Ship Motions and Wave-Induced Loads on High Speed Catamarans

by

Shinsuke MATSUBARA

M.E., The University of New South Wales (2005)
B.E.(Hons), The University of New South Wales (2000)

Submitted in fulfilment of the requirements for the degree of
Doctor of Philosophy

at

The University of Tasmania

The Australian Maritime College

The National Centre for
Maritime Engineering and Hydrodynamics

Supervisors:
Associate Professor Giles Thomas
Professor Michael Davis
Dr. Damien Holloway

June 2011

Blank page

Declaration of Originality

This thesis contains no material which has been accepted for a degree or diploma by the University or any other institution, except by way of background information and duly acknowledged in the thesis, and to the best of the my knowledge and belief no material previously published or written by another person except where due acknowledgement is made in the text of the thesis, nor does the thesis contain any material that infringes copyright.

Shinsuke MATSUBARA
May 28, 2011

Blank page

Statement of Authority of Access

This thesis is not to be made available for loan or copying for two years following the date this statement was signed. Following that time the thesis may be made available for loan and limited copying in accordance with the Copyright Act 1968.

Shinsuke MATSUBARA
May 28, 2011

Blank page

Abstract

Advancement in the design of large high-speed ferries demands comprehensive knowledge of ship motions and wave-induced loads to optimise their structural integrity. This investigation focused on the fluid structure-interaction problem experimentally to obtain such information.

Motions and loads were investigated by using two different high-speed catamaran models and a full scale ship. Firstly, a hydroelastic segmented model (HSM) of the INCAT 112 m class wavepiercer catamaran with centrebow was designed. It was tested in a towing tank for a range of head seas conditions to determine the motion responses, vertical bending moment (VBM) and slam loads. A second catamaran model was designed and tested in oblique seas in a model test basin (MTB) to examine the motions and asymmetric wave-induced loads. Thirdly, full scale measurements were performed during the delivery voyage of the INCAT 112 m Hull 064 from Hobart in Australia to Hakodate in Japan, to measure the motions and structural load responses.

The structural dynamic behaviour of the full scale vessel was replicated by the HSM model and the slamming and subsequent whipping behaviour were successfully modelled. As wave energy was consumed in the structural vibration of the model, the heave and pitch transfer function peaks reduced significantly when compared to the rigid configuration. The HSM test results also showed a strong non-linear motion response, with respect to wave height for this type of vessel, mainly due to the influence of the centrebow. The peak values for the VBM and slam loads were confirmed to be proportional to the square of the wave height for large waves. The MTB test model, which was not fitted with a centrebow, provided linear pitch, heave and roll motions for varying wave heights. The pitch connecting moment was found to be the dominant of the asymmetric wave loads and was linear with respect to wave height. During the full scale measurement programme, slamming phenomena were clearly recorded whilst crossing the Bass Strait. A reconstruction of the event, from the measured data, indicated that a slam event with subsequent whipping occurred with a bow down trim. Spectral analysis was used to detect the response frequencies of the VBM and machinery, with the frequency of the longitudinal mode increasing as the displacement reduced.

These experimental programmes, encompassing model and full scale measurements, have revealed valuable insights into the motion and structural dynamic behaviour of large high-speed catamarans. A comprehensive set of motion transfer functions, VBM and slam loads coefficients have been obtained, thus providing designers with important slam and wave load knowledge to aid the improved structural optimisation of these vessels.

Blank page

Acknowledgements

I would like to thank my supervisor Dr. Giles Thomas for his enormous support and understanding. His idea and insight to knowledge and cheerful positive thinking approach helped me to overcome the experimental and research difficulties and progress the project. His advice was so important for me to realise many aspects in a research and life.

I also would like to express deep sincere appreciations to Professor Michael Davis for his support and supervision in this project. His foreseeing idea and thoughts were essential and important in design and experiments. I have enjoyed learning how phenomena in reality can be interpreted into the engineering mathematics model with meaningful physical connections.

I would like to thank Dr. Damien Holloway for his advice and knowledge.

I am deeply grateful to towing tank staff: Towing Tank manager, Gregor Macfarlane, Dr. Jonathan Duffy, Tim Lilienthal, Kirk Meyer, Drew Honeychurch, Liam Honeychurch, and Richard Young. Their encouragement and generous support made me to achieve many experiments.

The model maker, Stuart Philips, made a beautiful model. I deeply appreciate for his challenge and dedication to construct such a complicated hydroelastic segmented model.

I would like to thank the project team students: Dr. Jason Lavroff, Walid Amin, Benjamin French, Jalal Shahraki, Stefan Winkler and Kim Chamberlin.

Post graduate researchers who kindly assisted experiments from the AMC basement: Roberto Ojeda, Bryce Pearce, Bruce Cartwright, Dr. Chin Bong, Dr. Vikram Garaniya, Hai Thanh Tran and Yohei Mozumi. With their generous support, many experiments were able to be conducted. I deeply appreciate for your kind support. Many special thanks should also go to Luciano Mason who always supports many researchers with his creative ideas and solutions.

I have received many supports from INCAT and Revolution Design: Robert Clifford, Kim Clifford, John Harris, Nick Wells, David Riseley, Mark Dewey, Tim Roberts, Gary Davidson and Gordon Stewart. Their kind encouragement kept me go through this project. I would like to express deep gratitude toward their kindness and support. Nick and John shared the spirit of INCAT with me. I will pursue their great positive spirit in my life.

I also would like to thank the INCAT hull 064 delivery voyage crews for a wonderful experience: Catp. Mike Jackson, Nick Wells, Leigh Tucker, Cameron I'Anson, Brendan StHill, Richard Roberts, Hiroaki Sato, Kouichi Nohara, Dick Calvert, Shigeru Miyata, Mikio Sato, Haruhito Moki, Toshiya Ito, Hidekazu Yamazaki, Nobuki Hiraga, Bob Chandler, Masashi Kikuchi, Naoyuki Saito, and Hidetoshi Tahara. With their supports, the valuable experimental data and log data were collected.

I also appreciate all the professors, lecturers and teachers, who I met and shared their wisdom and knowledge with me, for their passion and dedication toward education. I will carry and pass their spirit onto the next generations.

I would to express sincere appreciation to INCAT Tasmania, Revolution Design, the University of Tasmania and the Australian Maritime College, which form a collaborative research project team, for their support and findings. The project was also supported by the Federal Government through the Australian Research Council's industry linkage scheme.

I would like to sincerely thank my family and close friends for their kind support and encouragement. I would like to thank my wife, Mai for her great support and care.

Contents

List of Figures

List of Tables

Chapter 1

Introduction

1.1 Background

High speed catamarans have been developed over the last 40 years for a variety of commercial and military applications. The length of these vessels has increased with some recent new builds being over 100 m, with operational speeds above 35 knots. This increase in length and operational speed demands a greater understanding of their structural optimisation since they are operating in more severe wave conditions at higher speeds with the consequent increase in encounter frequency.

In order to optimise the structure, it is important to understand the wave load caused by hydrodynamic forces on the hull. These wave loads derive from both global wave-induced loads as well as impact slam-induced loads. Classification Societies develop the load cases to be utilised in the design process for ship, these load cases are usually the result of an experientially based program incorporating full-scale measurements and complimentary numerical predictions and physical model tests. For relatively novel craft, such as large high-speed catamarans, there is often a lack of full-scale data to enable appropriate load cases to be developed.

A key aim of this current work was to develop a methodology for determining the wave loads experienced by large high-speed catamarans, through experimental techniques. The INCAT type catamaran, with the centre bow and wave-piercer bow was used as the basis vessel for this investigation.

1.2 Problem Definitions and Scope

The present investigation consisted of three areas as follows:

- ship motion and wave loads on a hydroelastic segmented model in head seas;
- ship motion and wave-induced loads on a cross demihull loads model in oblique seas;
- full-scale measurements on the INCAT 112 m Hull 064 during its delivery voyage.

Each of these topics is now introduced.

1.2.1 Ship Motion and Wave Loads on a Hydroelastic Segmented Model

Generally, a high-speed catamaran has a thin bow with low reserve buoyancy which increases the chance of a bow nosedive and slamming in severe seas. In order to avoid the bow nosedive, the unique hull shape of the INCAT wave-piercer catamaran, whose details are explained in Section 1.4, was equipped with a centre bow. Although the catamaran with the centre bow can avoid the bow nose-dive effectively, it still inevitably experiences some slamming in large waves. The slam-induced loads on the centre bow influences the vertical bending moment of the demi-hulls, and these wave-induced loads are vital information for structural optimisation.

A wave-piercer catamaran with a centre bow is generally expected to behave with a non-linear response of ship motion with respect to wave height and speed. Hence, the experimental results, under a controlled environment, are essential to validate any numerical prediction program. Therefore, the results of this experimental programme can form the basis for design activities and numerical validation.

The measurement and prediction of the wave-induced and slam-induced loads can be conducted with or without the ship hydroelasticity of fluid-structure interaction. Past investigations, as presented in Section 1.3, show that the ship hydroelasticity problem has attracted the attentions of researchers in theoretical and numerical modelling. Previous investigations have reported many experimental results showing that the hydrodynamic wave force influences the structural response, often observed as an oscillatory motion of whipping in the time domain. However, a mutual interaction phenomena of fluid, dynamic motion and structure was rarely found in the reviewed experimental results. Hence, the hypothesis of ship hydroelasticity, as a mutually interaction between the fluid, motion dynamics and structural responses need to be demonstrated through experiments.

A primary objective of the current research was designing and utilising a catamaran hydroelastic segmented model, in order to measure the ship motion, wave-induced VBM on the demi-hulls and slam-induced loads on the centre bow. This would be done by simultaneously achieving ship hydroelasticity which simulates the slamming effect and subsequently occurring whipping phenomena.

The motion response of the wave-piercer catamaran in smaller waves and larger waves was also investigated for a range of speeds to ascertain the non-linearity of the motions and loads, both and slamming with respect to the wave height and speed. The effect of the ship hydroelasticity on motion and loads was investigated by comparing the motion response between the rigid model configuration and the elastic model configuration. The fluid-structure mutual interaction is difficult to determine from experimental data. The hypothesis of ship hydroelasticity is that fluid, fluid-induced dynamic motion and structure mutually interact, in theory. For experimental practice, in the past, many transient structural responses and transient motion responses were

presented individually, however evidence of the mutual interaction by the transient motion and structural response in the same time frame were not presented (to author's knowledge). The hypothetical system of the hydroelastic segmented model's behaviour is expected to be a complex interaction of the motions and loads. The ship motion is induced by the harmonic global wave excitation, simultaneously global wave-induced loads on the hull surface are generated. Large wave-induced ship motions cause the slam events, and the slam acts as the slam impact excitation force to the system. The slam impact excitation induces the subsequent whipping phenomena that causes the structure to vibrate at the resonant frequency of the VBM by the fundamental modal shape. Simultaneously, the motion of the ship is influenced by the whipping loads as the ship vibrates. This hypothetical behaviour of ship hydroelasticity is difficult to demonstrate from the experimental results and the analysis. (to author's knowledge)

Extensive calibration tests were conducted to ensure the load measurement system of the HSM was accurate. Modal tests in air and water were studied to measure the dry and wet modal resonant frequencies. Spectral and wavelet analysis were utilised for the measured loads to identify the response frequencies and modes.

The potential implication of the study is to form a basis which can validate the numerical solution of ship motion and wave loads prediction programs. The measured structure loads can be used for the structural optimisation to reduce the weight, hence it will lead to increase the speed of the catamaran vessels and to reduce the fuel consumption.

1.2.2 Cross Demihull Loads Model

The design evolution of the high-speed catamaran has led to an increase in the beam of the cross-bridge deck. This increases the bending moments on the cross-bridge deck. The transverse moments are the pitch connecting moment, split moment and pry moment. In the previous investigations, presented in Section 1.3, some studies have assessed the transverse vertical bending on the cross-bridge between the demi-hulls of the catamaran in beam seas. However, there have been no experiments conducted to measure the pitch connecting moment on the cross-bridge in oblique seas.

In order to measure the PCM, the novel design of the cross demihull loads (CDL) model was assessed in the model test basin for seakeeping tests in oblique seas. In addition to the PCM, the split and pry moments were also measured. Motion and load responses were investigated in relation to the wave height and speed.

The potential implication of this study is to form a basis which can validate the numerical solution of ship motions and wave loads prediction programs in oblique seas.

1.2.3 Full-Scale Measurement of INCAT 112 m During the Delivery Voyage

Full-scale measurements, during the delivery voyage from Australia to Japan in 2007, were conducted on the INCAT 112 m class, whose hull shape was used for the hydroelastic segmented model experiment. The vessel was equipped with strain gauges on the keel and steel column posts on the vehicle deck, accelerometers on the vehicle deck, and wave sensors. It provided an opportunity to record data over a long duration with variations in sea conditions and deadweight. The voyage log recorded the velocity speed, GPS locations, fuel quantity and sea conditions.

Spectral analyses were conducted on the accelerometer and strain gauges to determine the resonant frequencies. Frequency response analysis was conducted to investigate the wave response, VBM response and machinery response with the aid of the logged data. Dynamic attitude analysis on slamming event was investigated. The VBM resonant frequency variation during the delivery voyage from Australia to Japan was investigated. Second harmonic motions were observed in the model scale, therefore evidence of the second harmonic motion was investigated on the full-scale vessel.

The potential implication of this study would be to relate the full scale measurement to the experimental phenomena. The result of frequency response will be able to be used to advise the undesirable operational condition of the ship and machineries at seas.

1.3 Previous Investigations

Ongoing research and development has been conducted by industry and research institutions to extend the capability of high-speed catamarans. Generally, the high speed catamaran is built of aluminium, therefore structural design (Olkinuora et al. (1991)), welding method (Allday (1991)), fatigue problem analysis (Moan et al. (1991)) and repairing procedures have been extensively researched and developed. Vital information which is needed to progress the above development, is an understanding of the mechanism of wave-induced loads and the ability to efficiently predict them for design evaluation.

The starting point for ship hydroelasticity is the study of ship motion. Theoretical prediction of ship motion has been developed by strip theory with the two-dimensional oscillatory problem at the free surface in the frequency domain. Salvesen, Tuck, and Faltinsen (1970) outlined strip theory by considering the heave and pitch coupling and the sway, roll and yaw coupling. The original theory was proposed by Korvin-Kroukovsky and Jacobs (1957) and Korvin-Kroukovsky (1955, 1961). Many researchers have contributed to the development of strip theories for ship motion prediction in order to obtain the added-mass and damping coefficients (Gerritsma and Beukelman (1963), Smith (1967), Ogilvie and Tuck (1969), Smith and Salvesen (1970), Faltinsen (1971), and Faltinsen (1974)).

With respect to load of high speed vessel, Faltinsen and Zhao (1991) presented a simplified

method for the slender high Froude number ship. Wu, Hermundstad and Moan (1993) studied the hydroelastic analysis for the transfer function and modal response on a simplified hull form. Pedersen (2000) calculated the vertical bending moment at the longitudinal centre of gravity (LCG) of fast monohulls by employing Linear Strip Theory and Quadratic Strip Theory with a combination of Salvesen, Tuck, and Faltinsen's (STF) method (1970) and Gerritsma and Beukelman's method (1967). Kaplan and Dalzell (1993) presented wave-induced load predictions, including the effect of hull girder responses due to slamming. Hansen, Jensen and Pedersen (1995) extended the Quadratic Strip Theory to study long-term springing and whipping analyses, to predict the fatigue damage for the operational life time of the vessel.

The slender body theory has also been applied instead of strip theory. Vada (1995) extended the 3D radiation-diffraction program for ships with forward speed for hydroelastic responses to account for the deformation mode of motion, which is called SWAN. Results of SWAN for the rigid-body ship motion results were presented by Nakos and Sclavounos (1994) and Tønnessen, Vada and Nestegård (1993). However, the 3D slender body theory demands high computational consumption. As a solution, strip theory with a 2.5 time domain problem was utilised for the high forward velocity problem.

Holloway (1998) developed, for high-speed vessels, a 2d time domain approach high-Froude time-domain strip theory. Since it is a time domain method, it is possible to integrate with a slam prediction module component, which is an advantage of the time domain theory. In order to form an experimental basis for the slam numerical prediction module, two-dimensional drop tests of the centre bow hull shape were conducted by Whelan (2004). Davis et al. (2005a) analysed the ship motion response of a 86 m catamaran by the High-Froude time-domain Strip Theory. Davis (2004) and Davis et al. (2005) extended the theory to calculate the non-linear wave-induced loads. In addition, the validation of the High-Froude time-domain Strip Theory was conducted on 14 types of monohull and catamaran models in towing tanks by Davis and Holloway (2003). It is important to study the ship motion of catamarans prior to the load measurement test. Couser (1996) investigated the extensive resistance and seakeeping characteristic of a NPL round bilge series catamaran. He founds that the motion were linear with wave height provided that the motion were not too severe.

Hydroelastic models have been employed by many researchers, and the design and purpose of the different model types will be discussed in Chapter 2.1. Dessi et al.(2005) and Dessi, Mariani and Coppottelli (2007) used a monohull hydroelastic segmented model, and their analysis utilised the frequency domain decomposition in order to identify the modal parameters of the vibratorybehaviours. Heggelund et al. (2001) and Heggelund and Moan (2002) studied the global load analysis of a catamaran by the global FE model, with design loads calculated by the short-term stochastic calculations which accounted for the non-linear Froude Krylov and restoring force in regular waves.

Some researches have focused on the understanding of slamming. Slamming was first studied on the water landing of the seaplane floats by von Karman (1929). Wagner (1932) also devel-

oped two-dimensional theory for the water entry of a body which does not entrap air during impact.Yamamoto (1980) studied the fluid-structure interaction problem by incorporating the impact pressure due to slamming. Water impact pressure was measured experimentally on the flat plate by Okada (1995). Interestingly, their slam impact pressure wave pattern showed the Wagner type, which does not have a oscillatory response after impact. Miyamoto (1984, 1985) also demonstrated the Wagner type of slam impact pressure pattern by drop tests on low-deadrise angled wedges. Their results showed the Wagner-type impact near the adjacent point between the flat bottom surface and the round bilge. Their 45 degree wedge showed a slower rise of impact pressure spike when compared to the low-angle deadrise wedge. Yoshimoto (1997) and Takagi (1994) demonstrated a clear Bognold type of impact pressure wave with the air trapping.

Many researchers have investigated slamming on the model ship. Watanabe et al. (1988) tested a transparent bow model with high-speed video recording and the impact pressure measurement for the slam events in various speeds up to $F_n = 0.25$. Their results demonstrated that air trapped on impact could cause the maximum impact pressure to occur without the pressure sensor contacting the water. This visual observation can only be achieved with transparent models. Bow slamming of a large monohull was studied by Kvålsvold (1996).

For the high-speed vessel, Takemoto et al. (1993) conducted towing tank tests and full-scale measurement on a 40 m long monohull patrol vessel; the experimental model was equipped with a backbone beam to measure the vertical bending moment. Kapsenberg and Brizzolara (1999) and Sebastiani et al. (2001) investigated the hydroelastic effects of a high-speed monohull using model, which was equipped with a slamming panel load sensor at the top region of the bow flare. Their large angled bow flare showed the Wagner-type slam. They also conducted full-size measurement on the high-speed monohull vessel. McTaggart et al. (1997) conducted a hydroelastic test on a segmented model with backbone beams; they demonstrated a clear agreement between wave-induced load results and their 3D theory.

For monohull vessels, slamming can occur at the bow area and the flat bottom around the stern, and for catamarans the cross-deck structure between the two demi-hulls can be exposed to extreme loads due to a slam event. Kvålsvold and Faltinsen (1993) studied the local hydroelastic slamming on the wet deck of a catamaran. Studies of slamming on the cross-deck structure for catamarans were carried out by Grande and Xia (2002).

The wet deck slamming can cause a global structural response. The hydroelastic response of the vertical bending moment and vertical shear force of a catamaran was numerically simulated by Ge et al. (2002, 2005). Their experimental results of the slam event presented the response frequency with a harmonic series by spectral analysis. For the hydroelastic segmented model of the same catamaran, Wu et al.(1997) compared wave-induced loads in time history between the experimental and numerical results. They conducted the modal test in air, and successfully obtained the dry natural measured frequencies close to the calculated frequencies. Økland et al. (1998) also experimentally and numerically obtained the wet natural frequencies.

Transverse bending moments on the cross-bridge deck for catamarans and SWATHs in regular beam waves were studied by Kaplan (1991). However, there is little data available for the cross-demihull loads (CDL) between two demihull in oblique waves. This became a motivation for measuring CDL experimentally in this project, which is presented in Chapter 4 and 5.

In order to investigate slamming responses in full-scale, Thomas et al. (2003a) studied slam identification and occurrence on an 86 m wave-piercer catamaran. Thomas et al. (2001, 2003) incorporated the results of the slam response and FE analysis, including added mass calculated by the boundary element method developed by Doctors (1986, 1987) and further extend by Holloway (1998).

For the wave-induced loads by full-scale measurement, Sueoka et al. (1995) measured the structural loads on the fully submerged hydrofoil for a catamaran. Their results showed that the wave load on the foil was proportional to the wave height up to $H_w = 2.0\ m$.
There has been no previous experimental work conducted using a hydroelastic segmented model of a wave-piercer catamaran with a centre bow, to investigate ship motion and wave-induced loads. This generated the motivation to build the hydroelastic segmented model for measuring the response motion and wave-induced load of the VBM on the demihulls, and slam-induced forces on the centre bow. In particular, the centre bow force due to slamming impact with the forward velocity is a very unique problem, hence the novel design of the HSM experimental model was required.

1.4 Designs and Functions of INCAT 112 m Class

The INCAT 112 m class is a unique high-speed catamaran vessel, therefore, special mention of the hull features is necessary, as these strongly influence its ship hydrodynamics characteristics. The main features, which will be discussed here, are the wave-piercer bow, centre bow, centre bow arch, bow jaw demihull, transom stern, and cross-bridge deck, because the segmentation configuration needs to be designed with an understanding of the functions of these hull features.

1.4.1 Vessel Details

The INCAT 112 m class was, when it was launched, the world's largest catamaran vessel featuring both the wave piercer and centre bow. The INCAT 112 m Hull 064 was the first vessel in her class, and the principal particulars of the vessel are presented in Table 1.1. The vessel hull was the same as the hydroelastic segmented model used in the present study with only minor changes. The unique features of the vessel are detailed in Appnedix A.

The unique hull shape of the INCAT 112 m Hull 064 is presented in Figures 1.1 and 1.2. In order to maintain the continuous leading edge from the wave-piercer bow to the centre bow, a bow jaw is used, as shown in Figure 1.3. The centre bow starts forming the bow arch with the

Table 1.1: INCAT 112 m, principal particulars.

Design	
Builder :	INCAT Tasmania Pty Ldt.
Designer:	Revolution Design Pty Ltd.
Class Society:	Det Norske Veritas
Certification:	DNV +1A1 HSLC R1 Car Ferry "B" EO
Length overrall:	112.6 m
Length water line :	105.6 m
Beam of demihulls	5.80 m
Beam (moulded):	30.50 m
Draught:	3.74 m (from keel)
Speed:	40 $knots$
Capacites	
Gross tonnage:	10,841 $tonnes$
Deadweight:	Up to 1380 $tonnes$
Total Pax:	800 persons
Vehicle deck:	450 truck lane metres plus 193 cars or a total of 355 cars.
Pax	800 persons (including crews)
Vehicles	450 truck lane metres plus 193 cars or a total of 355 cars.
Axle loads	Tier 1 - 12 tonnes per axle. Tier 2 - up to 9 tonnes per axle.
Tankage:	
Fuel oil	900,000 $litres$
Fresh water	10,000 $litres$
Swage	5,000 $litres$
Lube oil	2 x 1,000 $litres$
ER Oily Water	4 x 150 $litres$
Genset Fuel Oil	2 x 1,238 $litres$
Machinery Installatins	
Main Engines:	4 x MAN 28/33D marine diesel engines, each rated at 9000 kW
Fuel consumption:	SFC of 190 g/kWh
Emissions:	< 10 g/kWh
Propulsion:	4 x Wartisla LJC 1500 waterjets configured for steering and reverse.
Trasnmission:	4 x ZF 60000 NR2H gearboxes
Ride Control:	Marine Dynamics' active ride control system.

demi-hulls, aft of the bow jaw, as shown in Figure 1.4. It is this area where the centre bow segment of the HSM is primarily exposed to the slamming loads, as described in Section 3.10.5. The wave-piercer bow, shown in Figures 1.5 and 1.6 is an extremely thin bow that can penetrate through the waves. The wave-piercer bow cutting through the water in high-speed operation is shown in Figure 1.6 during the delivery voyage. As can be seen in Figure 1.6, the wave-piercer bow does not have any reserve buoyancy to avoid a nosedive this lack of reserve buoyancy is compensated for by the centrebow.

A ride control system is equipped on the INCAT 112 m to reduce motions. A T-foil is installed behind the centre bow truncation bulkhead, and is shown in Figure 1.7. When the motion control is required, the T-foil will be deployed, and primarily acts as a motion damper to reduce the pitch and heave motion. Since the T-foil is situated at the centre-line of the vessel, it is not designed to reduce the rolling motion. For the roll motion, the trim tabs act as the roll motion damper, as well as the pitch and heave motion damper. Trim tabs are installed at an end of the demihull, below the water jets as shown in Figure 1.8. The demi-hulls are connected

using a cross-bridge deck, which is also called a slamming deck in some contexts. It provides an extremely large and wide area compared to a conventional monohull deck. Further details can be found in Appendix A for readers who are interested in a wave piercer catamaran with centrebow.

Figure 1.1: INCAT 112 m Hull 064

Figure 1.2: Frontal bow view of INCAT 112m Hull 064.

Figure 1.3: Side view of bow jaw connecting centrebow and wave-piercer bow.

Figure 1.4: Bottom view of centrebow arch.

Figure 1.5: Wave piercer frontal view.

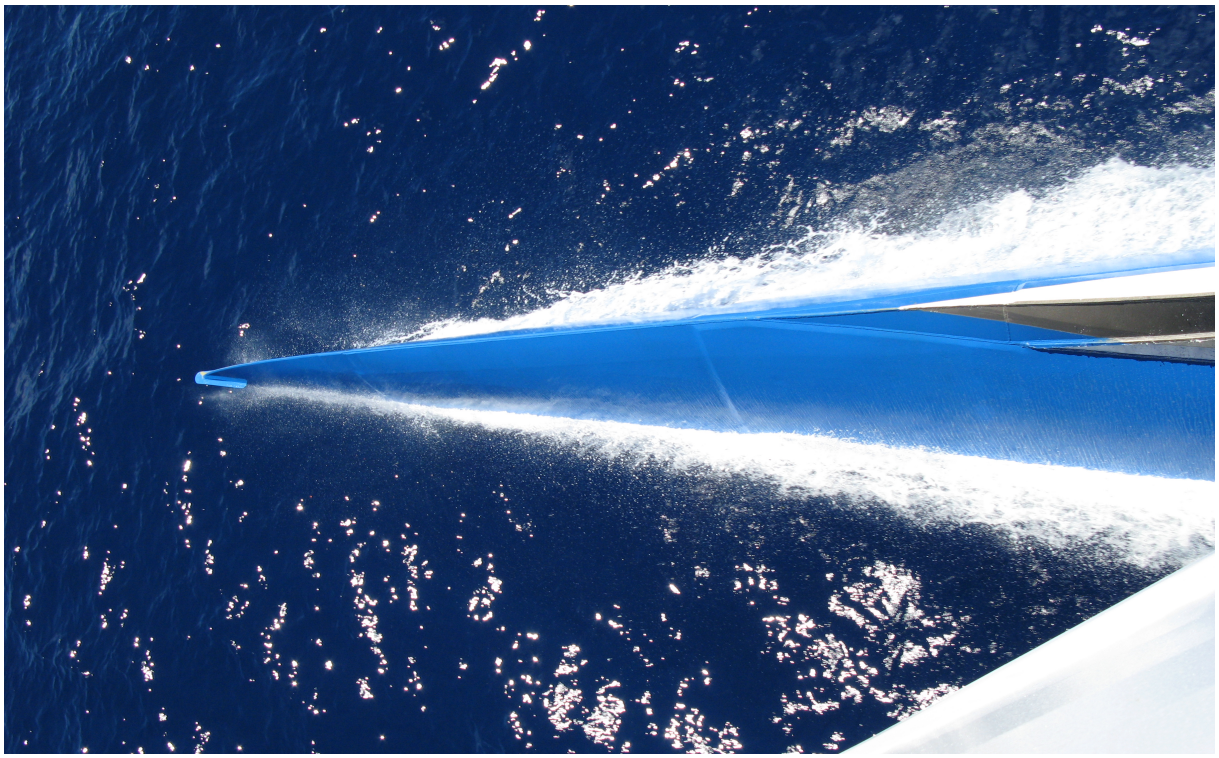

Figure 1.6: Plan view of wave piercer bow at speed.

Figure 1.7: Ride control system T-foil

Figure 1.8: Water jets

1.5 Outline of Thesis

This thesis consists of three major parts forming an extensive investigation into motions and wave-induced loads, as stated in Section 1.2. Past investigations utilising theoretical and experimental studies, with a focus on high speed catamaran, have been presented in Section 1.3
The first part of the thesis is the hydroelastic segmented model design and experiments. The design of the HSM is presented in Chapter 2.1: A review of the hydroelastic models is presented in Section 2.2. Since the present work focused on experimental works, the similitude and scaling for HSM experiments are explained in Section 2.3. The detailed design of the HSM is presented in Section 2.4.

The results of the HSM experiments are presented and discussed in Chapter 3. Prior to experimentation, many methods of calibration were conducted, as explained in Section 3.5 to ensure the load measurement capability. In Section 3.6, the modal tests in dry and wet conditions are presented; spectral and wavelet analysis were employed to identify the response frequencies. Interestingly, the calm water forward velocity induced a VBM, as explained in Section 3.7. Motion responses are presented in Section 3.9: the heave and pitch transfer functions were obtained and the hydroelastic effects on the ship motion are detailed in Section 3.10.5. Wave-induced load responses of the VBMs are presented in Section 3.10 and slam-induced loads in Section 3.10.4. The influential factors for the wave-induced loads are explain in Section 3.10.3. Analyses of the ship hydroelasticity demonstrated the mutual interaction between fluid-induced motion and structural response, as explained in Section 3.10.5. In Section 3.10.7, the slam resultant force position is discussed.

The second part of the thesis is the cross demihull loads experiments. The design of the CDL model is explained in Chapter 4; a novel design for measuring the pitch connecting moment was required, and is explained in Section 4.2.

The experimental results of the CDL experiment are presented in Chapter 5. Load cell calibration and ballasting were required, as explained in Section 5.4. Since motion sensors were used for the motion measurement, the Euler transformation was used for the acceleration data, as explained in Section 5.7. Motion and wave-induced loads response results are presented and discussed in Section 5.8.

The third part of the thesis is the full measurement on an INCAT 112 m class during its delivery voyage from Australia to Japan, as presented in Chapter 6. The onboard sensors and instrumentation are explained in Section 6.2. Analyses of the delivery voyage data is presented and discuss in Section 6.3. The transient slam history on the strain gauges and accelerometer data are presented, and the power spectral analyses were conducted to identify the frequency response for the VBM. The variation of VBM response from Australia to Japan due to the displacement variation of fuel consumption was obtained. A second harmonic motion was identified in the full scale and model scale, as explained in Section 6.3.5.

In Chapter 7, the conclusion to the work are outlined, including the implication of the research for vessel designers, classification societies, operators and researchers. Recommendation for future work are also presented.

1.6 Contribution to the Project by the Author

Unless acknowledged within the text, the author conducted all of the work described in this thesis. The work was undertaken by the author as part of an Australian Research Council Linkage project, 'Asymmetric and Nonlinear Unsteady Loads on High Speed Ferries', conducted in collaboration with Incat Tasmania Pty Ltd, Revolution Design Pty Ltd, the Australian Maritime College and the University of Tasmania.

Chapter 2

Development of the Hydroelastic Segmented Model

2.1 Introduction

A hydroelastic segmented model of the INCAT 112 m class catamaran was designed and constructed for this project to experimentally investigate ship hydroelasticity. The phenomena of ship hydroelasticity are interrelated effects that can be observed and measured in terms of ship motions, wave-induced loads and vibratory motions. Achieving such phenomena in an experimental environment depends on the appropriate selection from many possible designs. Therefore, the design of the model was an important and also rather complex process compared with that of conventional models for towing tank tests. The design of the hydroelastic segmented model, as shown in Figure 2.1, evolved through several iterations of the design spiral. The design involved many analytical decision-making processes based on satisfying scaling criteria, considering the technical feasibility within the experimental model and test facility, and referencing past examples of segmented models.

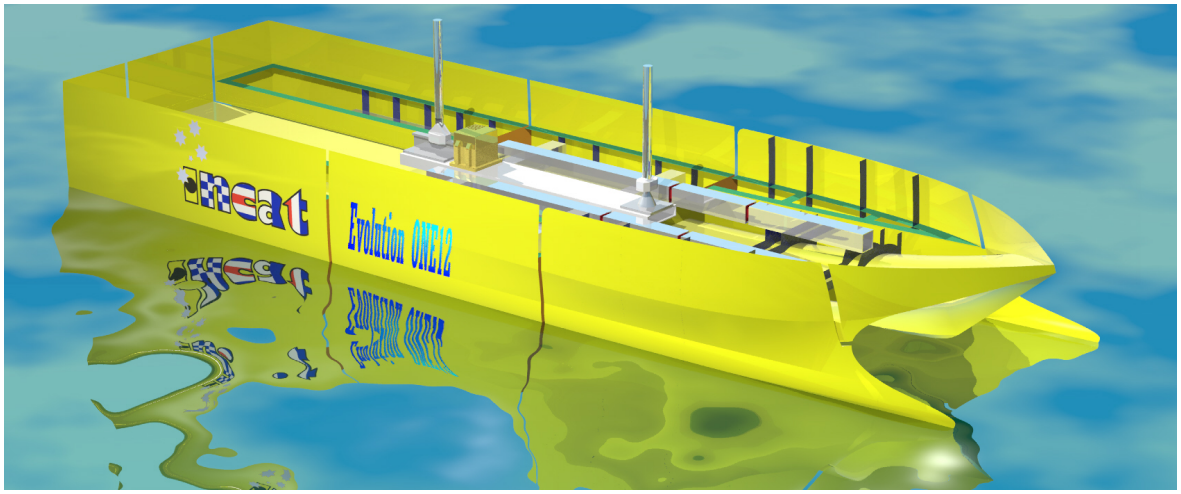

Figure 2.1: Rendered image for the INCAT 112 m class hydroelastic segmented model design

In this chapter, ship hydroelasticity is defined, then the objectives of the ship hydroelastic experiments are clearly set out to inform the conceptual derivation of the model and its design. In Section 2.2, the conceptual development of the hydroelastic segmented model is established by examining the different types of segmented models, and by reviewing some previous examples. These processes illustrate the functions, requirements and limitations of the final design. The scaling techniques are explained in Section 2.3, and the selection of the scaling methods was determined by the prioritisation of the design requirements and feasible limitations. The limitations arose not only from scaling aspects but also from the distinct features of the INCAT 112 m class. The unique features of the hydroelastic segmented model are explained in Section 2.4 with particular reference to the specific features of the INCAT 112 m class. The method of segmentation and construction process of the model are also explained in 2.4.

2.2 Concept of Hydroelastic Segmented Model

Defining the concept for the hydroelastic segmented model to satisfy the objectives of the experimentation is important in identifying the design criteria, informing the order of precedence over the design criteria for model construction, and in achieving successful ship hydroelasticity in the experiments.

2.2.1 Definition and Objective of Ship Hydroelasticity

A hydroelastic segmented model can be defined as a experimental ship model which can simultaneously experience and measure the interrelated phenomena consisting of ship motions, wave-induced loads and structural vibrations. Bishop and Price (1979), According to Bishop and Price expressed *Hydroelasticity* as simultaneous mutual interaction of the fluid flow and the structural elastic reaction. According to Faltinsen (2005), the hydrodynamic loading influences the structural elastic vibrations and the elastic vibration affects a fluid flow with a pressure field. Accordingly, ship hydroelasticity can be defined as mutually interacting effects between fluid and structural vibratory phenomena; wave loadings and/or ship motions causeing vibrations on the elastic hull, which in turn causes structural vibrations that affect fluid phenomena and/or ship motions simultaneously.

The hydroelasticity of a ship model can be achieved by many different types of hydroelastic modelling depending on the objectives of the design and its function. The objectives of these hydroelastic model tests were to measure ship motions and to gauge the structural loads which are caused by the integration of the hydrodynamic forces over the hull surface due to the wave and ship motion; hence to calculate the global wave-induced loads and slamming loads and to identify the modal response frequencies of whipping caused by the hydrodynamic forces. Determining the influence of the elasticity of the model structure on global ship motions was also one of the experimental objectives.

2.2.2 Categorisation of Ship Hydroelasticity

In order to satisfy the above objectives, the hydroelastic model was designed to measure structural loads and vibrational responses caused by ship motions and wave-induced loads. The structural loads and vibrational responses are influenced by the global stiffness distribution of the model. Therefore, the hydroelastic model had one function of representing the scaled model stiffness. A combination of the hull geometrical configuration and the elastic mechanism can achieve ship hydroelasticity. Such a configuration for hydroelastic model type can be selected from several different combinations of hull geometry type and elastic mechanism type. The hydroelastic model can simulate the dynamic response of fluid and structure interaction behaviour, such as a slam event with subsequent whipping behaviour, and also it can demonstrate the springing behaviour. Hence, the demonstration of ship hydroelasticity generally relies upon the selection of the elastic mechanism and the arrangement of segmentation for the experimental model.

In order to achieve one of the key objectives of measuring the wave-induced loads, three model types were considered as the design option: a hydroelastic continuous model; a rigid segmented model; and a hydroelastic segmented model. Each model type can be primarily characterised by a combination of two aspects: hull geometrical configuration type and flexural rigidity similitude.

A summary of the reviewed model types is presented in Figure 2.2. The first hull type is the continuous hull and the second is the segmented hull. The stiffness of the hull structures can be categorised into two model types: the rigid model and the hydroelastic model.

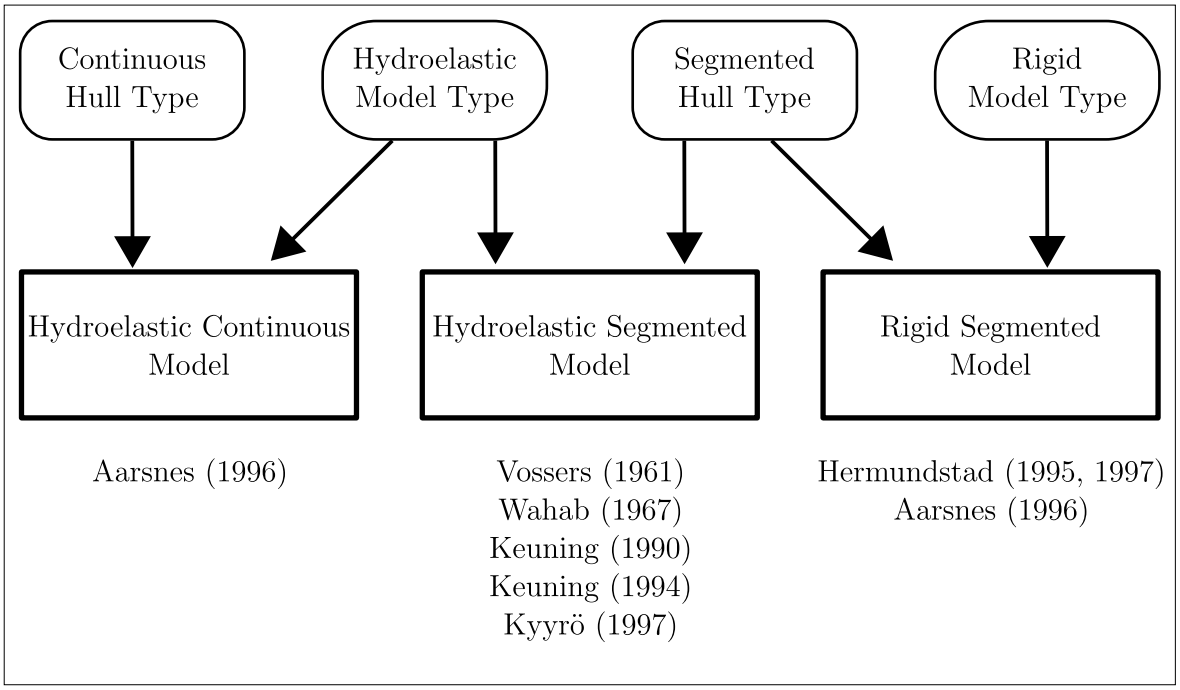

Figure 2.2: Classification of experimental models for ship hydroelasticity

By selecting a combination of the hull geometrical configuration type and the flexural rigidity similitude type, three main combinations are possible for experimental models that measure ship motions and/or wave-induced loads. Firstly, the combination of the hydroelastic model type and the continuous hull type forms the hydroelastic continuous model (HCM), whose details are explained in Subsection 2.2.3. Secondly, the combination of the rigid model type and the segmented hull type forms the rigid segmented model (RSM), which is detailed in Subsection 2.2.4. Thirdly, the combination of the hydroelastic model type and the segmented hull type forms the hydroelastic segmented model (HSM), which is explained in detail in Subsection 2.2.5. In addition, past experiments on ship hydroelasticity were reviewed in order to categorise the different types of models and hulls, and to identify onboard instrumentations and their functions.

2.2.3 Hydroelastic Continuous Model

The hydroelastic continuous model is a hybrid model of the hydroelastic model type and continuous hull type, as shown in Figure 2.2. The continuous hull integrates an elastic mechanism within its own hull shell structure which is constructed with an equivalent global stiffness and flexural rigidity and mass distribution of a full-scale ship.
The distinguishing feature of the hydroelastic continuous model is that the continuous single hull does not have any segmentation gaps, instead, the continuous single hull structure itself must display the equivalent structural vibratory responses, flexural rigidity to that of a full-scale ship. Having no segment gaps can be advantageous in that fluid flow is not disturbed.
The modal response frequency can be calculated in relation to flexural rigidity, global model stiffness and the governing equations of motion. These scaling and calculation requirements are similar for both the hydroelastic continuous model and the hydroelastic segmented model, and are detailed in Section 2.3.

In order to satisfy the required design, parameters are scaled from the full scale to the model scale vessel. Structural and modal analysis using the finite element method (FEM) analysis on the model structure is necessary for the model design prior to construction. The optimisation of the design, utilising the structural analysis, can provide the structural configuration and flexural rigidity which experiences the appropriate modal responses for ship hydroelasticity. However, at the construction stage, the model builder faces the difficulty of controlling the flexural rigidity of its hull structure, because with the FRP composites it is difficult to regulate the required accuracy of the cured composite material. Hence, it is difficult to achieve an accurate scaling in the structural characteristics on the hydroelastic continuous model. On the other hand, the concept of the hydroelastic segmented model simplifies the elastic mechanism to achieve the scaling of the structural frequency response and the flexural rigidity.

To measure the deformation of the flexible hull, strain gauges or optic fibres can be installed on the hull shell, generally attached on the inner face. The strain can be converted into structural loads using FEM analysis. Aarsnes (1996) tested a monohull model with the continuous hydroelastic model made of Divinycell foam and fibre glass/polyester resin, the thickness of these

materials was controlled to scale the required elasticity.

2.2.4 Rigid Segmented Model

A segmented model is divided into several linked segments. There are two model types that stem from the segmented model, depending on the purpose of experiments: the rigid segmented model (RSM) and the hydroelastic segmented model (HSM). Each rigid body segment of the RSM is embedded with a rigid bed (foundation) through load measurement mechanisms without elastic links. Consequently, the stiffness of the ship structure and its vibratory response, such as ship hydroelasticity, are not considered. On the contrary, the rigid body segments of a hydroelastic segmented model are linked with elastic link mechanisms, which are discussed in Subsection 2.2.5.

In order to avoid confusion betwen similar terminologies, the "rigid segmented model" refers to the assembled experimental segmented model with rigid body segments. The "rigid body segment" refers to each body part of the experimental model hull, after the hull was split by the segment cuts.

For both types, the segmented bodies are considered as rigid bodies, and assumed to be stiff enough to have no flexibility. A functional difference between the hydroelastic segmented model and rigid segmented model lies in the methods of measuring wave-induced loads, hence, the types of measured loads are slightly different as well. The hydroelastic segmented model is scaled on structural properties and vibrational responses from those of a full-scale ship, in conjunction with measuring the wave-induced load. On the other hand, the rigid segmented model focuses on the measurement of direct loads to each segment without the scaling of the structural properties.

The rigid segmented model is conceptually designed to transmit all the experienced loads on the hull to the load measurement system without losing them in structural deformation. Segments and components are not subjected to any deformation, so that collection of wave-induced loads are possible at load cell devices. Generally, the load cell devices link between a foundation and each rigid body segment. An adjacent segment is not directly connected; they are connected through the foundation. The foundation is firmly fixed to a towing tank carriage for the wave excitation force test or is attached on a oscillatory device for the radiation force test. Therefore, the rigid segmented model does not consider hydroelastic effects in the wave-induced load measurements.

Keuning (1990) used the rigid segmented model with a rigid girder. The model was divided into seven segments. Each segment was connected to a corresponding load cell, and the load cell was attached to the girder. Kyyrö and Holopainen (1997) also used the rigid segmented model with eight segments for a catamaran ship. The segmentation was uniquely made only on the port side demi-hull, and was assembled by the eight segments connected to a rigid crossbar aluminium backbone via three component forces/moment transducers. In the cases of Keuning

(1990) and Kyyrö and Holopainen (1997), the load cells were connected to the rigid foundation beam. Generally, load cells measured the vertical bending moments and vertical shear forces.

In another way to experimentally determine the structural loads caused by wave-induced loads, the vertical bending moment is measured by a load cell or force balance at the midship of a rigid segmented model. Since the maximum vertical bending moment can be expected to occur at the midship, the load cell/force balance is installed at the segmentation gap at the midship. Vossers and Riken (1961) used a strain gauge dynamometer installed at the midship of a rigid segmented model for the series 60 to measure the vertical bending moments. Wahab (1967) extended the work of Vossers and Riken by utilising a more complicated load measurement system. A comprehensive force balance was installed, which allowed the measurement of the vertical and horizontal bending moments, the shear forces and the torsional bending moment.

In the towing tank test, the rigid segmented model with oscillatory devices is conducted in order to obtain wave-induced loads due to the radiation wave force. The rigid segmented model, that is fixed to the towing tank carriage with no vertical motion and is then subjected to incident waves, produces the wave-induced loads due to wave exciting forces. The wave exciting force consists of the diffraction wave force and the Froude-Kriloff force. Speaking in the same manner for the hydroelastic segmented model, the wave-induced loads in a seakeeping test is composed of the wave exciting force and the radiation wave force. An example of a radiation force test on a rigid segmented model was presented by Keuning (1994), utilising two types of the scotch-yoke type, which demonstrated pure sinusoidal vertical motions. Sectional added mass and sectional damping for this project.

One advantage of using a rigid segmented model is that the wave-induced loads can be measured in a manner similar to strip theory. This allows the validation of strip theory in terms of the radiation force and wave exciting forces acting on each segment, which is similar to stripped segments. Since each segment is connected to a fixed foundation, the load cell calibration is simplified. Another advantage is that the number of segments can be large and feasible with the rigid segmented model compared with the hydroelastic segmented model. For radiation and wave excitation tests, the rigid segmented model does not require strict mass distribution in each segment in order to control the structural response frequency that is scaled from the the full-size ship. Therefore, an experimental model can be made of many segments, which results in more data points available for the structural loads calculation. The main disadvantage is that the rigid foundation is too heavy for high-speed vessels for seakeeping tests in smaller sized towing tanks. Thus, it was not suitable for the seakeeping test of high-speed vessels.

2.2.5 Hydroelastic Segmented Model

The hydroelastic segmented model, as shown in Figure 2.2, is conceptually a hybrid model of the hydroelastic model type and the segmented hull type. It is designed to easily achieve ship hydroelasticity and to measure ship motions, wave-induced loads and structural vibratory re-

sponses. For these purposes, the hydroelastic segmented model mainly consists of rigid segments and elastic mechanisms.

A hydroelastic segmented model is segmented into several rigid body segments whose features contribute to both the load measurement and the structural dynamic response. For the load measurement, the rigid body segments are ideally designed to capture all the hydrodynamic forces exerted onto the hull surfaces. The hull structures of the rigid body segments transmit the loads from the hull surface to the connected elastic links, therefore the rigid hull shells and rigid internal structures should not be deformed. The deformation for ship hydroelasticity should occur at the elastic links and the rigid segments are considered as solid bodies for the equations of motion.

Material selection of the rigid body segments is important to satisfy the maximum rigidity and light weight of the segments. A carbon fibre sandwich composite construction with a PVC core material is ideal for acquiring the maximum rigidity. The carbon fibre sandwich composite construction provides a stronger and more rigid structure for segmentation models than glass fibre sandwich composite or timber constructions. In addition to the advantage of the structural strength, the weight of the carbon fibre model is significantly lighter than glass fibre or timber models. A lighter model contributes to securing more freedom of ballasting, which is important to scale ship particulars.

An elastic mechanism is equipped with a load measurement system, which measures strain due to the vertical bending moments at the segmentation gaps with a structural dynamic response. A segmentation gap is defined here as a gap between two adjacent rigid body segments. The elastic mechanism can be selected from an elastic link with a strain gauge system, an elastic link with a load cell device system and a continuous elastic-backbone beam system. Each system has a different approach for simulating the elasticity of ship hydroelasticity.

The elastic link mechanism has two major functions. Firstly, the mechanism represents the elasticity of a ship, and secondly it measures structural loads due to wave-induced loads. The resultant loads of hydrodynamic forces integrated over the hull surface of the rigid segments, deflects the elastic links. The elastic link is associated with the two scaling properties of flexural rigidity and structural modal response frequency. It is necessary to scale the modal response frequency of the model from full-size with an appropriate selection of mass distribution and flexural rigidity. The desired flexural rigidity determines the stiffness of the elastic links. The stiffness and mass distribution affects the structural modal response frequencies. These details are discussed in Section 2.3.

The elastic link with a strain gauge system measures the strains at the segmentation gaps. The strain gauges are attached on the upper and bottom surface of the elastic link. The strain is caused by the vertical bending moment which resulted from the hydrodynamic forces on the rigid segmented hull surfaces. The strain of the elastic links is calibrated to measure the vertical bending moments at each segmentation gap.

In the measurement of wave-induced loads on the hydroelastic segmented model, controlling the structural response frequency is advantageous over the method used with the rigid segmented model introduced in Section 2.2.4. The hydroelastic segmented model can measure the wave-induced loads with the effects of the structural dynamic response, on the other hand, the rigid segmented model measures the wave-induced loads without the effects of the structural dynamic response.

An alternate solution to using the elastic links with a strain gauge system, is an elastic link with a load cell device. The load cell device connects between a facing wall of the rigid body segment and the end of an elastic link, where the other end of the elastic link is firmly attached to the wall of the adjacent rigid segment. This method was utilised by Hermundstad (1995), Hermundstad and Moan (1997)and Aarsnes (1996).

An advantage of utilising load cells is that the load measurements on six degrees of freedom about the three axes in the Cartesian coordinates system can be easily achieved, however, it can increase the model weight and the number of channels required for the measured data. A total number of channels for recording data would be significantly increased, thus, the consumption of the data acquisition system would be very expensive as well. From the aspect of mass distribution, many load cells and cables can be demanding on a smaller sized model. This would be determined by the feasibility of the model size, which also depends on the towing tank capacity. The elastic links with strain gauges can be easily manufactured in-house, in case any elastic links are damaged accidentally. Therefore, the elastic link mechanism would be a preferable solution for a hydroelastic experimental model of high-speed vessels, but this should be determined with many other aspects in the actual design process, in conjunction with the theory and scaling analysis.

As a different approach from the above two elastic link mechanisms, the continuous elastic-backbone beam system uses long beams or hollowed section bars for which the flexural rigidity is scaled down from the full-scale ship. The beams can be either a bar, a I-section beam, a hollowed section, or a combination made of steel or aluminium. The continuous backbone functions as the elastic properties for the experimental model.

Aarsnes (1996) used the backbone model with a continuous elastic-backbone beam system with a constant cross-sectional area. The elastic beam was connected to the rigid segments. For the load measurements of the backbone model, the backbone beam can be connected to the hull through the load cells, or strain gauges can be attached onto the backbone beam itself. By sophisticating the concept of the continuous elastic-backbone beam system, Dessi (2003) used a continuous backbone configuration with a variable transverse cross-section in a model of a high-speed monohull. This had the advantage of allowing the demonstration of a variation of the flexural rigidity along the longitudinal direction of the full-scaled ship. However, it requires many rigid segments, which can increase the difficulty of water tightness of the seams between the segments, or in an increase in weight due to more watertight bulkheads being required be-

tween each segment. Models for high-speed vessels have a limited displacement and it would be difficult to obtain the required modal shape and response frequency. It could result in many response frequencies, so that identifying the modal shape and response frequencies becomes difficult. Therefore, the elastic link with a strain gauge system and reduced number of rigid body segments is more suitable for the hydroelastic segmented model of a high-speed catamaran vessel.

In summary, a hydroelastic model is principally designed to measure the wave-induced loads and structural vibratory responses. The hydroelastic segmented model evolved from a consideration of the hydroelastic model type and the segmented hull geometry type.

For this project, the hydroelastic segmented model with elastic links with a strain gauge system was selected, based on the following advantages:

- a lighter sensor system and displacement;
- reducing the number of channels required for the data acquisition system;
- increasing the feasibility of controlling the structural modal responses and frequencies;
- securing water tightness of the segmentation gaps.

The hydroelastic segmented model consisted of three segment bodies for each demi-hull and one segment of centre bow, and was composed of carbon fibre composite rigid body segments and aluminium elastic links with strain gauges on the top and bottom surfaces. The design details of the hydroelastic segmented model for the INCAT 112 m are explained in Section 2.4.

2.3 Theory and Scaling for Hydroelastic Segmented Model

An appropriate selection of scaling analysis, based on similarity laws, is significant for any laboratory experiment to obtain the valid data that can be confidently applied to the full scale or used to validate numerical simulation models. The similarity laws for the design of the hydroelastic segmented model consist of the geometrical similarity, Froude similarity, dynamic similarity, flexural rigidity similarity, and the structural dynamic response similarity. However, it is a very challenging task to fulfil all of the scaling requirements, particularly due to small model size and the physical and technical constraints of the facilities. Thus, some conflicts among the similarity laws are expected when satisfying the scaling requirements. Therefore, taking into account the appropriate similarity laws for modelling ship hydroelasticity will likely result in a compromise based on prioritising the scaling requirements.

The set of required similarity laws and equations for designing the hydroelastic segmented model is shown in this section. Useful summarised fundamentals and experimental approaches of the similitude for the hydroelastic model were provided by Hermundstad (1995, 1995a), Aarsnes (1996), Maeda (1991), and the International Towing Tank Committee recommendation (1999).

The required scaling methods are briefly explained here, and their details and contributions to ship hydroelasticity are detailed in the following subsections. The geometrical similarity, defined in Subsection 2.3.1, determines the scale ratio of the full scale to experimental model scale. Once the scale ratio is defined, the Froude number provides the model speed for the experiments. Froude similarity is used for wave-making effects, as presented in Subsection 2.3.2. The governing parameters for dynamic similarity of ship motion is detailed in Subsection 2.3.3. The above similarity laws and parameters can be commonly seen in conventional ship motion experiments. However, the following similarity laws characterise the scaling for the special design of the hydroelastic segmented model. Specifically, the flexural rigidity similarity and structural dynamic response similarity are introduced in Subsections 2.3.4 and Subsection 2.3.5 respectively. Some similarity laws and parameters are constrained by the solution of the equations of motion presented in Subsection 2.3.6: three rigid segment system of a multi-body dynamics system. It determines the design values of the required dimensions and stiffness of the elastic link, and the modal response frequency of the hydroelastic segmented model. More details of the constraint are discussed in Subsection 2.3.6

2.3.1 Geometrical Similarity and Model Dimension Scale Ratio

Barenbaltt (1996) provides a definition of geometrical similarity, stating that the concept of physical similarity is a natural generalisation of the concept of similarity in geometry. Geometrical similarity is maintained by the geometrical scale ratio λ, between the full-size ship and model. The geometrical ratio is constant in all dimensions, hence the model possesses the same shape as the full scale. The geometrical scale ratio is an important factor, because it must be utilised in calculations for other similarity laws and scaling. Lloyd (1989) summarised model scaling laws for experiments, the geometrical scale ratio of the ship to the model defined as:

$$\lambda = \frac{L_s}{L_m} \tag{2.1}$$

where the subscript s is for the full scale ship, and m is for the experimental model. Therefore, the displacement of the scaled model with a fluid density correction, can be obtained as follows:

$$\Delta_m = \frac{1}{\lambda^3}\Delta_s \frac{\rho_m}{\rho_s} \tag{2.2}$$

where ρ is the density of the fluid and Δ is the displacement. Equation 2.2 can be rewritten in terms of the volume displacement as follows,

$$\nabla_m = \frac{1}{\lambda^3}\nabla_s \tag{2.3}$$

where ∇ stands for the volume displacement of the full-size ship or ship model depending on its subscript. Equation 2.1 is used for calculating the geometrical scale ratio from which the volume displacement of the experimental model is determined by Equation 2.3.

2.3.2 Froude Similarity and Scaling

Froude similarity and scaling between the full scale and the model scale ship governs the most important dynamic-similarity of fluid flow with respect to wave making effects. The wave making effects of a ship result from ship and fluid motions that are principally controlled by the gravitational forces. Froude similarity is a dynamic similarity for the wave-making effects:

$$F_n = \frac{V_s}{\sqrt{L_s g_s}} = \frac{V_m}{\sqrt{L_m g_m}} \tag{2.4}$$

The Froude scaling in the experiments binds the similarity to the forces associated with the inertia and gravity. Therefore, the Froude scaling on both experimental results and full-size data should be applied to the forces that arise from the gravitational and wave-making effects by considering the phenomena and its scaling component.

2.3.3 Dynamic Similarity

It is important to scale ship particulars for a dynamic similarity of ship motion, in particular, the mass distribution of the ship should satisfy the geometrical similarity. The mass distribution is represented by the location of the centre of gravity, and the mass moment of inertia.

Knowing the mass of the model, the mass moment of inertia is often expressed in terms of the radius of gyration. The location of the centre of gravity (CG) and the radius of gyration are geometrically scaled in the model-scale environment in order to achieve dynamic similarity with the full-scale ship. The radius of gyration (RoG), k_{RoG}, is obtained from the mass moment of inertia and mass as follows:

$$k_{RoG} = \sqrt{\frac{I}{M}} \tag{2.5}$$

The range of the pitch radius of gyration, k_5, for experimental models was recommended by Lloyd (1989) as follows:

$$0.2 \cdot LWL < k_5 < 0.25 \cdot LWL \tag{2.6}$$

where LWL is the length of the wetted waterline. The longitudinal centre of gravity (LCG) and the RoG are experimentally measured in the model scale. The LCG and RoG are adjusted to gain the appropriate values by weight distributions prior to experimentation. In order to achieve successful scaling of the LCG and RoG, it is important to provide a sufficient allowance of ballast weight distribution out of the total displacement.

2.3.4 Flexural Rigidity Similitude

Flexural rigidity is an important parameter for the structural and vibratory response in characterising hydroelasticity. The structural vibration and load response are dynamic phenomena induced by encountered waves in ship motions. It is necessary to model the flexural rigidity and structural dynamics similitude as correctly as technically possible. Flexural rigidity similitude, structural dynamics similitude and equations of motion for the mechanical dynamic system are

interdependent.

Flexural rigidity of the hydroelastic segmented model is achieved by the elastic link. Based on the concept of the hydroelastic segmented model outlined in Section 2.2, the flexural rigidity of the elastic links should be significantly smaller than the flexural rigidity of the rigid body segments, in order to achieve a clear structural response. Without a distinct difference in the flexural rigidities between the rigid segment of the hull and the elastic link, the hydroelastic segmented model cannot acquire appropriate structural dynamics. If the flexural rigidity is similar on both the rigid hull and the elastic link, deformations will occur on the rigid segments as well. This should be avoided for the hydroelastic segmented model, therefore regulating the flexural rigidity of elastic links is essential. The flexural rigidity required for the structural load scaling can be modelled in bending stiffness and shear stiffness scaling. The ITTC (1999) recommendation presents the following scalings:
Bending stiffness scaling is calculated as:

$$[EI]_m = \frac{1}{\lambda^5}[EI]_s \tag{2.7}$$

where I is the transverse cross- sectional second area moment and E is Young's modulus of the material. Shear stiffness scaling is:

$$[AG]_m = \frac{1}{\lambda^3}[AG]_s \tag{2.8}$$

where A is the cross-sectional area and G is the shear modulus of its material.

2.3.5 Structural Dynamics Response Similarity

A structural dynamic response similitude is modelled as a frequency response of the hull structure. The frequency response of a hydroelastic segmented model can be scaled by the following equation:

$$f_m = \sqrt{\frac{L_s}{L_m}} f_s = \sqrt{\lambda} f_s \tag{2.9}$$

where f is the response frequency. The response frequency can be a natural frequency of the model for the similitude of the structural dynamic response.

The natural frequency of the model can be considered in three situations. The first situation is the dry modal response frequency in air; the second situation is the wet modal response frequency without forward speed in the water; the third situation is the wet modal response frequency with forward speed in the water. Aarsnes (1996) successfully demonstrated the dry mode and wet mode tests, finding a distinct difference in the natural frequencies between the dry and wet modes. A difference in the natural frequencies would be expected and is caused by an influence of the added-mass of the water reducing the natural frequency. When the forward velocity of the model affects the added mass, then its natural frequency will also vary from the wet mode without forward velocity.

The target natural frequency of the model can be scaled using Equation 2.9. The natural frequency can be experimentally measured to satisfy the target natural frequency. The experimentally measured natural frequency of the hydroelastic segmented model can be adjusted by controlling mass distribution, bending stiffness (flexural rigidly) and the stiffness coefficient of the elastic link. The stiffness coefficient of the elastic link is calculated by the following equation,

$$k_{bar} = \frac{EI}{l_{bar}} \tag{2.10}$$

where l_{bar} is the length of the effective elastic part of the elastic link.

A prediction of the natural frequency can be obtained from a multi-body dynamics system with three rigid bodies and two elastic links. The system involves bending stiffness and the stiffness coefficient of the elastic link and mass distribution in the governing equations of motion. The multi-body dynamics system is explained in Subsection 2.3.6.

2.3.6 Multi-Body Dynamics System for Three Rigid Segments and Elastic Links

The multi-body dynamics system for three rigid segments with elastic links was developed to predict the natural frequency of the hydroelastic segmented model. The system was extended from the triple-beam system initially developed by Davis (2005). The multi-body dynamic system combines the governing equations of motion for three rigid bodies with the stiffness coefficient of the elastic links. Three equations of linear motion and three equations of angular motion were initially established, however, the constraints reduced the system to three linear equations with three degrees of freedom. Hence, a 3 x 3 matrix was formed, and then the determinate of the matrix was used to find the natural frequency.

The equations of motion for the multi-body dynamics system were modified from the triple-beam system in some areas, so that the system allowed the input of a variable local centre of gravity for each rigid body segment in the longitudinal direction with respect to a coordinate system of the corresponding rigid body segment. The free body diagram and coordinate systems of the mechanical dynamics system are defined in Figure 2.3. The forward segment, mid segment, and aft segment are considered to be rigid bodies. Each segment is jointed by an elastic link. The stiffness coefficient is defined by the dimension of the elastic link, whose calculation is given in 2.10.

The subscript i indicates an ith body segments, and the subscript j represents the coordinate axis. The numberings of the subscripts are as follows:

$i = 1:$ Longitudinal coordinate axis
$i = 2:$ Transverse coordinate axis
$i = 3:$ Vertical coordinate axis
$j = 1:$ Mid Segment
$j = 2:$ Forward Segment

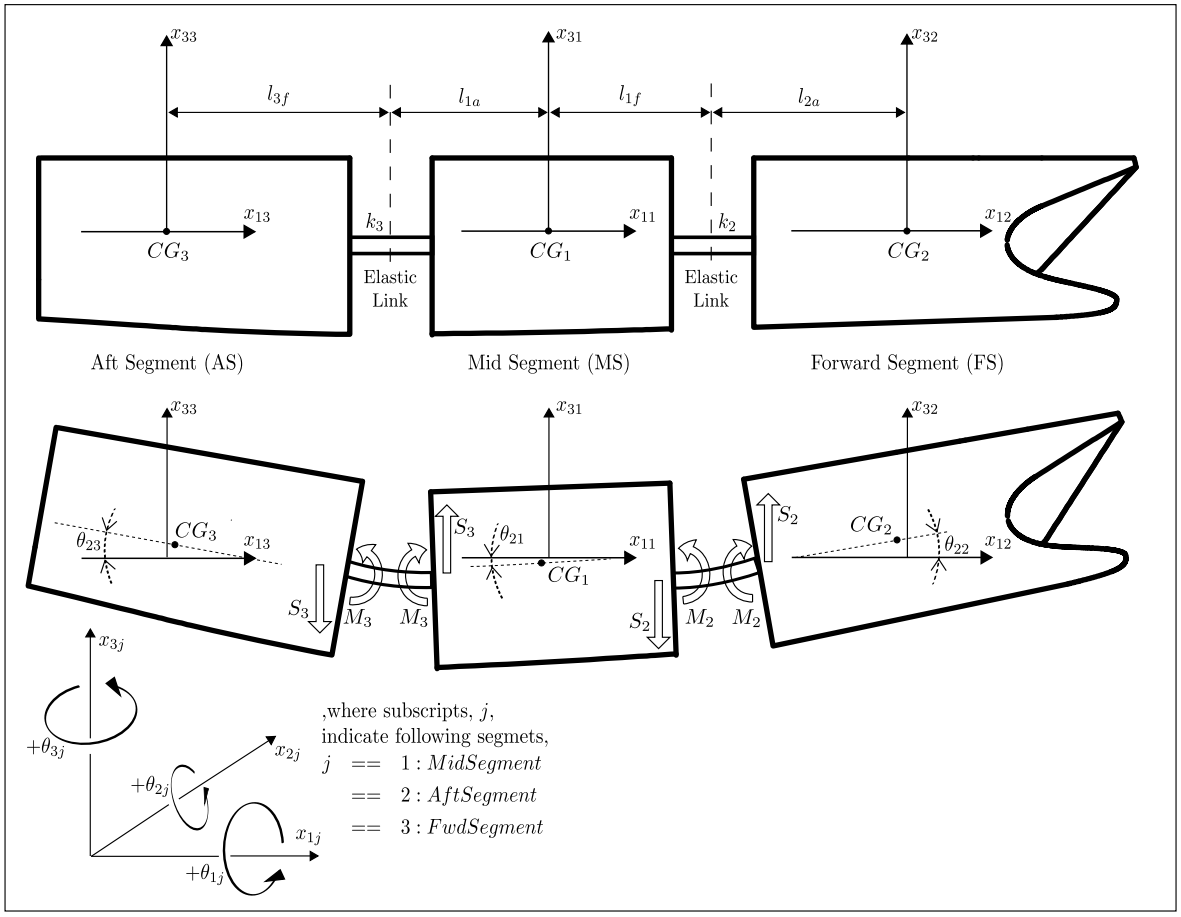

Figure 2.3: Free bodies diagram and coordinates system definition for the mechanical dynamics system

$j = 3:$ Aft Segment

The notations involved in the equations of the mechanical dynamics systems are defined as follows:

θ_{ij} ==: Angular displacement of ith segment about the coordinate axis, j

x_{ij} ==: Linear displacement of ith segment about the coordinate axis, j

m_i ==: Mass of ith segment

S_i ==: Shear force at the elastic link between ith segment and mid segment

M_i ==: Bending moment at the elastic link between ith segment and mid segment

k_i ==: Stiffness coefficient of the elastic link between ith segment and mid segment

r_{gi} ==: Radius of gyration of ith segment and mid segment

Each segment has its own local linear coordinate, and its centre of gravity moves with respect to the coordinates. The angular motion of each segment was considered about the transverse axis which passes through its own centre of gravity. The vertical shear force and longitudinal vertical bending moment are considered at the segmentation gaps.

Three segments were physically connected by the elastic links, therefore the centre of gravity of each segments on its corresponding coordinate system can be constrained. The geometrical

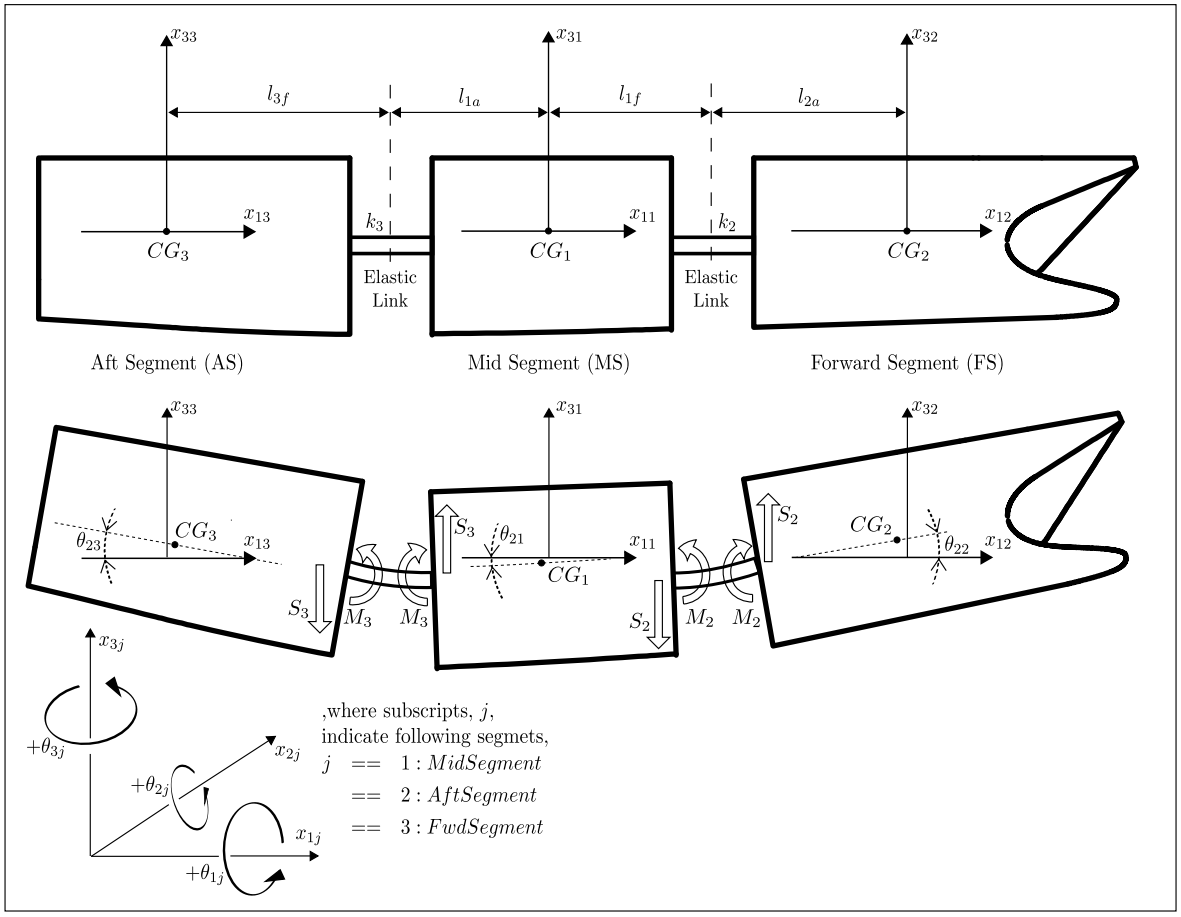

Figure 2.3: Free bodies diagram and coordinates system definition for the mechanical dynamics system

$j = 3:$ Aft Segment

The notations involved in the equations of the mechanical dynamics systems are defined as follows:

θ_{ij} ==: Angular displacement of ith segment about the coordinate axis, j

x_{ij} ==: Linear displacement of ith segment about the coordinate axis, j

m_i ==: Mass of ith segment

S_i ==: Shear force at the elastic link between ith segment and mid segment

M_i ==: Bending moment at the elastic link between ith segment and mid segment

k_i ==: Sti ness coe cient of the elastic link between ith segment and mid segment

r_{gi} ==: Radius of gyration of ith segment and mid segment

Each segment has its own local linear coordinate, and its centre of gravity moves with respect to the coordinates. The angular motion of each segment was considered about the transverse axis which passes through its own centre of gravity. The vertical shear force and longitudinal vertical bending moment are considered at the segmentation gaps.

Three segments were physically connected by the elastic links, therefore the centre of gravity of each segments on its corresponding coordinate system can be constrained. The geometrical

constraints of the centre of gravity are follows:

$$x_{32} = x_{31} - l_{1f}\theta_{21} - \ l_{2a}\theta_{22} \tag{2.11}$$

$$x_{33} = x_{31} + l_{1a}\theta_{21} + \ l_{3f}\theta_{23} \tag{2.12}$$

The equations of linear motion of each segment about the corresponding vertical ordinates are: For the forward segment:

$$S_2 = m_2\ddot{x}_{32} = m_2\left(\ddot{x}_{31} - l_{1f}\ddot{\theta}_{21} - l_{2a}\ddot{\theta}_{22}\right) \tag{2.13}$$

For the mid segment:

$$S_3 - S_2 = m_1\ddot{x}_{31} \tag{2.14}$$

For the aft segment:

$$-S_3 = m_3\ddot{x}_{33} = m_3\left(\ddot{x}_{31} + l_{1a}\ddot{\theta}_{21} + l_{3f}\ddot{\theta}_{23}\right) \tag{2.15}$$

The equations of angular motion of each segment about the corresponding transverse axis are: For the forward segment:

$$S_2 l_{2a} + M_2 = m_2 r_{g2}^2\ddot{\theta}_{22} \tag{2.16}$$

For the mid segment:

$$S_3 l_{1a} + S_2 l_{1f} - M_2 + M_3 = m_1 r_{g1}^2\ddot{\theta}_{21} \tag{2.17}$$

For the aft segment:

$$S_3 l_{3f} - M_3 = m_3 r_{g3}^2\ddot{\theta}_{23} \tag{2.18}$$

The vertical bending moments generated at the elastic links are:

$$M_2 = k_2\left(\theta_{21} - \theta_{22}\right) \tag{2.19}$$

$$M_3 = k_3\left(\theta_{23} - \theta_{21}\right), \tag{2.20}$$

where the stiffness coefficients of the elastic links, k_2 and k_3 can be obtained from Equation 2.10.

Derivation of Equations 2.11 to 2.20 are required to obtain the linear equations with respect to the angular displacements. This was carried out by eliminating the linear displacement, shear forces and moments from the equations of the multi-body dynamics system. For the normal mode of oscillation, each hull segment should be subjected to harmonic motion of the same frequency. Each hull segment also simultaneously passes through the equilibrium points. Therefore, such harmonic motions can be expressed as:

$$\theta_{2j} = \bar{\theta}_{2j}e^{\mathrm{j}(\omega t+\psi)}, \tag{2.21}$$

where ω is the angular frequency in radians per second, $\bar{\theta}_{2j}$ is the amplitude of the angular displacement, and j indicates the complex number in the temporal domain. From Equation 2.21, the following relationship can be obtained:

$$\ddot{\theta}_{2j} = -\omega^2 \theta_{2j} \tag{2.22}$$

Equation 2.22 eliminates the angular acceleration term in the system equations to reduce the number of variables. After the derivation, the matrix formed by the three linear equation can be obtained as in Equation 2.23.

After the matrix for the linear equation of the multi-body dynamics system was formed, the determinant of the matrix of Equation 2.23 can be determined for the natural frequency of the system. For convenience of notation, Equation 2.23 is simplifed to the following;

$$\begin{bmatrix} A & B & C \\ D & E & F \\ G & H & I \end{bmatrix} \begin{bmatrix} \theta_{21} \\ \theta_{22} \\ \theta_{23} \end{bmatrix} = 0 \tag{2.24}$$

The determinant for the above simplified matrix is;

$$|A\,(EI - FH) - B\,(DI - FG) + C\,(DH - EG)| = 0 \tag{2.25}$$

$$det\,(f) = A\,(EI - FH) - B\,(DI - FG) + C\,(DH - EG)\,, \tag{2.26}$$

where $f = \frac{\omega}{2\pi}$. Equation 2.26 can be treated as a function with respect to the vibrational frequency,f as the characteristic equation of the system. When the function intersects with the x-axis, the determinant is equivalent to zero. Therefore, the natural frequency of the system can be obtained at a frequency of the characteristic equation intersecting with the x-axis.

Once the natural frequency was obtained, the ratio of amplitude for each hull segmentation can be obtained. The natural frequency is substituted back into Equation 2.23. One of the amplitudes is set to be equal to one, then the normalised amplitude ratio can be obtained for the normal modes. For the kth normal mode, the kth normal mode oscillation can be expressed with the kth normal-mode oscillation-amplitude ratio, $\left(\frac{A_j}{A_{nj}}\right)^k$, and the kth amplitude, θ_A^k;

$$\theta_{ij}^k = \theta_A^k \left(\frac{A_j}{A_{nj}}\right)^k e^{\mathrm{j}\left(\omega_n^k t + \psi^k\right)}, \tag{2.27}$$

where nj is the segment whose angular displacement was set to 1 for the normalisation on angular displacement.

The aim of the multi-body dynamics system was to design a simplified prediction system with quantifiable physical variables with simple computations for feasible optimisation. Therefore it can contribute to the design of the hydroelastic segmented model and to the understanding of the influence of parameters on this particular mechanical dynamics system. The primary focus was to achieve a feasible scaling of the natural frequency. It is unfeasible to satisfy the stiffness coefficient of elastic link (Equation 2.10) which is required by the bending stiffness scaling (by

$$\begin{bmatrix} \left\{ \begin{array}{c} -\omega^2 m_2 l_{2a} \left(\frac{-m_3 l_{1a} + m_2 l_{1f}}{m_s} - l_{1f} \right) \\ +k_2 \end{array} \right\} & \left\{ \begin{array}{c} -\omega^2 m_2 l_{2a} \left(\frac{m_2 l_{2a}}{m_s} - l_{2a} \right) \\ +\omega^2 m_2 r_{g2}^2 - k_2 \end{array} \right\} & \left\{ \omega^2 m_2 l_{2a} \frac{m_3 l_{3f}}{m_s} \right\} \\ \left\{ \omega^2 m_3 l_{3f} \left(\frac{-m_3 l_{1a} + m_2 l_{1f}}{m_s} + l_{1a} \right) + k_3 \right\} & \left\{ \omega^2 m_3 l_{3f} \frac{m_2 l_{2a}}{m_s} \right\} & \left\{ \begin{array}{c} \omega^2 m_3 l_{3f} \left(-\frac{m_3 l_{3f}}{m_s} + l_{3f} \right) \\ -k_3 + \omega^2 m_3 r_{g3}^2 \end{array} \right\} \\ \left\{ \begin{array}{c} \omega^2 m_3 l_{1a} \left(\frac{-m_3 l_{1a} + m_2 l_{1f}}{m_s} + l_{1a} \right) \\ -\omega^2 m_2 l_{1f} \left(\frac{-m_3 l_{1a} + m_2 l_{1f}}{m_s} - l_{1f} \right) \\ -k_2 - k_3 + \omega^2 m_1 r_{g1}^2 \end{array} \right\} & \left\{ \begin{array}{c} \omega^2 m_3 l_{1a} \left(\frac{m_2 l_{2a}}{m_s} \right) \\ -\omega^2 m_2 l_{1f} \left(\frac{m_2 l_{2a}}{m_s} - l_{2a} \right) \\ +k_2 \end{array} \right\} & \left\{ \begin{array}{c} \omega^2 m_3 l_{1a} \left(-\frac{m_3 l_{3f}}{m_s} + l_{3f} \right) \\ -\omega^2 m_2 l_{1f} \left(-\frac{m_3 l_{3f}}{m_s} \right) \\ +k_3 \end{array} \right\} \end{bmatrix} \begin{bmatrix} \theta_{21} \\ \theta_{22} \\ \theta_{23} \end{bmatrix} = 0 \tag{2.23}$$

Equation 2.7) for the model scale length of 2.5 m. Aarsnes (1996) reported that the hydroelastic segmented model was not focused on matching the bending stiffness scaling. It was considered too difficult to achieve flexural rigidity similitude in the model scale. However, it is possible to match the structural response frequency of the hydroelastic segmented model between the model size and full size ship. The input data and results of the mechanical dynamics system for the hydroelastic segmented model are presented in Section 3.6.

2.4 Design of Hydroelastic Segmented Model

2.4.1 Design and Technical Feasibility of the Hydroelastic Segmented Model

The primary evaluation for the design and technical feasibility at the initial stage of the design spiral is the displacement of the experimental ship model. The displacement is important as it configures the length of the ship and the internal volume capacity for onboard devices and internal structure. Since the geometrical similarity should be maintained for the Froude scaling, the length and displacement mutually depend on each other. Once either the displacement or length is decided, the other dimension is determined based on the geometrical similarity. The INCAT 112 m class has a cruising speed of 38 K_n, therefore a Froude number for towing tank experiment of 0.604 is required. The model velocity is calculated using Equation 2.28 to obtain the Table 2.1.

$$F_N = \frac{V_s}{\sqrt{gL_{wl}}} \tag{2.28}$$

The model velocity was selected to be smaller than the maximum available speed of the towing tank carriage, and simultaneously a feasible model length for the towing tank was selected.

Table 2.1: Carriage speed feasibility calculation for the HSM

Length waterline (m)	Required carriage speed (m/s)
1.0	1.891
1.5	2.317
2.0	2.675
2.5	2.991
3.0	3.276
3.5	3.539
4.0	3.783
4.5	4.012
5.0	4.229
5.5	4.436

The calculations in Table 2.1 uses a ship length of 112 m to obtain the rational number for the geometrical scale ratio. These calculations show that there were no concerns regarding the design and technical feasibility with respect to the length of the model from 1 m to 5.5 m, where

the AMC towing tank carriage is capable of travelling at a velocity of 4.6 m/s.

After ensuring Froude scaling in the towing tank, the displacement of the experimental model could be determined. By concluding the displacement, the scale ratio of ship size to model size can be finalised. The model mass was calculated using Equation 2.2. The density of salt water, ρ_s for full-size scale and fresh water, ρ_m for the model scale were used 1025 kg/m^3 and 1000 kg/m^3, respectively.

Table 2.2: Model mass feasibility calculation for HSM to achieve the required Froude Number, F_N of 0.6039 in the towing tank experimentation.

Ship displacement (tonnes)	Ship Length (m)	Model length (m)	Scale ratio	Model displacement (kg)
2500	112	1.5	74.667	5.859
2500	112	1.75	64.000	9.304
2500	112	2	56.000	13.888
2500	112	2.25	49.778	19.775
2500	112	2.4	46.667	23.999
2500	112	2.5	44.800	27.126
2500	112	2.6	43.077	30.513
2500	112	2.75	40.727	36.104
2500	112	3	37.333	46.873
2500	112	3.25	34.462	59.595
2500	112	3.5	32.000	74.433
2500	112	3.75	29.867	91.549

In general, the smaller model displacement would not achieve design displacement due to ballasting and tow post weights for seakeeping experiments. A counterweight system can reduce the model displacements by physically lifting up the model, however the counterweight ballast system does add an extra mass moment of inertia to the ship's rigid body. Therefore, it is not appropriate for ship motion tests, because it affects the heave and pitch motion. As a result, the lower displacement was eliminated as an option for the target model displacement.

In conclusion, the length of 2.5 m was selected for the model. The advantage of 2.5 m is that the model provides longer test run in lengths, because it can travel at a relatively lower speed compared with larger models. Since the velocity can be low, the acceleration and deceleration period can be short as well. According to Hermundstad (1995), a short period with sufficiently steady conditions lasted from 2 to 6 seconds, using a 4.1 m hydroelastic segmented model. The 2.5 m class model can offer a period of steady conditions for more than 10 seconds in the towing tank at the AMC. The longer sampling period of steady conditions will increase the confidence and repeatability of the experimental results.

2.4.2 Demi-hull and Centre bow Segment and Segmentation Cuts

The HSM for the INCAT 112 m class, presented in Figure 2.4, was configured with forward transverse beams or cantilever beams to support the centre bow segment (CBS), as shown in Figures 2.4 and 2.5, respectively. The structural arrangements of both configurations are explained in Subsection 2.4.3. Each demi-hull was segmented into three rigid body segments separated with a 10 mm segmentation gap where the slits can be seen at the freeboard of the demi-hull in Figure 2.5. The segmentation gaps were sealed with latex rubber sheets, as shown in Figure 2.4. Two adjacent rigid segments were linked by an elastic link attached with strain gauges. The rigid bodies of the demi-hulls are, for convenience, named as the forward segment demi-hull (FSDH), the mid segment demi-hull (MSDH), and the aft segment demi-hull (ASDH), from the bow to the transom stern. A schematic diagram of the demi-hull is shown in Figure 2.6. The underside of the demi-hulls are shown in Figures 2.7 and 2.8. The segmentation of the centre bow was generated to be separate from the demi-hulls, as shown in Figures 2.9 and 2.10. The demi-hull and centre bow segmentation experienced many iterations of design, which are discussed below.

Figure 2.4: Hydroelastic segmented model with forward transverse beam configuration.

The centre bow is exposed to slamming in large waves. In order to understand this slamming effect, the centre bow was designed to measure the response of slamming forces by isolating the hydrodynamic force acting on the demi-hull, by being segmented from the demi-hulls.

Numerous ways of segmenting the demi-hulls were considered and evaluated in order to achieve

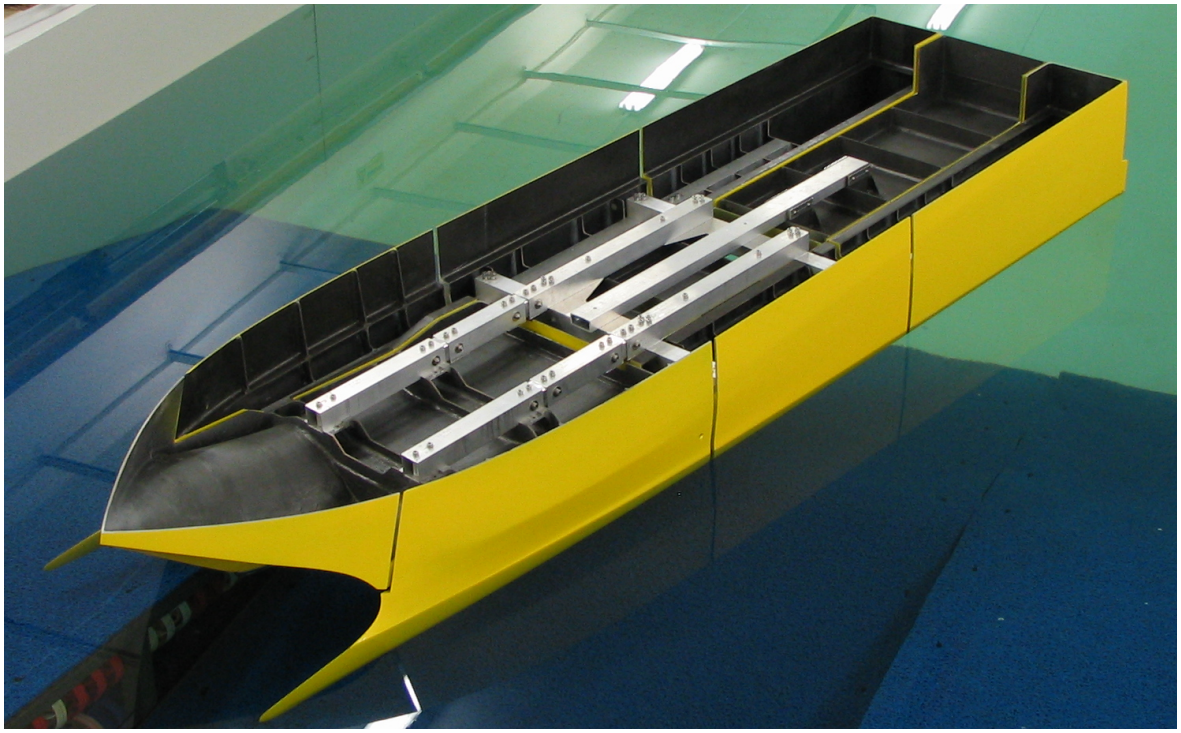

Figure 2.5: Hydroelastic segmented model with cantilever beam configuration.

the objective of the hydroelastic segmented model. The weight distribution and maximum strain response were some of the determining criteria for the locations of the segment cuts. In terms of the strain gauge response, larger vertical bending moments on the demi-hull generates larger strain responses on the demi-hull structure. Since generally large vertical bending moments occur around the midship (A larger strain response is beneficial to enhance the recorded data response), the location of the segmentation was designed to be closer to the midship of the demi-hull. However, the MSDH is necessary to maintain an adequate length in order to provide space for ballasting and the mid transverse beams (MTB) connecting between starboard and port side MSDH. It is essential that the LCG is placed within the MSDH so that the towing system can be attached on the MSDH through the MTB. A significant number of iterations of weight estimates were conducted as the design details evolved. The weight distribution was significant to achieve the modal response of the vessel and to ballast the vessel for controlling the location of the LCG, and the trim of the vessel.

As the demi-hull was divided into three segments, the CBS can be connected directly to the FSDH. This configuration is named as the forward transverse beam (FTB) configuration as shown in Figure 2.4. An alternate configuration was designed for the CBS to be supported by a cantilever from the transverse beams on the MSDH. This is called the cantilever configuration and is shown in Figure 2.5. An advantage of the FTB configuration is to demonstrate that the load transition from the CBS to FSDH is a realistic representation of the full-scale vessel. The loads on the centre bow transmit through the centre bow arch and bow jaw to the demi-hull. In the HSM, the rigid body of the CBS experiences the hydrodynamic forces, and its response load is delivered through the FTB to the rigid body of the FSDH. Therefore, the centre bow was

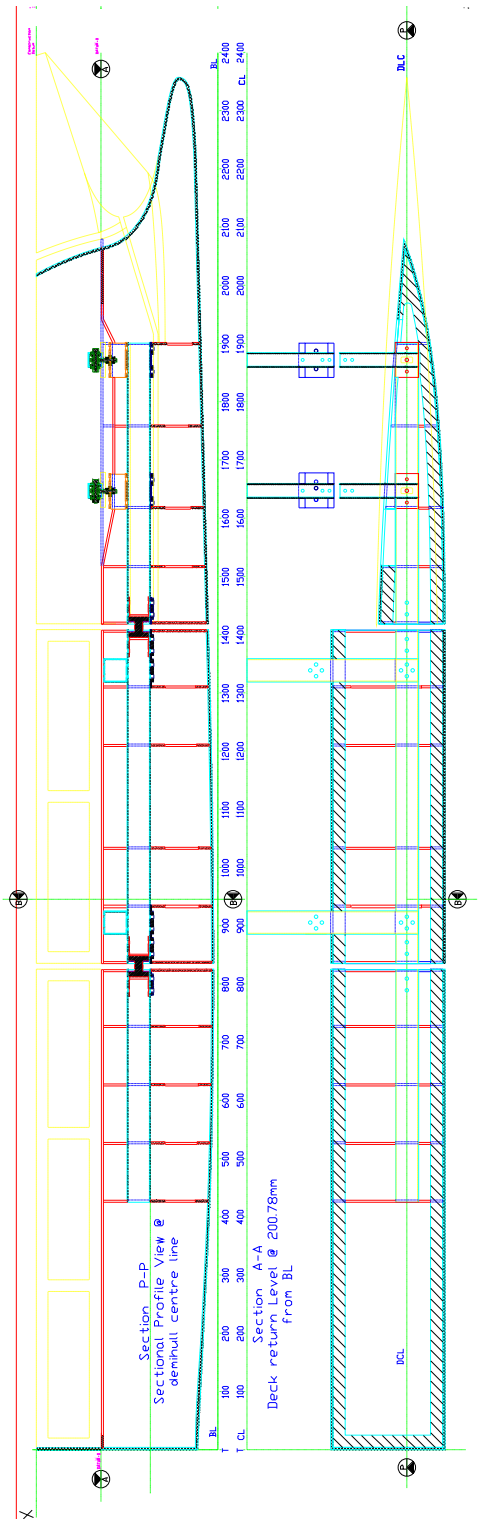

Figure 2.6: Hydroelastic segmented mode, general arrangement in the profile and plan view

also segmented from the demi-hulls in order to measure the loads onto the centre bow region. The centre bow segment end is aligned with the end of the FSDH, as shown in Figure 2.7. For the cantilever configuration, the measurement of the strain gauge data is possible at the same longitudinal location from the transom on both the demi-hulls and the centre bow, as shown in Figure 2.5.

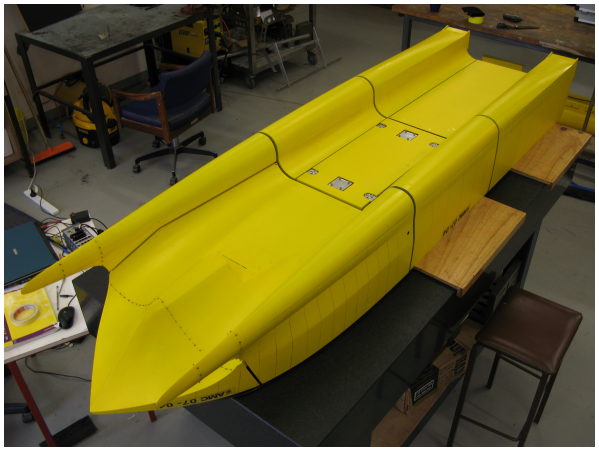

Figure 2.7: Segmentation of demihull and centre-bow (upside down view)

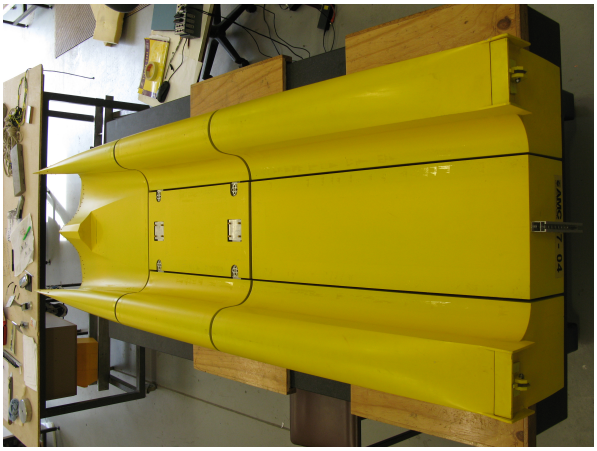

Figure 2.8: Segmentation of demihull and cross bridge deck (upside down view)

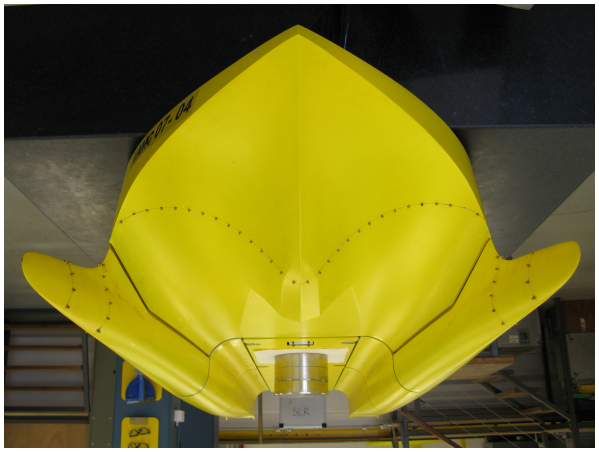

Figure 2.9: Segmentation cut on centrebow segment (front view)

Figure 2.10: Inboard side segmentation cut on centrebow segment (inboard view)

Segmentation on the centre bow required many iterations of design and evaluation to achieve the objective that the CBS collects the slamming force. Evaluations were made on the cuts in the longitudinal-vertical axis plane.

Firstly, the segmentation gap was placed along the peaks of the centre bow arch, as shown in Figure 2.11. This method (option 1) would ensure that the global wave effects would be acting on the demi-hull. However, the slamming force onto the centre bow was expected to be large around the centre bow arch peak. Placing the segmentation gap around the peak of the centre

bow arch would not be suitable for obtaining larger slamming forces. The demi-hull would be exposed to the slamming with larger waves, if the demi-hull contained some section of the centre bow arch.

For option 2 the segmentation gaps were located closer to the demi-hull side in order to avoid the demi-hull arch peak, as shown in Figure 2.12.

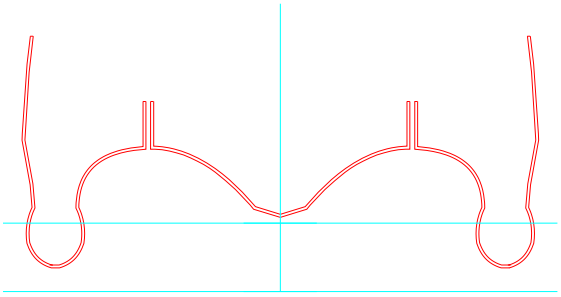

Figure 2.11: CBS segmentation gap option 1 at the centre bow arch peak

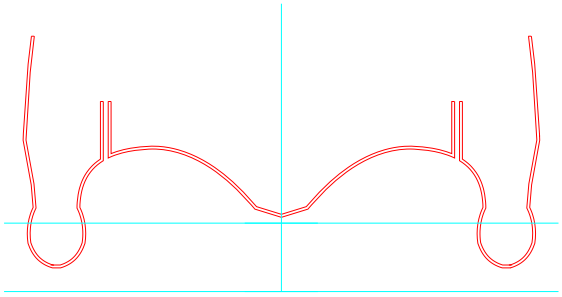

Figure 2.12: CBS segmentation gap option 2 at the centre bow arch half way

Slamming is unlikely to occur on the demi-hull of the wave-piercer bow, however, water flow momentum from the demi-hull might be disturbed by the acute angle of the segmentation gap. It was considered that the segmentation cut might be slightly higher, if the focus of experiments was to gain a clear slamming effect onto the centre bow.

The third option was to cut the hull near the intersection made by the demi-hull surface and centre bow surface, as shown in Figure 2.13. Option 3 would gather the slamming force more effectively than option 1 and option 2. However, the segmentation gap of option 3 caused a large opening in the hull surface of the centre bow arch, since the segmentation gap plane and surface did not cross vertically. The reason why the larger gap occurred in option 3 was that the segmentation gap was conventionally made by a cut in the vertical plane. The segmentation gap was too large in vertical plane, so a disturbance of fluid flow from the demi-hull to the centre bow could be expected. Since the segmentation cut had a vertical surface as the hull surface, the segmentation cut should be generated in the horizontal plane, which led to option 4.

The fourth option was to cut the segmentation gap in the horizontal plane to minimise the segmentation gap opening on the hull surfaces, as presented in Figure 2.14.
Option 4 had an ideal and larger area for the centre bow arch with the smaller segmentation gap, than those of the options 1, 2 and 3, in order to collect hydrodynamic force due to the slamming. Since the measurement of slamming is one of the primary focuses of the project, this location for the segmentation cut was used to measure the slamming load. However, option 4 did not have a retaining wall in case of a break occurring in the seal of the segmentation gap. Once the sealing is broken, the demi-hull compartment would be flooded.

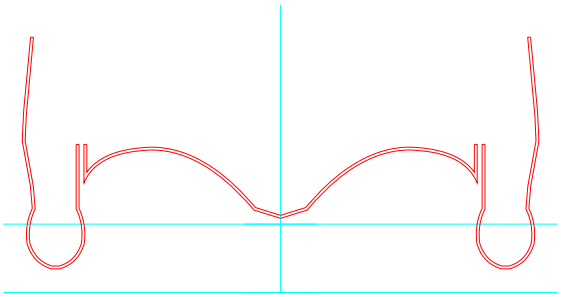

Figure 2.13: CBS segmentation gap option 3 on the demi-hull

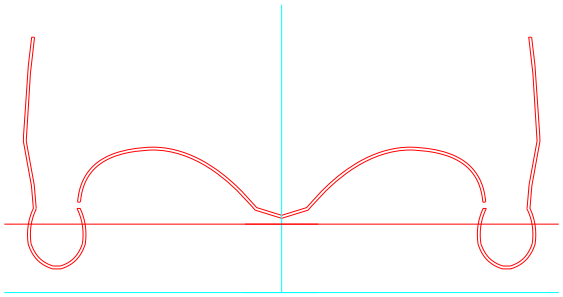

Figure 2.14: CBS segmentation gap option 4 on the demi-hull

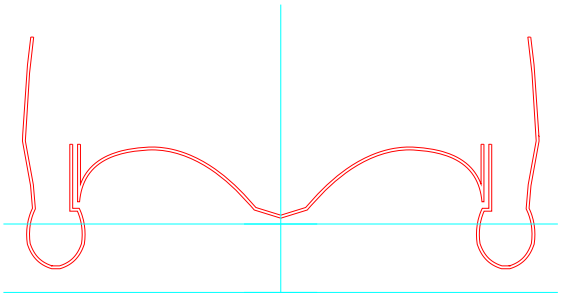

Figure 2.15: CBS segmentation gap option 5 on the demi-hull

In order to avoid this problem, a fifth method was developed, as shown in Figure 2.15. The location of the segmentation gap remained the same as in option 4. The segmentation gaps and retaining walls started at the top of the model, and at the bottom of the centre bow arch segmentation gaps were made at a 90 degree turn into the inboard direction. This reduced the aforementioned problem of larger spacing on the surface of the centre bow arch, as in option 3. This smaller segmentation gap would reduce the loss of capturing hydrodynamics forces onto the hull. As can be seen in Figure 2.15, there was a smooth continuous hull surface for the centre bow arch for slamming loading to the ship, and the segmentation gap was significantly smaller than the other options. In conclusion, option 5 was selected for the segmentation method between the centre bow and demi-hull.

The final design of the HSM can be decomposed into the six segments shown in Figure 2.16. The decomposed segments in the photo are from the left-hand side, starboard side aft segment demi-hull, port side aft segment demi-hull, mid segment demi-hulls, starboard side forward segment demi-hull, port side forward segment demi-hull, and centre bow with forward transverse beam configuration. The mid segment demi-hulls are still assembled with the cross-bridge deck.

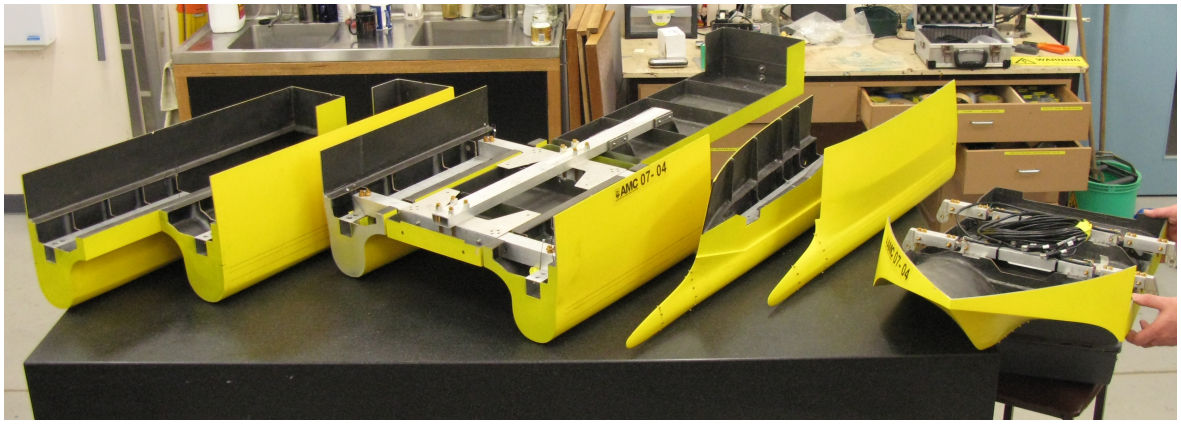

Figure 2.16: HSM segments

The starboard and port side forward segment demi-hulls are shown in Figures 2.17 and 2.18. The hull surface facing the centre bow arch clearly indicates a recess for the centre bow segment. The vertical height of the segmentation gap running horizontally from the aft end of the segment toward the bow was 6 mm. The segments were inclined towards the bow in order to make sure that the bow jaw was clear from the segmentation gap, so that the water flow would not be disturbed. This arrangement avoided placing overhung surface sections onto the forward segment demi-hulls, thus avoiding slamming effects on the demi-hull.

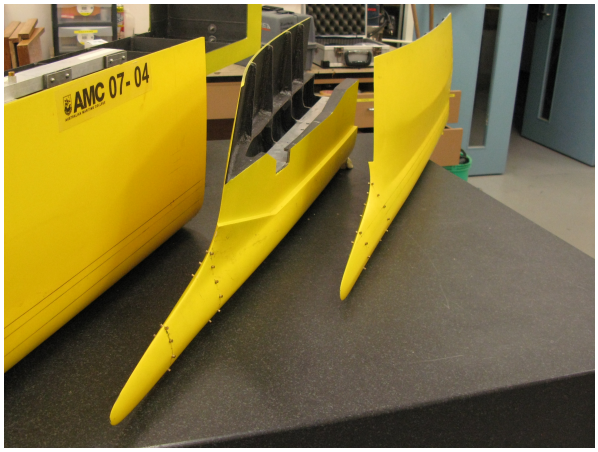

Figure 2.17: Forward segment demi-hull (forward view)

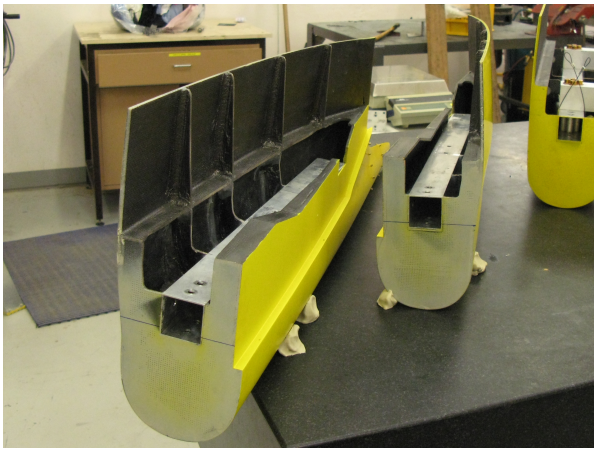

Figure 2.18: Forward segment demi-hull (aft view)

The aft segment demi-hulls are shown in Figures 2.19 and 2.20. The aft segment demi-hull has a tunnel arch as part of the demi-hull. Since the slamming load onto the cross-bridge deck was not a focus of the project, the arch was included in the demi-hull side to experience the maximum global wave load. At the transom of the aft segment demi-hull, the trim tab system was equipped as shown in Figure 2.19. Side plates were attached at the transom stern to extend the vertical wall surface of the hull.

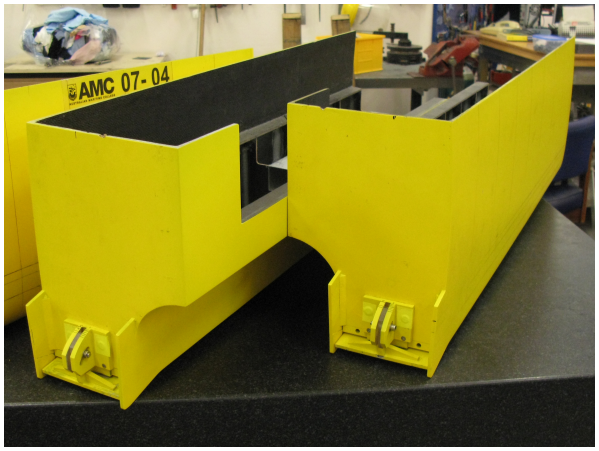

Figure 2.19: Aft segment demi-hull (aft view)

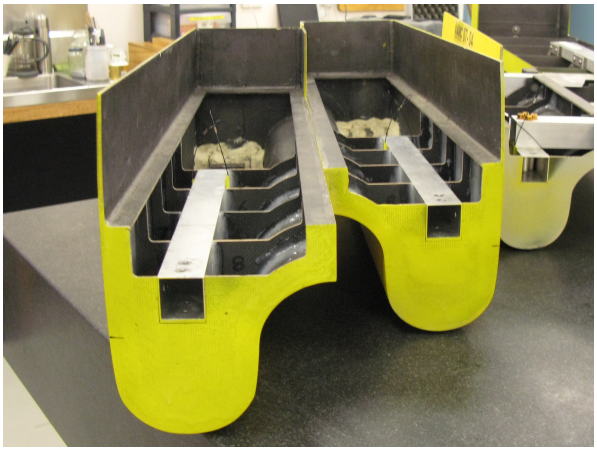

Figure 2.20: Aft segment demi-hull (forward view)

2.4.3 Backbone Beam Assembly and Structural Configuration

The overview of the structured arrangement with backbone beams installed in the demi-hulls and centre bow is shown in Figures 2.21 and 2.22. The backbone beam was supported by frames and a watertight bulkhead, therefore it is considered as a rigid part of the demi-hull structure. For the FTB configuration, the two forward transverse beams were connected to the forward segment demi-hulls, and the other two aft transverse beams were connected to the mid segment demi-hulls. The forward transverse beam was connected to pin-joint systems which were located on the backbone beam in the FSDH. The mid transverse beam was directly connected to the backbone beam, so that the starboard and port side mid segment demi-hulls formed one rigid body segment.

The backbone beam system, before assembly of the HSM is shown in Figure 2.23. This backbone beam configuration is for the cantilever configuration, however, the two longitudinal beams which were attached on the mid transverse beams, could be removed. The forward transverse beam configuration could replace the cantilever configuration used for the assembly stage of construction.

The demi-hull backbone beam was embedded into the frames, as can be seen in Figure 2.24. The bulkhead at the end of each segment secured the backbone beam and can be seen in Figure 2.20. The backbone beams were embedded into the frames and bulkheads in order to increase the integrity of the hull rigidity. The frames supported the backbone beam rigidity, so that the backbone beam was not subject to deflection. The backbone beams also contributed to the alignment of the segmentation joint. The aluminium hollow section of the backbone beam functioned as a female socket for the elastic link to join two adjacent segments. The locations of frames and bulkheads are shown in the schematic diagram in Figure 2.6. The frames had a cut-out openings to reduce the weight of the model. The frames were inserted in the model with a 100 mm spacing, where possible. If the spacing of 100 mm was not feasible, other alternate dimensions were selected for the frame spacing.

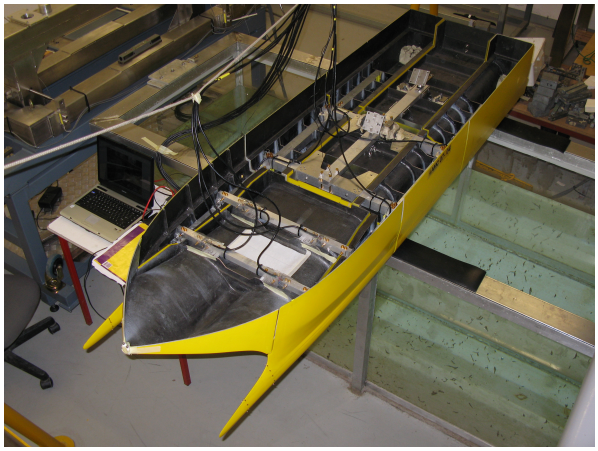

Figure 2.21: HSM internal structure arrangement (perspective view)

Figure 2.22: HSM internal structure arrangement (frontal top view)

The deck return, shown in Figure 2.24 was installed in order to increase the longitudinal strength. The deck return was created throughout both demi-hulls from bow to stern. With a similar structural function to the deck return, the tunnel arch was included in the demi-hull to increase the demi-hull rigidity.

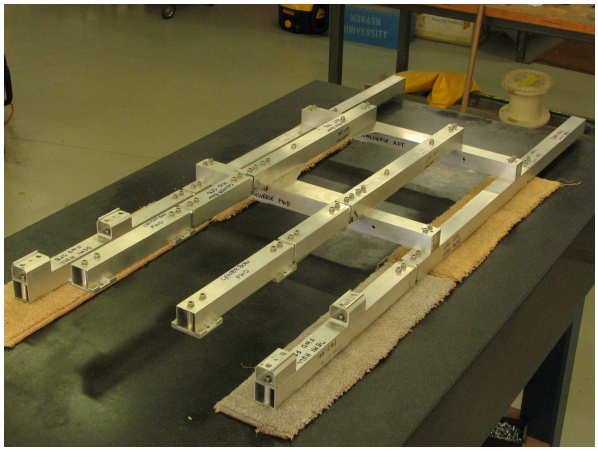

Figure 2.23: Backbone beam arrangement, cantilever configuration

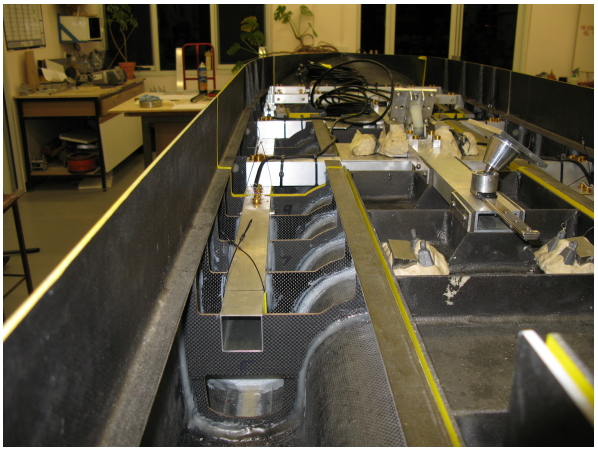

Figure 2.24: Backbone beam and ring frame arrangement

The cross-section of the backbone beam was also subjected to another consideration. A larger area moment of inertia contributes to the segment rigidity. However, it needs to be lightweight due to the lighter displacement of the model. Contradicting requirements led to the selection of the larger square hollowed section with thinner walls. It needed to be an adequate size to fit within the demi-hull and to provide enough access to the bottom of the demi-hull for ballasting.

The vertical position of the backbone beams was selected at the neutral axis of the mid segment of the vessel. Thus, the elastic link retained the neutral axis at the same height as those of the backbone beams. The vertical location of the backbone beams and elastic links were designed to be clearly above the designed waterline. In the case of flooding into the segmentation gaps,

water intrusion to the backbone beam or damaging the strain gauges on the elastic link could be avoided.

The local structure of the centre bow segment and its holding mechanism are discussed in Subsection 2.4.5, after mentioning the elastic links in Subsection 2.4.4.

2.4.4 Hydroelastic Stiffener Design for Flexural Rigidity

The elastic links contributing to the stiffness of the structure, were designed to be inserted into the aluminium square hollowed section of the backbone beams. Aluminium bolts secured the elastic link. The section of the elastic link with the strain gauge system had a simpler square section in order to simplify the manufacturing of the elastic link and calculating the flexural rigidity, EI, from the cross-section of the elastic link. Thus, it could control the stiffness character appropriately. The elastic links were machined from aluminium blocks by a CNC machine at the University of Tasmania.

The elastic link had two parts. Firstly, the elastic section to demonstrate the elasticity of the stiffness, and secondly rigid sections connected to the backbone beams. The elastic parts had the machined square section, functioning as the elastic length of the elastic link, l_{bar} in Equation 2.10. The elastic length and dimension of the square cross-section are important to calculate the stiffness coefficient of the elastic link for the equations of motion in the mechanical dynamic system, as presented in Subsection 2.3.6. The stiffness coefficient, k_{bar} is calculated in Equation 2.10. The strain gauges were placed at the longitudinal centre of the elastic part of the elastic link, on the top and bottom surface. The rigid parts of the elastic links had two holes for bolt fastening to secure the elastic link onto the backbone beam. With two securing holes, the elastic link and backbone beam increased the firmness of the clamping, and removed the slackness between the elastic link and backbone beams. A horizontal hole on the rigid part of the elastic link was also made to remove horizontal movement between the elastic link and backbone beam.

Two other types of link were also designed for the rigid hull configuration. By inserting the rigid link instead of the elastic link, the HSM could convert into a rigid model ship rather than a hydroelastic segmented model. The first type was a sold link, while the second type was a solid hollow link. The solid links, which were installed on the MSDH as shown in Figure 2.28, were utilised for the purpose of assembly during construction. The solid hollow link, which can be seen beside the MSDH on the work bench in Figure 2.28, was used for the non-hydroelasticity seakeeping test and resistance test. Thus, the influence of the elastic link on ship motions can be determined by comparing this with ship motions with the solid hollow link. The detail design of the elastic link was worked by Lavroff (2009)).

2.4.5 Centrebow Segment Connection

The centre bow can be fitted in two different ways, as mentioned in Subsection 2.4.2. The first connection method is the forward transverse beam configuration shown in Figures 2.25 and 2.26, and the second method is the cantilever beam configuration presented in Figure 2.27.

For the first method, the CBS was supported by the forward segment demi-hulls. There were two transverse beams to hold the centre bow. Each transverse beam was made of an aluminium hollow section 25 x 25 x 1.6 mm, which was smaller in size compared with the backbone beam in each demi-hull. It was split into three beam parts to form the FTB, and the adjacent beam parts were connected by elastic links to form the FTB, as shown in Figure 2.26. Both ends of the FTB were equipped with a pin-joint system so that no moment was produced about the longitudinal axis of the ship. The combination system of the pin joints and elastic links with strain gauges determined the load and its location of slamming onto the CBS. Aluminium mounts, which were placed on the frames of the CBS, were designed to support the FTB, and the aluminium mounts could also support the cantilever beam as in the second configuration.

For the cantilever beam configuration, the CBS was connected to the mid transverse beam on the MSDH, as shown in Figures 2.27 and 2.28. The cantilever beam was made of an aluminium hollow section 40 x 40 x 2.5 mm, which was the same as the backbone beam in the demi-hull segments, hence the elastic links were the same size as those for the demi-hull. Four elastic links with strain gauges were utilised to measure the location and load of the slamming resultant force onto the centre bow.

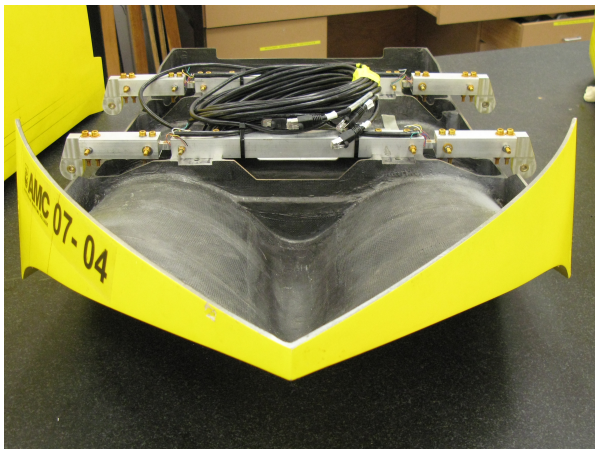

Figure 2.25: Centre bow segment (forward view)

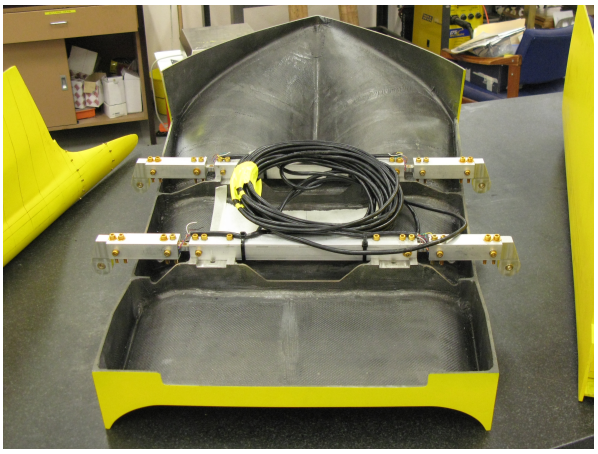

Figure 2.26: Centre bow segment (aft view)

The advantages of the FTB configuration are in the realistic structural arrangement and weight reduction in the total arrangement. With the FTB, the load from the CBS can be transmitted through the beam to the FSDH, which most likely occurs in the full-size ship. The pin-joint system for the FTB configuration could be utilised to gain a versatile measured system. A hole for the pin-joint system can be seen at both ends of the FTB in Figures 2.25 and 2.26. This was designed to aid the calibration system for load measurements on the CBS, which will be

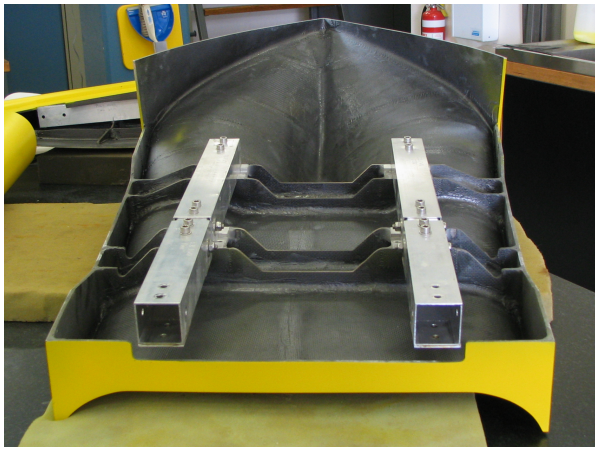

Figure 2.27: CBS cantilever configuration

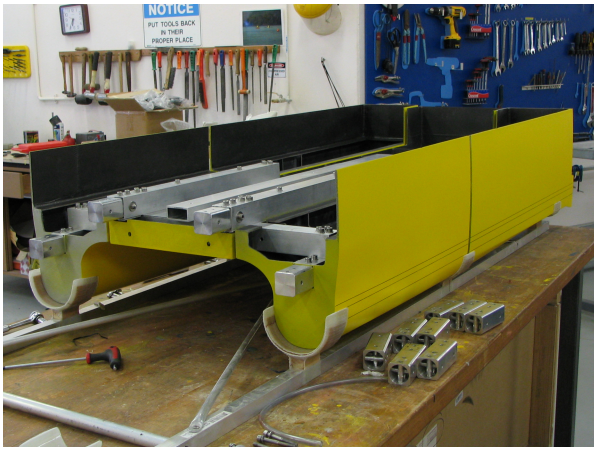

Figure 2.28: MSDH cantilever configuration with solid links attached on the MSDH. The solid hollow links are on the work bench top beside the MSDH.

described in Subsection 3.5.4. The drawback of the FTB configuration is that the physical isolation of slamming loads from the global wave load at the demi-hull elastic link is not possible. The elastic link on the demi-hull experiences the global wave-induced load and slamming load. Where there is interest in global waves on the demi-hulls, such as a validation of the numerical results based on theory, the slamming load needs to be isolated. However, this can be an advantage for measuring the total vertical bending moment of the demi-hull by slamming and global wave-induced load, if both loads need to be measured at the elastic link in the demi-hull.

The advantage of the cantilever configuration is the physical isolation between the slamming loads and global wave load at the elastic link in the demi-hull. Since the CBS does not connects to the FSDH and the mid segments, the slamming load is not transmitted to the FSDH.

During the series of experiments, the FTB configuration was selected because the load transition to segments was more aligned to a full-size ship.

2.4.6 Sealing of Segmentation

The sealing of segmentation gaps is important for watertightness. Trial and error was required to developed the adequate sealing technique. Ideally only the elastic link is connecting the adjacent rigid body segments, at the segmentation gap. However, this has the undesirable result of water leakage at the segmentation gaps, which may also cause the strain gauges at the elastic links to become wet. Since the load is measured only by the elastic links, the sealing ideally should not experience any loads. Therefore, a latex thin-rubber sheet was selected for sealing the gaps.

The latex rubber sheet required special attention during attachment to the model. During the preparation of the HSM, difficulty in achieving properly sealed seams was experienced. This was especially the case when the water-resistant adhesive tape overlapped another piece of water-

resistant tape, as this created a tiny gap through which the water could penetrate into the segmentation gap. In order to avoid water penetration, double-sided adhesive tape was utilised. Firstly, double-sided adhesive tape was attached to the edges of adjacent rigid body segments, and the latex rubber sheet, which was cut to the appropriate width, was layered to cover both the segmentation gap and the double-sided tape on both sides of the gap. The water-resistant tape was used to cover the edge of the latex rubber sheet, which was located right above the double-sided adhesive tape. The water-resistant tape was free from the gap and allowed a smooth water flow.

2.4.7 Trim Tab Design for the Hydroelastic Segmented Model

A trim tab was designed and installed in the hydroelastic segmented model as can be seen in Figure 2.19. The dimension of the trim tab was subjected to discussion and prioritisation of its function in the scaled experimental environment. The decision-making process focused on the hydrodynamic influence of the trim tab.

From the geometrical similarity point of view, the trim tab feature contributes to the water flow separation, and largely influences the transverse wave pattern after the transom walls. It is a wave-making effect related to the Froude effects. Therefore, it is important to install the trim tab in the model scale to maintain the geometrical similarity with respect to the wave-making effects. Hence, the trim tab was designed by maintaining the geometrical similitude of the trim tab area ratio and its installed location relative to the transom stern end.

2.4.8 Materials for the Hydroelastic Segmented Model

Material selection was one of the key factors to reduce the model mass. Since the target displacement of the HSM was extremely low for its experimental requirements, material selection was important. The lightest and most rigid material as possible was required for the rigid segments. Carbon fibre composite suited this requirement. The typical carbon fibre composite structure for the hull surface of the HSM consisted of two layers of gel coat of epoxy resin, carbon fibre cloth sheet, closed-cell core material, and carbon fibre cloth sheet with resin. The typical material properties of the carbon fibre cloth and core material are shown in Table 2.3.

Table 2.3: Carbon fibre cloth and closed-cell core material.

Item	Density	Thickness
Carbon Fibre Cloth	200 g/m^2	-
Closed Cell Core Material	50 - 70 kg/m^3	3mm

The closed-cell core material has the advantage that resin does not soak into the inside of the core cell. By applying less resin, it results in reducing the weight of the carbon composite structure, and hence the weight of the model.

Details of the construction process of the model are attached in Appendix B.

2.4.9 Weight Estimate and Optimisation

A significant number of detailed weight estimate calculations were required to develop the design for the hydroelastic segmented model. The most important activity for designing the HSM was to achieve a low lightship mass of the high-speed vessel. The weight estimates aided the structural design by idnetifing the unnecessary components as much as possible. Since Rhinoceros, a non-uniform rational B-spline (NURBS) surface modelling program, was used for detail design, a Rhinoceros macro program was developed to assist in the weight estimation. Although Rhinoceros is a surface modelling graphical application, the author extended its capability to solid modelling as much as technically feasible. Confident exercises on comprehensive weight estimation was inevitable to achieve the target displacement rigorously. The author developed the macro program to obtain the area, centre of gravity, and mass moment inertia data from the Rhinoceros model of the HSM. Without the powerful support of the macro program, the detailed weight estimate was literally impossible. Weight measurements of some components were not possible, so that weight estimates on those components were used, as described in Subsection 3.6.1 and Appendix C. It was also useful to predict the design and manufacturing feasibility in the design stage. Rhinoceros provided the rendering module package called Flamingo. Flamingo offers impressive rendering capabilities which are extremely useful for graphical presentation, as shown in Figure 2.1.

The principal particulars of the hydroelastic segmented model were presented with design and measured values in Table 2.4. A longitudinal centre of the gravity were measured by a pivot method on a levelled surface. A radius of gyration (RoG) for the pitch were measured by the swing method in pitch direction.

Table 2.4: Principal particulars of the hydroelastic segmented model

Particulars		Unit
Dispalcement	27.43	kg
LOA	2.426	m
Overall submerged length	2.383	m
Wetted surface area	0.919	m^2
LCG (v)	0.948	m
RoG for pitch	0.64	m

2.4.10 Conclusions

In this chapter, the selection process of the hydroelastic segmented model for the investigation of ship motions and wave-induced load responses with ship hydroelasticity was discussed, by investigating the available model types (hydroelastic continuous model, rigid segmented model and

hydroelastic segmented model) and adequate scaling techniques and theory for ship hydroelastic experiments. A novel experimental model that simultaneously measures wave-induced loads on the demi-hull and slamming loads on the centre bow with subsequent whipping, was designed and built in the model size of 2.5 m for the INCAT 112 m class.

The hydroelastic segmented model consisted of seven rigid body segments joined by elastic links. The elastic links were equipped with strain gauges for loads measurements. The model was required to satisfy the geometrical similarity, Froude similarity, radius of gyration, flexural rigidity similitude and structural dynamics response similarity. Some scaling laws and systems were coupled, hence all the similitudes and systems were satisfied with the exception of the flexural rigidity similitude.

Chapter 3

Hydroelastic Segmented Model Experiments in Head Seas

The experiments of the hydroelastic segmented model (HSM) for the wave-piercer high-speed catamaran were carried out in the towing tank at the Australian Maritime College (AMC) in Launceston, The primary aim was to investigate ship motion and wave-induced loads with ship hydroelasticity. Resistance tests and regular and irregular wave seakeeping tests in head-sea conditions were conducted on the HSM. Prior to the towing tank tests, extensive calibrations and modal frequency tests ,with impact excitation in air and water, with and without the forward velocity, were conducted to examine the load measurement system and natural frequency of the model.

The experimental objectives are presented in Section 3.1. The experimental facility, instrumentation and DAQ system are explained in Section 3.2. The experimental conditions are explained in Section 3.3, and a summary of the model information is given in Section 3.4. The calibration is explained in Section 3.5, and the modal tests are summarised in Section 3.6. The VBM induced by the forward velocity in calm water is presented in Section 3.7. The seakeeping result for the solid model and hydroelastic model are presented in Section 3.9, whilst the wave-induced loads are presented in Section 3.10.

3.1 Experimental Objectives and Hypotheses

The objectives of the hydroelastic segmented model experimentations were:

1. to investigate the hydroelasticity effect on the model;
2. to examine the influence of the hydroelasticity on ship motion and induced loads;
3. to obtain the motion response of heave and pitch in head seas;
4. to obtain the wave-induced VBM response of the demi-hulls and the slam-induced force on the centrebow;

5. and to investigate the mutual interaction of the ship motion and wave-induced loads due to ship hydroelasticity.

Uncertainty about the influence of ship hydroelasticity on ship motion and wave-induced loads uses one of the primary motivations for selecting a hydroelastic model. The hypothesis was proposed that the ship hydroelasticity mutually influences the ship motion and wave-induced loads on the structure. The ship motion is a response to the global wave motion influence, and the large ship motion causes the slam impact as an impulse excitation, leading to the whipping vibratory behaviour in the structure; this structural vibration may also influences the ship motion.
The ship motion responses were investigated since the wave-piercer high-speed catamaran, with a centre bow, is expected to show strong non-linearity in large waves, due to the extreme change in the hull form above the waterline.
The global wave load, slam-induced loads and ship motions are vital information for the design properties to be fulfilled for the industry and regulatory requirements, as high-speed vessel operations demand faster speeds, larger payloads, competitive seaworthiness, and fuel efficiency.

The major experiments carried out were as follows:

1. Calibration tests,
2. Dry and wet modal tests,
3. Seakeeping tests.

In order to investigate the vibratory response, spectral and wavelet analyses were utilised on the measured data. The major methods of analyses were as follows:

1. Spectral analysis,
2. Wavelet analysis,
3. Motion response analysis,
4. Load response analysis.

3.2 Experimental Facility and Devices

3.2.1 Towing Tank Facility

The Australian Maritime College has a 100 metre towing tank with a wave-maker device as shown in Figure 3.1. The design particulars of the towing tank are shown in Table 3.1.
The towing tank overview is shown in Figure 3.2. The general depth of the towing tank is 1.5 m. Due to the model size and clearance constraints between the model and towing tank moving carriage, the water depth was set to 1.4 m. The carriage runs on rails on the top surface of both

Table 3.1: Particulars of Towing Tank at Australian Maritime College

Length Overall	100	m
Standard Depth	1.5	m
Width	3.5	m
Maximum Carriage Speed	4.6	m/s

sides of the towing tank walls. The rails extend over the wet dock, where the model setting can be conducted by observing the model trim conditions through the glass sides of the wet dock.

Wave Maker: The paddle-type wave maker is installed at one end of the towing tank shown in Figure 3.3. The paddle is driven by a hydraulic system to generate the regular and irregular waves. The hydraulic system for the paddle is controlled by the wave generation program on the dedicated PC device for the wave maker.

Wave Dissipation Beaches: There are two types of wave dissipation system installed along the inner walls of the towing tank. On the port side of the carriage, this is a wave dissipation beach with an air pneumatic elevation system, as can be seen in Figure 3.3. On the starboard side, the snake-type wave dissipation tube system is available for resistance tests. At the other end of the towing tank to the wave-maker device, a permanently fixed wave dissipation beach.

The data acquisition system packages of the carriage onboard system are versatile and comprehensive types of sensors and systems are available. The general sensors are explained in Subsection 3.2.3, and the general DAQ systems are mentioned in Subsection 3.2.4.

3.2.2 Towing System

Tow Post System: The tow post system is essential to control the degrees of freedom for the experimental model in towing tank experiments. For these tests, the model was free to heave and pitch, whilst constrained in the other directions. The two-post system consists of the tow post frames and tow posts, LVDT sensors, and the dyno bed.

The forward tow post, running in vertical liner bearings, is connected to the load cell for the resistance measurements, and the load cell connects to a pin joint mount. The pin joint is mounted on the experimental model ship. The aft tow post is mounted to universal joints on a linear slider. Hollow stainless steel tow posts were utilised, since they provided sufficient strength and reliability for the large wave tests, but were lighter than the standard solid steel posts.

the experimentation.

Figure 3.1: AMC towing tank schematics (Image courtesy: AMC Towing Tank)

Figure 3.2: AMC towing tank facility during the HSM experiment.(Photographer: Bruce Cartwright)

3.2.3 Towing Tank Sensors

The towing tank is equipped with several devices to measure ship motion and wave height, as detailed in Table 3.2.

Table 3.2: List of Sensors on Carriage

Quality	Sensor and Systems
Carriage Speed	Taco Meter
Ship Motions	Linear Variable Differential Transformer (LVDT)
Wave Height	Capacitant Type Wave Probe
Wave Height	Ultrasonic Acoustic Wave Probe

Linear Variable Differential Transducer: Linear variable differential transducers (LVDT) are attached on the forward and aft tow post system to measure the vertical motion of the tow posts. The signals from the LVDT are sent to the signal-conditioning box dedicated to the LVDT. The signals of the LVDTs were used as synchronisation signals between the carriage onboard DAQ system and the CRIO system. The signals after the filter and amplifier and before the signal junction box were split with a T-junction joint and fed to the CRIO. The LVDTs were calibrated every morning prior to the experiment.

Capacitance Wave Probe: Capacitance wave probes were used for the moving wave measurement and static wave measurement. The capacitance wave probe requires a dedicated signal-conditioning box before its signal is sent to the filter and amplifier box.

Acoustic Wave Probe: The acoustic wave probe utilises an ultrasonic wave to measure the distance of the wave surface. With calibration data, the signal is converted to the wave height. The acoustic-type wave probe requires the dedicated signal-conditioning box.

Moving Wave Probe: A moving wave probe was placed on the carriage to measure the encountered wave height and frequency. The location and number of the moving wave probes used were dependent on requirements. For the seakeeping tests, one moving wave probe was placed at the LCG of the experimental model, and the moving wave probe was offset from the model to avoid the model generated waves. It was attached on the side of the vertical fin.

Static Wave Probe: The static wave probe was placed near the wave-maker device. The static wave probe provides measurements of the wave height and wave period generated by the wave maker. This wave data was obtained prior to the carriage starting to move.

Load Cell for Resistance Measurement: A load cell was used for resistance measurement. A Marin No. 8 load cell was used which was calibrated each morning.

3.2.4 General Data Acquisition Systems onboard the Towing Tank Carriage

A/D Converter Cards: A National Instruments A/D converter card was installed in the PC device onboard the carriage. Sixteen channels can be recorded with a voltage from -10 to 10.
Signal Junction Box: The signal junction box collects all signals for inputting to the A/D converter. The signal speed is input from the control box directly, but generally most signals are sent from the filter and amplifier unit.

Filter and Amplifier Unit: The filter and amplifier unit from the Matronix were installed. Whereas the signal can be filtered by low-pass filters by setting the cut-off frequency, no filtering was used in these tests. Gain on the amplifier was determined by obtaining the maximum possible voltage according to the maximum loads or displacement. The signals processed at the filter and Amplifier Unit, were sent to the signal junction box.
LVDT Junction Box: The LVDT junction box collects the sensor signals from the LVDTs on the forward and aft tow posts, and the signal is sent to the filter and amplifier box.

Strain Gauge Signal-Conditioning Box: The signals from the load cell for resistance measurement are sent to the strain gauge signal-conditioning box. The signal-conditioning box has the amplifier gain and voltage zero balance indicator. The zero voltage was balanced before the calibration.

Wave Probes Signal-Conditioning Box : The wave probe sends the signal to the wave probe signal-conditioning box. On the signal-conditioning box, a balance dial with a level indicator is available to use for zeroing before experimentation. The signal-conditioning box also has the gain amplifier.

3.2.5 Data Acquisition Systems

The National Instrumentation CompactRIO (CRIO) system was used for data acquisition for the strain gauge measurement of the elastic links, as shown in Figure 3.4.

The CRIO embedded system has a processing unit of an industrial 200 MHz Pentium class processor, and a real-time processor and reconfigurable filed-programmable gate array (FPGA) were used for control and acquisition applications. The CRIO I/O module is a small module that is fitted into the chassis, but the CRIO I/O module functions as the signal conditioning, conversion circuitry, and direct connection to the CRIO chassis. The CRIO can perform as a stand-alone DAQ system, or it can be controlled through a 10/100 Mb/s ethernet cable to view the web server on the CRIO. An FTP server was equipped on the CRIO, so that file transfers to a laptop PC were carried out by the FTP.

Figure 3.3: Towing tank with carriage in foreground

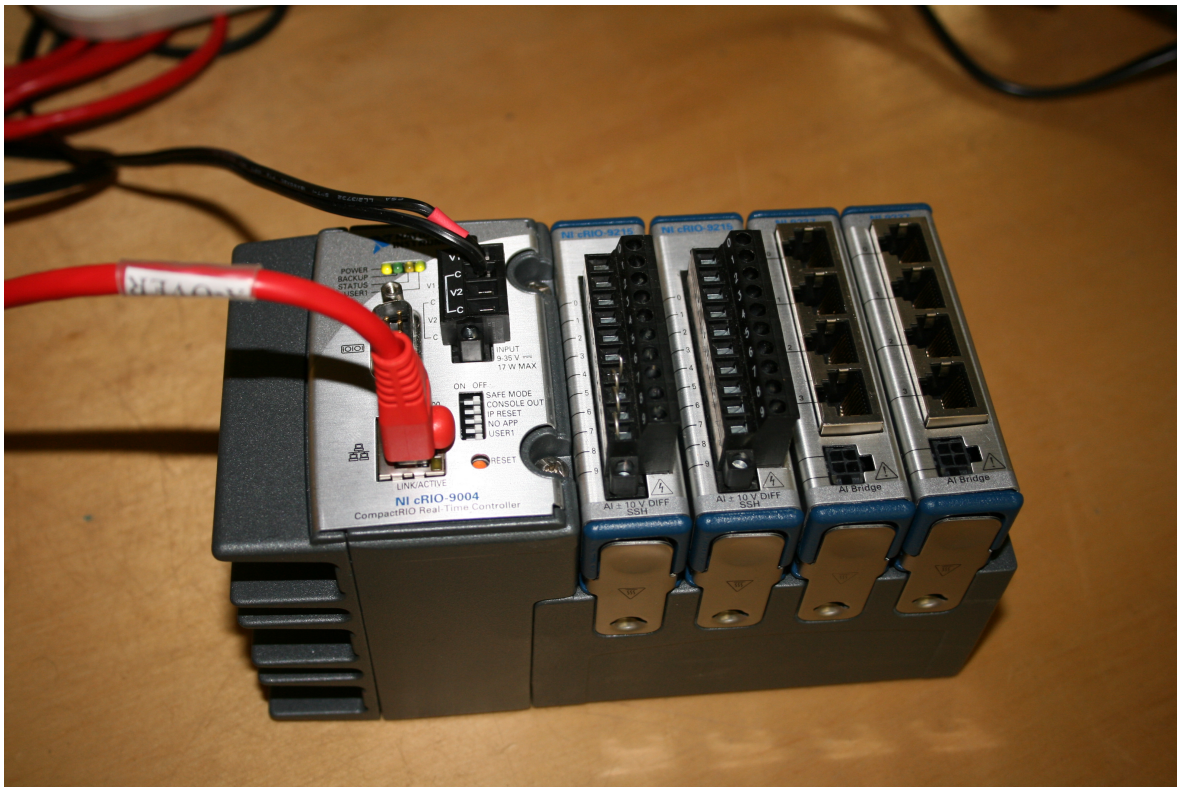

Figure 3.4: National Instrument, CRIO data acquisition device.

3.3 Experimental Phases and Conditions and Procedure of HSM

3.3.1 Experimental Phases

The experiments consisted of phases, conditions and runs. The different phases altered the settings of the segmented model. The changes to the model were relatively major and required several days of preparation. The varying conditions had different wave heights and model speeds with the same physical configuration of the hydroelastic segmentation model. Between each run, normally the wave frequency was changed. The run numbers were kept sequential throughout the entire set of experiments. Table 3.3 presents the phases for the experiments.

Table 3.3: Experimental phases

Phases	Test type	Hydroelasticity	Wave type	Forcus
Shake Down Phase	Resistance Seakeeping	Solid hollow link	Calm and Regular	Feasibility test of HSM
CWRPhase	Vibration and Resistance	Elastic link	Calm Water	Vibration with forward speed
HSM Phase 01	Seakeeping	Elastic link	Regular	Modal test
HSM Phase 02	Seakeeping	Elastic link	Regular	Seakeeping
HSM Phase 03	Seakeeping	Elastic link	Regular	Slamming load
HSM Phase 04	Seakeeping	Elastic link	Regular	Global wave load and speed
HSM Phase 05	Seakeeping	Elastic link	Irregular	Centrebow with pressure sensor

Firstly, the shake down phase was conducted to investigate the resistance and the seakeeping performance of the INCAT 112 m hydroelastic segmented model with a solid hollow link. The solid hollow link for the seakeeping test does not provide hydroelasticity, therefore it was a solid model. Comparing the results of the solid model to the results of the elastic-linked HSM, can determine the hydroelastic influence on the global ship motion. Therefore, the experimental data of the solid model is important for investigating the ship hydroelasticity contribution to the motions.

Next, the elastic link was installed in the model in the calm water vibratory resistance phase (CWR Phase) for the modal response test with ship hydroelasticity. The model was towed in calm water conditions, and the external impulse exciting force was applied to cause the modal response on the hydroelastic segmented model. It aimed to investigate types of modal behaviour and frequency in the different environmental conditions. Wet modal analysis, with and without forward velocity, and also the dry modal tests were conducted.

In the HSM Phase 01, seakeeping tests were conducted on the hydroelastic segmented model for the first time. Regular waves were selected to investigate the feasibility of the experimental

model withstanding the larger wave load. Calibration activities were also carried out to calibrate the strain gauges to known loads.

In the HSM Phase 02, the intention was to conduct seakeeping tests. Unfortunately, the CRIO data acquisition system for the strain gauges was compromised, therefore the experiment had to be cancelled. However, calibration data was obtained during this Phase before the incident occurred.

In the HSM Phase 03, larger regular waves were used for the seakeeping tests. Since slamming was expected to be the dominant wave loads, the acquisition of the slamming load data was the primary aim for the experiment. However, global wave loads still existed in larger wave conditions, so both slamming load and global wave load measurements were made to determine their characteristics.

In the HSM Phase 04, relatively smaller waves were selected to maintain the linearity assumption and the wave height was varied to investigate the motion and load linearity to the wave height. The forward velocity was varied to investigate the influence of velocity to the hydroelasticity.

In the HSM Phase 05, seakeeping tests with regular and irregular waves were conducted. A centre bow with pressure sensors was installed instead of the conventional centre bow segments, and as a result, the displacement of the segmented model was increased compared to the previous phases. In addition, the pressure sensors were installed on the centrebow. This phase was conducted by Chamberlin (2008) and the Author. Some results in irregular waves were presented by Chamberlin (2008), Winkler (2009), Thomas et al. (2009) and Thomas et al. (2010).

3.3.2 Experimental Conditions

Numerous conditions of the regular wave seakeeping tests were conducted and details are given in Table 3.4. The speed in the table indicates the equivalent full-size ship speed of the model during the experimentation, and the wave heights are indicated in the model scale. The capital letter C in the table stands for 'Condition'. This notation appears in many figures in the experimental results.

The wave heights were selected according to the expected slamming loads and global wave loads. For the global wave loads, relatively smaller wave heights were chosen as 20, 30 and 40 mm with an increment of 10 mm. These wave heights were expected to cause no slamming on the hydroelastic segmented model, so that effects of only the global wave loads would be measured. In addition, zero speed conditions were conducted for the lower range of wave heights.

For the wave range expecting the slamming loads, wave heights of 30, 60 and 90 mm were selected with increments of 30 mm. Only two speeds, 38 Kn and 20 Kn, were selected from service speeds of the INCAT 112 m class. The designed cruising speed is 38 Kn in normal

Table 3.4: List of phases and conditions for seakeeping tests for the design displacement in regular waves

Phase	**Link**	**Speed** (Kn)	**Wave Height** (mm)	**Completed Condition**	**Testing Run**
ShakeDownPhase	Solid Hollow Link	38	30	C09	-
			60	C12	-
			90	C13	-
		20	30	C08	-
			60	C11	-
			90	Not Conducted	-
HSM Phase01	Elastic Link	38	30	C20	-
			60	C25	C21
			90	-	C22
		20	30	C19	C16,C18
			60	-	-
			90	-	-
HSM Phase03	Elastic Link	38	30	-	-
			60	-	-
			90	C33	-
		20	30	-	-
			60	C27	-
			90	C30	
			120	C35	-
HSM Phase04	Elastic Link	0	20	C49	-
			30	C50	-
			40	C51	-
		20	20	C42	-
			30	C36	-
			40	C43	-
		30	20	C39	-
			30	C40	-
			40	C41	-
		38	20	C37	-
			30	-	-
			40	C38	-
		45	20	C44	-
			30	C47	-
		50	20	C45	-
			30	C46	-

conditions, and a reduced speed of 20 Kn for severe conditions.

In order to visualise the relationship of the selected environmental values for the many conditions, an experimental condition matrix is shown in Table 3.5. All the conditions in Table 3.5 utilised the same elastic link into the demi-hull backbone beam and into the forward transverse beam (FTB) configuration.

Table 3.5: Experimental variable matrix for the HSM

Wave height(mm)							
	120		C35				
	90		C30		C33		
	60		C27		C25		
	40	C51	C43	C41	C38		
	30	C50	C19, C36	C40	C20	C47	C46
	20	C49	C42	C39	C37	C44	C45
		0	**20**	**30**	**38**	**45**	**50**
		Speed (Kn)					

3.3.3 Experimental Procedure

The first step was was turning on the main power for the carriage drive. Under these circumstances, zero recording commences for first 5 seconds to produce the reference data for the moving data and the static data. system. Zero data recording was required for both these DAQ systems.

Then the wave maker was started. Once the fully developed waves started passing the static wave probe near the wave-maker device, the static recording was commenced for 10 seconds. This provided the data for the wave height.

The train waves took several seconds to reach the model. Once the wave arrived at the appropriate location, the carriage start switch was activated and the moving data recordings commenced on both the DAQ systems. When the carriage had travelled to the end of the towing tank near the wave-maker device, the carriage was stopped. The wave dissipation beaches were deployed to accelerate the damping of the wave in the towing tank.

3.4 The Model Setups

The model displacement was set to 27.42 kg, equivalent to the design displacement of the full-size ship of 2500 *tonnes*. The detailed mass and mass moment of inertia are presented in Figure C.1 in Appendix C. The ballast was set to achieve the level trim at the stationary position at the LCG of 948 mm from the transom wall of the model.

The trim tab angle was set for 7 degrees, after a series of resistance tests to determine the velocity and trim effects, as described in Subsection 2.4.7. For the elastic links between the segments, the types of the links were selected accordingly to Table 3.4.

3.4.1 Calibrations of the Measurement Devices

The LVTDs, wave probes, and resistance load cell were calibrated every morning. The wave probe calibration was conducted in absolute calm water conditions before the model was launched and disturbed the water surface.

The calibration of the strain gauges on the elastic links was important to obtain the vertical bending moment and resultant force of the slamming loads. The strain gauges were calibrated using many methods to increase the confidence in the measurement mechanism of the VBM and the resultant force of the slamming loads.

3.5 Elastic Links Calibrations

3.5.1 Strain Gauge calibration

The calibrations were conducted on the elastic link strain gauges on the demi-hull for measuring the vertical bending moment, and on the centre bow for measuring the slamming force and location. Calibrations on the strain gauges of the elastic links were conducted before and after each phase of experimentation. The hydroelastic segmented model had eight elastic links with strain gauges, and these are detailed in Table 3.6.

Table 3.6: Strain gauge location and signal channel number for elastic links

Channel No.	Segmentation Cut	Longitudinal position	Side
CH09	Demihull	Fwd	Port
CH10	Demihull	Aft	Port
CH11	Demihull	Fwd	Starboard
CH12	Demihull	Aft	Starboard
CH13	Centrebow	Fwd	Port
CH14	Centrebow	Aft	Port
CH15	Centrebow	Fwd	Starboard
CH16	Centrebow	Aft	Starboard

The methods of calibration were differentiated in terms of how the experimental model was supported. Two different calibration methods for the vertical bending moment were used for emulating the hogging and sagging conditions. For the hogging condition, a 'model-support cradle' method was utilised for a cantilever-type calibration. For the sagging condition, a 'multipurpose frame' hanging method was adopted. The calibration method for the centre bow was conducted using a 'benchtop' method.

The types of calibration were also varied in terms of the calibration jig and loading point distance from the strain gauges. For the vertical bending moment on the demi-hull, the first method used was a direct loading cable type, and the second method adopted an even-distribution loading bar and rods type. For the slamming loads on the centre bow, the centre bow calibration mould type was selected. The centre bow calibration mould was a centre bow female mould shape, which could be mounted on the centre bow when the model was upside down on the even-level benchtop.

The model-support cradle was used to calibrate the elastic links at the forward segmentation cuts and aft segmentation cuts of the demi-hulls. When the hydroelastic segmented model was supported at the mid segments and aft segments, the forward segmented was loaded with known weights. Similarly, when the aft segmented was loaded, the model was supported by the forward segments and mid segments. Further details are given in Subsection 3.5.2

The multipurpose frame was used to hang the model by steel wire cables either at the mid segments or at the forward and aft segments. The four steel-wire cables held the model at several

locations depending on the loading points. When the model was supported at the mid segments, the loadings were made in two ways; on the forward segment only; on both forward segments and the mid segments. It emulated the model being subjected to the hogging situation. The model was also hung from the forward and aft segments in order to load the calibration weights at the mid segments. This emulated the model being subjected to the sagging situation. Further details are given in Subsection 3.5.3

For the sign convention of the moment, the hogging vertical bending moment is defined as a positive moment. The sagging vertical bending moment is defined as a negative moment. This convention was used in Hughes (1998). For the slamming force, the positive force is defined to act upwards and the force causes the sagging vertical bending moment.

3.5.2 Strain Gauges Calibration for VBM by Hogging

The strain gauges on the elastic link at the demi-hull segmentation cut measured the vertical bending moment, and it was calibrated by two methods, a model-support cradle method and a multipurpose frame hanging method.

The schematic diagram for the model-support cradle is presented in Figure 3.5. The segmented model was placed on the model-support cradle. The demi-hull segments with the elastic links that were to be calibrated, were set to be free from the cradle constraint, so that the calibration on the strain gauges could be conducted.

The applied calibration force, F_c, was acting at a distance, l_{xf}, from a forward elastic link on the demi-hull. The applied force, $F_c l_{xf}$, generated an applied vertical bending moment at the elastic link. Therefore the vertical bending moment representing the hogging can be expressed as follows:

$$M_{Hf} = F_c l_{xf} \tag{3.1}$$

where M_{Hf} is the vertical bending moment of the forward elastic link at the forward segment gap of the demi-hull. Similarly, for the aft demi-hull segment gap the applied vertical bending moment, M_{H_a}, can be calculated as follows:

$$M_{Ha} = F_c l_{xa} \tag{3.2}$$

The strain gauges of the elastic link provides the strain ϵ_i, and it is calibrated to the known vertical bending moment:

$$M_{Hf} = C_{EL_i} \epsilon_i \tag{3.3}$$

$$M_{Ha} = C_{EL_i} \epsilon_i \tag{3.4}$$

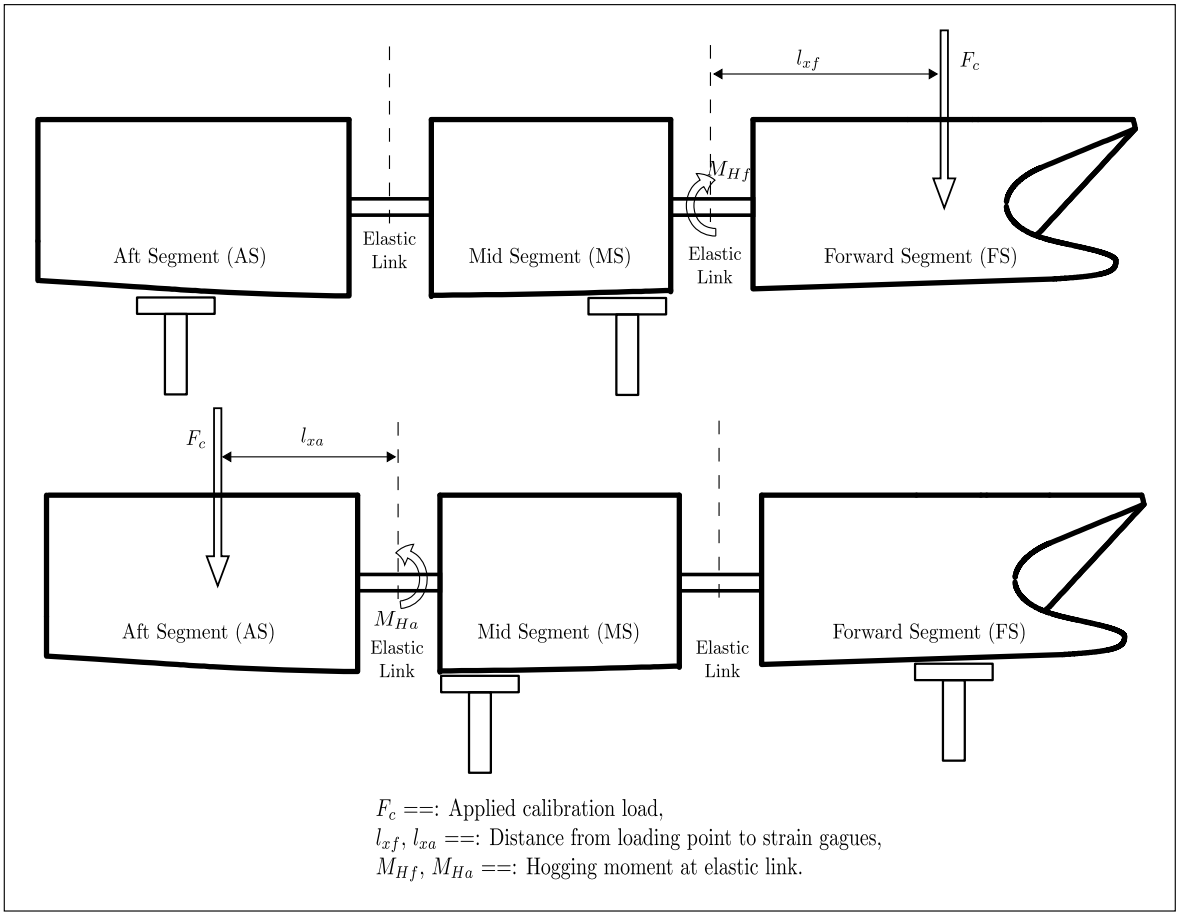

Figure 3.5: Calibration schematic diagram for the strain gauges on the elastic link on the demi-hull segment gap under hogging.

where the i is for ith channel of recorded data signals. The location of the elastic link and corresponding channel of the data signal are listed in Table 3.6. The calibration factors were obtained from the least-square method by fitting the linear regression line to the applied moment against the measured microstrain. Many sets of calibration were conducted to increase confidence in the calibration factors.

In order to obtain reliable calibration factors, several different types of jig were tested as follows:

1. Jig Type - 1: Direct loading cables and calibration weight boxes. Applying the calibration loads simultaneously on both demi-hulls.

2. Jig Type - 2: Even-distribution loading bar and rods. Applying the calibration loads simultaneously on both demi-hulls.

3. Jig Type - 3: Direct loading cable and calibration weight box. Applying the calibration loads on one side of the demi-hull only.

An advantage of Jig Type - 1 is that the calibration can proceed at any hook point on the model, however, the transverse alignment of applied load to the demi-hull centre-line is rather difficult, except for applying the calibration loads on the wave-piercer bow and transom stern

gunwale. In order to overcome this uneven distribution of calibration loads onto the model, Jig Type - 2 (the even-distribution loading bar and rods) was developed. The rod mounts can be precisely placed on the backbone beam on both demi-hulls, and the sharp rod edge supports the angled section loading bar that is equipped with a hanging calibration box at both ends. The angled section loading bar transversely crosses over the model. This system can apply the calibration load onto both the port and starboard demi-hulls, and a significant improvement of controlling the applied load position is a clear advantage to improve the repeatability of the calibration loading condition. Jig Type - 3 is similar to Jig Type-1 but loading only occurs on one side of the demi-hull. An advantage of Jig Type - 3 is that it produces a calibration result which can experimentally identify the structural mechanism consisting of the backbone beams, forward transverse beams and elastic sealing.

Using the above jigs, different loading positions were chosen to ensure the reliability of the strain gauges response on the elastic links. The loading positions were varied and are listed in Table 3.7, according to jig type.

Table 3.7: Loading position for strain gauge calibration on the demi-hull.

Loading segment [1]	Jig type [2]	Arm lever length [3] (m)	Load applied location
DHFS	Jig Type - 1	0.736	Wave piecer bow, centre line
DHFS	Jig Type - 2	0.185	Backbone beam
DHFS	Jig Type - 2	0.281	Backbone beam
DHFS	Jig Type - 2	0.41	Backbone beam
DHFS	Jig Type - 3	0.736	Wave piecer bow, centre line
DHAS	Jig Type - 1	0.83	Transom stern gunwale
DHAS	Jig Type - 2	0.105	Backbone beam
DHAS	Jig Type - 2	0.205	Backbone beam
DHAS	Jig Type - 2	0.305	Backbone beam
DHAS	Jig Type - 2	0.385	Backbone beam
DHAS	Jig Type - 3	0.83	Transom stern gunwale

[1] DHFS indicates the demihull forward segment.
DHAS indicates the demihull aft segment.
[2] Jig Type - 1 indicates direct loading cables and calibration weight box.
Jig Type - 2 indicates even distribution loading bar and rod.
Jig Type - 3 indicates direct loading cable (oneside demi-hull only).
[3] Length measured from the centre of the strain gauge and the applied load position for calibration.

The calibration factors for the bending moment can be affected by the distance between the loading point and the strain gauge location if the system or mechanism is not adopted correctly. In order to visualise the dominant influence of the arm distance to the calibration factors, the calibration factors are plotted against the arm distance in Figure 3.6 for the calibration case of the demi-hull aft segments.

It was found that the arm distance did not show a clear linear influence on the calibration factor. The calibration factor was rather scattered around its own mean values. Therefore the mean value of the calibration factors, that were selected from the suitable methods, were successfully

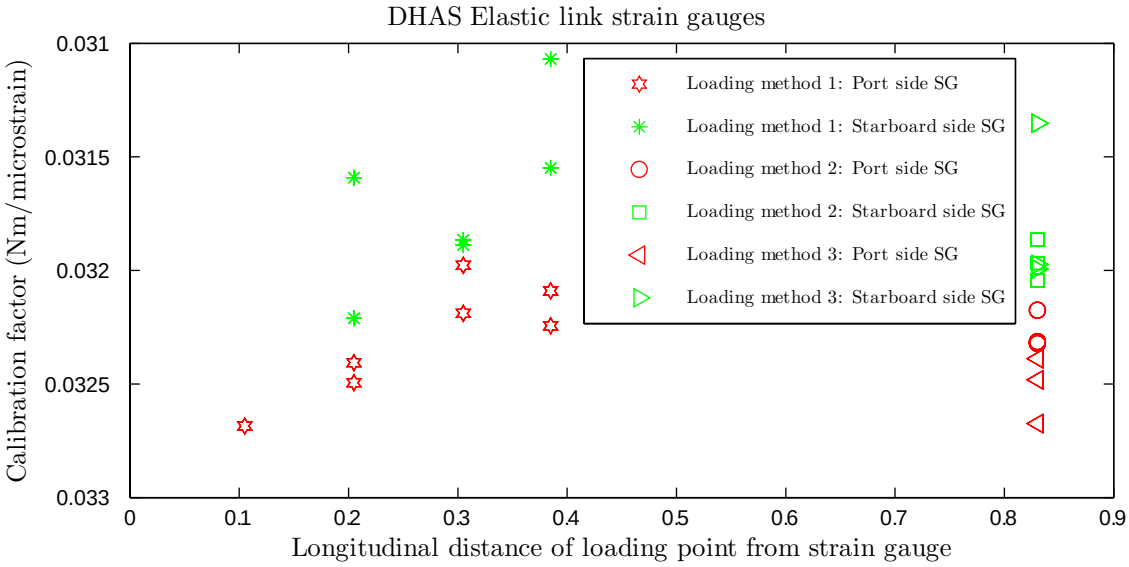

Figure 3.6: Calibration factors for elastic link strain gauges at DHAS.

obtained for the experiments.

The starboard and port side simultaneous loading method for the strain gauge calibration used an even-distribution loading bar and rods. The two rods, that were vertically placed on the backbone beams at the centre lines of both the starboard and port side demi-hulls, have a pointed edge which supports the even-distribution bar. The even-distribution bar was made of an angle bar with the cable attachment points at both ends of the bar. The calibration mass were hang from the cable attachment point. Therefore, this mechanism allowed the weight load to distribute evenly and accurately to the starboard and port side demi-hulls. The centre-line of the even-distribution loading bar was aligned to the centre-line of the experimental model, not to the demi-hull centre-line.

The calibration factors obtained for the elastic link at the forward segmentation cut on each demi-hull are presented in Table 3.8. The mean values of the calibration factors, standard deviation, and coefficient of variation were calculated for Ch09 and Ch11, respectively, at the port side demi-hull forward segment cut and at the starboard side demi-hull forward segmentation cut.

The results are very cosnsitent for both methods, Ch09 and Ch11. Two different methods resulting in similar results ensures the reliability of the calibration methods at the forward segment cut. The normalised relative error to the mean value of calibration factor, which can be described as the coefficient of variation, for the even-distribution loading bar and rods jig were $-1.6511e^{-02}$ for Ch11; therefore the error associated with this calibration factor can be considered as -1.65%.

Similarly, for the elastic link at the aft segmentation cut on each demi-hull, the calibration factors are shown in Table 3.9. The results also indicate that the two methods provided very

Table 3.8: Averaged calibration factors of elastic links at the forward segment demihull cuts

Calibration loading jig type	Segmentation cut sealing	Calibration factors		Standard deviation		Coefficient of variance	
$(Unit)$		CH09 $(\frac{Nm}{\mu strain})$	CH11 $(\frac{Nm}{\mu strain})$	CH09	CH11	CH09	CH11
Direct loading cables	Rubber sheet	-0.03095	-0.03087	1.8502E-04	4.5654E-04	-5.9788E-03	-1.4791E-02
Even distribution loading bar and rods	Rubber sheet	-0.03113	-0.03087	1.1676E-04	5.0964E-04	-3.7512E-03	-1.6511E-02

close calibration factors to each other. This indicates that the methods of calibration were valid for the elastic links at the aft segmentation cut as well. The maximum coefficient of variance was $-2.1697e^{-02}$ for Ch12 using the even-distribution loading bar and rods jig; hence, the error related to this calibration factor can be considered as -2.16%.

Table 3.9: Averaged calibration factors of elastic links at the aft segment demihull cuts on the demihull.

Calibration loading jig type	Segmentation cut sealing	Calibration factors		Standard deviation		Coefficient of variance	
$(Unit)$		CH10 $(\frac{Nm}{\mu strain})$	CH12 $(\frac{Nm}{\mu strain})$	CH10	CH12	CH10	CH12
Direct loading cables	Rubber sheet	-0.03227	-0.03196	7.8102E-05	8.5440E-05	-2.4203E-03	-2.6733E-03
Even distribution loading bar and rods	Rubber sheet	-0.03230	-0.03192	2.4315E-04	6.9261E-04	-7.5286E-03	-2.1697E-02

The interference of loading one side of the demi-hull utilising the direct loading cable jig was investigated and the results are compared in Table 3.10.
The values of the calibration factors for Ch10 and Ch12 at the aft segmentat cut were all close to each other. The asymmetric loading calibration also resulted in similar values to the symmetric loading. This indicated that the load applied at one side of the demi-hull did not affect the other side of the elastic links at the aft segmentation cuts. It also suggests that the rubber sealing did not transmit loads between each side of the demi-hull to significantly cause a large deviation in the calibration factors.

However, calibration factors for Ch09 and Ch11 at the forward segment cuts produced an interesting result. The asymmetric loading using the direct loading cable jig produced calibration factors which were higher than those from the other two symmetrical loading methods. The different results signify that the applied load at one side of a demi-hull transmitted to the other side of the demi-hull. Therefore, the calibration factors should not be used for calculating the measured load of the strain gauges. This result led to other calibration tests to ensure the summation of the measured moments for the elastic links at both starboard and port side forward

Table 3.10: Influence of calibration mechanism to the calibration factors of elastic links at the aft segmentation cuts on the demihull.

Calibration loading jig type	Segmentation cut sealing	Calibration factors			
(Segmentation cut location) (Channel Number) (*Unit*)		Port DHFS CH09 ($\frac{Nm}{\mu strain}$)	Stb. DHFS CH11 ($\frac{Nm}{\mu strain}$)	Port DHAS CH10 ($\frac{Nm}{\mu strain}$)	Stb. DHAS CH12 ($\frac{Nm}{\mu strain}$)
Direct loading cables (both demi-hulls)	Rubber sheet	-0.03095	-0.03087	-0.03227	-0.03196
Even-distribution loading bar and rods	Rubber sheet	-0.03113	-0.03087	-0.03230	-0.03192
Direct loading cable (one side of demi-hull only)	Rubber sheet	-0.03704	-0.03818	-0.03251	-0.03177

segment cuts of the demi-hull were equal to the applied loads at the centre bow. The results are shown in Subsection 3.5.3.

3.5.3 Strain Gauge Calibration for VBM by Sagging

The sagging condition was also repsresnted in the calibration by using a calibration frame. The model was hung from the calibration frame. A schematic diagram for this method is shown in Figure 3.7. The model was hanged by four thin steel wires attached on each forward and aft demi-hull segment. Calibration load was applied at seven different locations on the mid demi-hull segments using the mechanism of even-distribution loading bar and rods. This method was selected since it was found to be the most reliable method in the previous calibrations of the hogging conditions.
Calibration schematic diagram for the strain gauges on the elastic link on the demi-hull segmentation gap under hogging emulation.

$$M_{pa} = F_c l_{xc} - T_f l_T \tag{3.5}$$

Since the summed moment at the aft pin joint is zero, the following equation can be obtained:

$$F_c l_{xc} - T_f l_T = 0 \tag{3.6}$$

$$T_f = \frac{F_c l_{xc}}{l_T} \tag{3.7}$$

To establish a moment equation calculated about the forward pin joint:

$$M_{pf} = T_a l_T - F_c \left(l_T - l_{xc}\right) \tag{3.8}$$

When there is no moment acting on the forward pin joint:

$$T_a l_T - F_c \left(l_T - l_{xc}\right) = 0 \tag{3.9}$$

$$T_a = \frac{F_c \times \left(l_T - l_{xc}\right)}{l_T} \tag{3.10}$$

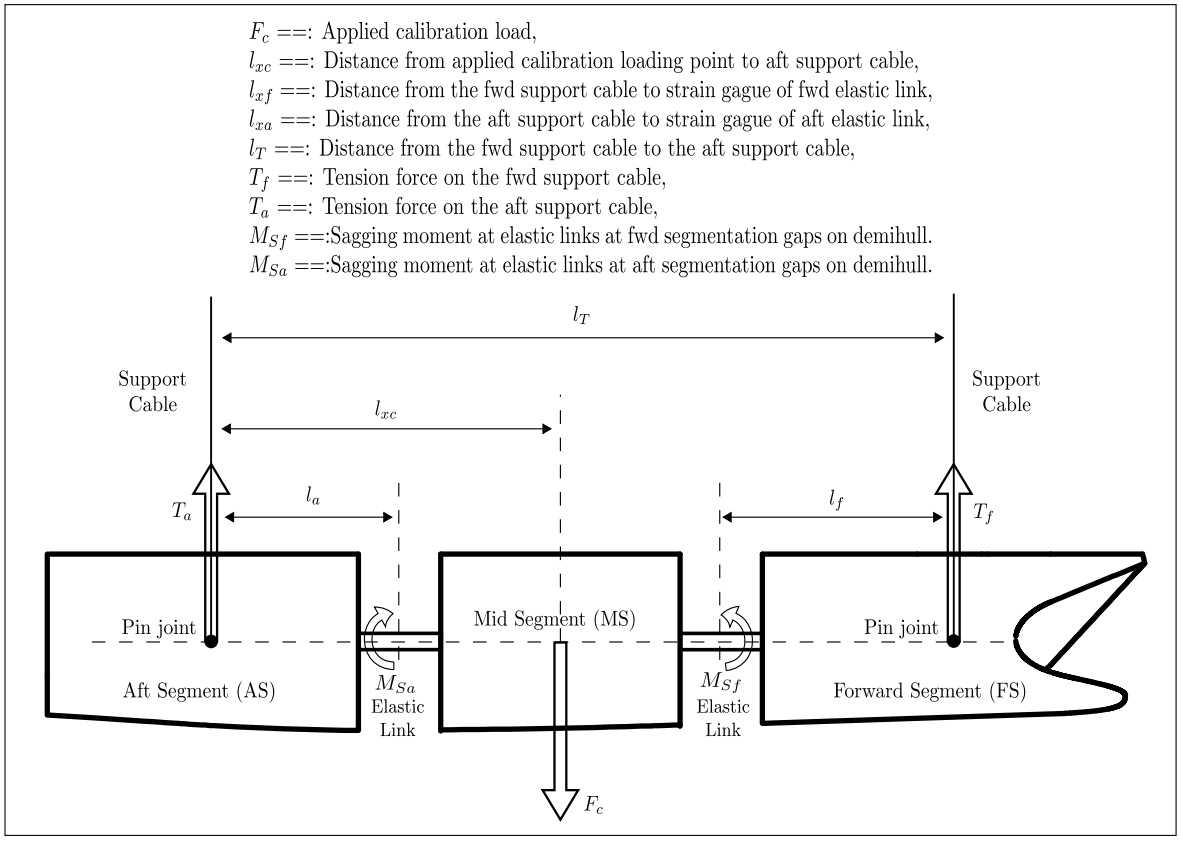

Figure 3.7: Calibration schematic diagram for strain gagues of elastic link on demihull segment gap under hogging

Next, calculating the moments at the elastic links are as follows:

$$M_{Sf} = T_f l_f \tag{3.11}$$

$$M_{Sa} = T_{fa} l_a \tag{3.12}$$

The strain of the elastic link can be obtained from the strain gauges of the elastic link, introducing the calibration factor to calculate the vertical bending moment. The following equation can be obtained for the forward and aft elastic links respectively:

$$M_{Sf} = C_{EL_{CH09}} \epsilon_{CH09} + C_{EL_{CH11}} \epsilon_{CH11} \tag{3.13}$$

$$M_{Sa} = C_{EL_{CH10}} \epsilon_{CH10} + C_{EL_{CH12}} \epsilon_{CH12} \tag{3.14}$$

Substituting Equations 3.7, 3.10, 3.13, and 3.14 into Equations 3.11 and 3.12, the following relationship can be obtained for calibration:

$$C_{EL_{CH09}} \epsilon_{CH09} + C_{EL_{CH11}} \epsilon_{CH11} = \frac{F_c l_{xc}}{l_T} l_a \tag{3.15}$$

$$C_{EL_{CH10}} \epsilon_{CH10} + C_{EL_{CH12}} \epsilon_{CH12} = \frac{F_c \left(l_T - l_{xc}\right)}{l_T} l_a \tag{3.16}$$

Calibration factors were obtained by using a least-square method. The calibration of the strain gauges of the elastic link at the demi-hull segments by the sagging method are presented in Table 3.11. Seven different loading positions on the demi-hull backbone beams were selected.

Table 3.11: Calibration factors of elastic links at the demihull segmentation cuts by sagging method. Calibration load were applied onto the both mid segments by even distribution loading bar and rods.

		Calibration factors			
(Elastic link position) (Channel number) (Unit)	Loading position (m)	Port DHFS CH09 ($\frac{Nm}{\mu strain}$)	Stb. DHFS CH11 ($\frac{Nm}{\mu strain}$)	Port DHAS CH10 ($\frac{Nm}{\mu strain}$)	Stb. DHAS CH12 ($\frac{Nm}{\mu strain}$)
Calibration factor	-0.141	0.03054	0.03176	0.03237	0.03221
	0.141	0.03117	0.03173	0.03141	0.03259
	-0.087	0.03108	0.03167	0.03220	0.03191
	0.087	0.03126	0.03149	0.03214	0.03216
	-0.041	0.03077	0.03162	0.03180	0.03279
	0.041	0.03148	0.03177	0.03149	0.03195
	0.000	0.03107	0.03170	0.03179	0.03215
Averaged calibration factor	-	0.03105	0.03168	0.03189	0.03225
Standard deviation	-	3.1189E-04	9.9906E-05	3.6479E-04	3.2424E-04
Coefficient of variation	-	1.0044E-02	3.1539E-03	1.1440E-02	1.0054E-02

The calibration factors showed consistent results, and the maximum coefficient of variation was $1.1440e^{-02}$. Even though the loading locations were changed along the backbone beam, similar calibration factors were successfully obtained indicating that the vertical bending moment was not influenced by the loading position.

The calibrations obtained by the different methods of hogging and sagging resulted in similar calibration factors. Hence, it is possible to use one signal calibration factor for each channel catering for both hogging and sagging. The standard deviations and coefficient of variations were calculated from each calibration. These calibration factors in Table 3.12 were used in the load calculation for the experimental data.

Table 3.12: Calibration factors of elastic links at the demihull segmentation cut.

(Elastic link position) (Channel number) (Unit)	Port DHFS CH09 ($\frac{Nm}{\mu strain}$)	Stb. DHFS CH11 ($\frac{Nm}{\mu strain}$)	Port DHAS CH10 ($\frac{Nm}{\mu strain}$)	Stb. DHAS CH12 ($\frac{Nm}{\mu strain}$)
Averaged calibration factor	0.03104	0.03130	0.03212	0.03206
Standard deviation	2.4658E-04	5.0957E-04	3.3932E-04	4.9598E-04
Coefficient of variation	7.9429E-03	1.6278E-02	1.0563E-02	1.5469E-02

The maximum coefficient of variance was $1.6278e^{-02}$ for Ch11 on average. Hence, the error related to this calibration factor can be considered as 1.63%.

The assurance calibration test was conducted by deploying the direct loading cable jig at the

centre bow tip. The applied loads at the centre bow tip were compared to the measured loads on both elastic links at both sides of the forward segmentation cuts. The summation of the measured loads were obtained to compare with the applied loads in Figure3.8, showing a clear linear relationship to the applied mass. Importantly, the summation of measured vertical bending moments from the strain gauges matched with the applied load at the centre bow. This showed that the forward transverse beam successfully transmitted the load from the centre bow to both the demi-hull segmentation cuts. It increased the confidence in measuring VBM loads at the forward segmentation cuts with the forward demi-hull elastic links capturing the load from the centre bow.

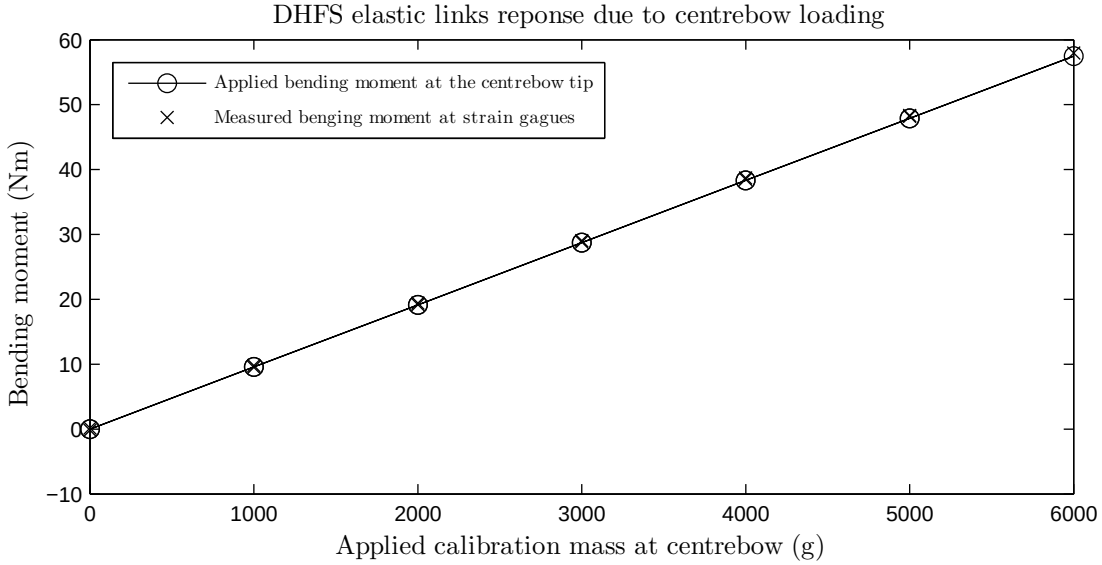

Figure 3.8: Comparison between the applied bending moment and measured bending moment at the strain gauges of the elastic links at the forward demi-hull segmentation gap.

3.5.4 Calibration for Slam-Induced Force and Location on the Centre bow

Initially, the individual calibration of each strain gauge of the elastic link was conducted, and the assembled calibrations were conducted in order to observe the integrated effects of the elastic link and mechanism of the centre bow arrangement. The schematic diagram of the centre bow is shown in Figure 3.9.

The slamming load distributed onto the centre bow is transmitted through the forward and aft FTBs to both the starboard and port demi-hulls. The moments are measured at the elastic links on the FTB. The moments are converted into vertical forces acting on each of the FTBs. The vertical forces are then combined to obtain the total slamming force and location.

For the calibration of the centrebow, the model was placed upside down on a level workbench. Two placement methods were carried out: Firstly, the demi-hull forward segment, demi-hull mid segment, and demi-hull aft segment were constrained and supported by the workbench for the free condition on the centre bow segment, so that both the CBS was not constrained. Secondly,

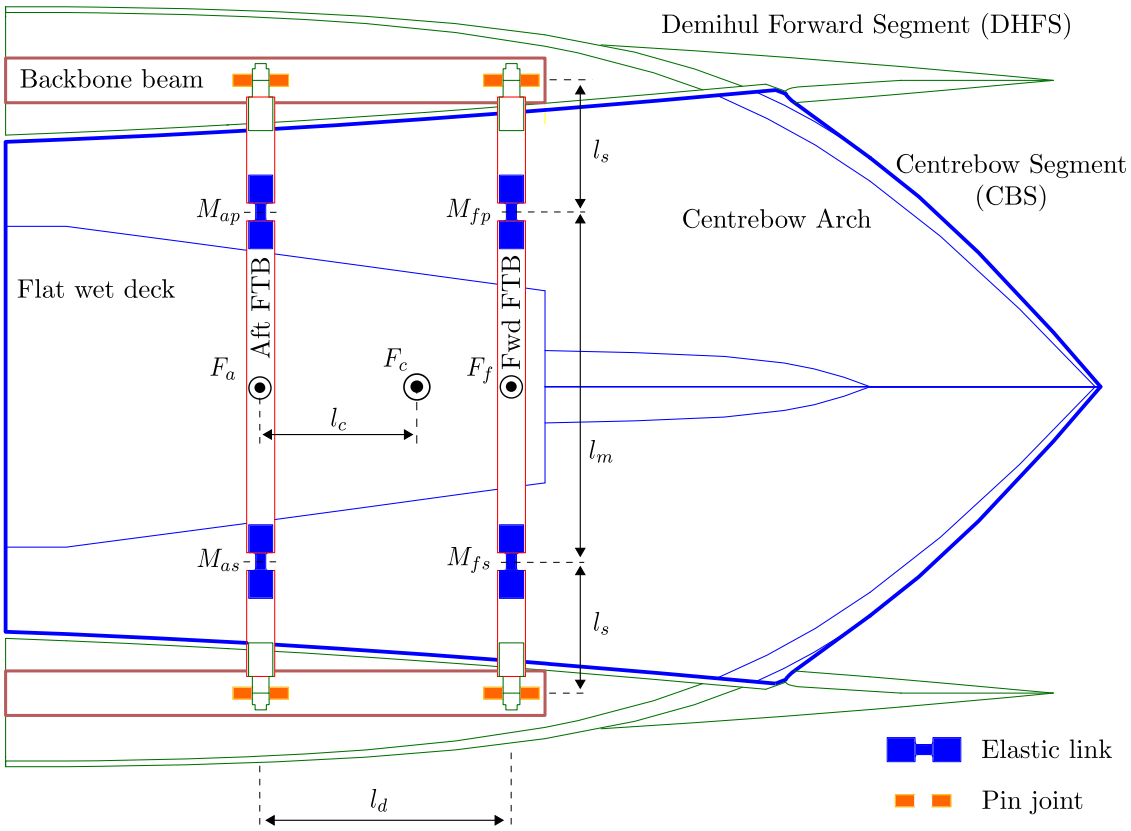

Figure 3.9: Calibration schematic diagram for strain gauges of elastic link on centrebow segmentation.

the demi-hull mid segments and demi-hull aft segments were supported by the workbench for the free condition on the centre bow segment and demi-hull forward segments, so that the centre bow segment and demi-hull forward segments were free to move. The centre bow mount was used for applying calibration loads, since the centre bow shape did not have a flat region.

The calibration and slamming force calculation equations were developed as follows, and the force diagram is presented in Figure 3.10.
The reaction force at the forward port pin joint can be expressed as:

$$R_{fp} = -\frac{M_{fp}}{l_s} \tag{3.17}$$

The vertical force equilibrium of the port forward FTB is:

$$R_{fp} = V_{fp} \tag{3.18}$$

Taking a moment equilibrium on the mid segment of the FTB about the starboard side elastic link is calculated as:

$$\frac{F_f l_m}{2} + V_{fp} l_m + M_{fs} - M_{fp} = 0 \tag{3.19}$$

Substituting Equations 3.17 and 3.18 into Equation 3.19, and simplifying the equation, the force on the forward FTB can be calculated as follows:

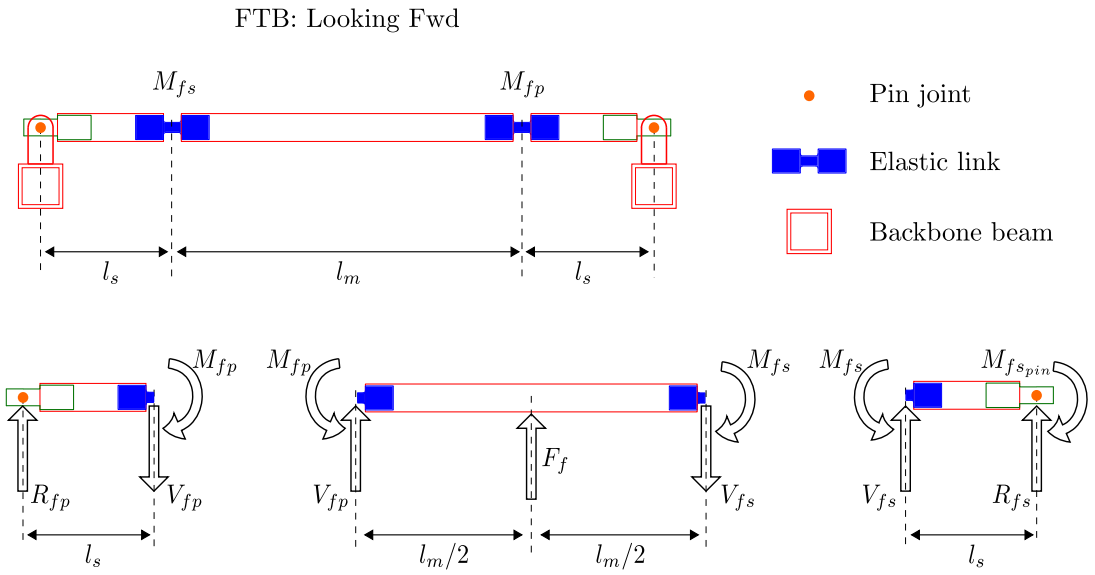

Figure 3.10: Forces diagram for loads acting on the forward FTBs on the centrebow for centrebow mount calibration. The subscript $_f$ is replaced with $_a$ for the aft FTB.

$$F_f = \frac{2M_{fp}}{l_s} + \frac{2\left(M_{fp} - M_{fs}\right)}{l_m} \tag{3.20}$$

Similarly, the force acting on the aft FTB can be calculated as:

$$F_a = \frac{2M_{ap}}{l_s} + \frac{2\left(M_{ap} - M_{as}\right)}{l_m} \tag{3.21}$$

The moment at the elastic link can be calculated with individual calibration factors:

$$M_{fp} = C_{EL_{CH13}} \epsilon_{CH13} \tag{3.22}$$

$$M_{ap} = C_{EL_{CH14}} \epsilon_{CH14} \tag{3.23}$$

$$M_{fs} = C_{EL_{CH15}} \epsilon_{CH15} \tag{3.24}$$

$$M_{as} = C_{EL_{CH16}} \epsilon_{CH16} \tag{3.25}$$

Finally, the total force on the centre bow can be calculated as:

$$F_c = F_f + F_a \tag{3.26}$$

Once the total force is calculated, then the force acting position of the total force can be calculated as:

$$l_c = \frac{F_f l_d}{F_c} \tag{3.27}$$

Due to the structural mechanics, the measured data and applied data experience slight discrepancies. Applied component forces at the forward FTB and aft FTB can be calculated from the applied total force as follows:

$$F_{f_{Applied}} = \frac{F_{c_{Applied}} l_{c_{Applied}}}{l_d} \tag{3.28}$$

$$F_{a_{Applied}} = \frac{F_{c_{Applied}} \left(l_d - l_{c_{Applied}} \right)}{l_d} \tag{3.29}$$

The difference between the applied loads and measured loads on each FTB are calculated as follows:

$$F_{f_{Diff}} = F_{f_{Applied}} - F_f \tag{3.30}$$

$$F_{a_{Diff}} = F_{a_{Applied}} - F_a \tag{3.31}$$

For convenience, this load difference is called the insufficient force, $F_{f_{Diff}}$ and $F_{a_{Diff}}$. The insufficient force was found to be a function of the applied force or measured force at each FTB. The results indicated a strong linearity between the insufficient load and applied load and measured load at the FTB, as shown in Figures 3.11, 3.12, 3.13, and 3.14. The least-square method was used to obtain an individual correction factor to the measured load. The individual correction factor and measured loads gives the calculated insufficient force. Summation of the calculated insufficient force and the measured loads provide the adjusted loads in Figures 3.11, 3.12, 3.13, and 3.14. The adjusted loads were calculated by the individual correction factor of the individual calibration set, not the correction factor calculated by a general method which can be valid for all the calibrations. The adjusted loads corresponded with the theoretical loads. This led to seeking a generalised method for an empirical formula of the correction factor.

In order to obtain the generalised method of the correction factors, the trend in the individual correction factors were investigated. The individual correction factor was found to be constant throughout a set of the individual calibrations. Therefore, the individual correction factors were calculated for all the calibration data sets. Then, the individual correction factors were plotted against the measured distance in Figure 3.15. This shows a linear trend of the individual correction factor with respect to the measured distance. To generalise the individual correction factor, an empirical equation of the correction factors to calculate a residual force were obtained by the least-square method as follows:

$$\Delta F_f = C_{f_{correction}} l_c \tag{3.32}$$

$$\Delta F_a = C_{a_{correction}} l_c \tag{3.33}$$

The correction factors of the empirical formula are plotted in Figure 3.15. Now, the measured corrected loads can be expressed by the measured loads and residual forces as follows:

$$F_{f_{Meas.Corrected}} = F_f + \Delta F_f \tag{3.34}$$

$$F_{a_{Meas.Corrected}} = F_a + \Delta F_a \tag{3.35}$$

The residual forces were calculated by the correction factor by the empirical formula, not by the individual calibration factor. Similar to Equation 3.26, the measured corrected total force is calculated as follows:

$$F_{c_{Meas.Corrected}} = F_{f_{Meas.Corrected}} + F_{a_{Meas.Corrected}} \tag{3.36}$$

Also the calculated distance for the measured corrected loading position can be calculated as follows:

$$l_{c_{Meas.Corrected}} = \frac{F_{f_{Meas.Corrected}} l_d}{F_{c_{Meas.Corrected}}} \tag{3.37}$$

Prior to the above integrated calibration on the centre bow, the individual calibration of elastic links was carried out utilising the calibration arm that had a loading distance of 0.2 m and 0.3 m. The calibration factor of the individual elastic links were obtained to convert the measured microstrain of the strain gauge to the bending moment at the elastic link. One end of the elastic link was clamped onto a horizontal level workbench, and the other end was inserted into the calibration bar made from an aluminium square hollow section. The calibration factors obtained for this individual calibration method obviously neglected the effects of the centre bow structural mechanism or latex sealing. The average calibration factors for Ch13 to 16 were calculated with standard deviations and coefficients of variation, and presented in Table 3.13.

Table 3.13: Calibration factors of elastic links on the centre bow segmentation.

		Calibration factors			
(Elastic link position) (Channel number) (Unit)	Loading arm (m)	Port Fwd CH13 $(\frac{Nm}{\mu strain})$	Stb. Fwd CH15 $(\frac{Nm}{\mu strain})$	Port Aft CH14 $(\frac{Nm}{\mu strain})$	Stb. Aft CH16 $(\frac{Nm}{\mu strain})$
Calibration factor	0.2 0.3	-0.0060397 -0.0060235	-0.0059723 -0.0059616	-0.0060518 -0.0060476	-0.0060589 -0.0060242
Averaged calibration factor	-	-0.0060316	-0.0059669	-0.0060497	-0.0060415
Standard deviation	-	1.1512E-05	7.6038E-06	2.9147E-06	2.4504E-05
Coefficient of variation	-	-1.9086E-03	-1.2743E-03	-4.8180E-04	-4.0559E-03

The calibration factors resulted in values which were very close for Ch13, Ch14, Ch15, and Ch16. The coefficients of variation were also small such that the maximum coefficient of variation among the four channels was $-4.0559x10^{-03}$. Hence, the mean error in the calibration factor was 0.41%. Therefore, the calibration factors could accurately provide the measured bending moment at each location.

The Figure 3.11 to 3.14 show examples of the loading effect on aft and forward FTB. The measured values were obtained by Equations 3.20 and 3.21 for the forward and aft FTBs, respectively.

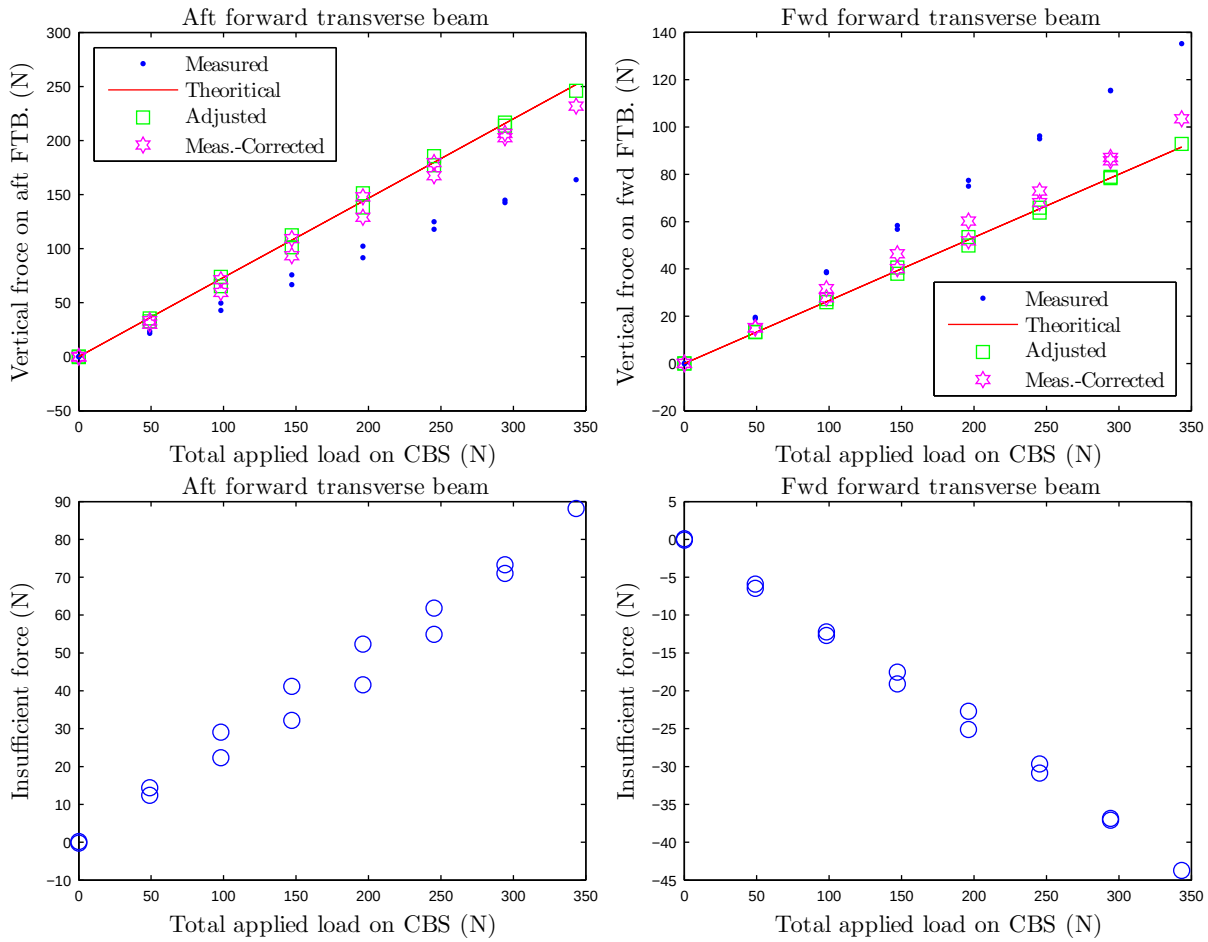

Figure 3.11: Example of calibration data for vertical forces on the forward transverse beams. The calibration load was applied at 1.707m from T. Phase 3, Calib. No.7.

The correction factors for residual forces between the measured forces and theoretical forces on individual forward and aft FTBs are presented in Figure 3.15.

After the loads on the forward FTB and aft FTB were measured and corrected by the correction factor obtained by the empirical formula, the total measured load with correction can be calculated. The total load with the correction indicated a closer match to the theoretical values than the total load without the correction during the calibration. The improvement in the correction factors for the total measured loads are shown in Figure 3.16.

The corrected measured loading positions for the corrected measured forces and the measured force are presented in Figure 3.17. The corrected measured loading position was improved compared with the measured loading position. Generally, the measured loading position was further towards the aft FTB than the applied loading point calibration. However, the correction factor for the residual forces successfully brought the measured loading position back to the expected loading position, as with the applied loads position.

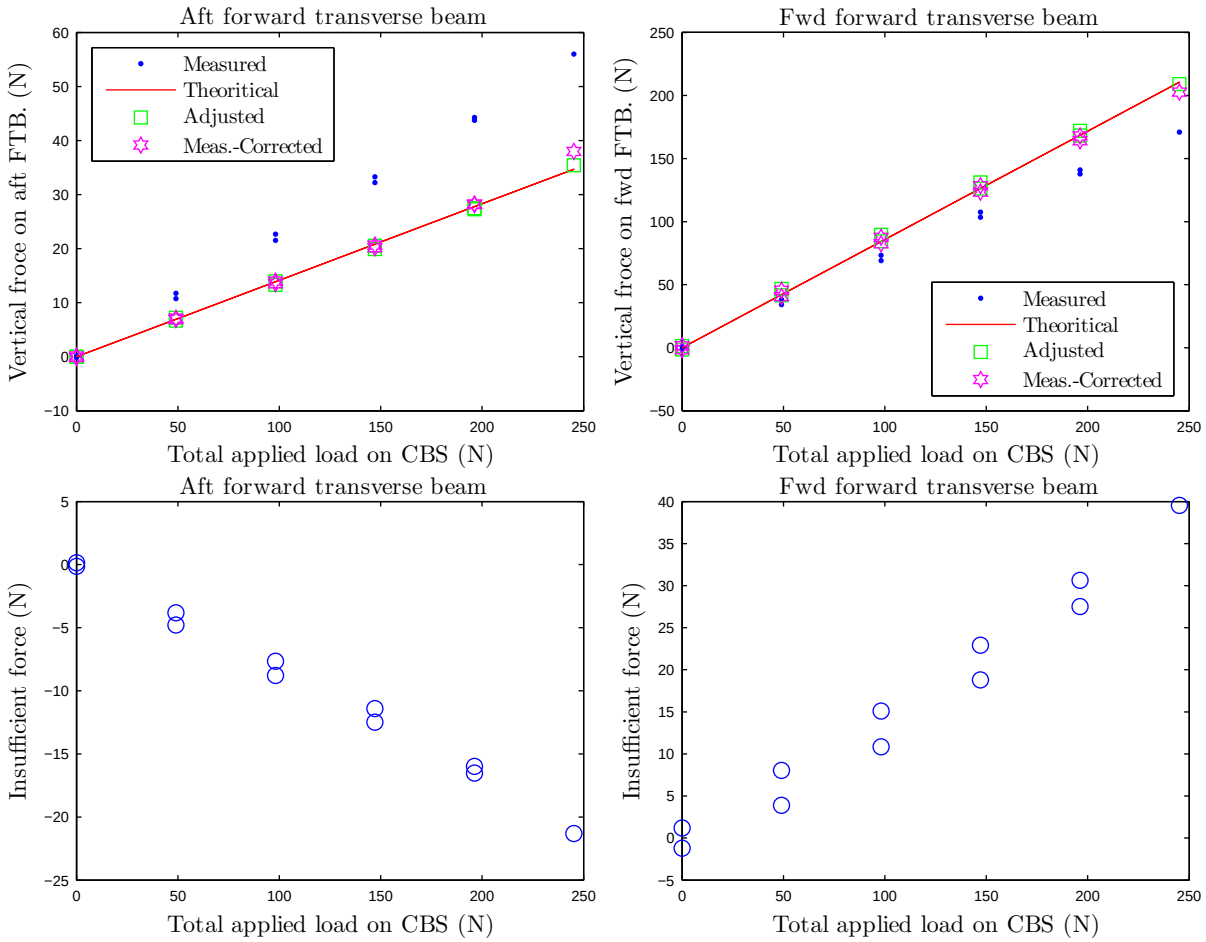

Figure 3.12: Example of calibration data for vertical forces on the forward transverse beams. The calibration load was applied at 1.84m from T. Phase 3, Calib. No.17.

The linear correction factor was required to compensate the discrepancy between the measured and expected values due to the load measurement mechanism of the centrebow and the forward transverse beam. The forward transverse beam is supported by the pin joints where small moments about the transverse axis of the model were inevitably generated.

Based on Equations 3.32 and 3.33, the following empirical formulas were obtained for the residual force calculations:

$$\Delta F_f = 3.6391 l_c - 0.4762 \tag{3.38}$$

$$\Delta F_a = -4.5463 l_c + 0.6901 \tag{3.39}$$

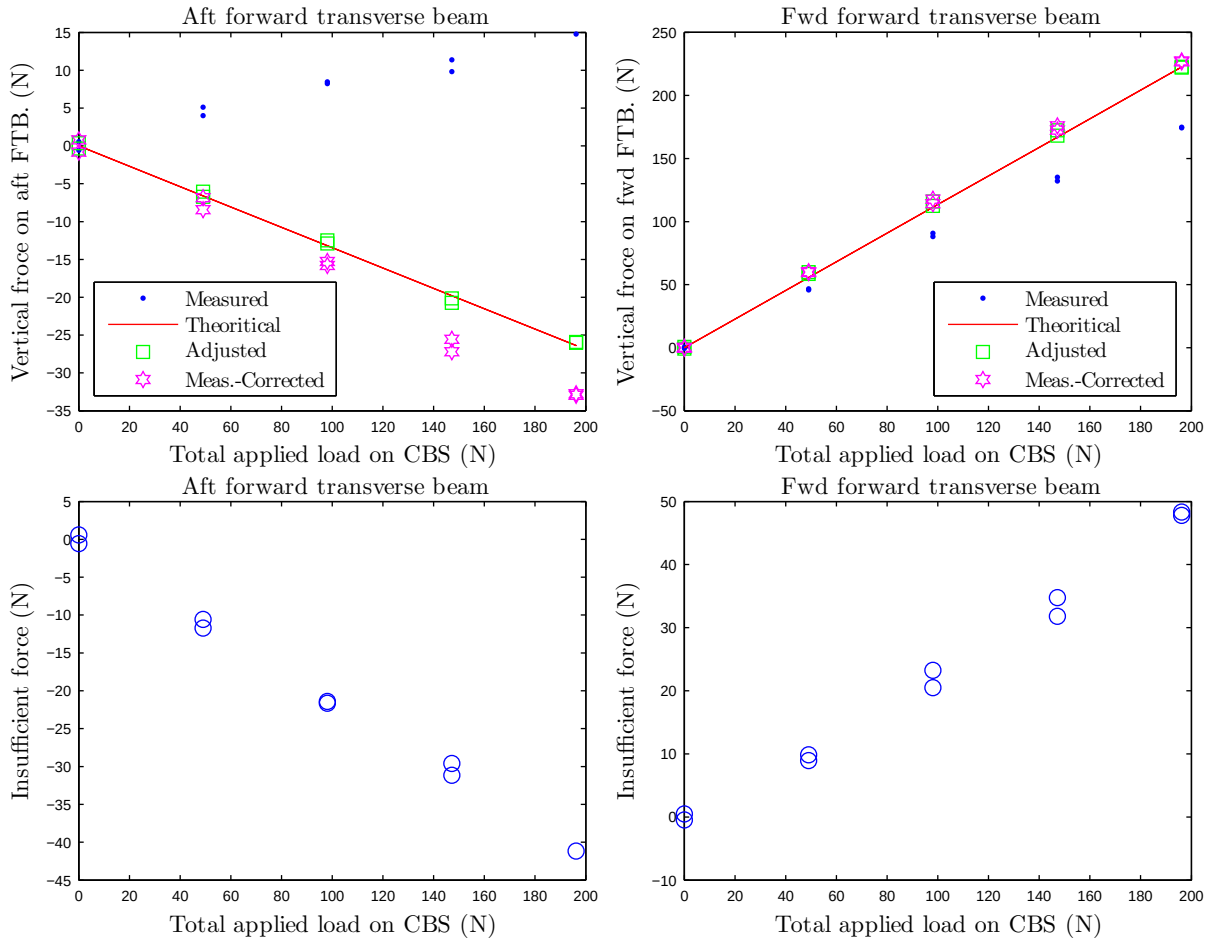

Figure 3.13: Example of calibration data for vertical forces on the forward transverse beams. The calibration load was applied at 1.902m from T. Phase 4, Calib. No.9.

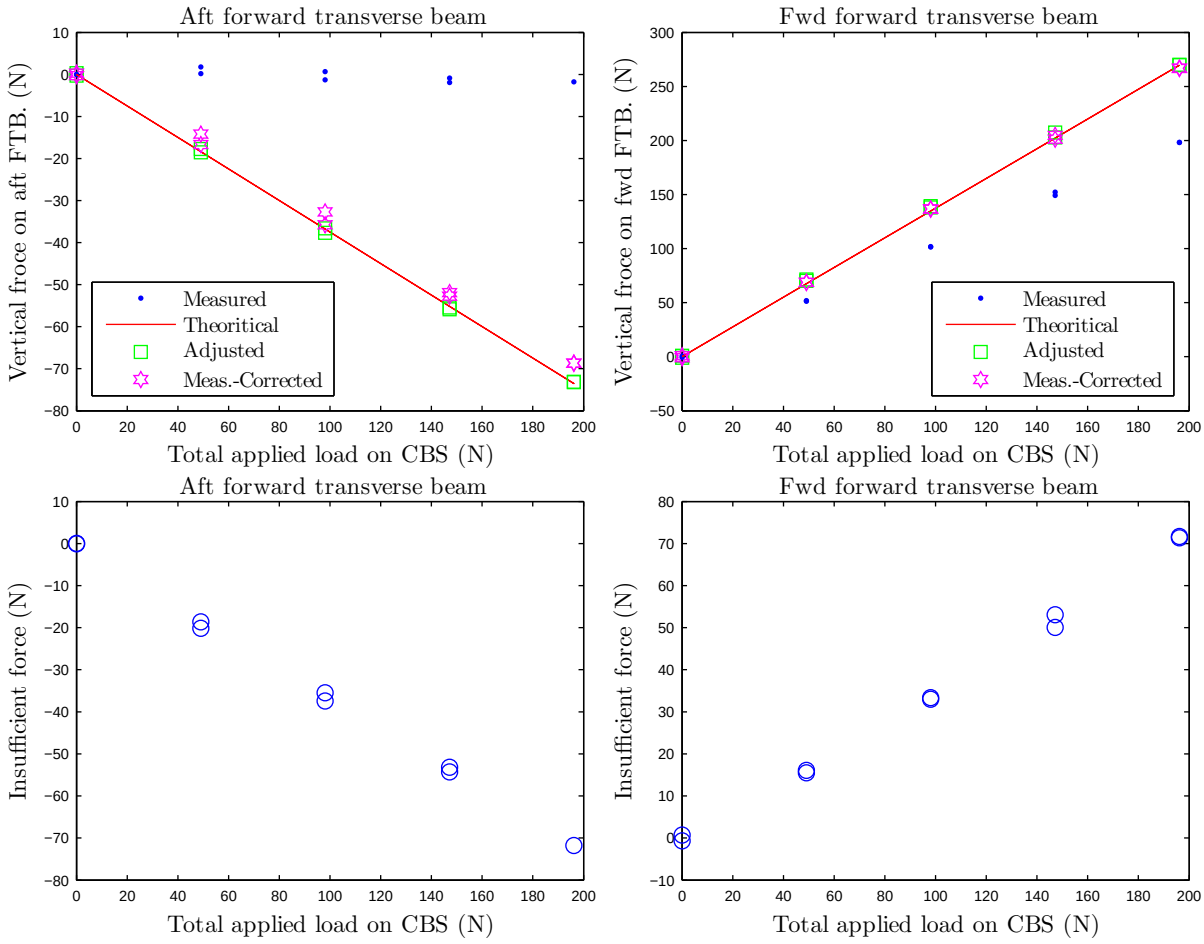

Figure 3.14: Example of calibration data for vertical forces on the forward transverse beams. The calibration load was applied at 1.956m from T. Phase 4, Calib. No.13.

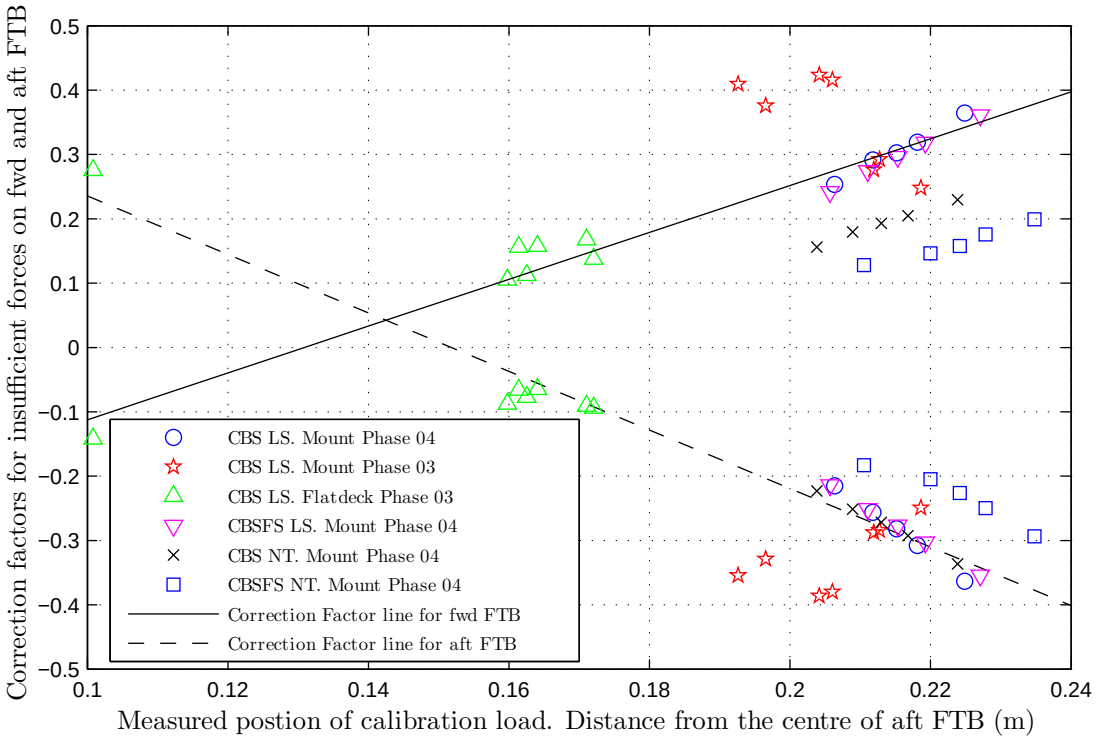

Figure 3.15: Relationship between correction factors and calibration load positions

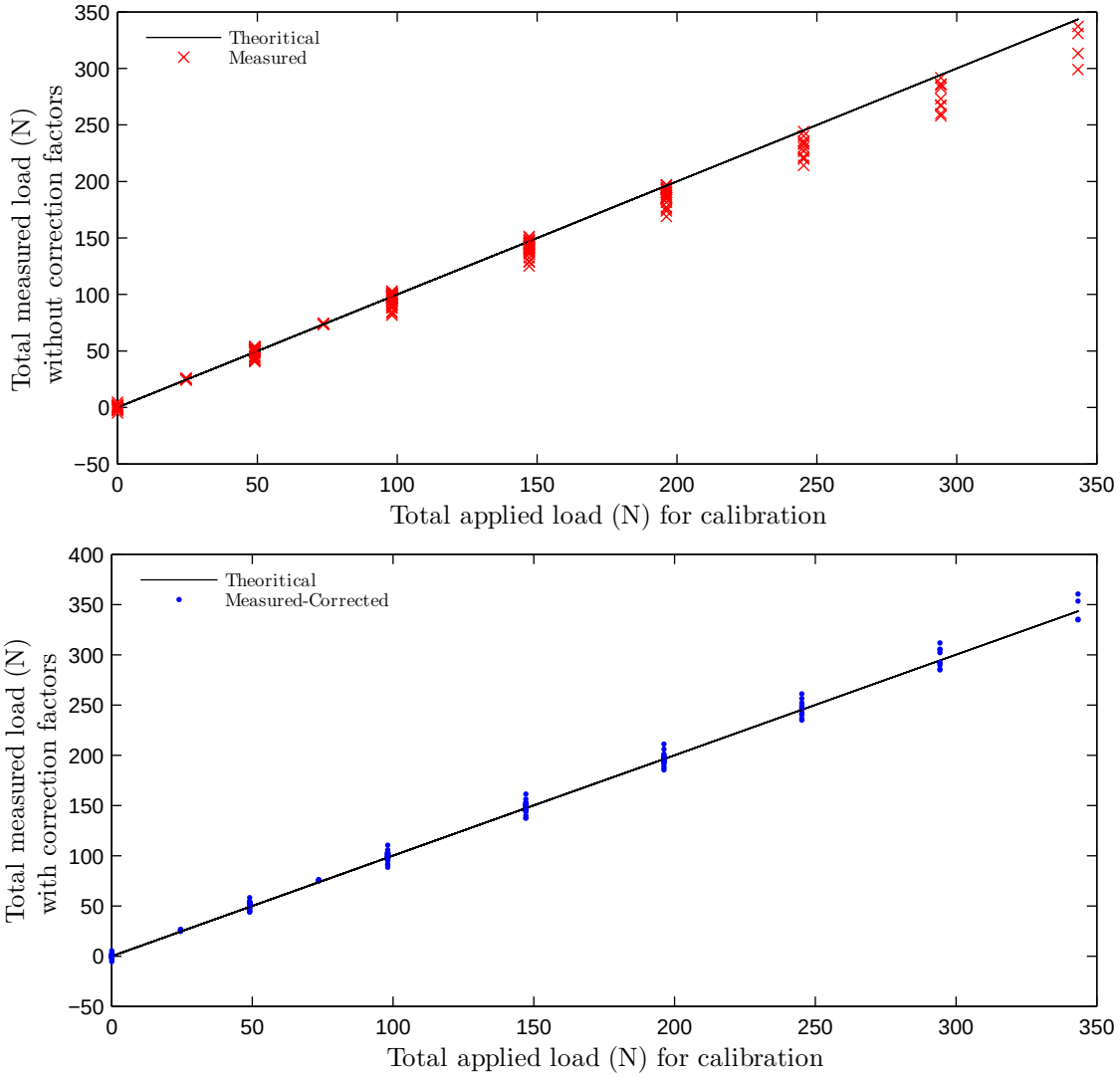

Figure 3.16: Total measured load improved by correction factors on the measured loads of forward FTB and aft FTB.

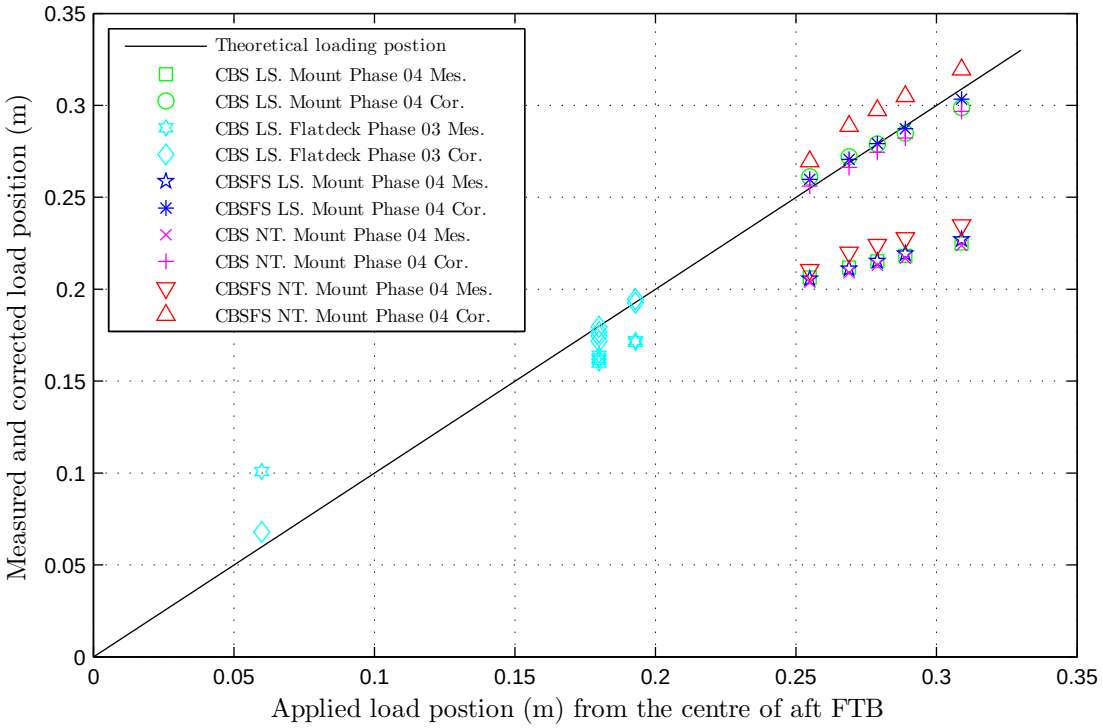

Figure 3.17: Comparison between measured load position and corrected load position for calibration load. Loading distance was measured from the centre of the aft FTB.

Table 3.14: Summary of model mass and details

Particulars	Mass	CG @ Local coordinate system			Mass moment of inertia		Radius of gyration	
		LCG	TCG	VCG	Pitch	Yaw	Pitch	Yaw
$(Unit)$ / Segments	(kg)	(m)	(m)	(m)	$(kg \cdot m^2)$	$(kg \cdot m^2)$	(m)	(m)
Forward Segments	6.939	0.3509	0.0030	0.1518	0.269598	0.583074	0.197113	0.289880
Mid Segments	11.956	0.1086	-0.0008	0.1784	1.019209	1.348975	0.291975	0.335905
Aft Segments	8.526	0.2540	-0.0028	0.1018	0.619631	1.265685	0.269587	0.385297
Total mass	27.420							
Reference coordinate frame		Zero @ local transom	Zero @ vessel centre-line	Zero @ base line	Local CG	Local CG	Local CG	Local CG

3.6 Modal Tests

The vibratory frequency of the HSM varies with different environments depending on whether it is under the influence of added-mass and hydrostatic restoring forces.

3.6.1 Particulars for the Mechanical Dynamics System and Calculated Results

The mechanical dynamics system, presented in Section 2.3.6, requires the input of particulars of the hydroelastic segmented model in order to simulate the vibratory response frequency and modal shape. In order to input the particulars, measurement of the mass distribution of the experimental model is required. The mass of the assembled segments and each individual component were measured, and the mass moment of inertia obtained by the bifilar method. Some component data were based on the Rhino Model data in order to obtain the detailed mass distribution, where the physical measurement was not feasible or practical.

The radius of gyration for the forward segment, the mid segment and the aft segment were calculated about the centre of the gravity of each segment, after the mass moment of inertia for the individual components was calculated for each segment. The results were presented in Table 3.14.

Table 3.15 shows the set of input values based on the mass distribution shown in Table C.1 for the mechanical dynamics system. The components of the starboard side and port side were combined for each corresponding segment. The length of the segment included half of the segmentation gap (10 mm).

The stiffness of the individual elastic link at the demi-hull was calculated as 12378 Nm/rad provided by theoretical stiffness of one elastic link. The starboard and port side of the stiffness needs to be summed to become 2×12378 Nm/rad. Therefore, the mechanical dynamics system for the hydroelastic segmented model assumed that the starboard and port side were treated as

Table 3.15: Input for the mechanical dynamics system

	Location	Symbols	Units	Input values
Mass	Mid Segment	m_1	kg	11.956
	Forward Segment	m_2	kg	6.939
	Aft Segment	m_3	kg	8.526
Length of segment	MS: Fwd length from LCG	l_{1f}	m	0.470
	MS: Aft length from LCG	l_{1a}	m	0.114
	FS: Fwd length from LCG	l_{2f}	m	0.588
	FS: Aft length from LCG	l_{2a}	m	0.356
	AS: Fwd length from LCG	l_{3f}	m	0.576
	AS: Aft length from LCG	l_{3a}	m	0.254
Radius of gyration	Mid Segment	r_{21}	m	0.291975
	Forward Segment	r_{22}	m	0.197113
	Aft Segment	r_{23}	m	0.269587
Stiffness of elastic link	Fwd Segmentation Cut	k_2	Nm/rad	2 x 12378
	Aft Segmentation Cut	k_3	Nm/rad	2 x 12378

one rigid body.

After inputting the mass distribution data from Table 3.15 into Equation 2.23, the determinant of the matrix can be found, and the natural frequency was obtained by finding the root of the characteristic equation obtained from the determinant matrix. The determinant in Equation 2.26 was plotted against the frequency in Figure 3.18.

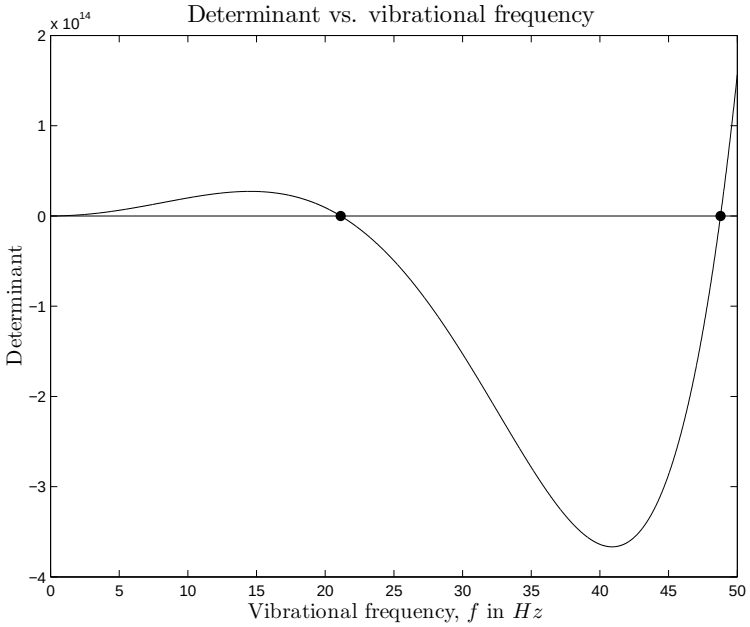

Figure 3.18: Natural frequency identification by the determinant of characteristic equations of the mechanical dynamics system.

The natural frequency of the first mode for the dry mode obtained by the mechanical dynamics system did not include any hydrodynamic influences, therefore this vibrational response frequency is recognised as a natural frequency of the hydroelastic segmented model that vibrates

in air. The results showed the first mode of the natural frequency, 22.02 Hz as the dry mode base on the theoretical stiffness of the elastic link. Holloway et al.(2006) used the effective stiffness method on elastic link. The effective stiffness was reduced from theoretical stiffness: 2 $\times$ 6321 Nm/rad for the froward elastic link; 2 $\times$ 8136 Nm/rad for the aft elastic link. The natural frequency based on the effective stiffness were 17.36 Hz.

Table 3.16: Dry mode results calculated by the mechanical dynamics system

	Respond natural frequency	
$(Unit)$ / Mode	(Hz)	
	1_{st} mode	2_{nd} mode
Dry Mode (Theoretical stiffness)	22.02	53.71
Dry Mode (Effective stiffness)	17.36	39.46

3.6.2 Modal Frequency Test in Dry Condition

The modal test for the dry mode was conducted by an impulse test. The model was hung in the multipurpose frame by elastic tension cables at four attached points on the backbone beam at the centre-line of the demi-hulls. The impact force was applied to different positions of the hull surface of the HSM. Due to the impact excitation, the HSM was vibrated at the resonance frequency of the demi-hull. The resonance frequency appears on the vertical bending moment of the demi-hull as a natural frequency of the fundamental mode. The resonance frequency can be diagnosed by spectral analysis, so power spectral density (PSD) of the VBM of all the elastic links on the demi-hull was obtained. The FFT method was used on the tapered VBM data in the time domain by the Hamming windows for the PSD. A summary of the resonance frequency of the elastic links on the demi-hull by the impact excitation are presented in Table 3.17. Selected examples of the spectral analyses results by the PSD are shown in Figures 3.19, 3.20, and 3.21.

The impacts were applied to the hull of the CBS, demi-hull mid segment, and wave-piercer bow of the demi-hull forward segment. All the response frequencies of all four sensors for all cases were extremely close to the average values of resonance frequency of the VBM. The resonance frequency in air was 16.46 Hz for the dry mode. Although different locations of the impact excitation were applied, the resonance frequency remained in the same frequency. Hence, the resonance was a global response of the HSM. It showed that the hydroelastic segmented model could be excited to demonstrate the natural frequency of the VBM effectively. It also experimentally confirmed that the resonance was independent of the applied impact positions.

Table 3.17: Modal test frequency response for dry mode

Run No.	CH 09 (Hz)	CH 10 (Hz)	CH 11 (Hz)	CH 12 (Hz)	Impact method
4	16.451	16.451	16.451	16.451	Impact on CBS
5	16.414	16.503	16.414	16.503	Impact on CBS
6	16.475	16.475	16.475	16.475	Impact on CBS
7	16.454	16.454	16.454	16.454	Impact on CBS
8	16.477	16.477	16.477	16.477	Impact on CBS
9	16.469	16.469	16.469	16.469	Impact on CBS
10	16.462	16.462	16.462	16.462	Impact on CBS
11	16.419	16.419	16.419	16.419	Impact on CBS
12	16.475	16.475	16.475	16.475	Impact on CBS
13	16.432	16.432	16.520	16.520	Impact on port. MSDH bottom
14	16.447	16.447	16.447	16.447	Impact on port. MSDH bottom
15	16.473	16.473	16.473	16.473	Impact on FSDH wave piercer bow
16	16.507	16.507	16.507	16.507	Impact on MSDH bottom
17	16.465	16.465	16.465	16.465	Impact on stb. FSDH wavepiercer
18	16.475	16.475	16.475	16.475	Impact on stb. FSDH wavepiercer
19	16.473	16.473	16.473	16.473	Impact on CBS
Average	16.461	16.466	16.466	16.472	

Wavelet analysis was conducted on the vertical bending moment of the elastic links on the demi-hull, and are shown in Figures 3.22 and 3.23. The continuous wavelet transforms with the

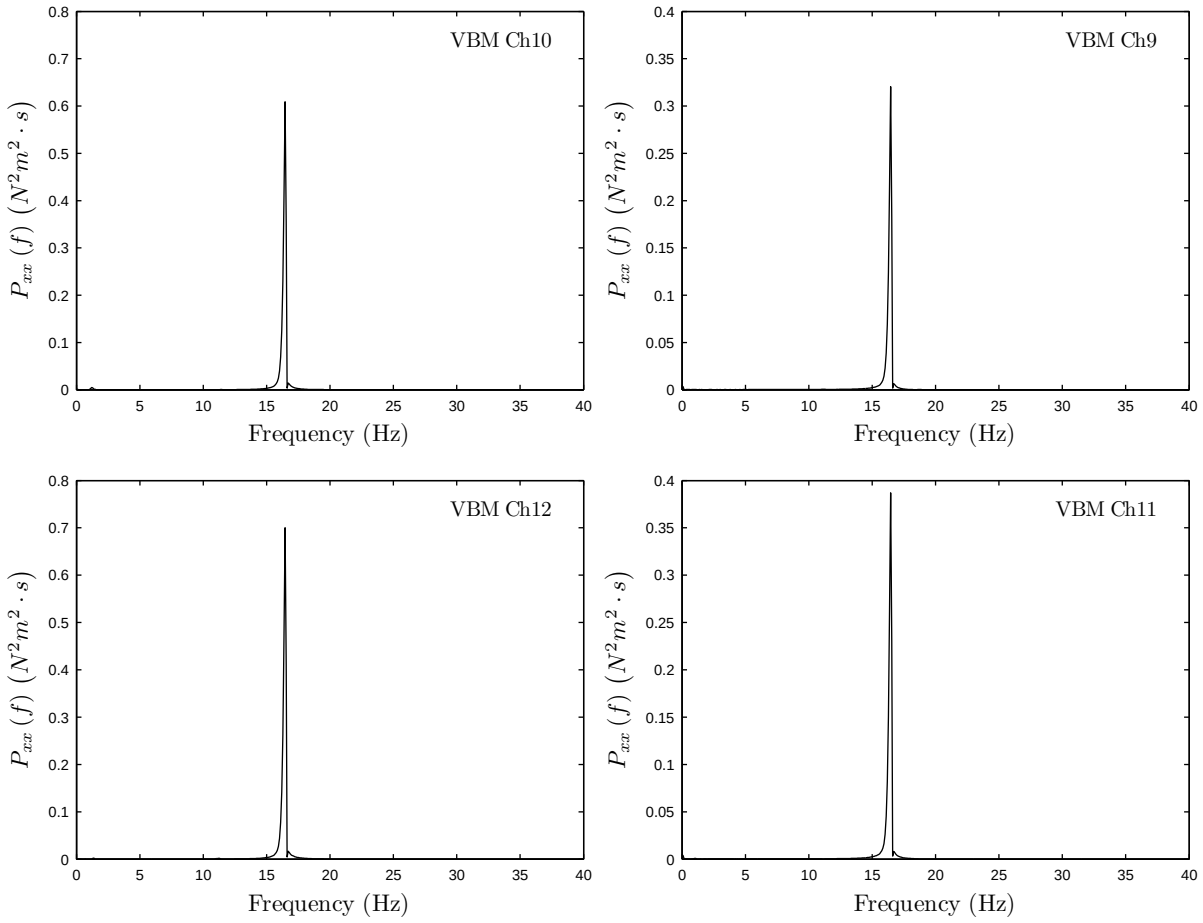

Figure 3.19: Modal analysis for dry mode. Power spectral density (PSD), $P_{xx}(f)$, for vertical bending moment (VBM) measured at the strain gauges at Ch9, Ch10, Ch11, and Ch12 in air. Dry mode Run No. 4. PSD was obtained by applying the Hamming window for data taper in the time domain, and no smoothing by a convolution in the frequency domain.

Morlet wavelet function were performed to investigate the VBM response at different positions of the elastic link with respect to the temporal domain and frequency domain. The frequency domain is equivalent to the *scalea* of the wavelet transform. The details of CWT are explained in Appendix E.

The wavelet results and the VBM magnitude were overlaid, the y-axis represents scale a. (A conversion of the scale a to the actual frequency can be referred to in Figure 3.35.) The colour at each $x-y$ point indicates the magnitude of the coefficient for the Morlet wavelet function.

For the case of applying the impact excitation on the CBS, the wavelet transform results showed the response of the coefficient for the Morlet wavelet function at scale $a = 10$, which is equivalent to 16.4 Hz based on the conversion by Figure 3.35. This frequency also matched with the response peak frequency of the PSD in Figure 3.19. It confirmed that the continuous wavelet

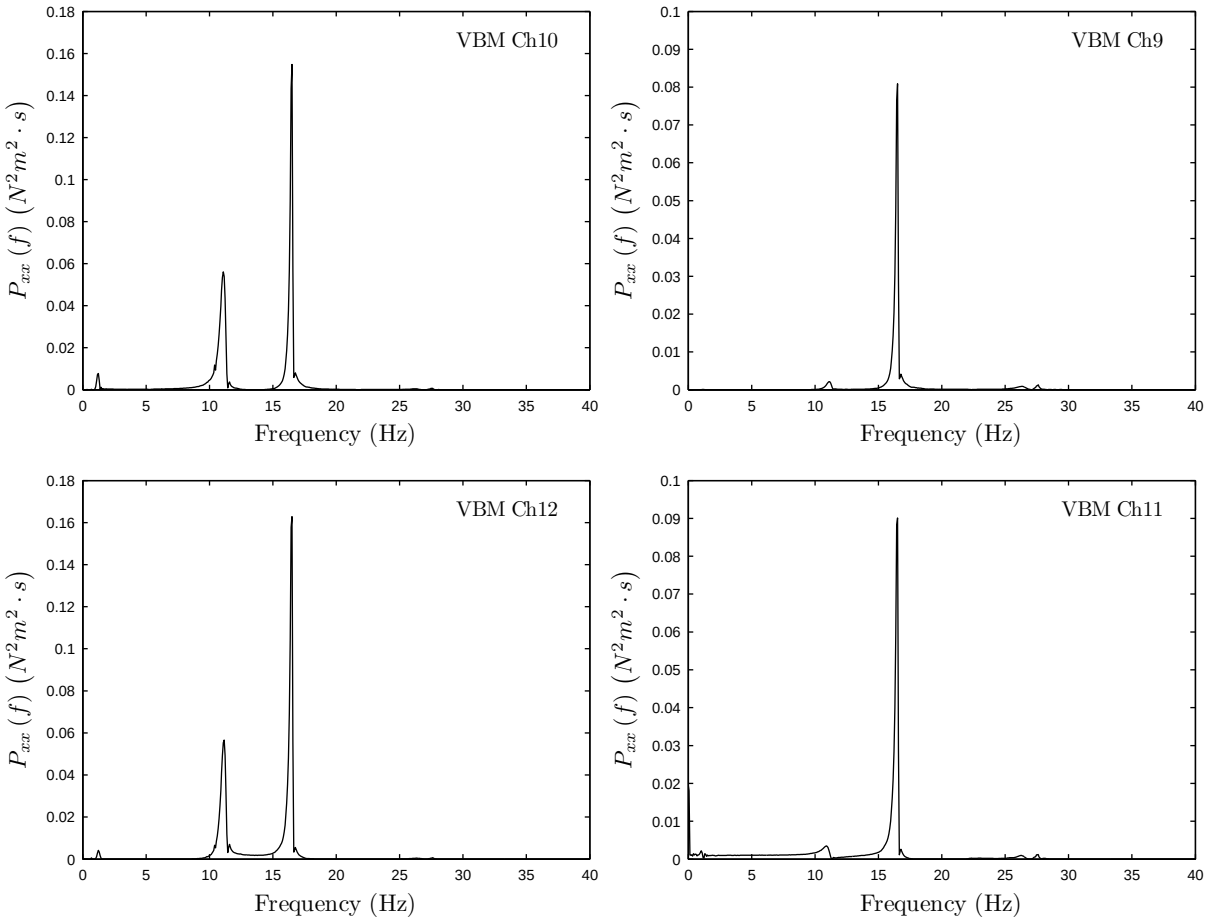

Figure 3.20: Modal analysis for dry mode. Power spectral density (PSD), $P_{xx}(f)$ for vertical bending moment (VBM) measured at strain gagues at Ch9, Ch10, Ch11 and Ch12 in air. Dry Mode Run No.16. PSD was obtained by applying the Hamming window for data taper in time domain, and No smoothing by a convolution in frequency domain.

transform with the Morlet function could detect the response frequency of the VBM. In the wavelet transform, the peak of the VBM oscillation coincided with the peak magnitude colour of the coefficient for the Morlet wavelet function and the peak of the VBM oscillation coincided with the peak magnitude colour of the coefficient.

The oscillatory VBM signals simultaneously responded with the same peak and trough phase at all the different elastic links in the time domain and continuous wavelet transform. Therefore, the response frequency was confirmed to be a fundamental mode of the natural frequency for the VBM in the dry situation.

The wavelet transform analysis could advantageously identify the impact force, if the impact excitation were generated near the elastic link. The impact excitation for Run No. 18, as shown in Figure 3.23, were made on the starboard wave-piercer of the demi-hull forward segment. The

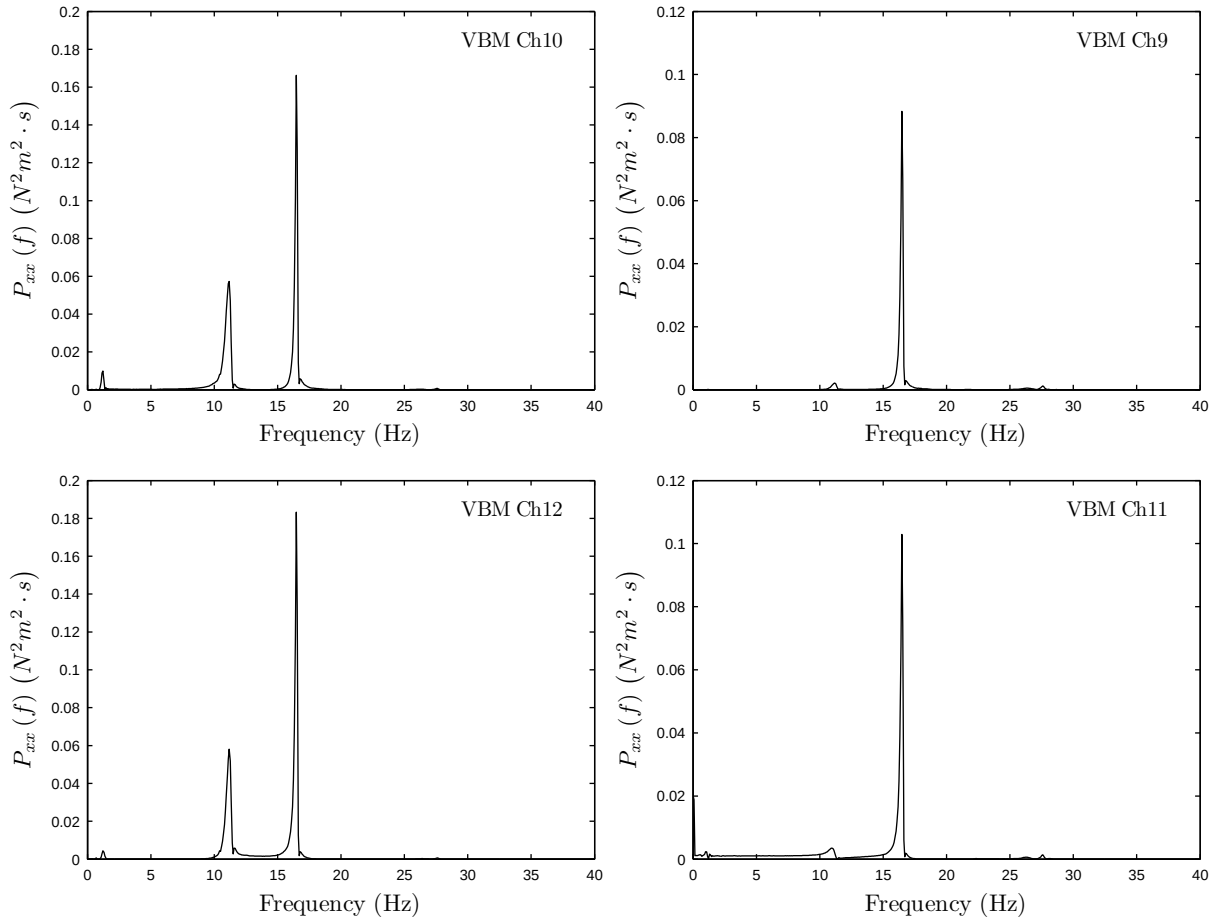

Figure 3.21: Modal analysis for dry mode. Power spectral density (PSD), $P_{xx}(f)$ for vertical bending moment (VBM) measured at strain gagues at Ch9, Ch10, Ch11 and Ch12 in air. Dry Mode Run No.18. PSD was obtained by applying the Hamming window for data taper in time domain, and No smoothing by a convolution in frequency domain.

closest elastic link to the impact position was at the elastic link for Ch11.
Due to the impact excitation, the high magnitude of the coefficient for the Morlet wavelet function for Ch11 was observed over a large range of the scale a from 10 to 40. It indicated that the impact excitation resulted in the coefficient of the wavelet transform with a large range of the scale a. Paradoxically, by utilising this unique characteristic, the occurrence of a large impact excitation could be identified by the continuous wavelet transformation.

It is somewhat similar to the spectral response of a single impulse excitation. The PSD of the impulse excitation itself, ideally appears as a constant magnitude response over the many frequency ranges. Similar responses appeared in the continuous wavelet transformation so that it could be used to distinguish the impulse wave excitation from the harmonic and random wave motion for sea conditions, hence this could be used for the slamming impulse identification.

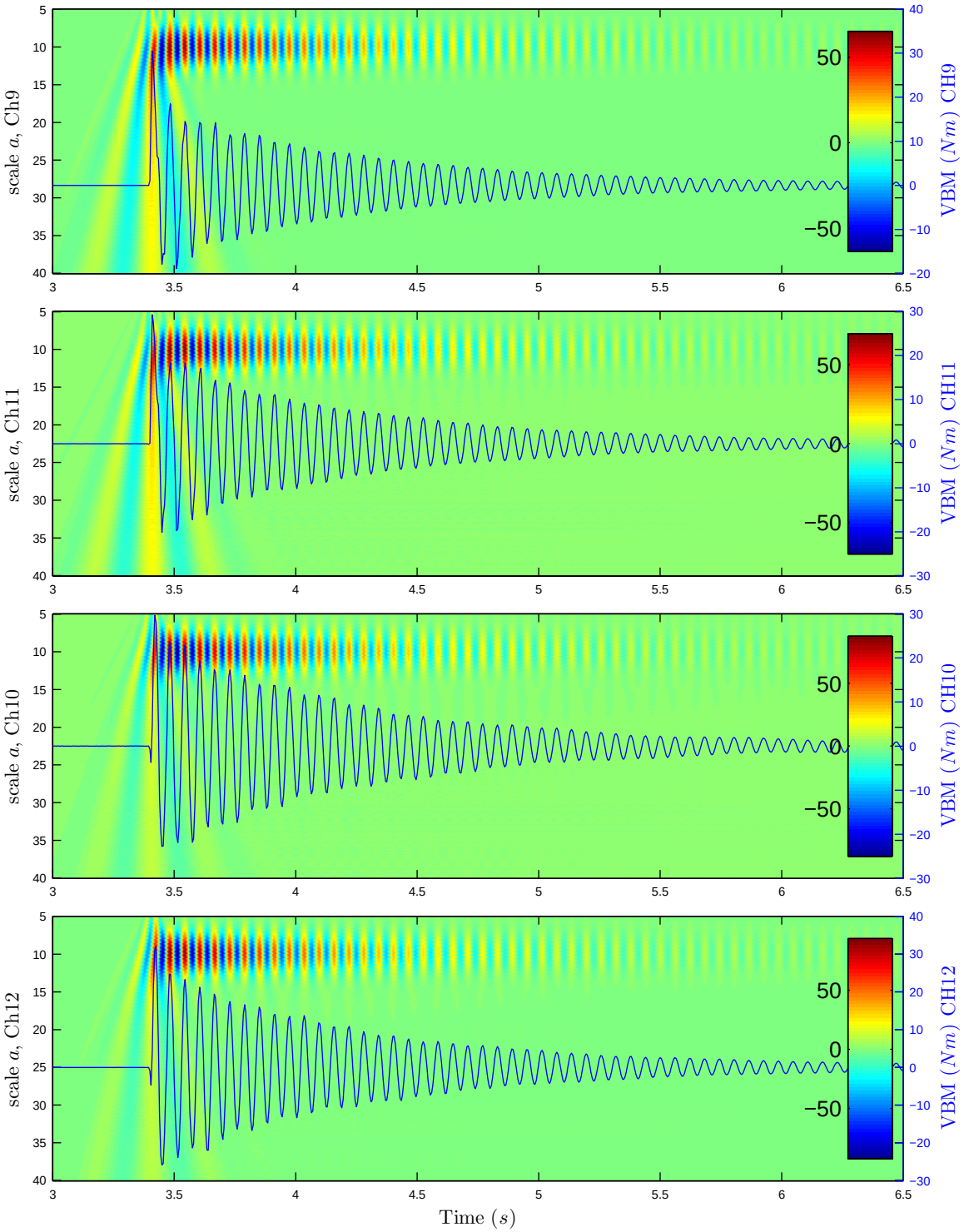

Figure 3.22: Modal frequency response of impact test on dry mode by wavelet analysis on the vertical bending moment (VBM) for Run No.4

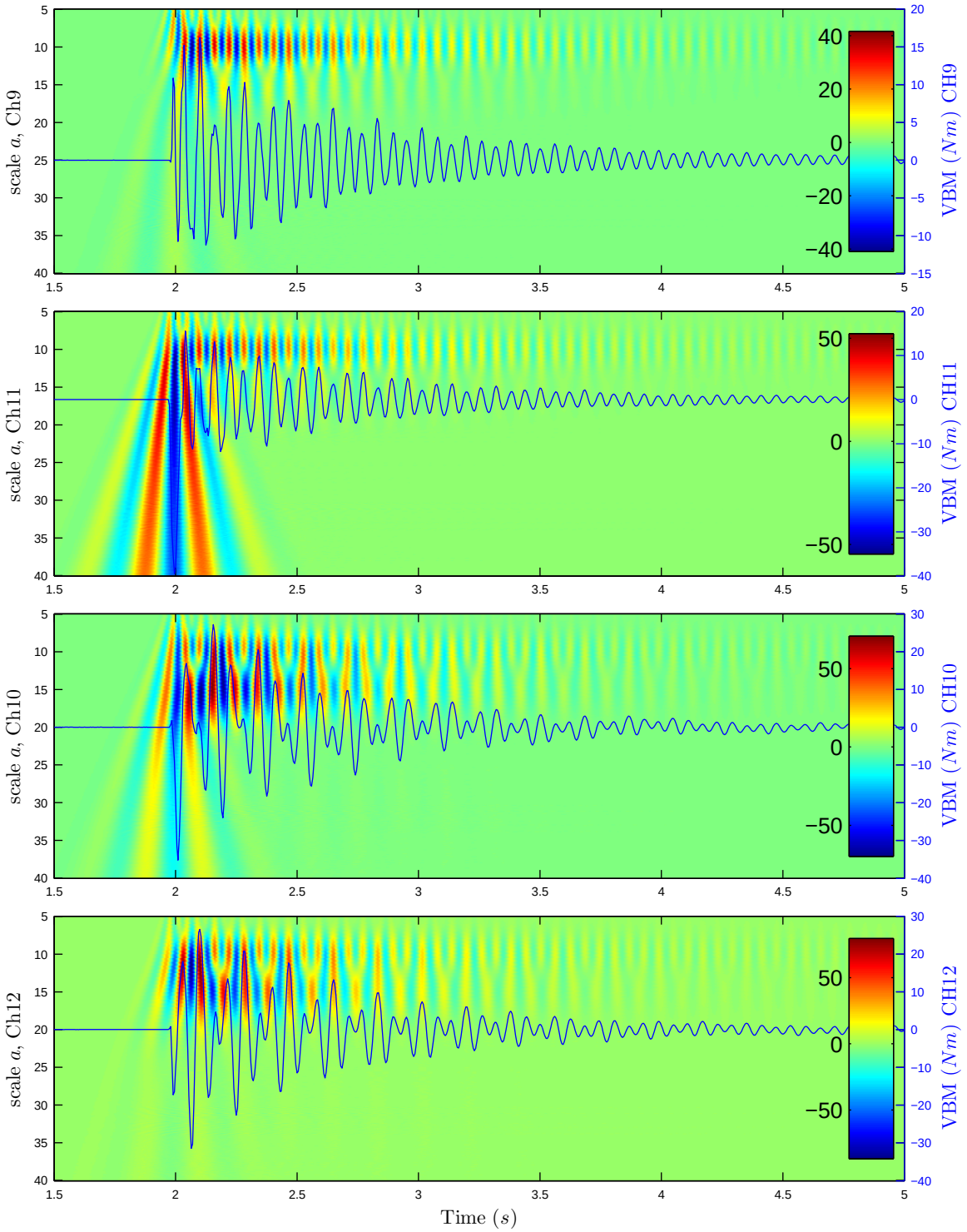

Figure 3.23: Modal frequency response of impact test on dry mode by wavelet analysis on the vertical bendign moment (VBM) for Run No.18

3.6.3 Modal Frequency Test in Wet Condition

Wet modal tests were conducted in calm water and disturbed water in the towing tank. Impulse excitation forces were generated on the centre bow segment to obtain the fundamental mode of the natural frequency of the VBM on the elastic links on the demi-hulls. In addition to the impact test, a drop test was conducted by releasing the CBS, which had been lifted by 220 mm from the lowest part of CBS to the water surface. The response frequencies were obtained by the power spectral analysis and continuous wavelet transform with the Morlet function.

The response frequencies of the VBMs on the demi-hull were obtained and are presented in Table 3.18. Selected examples of the PSDs are shown in Figures 3.24, 3.25, and 3.26. The results showed a consistent response frequency at Hz for the average of all the runs, and all four channels of the elastic links resulted in the same frequency.

Comparison between the dry and wet modal frequencies indicated a strong effect on the natural modal frequency. The surrounding water contributed to reducing the wet modal frequency by 18.6%. There was a reduction in the modal frequency caused by the addition of the added-mass effect and hydrostatic restoring effect to the structural vibratory system.

Table 3.18: Modal test frequency response for wet mode

Run No.	CH 09 (Hz)	CH 10 (Hz)	CH 11 (Hz)	CH 12 (Hz)	Impact method
8	13.358	13.358	13.358	13.358	Impact on CBS top
9	13.356	13.356	13.356	13.356	Impact on CBS top
10	13.401	13.401	13.401	13.401	Impact on CBS top
11	13.356	13.356	13.356	13.356	Impact on CBS top
13	13.412	13.412	13.412	13.412	Impact on CBS top
14	13.344	13.344	13.344	13.344	Impact on CBS top
15	13.357	13.357	13.357	13.357	Impact on CBS bottom
16	13.298	13.298	13.298	13.298	Impact on CBS bottom
17	13.360	13.360	13.360	13.360	Drop test (220mm)
18	13.333	13.333	13.333	13.333	Drop test (220mm)
19	13.358	13.283	13.283	13.283	Drop test (220mm)
20	13.310	13.310	13.310	13.310	Drop test (220mm)
21	13.309	13.309	13.309	13.309	Drop test (220mm)
Average	13.350	13.345	13.345	13.345	

The results of the wavelet analysis are shown in Figures 3.27 and 3.28. Again, the continuous wavelet transforms with the Morlet wavelet function were performed to investigate the VBM response in a similar manner to the dry mode. The response result of an impact excitation test in the calm water is shown in Figure 3.27, and the response result of a CBS drop test is presented in Figure 3.28.

The wavelet transformation response and VBM temporal signal in Figure 3.27 showed the hydroelastic segmented model was excited with the fundamental mode of the natural frequency of the VBM. At the same time, the colour of the coefficient for the Morlet wavelet function was the

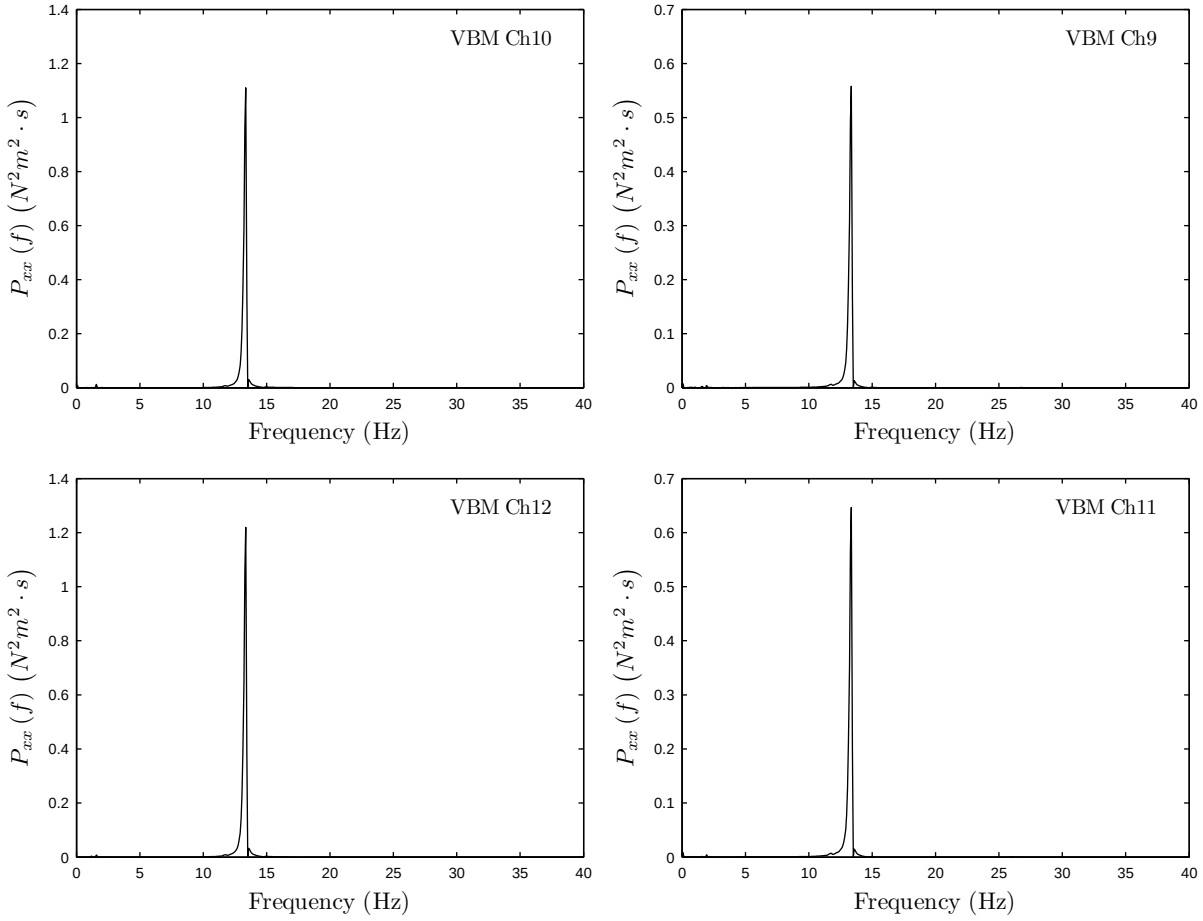

Figure 3.24: Modal analysis for wet mode. Power spectral density (PSD), $P_{xx}(f)$ for vertical bending moment (VBM) measured at strain gagues at Ch9, Ch10, Ch11 and Ch12 in calm water. Wet Mode Run No.8. PSD was obtained by applying the Hamming window for data taper in time domain, and No smoothing by a convolution in frequency domain.

same, and a decay in the response colour was similar among all the elastic links at a constant value of *scalea*. The wavelet response detected no other frequencies other than the fundamental mode.

Impulse excitation due to water impact, induced a red intensified long strip over a large range of *sclaea* at $t = 2.1$ seconds in the coefficient of the wavelet Morlet function for the wavelet transformation, as shown in Figure 3.28. Since the water impact excitation was supposed to generate the sagging VBM, the wavelet results and VBM time signal showed that the largest impulse response, that generated the hogging VBM, occurred as the subsequent reaction of the impulse excitation due to the water impact.

Using the wavelet analysis and wavelet transformation response with the Morlet wavelet function, the occurrence of the fundamental mode of the natural frequency of VBM on the HSM was

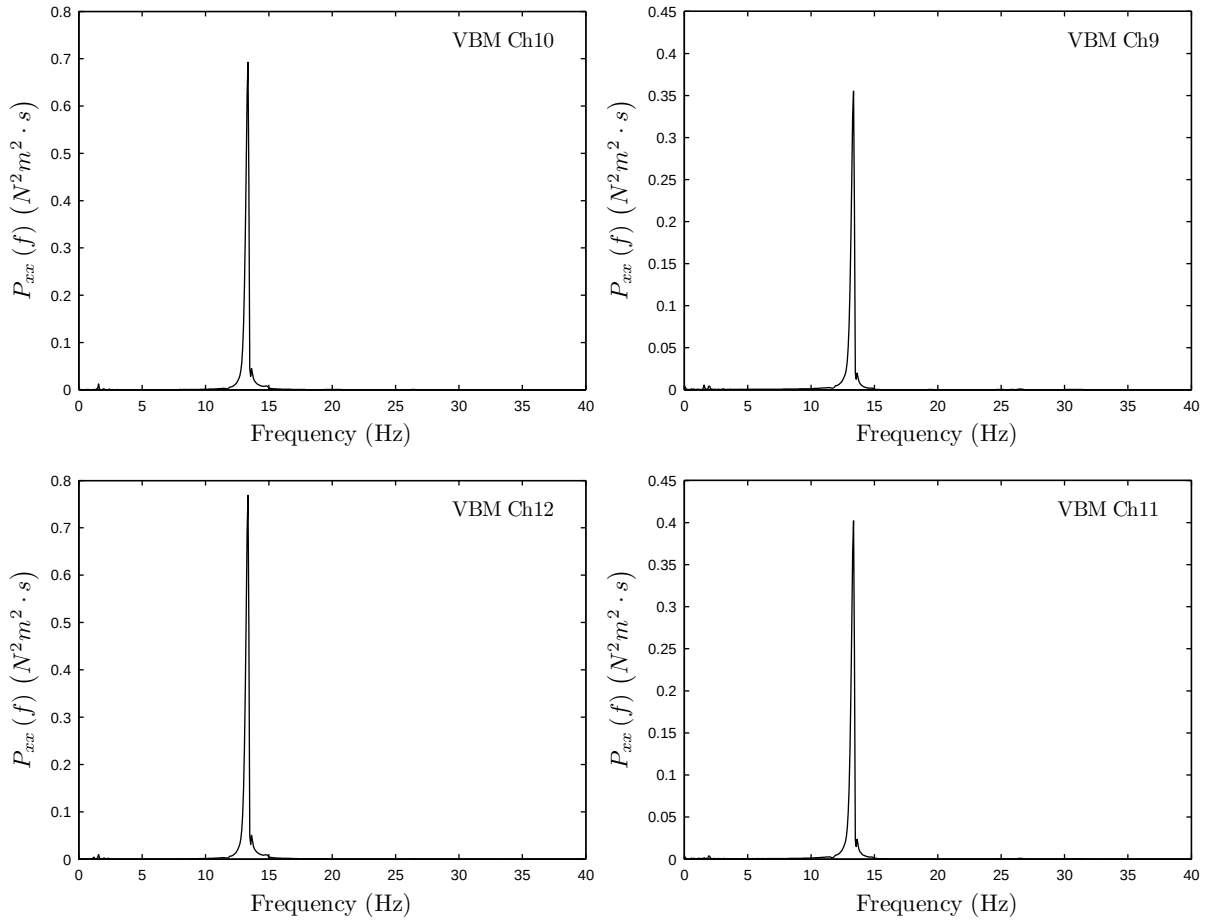

Figure 3.25: Modal analysis for wet mode. Power spectral density (PSD), $P_{xx}(f)$ for vertical bending moment (VBM) measured at strain gagues at Ch9, Ch10, Ch11 and Ch12 in calm water. Wet Mode Run No.15. PSD was obtained by applying the Hamming window for data taper in time domain, and No smoothing by a convolution in frequency domain.

confirmed in the air and water due to the impulse exciting force. This response was expected to appear in the seakeeping test due to the slamming impact as the impulse excitation to the model. In addition, the wavelet transform response can be potentially used as an identification tool for the impulse signals. The impulse signal on the VBM can be caused by either the water impact or the subsequent reaction to the water impact, whichever results in a larger impulse.

3.7 Forward-Velocity-Induced VBM Load in Calm Water

Investigation of the forward-velocity-induced VBM load in calm water was conducted. The power spectral analyses were conducted to find the resonance frequency on each elastic link strain gauge of the elastic link at the segmentation gap. The continuous wavelet analysis with the Morlet wavelet function was also deployed to analyse the temporal pattern of vibrational

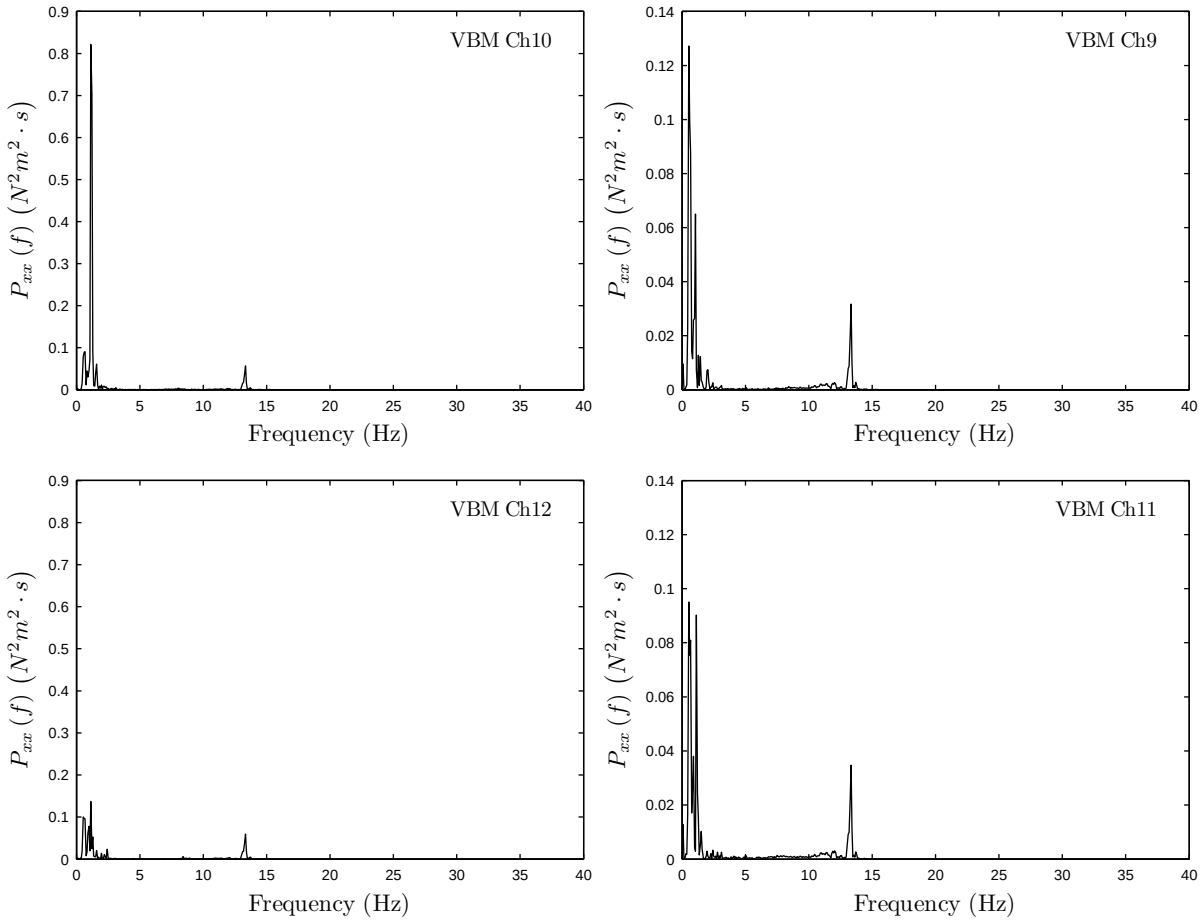

Figure 3.26: Modal analysis for wet mode. Power spectral density (PSD), $P_{xx}(f)$ for vertical bending moment (VBM) measured at strain gagues at Ch9, Ch10, Ch11 and Ch12 in calm water. Wet Mode Run No.18. PSD was obtained by applying the Hamming window for data taper in time domain, and No smoothing by a convolution in frequency domain.

occurrence.

Five different speeds were selected according to the speed of the seakeeping test. As shown in Table 3.5, 20, 30 , 38, 45, and $50Kn$ were chosen to study the influence of the forward velocity on the VBM and global and local vibration of the model. The sampling frequency of the carriage data acquisition system and CRIO data acquisition system was set to 200 Hz.

Since the induced motion was produced by the forward velocity in calm water, the sinkage and trim should be used for vertical displacement variation and angular displacement variation about the transverse axis of the model. However, the heave and pitch is also used in this section, since in some cases the motion behaves oscillatory.

3.7.1 Dynamic Attitude of the HSM due to the Forward Velocity

Dynamic attitude of the hydroelastic segmented model during the calm water run was plotted in the time domain. An example of the results of the dynamic attitude of the HSM for the speed of 38 Kn is shown in Figure 3.29. The speed, heave and pitch are plotted against time. Heave and pitch were calculated at the LCG of the model. Since the test was conducted in the calm water condition, pitch can be considered as the trim angle about the LCG. The results for 20, 30, 45, and 50 Kn are shown in the Appendix D.

For the 38 Kn case in Figure 3.29, the speed clearly reached the steady condition after $t = 12.5$ seconds. However, the heave continued to decrease to -5 mm until $t = 21$ seconds. After this point, the model experienced the lift force to increase the heave. The pitch angle also increased as the speed increased. Once the pitch became steady between t = 14 to 18 seconds, the heave still continued decreasing. After $t = 18$ seconds the pitch again started decreasing. The model was found to be subjected to small heave and pitch oscillatory motion due to the hydrodynamic effect of the running conditions. This seemed to be a harmonic motion induced by the forward velocity. Bow-up forces were generated by the resultant force of the hydrodynamics lift force, suction force, and transiently-varied hydrostatic forces onto the hull. The bow-up forces generated the vertical bending moment on the demi-hulls, which will be discussed in Subsection 3.7.2.

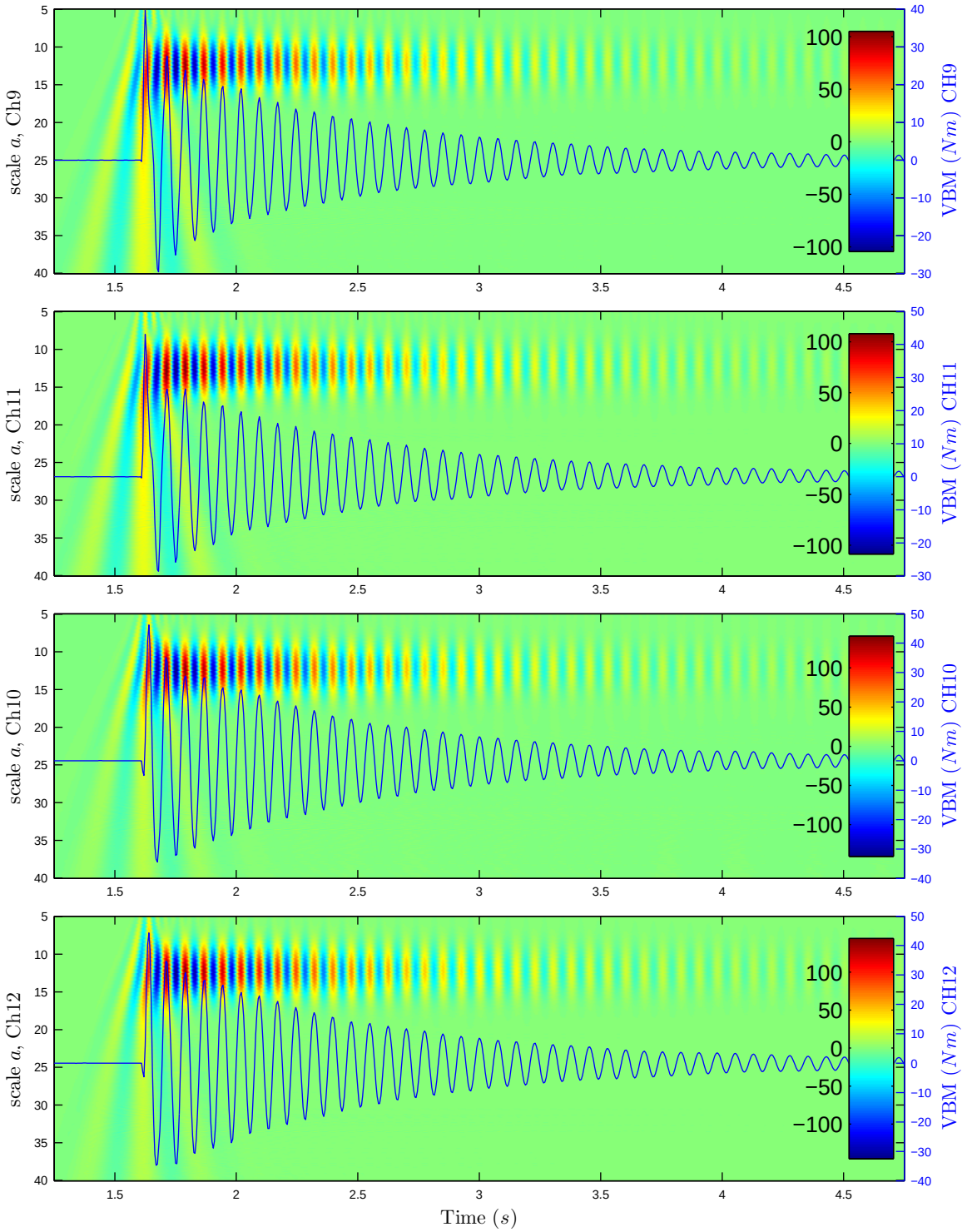

Figure 3.27: Modal frequency response of impact test on wet mode by wavelet analysis on the vertical bending moment (VBM) for Run No.8

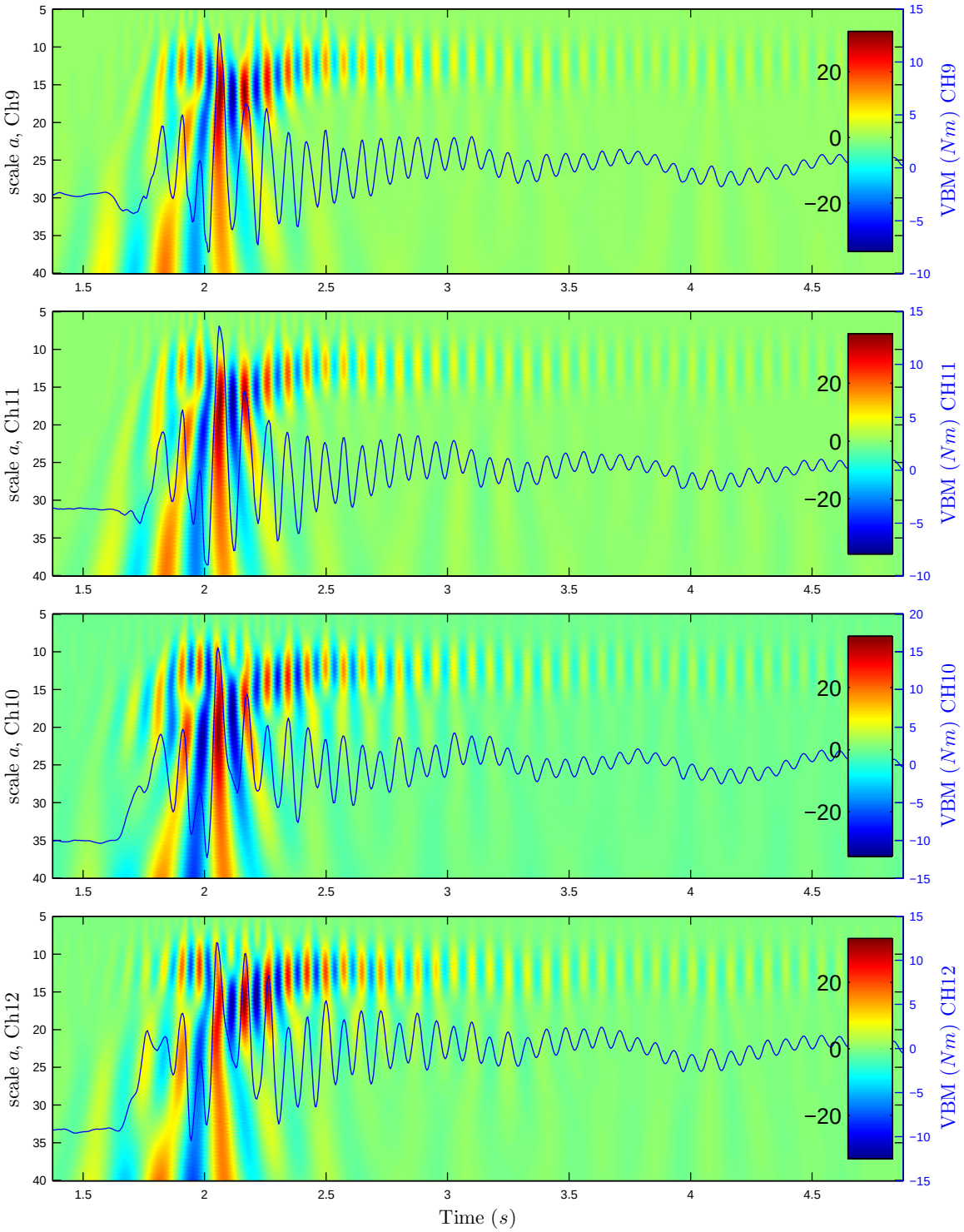

Figure 3.28: Modal frequency response of impact test on wet mode by wavelet analysis on the vertical bendign moment (VBM) for Run No.18

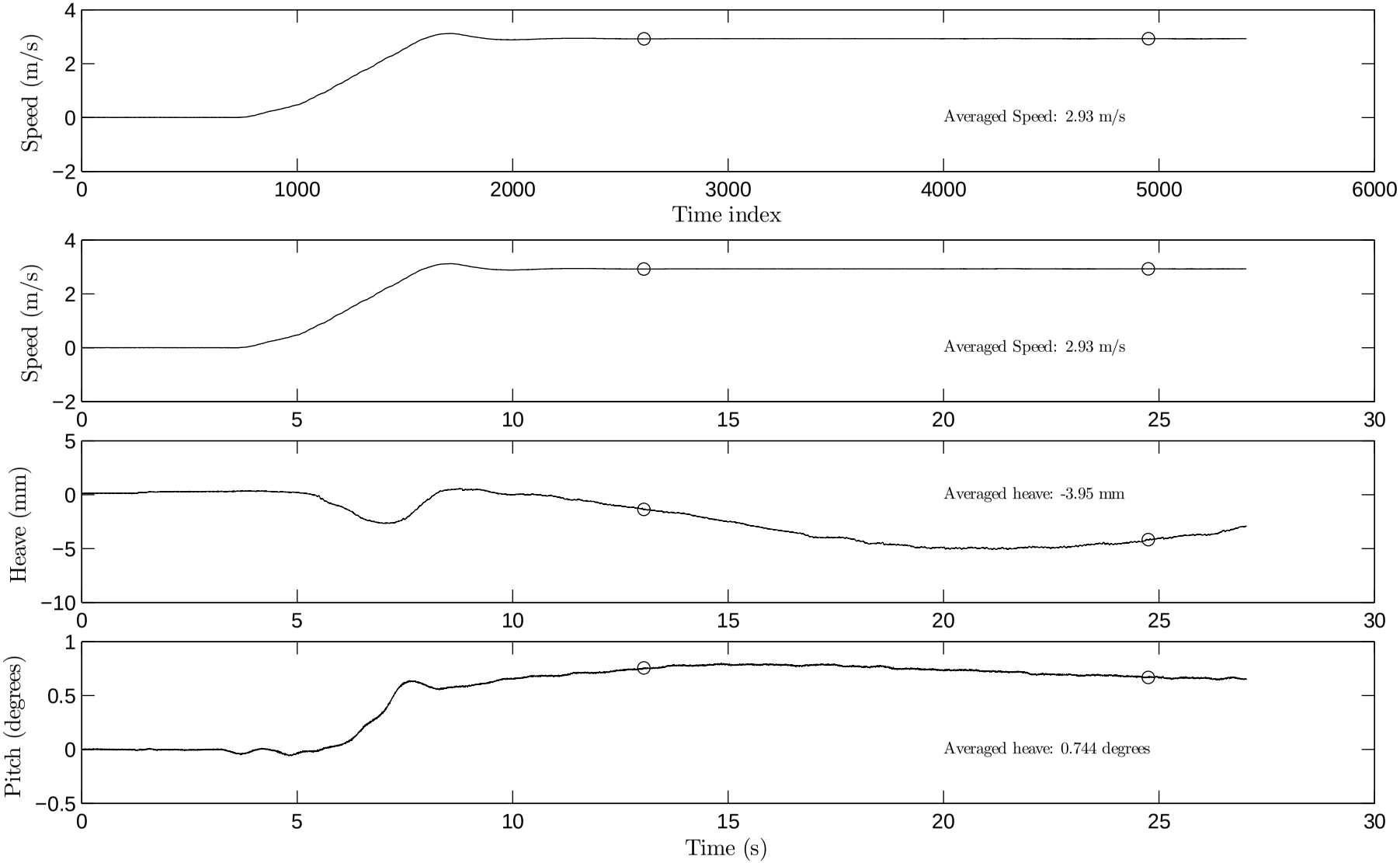

Figure 3.29: Dynamic attitude of calm water run with steady speed maintained at $F_n = 0.605$ for Run No. 815. Averaged values are calculated between two circles.

For the speed of 20 Kn in Figure D.5, the oscillation of heave and pitch remained throughout the run. In particular, pitch did not indicate any sign of attenuation of pitch amplitude during the run. Heave gradually increased with only small oscillations. Due to the slow speed, the suction of the model due to forward velocity was found to be quite small compared with the case of $30Kn$.

The case of 30 Kn is shown in Figure D.6. Similar to the case of 20 Kn, the small oscillation in heave and pitch motion was observed. Once the heave reached minimum values, which was caused by a suction at around $t = 14.5$ seconds, then the trend of the heave increased gradually. Although the pitch had a small oscillation, the trend of the pitch remained steady at about 0.75 degrees.

The case of 45 Kn is presented in Figure D.7. Positive heave values throughout the runs indicated a generation of the strong lift forces due to the forward velocity. The pitch linearly increased in its value throughout the run. It did not respond with any small oscillatory motion that could be seen in the slower speed cases.

The case of 50 Kn is presented in Figure D.8. Interestingly, the pitch was very constant at about 0.24 degrees, but the heave continued to increase in value. No small oscillation was found during the run. Overall, as forward speed increased, the period of the small oscillation of heave also increased. The heave and pitch about the LCG in calm water run caused the small oscillation, while the mean and trend of the heave and pitch were in a steady condition within a certain range.

3.7.2 Velocity-Induced VBM

The forward velocity varied the dynamic attitude of the model, hence it induced the change in the VBM on the demi-hull, as plotted at 38 Kn in Figure 3.30. The results for 20, 30, 45, and 50 Kn are shown in the Appendix D. After the model reached a steady velocity, the VBM remained at a constant value. The temporal variation of the heave did not affect the variation of the VBM significantly. The pitch attitude remained fairly constant at 0.74 degrees. The forward elastic links of Ch09 and Ch11 experienced the smaller vibration than the aft elastic links of Ch10 and Ch12. As a potential reason for this, it could be presumed that the transom stern flow induced the small vibratory motion, and some portion of its inertia was transmitted to the aft elastic links.

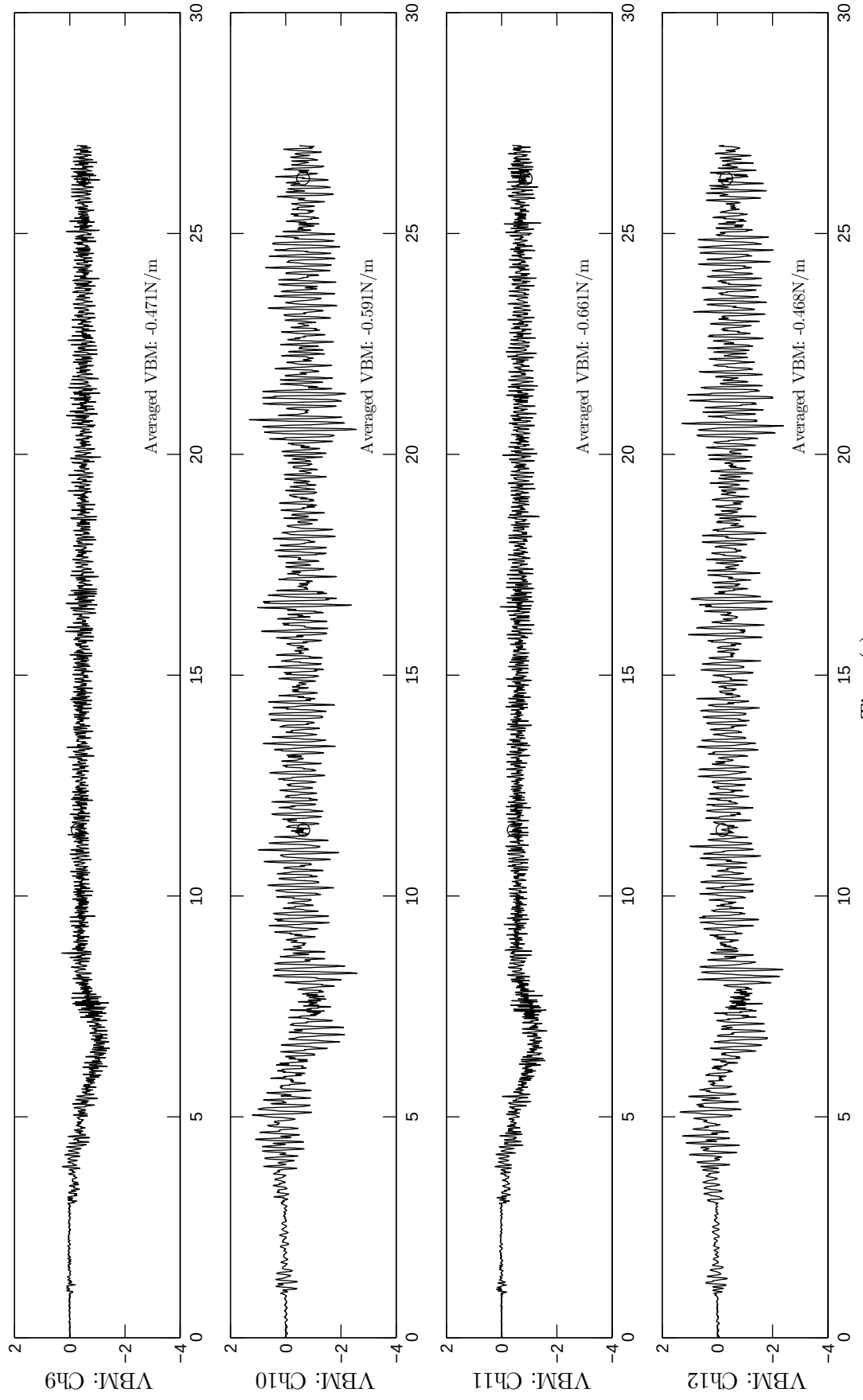

Figure 3.30: Vertical bending moment induced by the forward velocity during calm water run. The steady speed was maintained at $F_n = 0.605$. Run No. 815. Positive and negative values indicate the hogging and sagging VBM, respectively.

The forward velocity effect on the heave and pitch in calm water was investigated. The constant heave and pitch from the above five speeds were plotted against the forward velocity of the model, as shown in Figures 3.31 and 3.32. The heave (sinkage at LCG) was largest at 30 Kn. As the forward velocity was increased from 30 Kn, the heave values increased upwards. This indicated that there was a hydrodynamic lift generating on the demi-hull surfaces. Since there was an increase in the heave motion from 30 to 38 Kn, at the 38 Kn the model was under a semi-planing condition. Over 45 Kn, there was a strong hydrodynamic lift force acting on the hull surface of the model.

The trim angle (pitch) is shown in Figure 3.32. The maximum trim occurred at 30 Kn. As the speed increased, the trim results angle was reduced. The hydrodynamic lift forces were generated at aft of the LCG of the model, hence the trim moment was generated to induce the bow down as the speed of the model was increased. This indicated the centre of the acting position of the hydrodynamics lift force occurred at the aft of the LCG of the model to increase the bow-down trim moment.

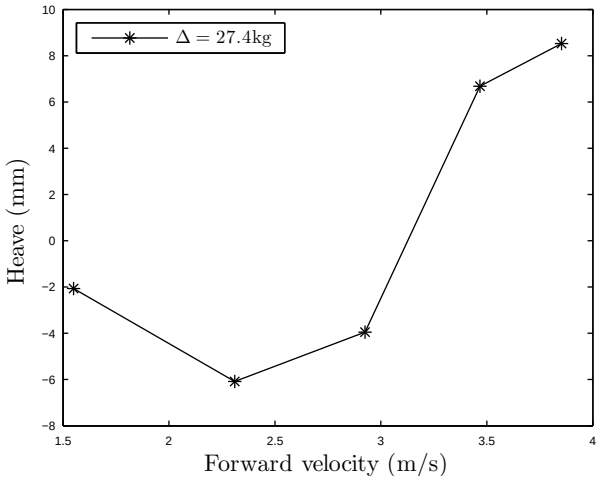

Figure 3.31: Forward velocity effect on heave at LCG

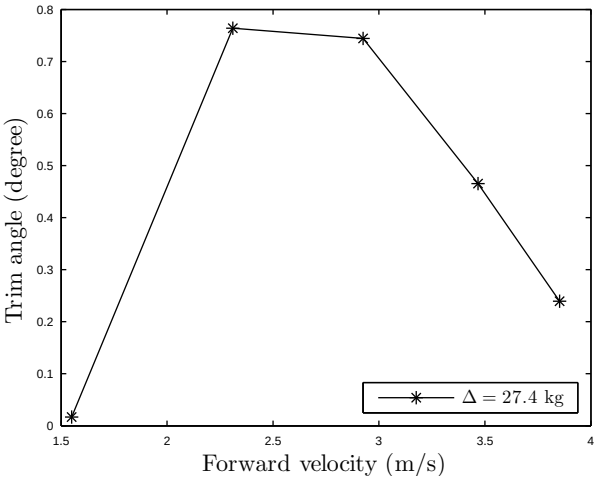

Figure 3.32: Forward velocity effect on trim angle at LCG

The vertical bending moment induced by the forward velocity is plotted in Figure 3.33. At the velocity of more than 30 Kn, the VBM increased as the velocity increased. Therefore, the increase of the bow-down trim moment due to the increase in the forward velocity, caused the VBM of the demi-hull in calm water to increase. Although the magnitude of the VBM induced by the forward velocity might appear to be small values, the forward velocity induced VBM effectively adjusted the measured VBM for the results of the seakeeping test in the regular waves. Therefore, it was essential practice to measure the VBM induced by the forward velocity in calm water.

3.7.3 Global and Local Vibration Identification by Spectral Analysis and Continuous Wavelet Transformation Analysis

Global and local vibration identification were archieved by the spectral analysis and continuous wavelet transformation (CWT) analysis. The PSD for the spectral analysis provides clearer

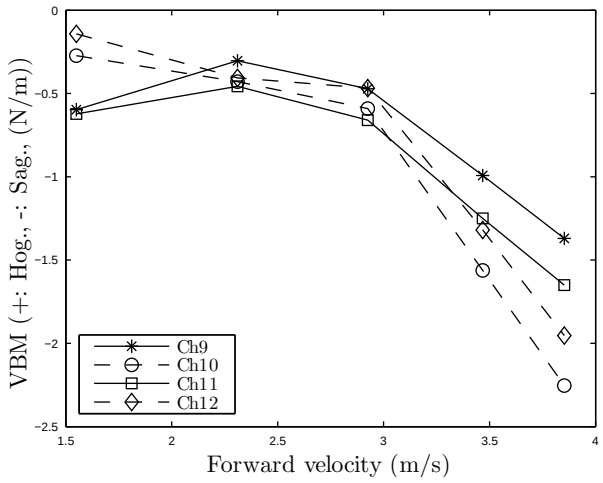

Figure 3.33: Vertical bending moment (VBM) induced by the forward velocity during the calm water run. VBM is plotted against the forward velocity. Positive values of VBM indicates the Hogging VBM and negative values of VBM indicate the sagging VBM

response frequency components of vibration than the CWT. However, the CWT can advantageously deliver the temporal information of the vibratory occurrence by distinguishing the response frequency components. Using this temporal information and frequency information recorded at multiple different locations appropriately, the global and local vibration identification was successfully established by the PSD and CWT. The details of CWT are presented in Appendix E.

Spectral analysis was conducted in order to identify the frequency response of the experimental model. The PSDs were computed by the periodogram method with the Fast Fourier Transform (FFT) method with the following procedure. Firstly, the mean value of the temporal raw data was subtracted from the temporal data to adjust the vertical shift in the original data. If the tread of the inclined values occurred, the de-trend of the temporal data can be applied. In order to avoid the spectral leakage, the taper was applied on temporal data before the FFT. The time window of the taper can be selected from the rectangular window, Hamming window, Hann window, and so on. The rectangular window does not have a taper effect, so all signals of the tapered data remain the same as the original. Thus both edges of non-tapered data could result in the spectral leakage around primary peaks of the response frequency. Once the temporal raw data was treated, the discrete Fourier transform (DFT) of the temporal raw data were calculated into the frequency domain. The power spectral densities were then obtained by multiplying the DFT and conjugate of the DFT, and divided by the number of the temporal data points and sampling frequency for the both-sided spectrum. To obtain the one-sided spectrum of the PSD for up to the Nyquist frequency, which is half of a sampling frequency, the above obtained PSD was multiplied by two. In this thesis, the PSD means PSD for the one-sided spectrum. If the smoothing is required in the frequency domain results, smoothing windows were applied by the convolution technique. Smoothing frequency domain data by the smoothing window was

also applied, if a further smoothing was required on the PSD. Smoothing was carried out by a convolution in the frequency domain with N number of smoothing windows. This method was implemented in Matlab to compute the PSD.

A methodological technique to analyse the vibratory motion was developed for the global and local vibration identification. The technique utilised the power spectrum analysis and CWT analysis. Firstly, the PSD identifies the key frequencies of the vibratory phenomena, and secondly, the CWT determines the temporal occurrence of the key frequencies. Thirdly, the CWT can also aid in distinguishing whether a component of the vibratory signal is the global or local vibration by applying the CWT analysis on different signal channels on the same temporal domain.

At the third stage, a comparative technique of the CWT results from different strain gauges is important for the successful global and local vibration identification. Generally, the wavelet analysis results are presented by means of a coloured map display, which shows the coefficient of the wavelet function. However, the coloured map has a disadvantage of hiding the relatively weaker signals compared with a strong signal in terms of the response magnitude of the coefficient of the CWT. Therefore, a visualisation of the signal with the moderate intensity became an essential technique. This technique was achieved by using the threshold display to enhance the magnitude of the target frequency. The enhancement technique on relatively weaker signals could be achieved by controlling the boundary limits of the coloured map display.

The power spectral density of the vertical bending moment was obtained for strain gauges on Ch9, Ch10, Ch11, and Ch12, when the hydroelastic segmented model was tested in the calm water run for five different speeds of F_n = 0.320, 0.478, 0.605, 0.717, and 0.797. The case of F_n = 0.605 is presented in Figure 3.34. The cases for F_n = 0.320, 0.478, 0.717, and 0.797 are presented in Figures D.1, D.2, D.3, and D.4, respectively, in Appendix D.0.1.

The PSD results, as shown in Figure 3.34, indicate that the forward velocity in the calm water also excited the HSM with the strong peak with the resonance frequency of the fundamental mode for the VBM on the demi-hull at 11.2 Hz. Also observed was a weaker response peak at 12.47 Hz. Focusing on both the frequencies in the wavelet transform result led to finding a variation of the resonant peak in the temporal domain. The details of this will be explained later with the CWT. However, the resonant peak at 11.2 Hz was the only resonant frequency which strongly responded at all four elastic links. Therefore, this frequency component indicated the global vibratory motion.

For the other speeds, clear resonant peaks were observed due to the forward velocity in calm water. This led to the conclusion that the forward velocity in calm water can induce the structural vibration. Hence, the fluid and structural interference from the fluid to the structure was confirmed for the ship hydroelasticity test.

The wavelet results with and without the enhancement technique on $RunNo.$ 815 is shown in

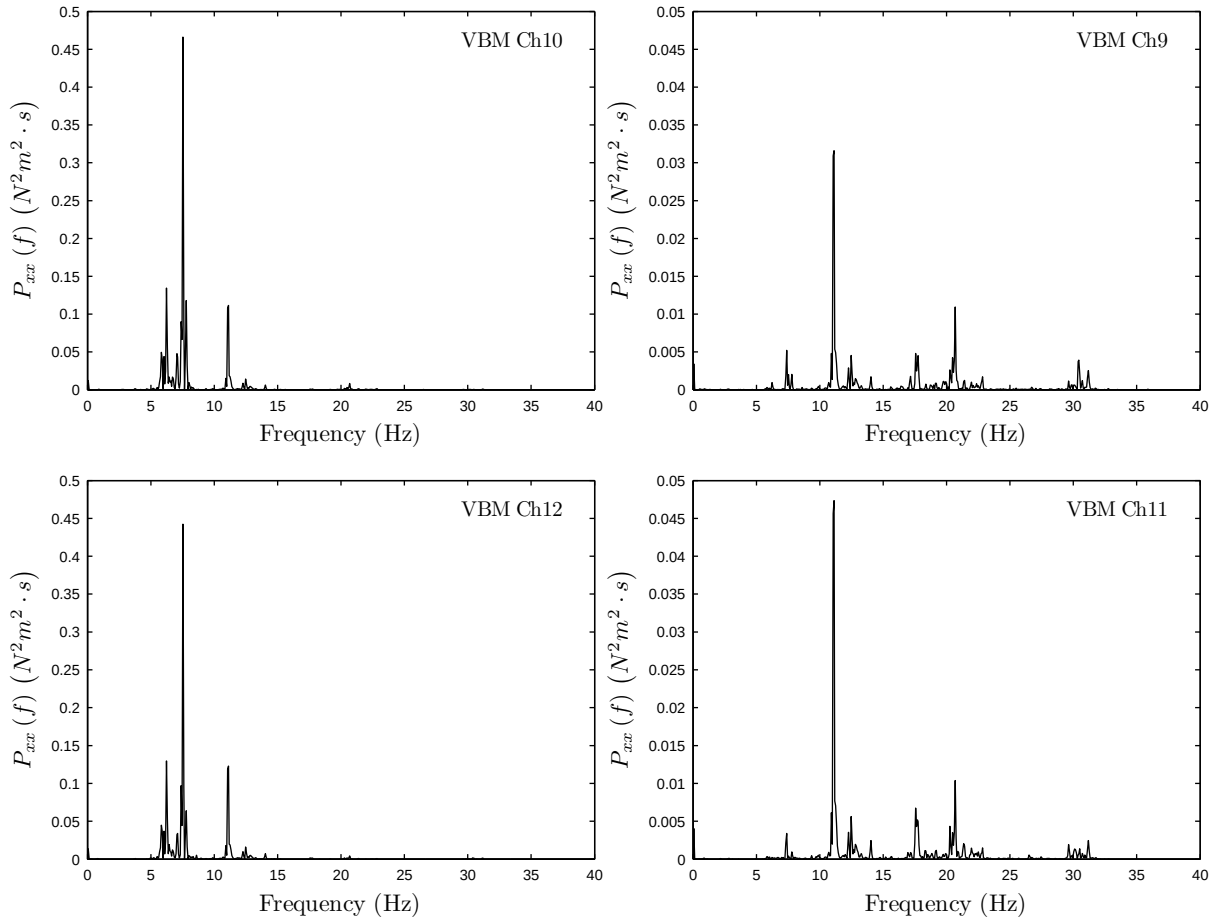

Figure 3.34: Power spectral density (PSD), $P_{xx}(f)$ for vertical bending moment (VBM) measured at strain gauges at Ch9, Ch10, Ch11 and Ch12 in calm water run at $F_n = 0.605$, Run No.815. PSD was obtained by applying the Hamming window for data taper in the time domain, and no smoothing by a convolution in the frequency domain.

Figure 3.36. The pseudo-frequency corresponds to the scale a values in the wavelet transformation as shown in Figure 3.35. By referring to the Figure 3.35, it enables the conversion of the frequency to the unit of Hz.

The Ch09 result at the port-side forward elastic link in Figure 3.36 showed the repetitive occurrence of the peak to trough fluctuated CWT coefficient indicating the harmonic vibratory response at around the scale $a = 15$, which is equivalent to 11.2 Hz in the frequency domain. On the Ch10, there was a strong response of the CWT coefficient at scale $a = 25$ (similarly, equivalent to 7.25 Hz). An enhancement technique was deployed by controlling the boundary limits of the coloured map display to between -1.5 and 1.5. Now, the boundary limits are the same as the Ch09 case. The fourth sub plot shows the enhanced result on Ch10. The Ch10 enhanced result clearly shows the response component at around the scale $a = 15$. Once the threshold was dropped on the 1.5 maximum on Ch10, the frequency components of 11.2 Hz and 20.68 Hz appeared in the colourmap display. This showed that the 11.2 Hz and 20.68

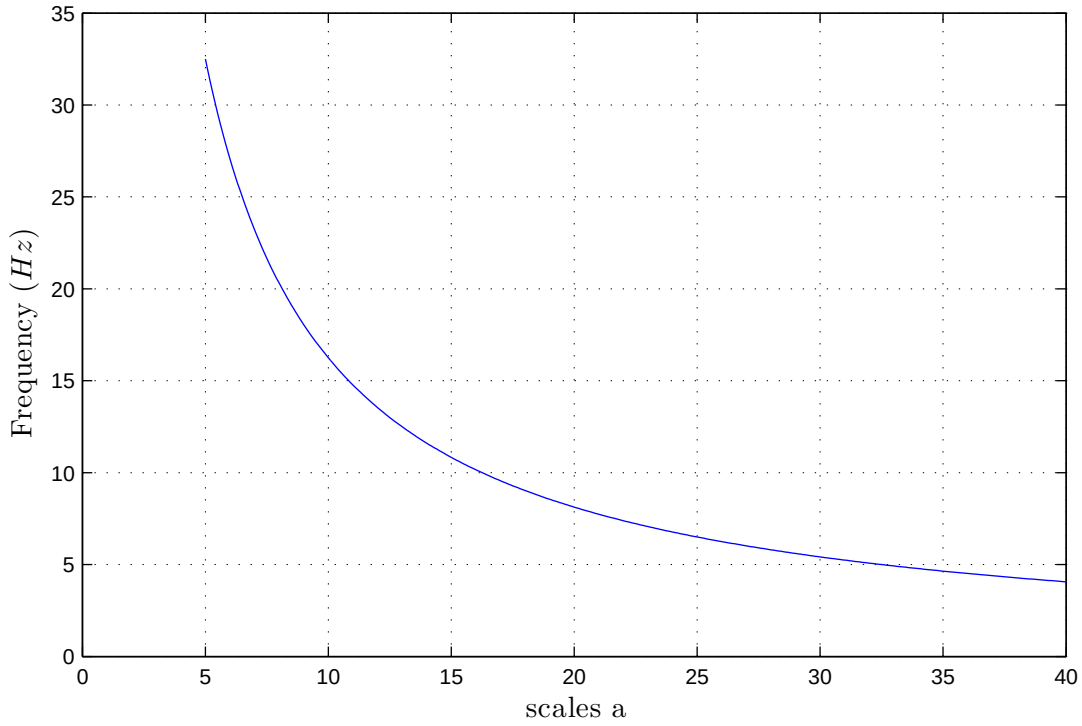

Figure 3.35: Pseudo-frequencies (Hz) corresponding to the scales a.

Hz (scale $a = 7.5$) response frequency components were existed in Ch10 as well, however these frequency components were attenuated by the stronger 7.52 Hz response component. Hence, it concludes that the harmonic vibratory response at 11.2 Hz was a global vibratory motion of the fundamental mode of the VBM for the HSM.

The global vibratory motion at 11.2 hz can also be confirmed by Figure 3.37. Since Ch09 and Ch11 at the forward elastic links showed the weak response at scale $a = 25$, the vibratory motion at 7 Hz can be recognised as the local vibratory motion occurring at the demi-hull aft segment of the model. Interestingly for Ch10 and Ch12, the colour pattern of the CWT coefficient indicated the phase differences of vibrations between the starboard demi-hull and port demi-hull were 180 degrees at 7.52 Hz. This indicated that the aft segments performed the local vibratory motion at 7.52 Hz, 180 degrees out of the phase between the demi-hulls.

Wavelet analysis was utilised for the global and local vibration identification. In order to compare the wavelet analysis results among the different strain gauges, the enhancement treatment was applied on some channels where the signals were extremely large, which attenuates relatively smaller signals. An example of the signal enhancement treatment is shown in Figure 3.36. The wavelet transform response showed a wavy response between 13.5 and 15.0 of scale a. In contrast when referring back to Figure 3.22, the CWT does not show the wavy response of resonance frequency in the scale a values. The CWT response occurred at a constant scale a. This is the reason for observing the resonance frequency shift in the temporal domain. The CWT in the calm water without the forward velocity responded at a constant value for the scale a values.

This comparison explains that the resonance frequency with the forward velocity was varied in the time domain. It presumed that the forward velocity of the fluid induced the resonant frequency shift in the temporal domain due to a oscillatory phenomena. The oscillatory phenomena was expected to be caused by the mutual interaction of the fluid motion and structural vibratory motion. Once the model structure was vibrated by the fluid motion, the hull surface affected the fluid domain, hence the characteristic of the fluid effect to the hull surface would be changed. This could result in a change in added mass to change the natural frequency, as can be seen in Figures 3.37 and 3.38 .

As with the resonant frequency at 11.2 Hz of a global vibratory motion of the model by PSD, the CWT results also confirmed the resonant frequency at 11.2 Hz (scale $a = 15$) appeared at all four elastic links, as shown in Figure 3.38. In addition, their VBM motion was in phase, hence the vibratory motion of the resonance frequency can be concluded as a fundamental mode of the natural frequency for the VBM of the demihull.

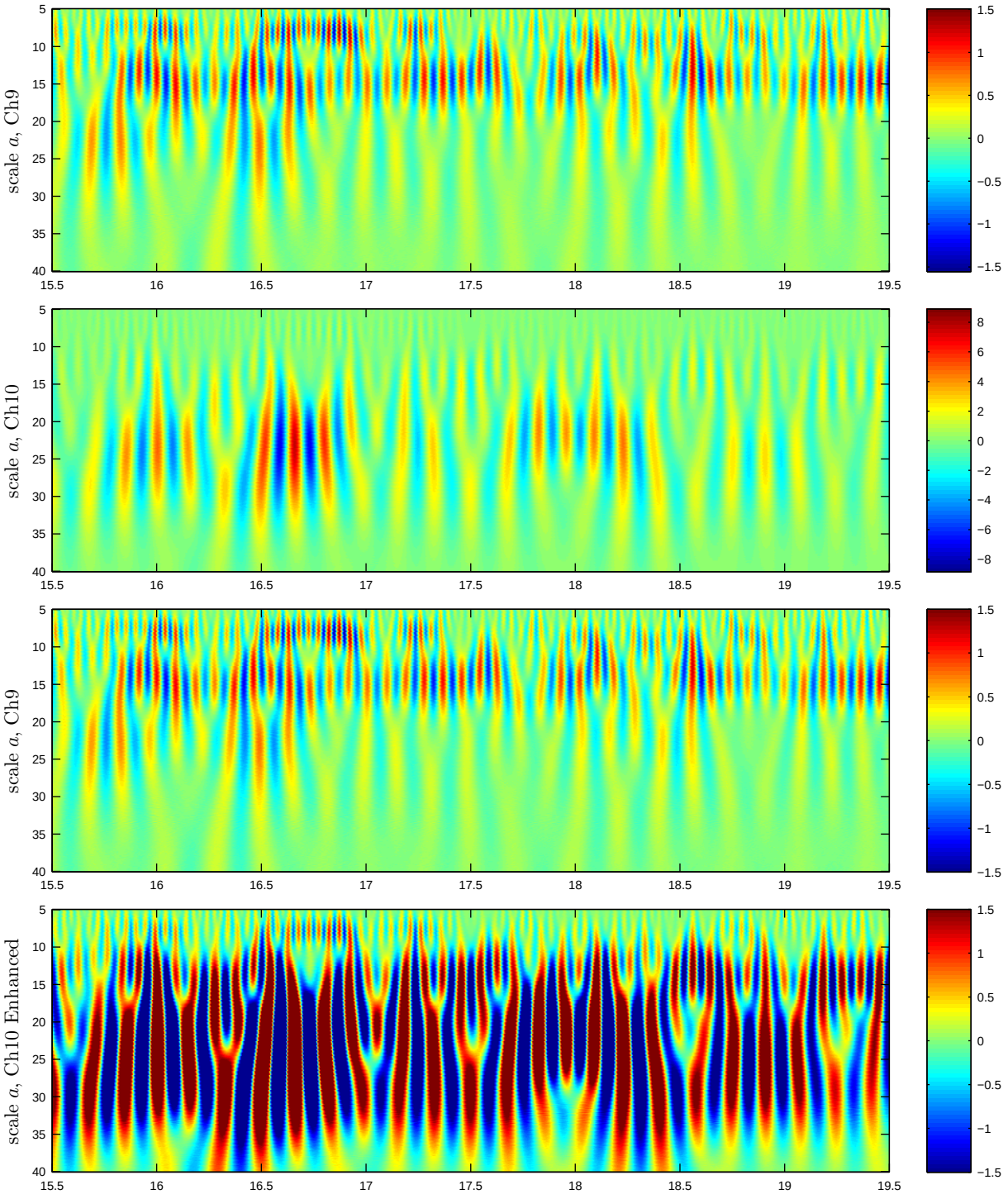

Figure 3.36: Global and local vibration identification by wavelet analysis for Run No.815. Signal enhancement treatment was applied on CH10 to compare with CH9.

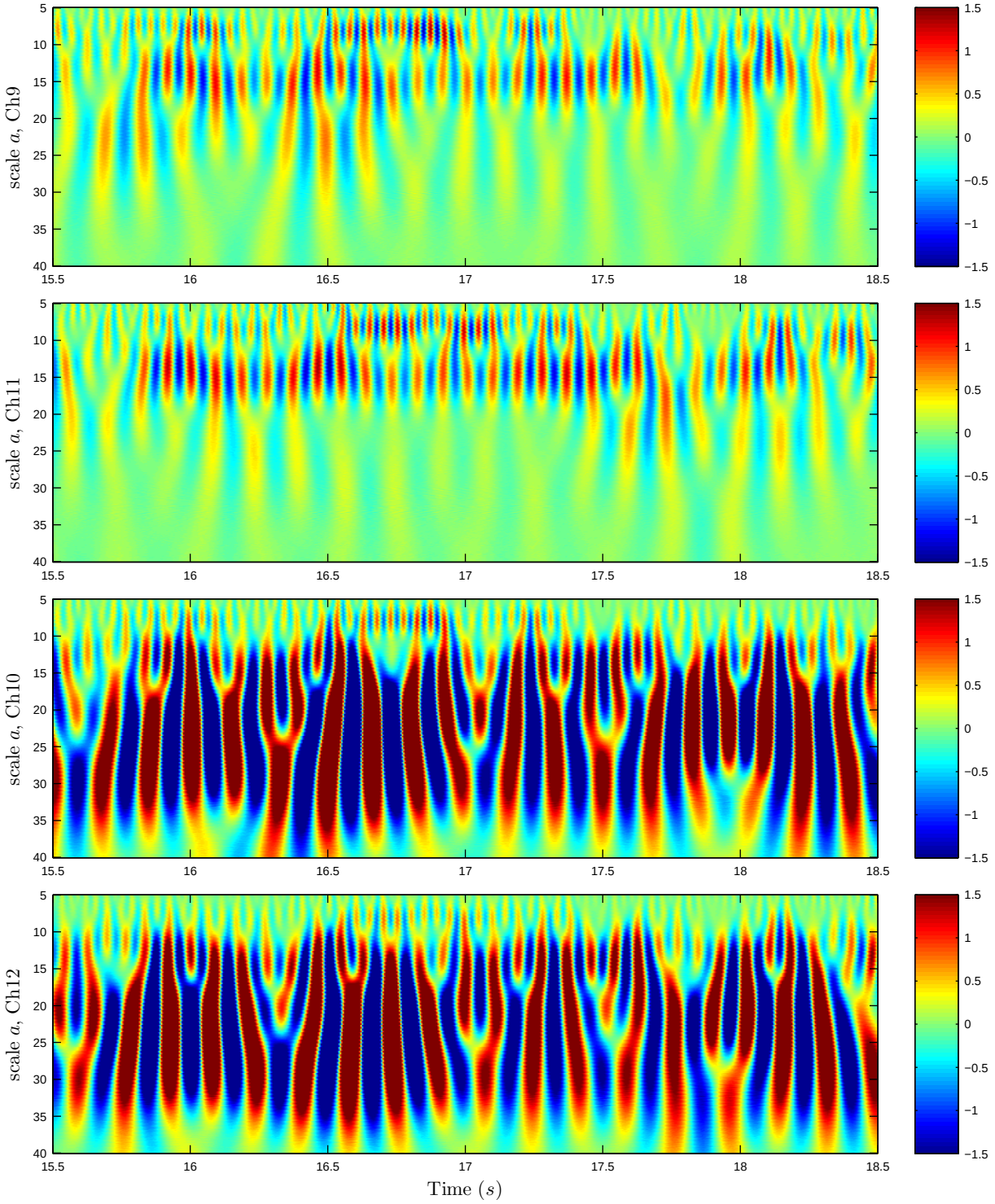

Figure 3.37: Global and local vibration identification by wavelet analysis on all demihull elastic links for Run No.815.

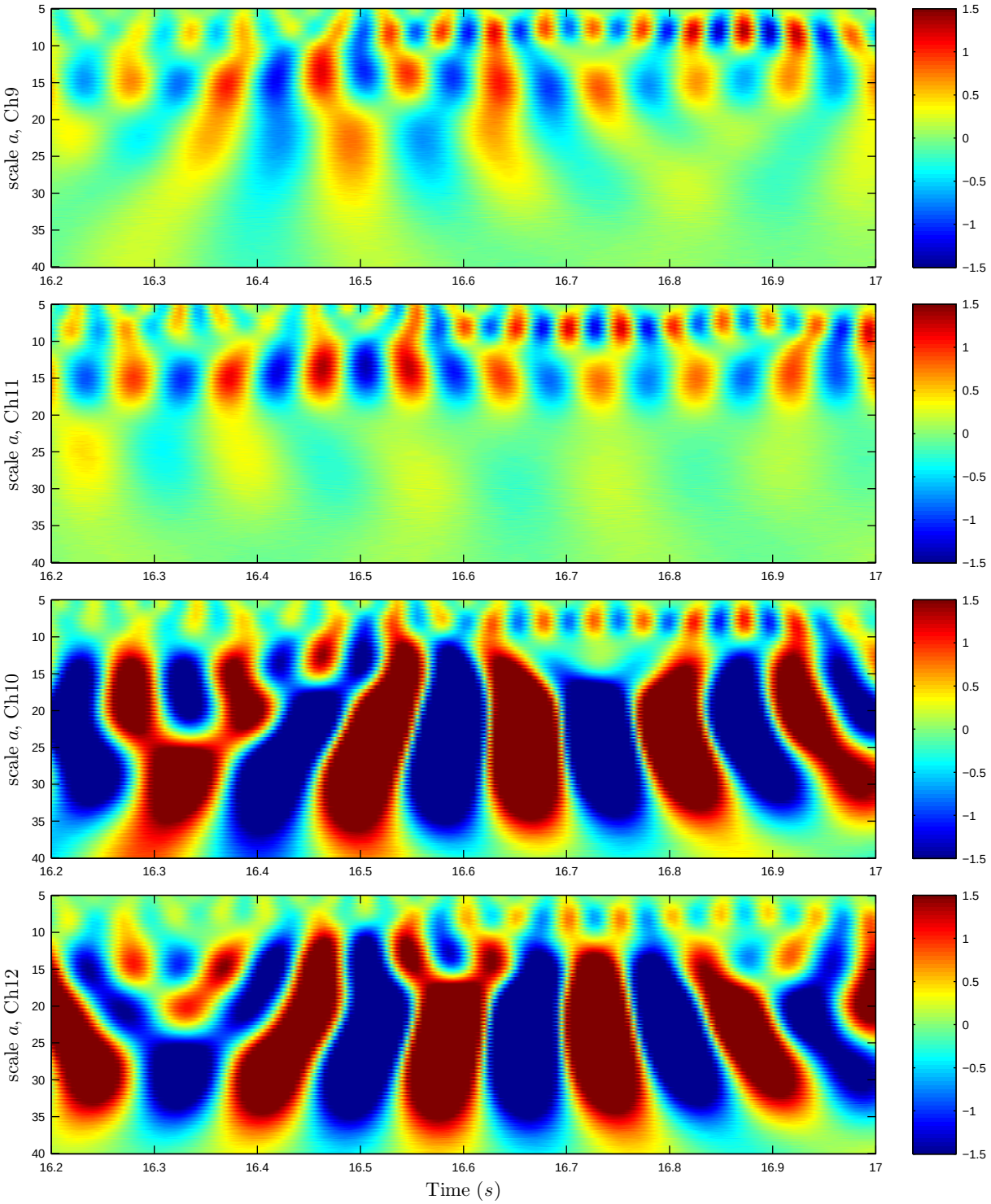

Figure 3.38: Global and local vibration identification by wavelet analysis on all demihull elastic links for Run No.815. Detail response of wavelet analysis.

3.8 Error Analysis for Ship Motions and Loads

Error analysis, using measurement uncertainty, was conducted on selected conditions. Between three and five repeated runs were conducted at selected wave frequencies for each condition. Two conditions, at 38 K_n, were presented here.

The system uncertainty, caused by the measurement system and its calibration, is not considered for the motion measurement. The calibrations error of the VBM and slam load measurement system were presented with the calibration factors in Section 3.5. The measurement uncertainty method used is the Measurement Uncertainty Analysis Principle and Methods by NASA (2010).

The random error for the heave and pitch motion can be calculated by the standard deviation of the sample mean for the non-dimensionalised heave and pitch data obtained for repeated runs. The standard deviation, s_x, of a sample of data is:

$$s_x = \sqrt{\sum_{k=1}^{n} \frac{(x_k - \bar{x})^2}{\nu}} \tag{3.40}$$

and the standard deviation in mean values $x_{\bar{x}}$ can be obtained as:

$$s_{\bar{x}} = \frac{s_x}{\sqrt{n}} \tag{3.41}$$

where n is the sample size, x_x is the kth measured value, $\bar{x}$ is the sample mean value and ν is the degree of freedom, equal to n-1.

Now, the measurement uncertainty due to the random error can be calculated by multiplying the standard deviation of measured samples by the t-distribution quantiles with 95% confidnce level, $t_{95,\nu}$:

$$u_{x_{ran}} = s_x t_{95,\nu} \tag{3.42}$$

$$u_{\bar{x}_{ran}} = s_{\bar{x}} t_{95,\nu} \tag{3.43}$$

The heave and pitch transfer functions are plotted with error bars of measurement uncertainty in the mean values, $u_{\bar{x}_{ran}}$, as shown in Figures 3.39 and 3.40. For the presented cases, the maximum measurement uncertainty error of the heave response, which was experienced at Condition 20, was ±3.72%. Similary, the maximum measurement uncertainty error of the pitch response, which was experienced at Condition 20, was ±2.13%. The measurement uncertainty error was therefore found to be small, providing the confidence in the experiemtnal motion data.

Similarly, the VBM responses on the demihulls measured at the forward and aft elastic links are plotted with error bars of measurement uncertainty in the mean values, $u_{\bar{x}_{ran}}$, as shown in Figures 3.41 to 3.44. Uncertainty error percentage of the VBM measured load at forward and aft segment cut for Condition 20 and 33 were calculated and presented in Table 3.19. There experienced the large error of more than 10%, however this was caused by either of following two

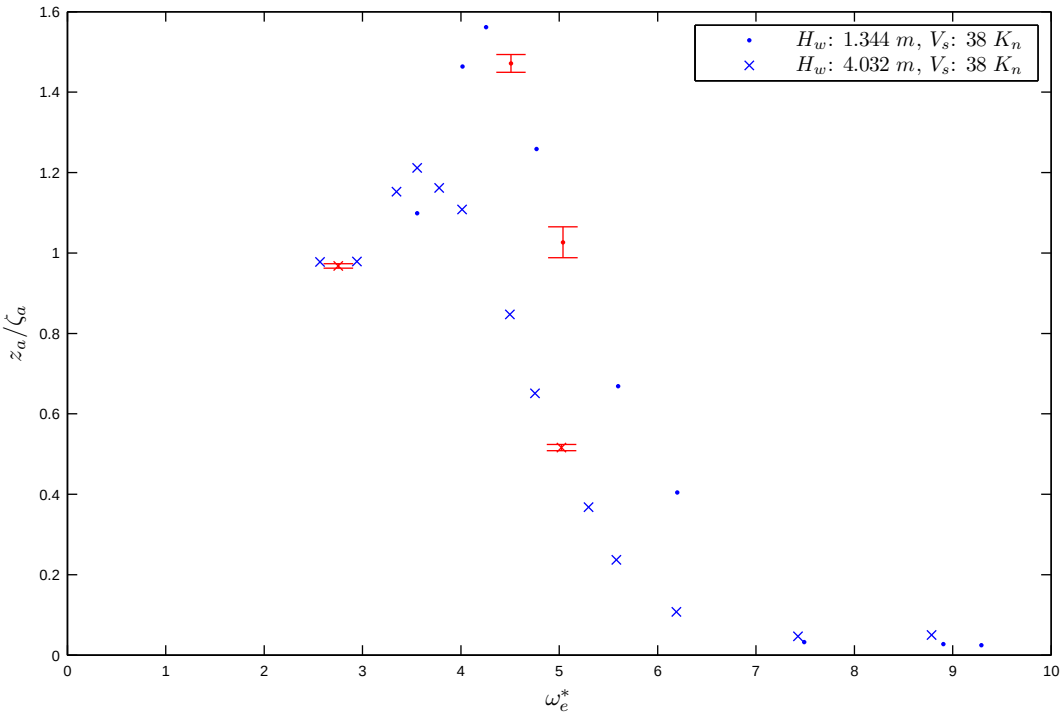

Figure 3.39: Error analysis for the heave transfer function.

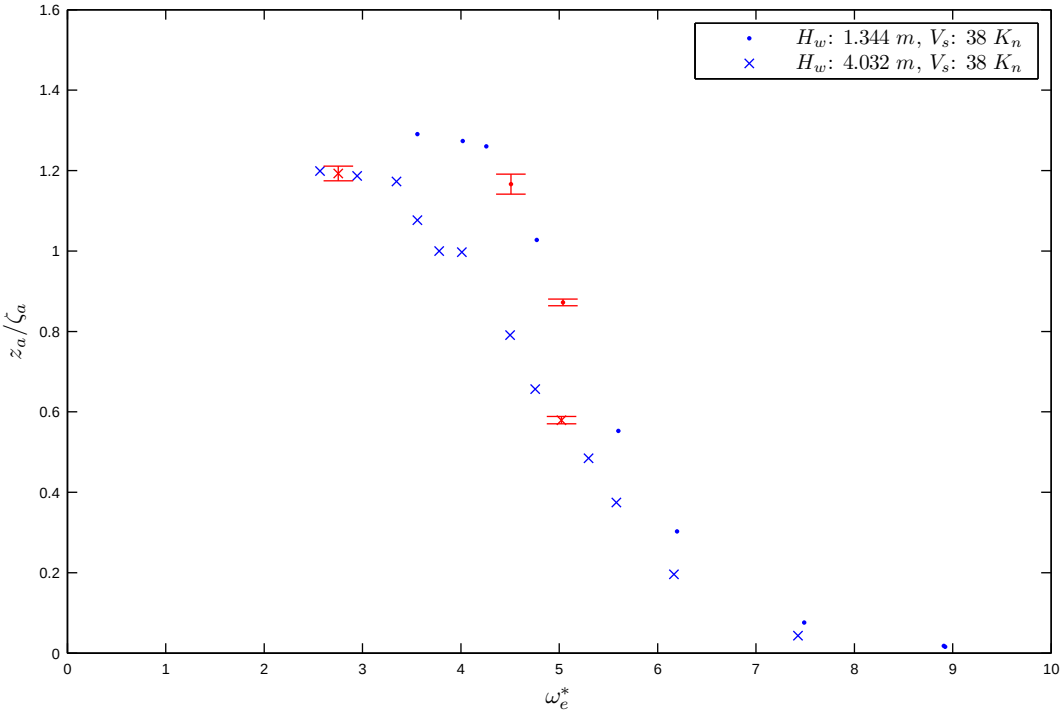

Figure 3.40: Error analysis for the pitch transfer function for Condition 20.

reaseons. For the Condition 20, the uncertainty error of 14.2% were calcuated, because of small mumber of repeted samples. This increased the value of the the t-distribution quantile. Hence the uncertainty error resulted in the large values. For the Condition 33, the error percentage of more than ±10% occured at small VBM maginitudes of less than 5 Nm in large waves. This was experienced at the aft segment cut. In the large wave, unseteady forces would be occured more than in smaller wave condtions, thereofore the increased in uncertainty error can be expected for the small magnitude of the measured VBM in large waves. Similarly, for a small maginitude of VBM, but in small wave cases, Conditon 20, large errors did not occur, even though the small maginitude were measured for the VBM. The error percenrtage in the bracket were calculated for the large magnitude of the VBM. The error percenrtage of the large magnitude of VBM was ±1.6%.

For the smaller wave, the maximum uncertainty error was ±6.6%. For the large wave, te maximum measured uncetainty error was claccted as ±3.7%. The measurement uncertainty error was therefore found to be acceptable by considering the measured magnitude of the VBM, providing the confidence in the experimental loads data.

Table 3.19: Uncertainty error percentage to mean value for the VBM measured loads.

	Fwd. EL	Aft EL	Fwd. EL	Aft EL
	Sag	Sag	Hog	Hog
Condition 20	±14.2%	±6.4%	±6.6%	±3.2%
Condition 33	±3.7%	±14.2%(±1.6%)	±3.5%	±12.9%(±0.64%)

The uncertainty analysis on the measured slam-induced force response was carried out for the Condition 33. The slam-induced force responses on the centrebow are plotted with error bars of measurement uncertainty in the mean values, $u_{\bar{x}_{ran}}$, as shown in Figures 3.45. For the large slam force, the maximum uncertainty error was ±5.2% in a large wave conditions. The measurement uncertainty error was therefore found to be acceptable, providing the confidence in the experimental slam-indcued loads data.

3.9 Seakeeping Results of the Hydroelastic Segmented Model

Transfer functions for the heave and pitch motions were obtained based on the peak-to-trough magnitude method, since this method of the peak and trough detection was the most suitable method to effectively calculate the wave-induced loads. The non-dimensional heave, z_a/ζ_a, and non-dimensional pitch, $\eta_{5a}/(k\zeta_a)$, were calculated, and were plotted with respect to the non-dimensional encounter wave frequency, ω_e^*.

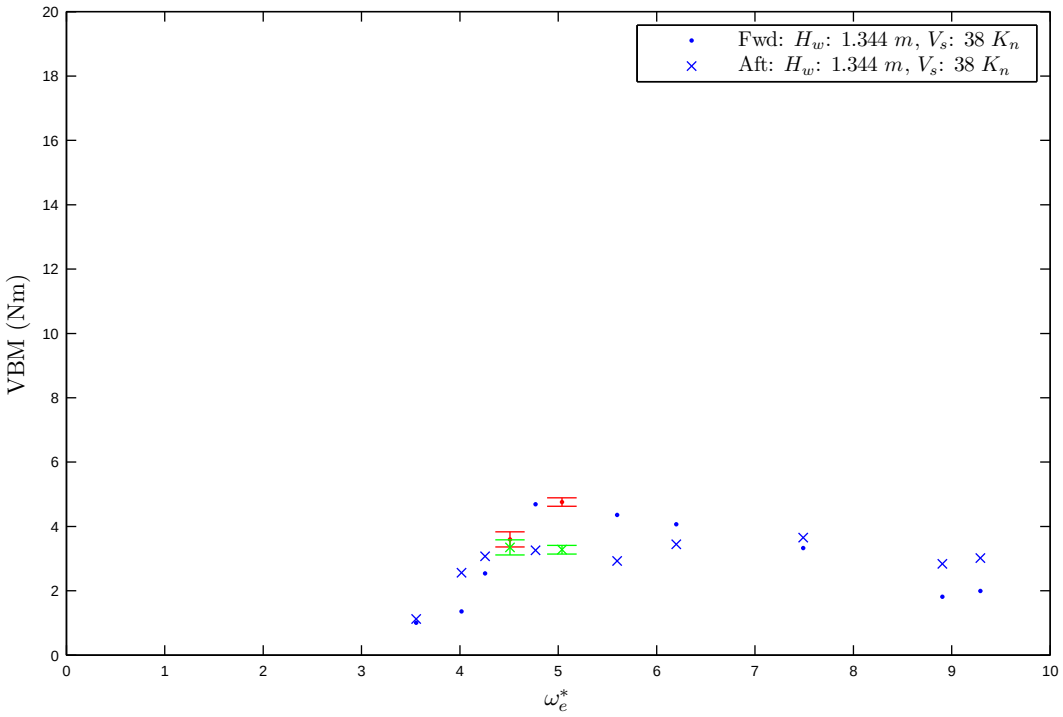

Figure 3.41: Error analysis for the measured Hogging VBM for Condition 20.

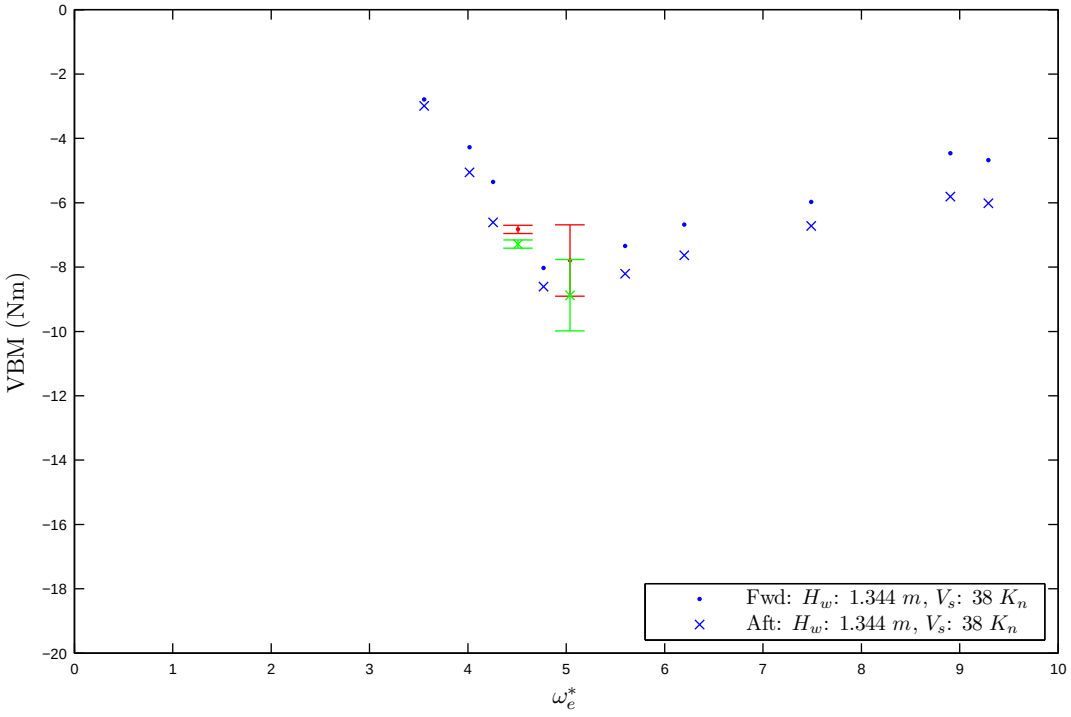

Figure 3.42: Error analysis for the measured Sagging VBM for Condition 20.

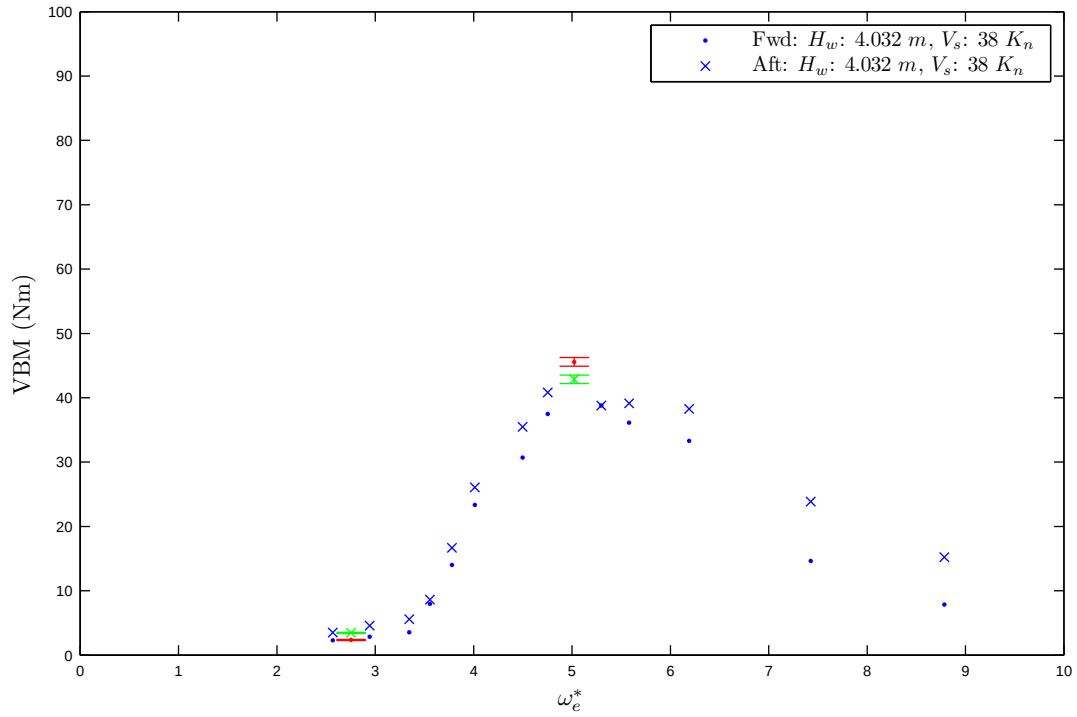

Figure 3.43: Error analysis for the measured Hogging VBM for Condition 33.

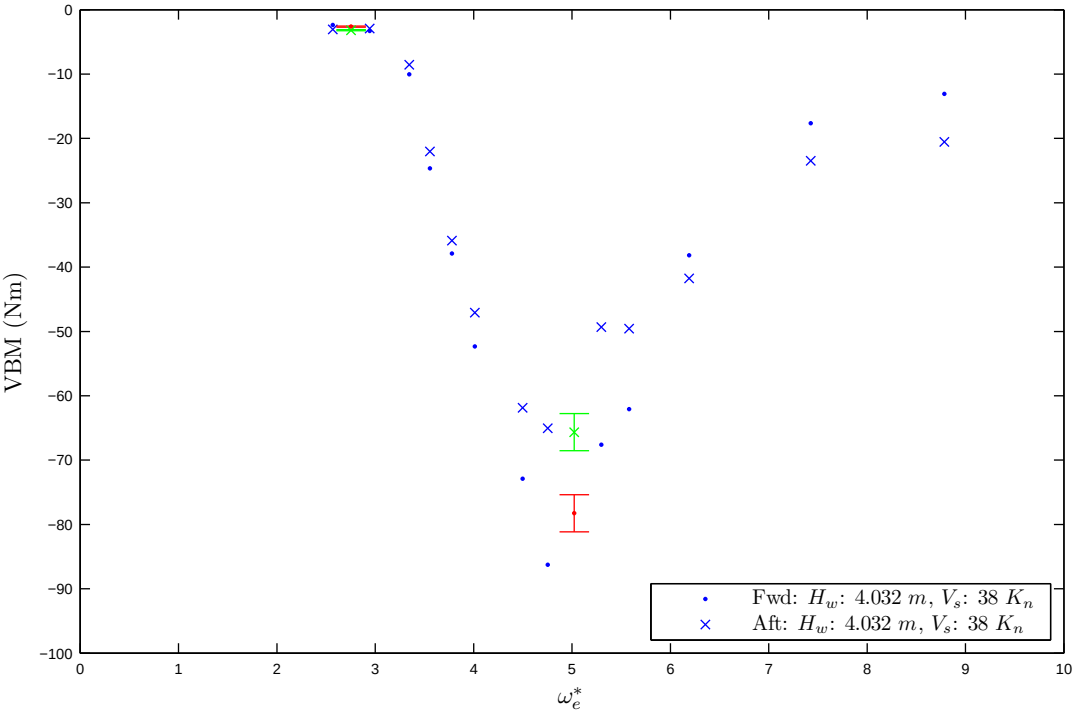

Figure 3.44: Error analysis for the measured Sagging VBM for Condition 33.

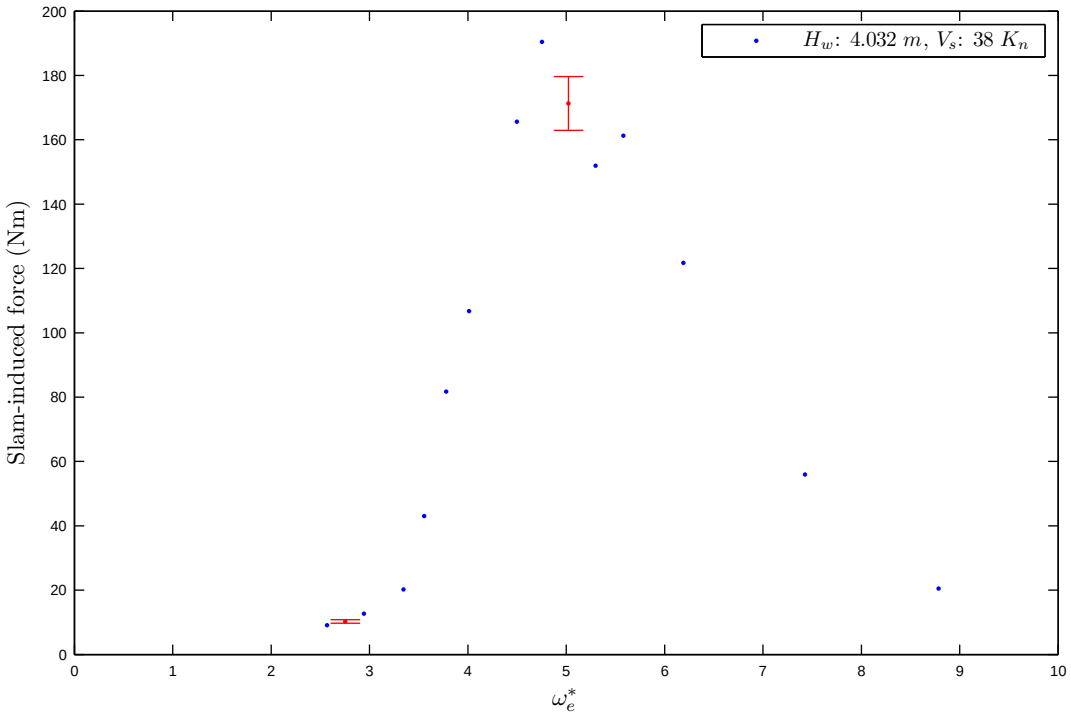

Figure 3.45: Error analysis for the slam-induced force reponse.

3.9.1 Hydroelastic Effects on Ship Motion

The influence of the elastic link on ship motion was investigated by comparing the different type of links between the rigid segments: i.e. solid hollow links (SHL) for the solid configuration and elastic links (EL) for the hydroelastic configuration, respectively. In total, five conditions were tested for the comparison at 1.55 and 2.94 m/s, details for each condition are shown in Table 3.4.

Transfer functions for the wave height of 1.344 m at the speed of 20 kn are shown in Figure 3.46 as an example comparison between the link type. Both the resonant peaks of the heave and pitch for the rigid configuration C8 and hydroelastic configuration C36 occurred almost at the same non-dimensional encounter frequency. Except for the resonant peak region, the magnitudes of the non-dimensional heave and pitch coincided. The other four cases are presented individually in Appendix F.

The transfer functions for the heave and pitch for 38 and 20 Kn conditions are presented in Figures 3.47 and 3.48, respectively.

As can be seen in the heave response, the hydroelastic configuration resulted in a slight reduction of the resonant peak magnitude of the transfer function compared to the rigid configuration. Differences in the resonant peak magnitude and frequency were investigated, and the results are shown in Figures 3.49 and 3.50. The heave resonant response was reduced more than the pitch resonant response. The difference for the pitch motion reduced as the wave height increased. On average, the resonance peak magnitude difference was 8% for the heave response, and 3.25%

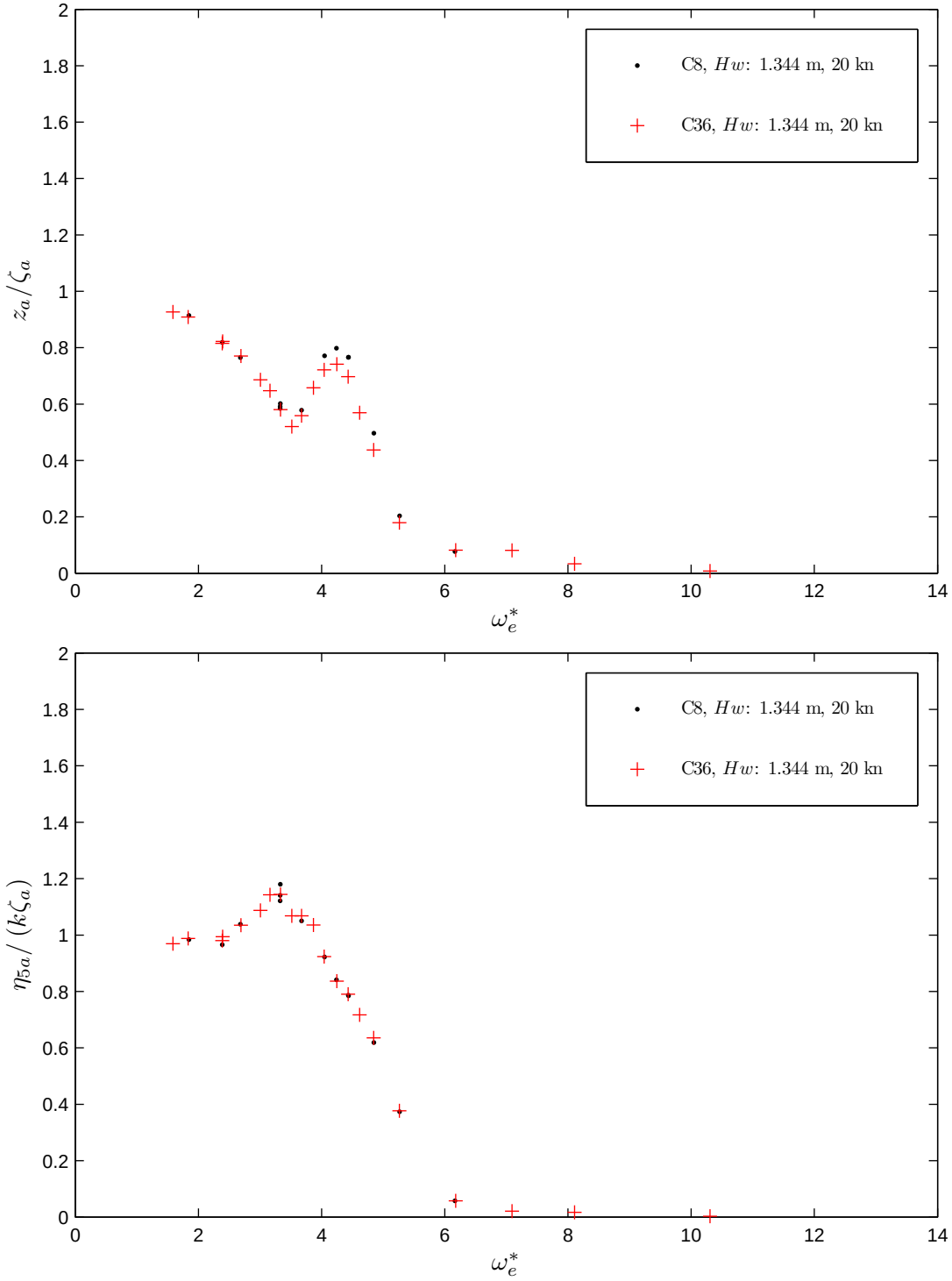

Figure 3.46: Elastic link influence to the RAOs for heave and pitch motions for the wave height, H_w/T = 0.39 plotted as a function of the non-dimensional encounter angular wave frequency, ω_e^*. The model speed was maintained at a constant speed of F_n = 0.32. (C8: Solid link, C36: Elastic link)

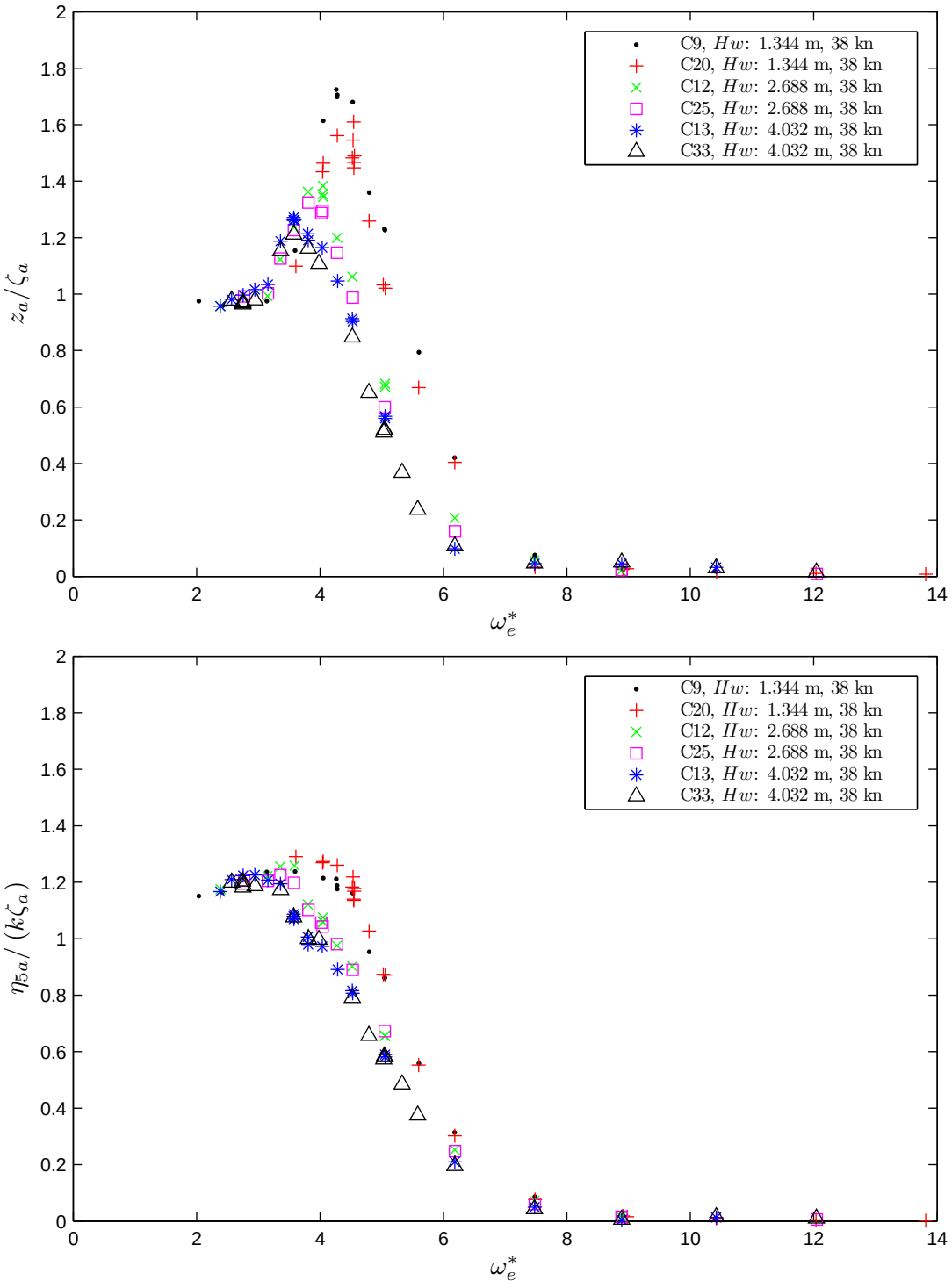

Figure 3.47: Elastic link influence to the RAOs fo heave and pitch motions by varying the wave height, H_w plotted as a function of the non-dimensional encounter angular wave frequency, ω_e^*. The model speed was maintained at a constant speed of $F_n = 0.60$.

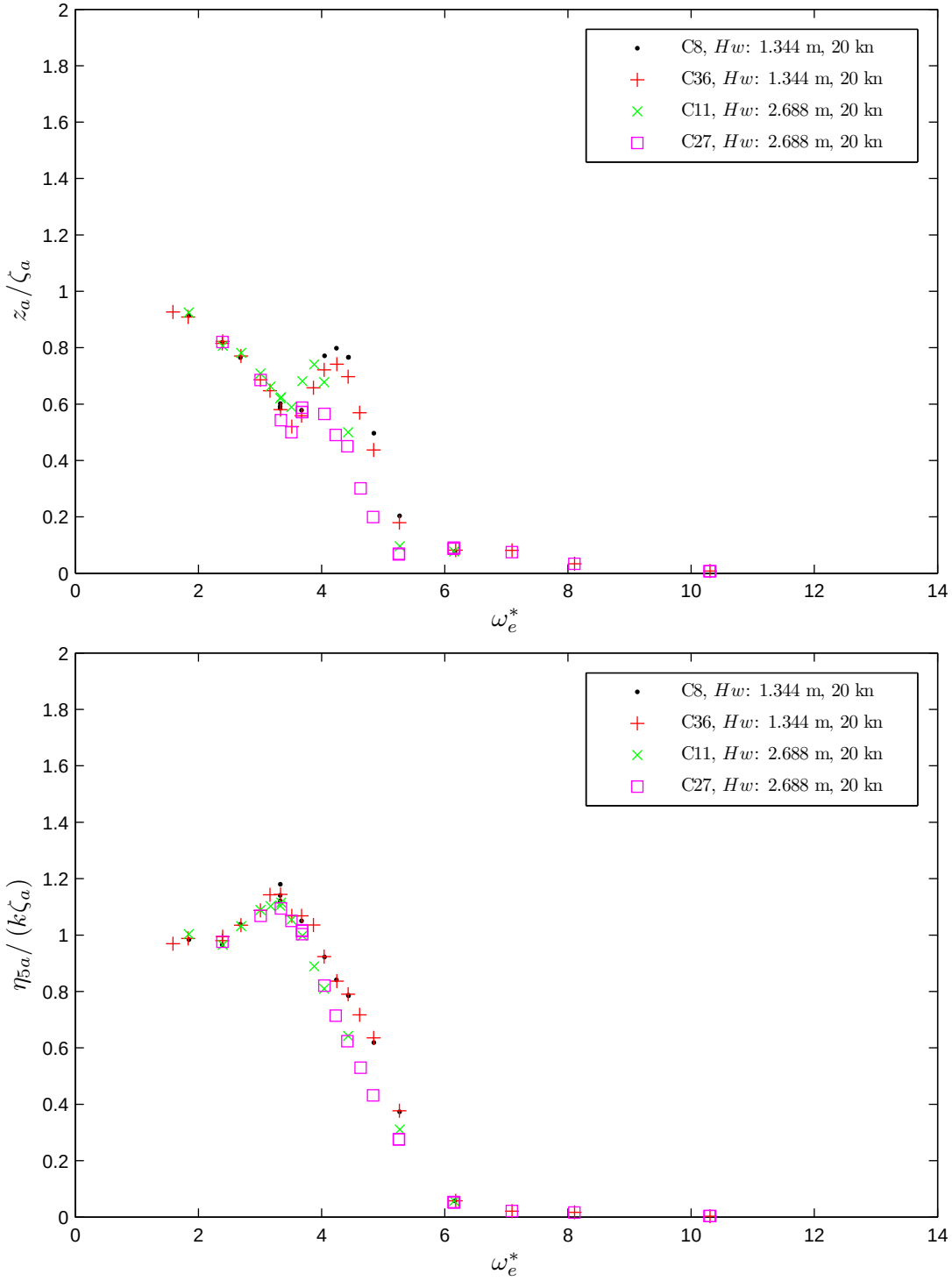

Figure 3.48: Elastic link influence to the RAOs for heave and pitch motions varying the wave height, H_w plotted as function of non-dimensional encounter angular wave frequency, ω_e^*. The model speed was maintained at a constant speed of $F_n = 0.32$.(C9,C12,C13: Solid link, C20,C25,C33: Elastic link)

for the response motion.

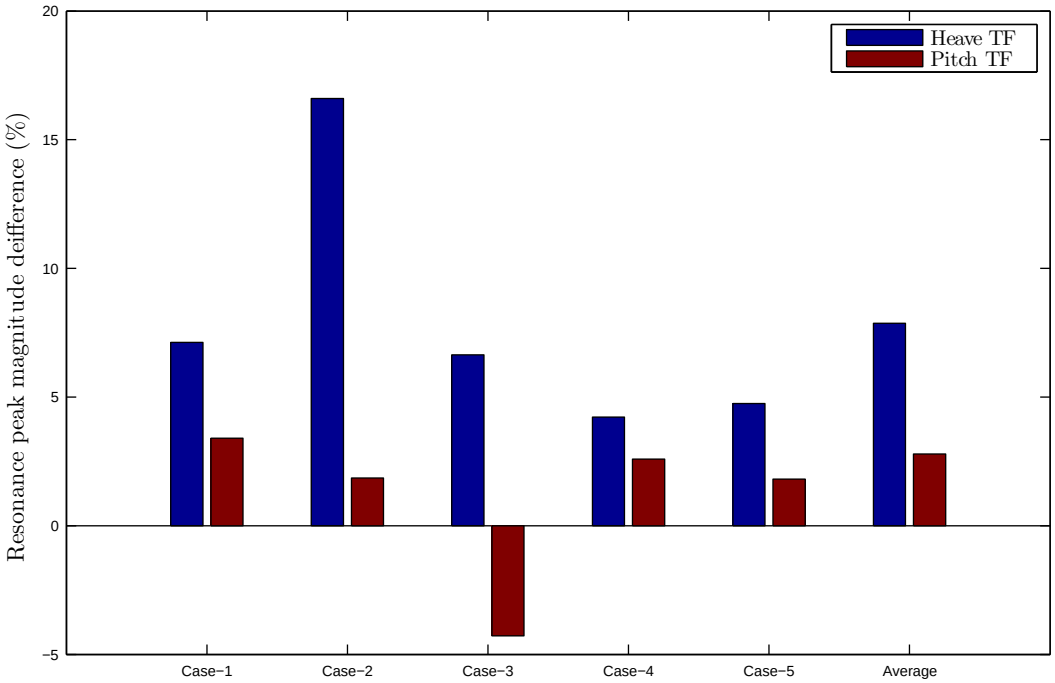

Figure 3.49: Absolute difference in resonant peak magnitude of the ship motion transfer function between the rigid model and HSM. The difference was calculated by $(Peak_{Rigid} - Peak_{Elastic})/Peak_{Rigid} \times 100$. Case-1: 20 Kn and $H_w = 1.344$ m; Case-2: 20 Kn and $H_w = 2.688$ m; Case-3: 38 Kn and $H_w = 1.344$ m; Case-4: 38 Kn and $H_w = 2.688$ m; Case-5: 38 Kn and $H_w = 4.032$ m.

The differences in the resonant frequencies did not indicate a clear tendency. The lower speed case did not show any clear difference in the resonant frequency between the solid and hydroelastic configuration. For the higher speed cases, a difference in the resonant frequency for the pitch motion was observed. At the 38 K_n case, the resonant peaks were reduced between 3 and 7%. With the reduction in the resonant peak magnitude, it indicated that the damping increased in the hydroelastic configuration compared to the rigid configuration. Presumbaly wave-indcued energy for the hydroelastic configuraiton was also absorbed into the deformation of the model in adition to the motions. Based on the oscillatory problem for strip theory, the reduction in motion causes the reduction in hydrodyanmic added mass. Assuming the hydrostatic restoring force was not affected significantly due to the small motion difference between the hydroelastic and rigid configuraiton at the high speed case, an increase in the resonant frequency would be expected with the hydrodyanmic reduced added mass. However, the experimental results presented the contrary results of a reduction in the resonant frequency. Therefore, it strongly supports the view that the damping effect was strongly dominated from the strucutral dammping of hydroelastic configuration, not from the hydrodynamic effcts. This experimentally showed that ship hydroelasticity did have a small influence on its the ship motion at both the low and high speed tested, and on its resonant frequency at the high speed tested.

The resonant frequency reduction due to ship hydroelasticity was more dominant in the higher

speed case of 38 Kn, because the pitch and heave motion were larger than those of the lower speed cases. Therefore more drastic changes in added mass and the damping factors for the ship motions and structural vibration between the hydroelastic and rigid configuration can be expected to be a reason of the resonant frequency reduction. The elastic links in the hydroelastic configuration were prone to cause a small vibration of the model structure, and then the small oscillation caused more energy dissipation into water. As conventionally the ship motion oscillation causes the energy dissipation into the water field, this small perturbed oscillatory motion of the fluid induced by the structural vibration additionally increased the damping effect for the ship motion. On contrary, the rigid configuration does not have structural vibration, it does not induce the hydrodynamic damping effects due to the vibration. Therefore, the HSM in the hydroelastic configuration increased more hydrodynamic and structural damping factor than in the rigid configuration. This experimental result showed that ship hydroelasticity was experimentally demonstrated on the HSM successfully.

The key factor of the reduction in motion was considered to be the hydroelastic phenomena. In the rigid configuration the wave loads transmitted to the model were consumed as an energy of ship motion. However for the hydroelastic configuration, the wave load transmitted to the model was used for structural vibration as well as for ship motion. It evidentially showed that the hydroelasticity of the ship affected the motion to some extent.

3.9.2 Seakeeping Results for the Hydroelastic Segmented Model

Transfer functions (TF) for the heave and pitch response for the hydroelastic configuration were obtained from the experimental data in the head-sea conditions. The non-dimensional heave, z_a/ζ_a, and non-dimensional pitch, $\eta_{5a}/\left(k\zeta_a\right)$, were calculated based on the peak-to-trough magnitude method, and were plotted with respect to the non-dimensional encounter wave frequency, ω_e^*. The linearity of the heave and pitch responses were observed to assess the influence of the wave height and vessel speed on the motions.

Transfer functions for non-dimensional heave and non-dimensional pitch were plotted against ω_e^* at constant speeds of 20 K_n, 30 K_n, 38 K_n, 45 K_n, and 50 K_n, with a variation in the wave height, and are shown in Figures 3.51, 3.52, 3.53, 3.54, and 3.55, respectively.

At the constant speed with varying wave height, in general the resonant peak magnitudes of the non-dimensional heave were reduced as the wave height increased. Exceptionally, the case of 20 K_n showed the decrease of the resonant peak in smaller waves of up to 2.688 m, as shown in Figure 3.51. For the larger wave height cases of 4.032 and 5.376 m, interestingly the resonant peak of the non-dimensional heave rose again. In Figures 3.51, 3.52,and 3.53, the heave transfer function indicated a distinct non-linearity of the heave response with respect to the wave height between the range of ω_e^* from 3 to 6, which is referred to here as a non-linear response region. The resonant heave peak always occurred within this non-linear region. The resonant peaks were generally found around the range of ω_e^* from 3.5 to 4.5. The non-dimensional resonant frequency

for a heave resonant peak was reduced as the wave heights were increased when maintaining a constant speed, as shown in Figures 3.51, 3.52, and 3.53. Above the $\omega_e^* = 6$, the heave response became significantly smaller, hence there was a clear linearity with respect to the wave height at 20 and 30 K_n.

The results at the constant speeds, as presented in Figures 3.51, 3.52, and 3.53, showed the heave resonant peak was reduced as well. This indicate, based on an implication of strip theory, that the vertical large heave displacement due to the larger wave height increased the added-mass factor and/or reduced the stiffness factor (hydrodynamic restoring factor) for ship motion, hence z_a/ζ_a of the heave resonant frequency was reduced. The added masswas increased because of the larger motion amplitude due to the large wave height. In addition, the centre bow effectiveness in larger waves, might also contribute to increasing the added-mass and damping factors. The hydrostatic restoring factor is generally obtained as $\rho g B_x$ for the sectional hydrodynamics coefficient used by Doctors (1999) and Lloyd (1989). As the wave-piercer bow was fully submerged into, and jetted out of the large waves, the local waterline beam length, B_x, for the hydrostatic restoring force factor became zero. Hence, in larger waves, the more reduction in the hydrostatic restoring factor of the wave-piercer was expected compared with the hydrodynamic restoring factor in smaller waves. However, as the wave-piercer bow becomes fully submerged, the centrebow provide a reserve buoyancy to generate the hydrostatic restoring factor. From the observation of the reduction of heave resonant peak magnitude, the damping effect of centrebow show significantly effectiveness for reducing the heave and pitch motion.

For the small wave heights up to 2.688 m in 20 K_n, the resonant peak was reduced due to the increased damping effect, as shown in Figure 3.51. For the 38 Kn cases in Figures 3.53 and 3.52, the damping effect effectively reduced the non-dimensional heave resonant peak as the wave height was increased. For larger wave heights, the wave-piercer bow effectively penetrated into the wave by avoiding the bow being lifted by the waves. As a consequence, it increased the damping effect and reduced the heave resonant peak magnitude of the heave transfer function.

The case of the 50 K_n showed that the resonant peak magnitude was smaller than the one for 45 K_n for the lower wave heights, H_w, of 0.896 and 1.344 m. The case for $V_{K_N} = 45$ and 50 K_n are shown in Figures 3.54 and 3.55, respectively. The resonant peak magnitudes of heave response at the lower wave height range of 0.896 and 1.344 m behaved in a similar manner Interestingly, the response peaks remained within a small range of ω_e^* around 4.5 as shown in Figures 3.54 and 3.55.

The transfer functions showed the strong non-linearity of the heave and pitch response at the resonant peak region with respect to the wave height variation at a constant speed.

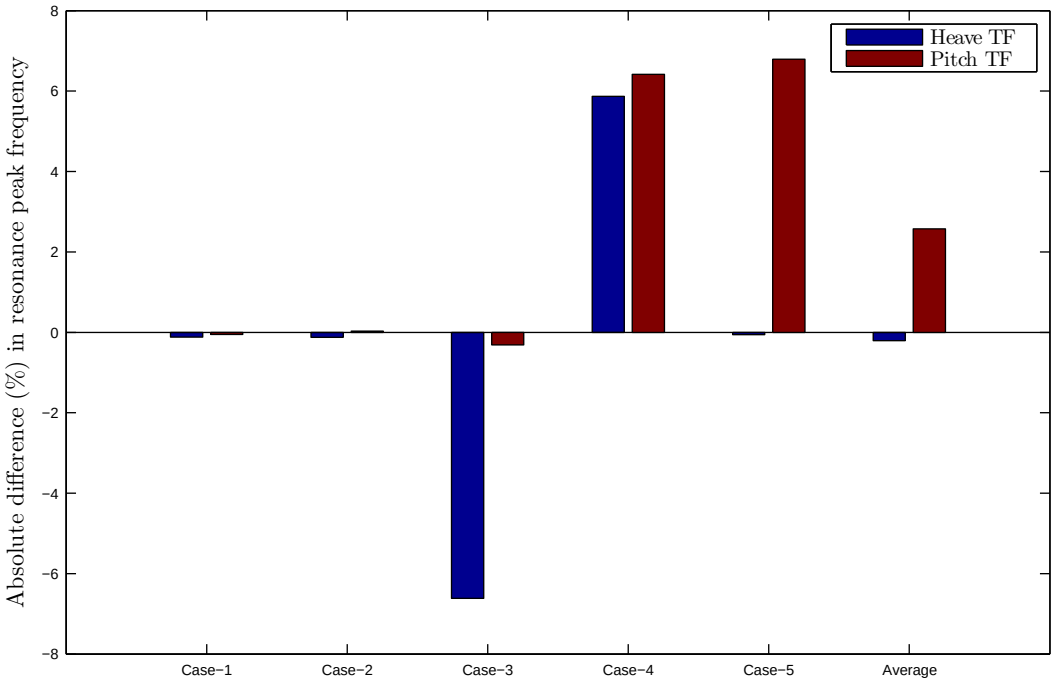

Figure 3.50: Absolute difference in resonant peak frequency of the ship motion transfer function between the rigid model and HSM. The difference was calculated by $(Peak_{Rigid} - Peak_{Elastic})/Peak_{Rigid} \times 100$. Case-1: 20 Kn and $H_w = 1.344$ m; Case-2: 20 Kn and $H_w = 2.688$ m; Case-3: 38 Kn and $H_w = 1.344$ m; Case-4: 38 Kn and $H_w = 2.688$ m; Case-5: 38 Kn and $H_w = 4.032$ m.

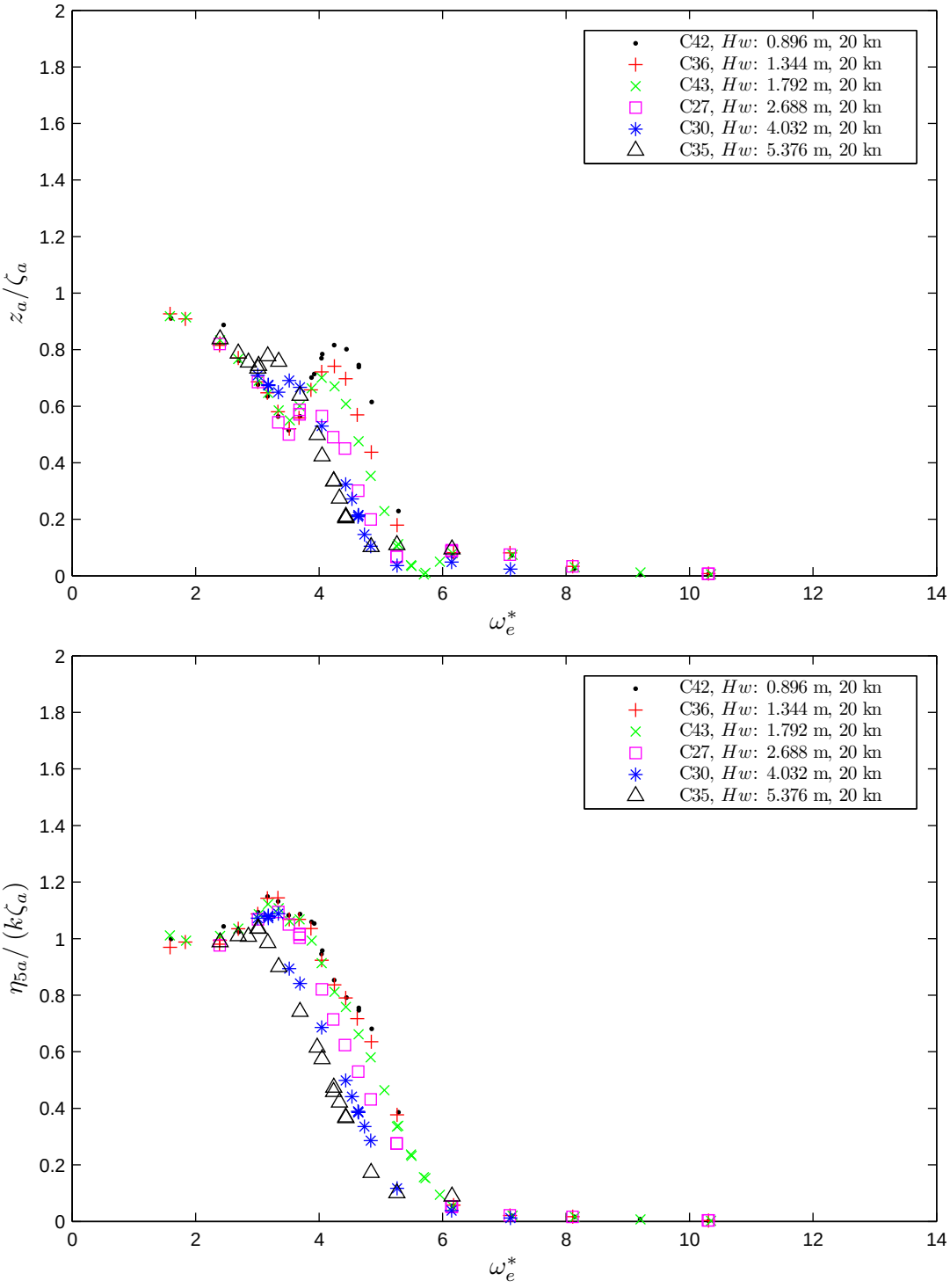

Figure 3.51: Comparison of RAOs for heave and pitch motions by varying the wave height, H_w plotted as a function of the non-dimensional encounter angular wave frequency, ω_e^*. $F_n = 0.32$.

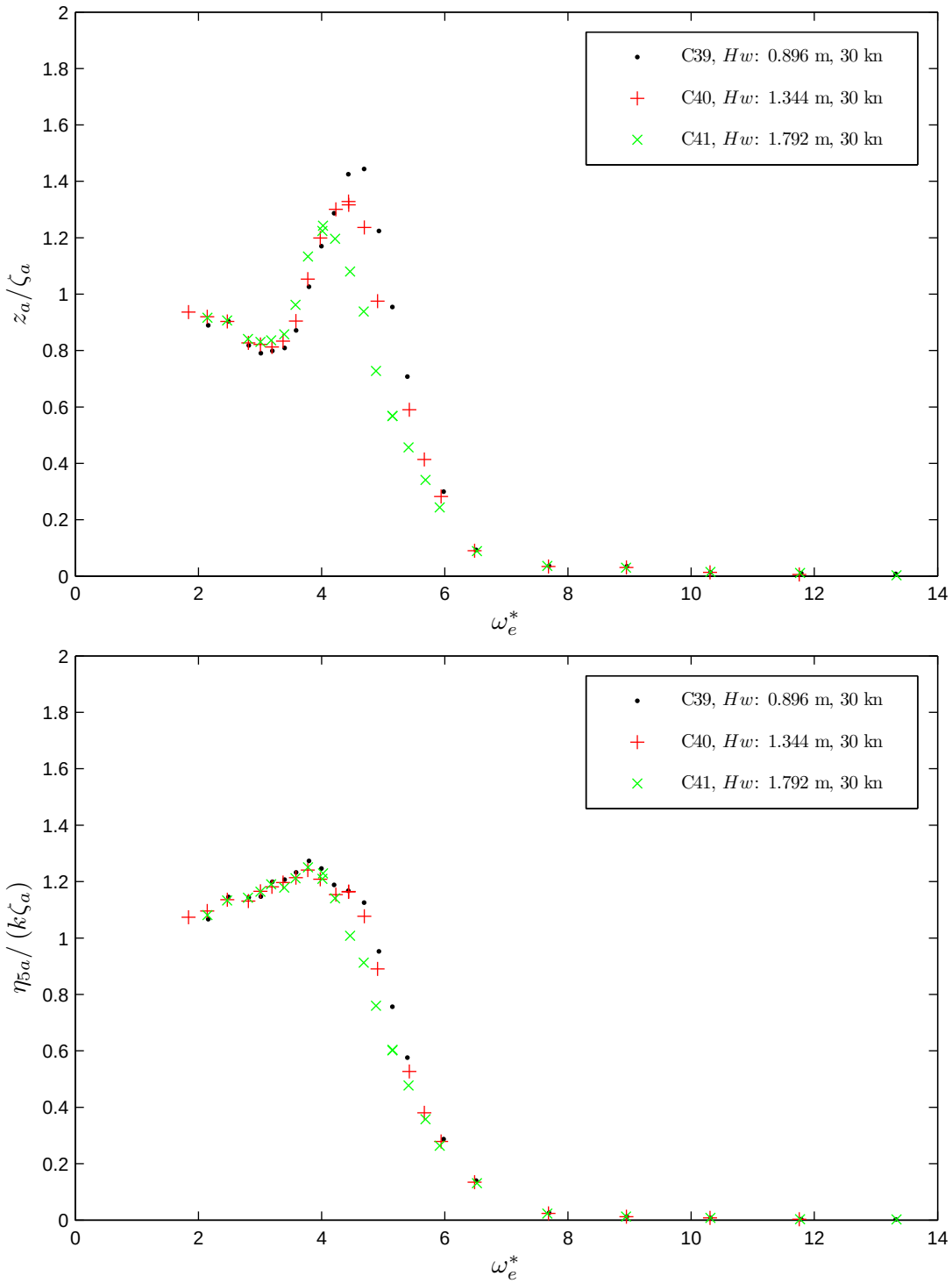

Figure 3.52: Comparison of RAOs for heave and pitch motions by varying the wave height, H_w plotted as a function of the non-dimensional encounter angular wave frequency, ω_e^*. $F_n = 0.48$.

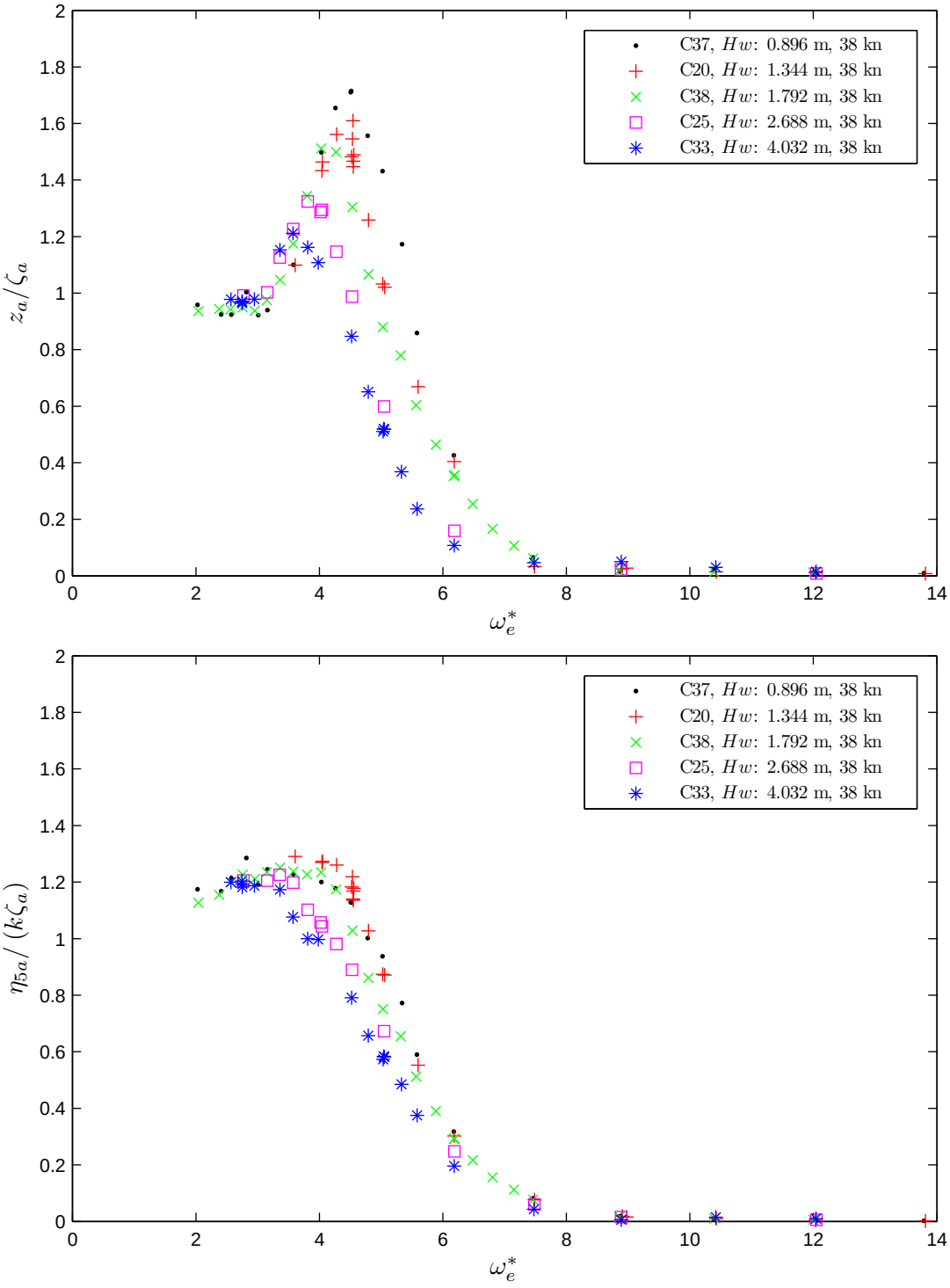

Figure 3.53: Comparison of RAOs for heave and pitch motions by varying the wave height, H_w plotted as a function of the non-dimensional encounter angular wave frequency, ω_e^*. $F_n = 0.60$.

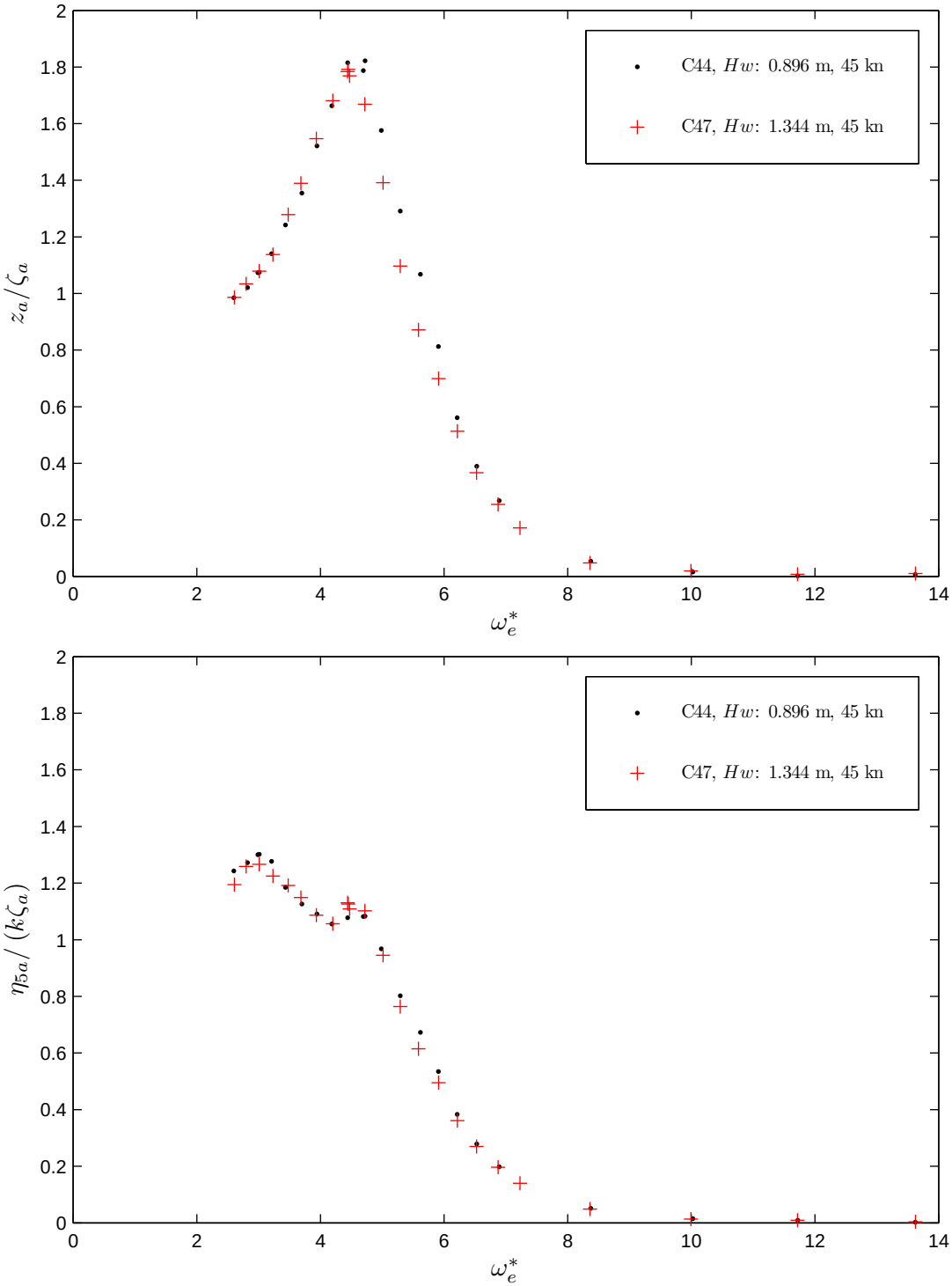

Figure 3.54: Comparison of RAOs for heave and pitch motions by varying the wave height, H_w plotted as a function of the non-dimensional encounter angular wave frequency, ω_e^*. $F_n = 0.72$.

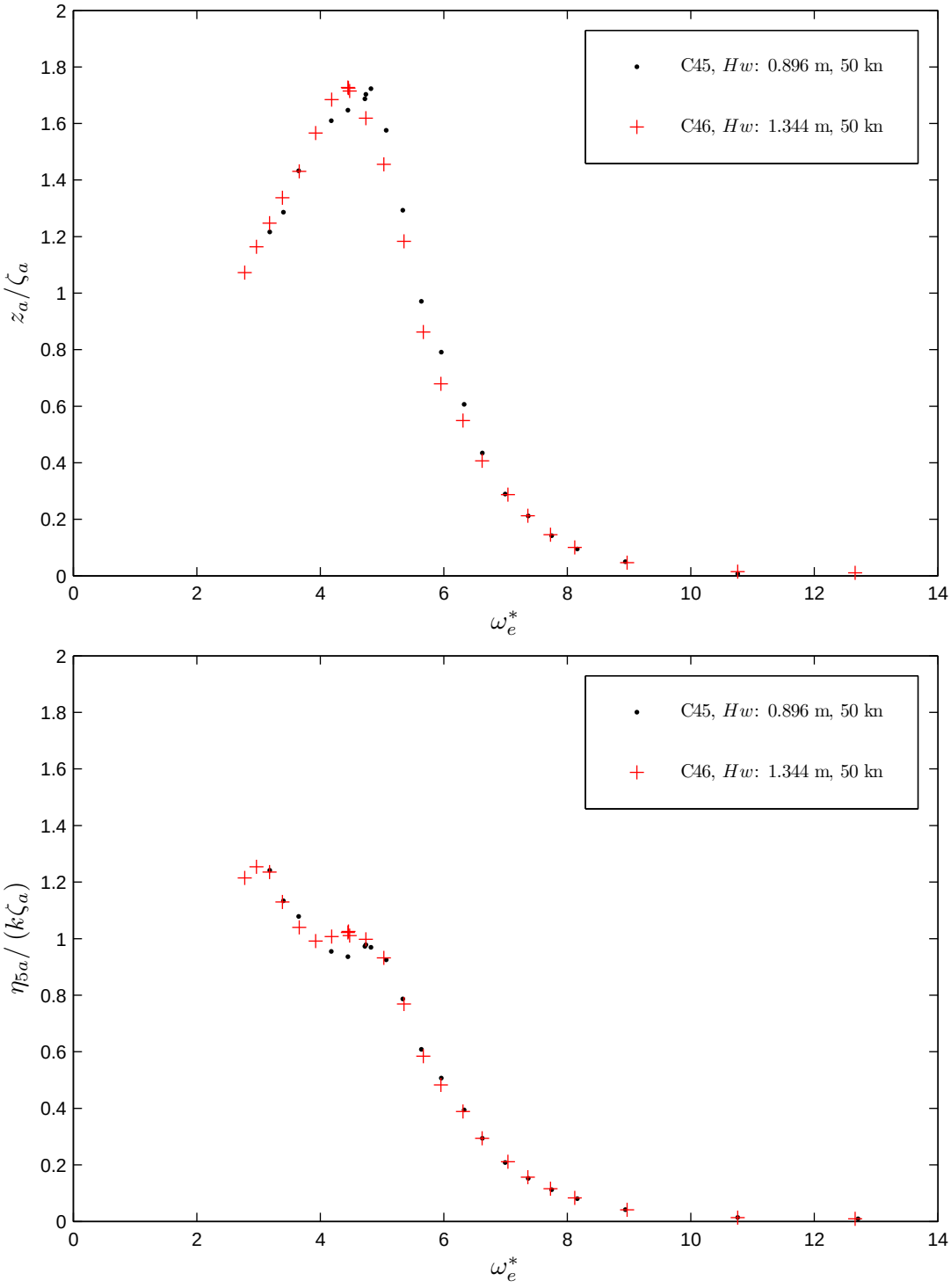

Figure 3.55: Comparison of RAOs for heave and pitch motions by varying the wave height, H_w plotted as a function of the non-dimensional encounter angular wave frequency, ω_e^*. $F_n = 0.79$.

Transfer functions for the non-dimensional heave and pitch response plotted against the non-dimensional encounter wave frequency at the constant wave height of 20 mm, 30 mm, and 40 mm, are presented in Figures 3.56, 3.57, and 3.58, respectively.

The resonant frequencies of heave responses at the same wave height were almost constant regardless of the change in the velocity. The resonant frequency of the heave and pitch were dependent on the encounter wave frequency. The resonant peak of the heave response increased as the velocity increased at a constant wave height, for the cases of 20, 30 and 38 K_n. The heave and pitch response showed a strong non-linearity with respect to the ship speed at constant wave height. As the speed increased, generally the heave resonance increased, this was observed up to $V_{KN} = 45\ K_n$.

Faltinsen (2005) demonstrated that the increase in model speed resulted in the higher wave exciting force for resonant heave motions; the higher wave exciting forces enhanced the heave amplitude. The wave exciting force of the heave consists of the Froude-Kriloff force and diffraction forces, which can be increased by the velocity at the stern of the vessel. This was presented by Doctors (1999). Therefore, the increase in the velocity results in the increase in the heave resonant peak at a constant wave height for the moderate speed range up to $F_n = 0.72$.

The resonant peak magnitudes for the heave and pitch for all the conditions were obtained and plotted against the velocity, as shown in Figure 3.59. The heave resonant peak occurred at 45 K_n, and increased as the velocity increased up to 45 K_n. The pitch motion showed the maximum resonant peak either at 38 and 45 K_n. Generally, the resonant peak magnitudes of the heave and pitch transfer function were reduced as the wave height increased. Both the transfer function for the heave and pitch responses showed strong non-linear behaviour to both wave height and velocity.

These results provide a variable insight into the behaviour of a wave-piercing catamaran with a centrebow. Not only can they be used to asses the motion in a range of realistic condition, although use in this way should include caution due to the strong non-linear behaviour, they are also an important data set for validating seakeeping numerical codes. One factor to bear in mind is that these results are for a bare hull with no ride control (RCS) system fitted, a RCS will likely to alter the motion significantly for the full scale vessel.

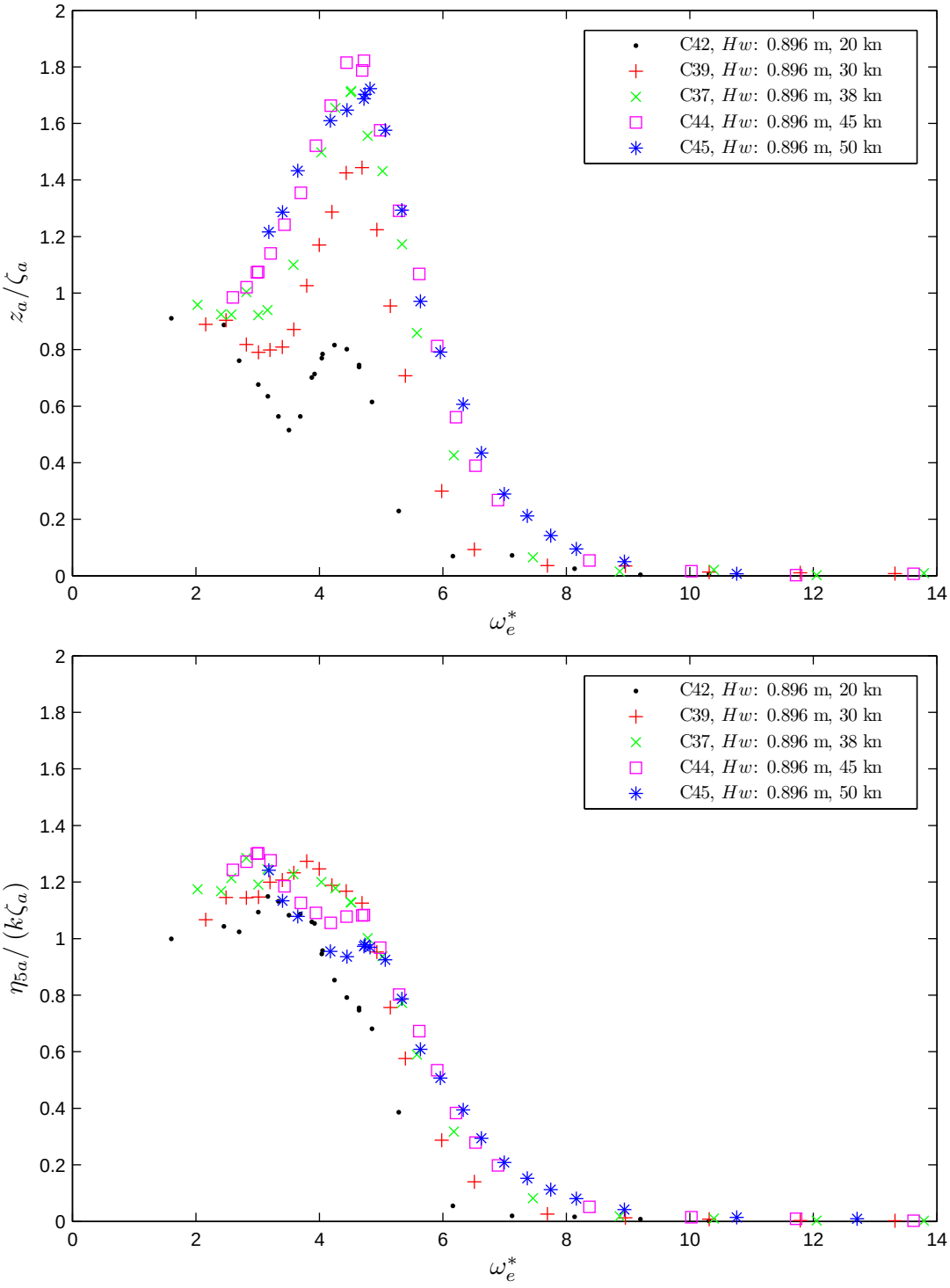

Figure 3.56: Comparison of RAOs for heave and pitch motions by varying the speed, V_{KN} plotted as a function of the non-dimensional encounter angular wave frequency, ω_e^*. $H_w/T = 0.26$.

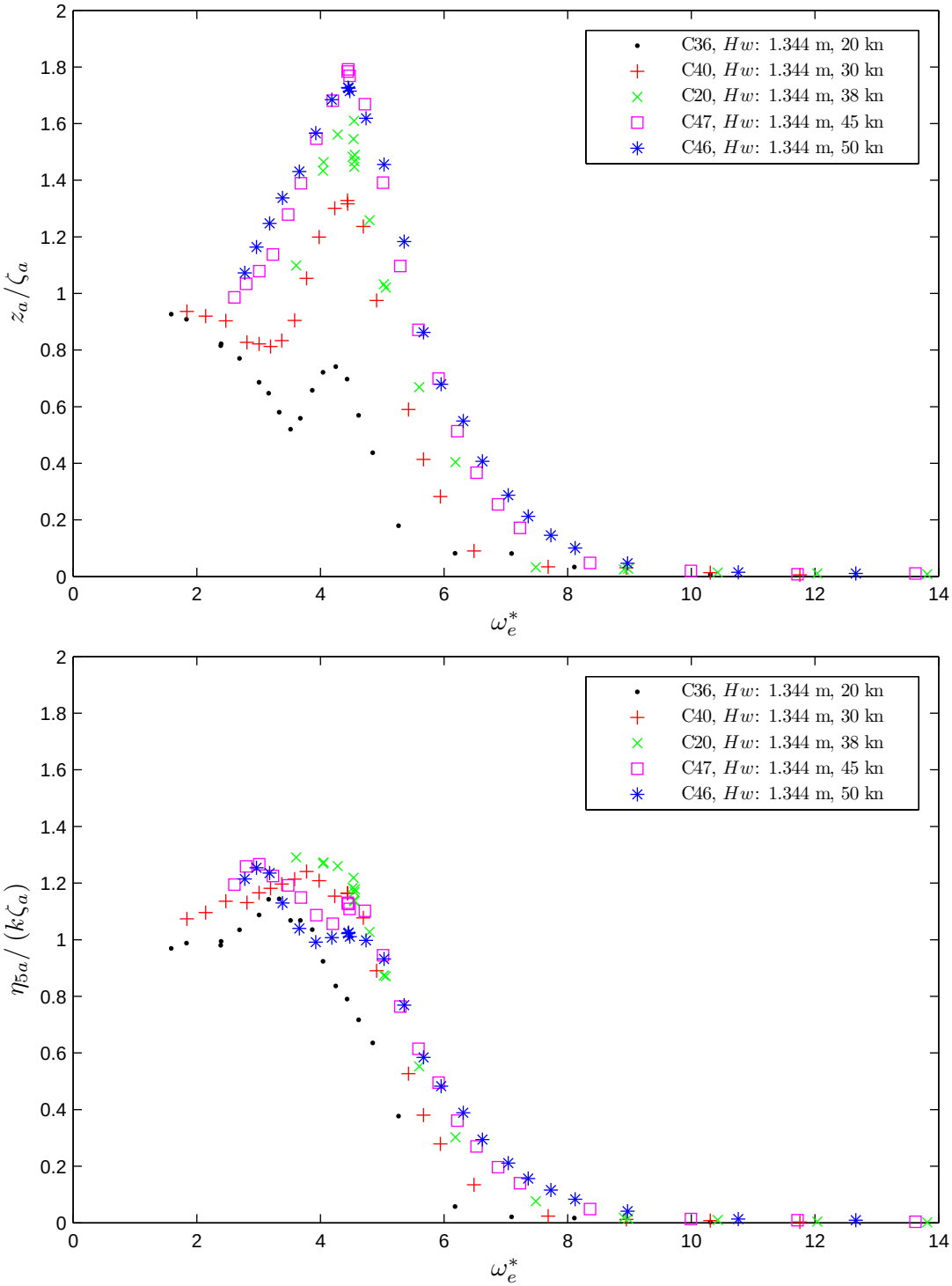

Figure 3.57: Comparison of RAOs for heave and pitch motions by varying the speed, V_{KN} plotted as a function of the non-dimensional encounter angular wave frequency, ω_e^*. $H_w/T = 0.39$.

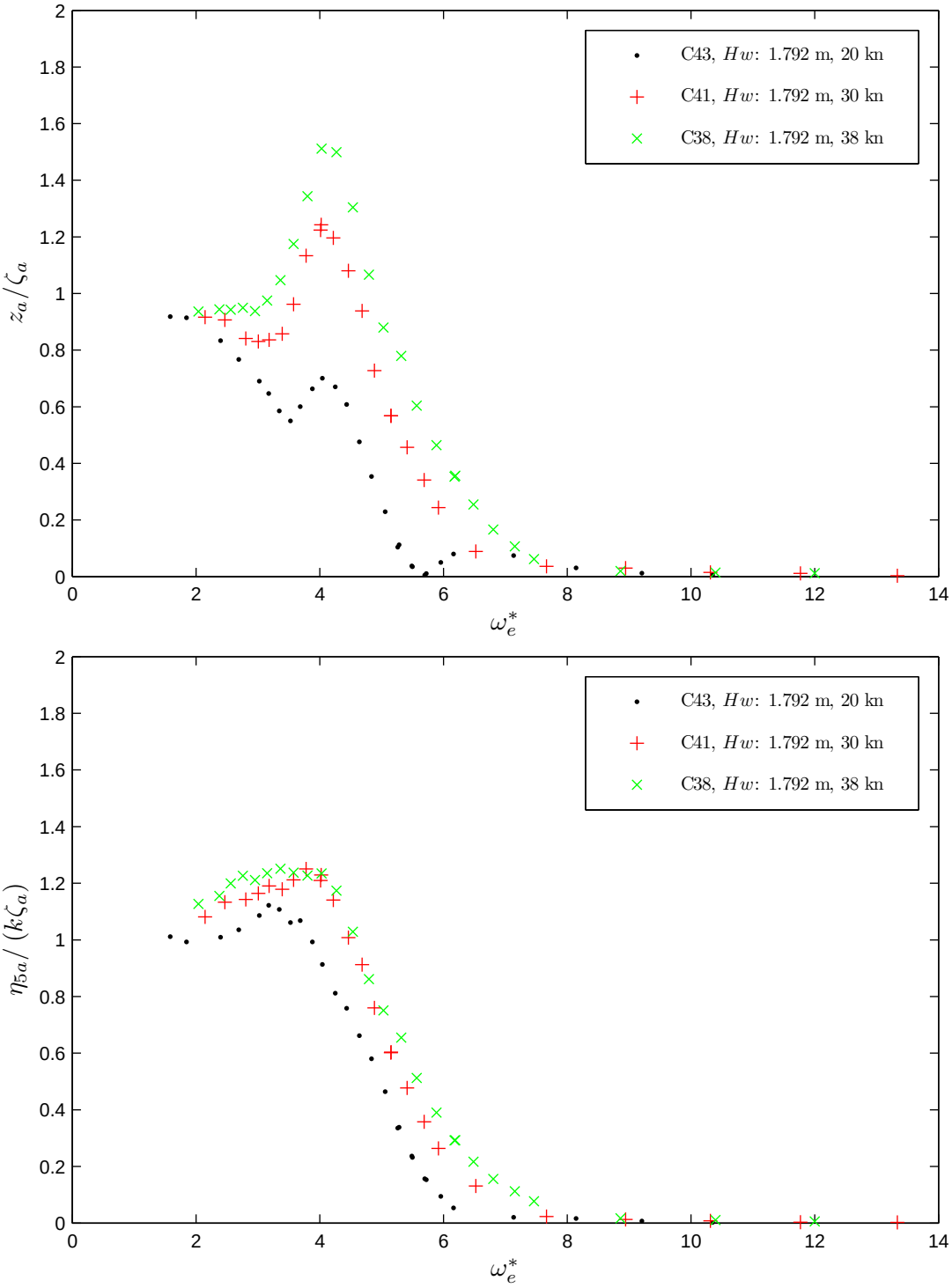

Figure 3.58: Comparison of RAOs for heave and pitch motions by varying the speed, V_{KN} plotted as a function of the non-dimensional encounter angular wave frequency, ω_e^*. $H_w/T = 0.52$.

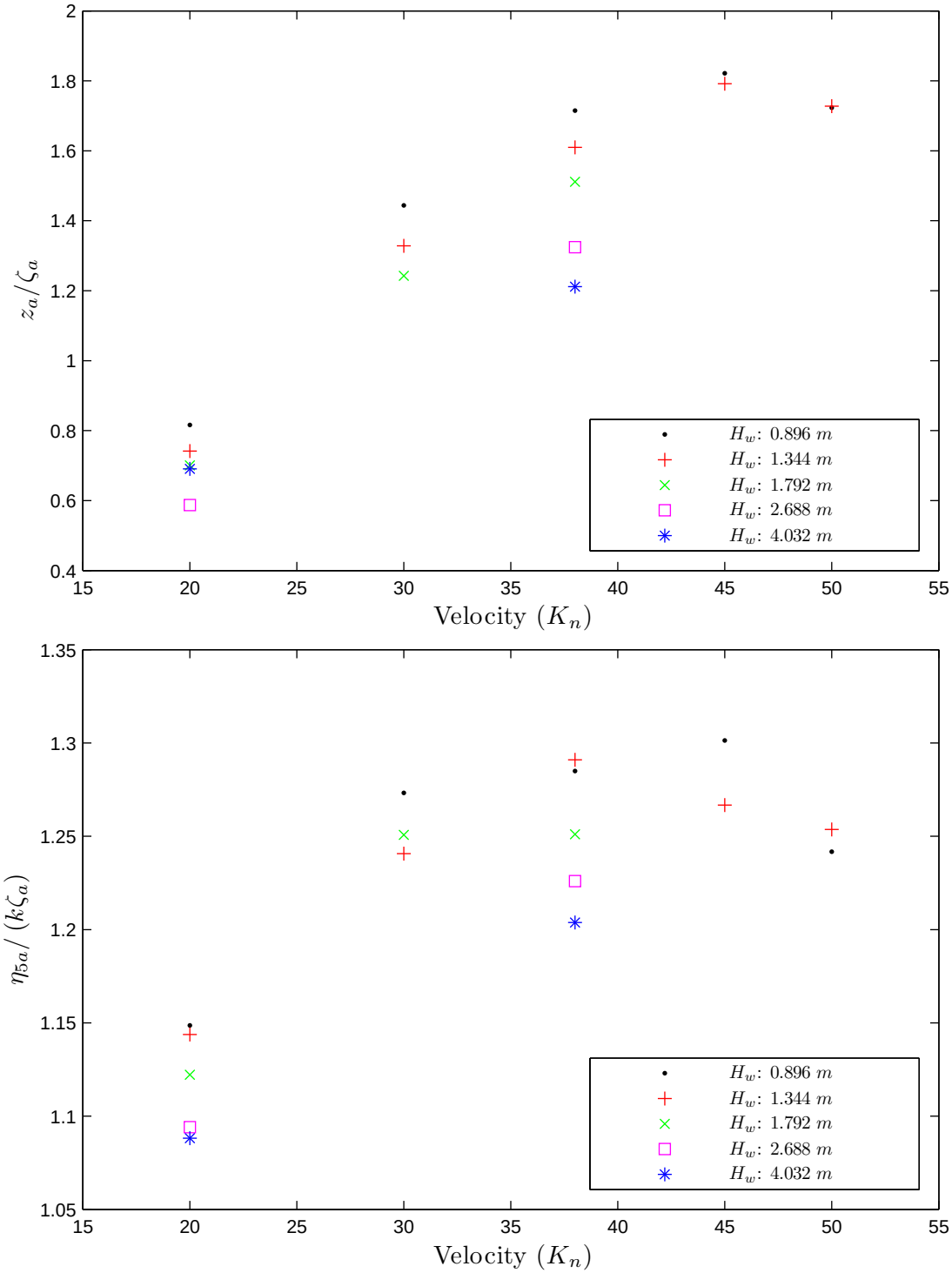

Figure 3.59: Resonance peak comparison for heave and pitch motion transfer function under the hydroelastic configuration

3.10 Wave Loads Results

Wave-induced loads in head-sea conditions were obtained; generally, the VBM in small waves without a slamming is a global wave-induced load, whilst for large waves, the VBM is a combination of global wave-induced load and slam load. The slam load is a localised impact wave force onto the centre bow. Based on the obtained calibration factors explained in Section 3.5, the VBM and slam-induced loads were obtained in the post processing.

3.10.1 Measured Wave-Induced Loads on Demihulls for Small and Large Waves

The VBMs were successfully obtained from the elastic links at the segmentation gaps on the demi-hulls. The wave-induced VBM was found by subtracting the forward-velocity-induced VBM in the calm water from the total measured VBM. The measured wave-induced VBM responses were obtained by the peak-to-trough method for sets of adjacent peaks and troughs in the time domain. Hereafter, VBM is used to denote the measured wave-induced VBM. Since the slam force was expected to contribute mainly to the sagging VBM rather than the hogging VBM, the hogging and sagging VBM responses were also obtained. Generally, the hogging VBM is measured in positive values and the sagging VBM is measured in negative values. The positive slam force acting upwards onto the centre bow in the vertical axis generates the sagging moment, which is a negative value.

Examples of the VBM responses at the forward elastic links are presented for small and large wave conditions at 20 K_n in Figures 3.60 and 3.61, respectively. The magnitude of the VBM was used in the model scale, although the environmental condition values are described in the full-scale values for convenience.

For the small wave cases in Figure 3.60, the peak-to-trough VBM showed a constant increase especially around the resonant peak regions, as the wave height was increased from 0.896 to 1.792 m. The sagging VBM also increased as the wave height increased. For the large wave height cases at 20 K_n in Figures 3.61, a distinct difference in the magnitude for the VBM was observed. In addition, the absolute magnitude of sagging and hogging VBM differed from each other. The absolute values of the sagging VBM were larger than for the hogging VBM, because the slamming force contributed to the sagging VBM. Selected further examples of VBM responses at the forward and aft elastic links at 20 and 38 Kn in small and large waves are presented in Appendix G.

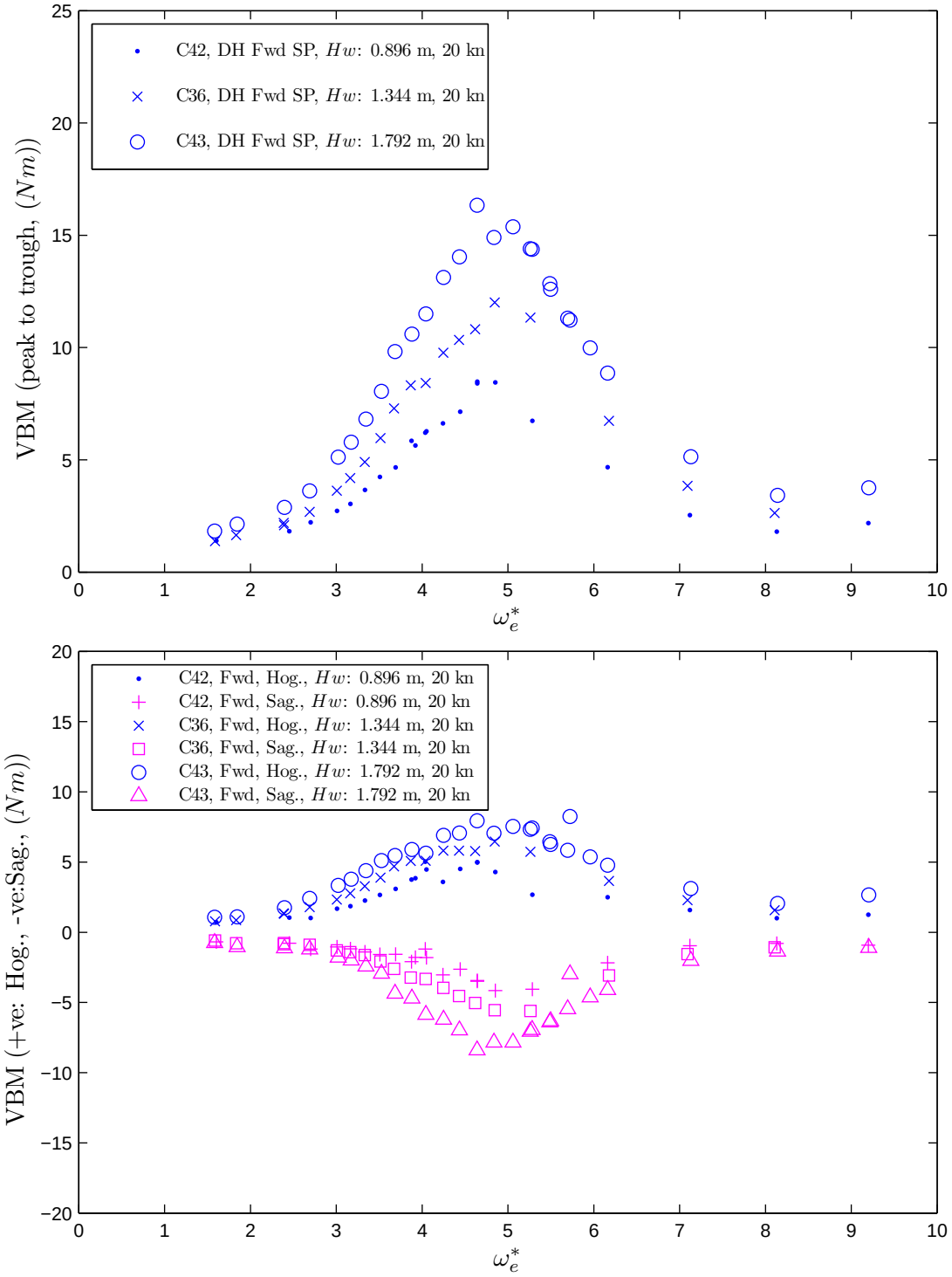

Figure 3.60: Vertical bending moment (peak to trough) and hogging and sagging vertical bending moment at forward elastic links by varying the wave height, are plotted with respect to non-dimensional encounter angular wave frequency, ω_e^*. The model speed was maintained at the constant speed of $F_n = 0.32$.

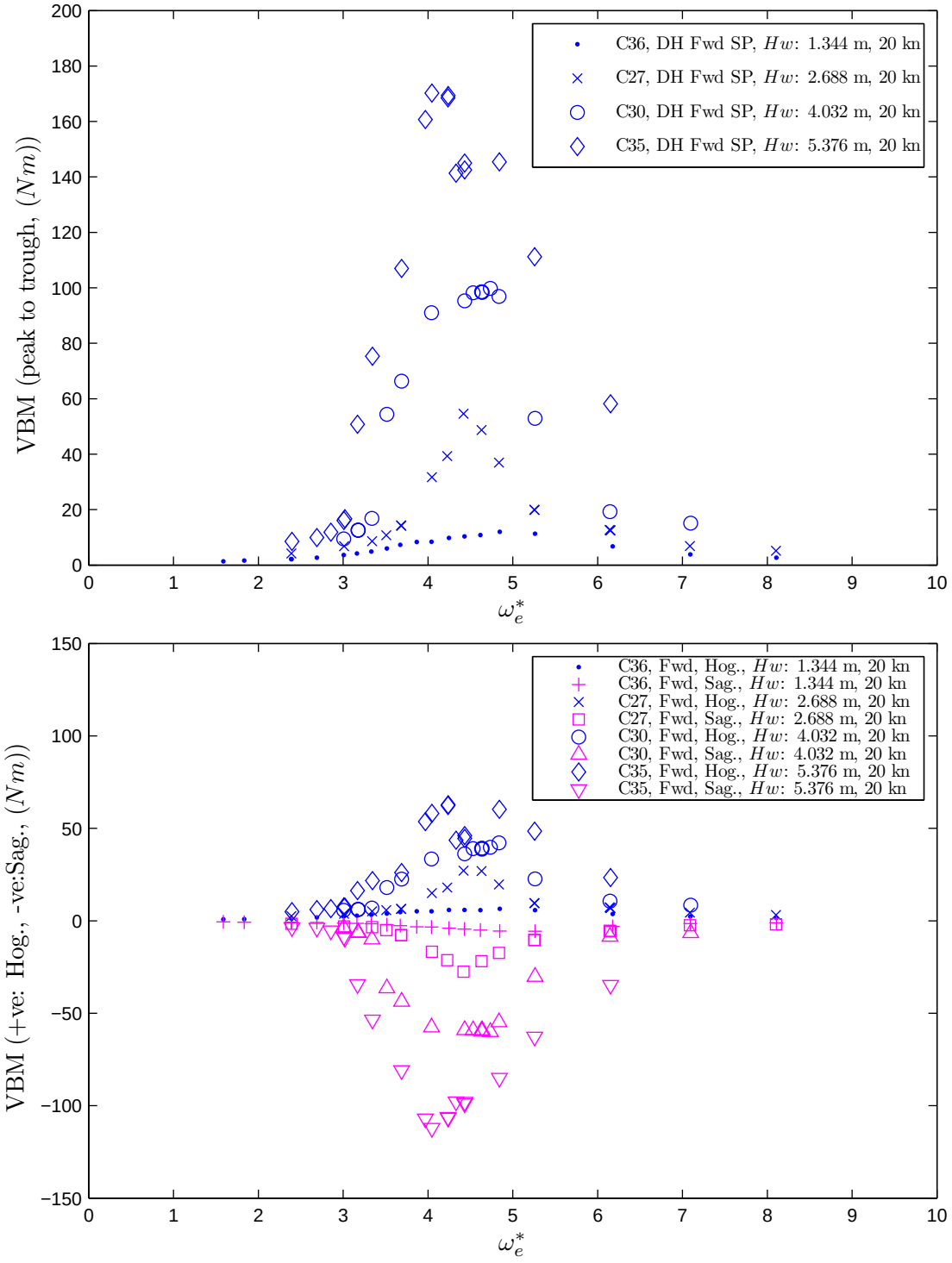

Figure 3.61: Vertical bending moment (peak to trough) and hogging and sagging vertical bending moment at forward elastic links by varying the wave height, are plotted with respect to non-dimensional encounter angular wave frequency, ω_e^*. The model speed was maintained at the constant speed of $F_n = 0.32$.

General trends in the VBMs for wave height and speed variation were investigated. Since the sagging VBMs presented larger absolute values, the sagging VBM was used to map out a pattern of peak magnitude for the sagging VBM response in Figure 3.62. Generally, the increase in speed resulted in the increase in the sagging VBM. Larger wave heights caused larger sagging VBMs. The influence of the wave height was more dominant to the VBM peak magnitude than the influence of the velocity. The VBM was plotted against the ratio of the wave height squared to the draft squared, as shown in Figure 3.63. Interestingly, the data points showed two types of linear trend. This implied that there were at least two different key factors to the wave-induced VBM, depending on the wave height range. For the lower wave heights, the gradient of the linear trend was smaller. It can be presumed that the slamming effects on the VBM on the HSM became apparent above $H_w^2/T^2 = 0.54$, corresponding to the higher end of the lower wave height region. From this discovery, it shows that the wave height squared factor should be included in the non-dimensional coefficient for the VBM in large waves, which will be discussed in the following subsection.

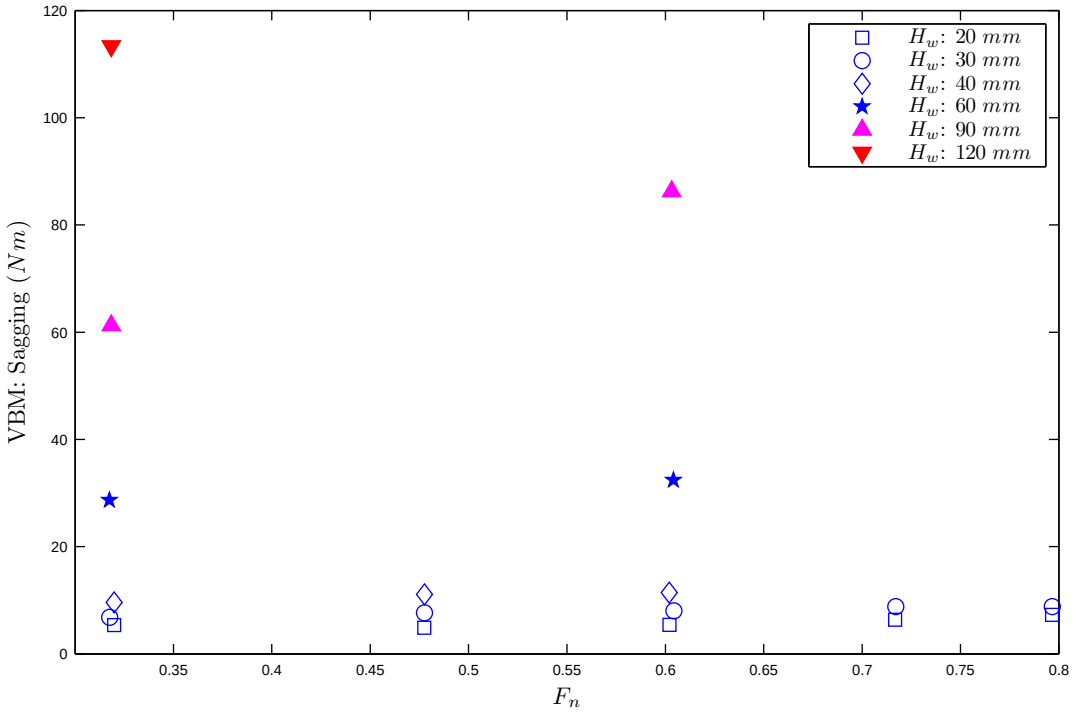

Figure 3.62: Maximum sagging vertical bending moment against the Froude Number, F_n.

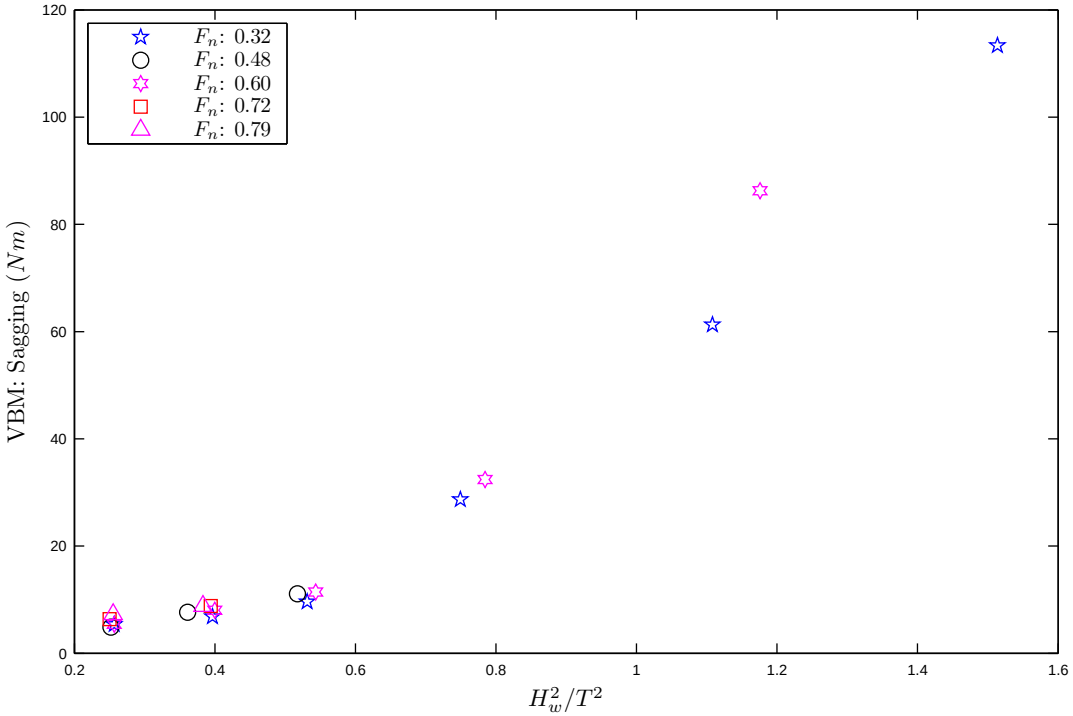

Figure 3.63: Maximum sagging vertical bending moment against the ratio of wave height squared to draft squared.

3.10.2 Non-dimensional Coefficient for VBM and Slam-Induced Loads

In order to investigate the factors affects the VBM, many non-dimensionalised coefficients were investigated. Colwell (1995) used a bending moment coefficient as follows:

$$C^*_{VBM_{Colwell}} = \frac{VBM}{\rho g L^2 B H_w} \tag{3.44}$$

where the VBM is the measured wave-induced vertical bending moment, ρ is the water density, g is the acceleration due to the gravity, L is ship length, B is ship beam, and H_w is a wave height. As an alternate approach, instead of L and B, the volume displacement, ∇ is used for the following coefficient, $C^*_{VBM^{01}}$:

$$C^*_{VBM^{01}} = \frac{VBM}{0.5\rho g H_w \nabla} \tag{3.45}$$

Equation 3.45 has a linear wave height factor. Since the forward velocity of the vessel influences wave exciting forces for the response motions, the velocity term, V_s can be alternatively included in the vertical bending moment coefficient as follows:

$$C^*_{VBM^{02}} = \frac{VBM}{0.5\rho V_s^2 H_w \nabla^{\frac{2}{3}}} \tag{3.46}$$

Next, as the VBM was linear to H_w^2/T^2 in the large wave height range as shown in Figure 3.63, the wave height squared was included in a coefficient. Consequently, the VBM coefficient includes the square of the wave height showed intriguing results for a certain range of wave height as such the coefficient follows:

$$C^*_{VBM^{03}} = \frac{VBM}{0.25\rho g H_w^2 \nabla^{\frac{2}{3}}} \tag{3.47}$$

$C^*_{VBM^{03}}$ is similar to $C^*_{VBM^{01}}$, however the contribution of the wave height are different.

The slam-induced force coefficient was also considered in a similar manner to the VBM coefficient. The wave height factor was consider for the following slamming coefficient:

$$C^*_{Slam^{01}} = \frac{F_{Slam}}{\rho g H_w \nabla^{\frac{2}{3}}} \tag{3.48}$$

Next, the velocity squared was considered as a key factor as follows:

$$C^*_{Slam^{02}} = \frac{F_{Slam}}{0.5\rho V_s^2 H_w \nabla^{\frac{1}{3}}} \tag{3.49}$$

For the slamming load, the wave height squared was also considered:

$$C^*_{Slam^{03}} = \frac{F_{Slam}}{\rho g H_w^2 \nabla^{\frac{1}{3}}} \tag{3.50}$$

For this project, the VBM coefficients were calculated from the measured wave-induced VBM as defined in Subsection 3.10.1. The slam-induced force coefficients were calculated from the corrected-measured slam-induced forces as defined in Subsection 3.5.4

3.10.3 Vertical Bending Moment Non-Dimensionalised Coefficient

The wave-induced VBM coefficients were obtained based on Equations 3.45, 3.46, and 3.47. The VBM coefficient responses against the non-dimensional encounter frequency are presented for many variable sets of conditions. The wave height varied from 20 mm to 120 mm, and the speed ranged from 1.55 to 3.86 m/s. Since the absolute magnitude of sagging and hogging VBMs can differ largely from each other due to the slamming force components, three types of coefficient were obtained for the peak-to-trough hogging and sagging values. The hogging and sagging VBM is denoted by the subscript of VBM with Hog and Sag, respectively. The superscript of VBM is indicated as per the equations described in Subsection 3.10.2.

For smaller wave heights from 20 to 40 mm, the severe slamming force was not expected, but was expected in large wave conditions. The VBM coefficient responses for small and large wave height conditions are collectively presented in Appendix H and I, respectively.

The effect of the small wave height on the VBM coefficient response was investigated. The VBM coefficients calculated by Equation 3.45 are presented in Figures H.1 to H.10. At 20 K_n, the coefficient $C^*_{VBM^{01}}$, $C^*_{VBM^{01}_{Hog}}$, and $C^*_{VBM^{01}_{Sag}}$ for the equivalent full scale wave heights of 0.896, 1.344 and 1.792 m for 20, 30 and 40 mm in the model scale, followed the same trend to show the linearity at 20 K_n in Figure H.1 and H.2. The linearity could be observed on both the forward and aft links. Other speed conditions are also presented in Appendix H. The linear trend of the VBM response being proportional to the wave height at a constant speed was confirmed by the coefficients $C^*_{VBM^{01}}$, $C^*_{VBM^{01}_{Hog}}$ for the lower wave height cases of 0.896 and 1.344 m. The wave height-to-draft ratios, H_w/Tm were 0.26 and 0.39 respectively. Interestingly, this linearity of the VBM response to the small wave height was observed up to 50 K_n.

The VBM coefficients $C^*_{VBM^{03}}$ for the forward and aft elastic links were obtained by Equation 3.47 , and are presented for the wave heights of 0.896, 1.344 and 1.792 m at 20 and 38 K_n in Figures H.15 to H.18. The VBM coefficient responses did not show any linear relationship with the small wave heights in all the speed ranges. Therefore, the other speed cases of 30, 45 and 50 K_n are not presented. The VBM response for smaller wave height conditions of less than H_w/T = 0.52 did not show a linear relationship with respect to the square of the wave height.

The VBM coefficients $C^*_{VBM^{02}}$ obtained by Equation 3.46 for the forward and aft elastic links are presented for the wave heights of 0.896, 1.344 and 1.792 m at 20 and 38 K_n in Figures H.11 to H.14. The wave velocity squared factor is included in the coefficient $C^*_{VBM^{02}}$. However, the VBM coefficient responses of $C^*_{VBM^{02}}$ were similar to the VBM coefficient responses of $C^*_{VBM^{01}}$, since the wave speed for the response comparisons was constant and the wave height effect was of same order. The velocity variation effects on the VBM coefficient at the same wave height are presented later.

The effects of the large wave height on the VBM coefficient response were investigated. For large wave heights of 1.344, 2.688, 4.032, and 5.376 m, the VBM coefficients calculated by Equation

3.45 are presented in Figures I.1 $\sim$ I.4. The coefficient, $C^*_{VBM^{01}}$ increased as the wave height increased, where the coefficient contained only the wave height factor. Although the coefficient $C^*_{VBM^{01}}$ was suited for the lower wave height cases, it was not appropriate for the large waves.

The VBM response coefficients $C^*_{VBM^{02}}$ obtained by Equation 3.46 were calculated for large wave heights of 1.344, 2.688, 4.032, and 5.376 m, however, it did not show any significant phenomena. Therefore, the results are not included for the large wave heights at a constant speed.

The VBM coefficients $C^*_{VBM^{03}}$ obtained by Equation 3.47 are presented for the forward and aft elastic links for the wave heights of 1.792, 2.688, 4.032, and 5.376 m in Figures I.5 to I.8. The VBM coefficient response showed trends in each condition at a constant speed. The resonant peaks of the sagging VBM at a constant speed were very similar to one another at the wave heights of 2.688, 4.032 and 5.376 m, and could be observed in both the 20 and 38 Kn cases. The maximum response magnitude of the VBM coefficients $C^*_{VBM^{03}}$ was fairly constant with variation in the wave height. This indicated the linearity of the maximum response magnitude to the wave height squared. A resonant peak analysis for the sagging VBM is given later.

Next, the effects of the forward velocity on the VBM coefficient response were investigated. The VBM coefficients calculated by Equation 3.45 for the forward velocity effects were investigated. The VBM response coefficient $C^*_{VBM^{01}}$at a constant wave height of 0.896, 1.344 and 1.792 m were compared to the effect of the speed variation of 20, 30, 38, and 50 K_n in Figures J.1 to J.6 in Appendix J. The peaks of the coefficient responses did not occur at the same frequency for a constant wave height with variations in the speed, because there was no velocity factor in the coefficient $C^*_{VBM^{01}}$. However, the response peaks showed similar maximum magnitudes for some cases.

The VBM response coefficient $C^*_{VBM^{02}}$, the forward and aft elastic links at a constant wave height of 0.896, 1.344 and 1.792 m were compared to the effect of the speed variation of 20, 30, 38, and 50 K_n in Figures J.7 and J.16. Although the velocity squared factor was involved in the coefficient $C^*_{VBM^{02}}$, no linearity of the VBM coefficient to the square of the velocity was observed. Whilst a vertical velocity may be appropriate for the VBM coefficient, the vertical velocity is rather difficult to predict at the preliminary vessel design stage. Therefore, the coefficients were constructed by focusing on the vessel and conditional parameters, rather than response variables. For the large wave case, there were no linear trends; the VBM coefficient response was non-linear with respect to the square of the forward velocity.

The VBM coefficient $C^*_{VBM^{03}}$ for the forward and aft elastic links at the 20 and 30 mm cases are shown in Figures J.17 to J.20. The VBM coefficient $C^*_{VBM^{03}}$ also did not show any improvement compared to the VBM coefficient $C^*_{VBM^{01}}$ for a smaller wave height range.

Whilist the magnitude of the VBM was increased with the velocity, the linear effect of the forward velocity squared to the vertical bending moments was not observed in lower wave height, as shown in Figure 3.63. The reason why the forward velocity was less influential on the VBM

coefficient is that the VBM is subjected to the vertical motion rather than ship longitudinal motion, such as the forward velocity. The vertical velocity is probably suitable for the VBM coefficients including the speed factor, however, the vertical velocity is not an easily available parameter at the preliminary design stage of the vessel.

The maximum sagging VBM coefficients were selected from each condition in order to investigate the linear characteristics of the VBM resonant peaks. As can be seen from the linear trends in Figure 3.63, the wave height factor and wave height squared factor were found to be influential to the VBM in small and large waves, respectively. The wave height case is presented in Figure 3.64 and the square of the wave height case is presented in Figure 3.65. The VBM response shows a linear relationship to the wave height in the small wave height range, as shown in Figure 3.64. It probably implies that this VBM linearity to the wave height was true before the model experienced the slamming load onto the centre bow. When the model was subjected to the large wave height, the VBM resonant peak was linear to the square of the wave height, as shown in Figure 3.65. This discovery indicated that the wave height squared value was significant for the VBM resonant peak in large waves. The analyses on the HSM experiments discovered that the wave height linearly influenced the VBM response up to $H_w/T = 0.52$ for the small wave height, and the wave height squared linearly influenced the VBM peak response above $H_w/T = 0.52$ for the large wave height. The linear response with respect to wave amplitude for small wave heights is probably due to the dominance of the Froude-Krylov force for these conditions.

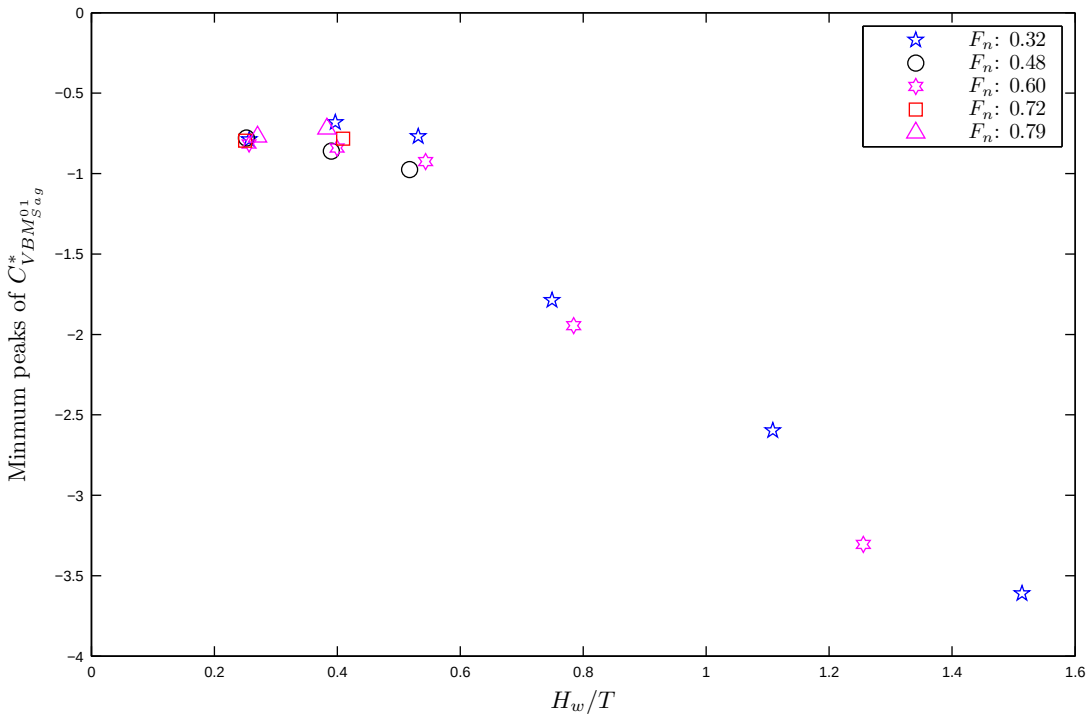

Figure 3.64: Minimum peaks of non-dimensional coefficient for sagging moments, $C^*_{VBM^{01}_{Sag}}$ plotting against the ratio of wave height to draft.

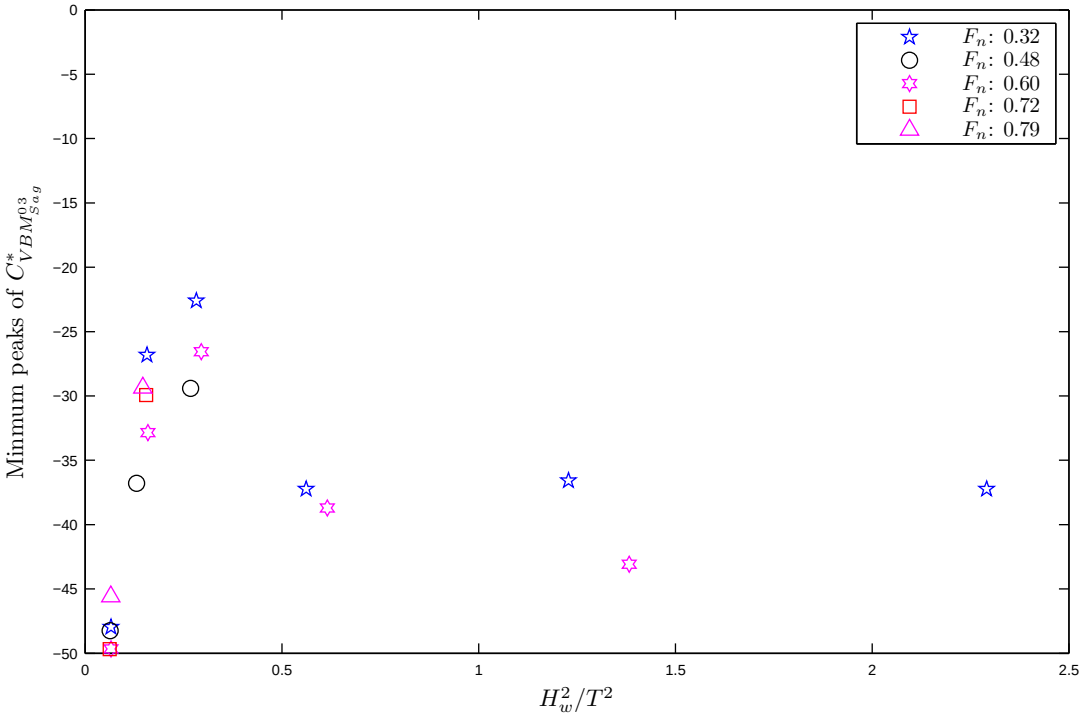

Figure 3.65: Minimum peaks of non-dimensional coefficient for sagging moments, $C^*_{VBM^{03}_{Sag}}$ plotting against teh ratio of wave height squared to draft squared.

3.10.4 Slamming Loads

The slam-induced load and its resultant force location were calculated from the measured strains of the elastic links on the centre bow. The method of calculation was explained in Subsection 3.5.4. Severe slamming events clearly occurred with relatively large wave heights, when the wave height-to-draft ratio H_w/T was more than 0.79.

The slam-induced loads were plotted against the non-dimensional encounter frequency. Examples of the slam-induced load response for the 20 and 38 K_n cases are presented in Figures 3.66 and 3.67. Similar to the VBM response, the peak-to-trough force, positive force and negative force are presented, where the positive force is the slamming force acting upward on the hull surface. Evidently, the larger wave height caused the larger slam load response. The resonant frequency generally occurred at the same non-dimensional encounter frequency at the same speed, however, the 120 mm wave height cases showed a slight offset in the resonant frequency. The positive force of the slamming was larger than the negative force.

The slam-induced force coefficients were investigated. Many coefficients that can be constructed only with the design and environmental parameters were explored. Three factors similar to the VBM coefficients are presented in Appendix K. The three factors are the wave height effect, velocity squared factor, and wave height squared factor involved in Equations 3.48, 3.49, and 3.50, respectively. The slam-induced force coefficient responses are presented for the large wave cases of 1.344, 2.688, 4.032, and 5.376 m at the 20 and 38 K_n in Figures K.1 to K.6 in Appendix K.

In general, the slam-induced force coefficient response did not show a trend regardless of the wave height or forward velocity. A non-linear response of the slam-induced force was observed. It could be assumed that the centre bow response was subject to the mechanics of the wave and ship dynamics to cause the slam impact. At 38 K_n in the higher wave height, the response peak magnitude of the slam-induced force coefficient $C^*_{Slam^{02}}$, indicated a possibility of linearity to the velocity squared. However, it requires further experiments to confirm the linearity of the slam-induced force to the velocity squared in higher wave heights at higher speed ranges.

The three factors of the wave height, square of the forward velocity and the square of the wave height are presented as an example. The slam-induced force coefficient $C^*_{Slam^{01}}$, that includes the wave height factor is presented in Figure 3.68. The slam-induced force coefficient $C^*_{Slam^{02}}$, that includes the velocity squared factor is shown in Figure 3.69. The slam-induced force coefficient $C^*_{Slam^{03}}$, that includes the wave height squared factor is shown in Figure 3.70. There was no single general response trend for the slam-induced force. However, there were two linear trends for the maximum response of the slam-induced force among the above coefficients.

Firstly, for the higher speed cases of $F_n = 0.60$ in large wave conditions, the slam-induced force coefficient $C^*_{Slam^{02}}$ response showed that the peak magnitudes of the slam-induced load responses at a higher speed were constant at H_w/T greater than 0.79. This could indicate that

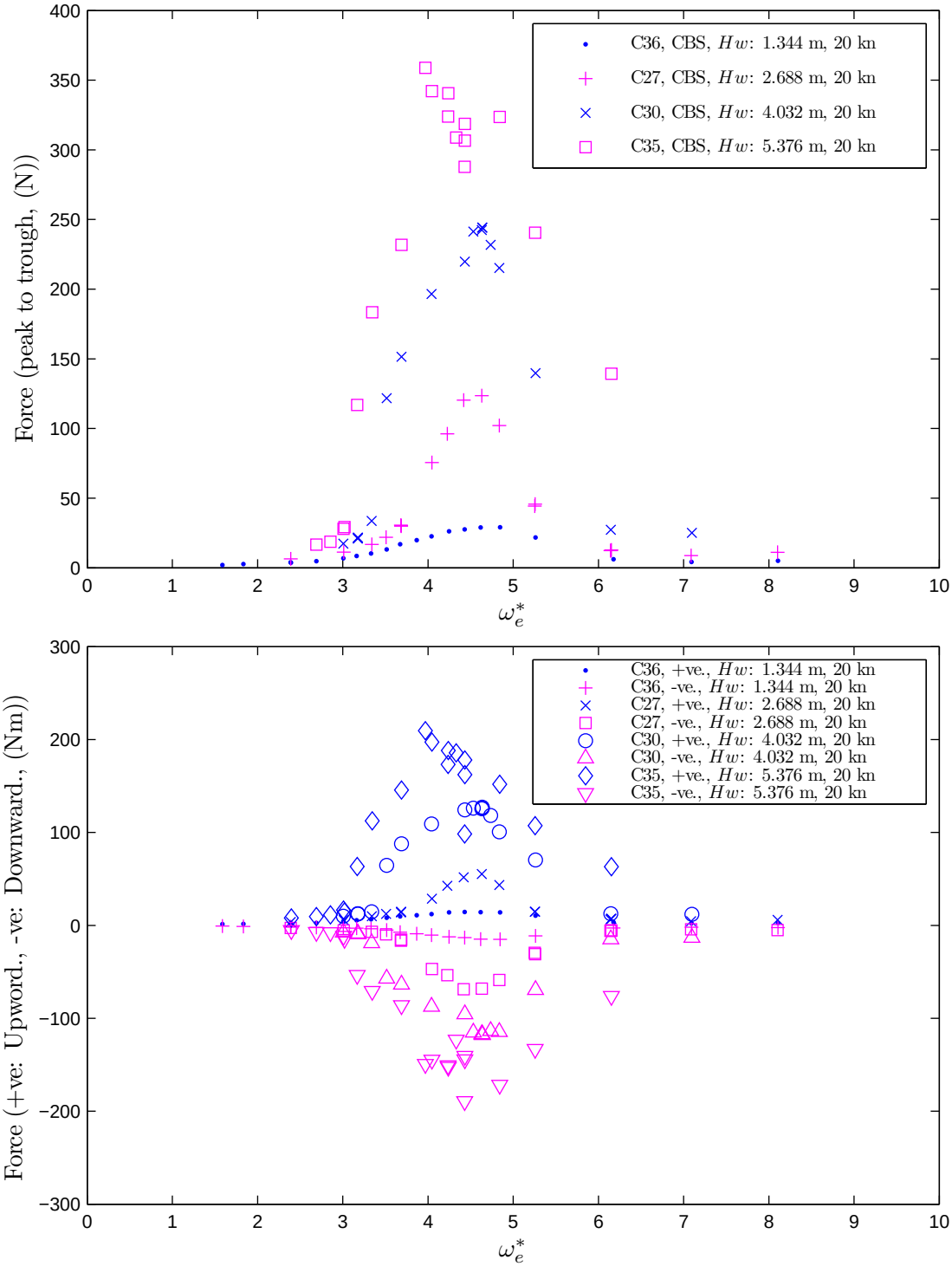

Figure 3.66: Slam force (peak to trough) response and positive and negative slam force response by varying the wave height, are plotted with respect to the non-dimensional encounter angular wave frequency, ω_e^*. $F_n = 0.32$.

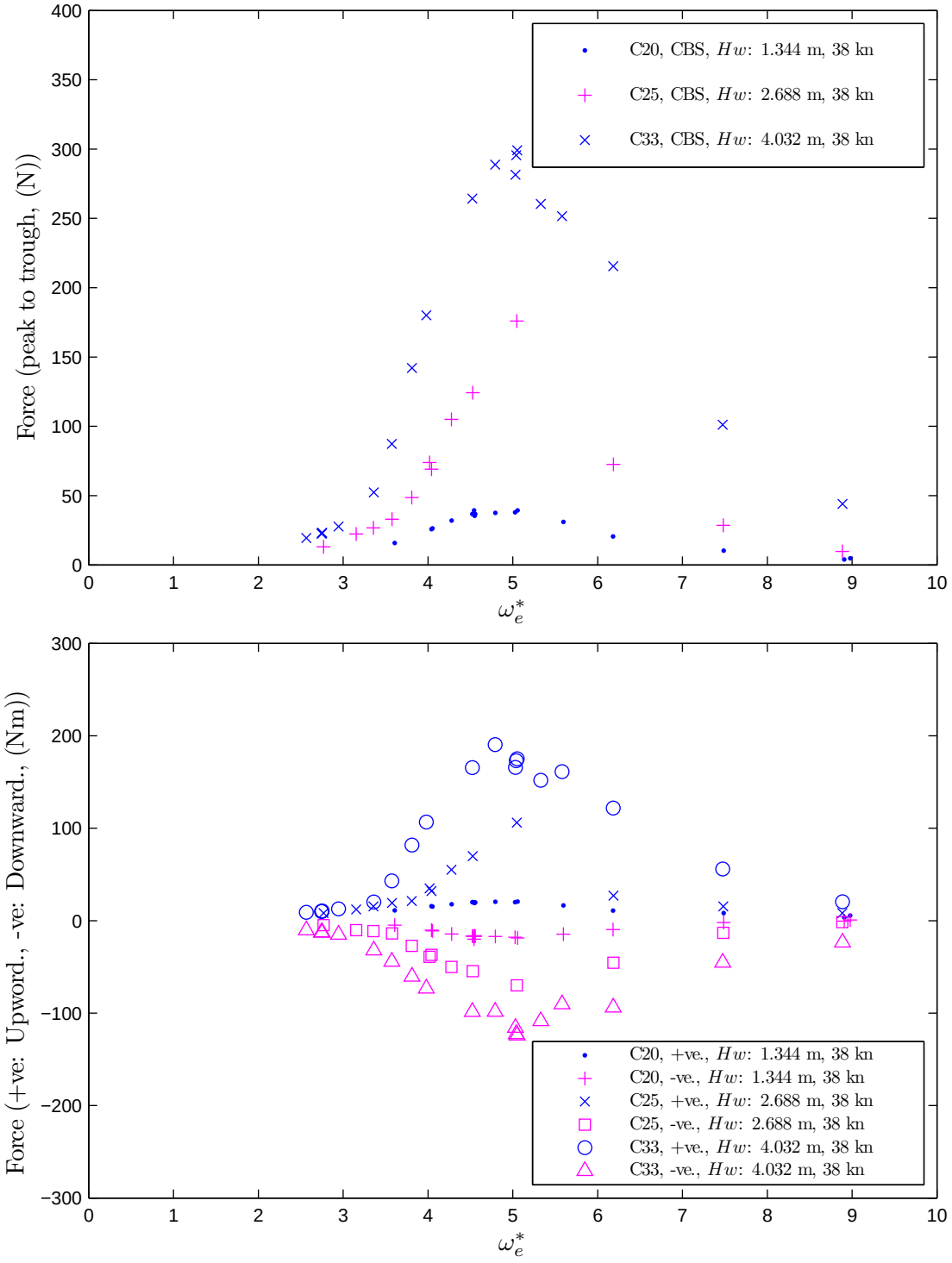

Figure 3.67: Slam force (peak to trough) response and positive and negative slam force response by varying the wave height, are plotted with respect to the non-dimensional encounter angular wave frequency, ω_e^*. $F_n = 0.6$.

the maximum slam load at the higher forward speed was linear to the forward velocity squared. Since the forward velocity has a relationship with the vertical velocity response of the CBS, further investigation will be needed to confirm the findings.

Secondly, for the lower speed cases of $F_n = 0.32$ in large wave conditions, the slam-induced force coefficient $C^*_{Slam^{03}}$responses showed that the maximum peaks of the coefficient responses were constant at H_w/T greater than 0.79. This could indicat that the maximum slam-induced load at the lower forward velocity cases of $F_n = 0.32$ was linear to the wave height squared for large waves. At the lower forward velocity, the velocity might not affect the slam-induced force as much as the wave height affects it.

It was difficult to clearly and conclusively determine the most influential parameter of the slamming load out of the design dimensional and environmental parameters. Therefore, further experiments would be required with a more comprehensive measurement system of the centre bow for the slam-induced force. In particular, attention to the measurement of the longitudinal slam-induced load might be useful, since the current configuration was designed for the measurement of the vertical slam-induced force ondly.

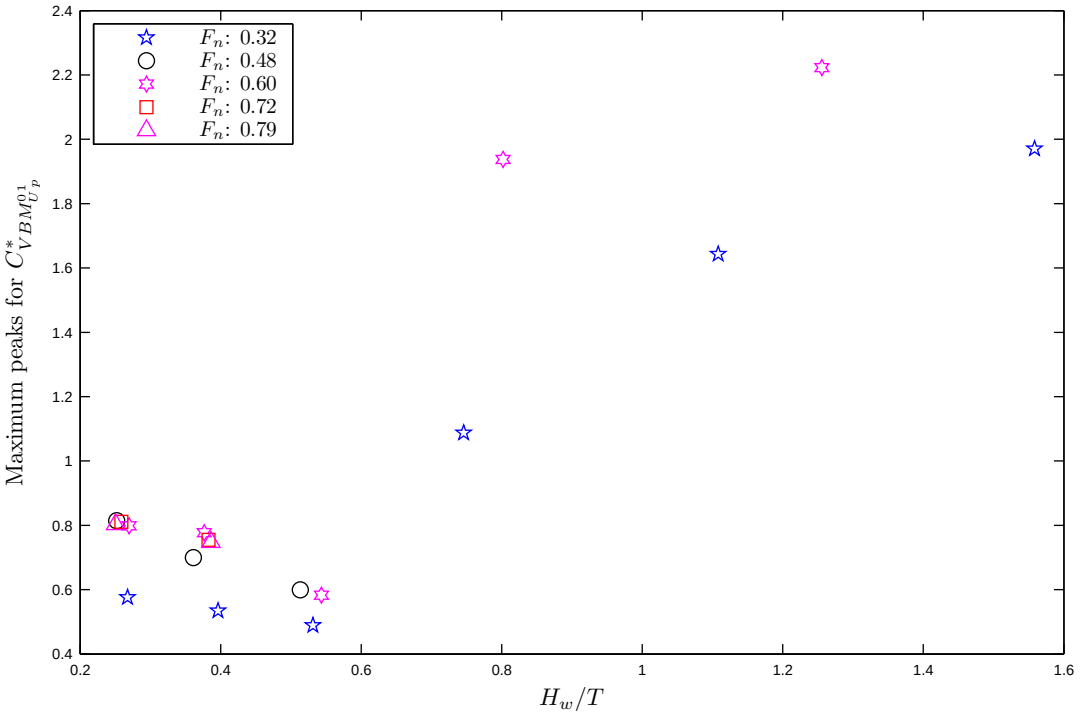

Figure 3.68: Minimum peaks of non-dimensional coefficient for sagging moments, $C^*_{VBM^{01}_{Sag}}$ plotting against the ratio of wave height to draft.

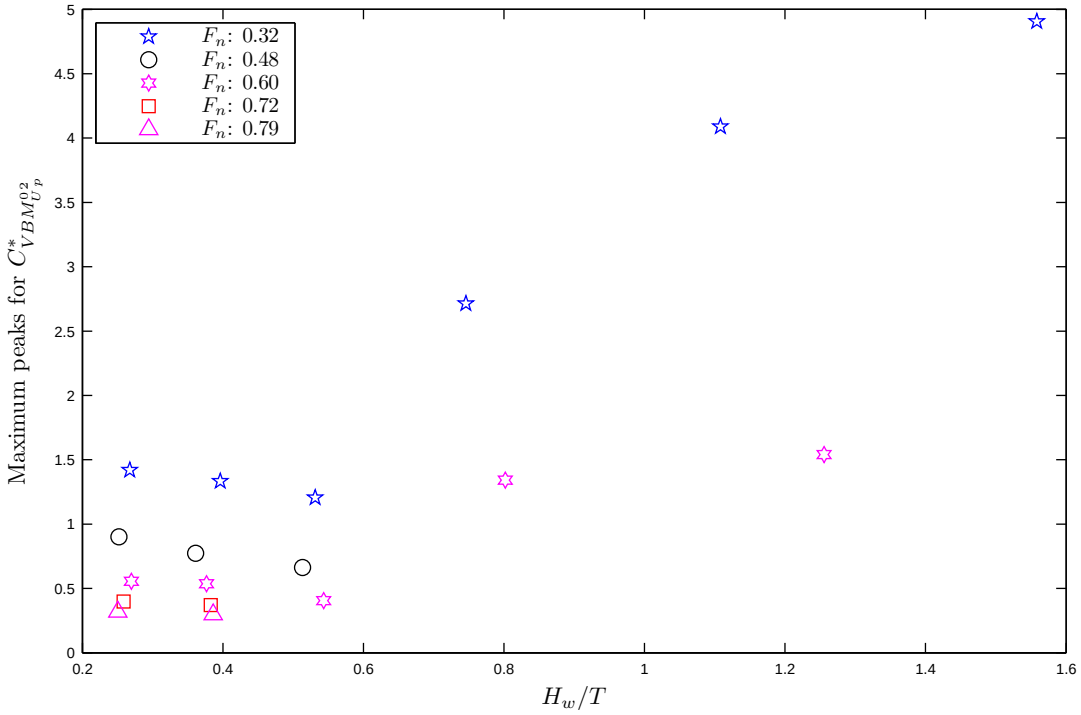

Figure 3.69: Minimum peaks of non-dimensional coefficient for sagging moments, $C^*_{VBM^{02}_{Sag}}$ plotting against the ratio of wave height to draft.

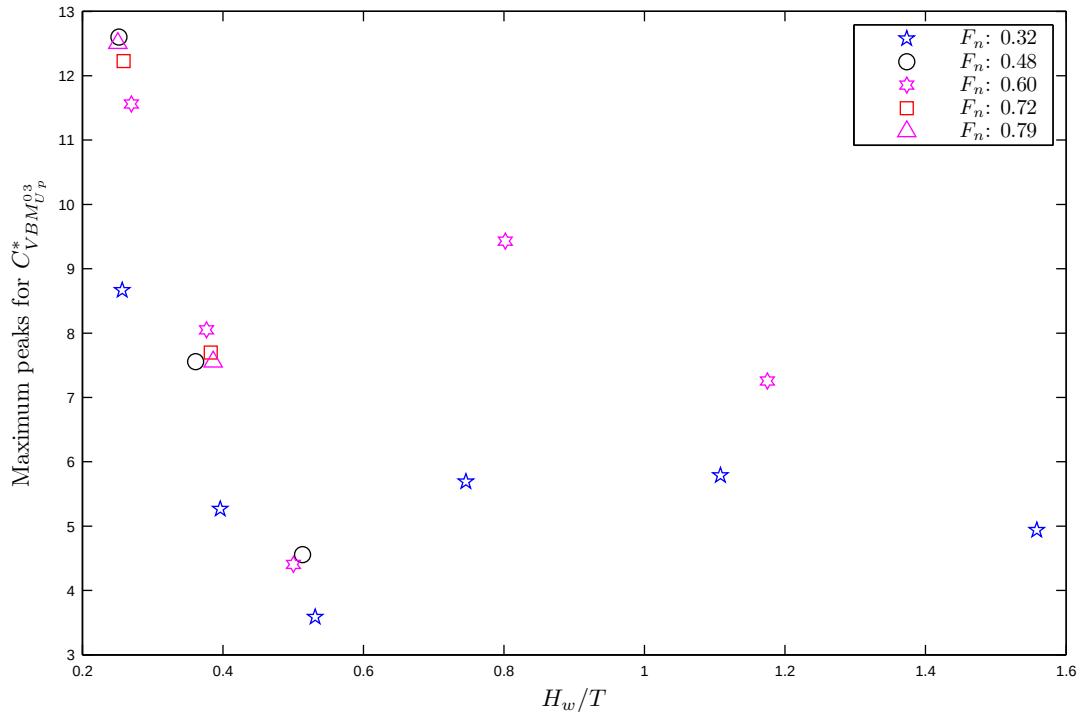

Figure 3.70: Minimum peaks of non-dimensional coefficient for sagging moments, $C^*_{VBM^{03}_{Sag}}$ plotting against the ratio of wave height to draft.

3.10.5 Ship Hydroelasticity on Motion, Global Wave and Slamming Load

The interaction between the global wave-induced loads on the demi-hull, slam-induced loads on the centre bow and ship motion was investigated. The heave and pitch motion, VBM and slamming loads were plotted in a synchronised time domain. The VBMs of both the starboard and port side demi-hulls were summed to form the forward and aft VBM at elastic links at the segmentation gaps. A positive slam force indicates an upward force that was applied onto the hull. An example of large wave cases of 90 mm is presented in Figure 3.71. for the larger magnitude of slam-induced forces. At the same wave height, the example of slam cases at a non-response peak is presented in Figure 3.72. For a small wave height case, the heave and pitch motion, VBM and slam loads were plotted in a synchronised time domain in Figure 3.73.

For the large wave case of 90 mm, as shown in Figure 3.71 for $RunNo.457$. The model experienced the largest VBM and slam loads response at 38 K_n at the incident wave frequency of 0.7 Hz. As the slamming force increased, the absolute magnitude of sagging VBMs also increased. Interestingly, the resonant peaks of the VBM response did not occur at either the heave or pitch motion resonant frequency, but instead occurred at a higher frequency than the heave and pitch resonant frequency. The heave motion in time constructed the sinusoidal curve at the upper parts of the oscillatory heave motion. At the lower part, there can be seen two clear deformations of the curve on the oscillatory heave motion before and after the heave trough. The cause of the deformation is discussed in later with vertical heave acceleration. At 9.6 seconds, the VBMs started decreasing with a small oscillation up to 9.67 seconds, and the slam force also started to increase simultaneously. After 9.67 seconds, the more aggressive increases in the sagging VBM and slam force can be observed. The first increases were likely to be caused by the global wave-induced load, as the wave-piercer bow and centre bow were submerged into the water, but before the centre bow arch is fully submerged. The second increases were caused by the slamming impact, as the centre bow arch was filled with water. In the large waves, the wave-piercer bow was completely out of the water, after the slamming. The VBM showed the clear whipping behaviour after the slamming events. The peak and trough of the whipping event for the forward and aft elastic links occurred simultaneously, hence the fundamental mode of the natural frequency for the resonant VBM response can be confirmed from the experimental results. For the peak and trough in $RunNo.457$, the whipping could not be dissipated completely due to the short duration of the encounter wave period of the regular wave.

For the large wave case of 90 mm, as shown in Figure 3.72 for $RunNo.440$, the heave and pitch experienced the oscillatory motion with a large distortion due to the influence of the structured loads induced by the global wave-induced loads and slam-induced loads. The whipping oscillation that occurred in the VBM signal was relatively large compared to the global-wave loads oscillation. The slam occurred due to the large wave and subsequently the whipping phenomena was induced at the fundamental mode, since the VBMs at the forward and aft elastic links showed the simultaneous occurrence of the whipping peak and trough. From $RunNo.457$ and $RunNo.440$, the results confirmed that the slam impact induced the whipping phenomena at the fundamental mode.

For the small wave, the heave and pitch motion, the VBMs and the slam force are shown in Figure 3.73. The heave and pitch motions in the small wave were not distorted as much as those observed in large wave. The whipping behaviour was also smaller than for the large wave, therefore the structural load influence on the motion could be expected to be reduced. The heave and pitch formed a smoother sinusoidal motion due to less structural response for ship hydroelasticity. It paradoxically supports the hypothesis that ship hydroelasticity influences the ship motion. Interestingly, some vibratory motion was observed such as a springing behaviour in the VBMs.

Ship hydroelasticity was experimentally observed by discovering evidence of a mutual interaction between ship motion induced by waves and structural vibratory loads. The heave and pitch acceleration were numerically calculated by the five-point symmetric formula of the finite difference scheme for the second derivative of the heave. The five-point formula is more accurate than other formulas as demonstrated by Fletcher (1991). Since the calculated acceleration contained higher frequency oscillation, 25 Hz of the law-pass Butterworth filter was used to extract useful acceleration information. As can be seen from the heave motion in Figure 3.74, a region near the trough of the heave has a distorted sinusoidal curve shape. Therefore, this could lead to a supposition that external forces influenced the heave motion when the HSM was well submerged into the water. The heave acceleration was calculated to compare with the heave motion and VBM loads. The maximum heave acceleration occurred when the maximum sagging VBM was experienced. It also coincided with the timing of the maximum slamming force acting on the centre bow. Hence, the slamming forces increased the positive heave acceleration upwards to cause the sagging VBM. The subsequent maxima and minima of the heave acceleration also corresponded to the subsequent minima and maxima of the VBM loads, respectively, which was whipping behaviour. This synchronisation in time, was observed strongly for about three complete oscillations after the full development of the whipping phenomena induced by the slamming. The heave motion time trace did not show clear effects due to the slamming and subsequent whipping towards the ship global motion. However, the heave acceleration showed a clear effect in its oscillation due to the slamming and subsequent whipping. The heave acceleration is a motion property of the heave, hence the heave acceleration motion and VBM whipping motion interacted mutually. The large ship motion in large waves caused the slamming impact and subsequent whipping events, then both loads influenced the heave acceleration, hence the heave motion was altered.

The experimental model evidentially demonstrated the mutual interaction of the fluid-induced motion and structural vibratory loads for the purpose of the HSM hydroelasticity. Furthermore, this discovery experimentally validates the hypothesis that ship hydroelasticity influences the ship global motion. It also concludes that the reduced heave and pitch resonant peaks, as shown in Figure 3.49, was caused by the ship hydroelasticity. The ship motion induced by the fluids of the large global waves and the forward velocity caused the slam event. The harmonic excitation of the global waves caused the global wave-induced VBM, and the impulse excitation of the slam event caused the slam-induced VBM and subsequent whipping response with the fundamental

mode of the natural frequency for the VBM of the demi-hulls. The whipping oscillatory motion of the VBM was synchronised in time with the heave acceleration oscillation of the heave motion. In addition, ship motion was modified because of this interaction. This clear mutual interaction of the fluid-induced motion and structural load response showed that the hydroelastic segmented model achieved and demonstrated the ship hydroelasticity experimentally, that caused the fluid-structure interaction.
Spectral analysis on the VBM of each individual run was completed to identify the encounter wave frequency, VBM resonant frequency and other response frequencies of the HSM. Selected examples of the power spectral densities (PSD) are discussed here. The power spectral density of VBMs are presented for a case of the relatively smaller wave height of $H_w = 30\ mm$ in Figure 3.75. A case of the relatively large wave height of$H_w = 90\ mm$ mm was selected for the power spectral density for $RunNo.440$ and $RunNo.457$, which are shown in Figures 3.76 and 3.77, respectively.

The VBM PSD of the smaller wave height case in Figure 3.75 showed that the frequency of the maximum response peak coincided with the encounter wave frequency of a harmonic excitation. Furthermore, it was the dominant response peak magnitude in the PSD. The VBM resonant natural frequency of 12.7 Hz appeared with a relatively small peak magnitude compared to the response peak magnitude at the encounter wave frequency. The VBM resonant frequency was the natural frequency of the VBM that occurred by whipping behaviour, hence it varied depending on the environmental condition, such as wave height and forward velocity. The results of the PSD indicated that even a small wave oscillation could induce the VBM resonant vibratory motion.

On the other hand, in the large wave height case of Run No. 457, with the resonant encounter wave frequency to cause the VBM resonant response, as shown in Figure 3.76, the strong harmonic series of the encounter wave response frequency of the VBM can be observed in the PSD, while the first response peak matched with the encounter wave frequency. The VBM resonant frequency corresponded to the natural modal frequency of the VBM based on the individual condition. The VBM resonant frequency with the large wave can be determined with a clearly identifiable response peak magnitude in the PSD. The VBM resonant frequency coincided with the response frequency in multiples of the encountered wave frequency. From these results and the time plot results from Figures 3.71 and 3.72, a system for the fluid-structure interaction can be confirmed. In the large wave condition, the fluid-structure interaction of the HSM formed an integrated system composed of two excitations: a harmonically excited oscillation of the global wave load, and an impulse excitation caused by the slamming forces induced by the ship motion. When the two excitation systems were in phase, the complex system induced the large whipping response, as shown in Figure 3.71, which occurred at the VBM resonant peak frequency. Furthermore, the attuned VBM loads that responded to the harmonic wave excitation and to the impulse slamming excitation, resulted in the maximum magnitude peak of the VBM load response among the conditions for $H_w = 90\ mm$. The harmonic wave excitation and the impulse slamming excitation were also induced by the ship motion responses, which was also induced by harmonic global wave motion in regular waves. Therefore, the integrated system is categorised

in the fluid-structure interaction problem.

From the modal test in Subsection 3.6, the VBM modal frequency in wet mode in the calm water was 13.35 Hz. In the small wave height, as shown in Figure 3.73, the VBM resonant frequency was observed at 12.06 Hz. In the large wave height case, as shown in Figure 3.76, the modal response frequency of the VBM occurred at 11.41 Hz. The VBM resonant frequencies varied depending on the model and environmental conditions.

For the non-resonant encounter wave frequency of the VBM response in the large wave height case of $RunNo.440$ shown in Figure 3.77, the encounter wave response frequency and modal frequency of the VBM was observed. Interestingly, the harmonic series of the encounter wave response frequency of the VBM PSD was not as strong as in the case of the resonant encounter wave frequency. However, the modal frequency of the VBM was also in the multiples of the encounter wave response frequency. The phase difference of ship motion and global wave caused a lower magnitude of ship response, hence lower VBM, although the wave height was large. The small ship response also reduced the impact of the slamming magnitude. In addition, the VBM responses due to the slam-induced whipping and global wave-induced loads were not in phase, therefore the total magnitude of the VBM load was reduced, as can be seen in Figure 3.72.

Spectral analysis by the power spectral density on individual runs showed that the VBM resonant frequency occurred at the whipping frequency in multiples of the encounter wave response frequency. The VBM resonant frequency varied within some ranges, due to the wave profiles around the model and its motion. Clearly more added mass can be expected in large waves than in small waves, and also the wave-piercer bow emerging from the water results in the reduction of the hydrostatic restoring factor. The combination of added mass and hydrostatic restoring force factor are the dynamic parameters of the response system, and they consequently increased and reduced the natural frequency of the VBM dynamically based on the environmental conditions and ship motion response. When the natural frequency of the response system coincided in multiples of the encounter wave response frequency in phase, the VBM resonant frequency can appear. For Condition 33 of the 90 mm wave height, the VBM resonant frequency with the large response magnitude of VBM loads occurred at the static wave frequency of 0.7 Hz. The results showed that the slam event caused the whipping with the fundamental mode of the natural frequency for the VBM exciting the demi-hull structures.

For larger wave heights, a strong harmonic series of vibrations occurred, therefore spectral amplitude cannot be used to obtain the load response by a method of response amplitude operator using the PSD. The response magnitudes, other than at the encounter wave frequency, were significantly large and cannot be ignored. Therefore, it is rather difficult to use the power spectral method for obtain the RAO. Hence, the peak-to-trough method can be used for VBM and slam load responses with the large wave heights.

3.10.6 Slamming and Centrebow Inertial Forces

The slam-induced force measured by the strain gauges installed on the centre bow FTB could be influenced by the inertia force of the centre bow. Hence, the slam-induced forces might differ from the total actual slam load applied to the CBS hull surface due to the CBS inertial force. For convenience in this thesis, the slam-induced force indicates the slam-induced force measured on the CBS measurement system, and the actual slam force indicates the total actual slam force with the inertial effects. Therefore, the influence of inertial force on the slam-induced force was investigated. The inertial force can be determined by multiplying the centre bow mass and the acceleration at the LCG of the centre bow segment. The actual total slam-induced force can be equated to the summation of the CBS inertial force and the measured slam-induced force at the centre bow FTBs measurement system.

Since the accelerometer was not installed on the cetnrebow for the experiment, the vertical acceleration of the centre bow was numerically calculated at the LCG of the centre bow segment. The vertical displacement at the centre bow LCG was extrapolated from the heave and pitch motion in time. The five-point symmetrical formula of the finite difference scheme for the second derivative on the vertical displacement was utilised to calculate the vertical acceleration at the centre bow LCG of 1.842 m from the transom of the model. The calculated vertical acceleration was treated with a low-pass Butterworth filter at 25 Hz. The centre bow mass weighed 2.40 kg to calculate the CBS segment inertial force.

The result for Run No. 457 is shown for the CBS inertia force, VBM and slam-induced load in Figure 3.78. A maximum slamming load of 176.8 N occurred at $t = 9.665$ and the corresponding inertial force was calculated as 36.7 N. At the maximum slam load, the actual slam load could be increased by 20.8% of the measured slam-induced force. Although the acceleration was estimated from the LVDT data for the heave and pitch motion that might not reflect an exact motion of the CBS small vibration due to whipping, the maximum vertical acceleration calculated by the numerical method showed a good agreement with the measured values of maximum acceleration presented by Amin (2009). The model configuration and displacement was slightly different between this experiment and an experiment conducted by Amin.

At $t = 9.59$ seconds, the inertia force was zero which indicates that the vertical acceleration of the centre bow was also zero. Interestingly, the slam-induced load was also close to zero. This time point was the beginning of the initial rise for the slam event. From the slam-induced load and VBM load of the time response, two phases of the increase in slam-induced load and VBM can be observed . The first phase was from $t = 9.6$ to 9.67 seconds and the second phase from $t = 9.67$ to 9.78, both associated with rapid increases in an extremely short time period. The increased load magnitude for slam-induced force at the first phase was 79.4 N, and the increased magnitude of slam-induced force at the second phase was 108.6 N. Interestingly, the VBM also behaved in a two-phase pattern in a synchronised manner with the slam-induced force. The positive slam-induced forces on the centre bow caused the sagging VBM on the demi-hull. This meant that the VBM and slam force showed strong interference with each other.

The actual slam force could be increased by the inertial forces. However, the accelerometer data was not available for this experiment, and the slam-induced force measured by the CBS FTB mechanisms was used for the analyses. Therefore, installing an accelerometer on the centre bow is strongly recommended for future experiments.

3.10.7 Slam Resultant Force Position on Centrebow

The centre bow arrangement with the forward transverse beam was design to measure the slam resultant force and position. The calculation and calibration method were explained in Section 3.5. Slam resultant force and slam resultant force location in the time domain are presented in conjunction with a general arrangement of the centre bow and forward segments in Figure 3.79. The unit of the left-hand side vertical axis indicates the slamming resultant forces calculated by the correction method described in Subsection 3.5.4. Two resultant force positions are displayed for the corrected slamming resultant force (SRF) position and non-corrected slamming force position, whose unit is placed in the right-hand side vertical axis. The schematic diagram of the general arrangement is scaled accordingly to the coordinate of the slamming resultant force location. The origin of the SRF position is referenced to the transverse centre-line of the aft forward transverse beam, as shown in Figure 3.79.

Slamming forces increased with a small oscillation to $t = 13.35$ seconds, and simultaneously the SRF position moved forward to around 0.38 m. This was because the hydrostatic restoring force at the centre bow LCG was generated and moved forward, as the centre bow submerged into the wave. After 13.35 seconds, the rapid increase in the slamming forces can be observed. The slamming impact occurred onto the centre bow arch surface after $t = 13.35$ second. At the peak of the slamming force, the SRF position formed the local minimum after $t = 13.35$ seconds. Before the local minimum was formed, the SRF position shifted about 85 mm backwards. This indicated that the mass of water was transported by guidance of the centre bow arch. The centre bow arch contributed to distributing the SRF location in time. The comparison of the time trace between the corrected SRF and non-corrected SRF position showed that the corrected SRF position was a more realistic situation, and that the corrected SRF position was experienced in front of the centre bow truncation bulkhead, where the displaced volume of the centre bow was available for large waves. The centre bow truncation wall is located in front of the forward FTB. The SRF location sometimes generates large values due to the mechanical arrangement, however, the maximum slamming force always provided consistent repeatable values for the SRF location.

The corrected SRF position lies forward of the bow at t = 13.4 seconds. This phenomenon is due to the measured slam force values changing from positive to negative values, the zero load cases creates a numerical anomaly.

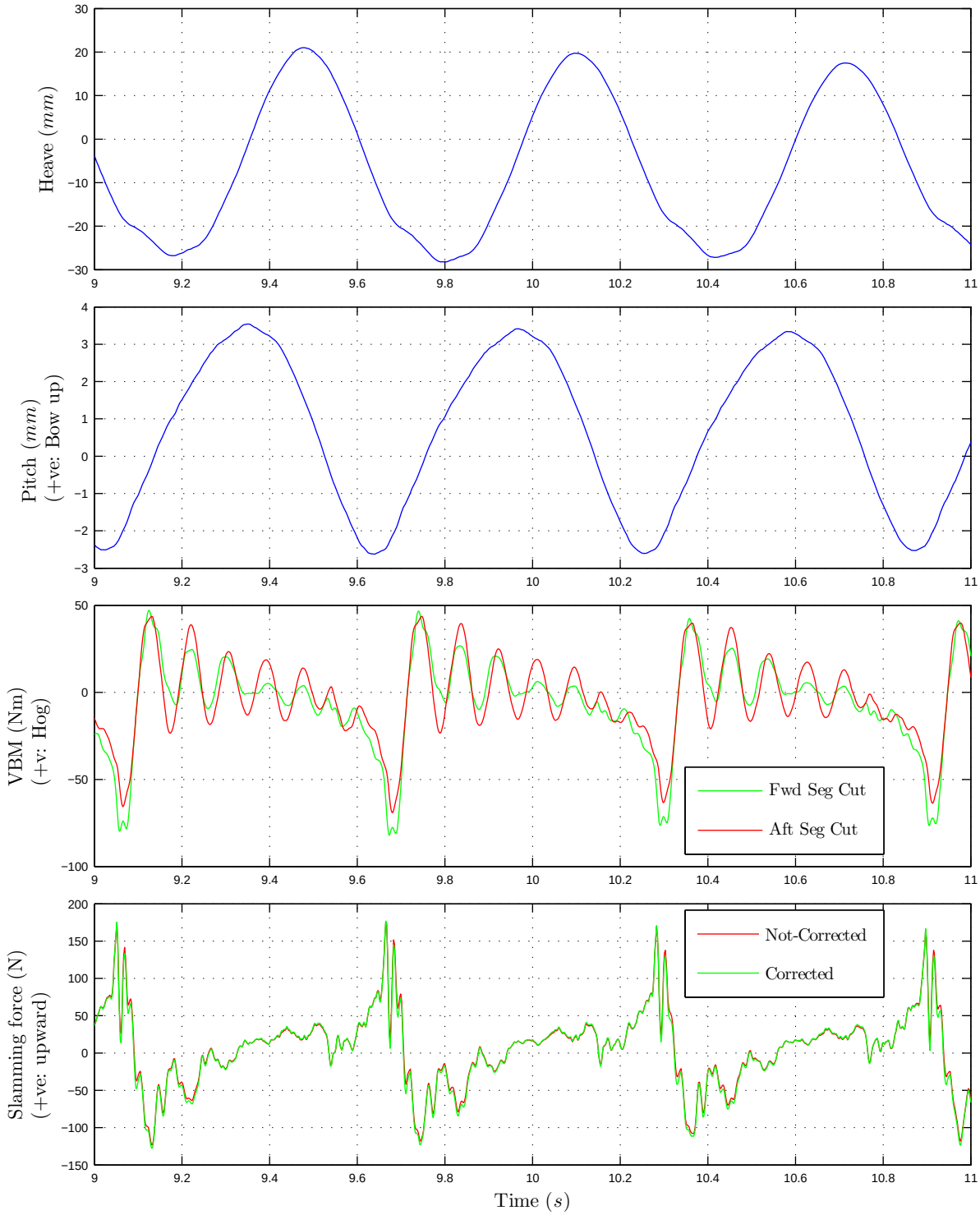

Figure 3.71: Vertical bending moments and slamming force with heave and pitch motion in time domain for Run No.457. VBMs were calculated by summing both stb and port side segmentation cuts for the fwd and aft segments, respectively. Both corrected and not-corected slamming forces were presented.

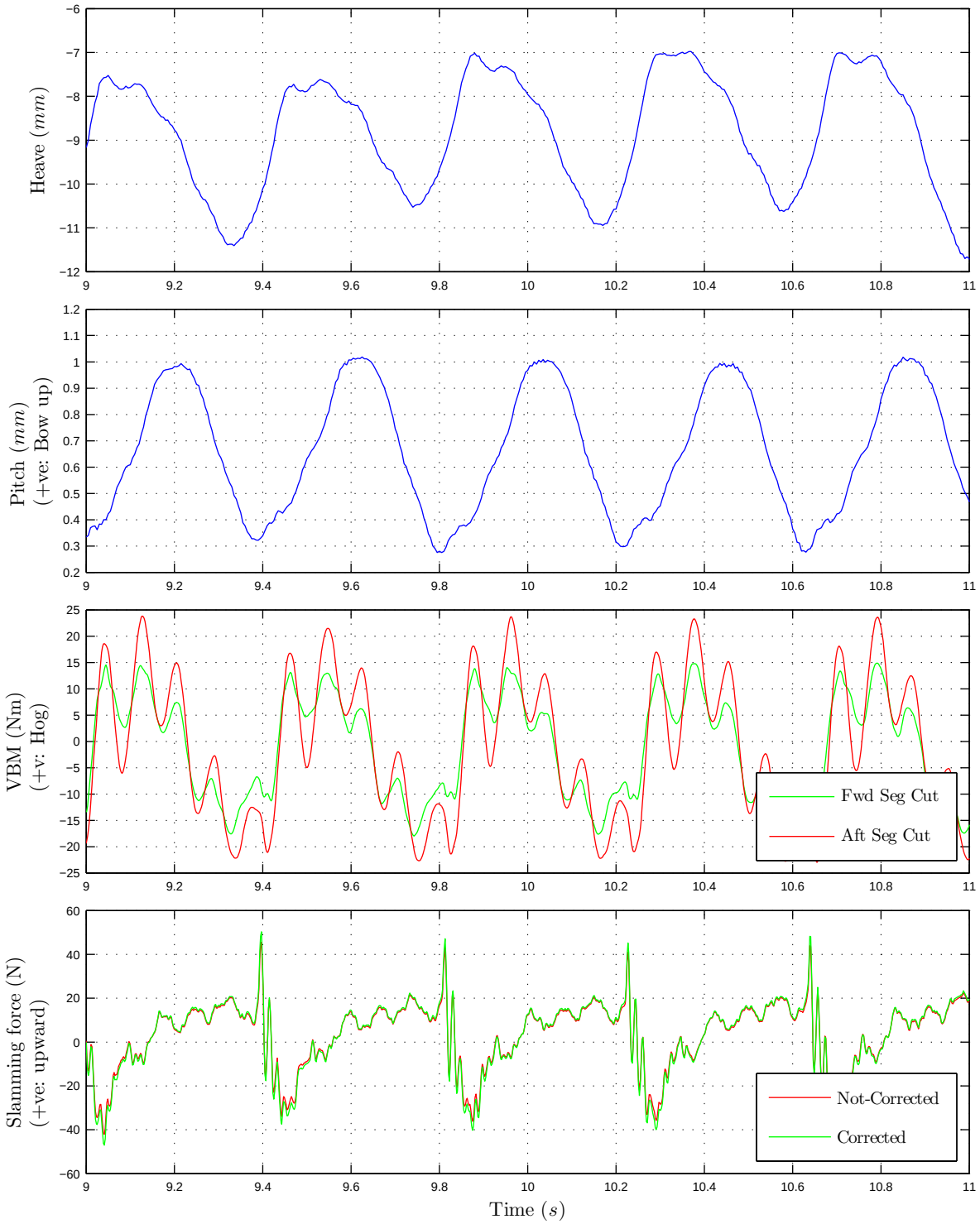

Figure 3.72: Vertical bending moments and slamming force with heave and pitch motion in time domain for Run No.440. VBMs were calculated by summing both stb and port side segmentation cuts for the fwd and aft segments, respectively. Both corrected and not-corected slamming forces were presented.

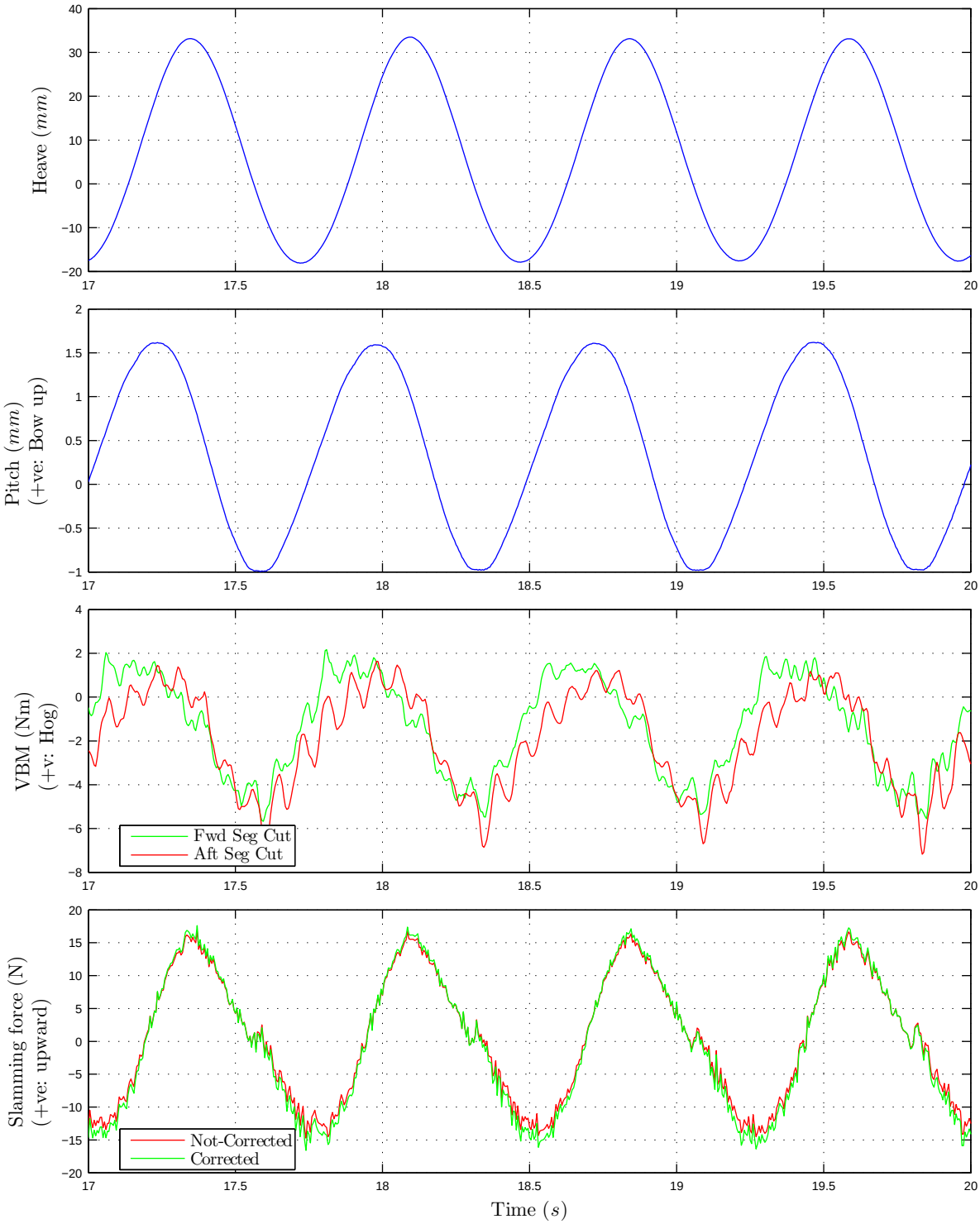

Figure 3.73: Vertical bending moments and slamming force with heave and pitch motion in time domain for Run No.797. VBMs were calculated by summing both stb and port side segmentation cuts for the fwd and aft segments, respectively. Both corrected and not-corected slamming forces were presented.

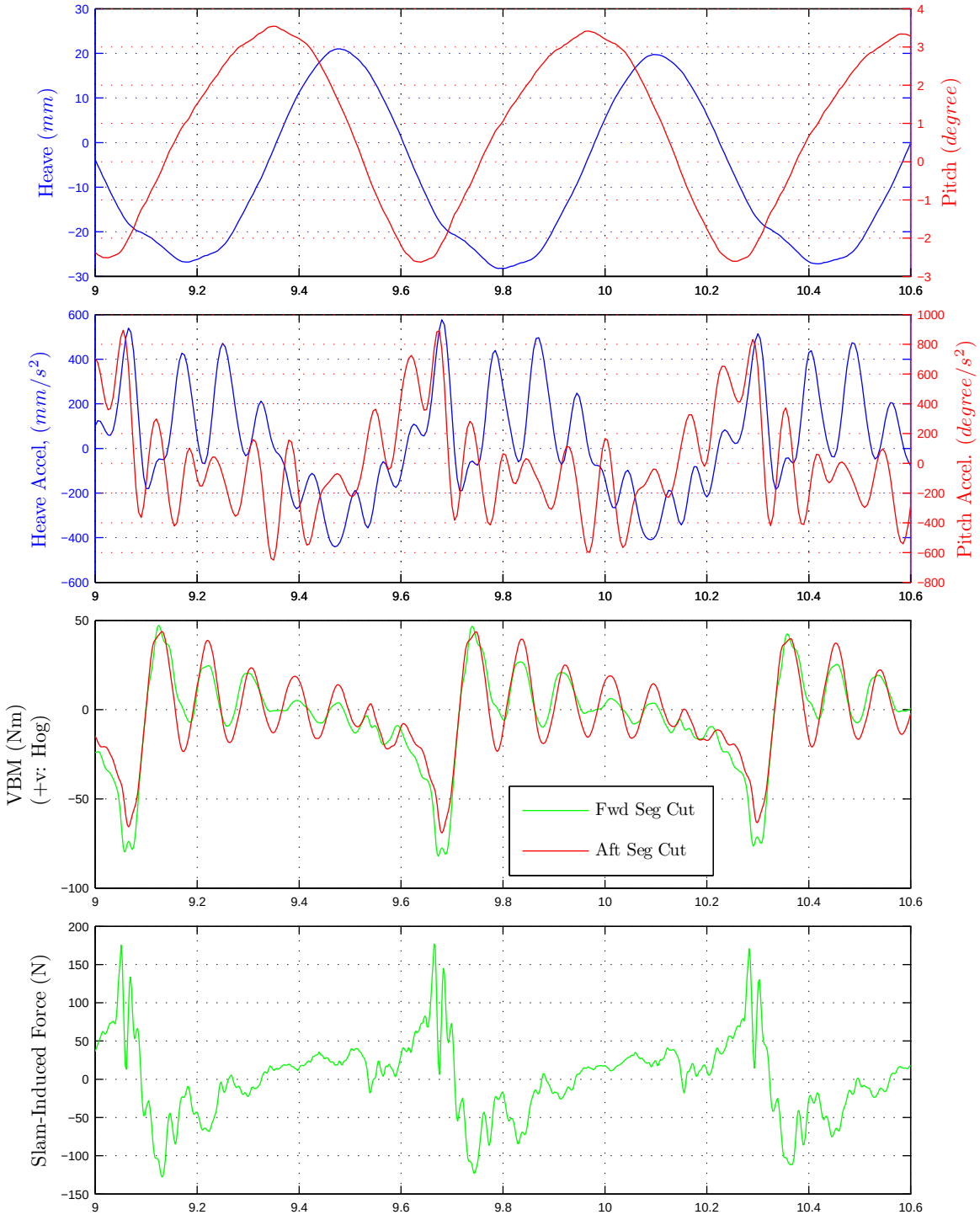

Figure 3.74: The heave and pitch displacements, the heave and pitch accelerations at the model LCG, the VBM at the forward and aft segmentaiton cut and the corrected slam-induced forces on the cetnrebow segment were synchronisedin the time domain for Run No.457.

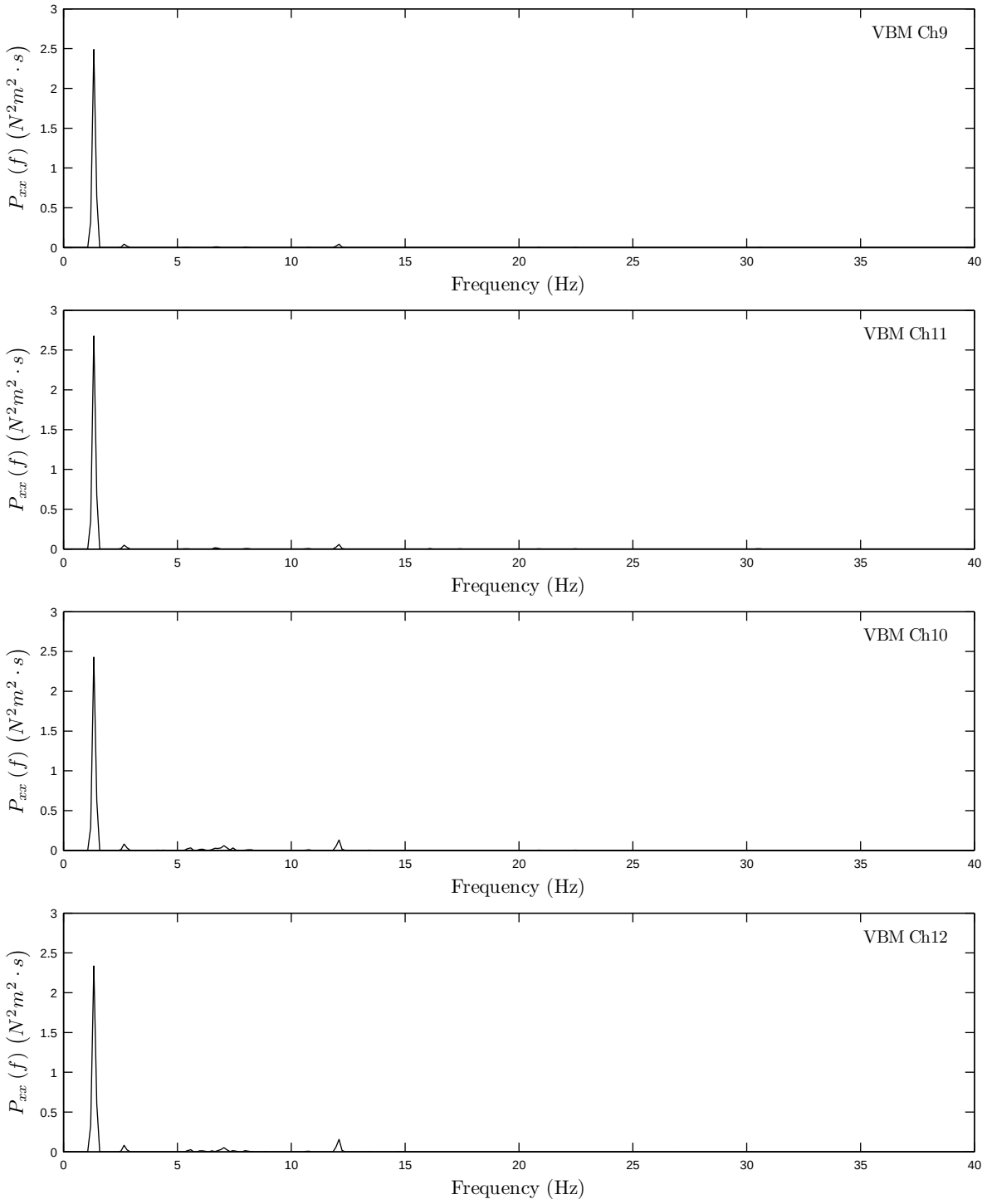

Figure 3.75: Power spectral density (PSD), $P_{xx}(f)$ for vertical bending moment (VBM) measured at elastic links for Ch9, Ch10, Ch11 and Ch12 in regular wave height, $H_w = 30.3$ mm and wave frequency f_s =0.577 Hz at $F_n = 0.717$. The measured encounter wave frequency by the moving wave probe at LCG was 26.9 Hz. Run No.797 PSD was obtained by applying the Hamming window for data taper in time domain, and No smoothing by a convolution in frequency domain.

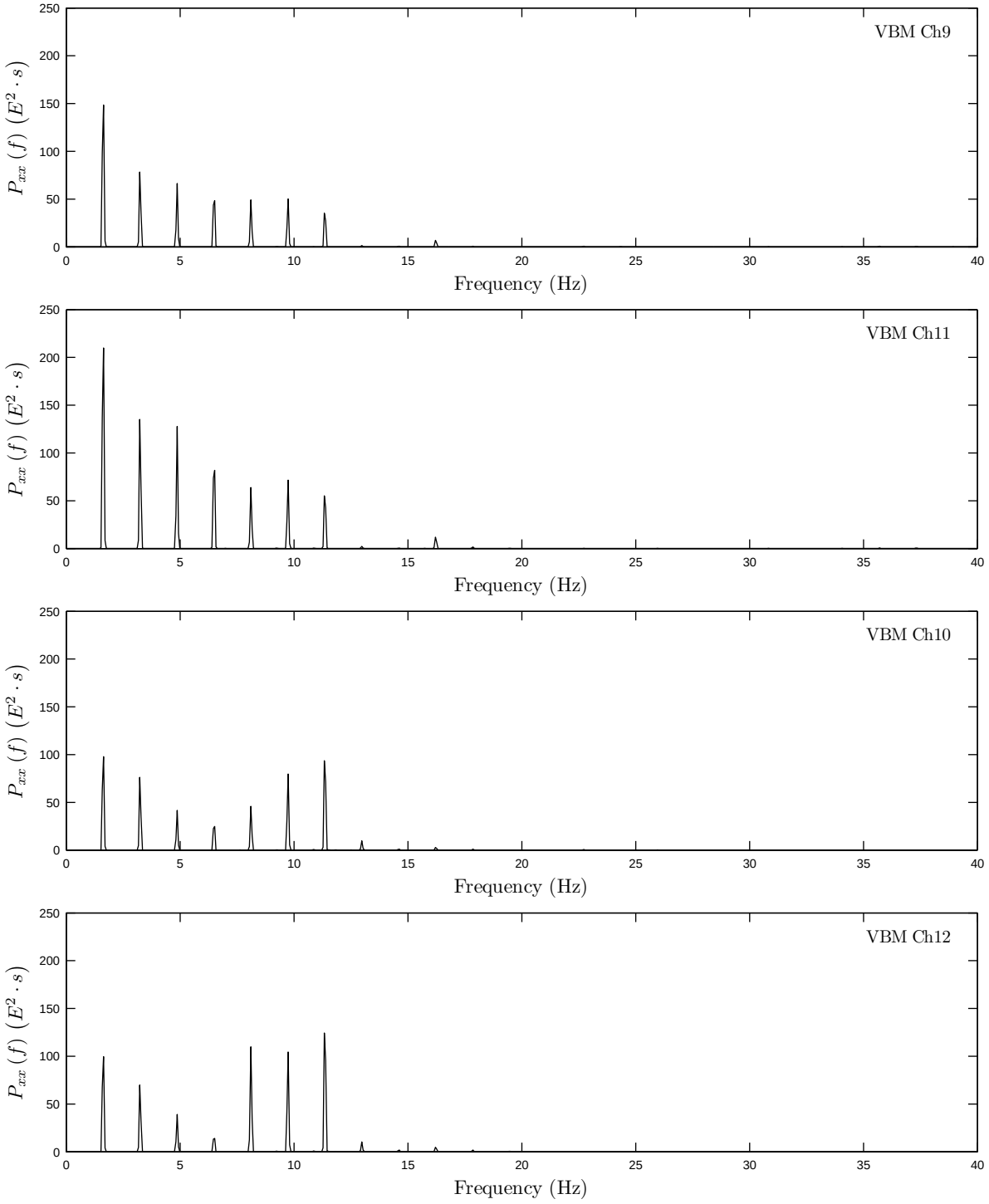

Figure 3.76: Power spectral density (PSD), $P_{xx}(f)$ for vertical bending moment (VBM) measured at elastic links for Ch9, Ch10, Ch11 and Ch12 in regular wave height, $H_w = 90.5$ mm and wave frequency f_s =0.7 Hz at $F_n = 0.603$. The measured encounter wave frequency by the moving wave probe at LCG was 77.6 Hz. Run No.457 PSD was obtained by applying the Hamming window for data taper in time domain, and No smoothing by a convolution in frequency domain.

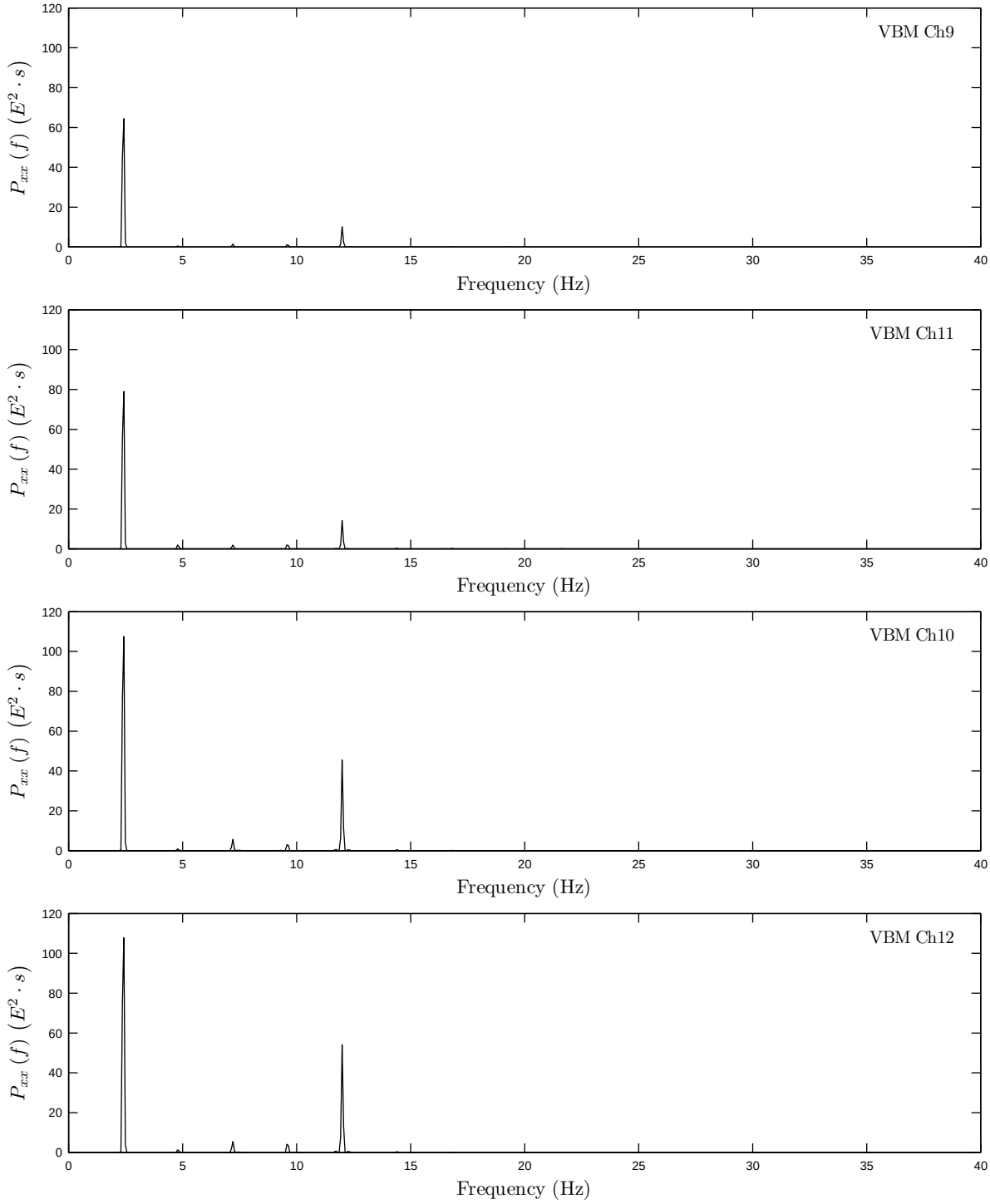

Figure 3.77: Power spectral density (PSD), $P_{xx}(f)$ for vertical bending moment (VBM) measured at elastic links for Ch9, Ch10, Ch11 and Ch12 in regular wave height, H_w = 90.9 mm and wave frequency f_s =0.9 Hz at F_n = 0.604. The measured encounter wave frequency by the moving wave probe at LCG was 60.3 Hz. Run No.440 PSD was obtained by applying the Hamming window for data taper in time domain, and No smoothing by a convolution in frequency domain.

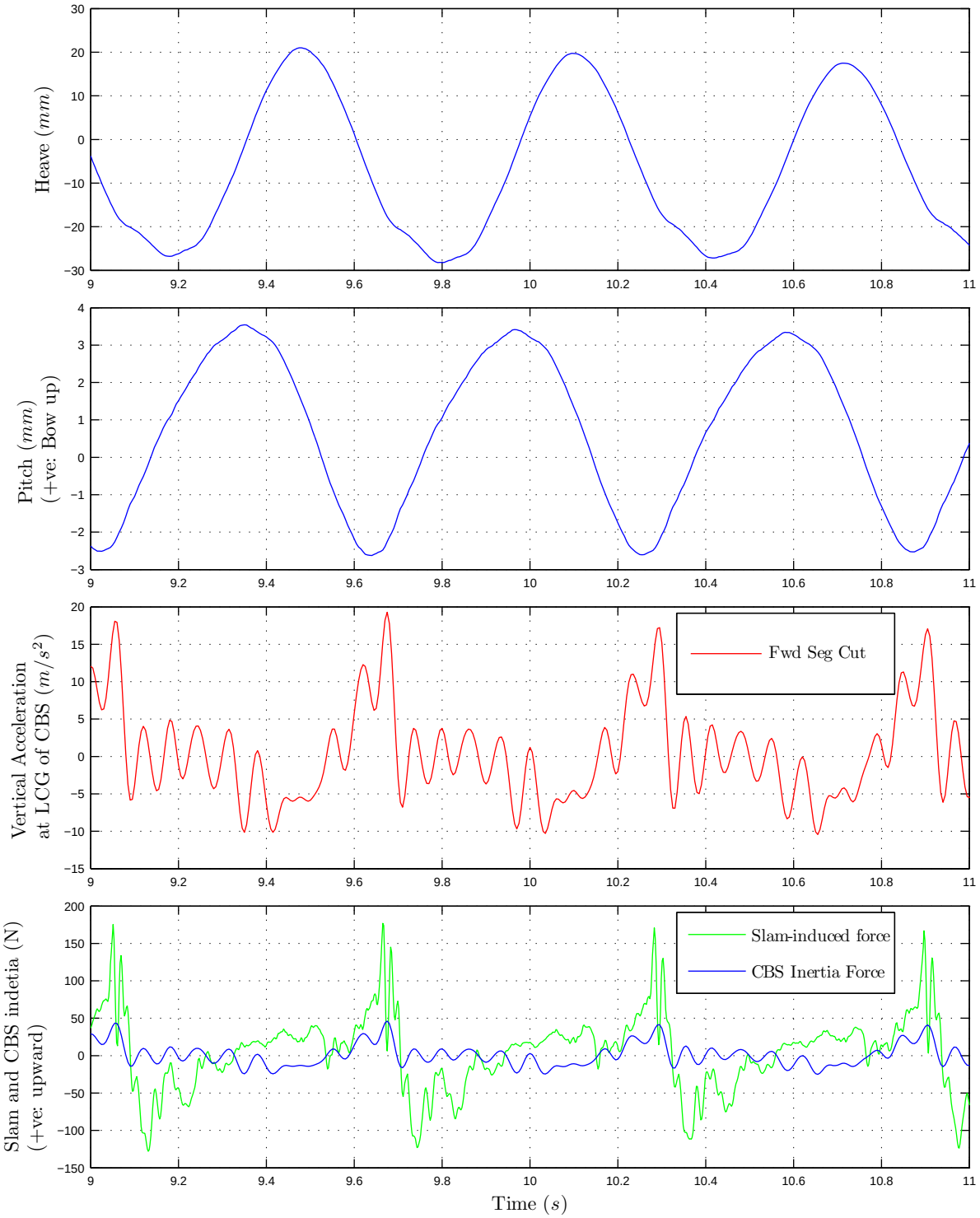

Figure 3.78: The heave and pitch motion at the model LCG, and the vertical acceleration at the CBS LCG in time domain for Run No.457. The corrected slamming forces and CBS inertial force were presented.

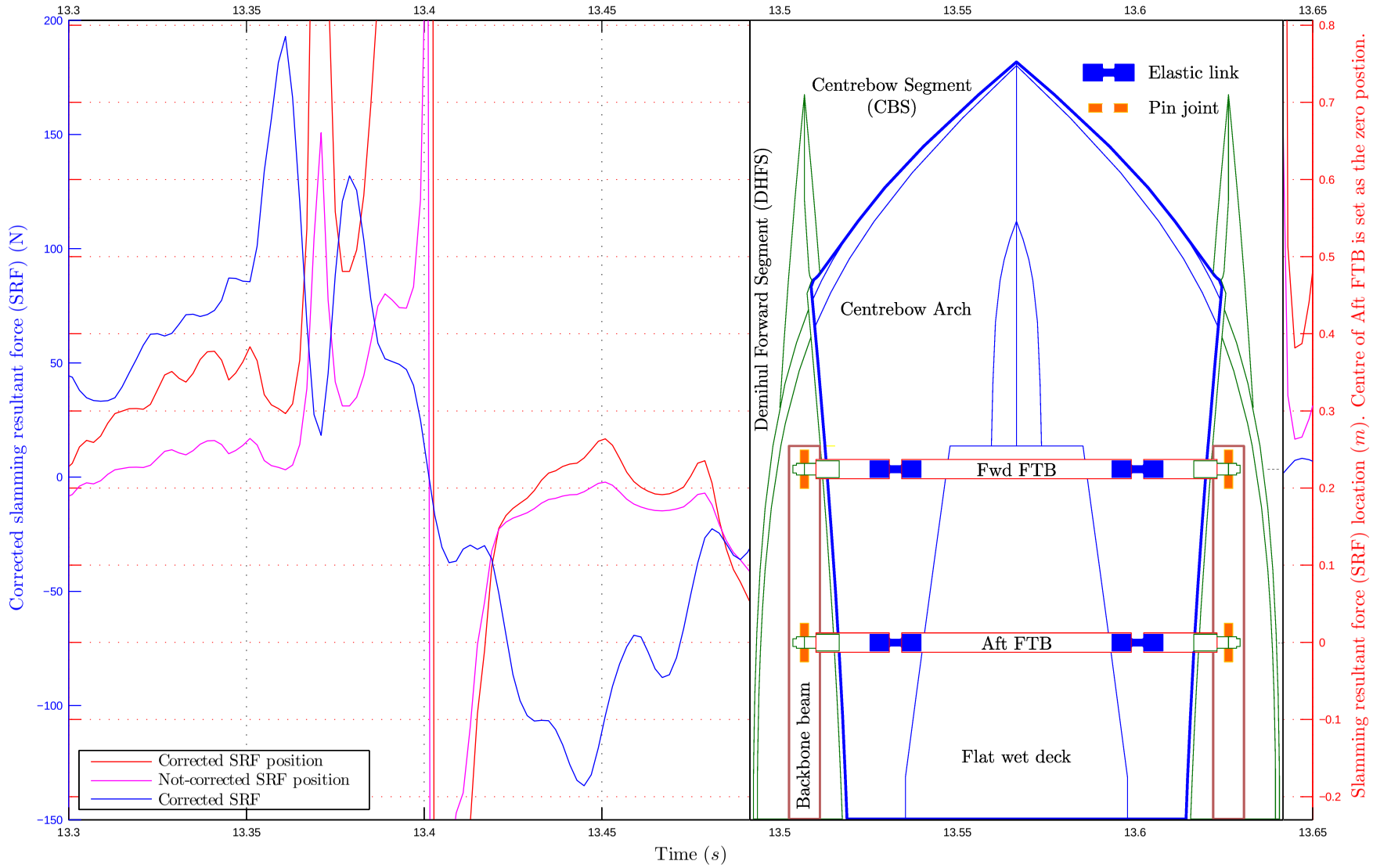

Figure 3.79: Slamming resultant force (SRF) and SRF location for Run No.457. Both corrected and not-corrected SRF location are presented.

Slam resultant force positions were determined based on the procedure explained in Subsection 3.5.4. The corrected slam resultant force position and non-corrected position are presented for Condition 35 in Figure 3.80. The positions for the hogging and sagging condition are shown. The positions for the sagging were located further forward than the one for the hogging. The sagging VBM was influenced more by the slamming forces, hence, the SRF position due to sagging was used for the analyses of the SRF position. The corrected positions and non-corrected positions showed significant differences for Condition 35. On the basis of the FTB mechanism discussed in Subsection 3.5.4, the corrected position was used for the analyses of the SRF position.

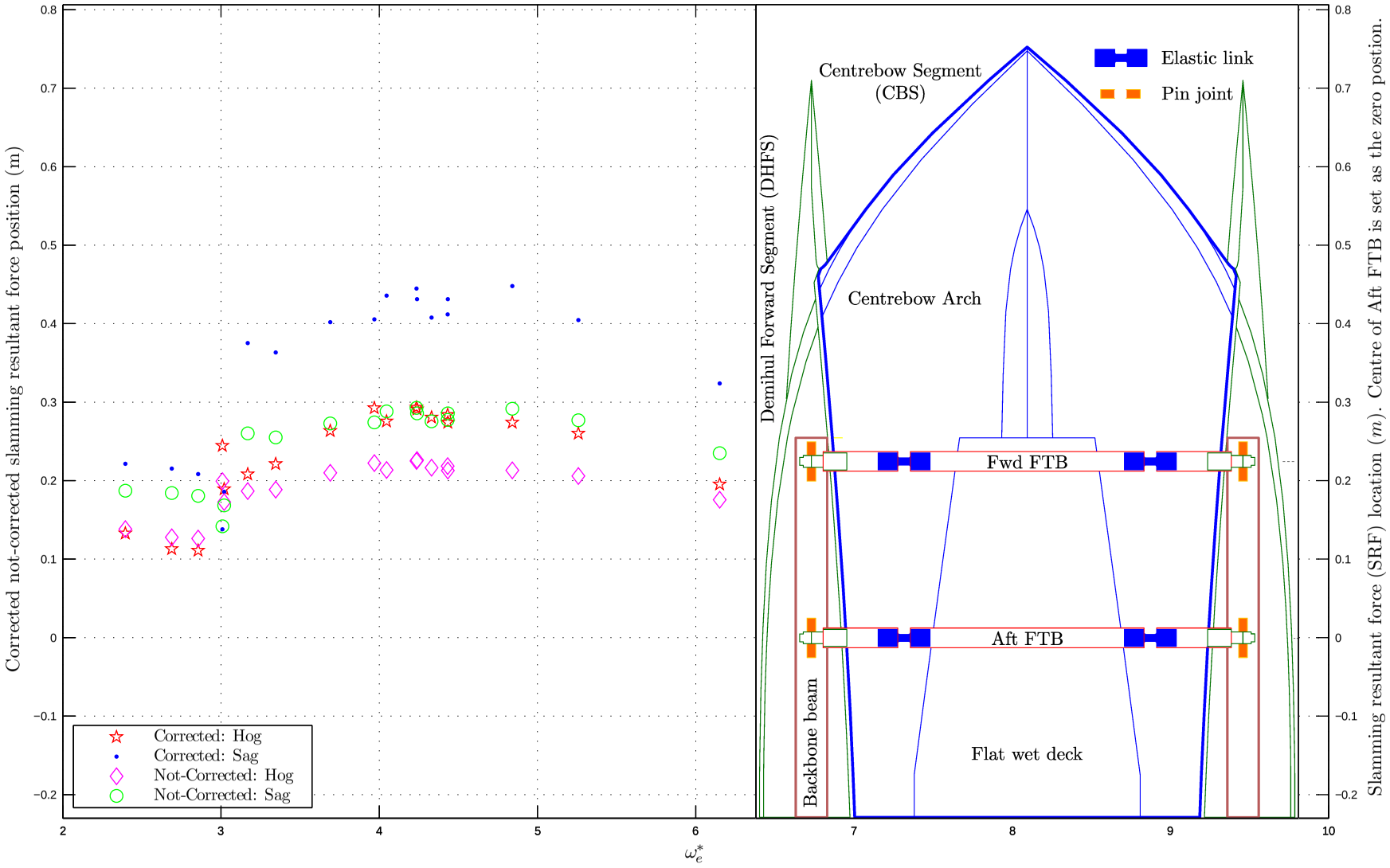

Figure 3.80: Slamming resultant force (SRF) location for sagging. Both corrected and not corrected location were presented. Condition 35

The slamming resultant force positions were plotted for large wave cases. Wave height effect on the location were plotted against ω_e^* for 1.55 and $2.94 m/s$, as shown in Figures 3.81 and 3.82, respectively. Similarly, the velocity effect on the location is shown in Figure 3.83.

As the wave height became larger, the position of the slamming resultant force was located at the forward part of the centre bow at both 20 and 38 Kn, as shown in Figures 3.81 and 3.82, respectively. For the larger wave, the centre bow arch was filled with the water in a shorter period than for the smaller wave. Smaller waves could travel farther aft to cause the maximum resultant loading position further behind. In order to cause this, a smooth transition of water is required, and it can be expected that the centre bow arch successfully transfers the water in the longitudinal direction at the event of the centre bow submergence.

As the vessel speed became faster, the position of the slamming resultant force was located at the forward part of the centre bow, as shown in Figure 3.83. The water travelled relatively to the centrebow farther back in the longitudinal direction, therefore the higher velocity resulted in the location of the resultant forces occurring farther back.

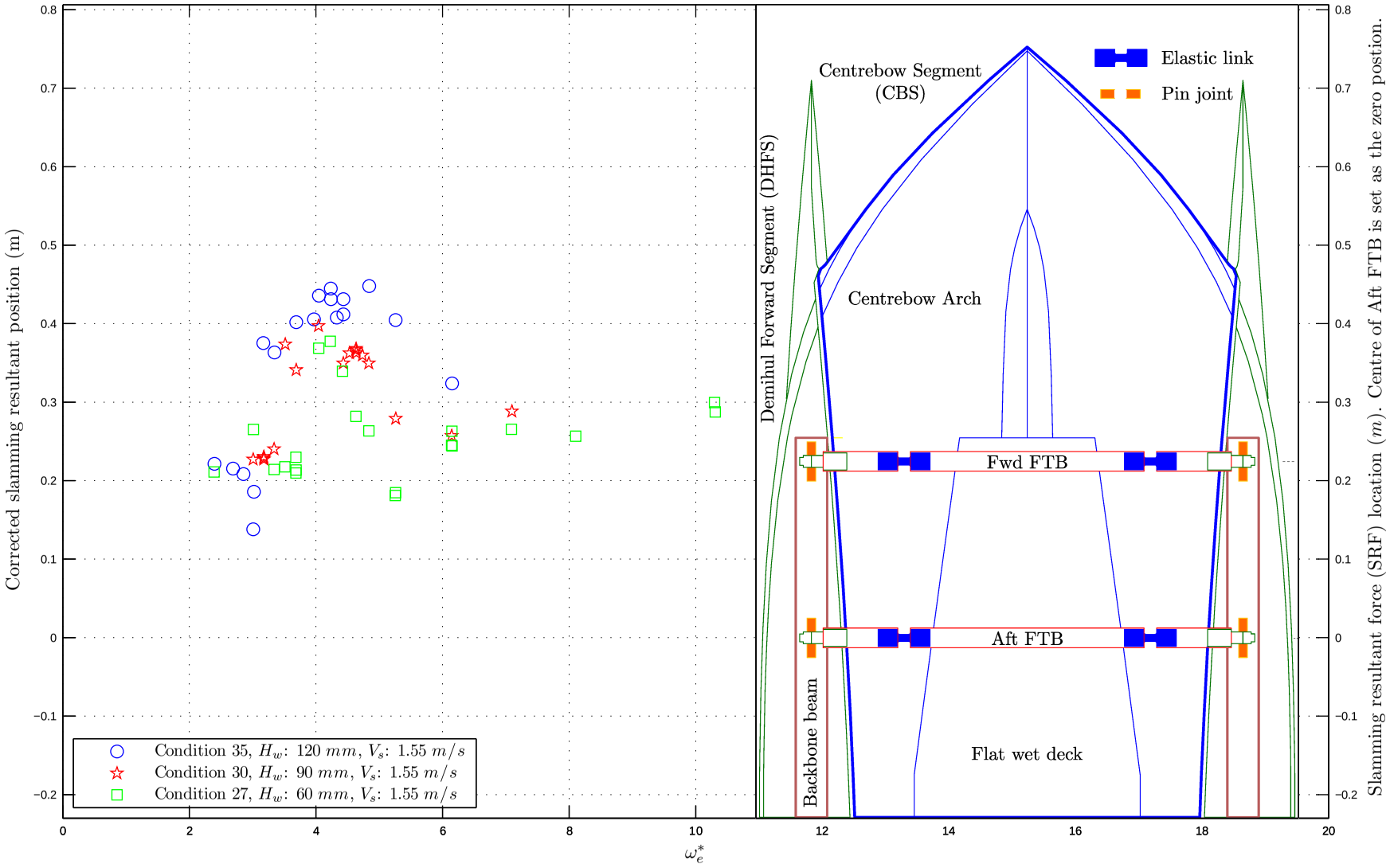

Figure 3.81: Slamming resultant force (SRF) location for sagging. Both corrected location were presented. V_s is constant at 1.55 m/s.

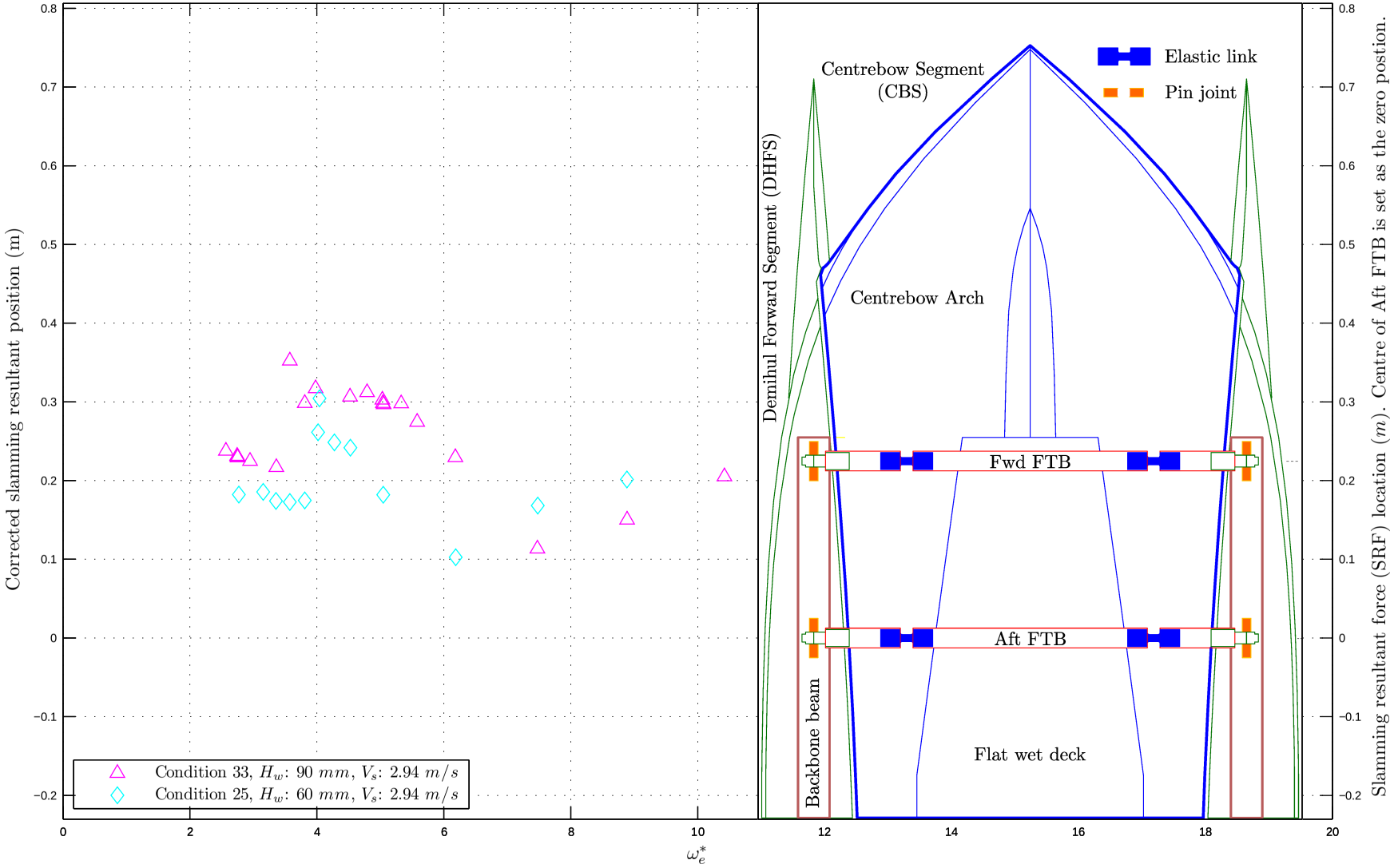

Figure 3.82: Slamming resultant force (SRF) location for sagging. The corrected location are presented. V_s is constant at 2.94 m/s.

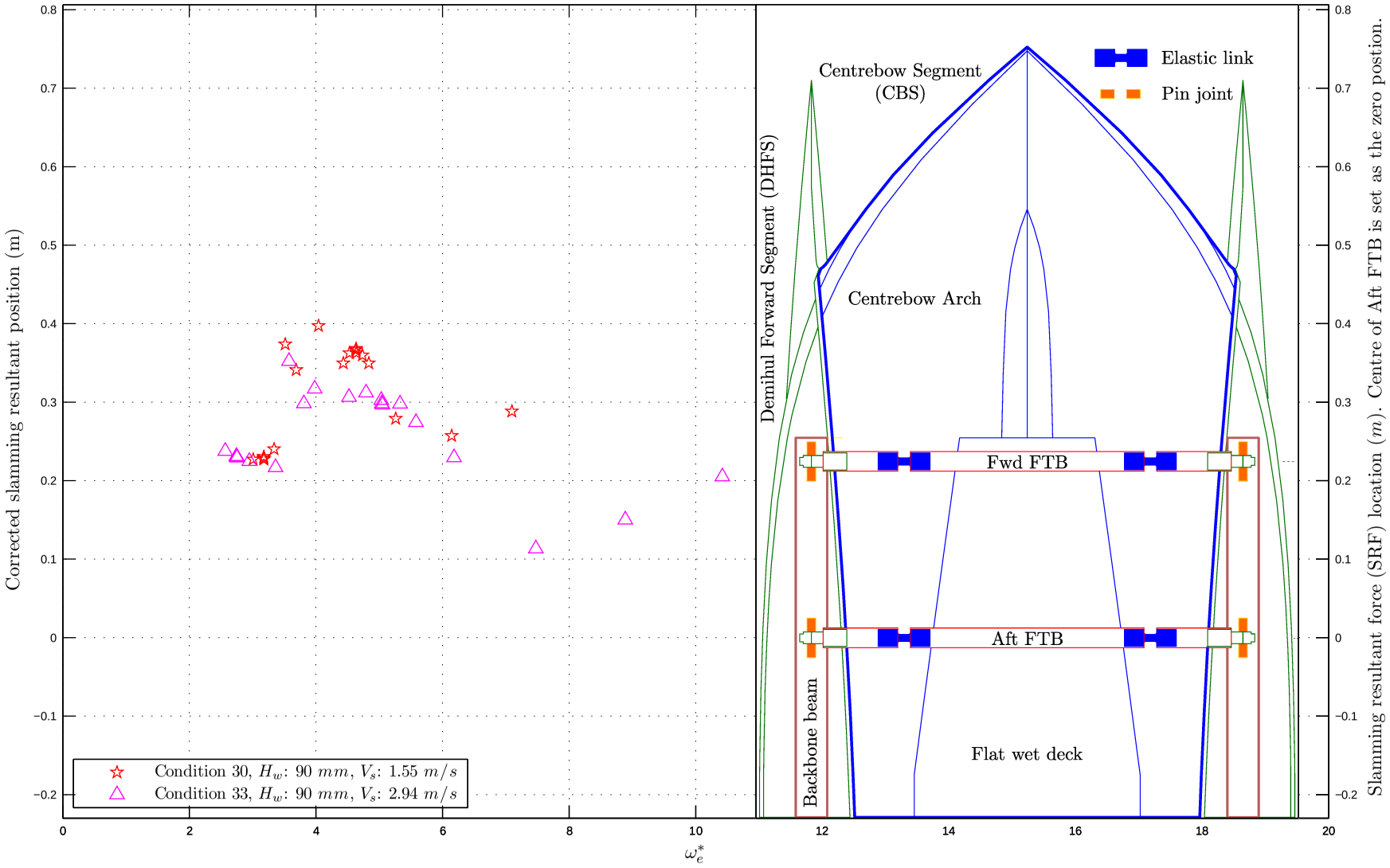

Figure 3.83: Slamming resultant force (SRF) location for sagging. Both corrected location are presented. H_w is constant at 90 mm.

The slam-induced resultant force magnitude and position were examined for the centre bow region for larger slamming loads. Three cases are presented in Figures 3.84, 3.85 and 3.86, two cases of variation in wave height at 20 and 38 K_n, and one case of variation in velocity at the wave height of 90 mm.

Figure 3.84 compares the wave height of 120, 90 and 60 mm at 20 K_n. The larger wave at a constant wave speed generated the slam force towards the forward area of the centre bow than the smaller wave. A large wave simply reaches to the peak of the centre bow arch quickly to generate the maximum loads as slamming, before the wave can travel backwards. Therefore the SRF position of the large waves occurred at a forward area of the CBS. As wave height reduces, the wave can move further before the water can reach the peak of the centre bow arch to cause the maximum slamming loads. Therefore the SRF position in small waves occurred at further back than in large waves. The centre bow arch is designed to guide water along the arch side to the arch peak. For the 38 K_n cases in Figure 3.85, same tendencies were observed to the 20 K_n cases.

Most of the large slam-induced forces of more than 100 N occurred in front of the centre bow truncation wall. The slam maximum impact occurred as the water filled the centre bow arch.

An intriguing phenomena was evident in a few observations of the slam force at more than 100 N which appeared behind the centre bow truncation bulkhead wall for both $H_w = 90$ and 60 mm at 38 K_n. This could imply that the faster water flow of the wave due to the higher model velocity was guided by the centre bow arch and transferred further back to the arch peak in a short time period, before the maximum slam loads were fully developed at the slam resultant force position. Therefore the SRF position occurred behind the centre bow truncation wall. The influence of forward velocity is shown in Figure 3.86 at the constant wave height of 90 mm. Clearly, the higher velocity conveyed the water further back onto the centre bow arch to cause the maximum slam force.

A gap can be seen without any data points of SRF position between 20 and 30 N in the Figures 3.84 and 3.84. Above the gap the slamming impact was induced in most cases, and below the gap the gentle water entry without a water impact occurred.

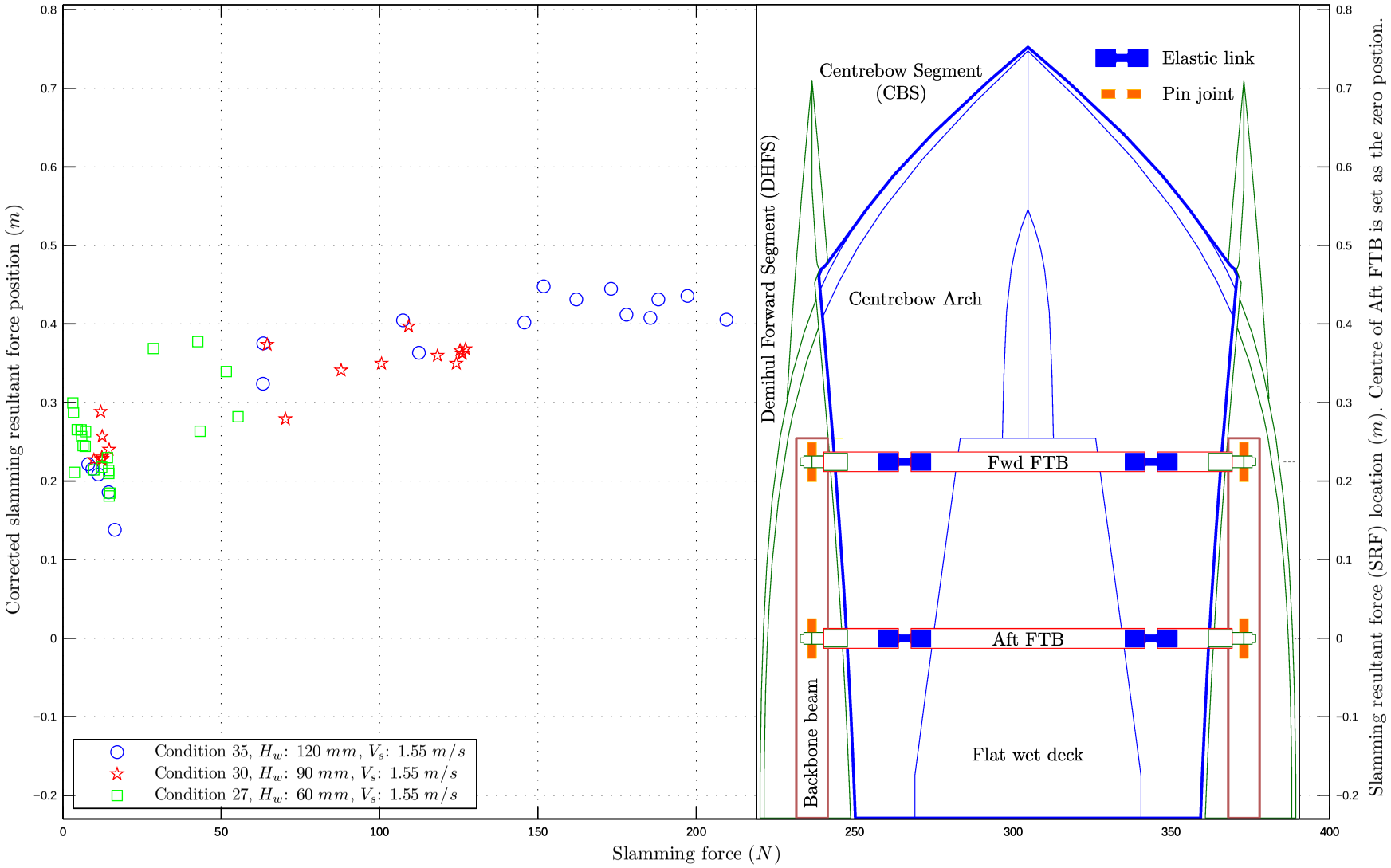

Figure 3.84: Slamming resultant force (SRF) location for sagging vs slamming load. V_s is constant at 1.55 m/s.

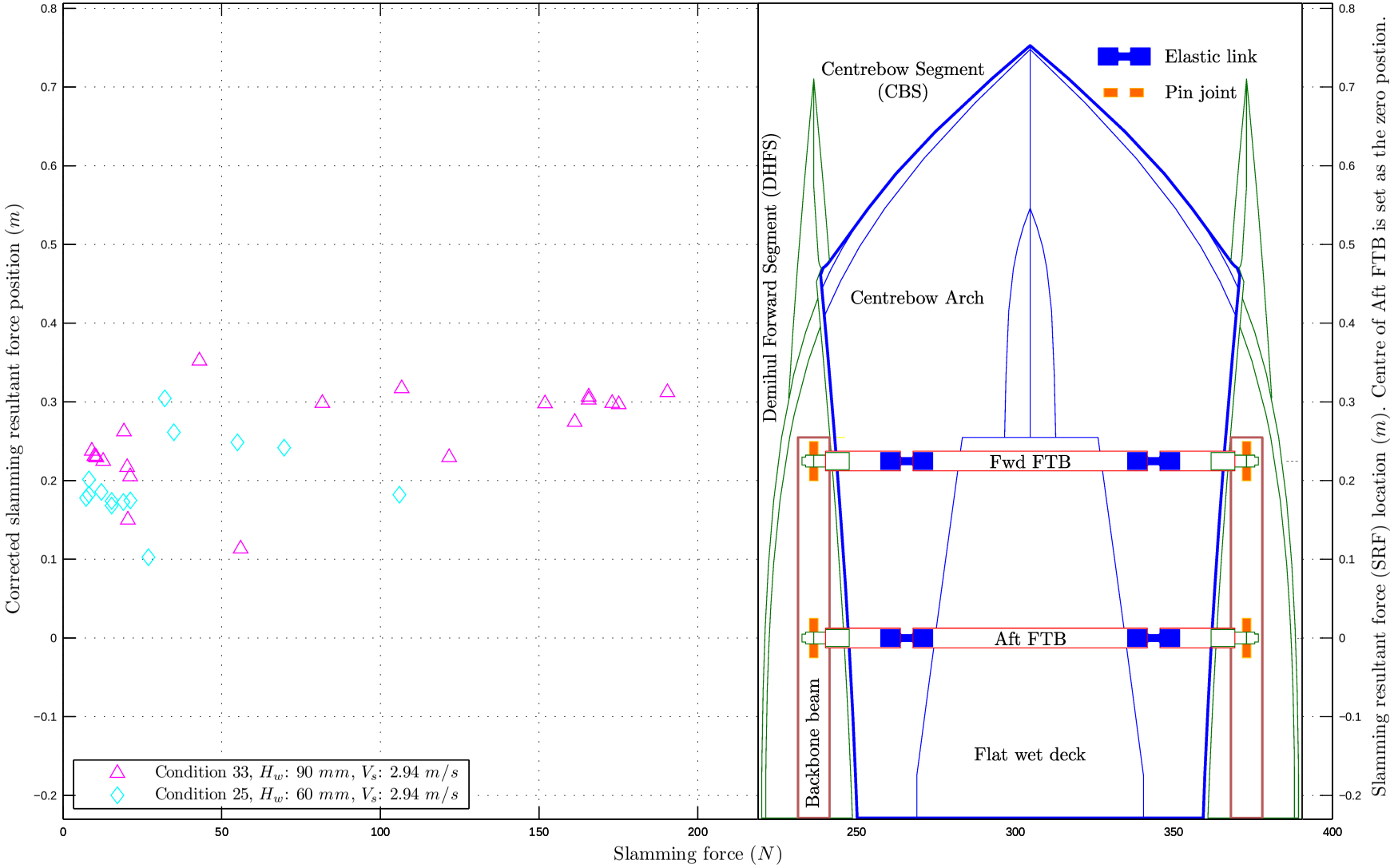

Figure 3.85: Slamming resultant force (SRF) location for sagging vs slamming load. V_s is constant at 2.94 m/s.

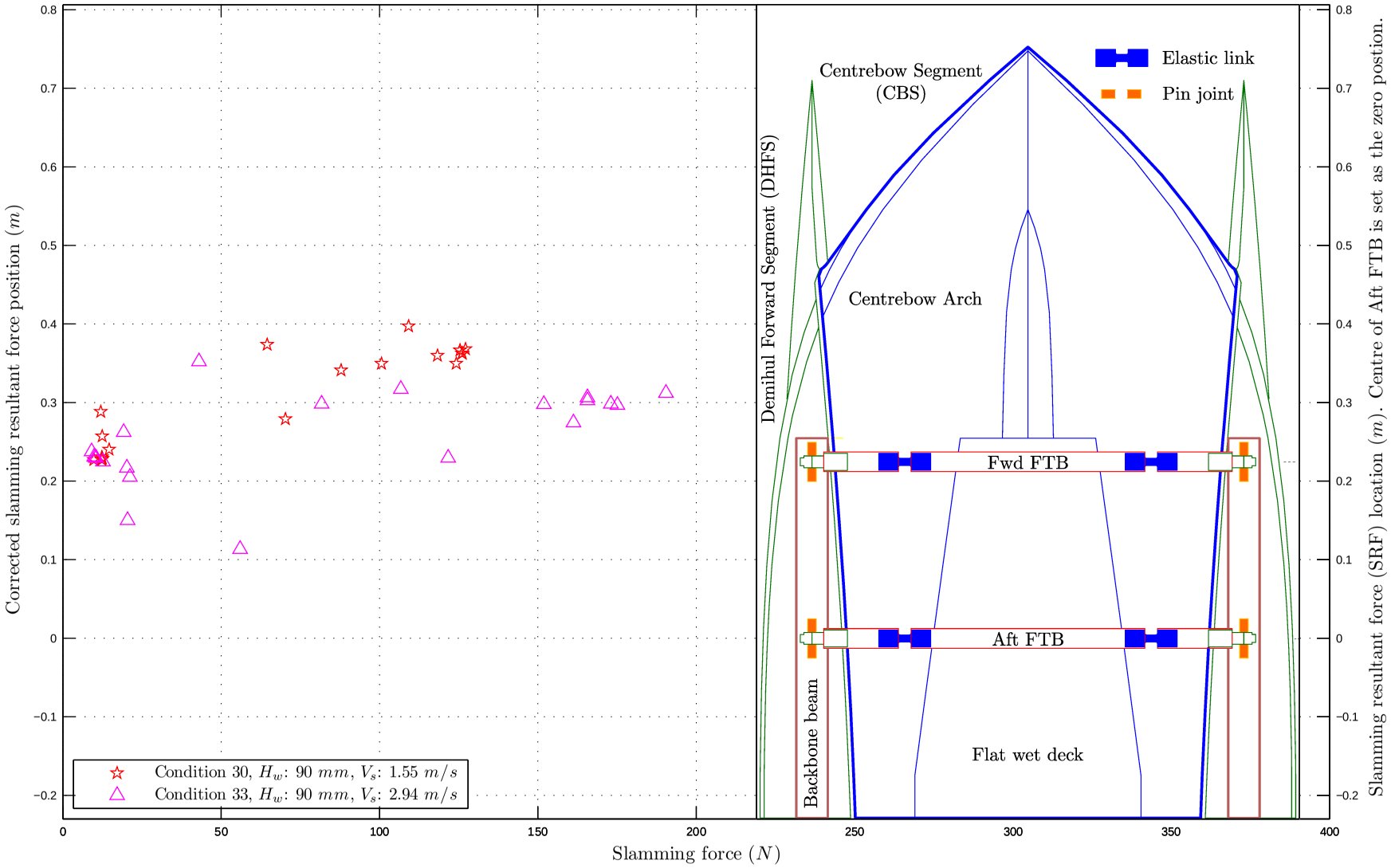

Figure 3.86: Slamming resultant force (SRF) location for sagging vs slamming load. H_w is constant at 90 mm.

3.10.8 Response Interactions for Wave-Induced VBMs on Demi-hulls and Slam-Induced Moments on the Centre bow

The wave-induced VBM response on the demi-hulls and slam-induced force response were compared for the response peak occurrences at 20 and 38 K_n in Figure 3.87 and 3.88, respectively; the maximum magnitude of the slam-induced force response occurred at $\omega_e^* = 4$ to 5 and 5 for 20 and 38 K_n, respectively. The maximum magnitude of wave-induced VBM responses also occurred at the same encounter frequency, as expected. This shows that the maximum magnitude of the VBM response is strongly influenced by the slam forces.

For 20 $K_n$in the higher frequency region,the magnitude of the wave-induced VBM response reduced as the magnitude of the slam-induced force response decreased. In contrast, for 38 K_n in the higher frequency region, the magnitude of the wave-induced VBM response did not reduce as the magnitude of the slam-induced force response did not decrease. It can be presumed that encounter wave excitations of higher frequencies maintains the VBM loads at higher magnitudes, before the VBM load can be dissipated between each cycle of wave-induced load excitations. The period between the peak of the load excitation was shorter in the higher encounter wave frequency, therefore the wave-induced VBM load response system did not have enough time to release the energy of the wave-induced VBM loads on the structure. From the comparison of the 20 and 30 K_n cases, it was found that the wave-induced VBM response of the demi-hull and slam-induced force response of the CBS were mutually associated.

The distance from a slam resultant force position to an elastic link position act as an lever arm for slam-induced force to calculate the slam-induced moment at an elastic link.

The VBM was compared with the slam-induced moment (SIM) at the forward and aft segmentation cuts on the demi-hull calculated by multiplying the slam force and its resultant force position. The case of Condition 35 for sagging moments is presented in Figure 3.89. For sag, the VBM peak and slam-induced moments peak occurred at the same non-dimensional encounter frequency. The magnitudes of the VBMs measured at the elastic link were always smaller than the calculated values of the slam-induced moments. This suggests that the energy generated by the slam forces was absorbed not only into the VBM on the structure, but also into the ship motion and whipping motion.

The slam moments for larger waves were plotted against the VBM at both the forward and aft segmentation cuts, as shown in Figures 3.90 and 3.91. The linear relationship between the wave-induced VBM and slam-induced moment were observed. Again, this indicated that slam forces were the significant factor for generating the VBM on the demi-hulls. The linearity relationship between the wave-induced VBM and slam-induced moment was discovered.

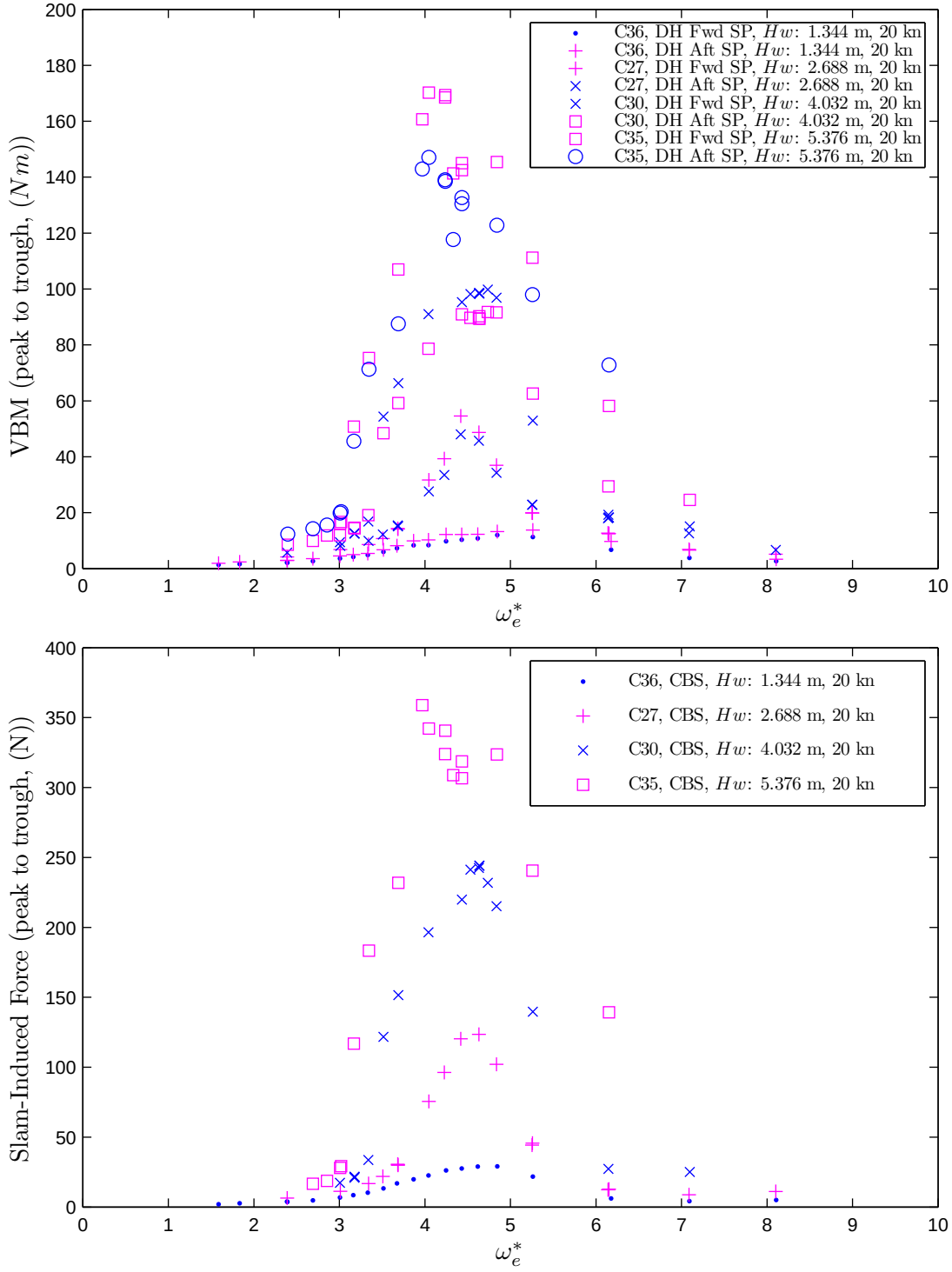

Figure 3.87: RAO Comparison between slam force (peak-to-trough) and VBM (peak-to-trough) by varying the wave heights, plotted as a function of the non-dimensional encounter wave frequency, ω_e^*. The model speed was maintained at a constant speed of Fn = 0.32.

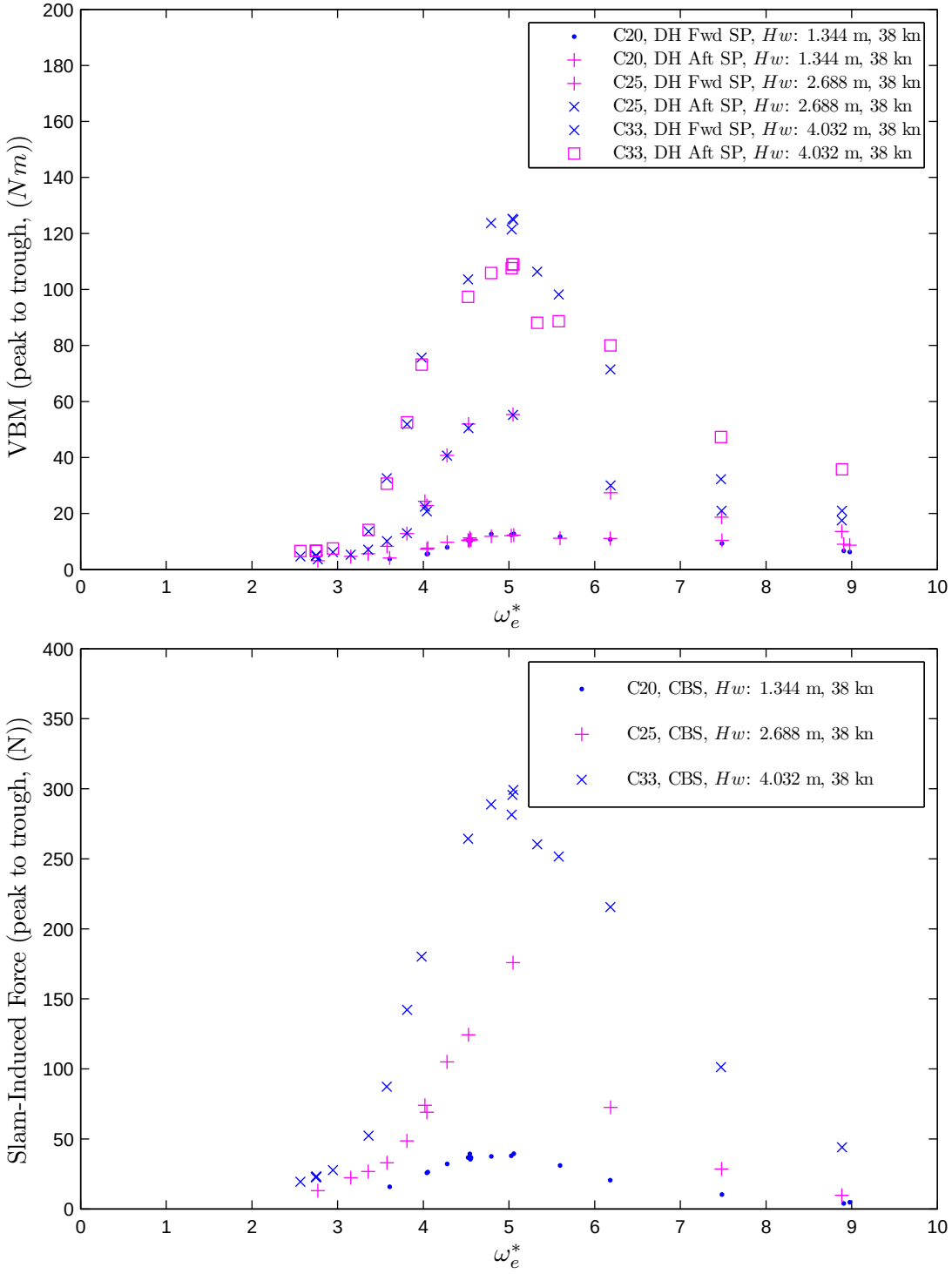

Figure 3.88: RAO Comparison between Slam force (peak to trough) VBM (peak to trough) by varying the wave height, are plotted as function of non-dimensional encounter angular wave frequency, ω_e^*. The model speed was maintained at a constant speed of $F_n = 0.60$.

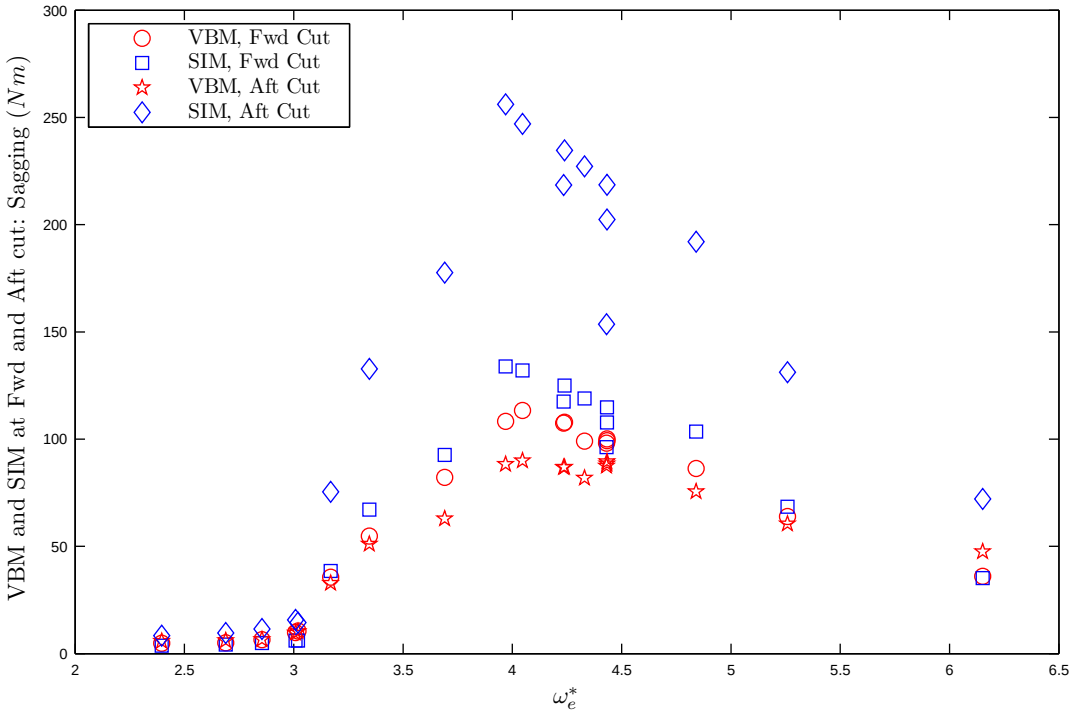

Figure 3.89: Absolute magnitude for sagging vertical bending moment and slam induced momenet (SIM). Condition 35

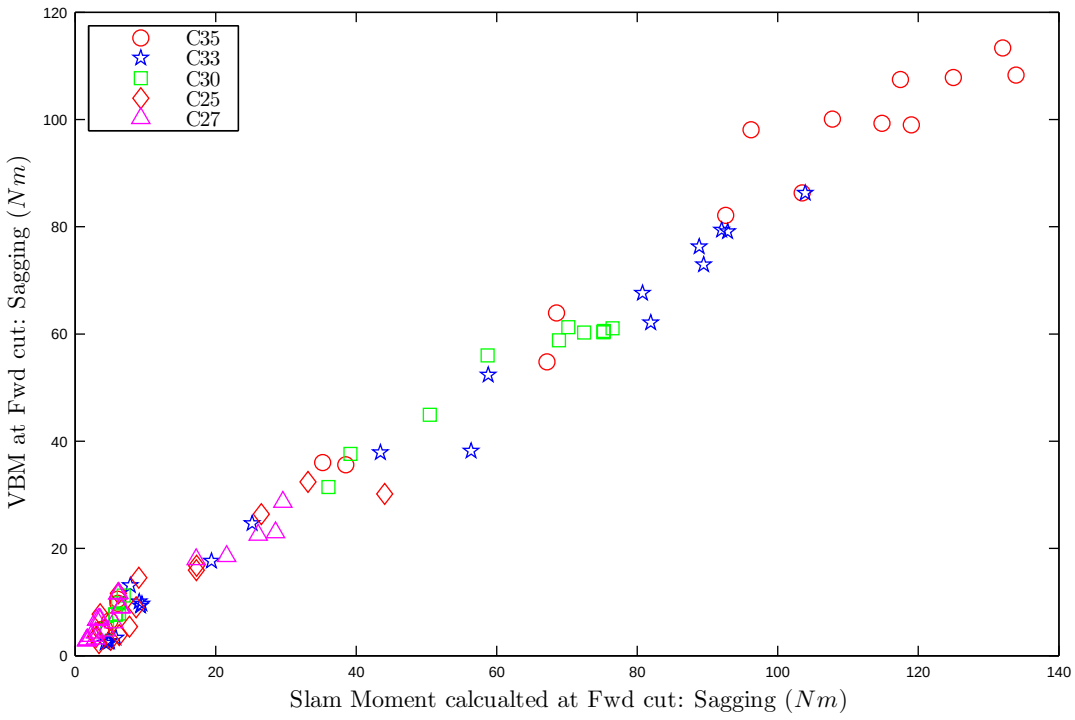

Figure 3.90: Vertical bending moment vs. slam moment at forward cut on the demihull

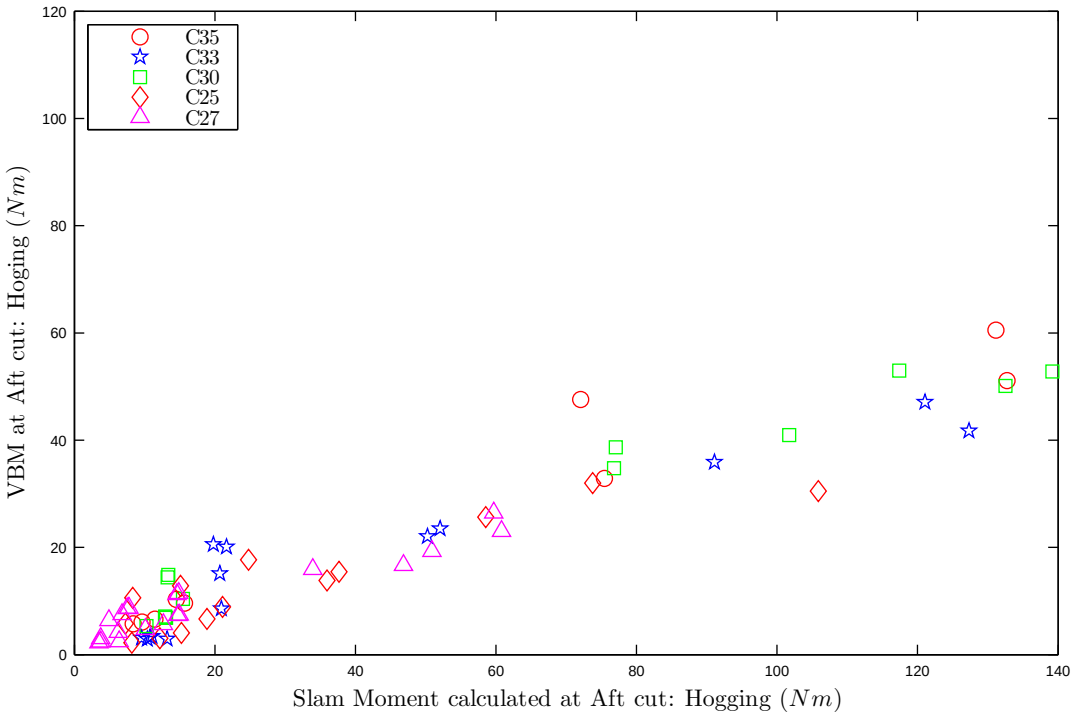

Figure 3.91: Vertical bending moment vs. slam moment at aft cut on the demihull

3.11 Conclusions

The hydroelastic segmented model experimentation was successfully conducted based on a range of experimental programs. The experimentation consisted of the calibration, modal and Seakeeping test.
Extensive calibrations were conducted for ensuring the load measurement mechanism. The elastic links on the demihull segment cut and on the centre bow forward transverse beams. The maximum error magnitudes associated with calibration were found to be 2.16 and 0.41% for the elastic links on the demihull segmentation cuts and on the centrebow, respectively. The correction method on the slam-induced force on the centre bow was developed and validated to improve the measurement on the slam resultant force position.

Modal tests with the impulse excitations were conducted by employing the spectral analysis (by the power spectral density (PSD)) and wavelet analysis and identify the resonant frequency as a natural frequency for the VBM of the demihulls. The dry modal frequency in air occurred at 16.46 Hz, and the wet modal frequency in calm water occurred at 13.45 Hz. Wavelet analysis by continuous wavelet transformations confirmed that these identified frequency were the fundamental modal frequency for the natural frequency of the VBM for the HSM. The wet mode results showed that the added mass and hydroelastic restoring factor significantly reduced the modal frequency by 7.4%. The combination of the spectral and wavelet analysis was found to be effective for frequency response and modal analysis to integrate analysed information in the both domains. The repeatability of the modal tests was excellent, and it indicated the HSM was successfully capable to responded to the excitation force and to response with the modal frequency.

The heave and pitch transfer function showed that heave and pitch responses were characterised with strong non-linearity with respect to the wave height and to the forward velocity. The non-linear response was caused by the geometrical non-linearity of the thin wave-piercer bow and centre bow.

Ship hydroelastic effects were investigated by comparing the motions for the model set-up with the solid and elastic links. The heave and pitch response of the elastic model were reduced an average of 8 and 3.25% difference respectively between the two configurations, indicating that ship hydroleasticity influenced ship motion due to some fluid-idnuced energy comsumed into the strucutral vibraiton as well as ship motions.

The wave-induced VBM coefficient responses were obtained for a range of formulations. The different coefficients were investigated for the influential factors for the wave-induced VBM response. The wave-induced VBM response in small wave conditions was linearly proportional to the wave height at the same forward velocity. For large wave conditions, the peak magnitudes of the wave-induced VBM responses were linearly proportional to the square of the wave height at the same forward velocity.

Slam-induced force coefficients were obtained. However, it was difficult to conclude the definitive factor, since the forward velocity did not show any dominant trend. The dominant factor would be expected to be the vertical velocity, however vertical velocity is the response value as an output, rather than the conditional value as an input. Therefore it was difficult to determine a factor for the slam-induced loads to form the basis of the load prediction.

The ship hydroelasticity of the HSM mutually influenced the ship motion and wave-induced loads of the structure. The ship motion responding to the large global wave acted as a harmonic excitation, and the induced large response of the ship motion response resulted in the impulse excitation induced by the slam impact. The slam-induced loads onto the centre bow induced the subsequent whipping vibratory behaviour of the demi-hull structure, where the fundamental mode of the resonant frequency of VBM was excited. The structural vibration also influenced the ship motion simultaneously as the global waves affected the ship motion. This was observed in the simultaneous coexistence of the vibratory phenomena both in the heave acceleration and in the VBM whipping. The hypothesis of ship hydroelasticity and its mechanism presented in Section 3.1 was therefore successfully discovered.

This observed phenomena raised the importance of ship hydroelasticity for ship motion and wave-induced loads measurement on the VBM and slam event, since the whipping also altered the VBM induced by the global waves. It can also be concluded that the demi-hull whipping induced by the slam impact was important for the experimental measurement for the wave-induced VBM and slam-induced force on the centre bow.

Slam resultant force position on the centre bow was investigated. Most of the severe slams occurred in front of the centre bow truncation bulkhead. A larger wave at the same speed caused the SRF position to be further forward; higher forward velocity caused the SRF position further back than the slower speed.

The interaction between the wave-induced VBM response and the slam-induced moment was investigated. A linear relationship exists between the wave-induced VBM and the slam-induced force. It showed that the slam-induced force dominantly influenced the wave-induced VBM.

The hydroelastic segmented model experimentation was successfully conducted by achieving ship hydroelasticity to obtain the ship motion response, wave-induced VBM response on the demi-hull and slam-induced force responses on the centre bow for the wave-piercer high-speed catamaran.

Chapter 4

Development of Cross-Demihull Loads Model

Catamaran vessels are subject to a pitch connecting moment (PCM), split moment and pry moment generated on their cross-bridge structure in oblique seas. The cross-bridge structure joins the starboard and port demi-hulls. Hence these loads are called as cross-demihull loads. In order to simulate these phenomena and to quantify the moments due to oblique global waves, the Cross-Demihull Loads (CDL) model was developed and tested in oblique-sea conditions at the Model Test Basin at the Australian Maritime College (AMC).

For the main part of the these model tests, the influence of global waves on ship motion and wave loads in the oblique sea was investigated in the model test basin test; therefore, the slamming phenomena was not considered in the the CDL model test.

In the present chapter, a novel experimental approach to measuring the pitch connecting moment of a catamaran, achieved by a geometrical arrangement and mechanical design, is introduced. The conceptual approach of solving the measurement difficulty of CDL is explained in Section 4.1. The hull design and CDL measurement are presented in Section 4.2. The detailed design of the CDL measurement system was carried out by Tim Lilienthal, Research Engineer at the National Centre for Maritime Engineering and Hydrodynamics, AMC. The onboard measurement devices and data logging systems are explained in Section 4.3.1.

4.1 Development of CDL Model

Extensive design development of the CDL model was carried to result in a catamaran model measurement of the cross-demihull loads.

4.1.1 Conceptual Derivation of CDL Model

Primarly, the CDL model was developed in order to measure the moments between the starboard and port demi-hulls in response to ship motion.

The measurement mechanism and location can derives both the method of measuring the CDL and the geometrical configuration of a cross-bridge structure. With the limited number of channels on the data acquisition system being used (National Instruments CRIO DAQ system), the number of possible load sensors was also limited. A single location of load measurement has the advantage of simplifying and integrating all forces and moments at the one location, and also simplifies the cross-bridge structure and load measurement device. The calibration process is also significant to allow accurate measurement of the response load of the integrated hydrodynamic force on the hulls of the catamaran, therefore a single load measurement device was chosen. The Advanced Mechanical Technology, Inc. (AMTI) MC3A-250 load cell was available, it allowed measurement of forces and moments in six degree of freedom. It was also important to investigate the resonant frequency of the load measurement sensor.

Since the environment of the experimental facility demands motion measurements using an onboard system, a comprehensive and integrated data acquisition system, the CRIO, was selected. The model test basin has no carriage on which an operator can embark, however, a cable towing system is available. The cable tow system can be equipped with a moving platform where the DAQ system can be placed. The motion measurement was carried out by means of a inertial sensor fixed on the model.

A new towing mechanism was designed such that the towing force and its generated moment were not applied to the load cell measuring the cross-demihull loads. Since the towing mechanism constrains the motions of the experimental model, careful consideration of the effects of the constraint made by the towing mechanism and system on the ship motion and measured loads was required. In particular, the pitch connecting moment should be free from the moment generated by the towing force. Details of this mechanism are discussed at length in Subsection 4.2.3.

4.2 Design of the CDL Model

The NPL 5b hull form was selected for the CDL model, it is a generic hull form designed for high speeds and possesses a round bilge hull form. The generic hull type was chosen for the hull geometry for these tests instead of the INCAT 112 m hull shape, primarily to allow for a simpler model set up, avoid strong non-linearities in the motion and loads responses and negate possible slam occurrence. This approach was taken, because the CDL catamaran model experiment has not been experimentally attempted in the past (to author's knowledge).

4.2.1 LCD Model Hull Form and Configuration

Principal particulars of the NPL 5b model are listed in Table 4.1, and a body plan of the NPL 5b is presented in Figure 4.1.

Table 4.1: Principal particulars of NPL PCM model

Displacement	Δ	30.000	kg
Length overall	L_{OA}	2625	mm
Length Water Line	L_{WL}	2467	mm
Beam overall	B_{OA}	900	mm
Beam for Demi-hull	B_{DH}	250	mm
Draft	T	88	mm

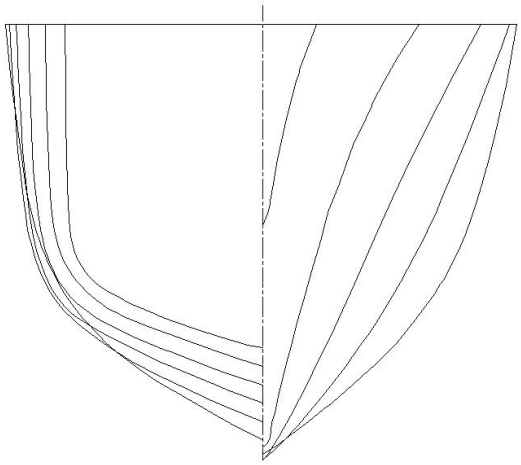

Figure 4.1: NPL 5b body plan

Hull Shape

The NPL 5b, hull form is not wall sided at the water line so it does not comply with the linearity assumption for strip theory of ship motion. So this hull geometry characteristic might be expected to experience slight non-linearity with respect to the wave height in the experimental results. Although the INCAT 112 m hull form has a round bilge hull form until the water jet tunnel intake, the NPL 5b has a V-shaped bottom hull. However, this V-shaped bottom hull was expected to increase directional stability while the model was subjected to oblique seas. The NPL hull form has a transom stern, which is generally observed in high-speed catamaran ferries with water jets.

The body plan of the NPL 5b shows a sharp bow stem that leads to the keel line within two body sections. Once the bow stem reaches the keel line it continues to the mid section. The bow area has a pronounced V shape. After the mid section, the keel profile is gradually raised to the stern. The transom stern has a wide V-shaped stern bottom with round bilge corners, where the INCAT 112 m has a more rounded bottom hull form towards the stern and a flat bottom at the stern for the inlets of the water jet tunnels.

General Model Configuration

The general experimental configuration is shown in Figures 4.2 and 4.3. The two demi-hulls were

joined with a single aluminium tube, supported and locked by the truss frame system rigidly mounted on the deck of the hull. The truss frame clamped the aluminium tubes so that the force was transmitted to the load cell, measuring the moments, located on the centreline of the vessel. The details of the cross-bridge are explained in Subsections 4.2.2 and 4.2.3.

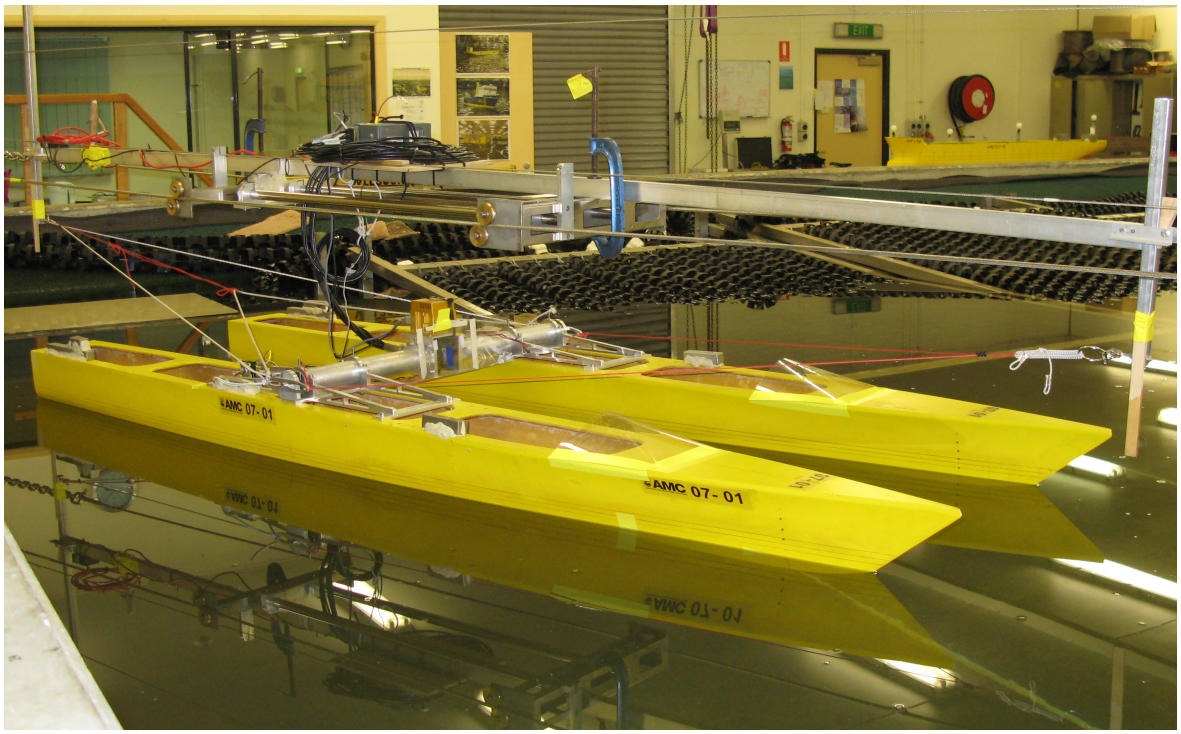

Figure 4.2: CDL model (frontal perspective view)

Model Displacement

The model displacement was set at 30.0 kg and was selected in order to maintain a similar displacement to the hydroelastic segmented model for the INCAT 112 m class.

Demihull Separation

The demi-hull separation was set at 900 mm to achieve the largest feasible transverse span of the cross-bridge structure. Since the oblique angle to a head-sea direction was relatively small due to the facility constraints, the demi-hull separation was maximised in order to produce an enhanced PCM signal. A larger demihull separation will produce a greater PCM due to the increased moment between the hulls and the increased offset between wave crests acting on the separate hulls.

4.2.2 Transverse Cross-Bridge

The transverse cross-bridge tube joining the two demihulls was split into two to allow the insertion of the load cell to measure the moments and forces at the centre-line of the model. The outer ends of the transverse cross-bridge tube beams were supported by the truss frame

Figure 4.3: CDL model (rear perspective view)

system shown in Figures 4.4 and 4.5. The transverse centre-line of the tube beams was aligned with the centre of the load cell, so the towing mechanism was designed to be aligned with this axis. The towing mechanism will be discussed in Subsection 4.2.3.

4.2.3 Towing Mechanism

The transverse cross-bridge system is shown in Figure 4.6. In order to avoid any undesirable towing moments, geometrical and mechanical solutions to the arrangement of the towing point relative to the load cell location were considered. The geometrical solution involved the towing force running through the centre-line of the aluminium tube beam and load cells, as this does not generate additional pitch connecting moments. Also the transverse cross-bridge tube was placed at the LCG of the experimental model. The towing cable was attached to a hole on a small arm that was pin-jointed to the base of the frame, as shown in Figure 4.7. The mechanical solution involved the pin-joint being supported by a ball bearing to ensure the free rotation of the small arm, thus reducing the moment generated by the towing force. Therefore, the PCM was expected to be free from the influence of the towing force.

The forward end of the towing arm was attached to a non-stretch static cable, while the aft end of the arm was connected to elastic cables in order to avoid excessive sway motion during towing. When the forward static cable is towing the ship, the towing force is applied through the small arm to the centre axis of the aluminium tube.

The split moment was expected to be nearly free from the influence of the towing force, since

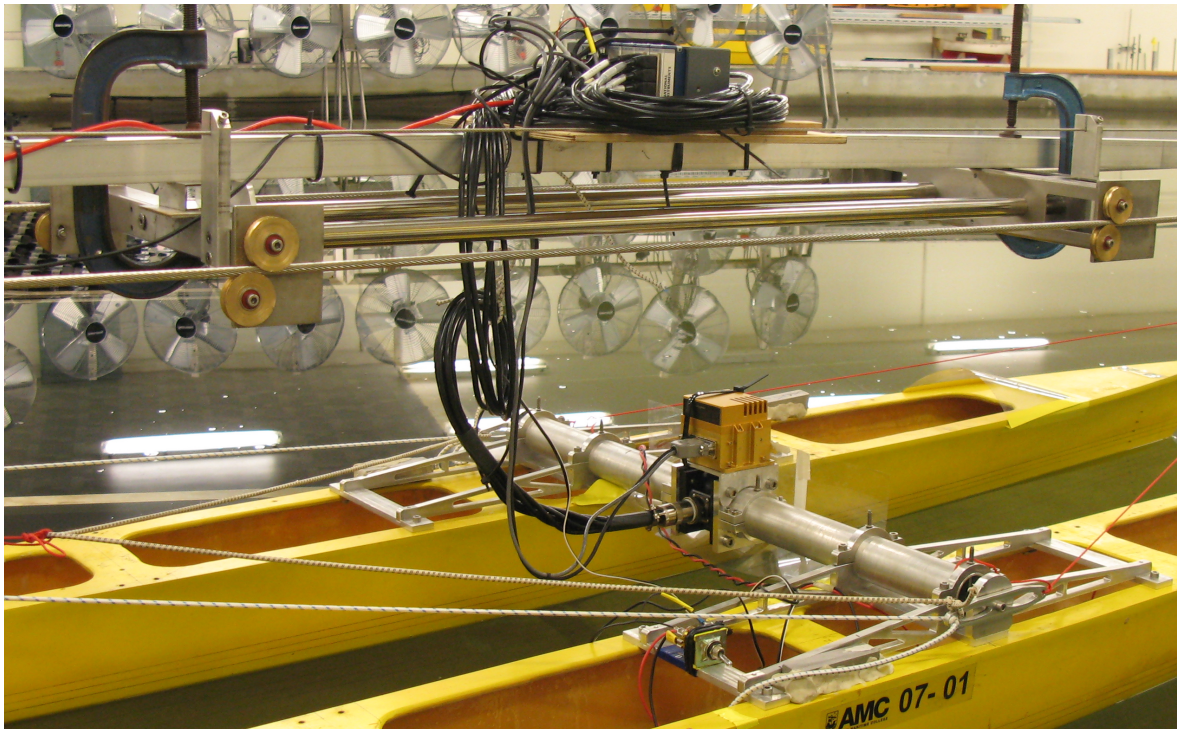

Figure 4.4: CRIO DAQ on the moving carriage, NAV420 motion sensors and AMTI laad cell

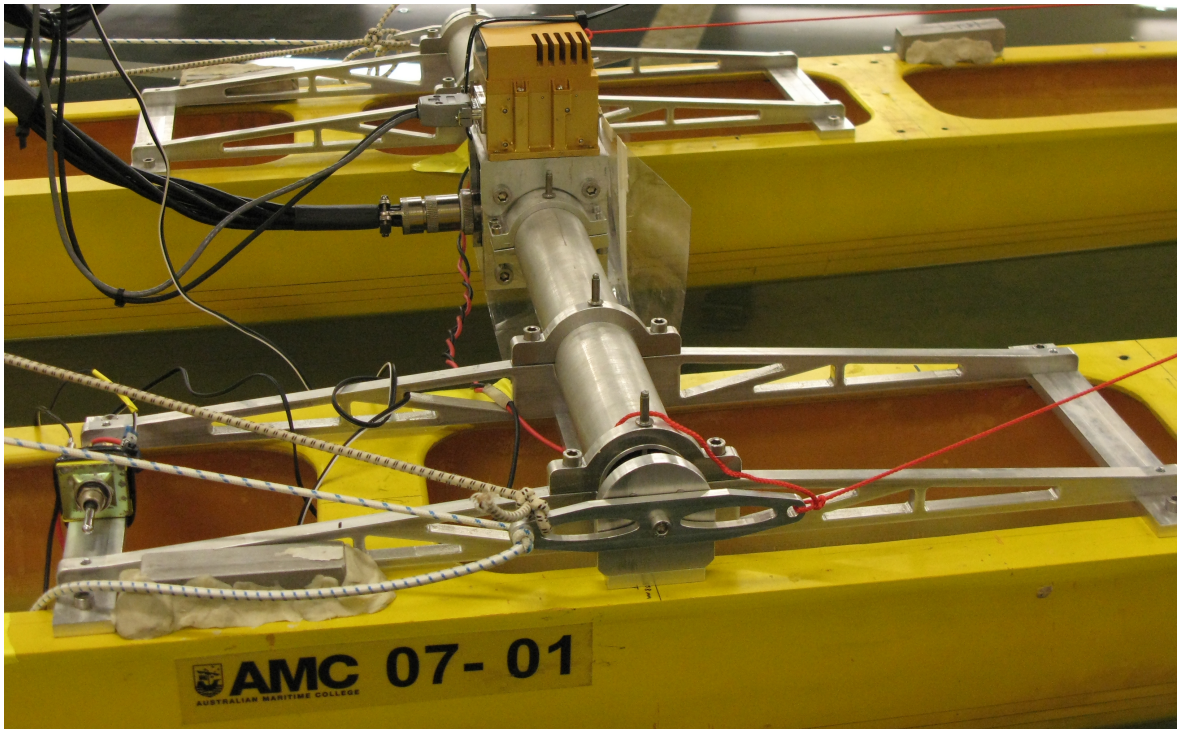

Figure 4.5: Cross-bridge frame system and NAV420

the pin-jointed arm was designed to reduce the force that acts on the model in the vertical axis. The towing cable was set as close as possible to be parallel to the horizontal plane. Therefore, the applied force was expected to act normal to the transverse vertical plane where the split moments would be acting.

Pry moment is likely to be affected by the towing force, since the connection of the pin-jointed arm was fixed for motion in the horizontal plane. This would transfer the towing load to the cross-bridge aluminium beam tube. In view of the towing capability, this was a compromise in the towing system. Since a self-propelled model was not technically feasible to achieve the desired speed, due to the size of the model test basin, towing the model by an external force was unavoidable.

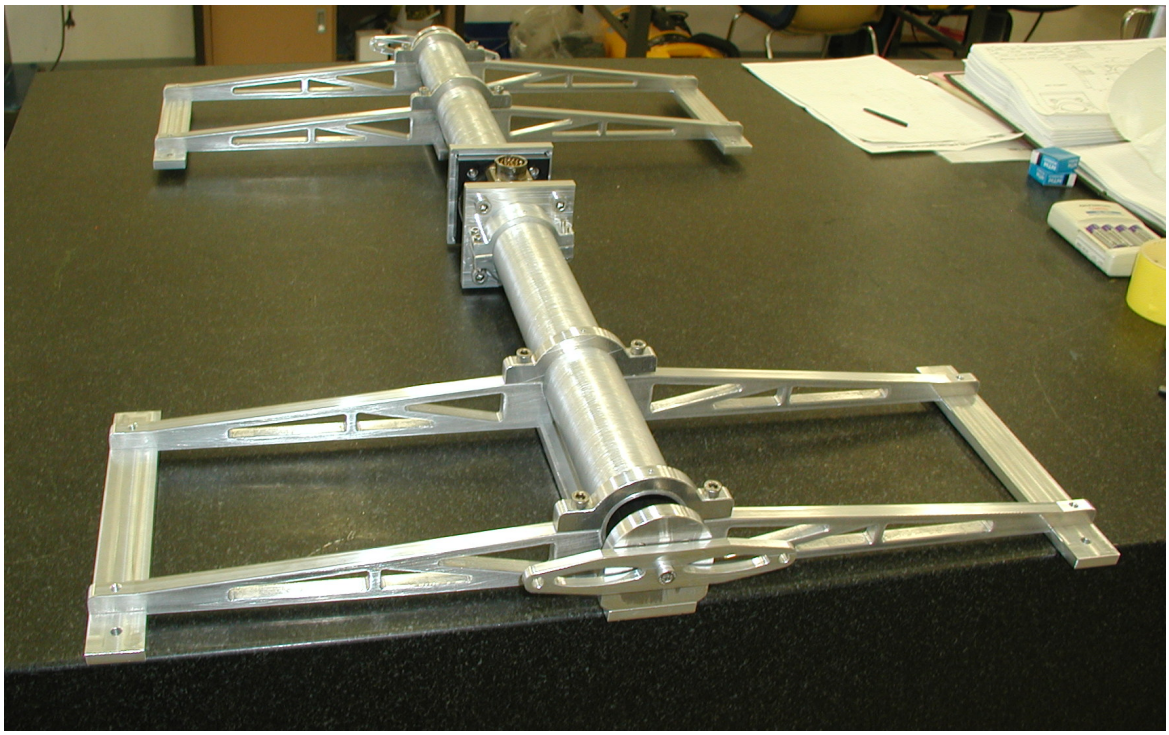

Figure 4.6: Transverse cross bridge aluminium tube beam, bare system. Detail designed and assembled by Timothy Lilienthal

4.3 Onboard Measurement Device and DAQ System

4.3.1 CDL Moment Measurement System

Location

The longitudinal location of the CDL measurement was chosen as the LCG at level trim. In the transverse direction it was located on the centre-line of the model, ensuring it was located at the transverse centre of gravity (TCG).

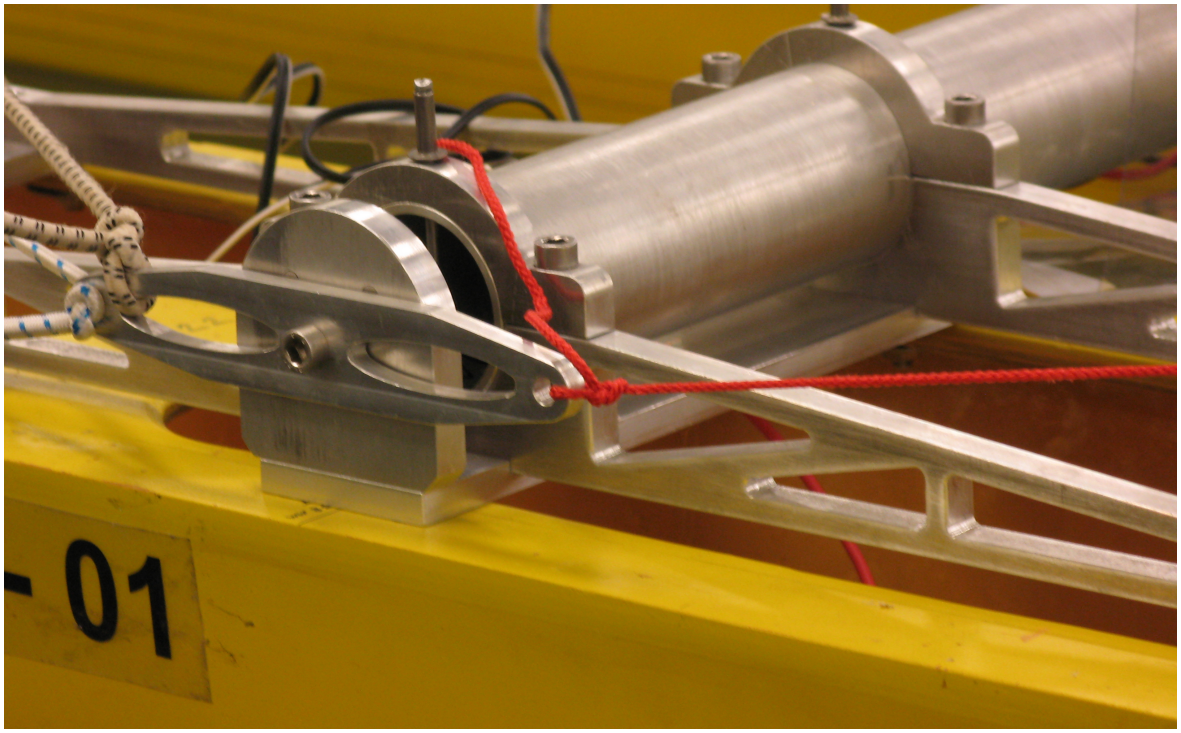

Figure 4.7: Transverse cross bridge tube, mounted on the CDL model

The force and moment sensor, AMTI MC3A-250, was selected, not only because of the six degrees of freedom measurement capability, but also because of its durability. The AMTI MC3A, shown in Figure 4.8, is equipped with elastomeric O-ring seals to protect the internal strain gauges and wiring from moisture exposure. The housing of the load cell is manufactured from a high strength aluminium alloy with an anodised surface finish to prevent exterior corrosion. These functions suited a sensor which was required to be used in the model test basin and operate close to the water.

The lowest resonant frequency of the AMTI MC3A-250 is 500 Hz according to its specifications with oscillatory motions expected to occur well below a frequency of 500 Hz, the measured signal data should not be affected by resonance of the load cell. The data cable from the load cell was connected to the strain gauge modules of the CRIO data acquisition system. The cables can also transfer undesirable load to the model. As a countermeasure, the cables were placed on the centre-line of the model. Since the load cell was placed at the centre-line as well, a lever arm and a tow force generating ting the undesirable moments was considered to be negligible.

4.3.2 Motion Measurement System

The NAV420, as shown in Figure 4.9, was used for the motion measurements. Linear Accelerations in heave, sway and surge, angular rates and angular displacement for roll,pitch and yaw were measured by the NAV420. The NAV420 was connected to a RS232 connection on the main unit of the CRIO measurement system. The NAV420 sensor was required to be placed on the centre of the vessel. Having the single aluminium tube crossing between the two demihulls, a

base was made above the load cell to fix it on.

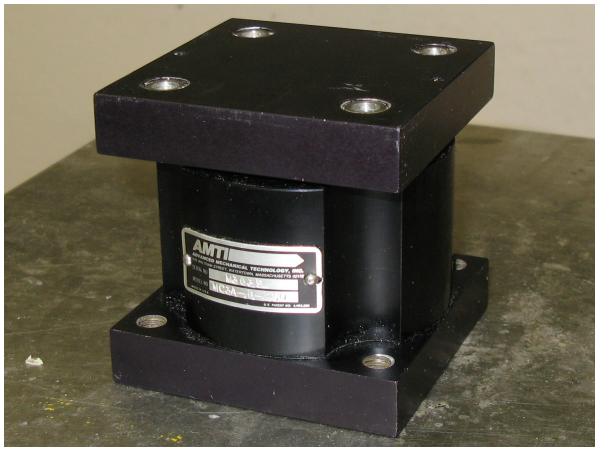

Figure 4.8: AMTI load cell (6 DoF)

Figure 4.9: NAV 420

4.3.3 Data Acquisition System, CRIO

The CRIO was utilised as a semi-automatic data acquisition system, since it had to be placed remotely from the experimental operators. The CRIO was placed on a moving platform located on the winch cables above the model. The moving platform was supported by the two static cables and driven by one moving cable at its centre.

The CRIO produced two types of output data files. The first containing the motion data from the NAV420, while the second file contained the load data from the load cell data.

Chapter 5

Cross-Demihull Loads Model Experiments

5.1 Experimental Facility

5.1.1 Model Test Basin Facility

The CDL model experiments were conducted in the model test basin at the Australian Maritime College. The model test basin has the following dimensions:

Table 5.1: Particulars of model test basin at Australian Maritime College

Length overall	35	m
Standard Depth	0.8	m
Width	12	m
Tow Cable Speed	$0 - 3.8$	m/s

The model test basin (MTB) is equipped with towing cables and a winch system. A multi-panel wave maker is located at one end to generate the regular and irregular waves. The other end of MTB is equipped with a wave dissipation beach. The electrical winch motor is situated at the wave maker end, and the wheel sheave unit for the winch cable to turn around is situated at the opposite end. Between the electrical motor stand and the sheave wheel stand, static and dynamic steel cables were pitched across the MTB. The two static tension cables functioned as the guide cables for a small moving platform, and a dynamic cable towed the model and the moving platform. Both the electrical motor stand and the wheel sheave stand were mounted on frames which could be moved around in the MTB. It allowed for oblique-sea conditions by towing the model diagonally across the MTB.

5.1.2 Wave Generation and Dissipation Control Systems

The wave maker consists of 16 panels of a wave paddle system, which can be seen in Figure 5.1. Each panel is controlled by a linear cable operated by an electrical motor. The wave maker is

operated by a PC at the control station at the side of the basin.

The wave dissipation beach is located at the opposite end of the wave maker to minimise the reflection of waves. The wave dissipation beach consists of multiple layers of swimming pool snakes for dissipating wave motions under the water surface. The framed swimming pool snake units, shown in Figure 5.2 are inclined into the water to assist dissipation of the surface wave.

Figure 5.1: Wave makers

5.1.3 Towing Cable System

The towing cable system can be configured to achieve head-sea and oblique-sea conditions by relocating the tow cable winch stand and cable wheel stand. The cable can be placed parallel to the longitudinal wall, or diagonally across the model test basin from one corner to the other diagonal corner. For the oblique sea angle of 20 degrees was selected for this experiments. The towing cable control unit is located on the control station where the data acquisition system is placed along the side of the model test basin. The winch and drum system, shown in Figure 5.3, are located behind the wall of the wave maker side. The winch drives the drum in order to control the moving cables. The moving cables are led to a wheel sheave at the other end, supported by the wheel sheave stand shown in Figure 5.4. The wheel sheave stand is also located outside of the basin. Static cables are also installed between the winch unit and wheel sheave unit. The static cables can be tensioned at the wheel sheave stand end. Its function is to guide the cables for a small moving platform which can store small devices. In this case, the moving platform was used for the base of the CRIO data acquisition system.

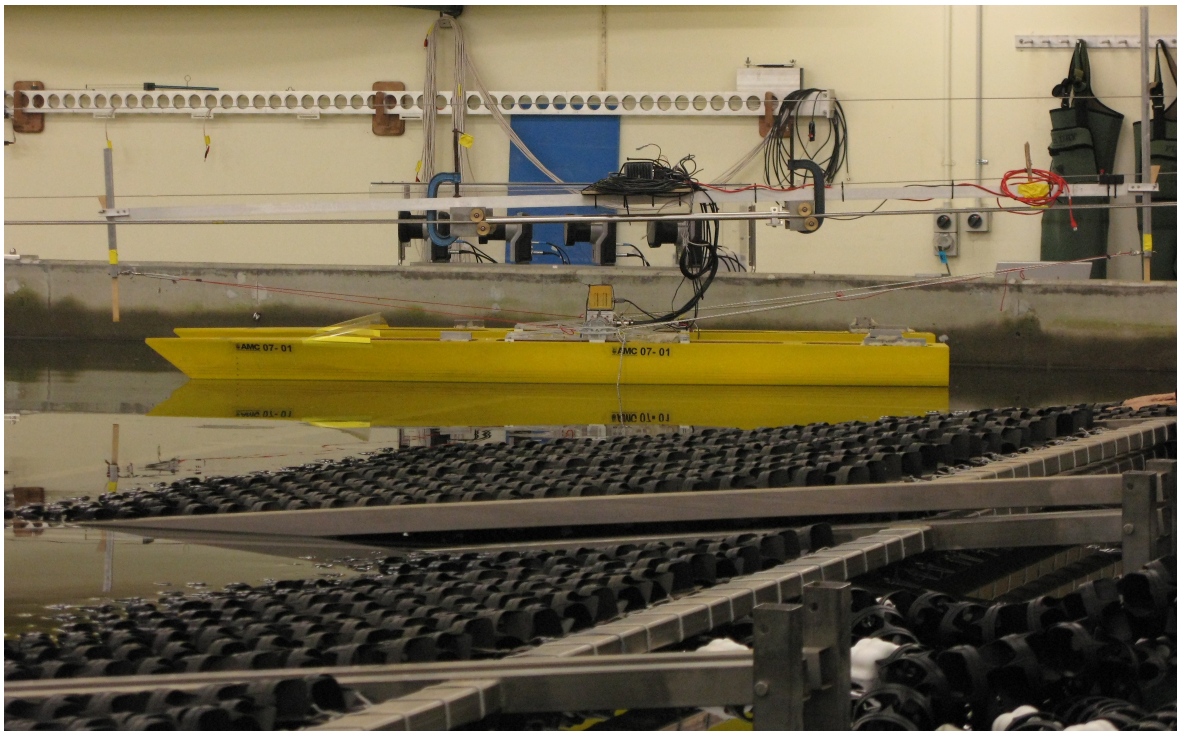

Figure 5.2: Wave dissipation beach

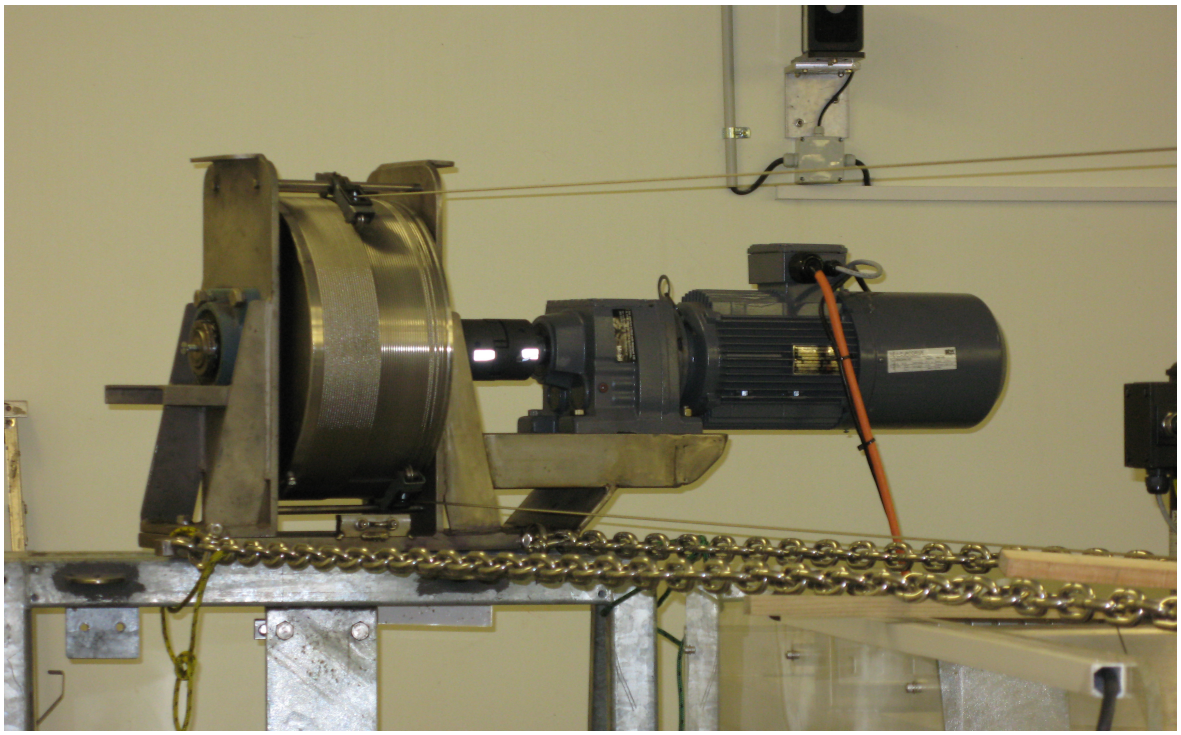

Figure 5.3: Electrical winch and cable drum. Detail designed and assembled by Tim Lilienthal

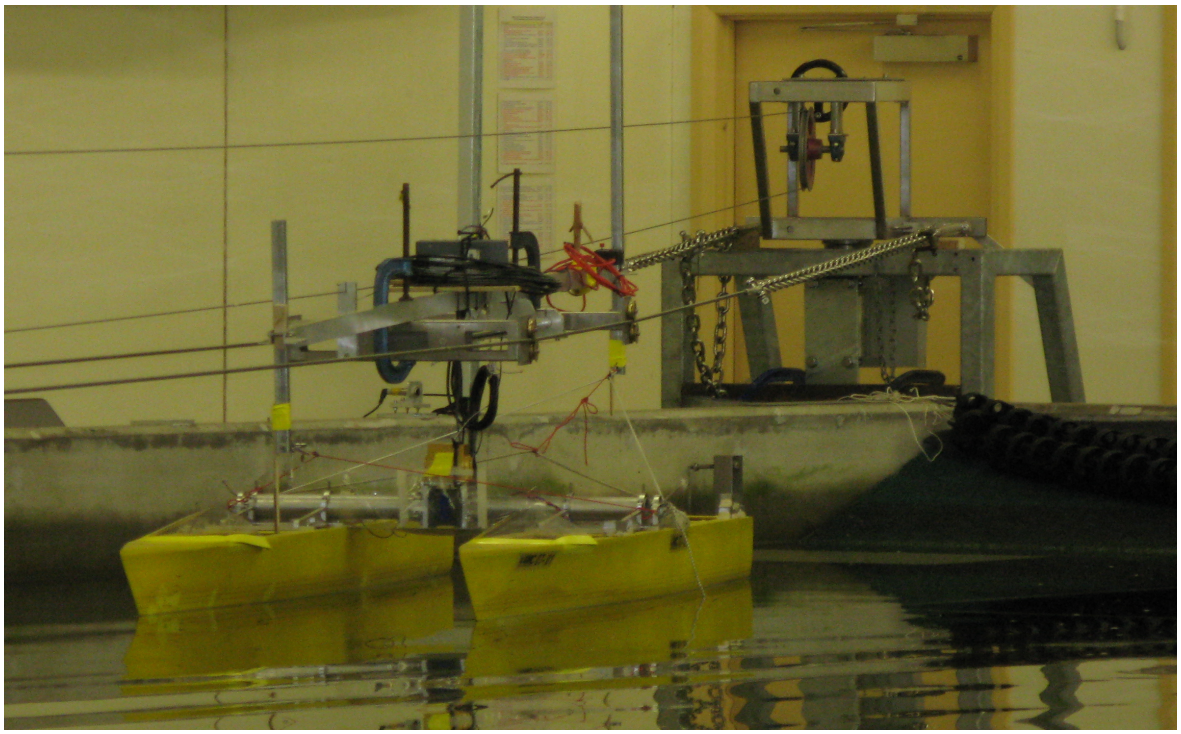

Figure 5.4: Wheel sheave units and frame. Detail design and assembly by Tim Lilienthal

5.2 CDL Model Settings

5.2.1 Degrees of Freedom and Constraints for Ship Motion

In order to successfully tow the model in oblique seas, the degrees of freedom (DoF) and constraints for ship motions needed to be preselected. The DoFs and constraints are listed in Table 5.2. This was achieved by the towing mechanism and system with pin-jointed arms on the transverse beam of the CDL model.

Table 5.2: Degrees of freedom in ship motion

i **or** j	**Motion**	**Free or Constrained**
1	Surge	Constrained
2	Sway	Constrained
3	Heave	Free
4	Roll	Free
5	Pitch	Free
6	Yaw	Constrained

5.3 Data Acquisition System for CDL Model Test

Two systems for data acquisition were used for the PCM model tests. Carriage speed, wave height, ship motion, and forces and moments were measured in each run. A conventional data acquisition system of National Instrumentation was deployed for measuring the carriage speed and wave height. Ship motion and loads were recorded by the CRIO systems onboard the CDL model.

5.3.1 Conventional National Instrumentation and DAQ programs

The towing winch motor has a device to measure cable speed, this was used to determine the vessel speed. A capacitance type of wave probe at a stationary location was used for measuring the wave height during each run. The wave probe was connected to a wave probe signal conditioning box, and to an amplifier and filter box, and the amplified signal was fed into the junction box. From the junction box, all signals were delivered to an A/D converter card then onto the desk top PC. The signals were recorded by the in-house AMC DAQ program written using Labview.

5.3.2 CRIO System for AMTI Load Cell and NAV420 Mode

The CRIO was again utilised for the CDL test. The two strain gauge modules on the CRIO system were used to measure the AMTI load cell data. The strain gauge modules received the 3-forces and 3-moments signal, and were processed to obtain the micro strain. The CRIO also has a RS232 connection to receive the data signal from the NAV420. The CRIO recorded two data files for each run for the AMTI load cell and NAV420 data. On the files, the start time of the experiment was recorded, therefore it was possible to synchronise both signals.

5.4 Calibration of the CDL Model

5.4.1 Load Cell Calibration

The load cell AMTI was calibrated prior to the experiment. The AMTI load cell was mounted on a level working bench to calibrate all forces and torques in six degrees of freedom against the applied loads. A summary of calibration factors is listed in Table 5.3. A lever arm was assembled through a jig that allowed the applied load to be generated at the centre-line of the load cell. The lever arm distance was measured and the calibration weights were applied. Both the positive and negative directions for the known moment were applied for calibration factors.

Table 5.3: Averaged calibration factors of AMTI load cell for PCM model

Force and Moment	Vertical F.	Longitudinal F.	Transverse	Pry M.	Split M.	Pitch C.M.
Load component	Fx	Fy	Fz	Mx	My	Mz
Unit	$\frac{g}{\mu\epsilon}$	$\frac{g}{\mu\epsilon}$	$\frac{g}{\mu\epsilon}$	$\frac{g}{\mu\epsilon}$	$\frac{g}{\mu\epsilon}$	$\frac{g}{\mu\epsilon}$
Average	39.15948	38.44861	152.79861	0.74608	0.74504	1.06519
Positive direction to	Down	Fwd	Starboard	X-axis (CCW) [1]	Y-axis (CCW) [1]	Z-axis (CCW) [1]

[1] CCW indicates counter-clockwise direction.

5.4.2 Ballasting

Ballasting the CDL model was conducted throughout the iterations of the radius of gyration measurements and the inclining test, using the wet dock. The measured mass of each component and ballast mass locations are presented in Table 5.4.

Table 5.4: NPL PCM model, mass measurement and ballast mass location

Components	Mass	X	Y	Z
Unit	(g)	(mm)	(mm)	Location
Demihull Stb	5819	-	-	-
Demihull Port	5438	-	-	-
AMTI	849	-	-	-
PCM beam Stb.	617	-	-	-
PCM beam Port	618	-	-	-
Xbow base & 4Stb bolts	147	-	-	-
AMTI bolt (port)	26	-	-	-
Battery cables	117	-	-	-
NAV420 & Cables	616	-	-	-
AMTI Cables	125	-	-	-
Ballast Stb 1	478	1988	-650	Keel
Ballast Stb 2	542	1608	-745	Deck Outer
Ballast Stb 3	515	1138	-650	Keel
Ballast Stb 4	534	933	-745	Deck Outer
Ballast Stb 5	1370	888	-650	Keel
Ballast Stb 6	533	463	-650	Keel
Ballast Stb 7	1428	193	-745	Deck Outer
Stb. Battery	2198	1628	-650	Keel
Ballast Port 1	330	1978	650	Keel
Ballast Port 2	531	1598	745	Deck Outer
Ballast Port 3	845	1138	650	Keel
Ballast Port 4	532	928	745	Deck Outer
Ballast Port 5	1471	863	650	Keel
Ballast Port 6	517	363	650	Keel
Ballast Port 7	1511	188	745	Deck Outer
Port Battery	2248	1608	650	Keel
Total mass	29955			

5.4.3 Measuring the Radius of Gyration and $\overline{GM}$

Two measurement methods were conducted for the pitch radius of gyration (RoG). The first method was the pendulum method for pitch and roll radius of gyration. The second method was the bifilar method for yaw radius of gyration. The vertical centre of gravity (VCG) was

found through the swing test. The inclining test at the wet dock area of the towing tank was conducted to find the transverse $\overline{GM}$.

Figure 5.5 shows the pendulum method for measuring the roll radius of gyration, whilst Figure 5.6 shows the pendulum method for measuring the pitch radius of gyration. For yaw radius of gyration, the bifilar method was utilised as shown in Figure 5.7. The VCG was obtained from the inclining method during the pendulum method test. After controlling the radius of gyration and ballasting tests, the GM was obtained by the inclining test at the wet dock. The results are summarised in Table 5.5.

The radius of gyration for the roll and pitch can be determined by the pendulum method. First in order to find the length, the $\overline{OG}_M$ between from VCG to the pivot point, O are,

$$\overline{OG}_M = \frac{w_b\, d}{W_M \tan(\theta')}, \tag{5.1}$$

where w_b is the moving weight for inclining the model, d is a shifted distance of the moving weight, W_M is the weight of the experimental model and $\theta^{'}$ is an inclined angle of the model due to shifting the moving mass. The mass moment of inertia, including the swing system, can be found by swinging the model. The measured period $T^{'}$ is substituted into Equation 5.2 and the period was averaged from 10 swing oscillations.

$$I^{'} = \frac{W_M \overline{OG}_M\, T'^2}{4\pi^2} \tag{5.2}$$

Next, the mass moment of inertia about the model centre of gravity can be calculated from Equation 5.3.

$$I_M = I^{'} - W_M \frac{(OG_M)^2}{g} \tag{5.3}$$

Finally, the roll radius of gyration k_{xx} can be found as follows:

$$k_{xx} = \sqrt{\frac{I_M}{W_M/g}} \tag{5.4}$$

Similarly, the pitch radius of gyration k_{yy} can be determined by the same swing method with in the different orientation.

While measuring the RoG for pitch and roll, a length from the pivot point to the VCG influenced the roll RoG, since the distance contribution became larger in comparison to the mass moment of inertia for the model only. Therefore, the length from the pivot point to the deck surface of the model was shortened from 0.734 m, as the setting shown in Figure 5.5, to 0.326 m.

After the bifilar method was used for measuring the yaw radius of gyration, an inclining test was used to measure $\overline{GM}$. For the inclining test, the moving mass was placed at the LCG of the vessel on its centre-line. An inclined angle of the model and a shifted distance of the moving mass were measured to calculate $\overline{GM}$, using Equation 5.5. This process was repeated several times and the $\overline{GM}$s were averaged.

$$\overline{GM} = \frac{w\, l}{W_M \tan(\theta)}, \tag{5.5}$$

where w is the moving mass in kg, l is a shifted distance of the moving mass in m, Δ is the mass of the model in kg and θ is the inclined angle of the model due to shifting the moving mass.

The measured RoG and $\overline{GM}$ are presented in Table 5.5.

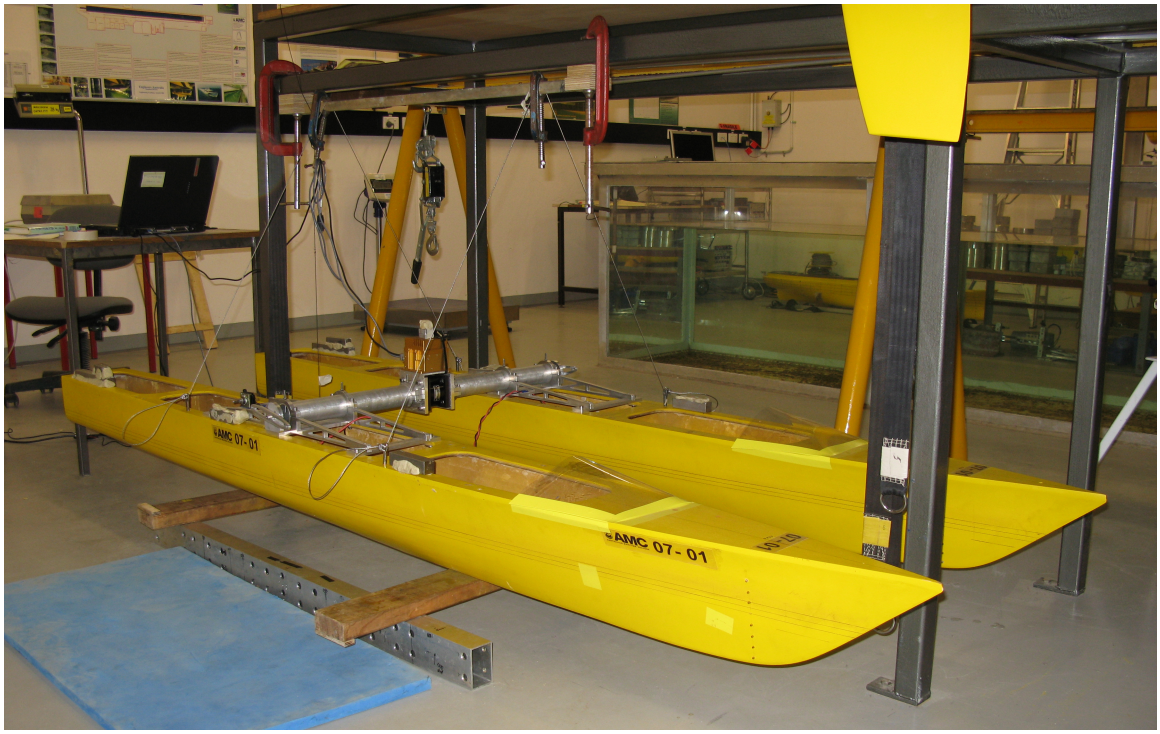

Figure 5.5: Roll radius of gyration measurement by swinging method

Table 5.5: CDL model, measured particulars

Particulars	Unit		Method
VCG	(m)	0.127	Inclining
GM (Roll)	(m)	2.476	Inclining
Roll RoG	(m)	0.337	Swing
Pitch RoG	(m)	0.553	Swing
Yaw RoG	(m)	0.656	Bifilar

5.5 Non-Dimensional Coefficients

Various non-dimensional coefficients for the pitch connecting, pry and split moments were considered. For a similarity of coefficients for these moments, the pitch connecting moment (PCM) is considered here. Using the submerged ship length, L_{wl}, a non-dimensional PCM coefficient can be expressed as:

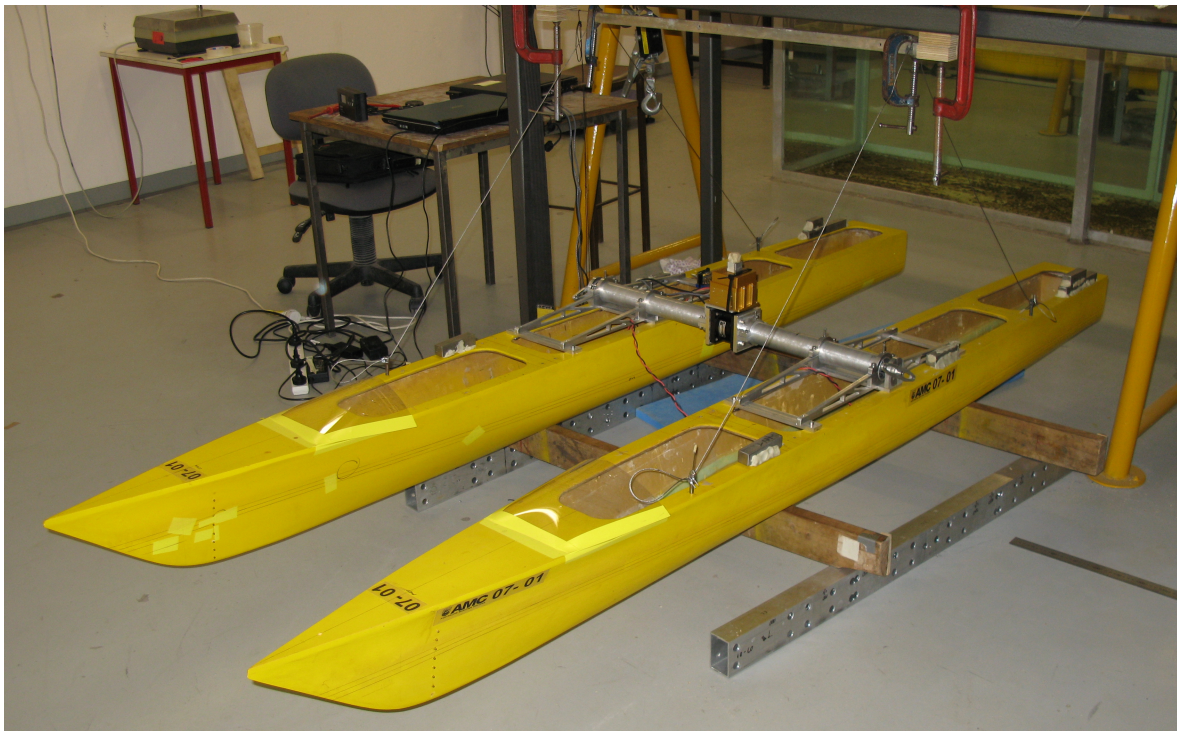

Figure 5.6: Pitch radius of gyration measurement by swinging method

Figure 5.7: Yaw radius of gyration measurement by bifilar method

$$CM_z = \frac{Mz}{0.5\rho L_{wl}\nabla^{\frac{2}{3}}V_s^2}, \tag{5.6}$$

where M_z is the pitch connecting moment. However, Equation 5.6, does not include the wave height term, which is presumably expected to have a large influence on hydrodynamic forces acting on the hull surface. In order to include the wave height effect into the non-dimensional PCM coefficient, a ratio of the wave height to submerged ship length is introduced as follows:

$$H_w^{ND} = \frac{H_w}{L_{wl}} \tag{5.7}$$

Substituting Equation 5.7 into Equation 5.6 gives the following equation:

$$CM_z^{01} = \frac{Mz}{0.5\rho L_{wl}\nabla^{\frac{2}{3}}V_s^2 H_w^{ND}} \tag{5.8}$$

Equation 5.8 can also be expressed as follows:

$$CM_z^{02} = \frac{Mz}{0.5\rho H_w\nabla^{\frac{2}{3}}V_s^2} \tag{5.9}$$

Similarly, the subscript of the coefficient for split and pry moment can be varied as shown in Figure 5.13.

5.6 Experimental Methodology

5.6.1 Experimental Conditions

In total seven conditions were tested. Firstly, a heavier displacement in the head-sea condition at the Model Test Basin at AMC was used in order to compare with past experiments which had been conducted in the Towing Tank at AMC. This comparison was conducted to ensure that the new towing arrangement gave results in the existing facility
The experiemental investigation focused on the linearity of ship response motion and wave-induced loads due to the wave and speed of the vessel. Five conditions varying the wave height and speed in oblique seas were conducted, as shown in Table 5.6.

Table 5.6: CDL model test conditions in oblique sea

40mm		Condition 04	
30mm	Condition 06	Condition 03	Condition 07
20mm		Condition 05	
H_w/V_s	1.25m/s	2.00m/s	2.75m/s

The above combination of test conditions allowed the investigation of the influence of the wave height and vessel speed on ship response motion and wave loads. For the investigation of wave height influence on both the ship motion and wave load, the speed of the model was set to 2.0 m/s, and similarly for the observation of the speed influence, the wave height was set to 30 mm. Smaller wave heights were selected to gain global wave effects without a slamming effect,

so that a linear relationship would occur in the response of ship motion and wave-induced motion.

5.6.2 Experimental Procedure

The experimental procedure was slightly different from the towing tank procedure, since there were no operators onboard the moving carriage. Therefore, once the experimental run started, the CRIO on the moving platform could not be controlled by the operators. Therefore, the CRIO needed to be a semi-automatic standalone recording system. The experimental procedure for the PCM model test at the model test basin was as follows:

1. Recording the zero condition for the static wave probe on the control station DAQ system.
2. Start recording the zero data on CRIO DAQ system.
3. Start wave maker to generate the wave.
4. Start recording the moving data on CRIO DAQ system.
5. Run the winch after wave had fully developed.
6. Stop the wave maker.
7. Reverse the towing cable to bring back the model to the original position.
8. Connect CRIO and the laptop PC.
9. Extract the recorded data from CRIO to the laptop PC.

5.7 Post Processing Analysis for PCM Model Test

Analysis codes for ship motion and wave-induced loads were developed in Matlab. There were two sets of running data recorded by the data acquisition system, CRIO. The NAV420 measured the ship motion data and the AMTI load cell measured the loads in the time domain. Transfer functions for the heave, pitch, and roll motions were obtained from the NAV420. The wave-induced load responses were obtained from the AMTI load cell data. The ship motion data measured by the NAV420 required a coordinate transformation on the axis accelerations.

5.7.1 Motion Analysis on the NAV420

The NAV420 provided the motion data in the time series, the coordinate system for which is defined in Figure 5.8. The actual device is shown in Figure 4.9 and a sample of NAV420 raw data was shown in Figure 5.9.

Since the NAV420 was mounted on the model, the vertical acceleration was measured in the moving coordinate system. The acceleration in the moving coordinate system was transformed into the acceleration in the fixed coordinate system using the Euler transformation. The Euler transformation was utilised on the vertical acceleration obtained from the NAV420 motion.

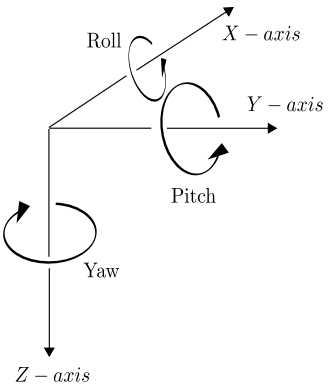

Figure 5.8: Coordinate system of NAV420 relating to the ship motion. When the connector is facing the user, the axes are defined as following: $X - axis$ from the face with the connector through NAV420 to the other face, $Y - axis$ along the face with connector from left to right, and $Z - xis$ along the face with the connector from top to bottom.

Generalised equations for the Euler transformation in the right-hand side coordinate system was used. Equation 5.10 transforms the values from the fixed coordinate to the moving coordinate by a roll angle, θ_{roll}. Next, the transformation by pitch motion about the $Y - axis$ could be carried out using Equation 5.11. Finally, the transformation due to the yaw angle could be calculated by Equation 5.12.

$$\begin{bmatrix} X_1 \\ Y_1 \\ Z_1 \end{bmatrix} = \begin{bmatrix} 1 & 0 & 0 \\ 0 & \cos\theta_{roll} & -\sin\theta_{roll} \\ 0 & \sin\theta_{roll} & \cos\theta_{roll} \end{bmatrix} \begin{bmatrix} X_0 \\ Y_0 \\ Z_0 \end{bmatrix} \tag{5.10}$$

$$\begin{bmatrix} X_2 \\ Y_2 \\ Z_2 \end{bmatrix} = \begin{bmatrix} \cos\theta_{pitch} & 0 & \sin\theta_{pitch} \\ 0 & 1 & 0 \\ -\sin\theta_{pitch} & 0 & \cos\theta_{pitch} \end{bmatrix} \begin{bmatrix} X_1 \\ Y_1 \\ Z_1 \end{bmatrix} \tag{5.11}$$

$$\begin{bmatrix} X_3 \\ Y_3 \\ Z_3 \end{bmatrix} = \begin{bmatrix} \cos\theta_{yaw} & -\sin\theta_{yaw} & 0 \\ \sin\theta_{yaw} & \cos\theta_{yaw} & 0 \\ 0 & 0 & 1 \end{bmatrix} \begin{bmatrix} X_2 \\ Y_2 \\ Z_2 \end{bmatrix} \tag{5.12}$$

Combining the above equations, the 3D rotational matrix results in Equation 5.13.

$$R_{rot} = \begin{bmatrix} \cos\theta_{yaw} & -\sin\theta_{yaw} & 0 \\ \sin\theta_{yaw} & \cos\theta_{yaw} & 0 \\ 0 & 0 & 1 \end{bmatrix} \begin{bmatrix} \cos\theta_{pitch} & 0 & \sin\theta_{pitch} \\ 0 & 1 & 0 \\ -\sin\theta_{pitch} & 0 & \cos\theta_{pitch} \end{bmatrix} \begin{bmatrix} 1 & 0 & 0 \\ 0 & \cos\theta_{roll} & -\sin\theta_{roll} \\ 0 & \sin\theta_{roll} & \cos\theta_{roll} \end{bmatrix} \tag{5.13}$$

The values in the moving axis coordinate can be transformed by the inverse matrix of the Euler transformation matrix, R_{rot} in Equation 5.13 to the value in the fixed axis coordinate.

$$\begin{bmatrix} X_f \\ Y_f \\ Z_f \end{bmatrix} = [R_{rot}]^{-1} \begin{bmatrix} X_m \\ Y_m \\ Z_m \end{bmatrix} \tag{5.14}$$

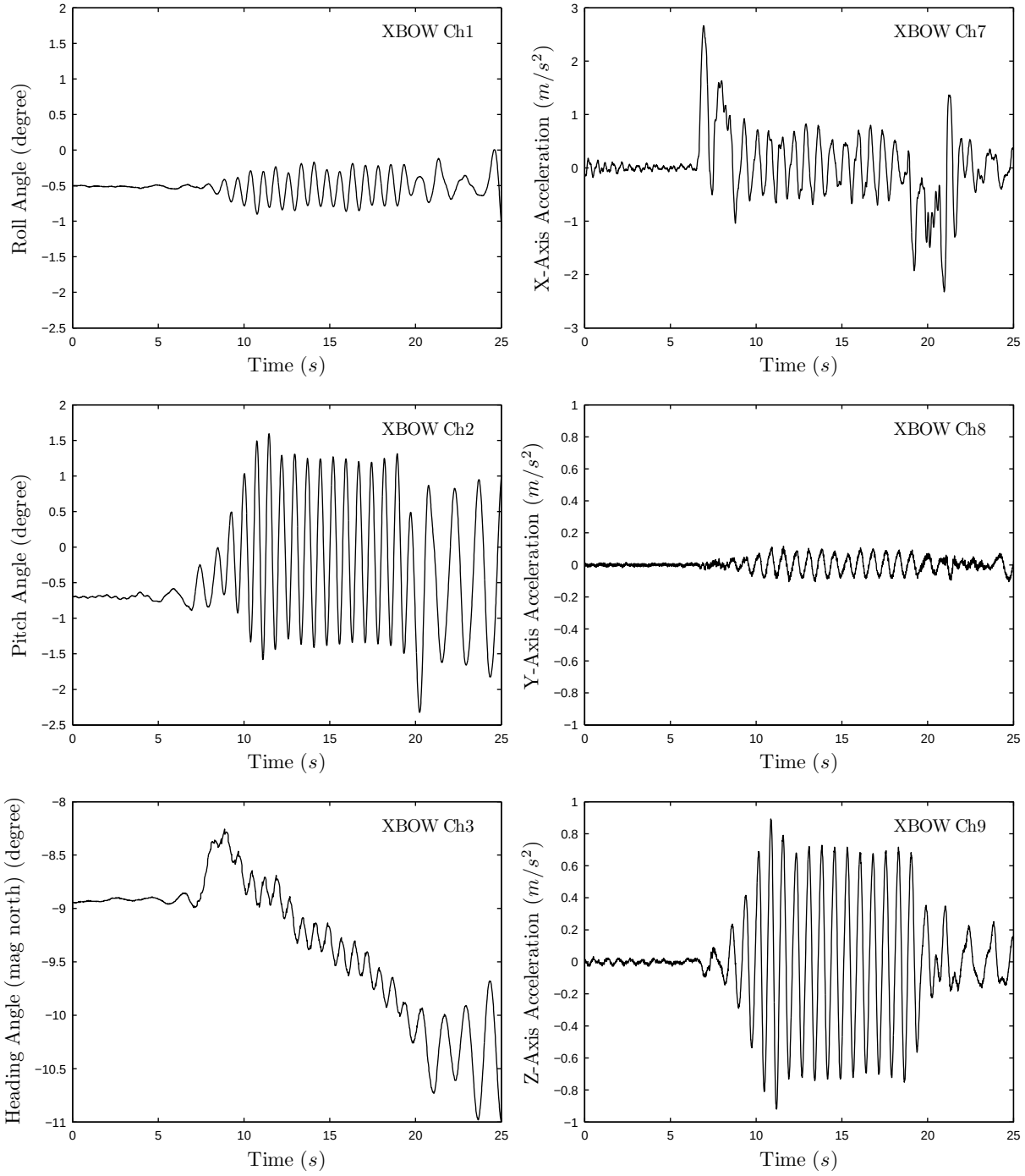

Figure 5.9: Motion data in time domain, Run No.51

The acceleration measured by NAV420 in the moving axis coordinate can be converted to the acceleration in the fixed axis coordinate system using Equation 5.14. Special attention to the input values of the measured rotational angles by NAV420 was required, because the measured rotational angle values were recorded as a rotational angle of the moving axis with respect to the space fixed coordinate system. Therefore, the rotational angle for transforming the accelerations from the moving axis to the fixed axis coordinate system, should be the opposite sign to the measured values of the rotational angle. This negative measured rotational angle should be used to form the 3D rotational matrix in Figure 5.14.

The acceleration in the fixed coordinate system was numerically integrated into the vertical displacement, which is equivalent to the heave motion. Examples of the numerical integration are shown in Figure 5.10. The validity of the above method can be observed in the results of the transformed acceleration in the X and $Y - axes$. In the recorded data, the measured acceleration started with an offset from the zero acceleration, when the model was stationary in calm water conditions. After the coordinate transformation from the moving to the fixed coordinate system, the accelerations about the X and $Y - axes$ were appropriately corrected to zero acceleration in calm water.

After the acceleration was transformed into the fixed coordinate system, it was integrated into the heave velocity, and was de-trended into a linear component due to the numerical integration. The heave velocity was then integrated to obtain the heave displacement. The results of the integration process are shown in Figure 5.11.

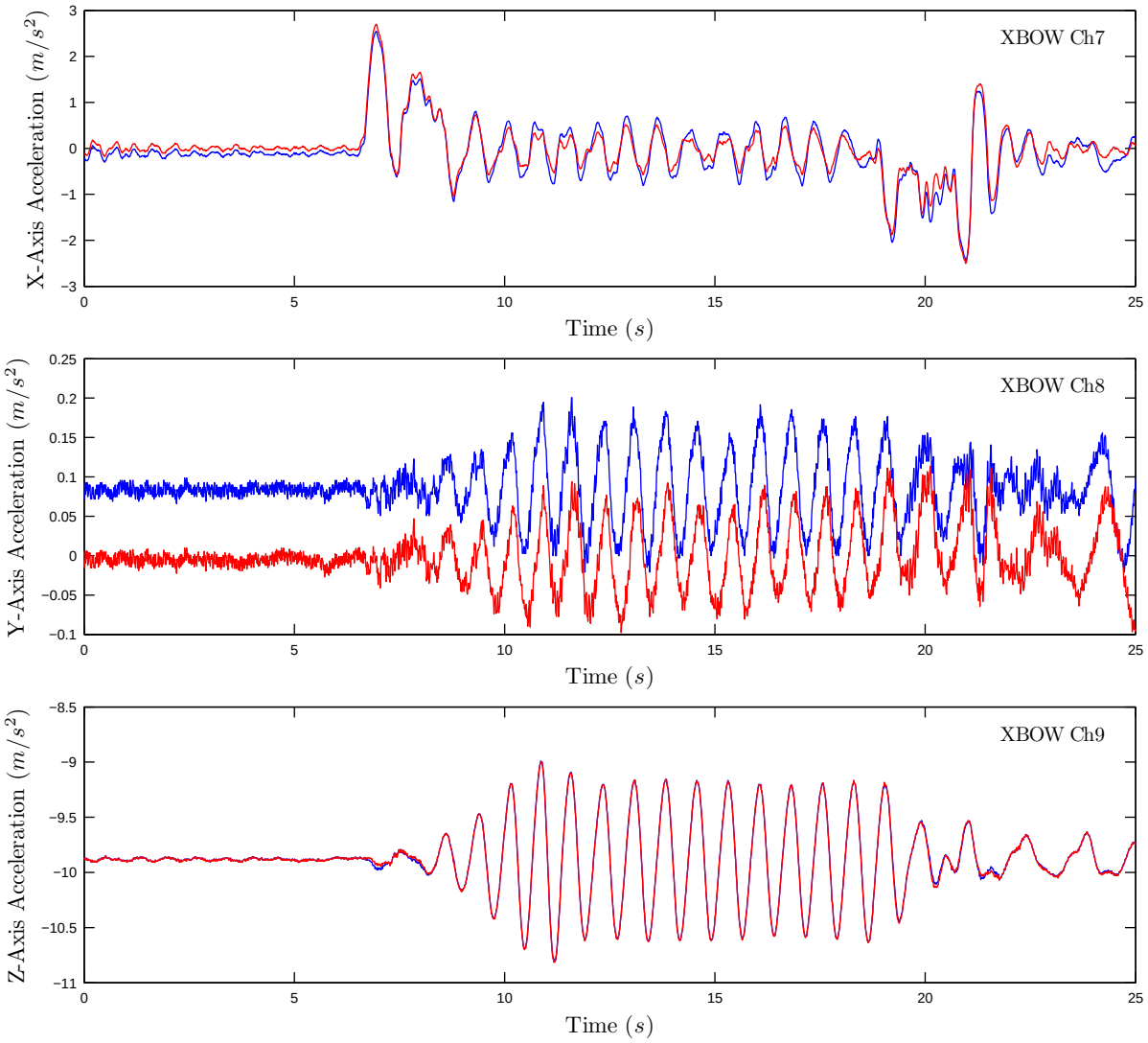

Figure 5.10: Acceleration trasnformation from the moving axis coordiante system to fix axis coordinate system. Blue lines indicate the measured value by NAV420, and red line indicates the transformed values., Run No.51

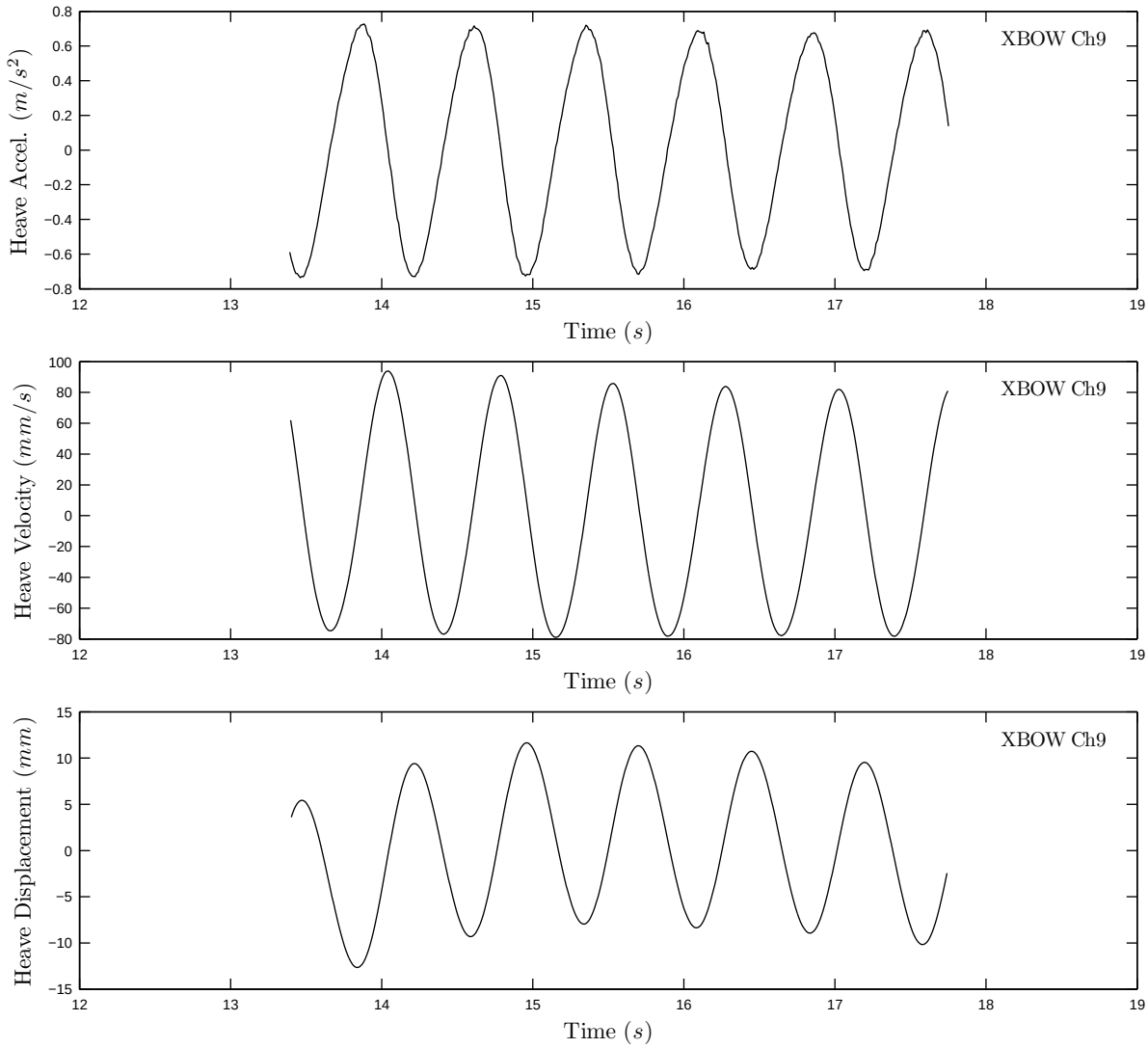

Figure 5.11: Calculated heave by numerically integrating the acceleration. Run No.51

5.7.2 Coordinate System for the AMTI Load Cell

The definition of pitch connecting, pry and split moments are shown in Figure 5.12. The coordinate system and load direction are shown in Figure 5.13 in relation to the ship coordinate system. The vertical axis for the force, F_x, and pry moment, M_x, was set to positive in the downwards direction. The horizontal axis for force, F_z, and pitch connecting moment, M_z was set to positive in the starboard direction. The longitudinal axis for the force, F_y, and split moment, M_y, was set to positive in the forward direction. The load cell arrangement is shown in Figures 4.4 and 4.5.

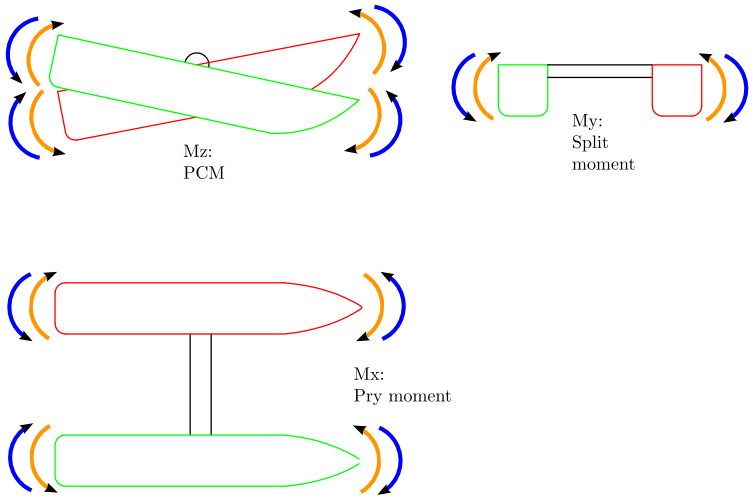

Figure 5.12: Pitch connecting, pry and split moment definition for catamaran vessels.

The measure forces and moments were plotted against the time shown in Figure 5.14. For the moments, the pitch connecting moments, M_z, clearly indicated the sinusoidal motion with larger amplitude compared with the pry moment, M_x, and split moments, M_y. The pry moment, M_x, indicated some oscillatory motion, however clear sinusoidal motions could not be measured. On the other hand, the measurement of the split moment resulted in a sinusoidal wave with a small amplitude. The peak-to-trough detection analysis was conducted to obtain the load response. The moments were used to obtain the wave-induced load response for the pitch connecting moment, pry moment and split moment.

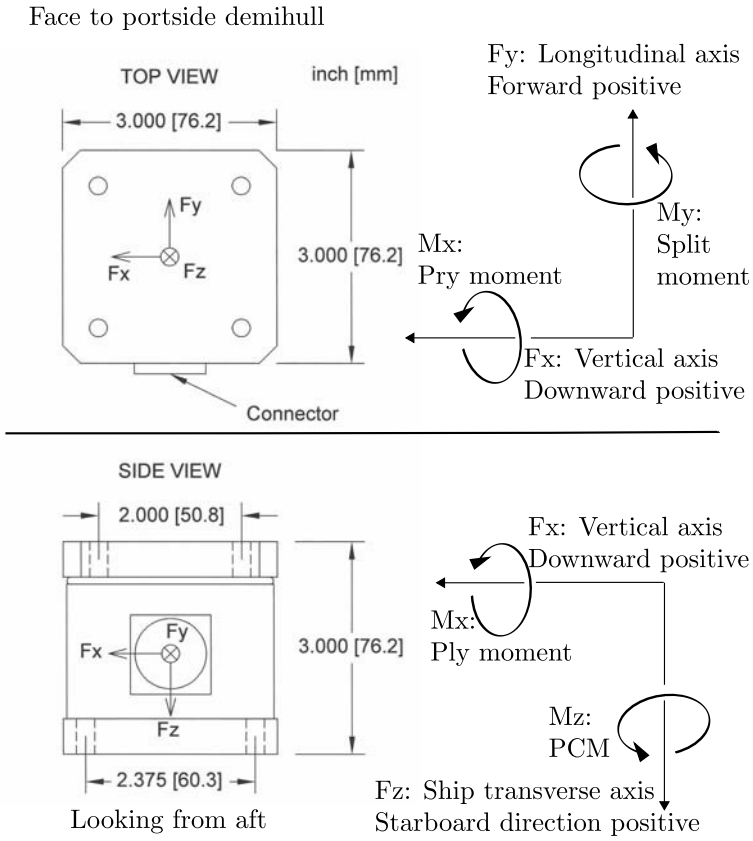

Figure 5.13: Definition of the coordinate system and measured load direction for the load cell, AMTI MC3A 250, with respect to the ship coordinate system. PCM indicates the pitch connecting moment. The notations of forces and moments, F_x, F_y, F_z, M_x, M_y, and M_z correspond to the notations in the figures in Chapter 4 and 5 as in the coordinate system of the load cell.

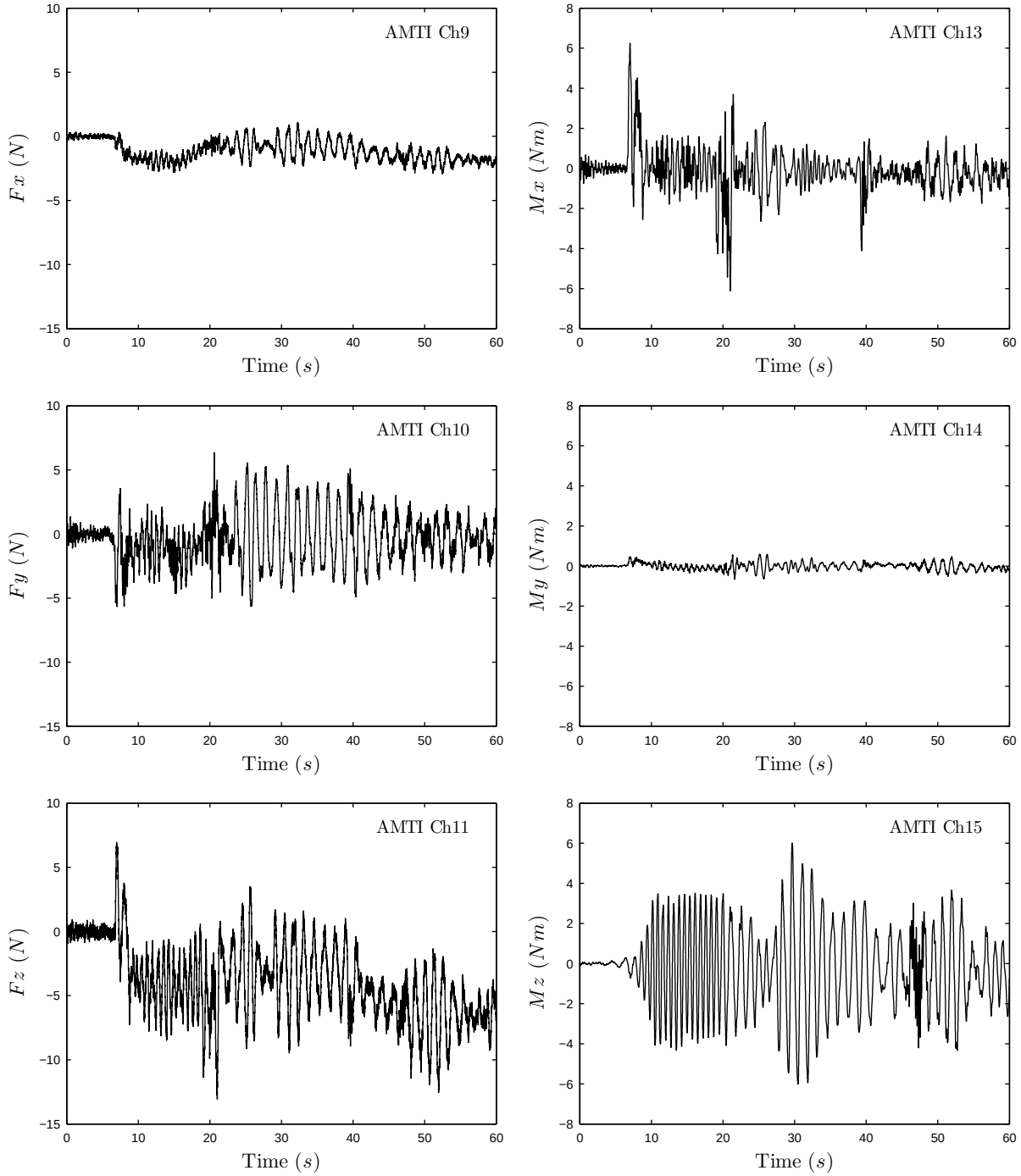

Figure 5.14: Forces and moments of AMTI load cell in time domain. Fx-axis is positive to the downward of the ship's vertical axis, Fy-axis is positive to the forward of the ship's longitudinal axis, and Fz-axis axis is positive to the starboard side of the ship's transverse axis. Mx is the split moment, My is the prying moment, and Mz is the pitch connecting moment. Run No.51

5.8 Results for Motions and Wave-Induced Loads

Sample ship motion data in six degrees of freedom (DoF) are plotted in Figure 5.9 in the time domain; a peak-to-trough detection was conducted on the wave and motion data to obtain the transfer function (TF).

Figure 5.14 plots an example measurement by the AMTI load cell for the forces and moments of the AMTI load cell in six DoFs. The loads and their coordinate definitions were given in Figure 5.13. Based on the calibration factor discussed in Subsection 5.4.1, the raw data of the AMTI load cell was converted to moments and a peak-to-trough detection was performed on the moments in order to calculate the load response. Non-dimensional coefficients for the pitch connecting moments, pry moment and split moment, as discussed in Section 5.5, were used to present the wave-induced load response.

5.8.1 Ship Motions in Head Sea for CDL Model

A head-sea condition was conducted in the towing tank and model test basin in order to compare differences in motion response due to the facility and instrumentation. Heave and pitch transfer function comparisons between the towing tank, where LVDTs were used to measure motions, and model test basin are presented in Figures 5.15 and 5.16, respectively. Condition 01 was a head-sea condition at a constant wave height of 30 mm in regular waves with speed of 2.0 m/s. The displacement was 36.6 kg.

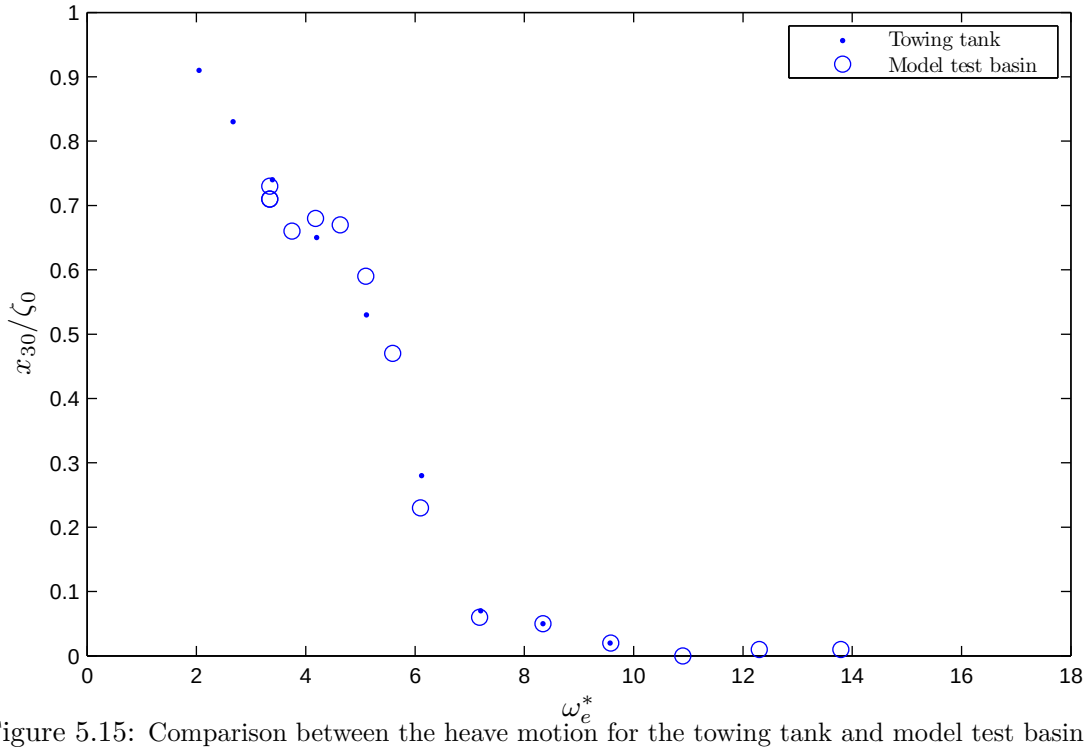

Figure 5.15: Comparison between the heave motion for the towing tank and model test basin tests

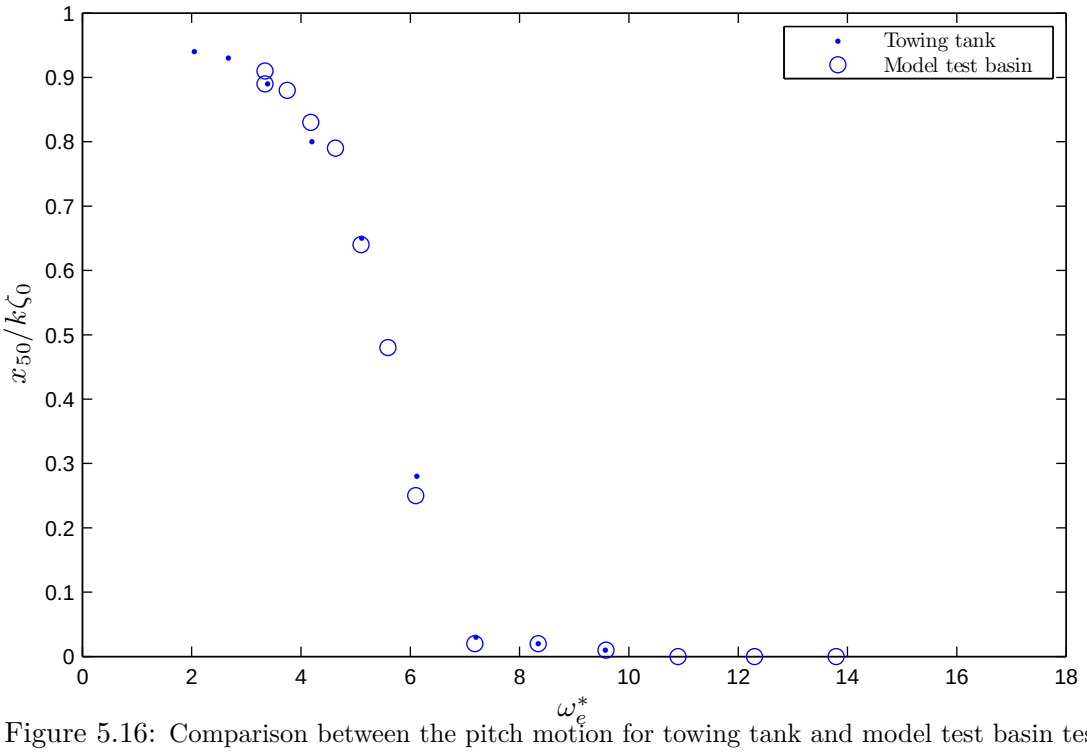

Figure 5.16: Comparison between the pitch motion for towing tank and model test basin tests

The heave transfer function, as shown in Figure 5.15, indicated that the trend of the heave motion was similar with a maximum deviation of 10%. The discrepancy may due to differences in towing technique, water depth or instrumentation. The pitch transfer function in Figure 5.16 showed clear agreement between the two sets of data. Hence, the test system and NAV420 were considered suitable for the purpose of measuring the ship motion in the model test basin.

5.8.2 Comparison between Head Seas and Oblique Seas

Condition 02 was a head-sea condition at a wave height of 30 mm in regular waves, while the displacement of the NPL model was 30.0 kg. The vessel speed was set at 2.0 m/s. The displacement remained the same for conditions 02, 03, 04, 05, 06, and 07 in oblique seas.

The difference between condition 02 and condition 03 was only the heading angle. Comparisons of the TFs for heave and pitch motion are plotted in Figure 5.17. The oblique angle was 20 degrees. Generally for the heave and pitch, there was little difference between the head seas and oblique seas. However, for the pitch TF the oblique-sea case experienced significantly over responses below the non-dimensional encounter wave frequency, $\omega_e^* = 5.5$.

5.8.3 Ship Motions in Oblique Sea for PCM Model

The influence of wave height on ship motions were investigated. The wave heights, H_w, of 20,30, and 40 mm were selected by satisfying the condition that the wave height was relatively smaller than the draft of the experimental model. The linear wave assumption was attempted

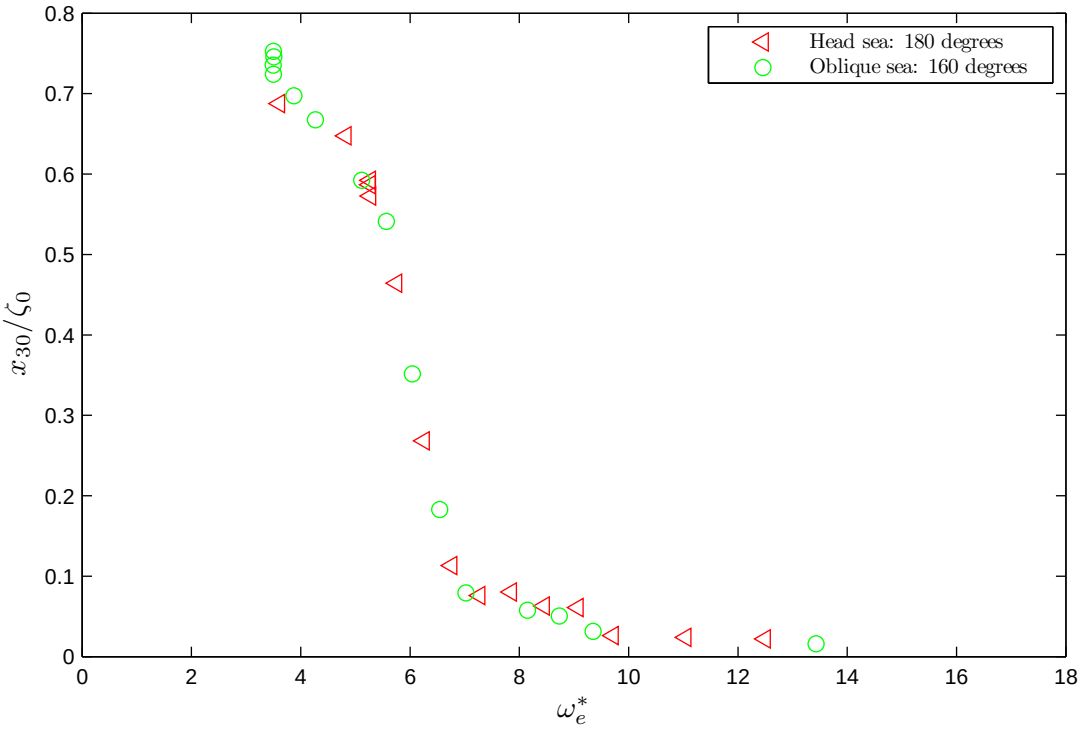

Figure 5.17: Comparison between the head sea and oblique sea on heave motion transfer function. H_w = 30 mm, V_s = 2.0 m/s.

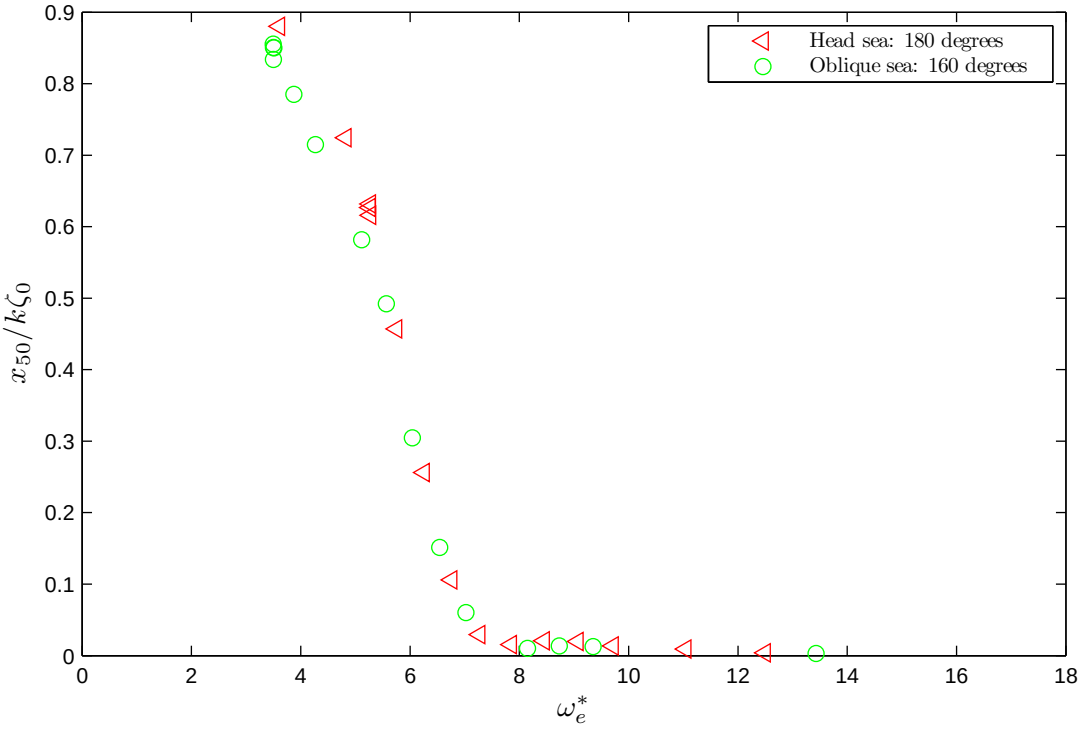

Figure 5.18: Comparison between the head sea and oblique sea on pitch motion transfer function. H_w = 30 mm, V_s = 2.0m/s.

experimentally by selecting a relatively small wave height. The heave, roll and pitch TFs were obtained. In conditions 03, 04 and 05, the velocity of the vessel remained constant at 2.0 m/s and the wave height, H_w, was varied during the experiments to observe the effect of wave height on the ship motion response and wave-induced load response.

In Figure 5.19, the heave motion TF, $\frac{x_{30}}{\zeta_0}$ for conditions 04, 03 and 05 were plotted against the non-dimensional encounter wave frequency. The heave motion showed clear linearity with respect to the wave height variation when a constant model speed was maintained. The variation in wave height was selected to be relatively small compared to the draft of the experiment model. The heave motions of conditions 03, 04 and 05 showed slight humps at ω_e^* of around 4.67. At ω_e^* of around seven, the heave motion response decreased quite significantly. These trends in TFs were similar in conditions 03, 04 and 05.

In Figure 5.20, the roll motion TF, $\frac{x_{40}}{k\zeta_0}$ for conditions 04, 03 and 05 were plotted against the non-dimensional encounter wave frequency, ω_e^*. The roll motion also showed a high linearity with respect to the wave height when a constant vessel speed of the model was maintained under the condition of smaller wave heights.

In Figure 5.21, the pitch motion, $\frac{x_{50}}{k\zeta_0}$, for conditions 04, 03 and 05 are plotted against the non-dimensional encounter wave frequency. Clear agreement between the pitch motion TFs of the different wave heights also indicated linearity with respect to the wave height at the constant speed of the model. It also experimentally verified that the roll motion had a linear response to the wave height which was relatively small compared to the ship draft.

Overall, the ship motions of heave, roll and pitch in the oblique response at a constant speed, responded in a linear fashion to the wave height, where the wave height was relatively small in comparison to the ship draft.

The influence of ship speed on ship motion was investigated in an oblique-sea condition. The wave height was maintained at a constant 30 mm, with velocity varied to 1.25, 2.00 and 2.75 m/s. Ideally, speeds of 1.00 and 3.00 m/s would have been preferred, however the number of encounter waves was important to develop the load responses.

In Figure 5.22, the heave motion TFs, $\frac{x_{30}}{\zeta_0}$ for conditions 06, 03 and 07 are plotted against the non-dimensional encounter wave frequency, ω_e^*. The heave motion showed a strong non-linearity with respect to the vessel speed at the constant wave height. In condition 07 with a velocity V_s of 2.75 m/s, the heave response showed a dominant peak at ω_e^* of around 5.6, with a peak value of 1.26. The TFs reduced with reduction in the forward velocity of the experimental model. The reduction of heave response was significant, which complies well with operational practice for high-speed ferries, such that reducing the vessel speed in large wave conditions is recommended to reduce the ship motion. From the reduced amount of the heave motion seen as the speed decreased, the reduction in ship velocity in large waves can be observed and recommended as an effective method to reduce the heave motion for safe ship operation.

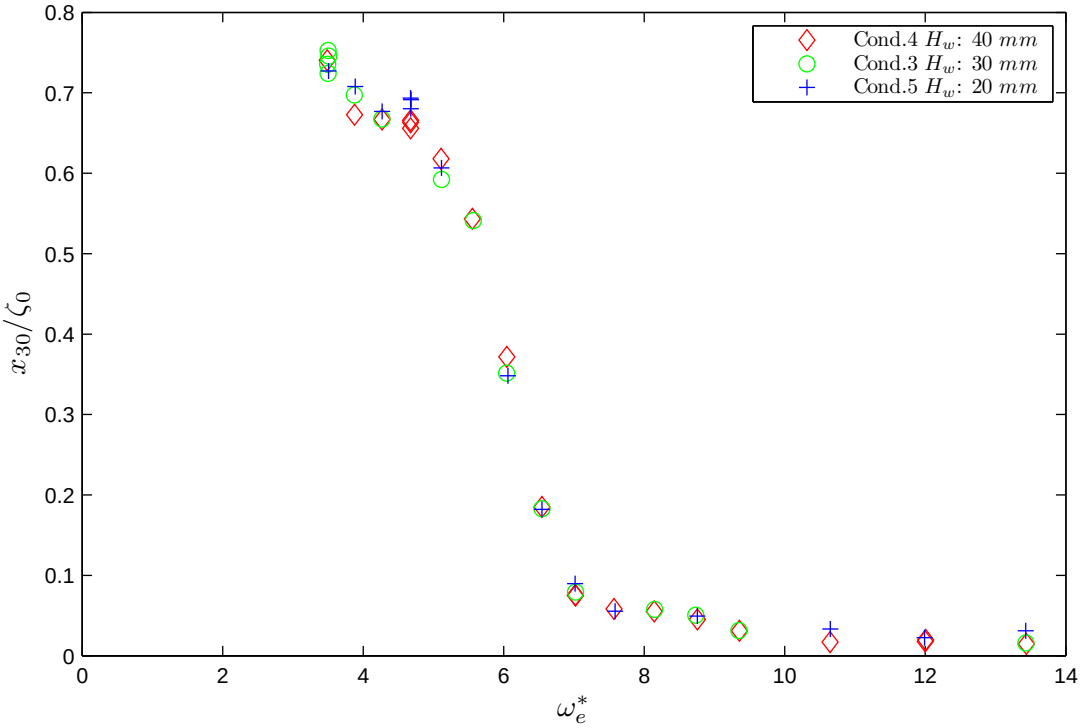

Figure 5.19: Heave Motion TF for the PCM Model is plotted non-dimensional encouter wave frequency.

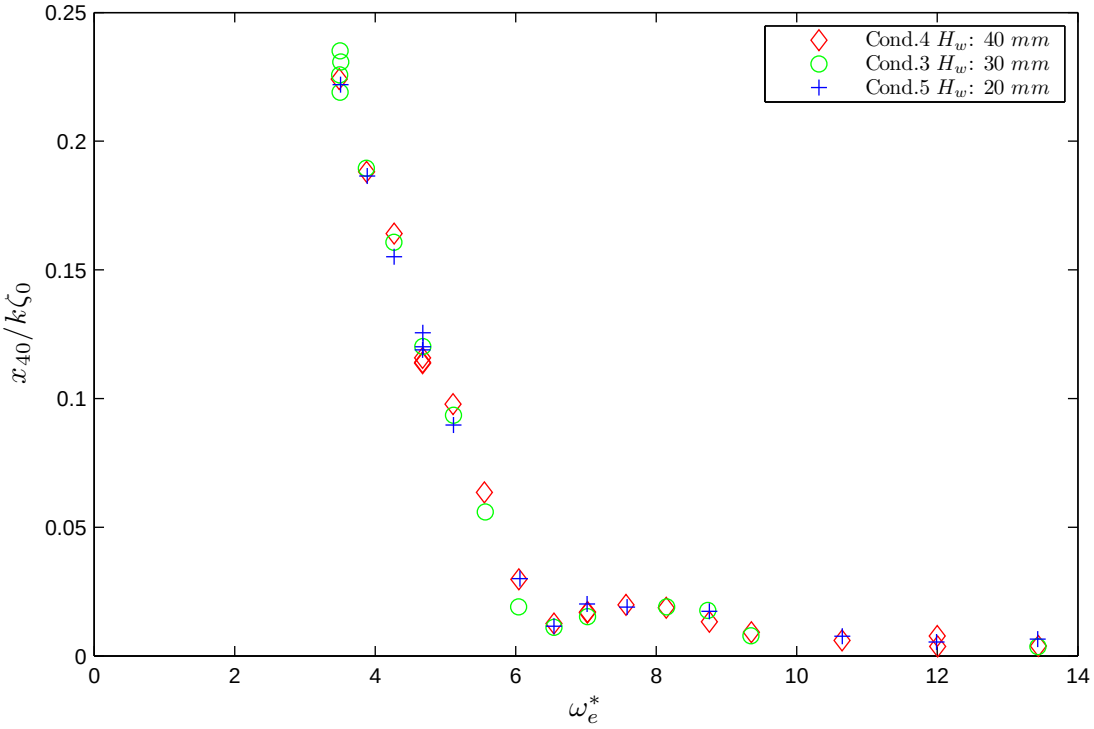

Figure 5.20: Roll motion TF for the CDL model plotted against the non-dimensional encounter wave frequency

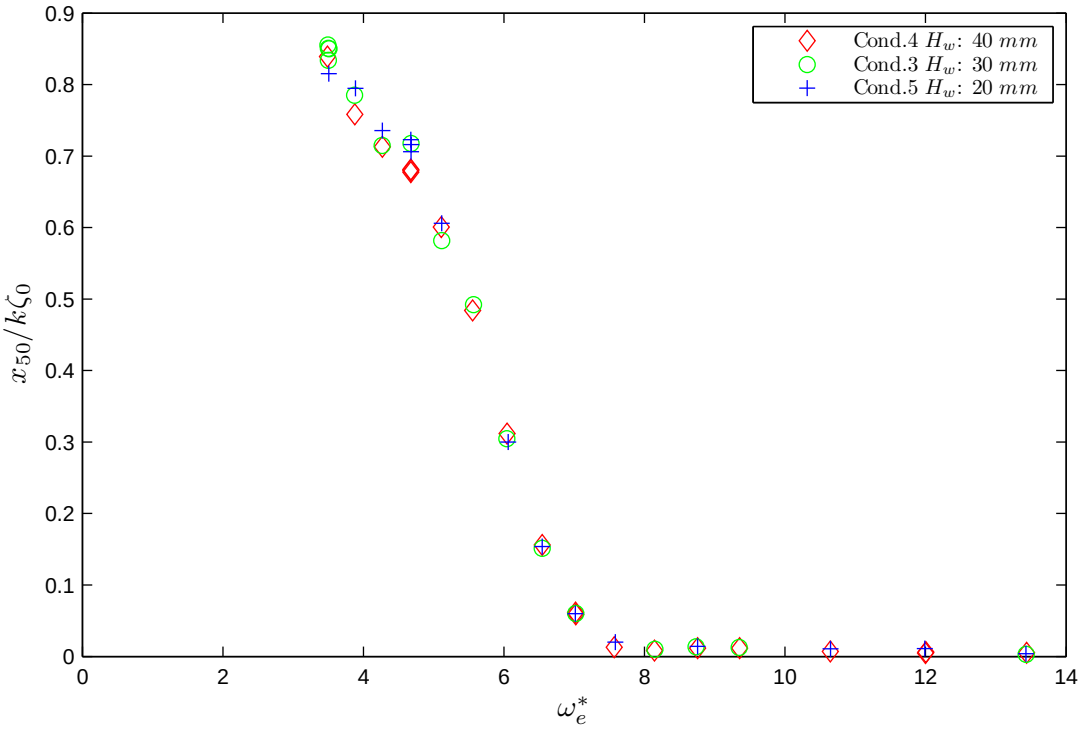

Figure 5.21: Pitch motion TF for the CDL model plotted against the non-dimensional encounter wave frequency

In Figure 5.23, the roll motion TFs, $\frac{x_{40}}{k\zeta_0}$ for conditions 06, 03 and 07 are plotted in non-dimensional values against the non-dimensional encounter wave frequency, ω_e^*. The roll motion indicated a strong non-linearity with respect to the vessel speed at the constant wave height. Roll motion was also reduced as the vessel speed reduced. A local peak was observed at ω_e^* of 5.7 in Condition 07.

In Figure 5.24, the pitch motion TF, $\frac{x_{50}}{k\zeta_0}$ for conditions 06, 03 and 07 are plotted in non-dimensional values against the non-dimensional encounter wave frequency, ω_e^*. The pitch motion also indicated a strong non-linearity with respect to the vessel speed at the constant wave height. Pitch motion also had a larger response as the ship velocity increased.

Overall, the velocity variation tests did not show the linear relationship between vessel speed and motion response. However, increase in the velocity resulted in a large increase of motion response for the NPL5b catamaran model.

The uncertainty error analysis was conducted using the method described in Section 3.8. The uncertainty error of the heave, pitch and roll TFs are presented for the above constant wave height cases in Figures 5.22 to 5.24. The maximum uncertainty occurred at the resonant peaks for $V_s = 2.75\ m/s$: heave = $\pm 3.2\%$, pitch = $\pm 3.3\%$ and roll = $\pm 15.7\%$. The uncertainty for roll was large. Since the magnitude of the non-dimesional roll was small, a small deviation of

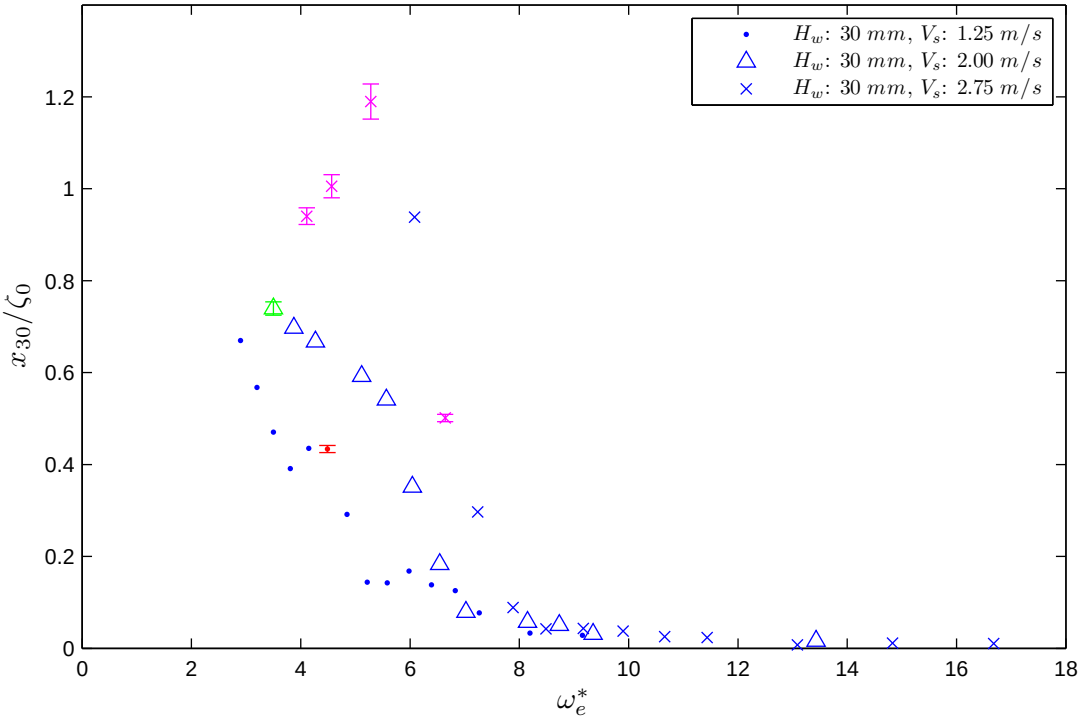

Figure 5.22: Heave motion TF for the CDL model plotted against the non-dimensional encounter wave frequency.

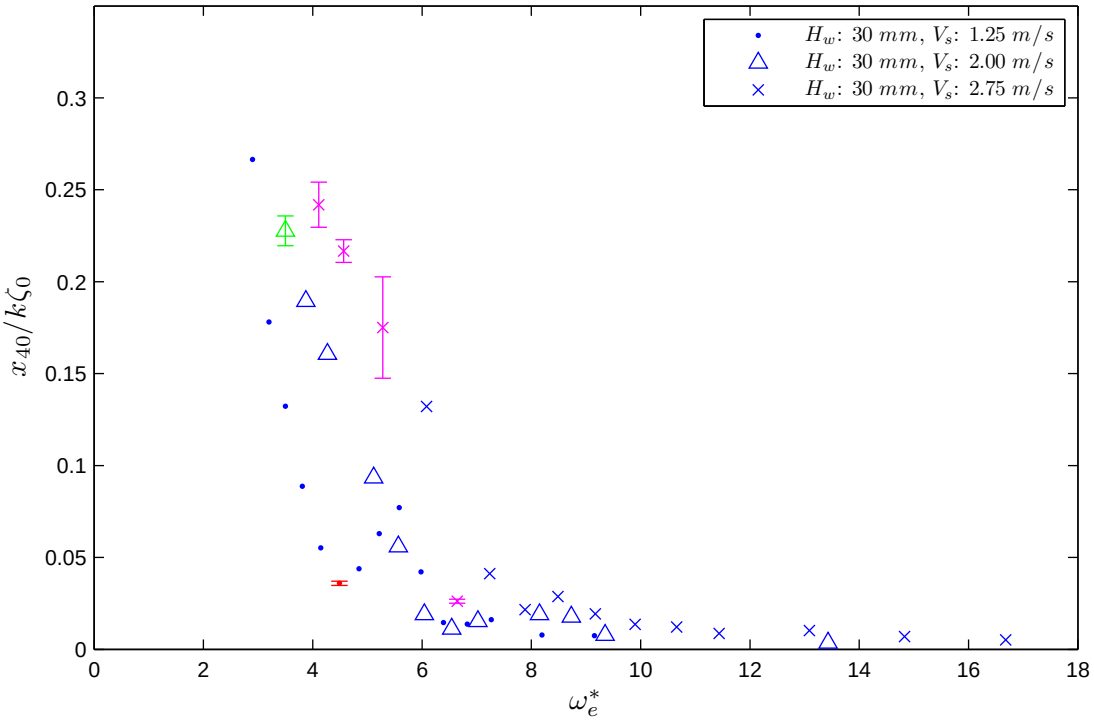

Figure 5.23: Roll motion TF for the CDL model plotted against the non-dimensional encounter wave frequency.

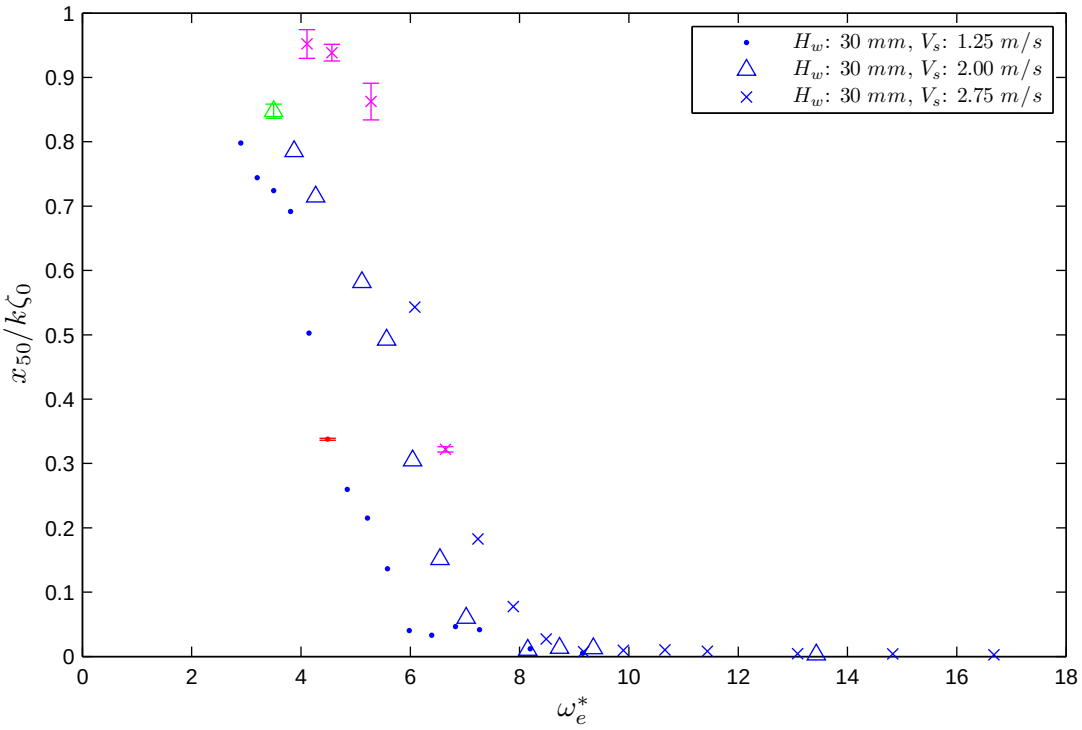

Figure 5.24: Pitch motion TF for the CDL model plotted against the non-dimensional encounter wave frequency.

magnitude resulted in the large error. For the motion TF, the uncertainty error was generally small enough to provide confidence in the experimental data.

5.8.4 Structural Loads Results

In Figure 5.25, the PCM, M_Z is plotted with respect to the non-dimensional encounter wave frequency, $\omega^{(*)}{}_{(e)}$, in dimensional values. The vessel speed remained constant at $2.0m/s$, and the wave heights were set at 30, 40 and 50 mm in conditions 04, 03, and 05 respectively. All cases of wave height followed a similar pattern in the PCM values with offsets. An increase in the wave height was observed in order to gain an increased PCM with a constant increment of the PCM value. For these three conditions, the first highest values of PCM appeared at the incident wave frequency f_W =0.8. This indicated that wave height did not influence the incident wave frequency at which the maximum PCM responses were first generated for a constant model speed.

Similarly, the pry moment is plotted against the incident wave frequency in 5.26 for conditions 04, 03 and 05. Measurement of the pry moment, M_x, was found to be more challenging than measurement of the pitch connecting moment, M_z, and split moment, M_y. At the same incident frequency, the pry moment seemed to fluctuate with the values of the measured moments.

The split moment, M_y, for conditions 04, 03 and 05 are shown in Figure 5.27. Although the

measured moment values were relatively smaller than the other moments, the results show that there was a clear influence of the wave height on the measured values of the split moment.

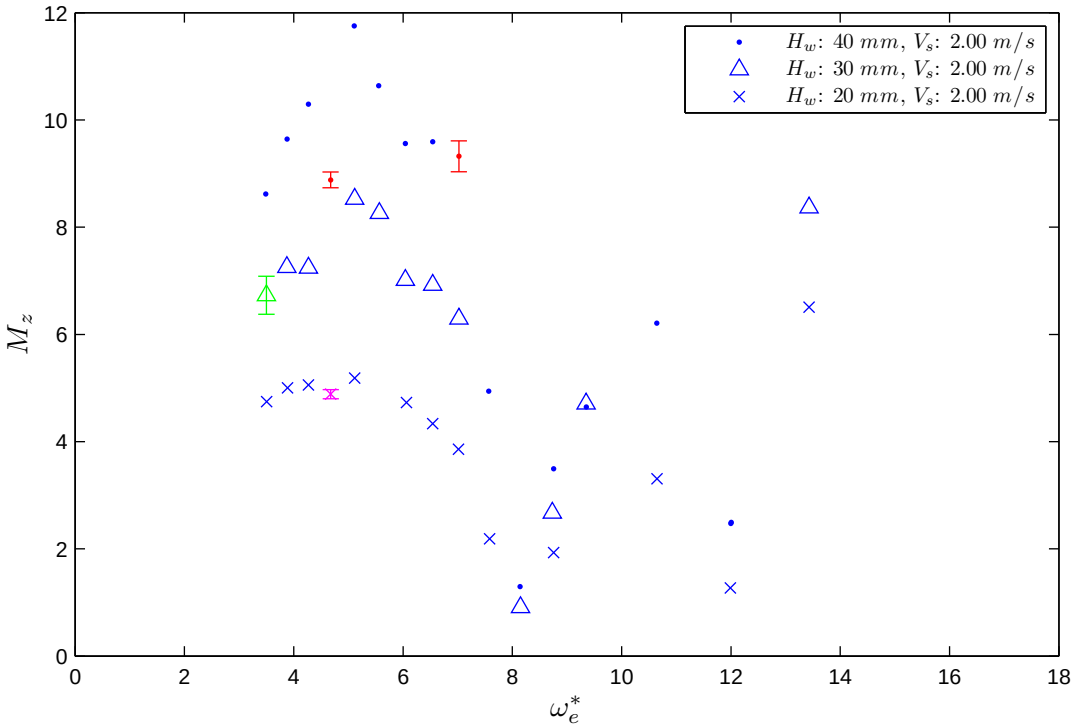

Figure 5.25: Pitch connecting moment response for the CDL model is plotted against the non-dimensional encounter wave frequency with uncertainty error bars.

The uncertainty error analysis was conducted on the load response using the method described in Section 3.8. The uncertainty error of the PCM, pry moment and split moment response are presented for the constant speed cases in Figures 5.25 to 5.27. The maximum uncertainty error of the PCM was ±5.3%, the split moment was ±19.1%, and the pry moment was ±34.4%. The large error occurred for pry moment because the measured values were small, and as explained in Section 4.2.3, some error due to the towing mechanism was expected. The pry moment was particularly challenging to measure due to possible contamination of the moment by the towing force. As can be seen in the measured magnitude variation among the PCM, pry moment and split moment, the uncertainty for measuring loads was generally acceptable to provide confidence in the measured data.

In order to investigate the linearity of wave-induced load responses influenced by the wave height, the non-dimensional coefficient was introduced. The non-dimensional wave-induced load responses were calculated using Equation 5.8 for pitch connecting moments, pry moments and splits moments.

A trend of linear response for the PCM with respect to the wave height is shown in Figure 5.28 for conditions 04, 03 and 05, where the vessel speed was maintained at a constant 2.0 m/s with

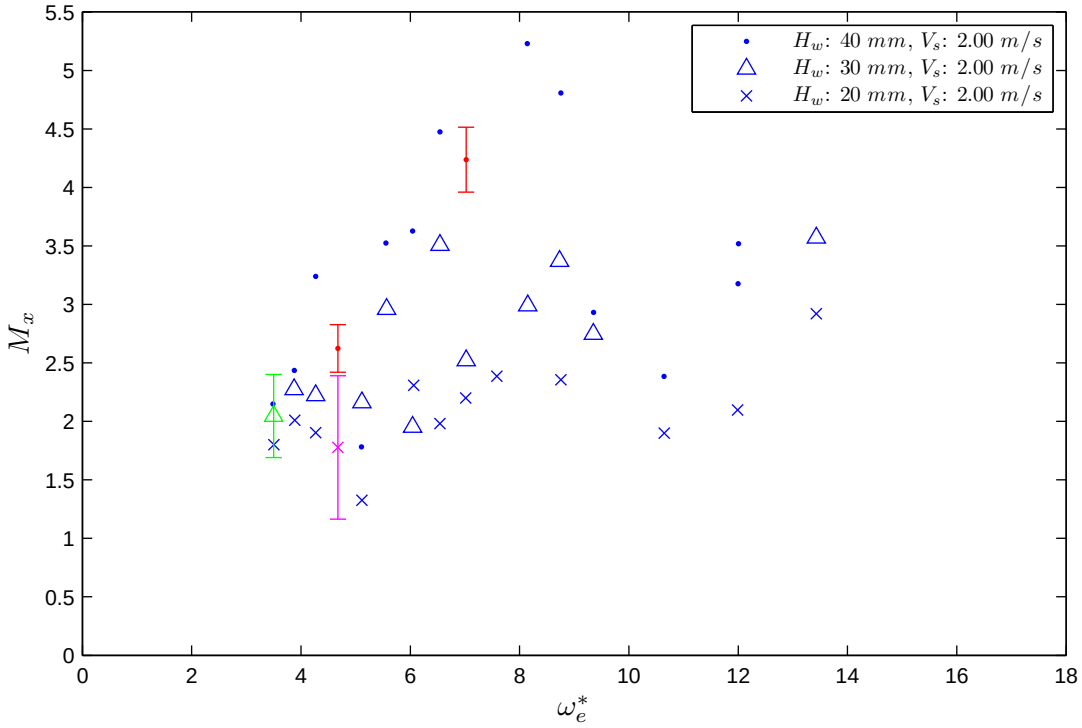

Figure 5.26: Pry moment response for the CDL model is plotted against the non-dimensional encounter wave frequency with uncertainty error bars.

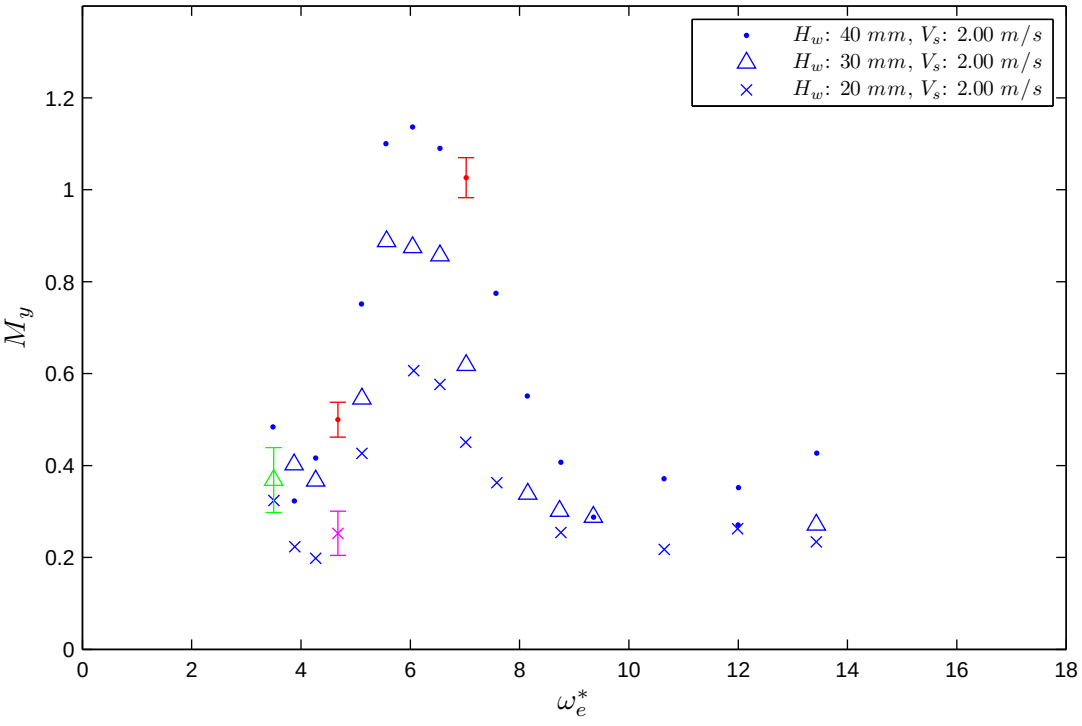

Figure 5.27: Split moment response for the CDL model is plotted against the non-dimensional encounter wave frequency with uncertainty error bars.

varying wave height, H_w, of 40, 30 and 20 mm, respectively. The general trend of the curves of the PCM response coefficients were similar to each other, although there was some deviation around ω_e^* of 6.3 to 7.6. The response of the PCM to wave height generally indicated a linear relationship when the wave height was small compared to the vessel draught.

Non-dimensional load responses for the pry moments are shown in Figure 5.29 for condition 04, 03 and 05. The non-dimensional wave-induced load values were rather scattered over the same range. It seems that the pry moments did not show the linear relationship with respect to wave height with a constant vessel speed. However, since the model was primarily designed to measure the pitch connecting moments, the measurement of the pry moment was expected to be difficult, as the towing mechanism system was not designed for pry moment measurement. This was discussed in Subsection 4.2.3.

The split moments at constant speed with varying wave height are shown in Figure 5.30 for conditions 04, 03 and 05. A trend in the linear relationship of wave height to the measured split moments was obtained, and it especially improved around the peak values. This result of a linear response was found to be a remarkable phenomenon when considering that the measured values of split moment were relatively smaller than the pitch connecting moment. As the magnitude of the split moment decreased, the deviation of non-dimensional split moment coefficient became larger due to the small value of split moments.

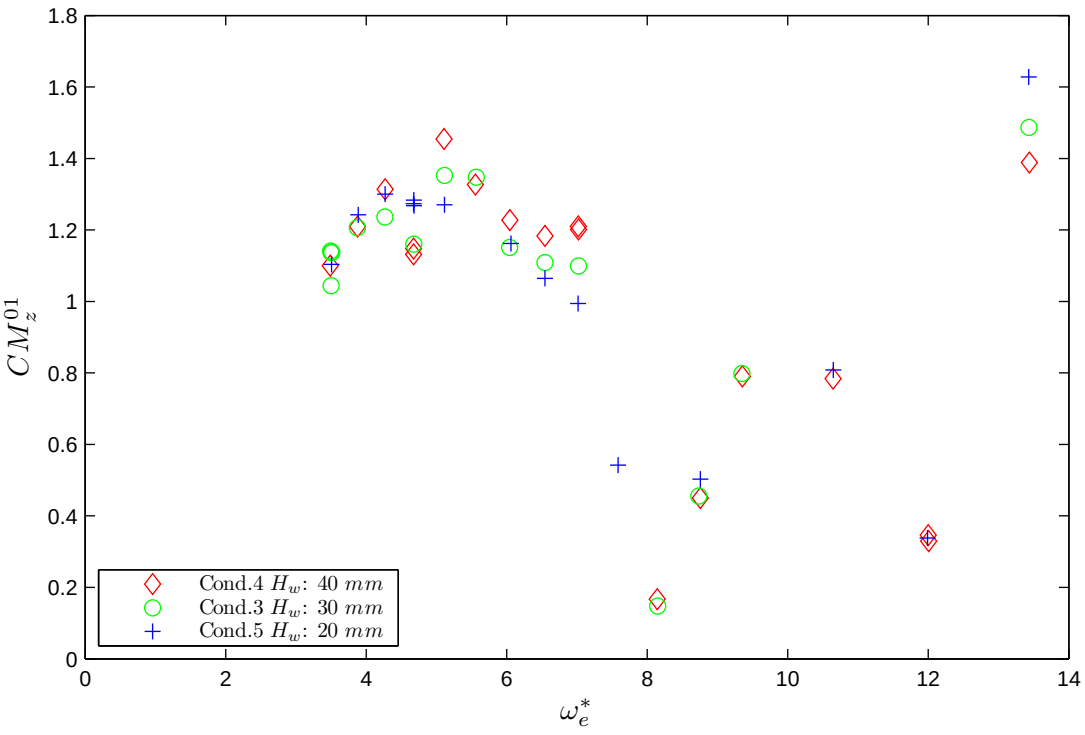

Figure 5.28: Pitch connecting moment RAO for the PCM Model is ploted non-dimensional encouter wave frequency.

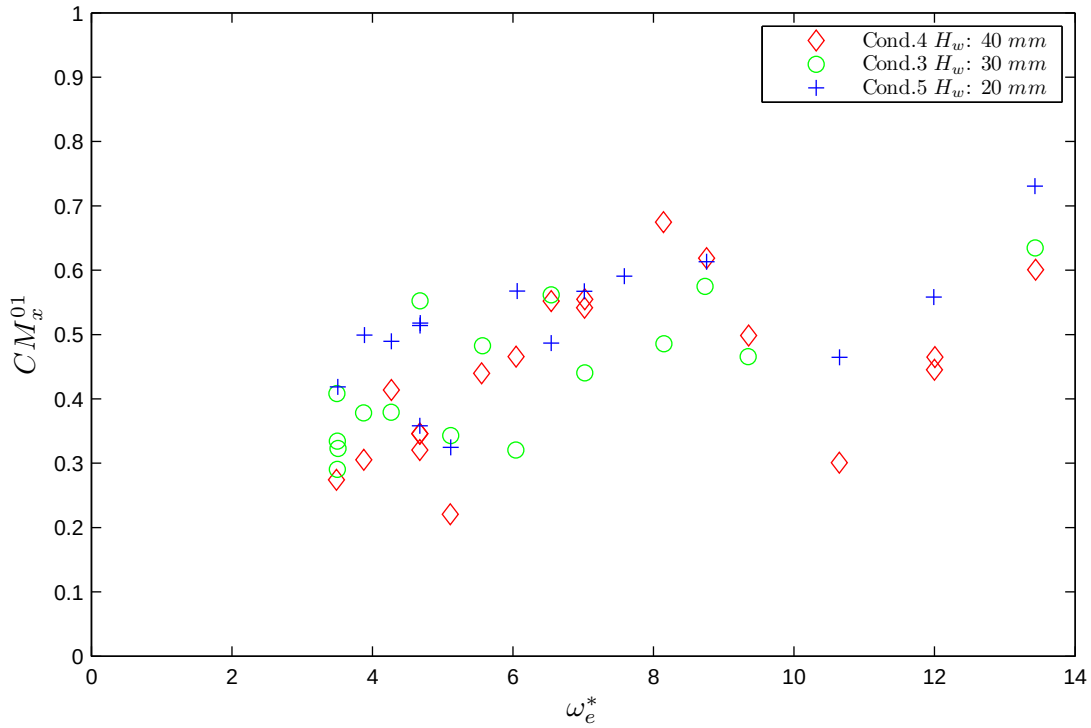

Figure 5.29: Ply moment RAO for the PCM Model is ploted non-dimensional encouter wave frequency.

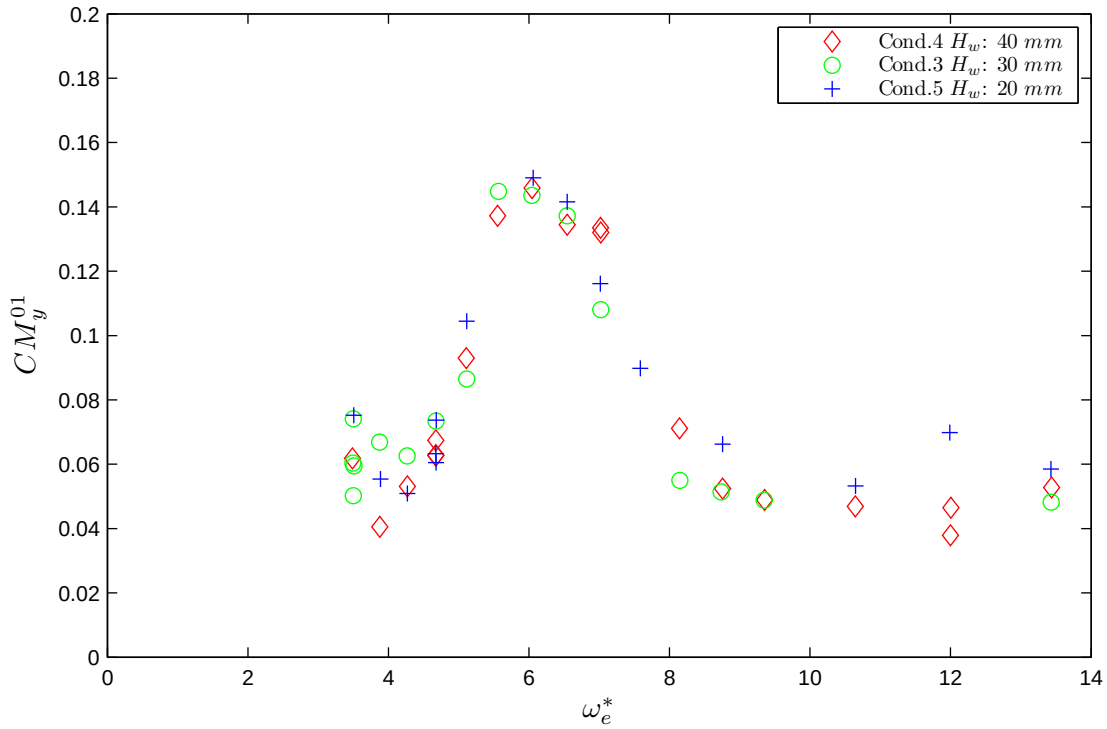

Figure 5.30: Split moment RAO for the PCM Model is ploted non-dimensional encouter wave frequency.

The influence of the velocity on the measured wave-induced loads at a constant wave height was investigated. The wave height was maintained constant at 30 mm, and the vessel speed varied at 1.25 m/s, 2.00 m/s and 2.75 m/s for the conditions 06, 03 and 07 respectively.

The non-dimensional pitch connecting, pry and split moments for three conditions of varying vessel speeds are plotted in Figures 5.31, 5.32 and 5.33 against the non-dimensional encounter wave frequency. The result clearly shows a non-linear relationship between the vessel speed and all the moments.

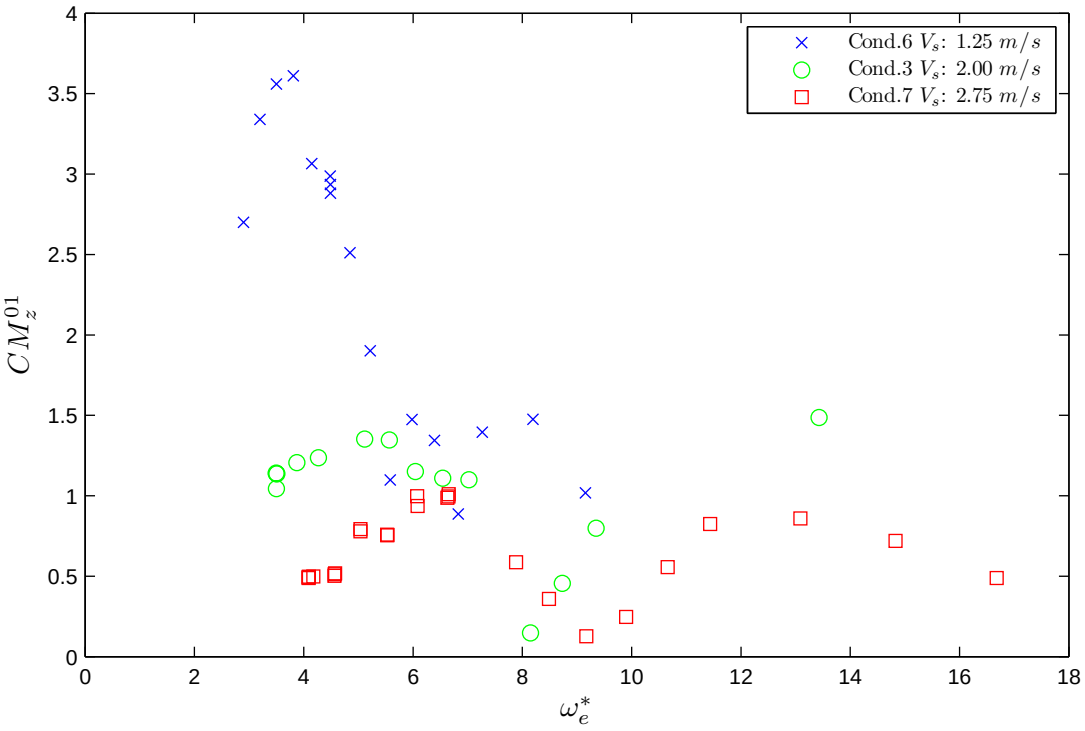

Figure 5.31: Pitch moment RAO for the PCM Model is ploted non-dimensional encouter wave frequency.

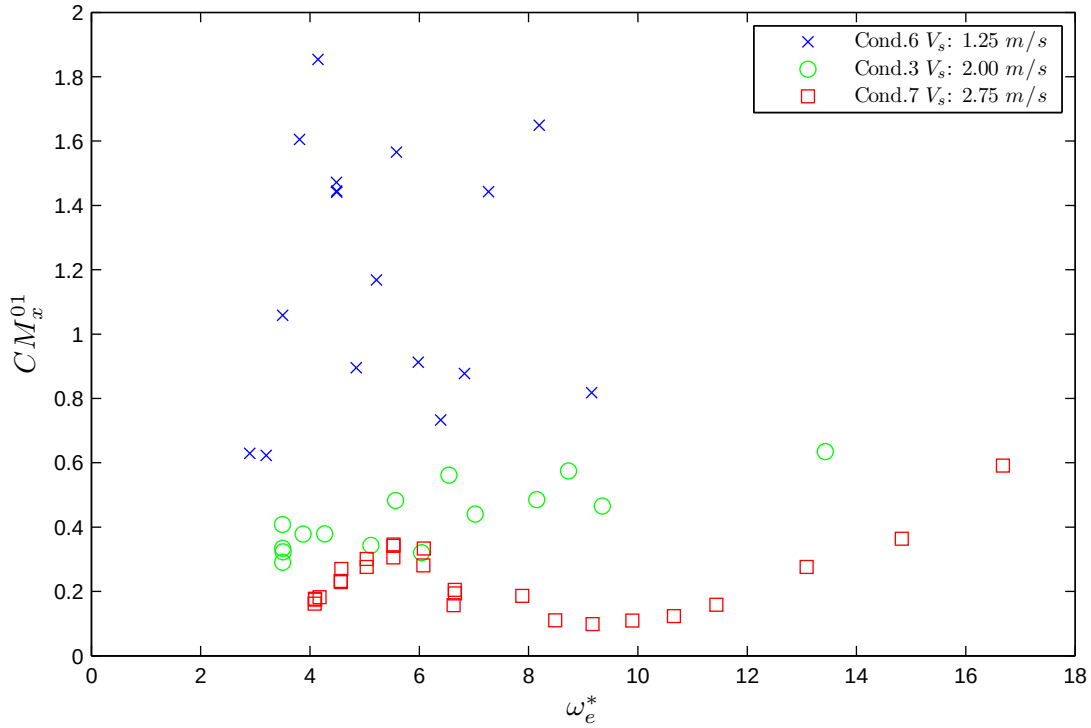

Figure 5.32: Ply connecting moment RAO for the PCM Model is ploted non-dimensional encouter wave frequency.

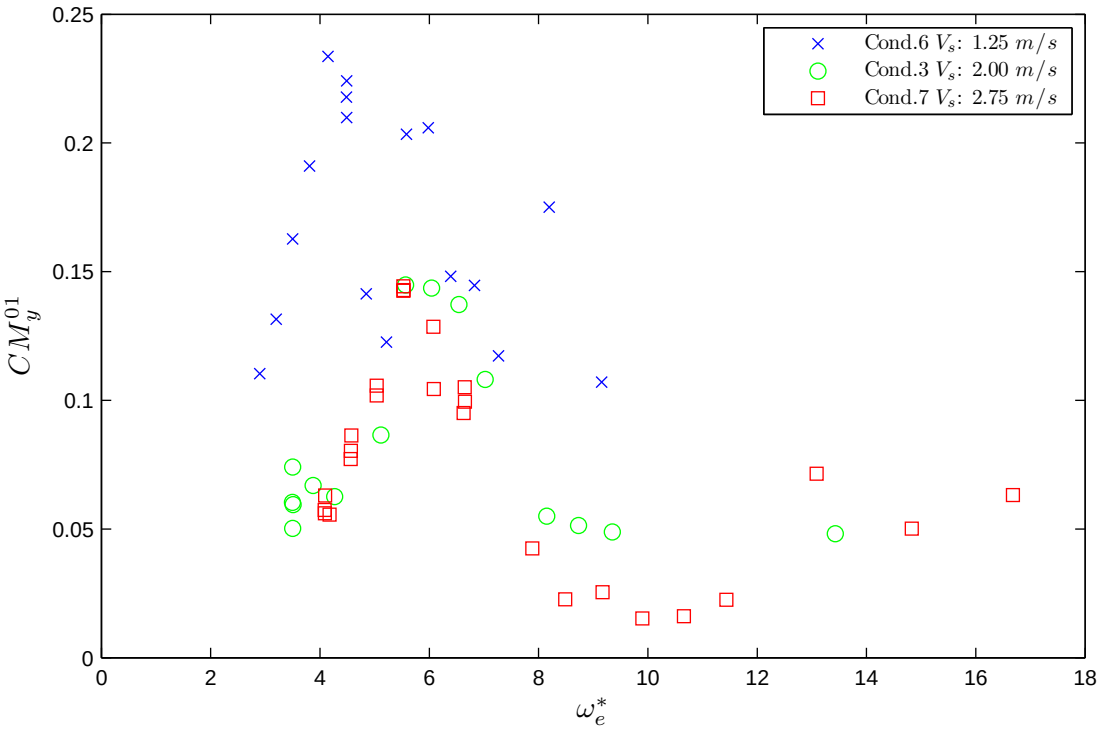

Figure 5.33: Split moment RAO for the PCM Model is ploted non-dimensional encouter wave frequency.

5.9 Conclusions

In conclusion, the pitch connecting moments were successfully measured by the designed mechanism of the CDL experimental model. The motion data, successfully obtained by the NAV420, produced the heave, pitch and roll transfer functions in oblique seas. The AMTI load cell successfully measured the pitch connecting moments, pry moment and split moment on the cross-bridge of the catamaran. The experimental conditions were designed to obtain the wave height and vessel speed effects on ship motion and wave-induced load response.

The linearity of the motion response against the wave height and speed variation were investigated using a relatively small wave height compared with the model draft. The motion TF for heave, pitch and roll indicated good linear relationships between the wave height and the measured motions. Contrary to this, the vessel speed did not linearly influence the motion responses. Increased velocity of the model resulted in significantly larger motion responses.

For the wave-induced load response, the pitch connecting moment showed a linearity between the wave height and the load response. The results of the pry moment did not show clear linearity against the wave height. The towing mechanism inevitably influenced the measured pry moments, which was expected prior to the experiment. The load response of split moment was particularly small, however, around the peak region linearity against the wave height was observed. The wave-induced load response did not show a linear relationship with the vessel speed.

The realisation of the cross demihulls loads and the achievement of its measurement methodology are important to validate the numerical prediction for design values of cross bridge of catamaran in the oblique seas. As the ship evolves a longer hull length, larger displacement and wider beam, the cross bridge loads will be one of significant structural loads to be calculated with durable and reliable, yet feasible values for a required large wave conditions. Since the experiment of measuring the cross demihull loads were not attempted before (to author's knowledge), the novel approach of cross demihull load mechanism were tested for linear range waves to assure its capability. The PCM and split moments were successfully measured and showed the linear response to the wave heights. This data can form a basis to validate the numerical prediction. As a recommendation, larger oblique angle and large wave hight can be considered to expand the research envelope.

Chapter 6

Full-Scale Measurement on INCAT 112m Hull 064

Full-scale measurements of the INCAT 112 m class were conducted, with the author joining the delivery voyage of the first vessel of this class (Hull 064) from Hobart in Australia to Hakodate in Japan in 2007. During the delivery voyage, comprehensive observation records and measurements were carried out on ship speed and main engine performance, fuel consumption, ship motion, sea condition, structural load and acceleration.

The delivery voyage provided valuable data and observations at full scale for various speeds and sea conditions. After leaving Brisbane in Australia and passing the Latangai Island, as shown in Figure L.4, the sea condition in the middle of the Pacific Ocean was so calm that waves were not identifiable. However, the vessel experienced rough seas when crossing Bass Strait between the mainland of Australia and Tasmania. The rough-sea conditions allowed successful data recording which contained slamming and whipping effects. Filtering and spectral analysis on the measured data at multiple sensors elucidated the response frequency of ship motion, ship structure and main engine vibration.

In this Chapter, the delivery voyage route map and selected log, which are associated with the measured data, are explained in Subsection 6.1.1. The instrumentation for the onboard measurement system is discussed in Subsection 6.2. The experimental results and analysis are presented in Section 6.3. The unique vessel features of INCAT 112 m Hull 064 are explained in Subsection 1.4.

6.1 Delivery Voyage Data

6.1.1 Delivery Voyage Route

The maiden delivery voyage of the Hull 064 was made in 2007. The vessel departed from Constitution Dock in Hobart for Japan at 0600 hr on the $4th$ of August, 2007. After leaving Hobart, the ship stopped for bunkering at Gladstone and Brisbane. From Brisbane the delivery voyage was made in one leg to Hakodate in Japan.

The voyage track from Hobart to the coast off Sydney is presented in Figure 6.1. The comprehensive set of route maps of the delivery voyage are presented in Appendix L.

Figure 6.1: Vessel locations crossing Bass Strait during the voyage from Hobart to off Sydney

The most useful voyage data for analysis were obtained in the Bass Strait, since the vessel experienced rough-sea conditions, with the significant wave height, recorded by the TSK processing

device varying from 2.9 m to 3.2 m.

In Bass Strait, the waves generally came from a westerly direction, so the wave direction relative to the vessel changed from the bow-quartering seas, to beam seas, to following seas as the vessel crossed through Bass Strait. During the bow-quartering seas the vessel experienced both pitch and roll, while at beam seas the roll motion became the dominant phenomena. The vessel showed least motion in following seas.

6.1.2 Ship Displacement Variation

The ship displacement varied as fuel (marine gas oil) was consumed during the cruise and added through bunkering at ports. Ship displacement variation, as shown in Figure 6.2, was calculated based on the fuel gauges recorded in the voyage log. Each dot indicates the vessel displacement at the logged time. Based on this data, a vessel displacement interpolation program was created in Matlab, which is able to compute the expected vessel displacement based on the time of the recorded data for the sensors.

6.2 Delivery Voyage Instrumentation

Accelerometer, strain gauges and a TSK wave height meter system with a dedicated vertical accelerometer were installed for measuring the acceleration, ship motion, strain response of the structures and the encountered wave environment. General arrangement with sensor locations are presented in Figure 6.7.

6.2.1 Wave Height Meter

A shipborne wave height meter was fitted to the forwarded end of the centre bow, as shown in Figure 6.3. The wave height meter (microwave sensor) has a dome shape housing, installed just to starboard of the anchor. The cable of the microwave sensor was connected to a junction box, shown in Figure 6.4, in the centre bow void. The dedicated TSK vertical accelerometer sensor was placed adjacent to, and connected to, this junction box. The data was sent to the signal processor unit equipped with a digital indicator for significant wave height. Due to anchoring at Gladstone the wave sensor unit was removed once, however it was re-installed at Brisbane prior to departure for the final leg. Therefore, data acquisition was not performed during the voyage from Gladstone port to Brisbane port.

The wave sensor unit sends a microwave to the water surface. The wave meter sensor system utilises a Doppler shift of the microwave to measure the variation in the distance between the microwave sensor unit and water surface, which is measured as the relative wave height (RWH). The accelerometer white box, shown in Figure 6.3, held the accelerometer sensor that was mounted on double axis gimbals in an oil-filled bath. The accelerometer sensor motion is damped by the

oil, whose viscosity is chosen to avoid resonance of the sensor from the wave-induced ship motion.

6.2.2 Strain Gauges

In total eight strain gauges were mounted on the keel of each demi-hull and steel posts on the vehicle deck. On each demi-hull, two longitudinal locations on the keel were selected for measuring strains. The positions were selected to be similar to the strain gauges' positions on the hydroelastic segmented model. The forward segmentation cut and aft segmentation cut on the hydroelastic segmented model corresponded to $Frame\ No.\ 52.7$ in $Void{-}4$ and $Frame\ No.\ 31$ in $Void{-}7$,(A frame spacing is 1.2 m). Since $Void{-}4$ is the forward fuel tank, it was impossible to access in order to install strain gauge sensors. Hence, the forward strain gauges for the full-scale ship were alternatively shifted to $Void{-}3$, a pump room void, as it is a dry void. $Void{-}7$, a fuel pump room, was accessible for installing the strain gauges. For the strain gauges attached to the vertical column, the aft-most column and the forward-most column were selected for the strain measurements. Strain gauges were installed symmetrical to the longitudinal axis of the vessel. Sensors locations are presented in Figure 6.7.

6.2.3 Accelerometer Sensors

All four accelerometers were installed on the vehicle deck. One accelerometer sensor was located on the forward just behind the centre bow bulkhead on the centre-line of the vessel. The remaining three accelerometers were placed at the same longitudinal position on the vehicle deck. One accelerometer was situated on the vessel centre-line. Other accelerometers were placed at the starboard side and port side edge of the vehicle deck and transversely symmetrical to the centre-line of the vessel.

The main engine rotational speed (RPM) can be calculated from the subharmonic frequency of the main engine vibratory motion. The subharmonic frequency was obtained from the clear response frequency in the power spectral density of the acceleration data. The power spectral density (PSD) is discussed in detail in Section 6.3.3. The main engine RPM variation during the delivery voyage is shown in Figure 6.5.

During the delivery voyage a malfunction of the dedicated accelerometer sensor of the TSK wave height sensor system occurred. Therefore, another means of obtaining the encountered wave data was attempted by utilising the accelerometer and strain gauge data. The frequency of the encountered wave is generally expected to coincide with the response frequency of the accelerometer and strain gauge data in the PSD, over an expected range of the encountered wave frequency. These characteristics were utilised to find the encountered wave frequency (period) for the vessel as a countermeasure of the malfunction. Histograms of the dominant encountered wave periods are shown in Figure 6.6.

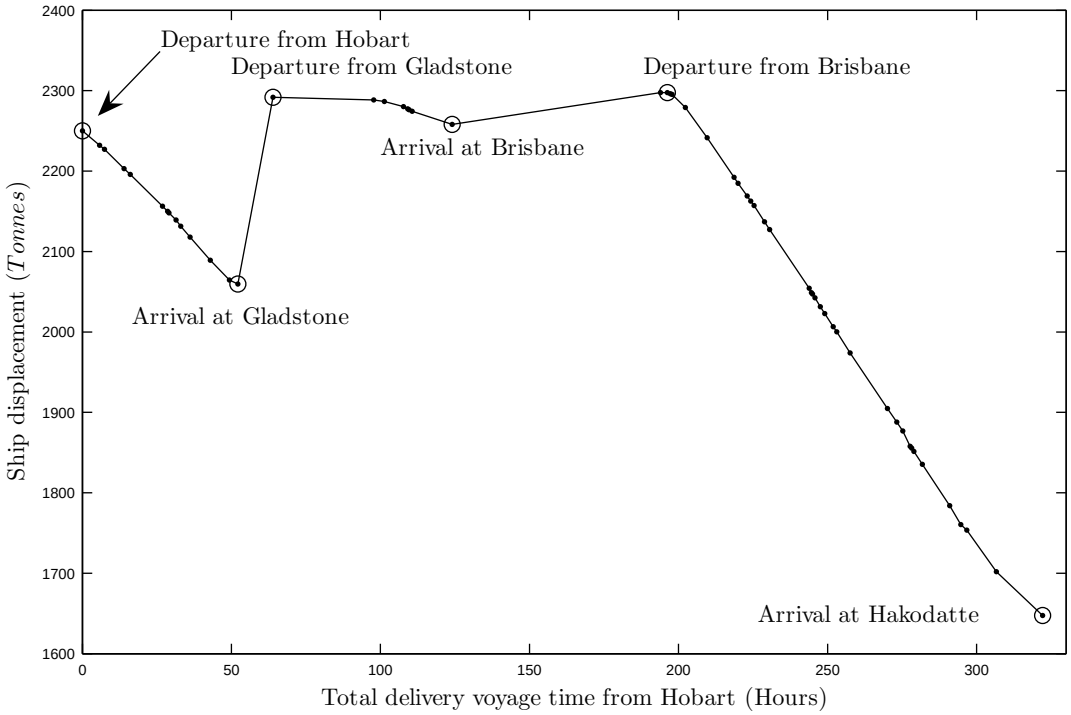

Figure 6.2: Displacement time variation of Hull 064 due to fuel bunkering and consumption during the delivery voyage from Hobart to Hakodate in 2007.

Figure 6.3: Wave sensor mounted on the centrebow.

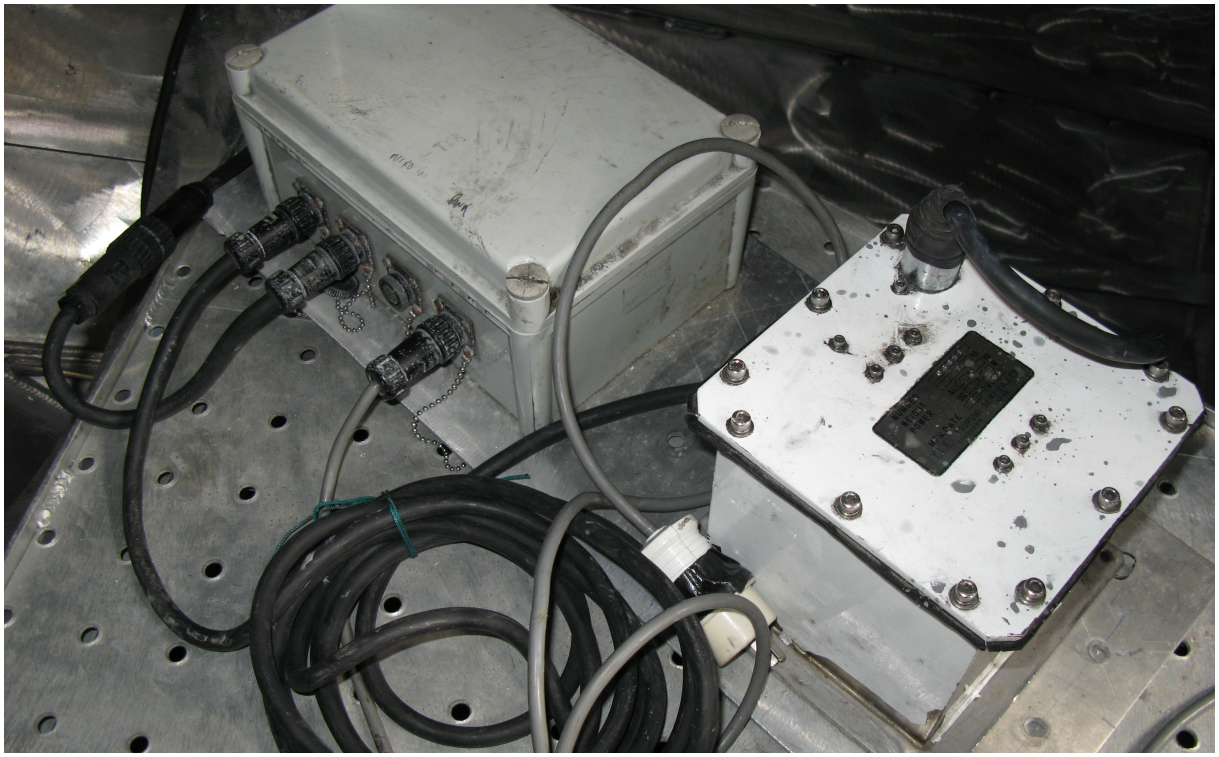

Figure 6.4: TSK motion sensor.

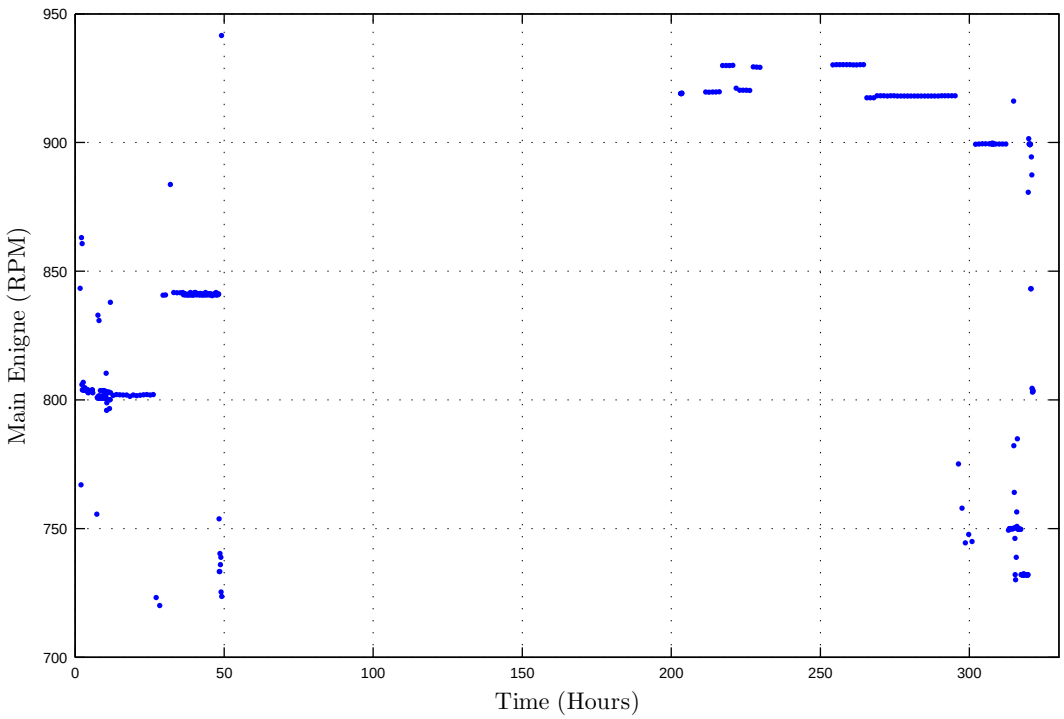

Figure 6.5: Main engine rotational speed (RPM) during the delivery voyage. Main engine RPM was calculated from the subharmonic frequency of main engine vibratory motion. The subharmonic frequency of Ch02 (Aft accelerometer sensor) was used for the RPM calculation).

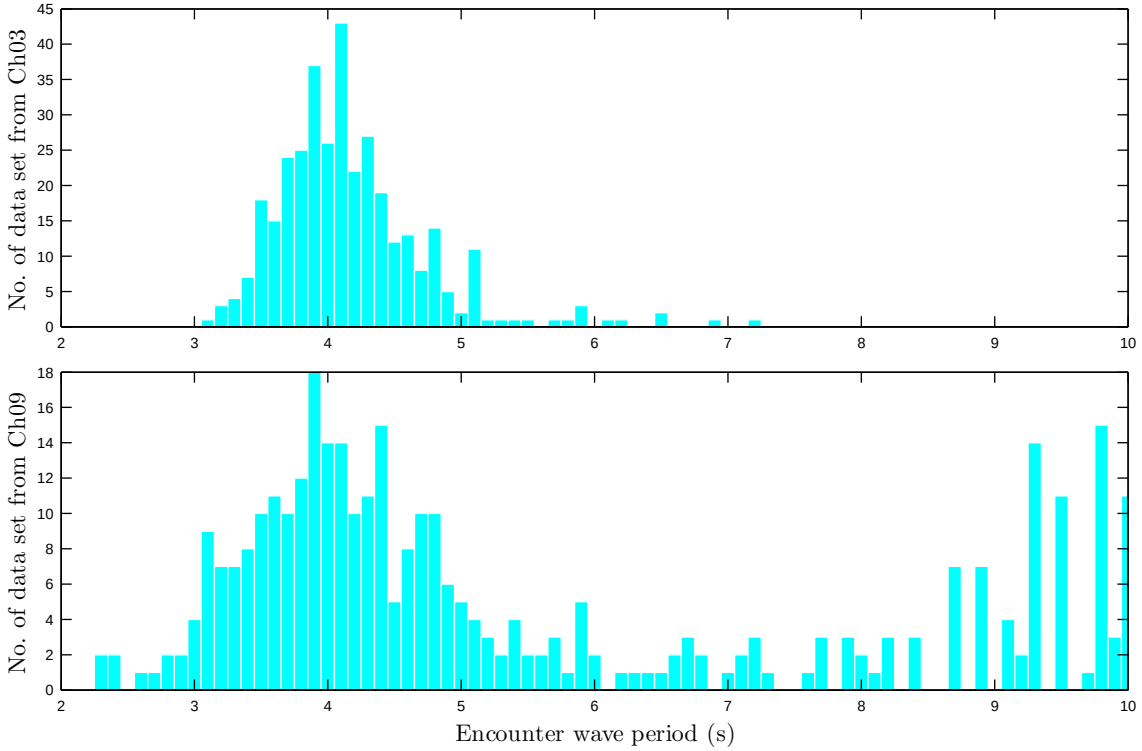

Figure 6.6: Response period distribution of sensors corresponding to the encounter wave period for the dominant waves of data set. The response periods were obtained from the local maximum peak of power spectral density on Ch03 (Accelerometer sensor) and Ch09 (Strain gauge sensor) bounded between 0.1 Hz to 1.0Hz

Channel sensors were selected due to the similar results among the same type of sensors. The accelerometer sensor (Ch03) showed only the primary encountered wave period which ranged between 3 and 7 seconds. On the other hand, the strain gauge sensor (Ch09) detected not only the primary encountered wave but also the lower frequency components, which is discussed in Section 6.3.5.

6.2.4 Calibration

Calibration of the accelerometers was conducted at Hakodate after arrival. An uprighting and inverting calibration was conducted for +1 g and -1 g, respectively. Sensitivity and calibration are presented for each sensor in Table 6.1. Unfortunately, the accelerometer sensor #4 lost signal during the delivery voyage. Therefore, an expected calibration factor for the #4 sensor was calculated based on past data. The sensitivity ratio of the #4 / #2 of this calibration was multiplied to the sensitivity of the #2 sensor in past data to obtain the expected sensitivity for the #4 sensor.

The acceleration was recorded in voltages so that the zero acceleration reference, which is equivalent to +1 g of gravity, was measured in calm water during the mooring. For the presentation

Table 6.1: INCAT 112m *Hull* 064, accelerometer calibrations.

Accelerometer ID No.	(Unit)	#4	#2	#1	#3
<DAQ Channel No.>		<Ch1>	<Ch2>	<Ch3>	<Ch4>
Output, Upright: +1 g	*volts*	NA	0.5970	0.6273	0.5746
Output, upside down: -1 g	*volts*	NA	-3.8833	-4.3148	-4.6737
Output, Difference: +2 g	*volts*	NA	4.4802	4.9421	5.2483
Sensitivity	$volts/g$	2.2745	2.2401	2.4710	2.6242
Calibration factor	$(m/s^2)/volts$	4.3131	4.3792	3.9700	3.7383
Past Sensitivity 1	$volts/g$	1.83	1.8	2	2.2
Past Sensitivity 2	$volts/g$	1.81	1.785	1.99	2.17

of acceleration data, the gravitational acceleration was subtracted from the total measured acceleration, with the positive acceleration being defined as upward.

6.3 Analyses and Results for the Delivery Voyage

6.3.1 Main Engine and Water Jet Shaft Response

Four main engines were installed on Hull 064 and each main engine drives a water jet impeller through a gear box and jet shaft. Rotational speeds of the main engines and jet shafts were logged during the delivery voyage, since the main machinery components was generally expected to generate a vibrational response. Selection of the RPM speed for the main engines and jet shafts are presented in Table 6.2. It contributed to the frequency response of accelerometers and strain gauge sensors to the vibrations caused by the main engines or water jet shafts.

Table 6.2: INCAT 112 *m Hull* 064, main engine and jet shaft RPM

08-08-2007 1721hr	POME	PIME	SIME	SOME	POJS	PIJS	SIJS	SOJS
RPM	651	649	651	657	306	300	305	311
Frequency (Hz)	10.85	10.82	10.85	10.95	5.10	5.00	5.08	5.18
Subharmonics (Hz)	5.43	5.41	5.43	5.48	2.55	2.50	2.54	2.59
04/08/2007-1650hr								
RPM	795	795	801	796	372	372	376	376
Frequency (Hz)	13.25	13.25	13.35	13.27	6.20	6.20	6.27	6.27
Subharmonics (Hz)	6.63	6.63	6.68	6.63	3.10	3.10	3.13	3.13
06/08/2007-0041hr								
RPM	841	840	843	840	394	390	390	391
Frequency (Hz)	14.02	14.00	14.05	14.00	6.57	6.50	6.50	6.52
Subharmonics (Hz)	7.01	7.00	7.03	7.00	3.28	3.25	3.25	3.26
12/08/2007-2319hr								
RPM	919	920	919	920	428	431	429	433
Frequency (Hz)	15.32	15.33	15.32	15.33	7.13	7.18	7.15	7.22
Subharmonics (Hz)	7.66	7.67	7.66	7.67	3.57	3.59	3.58	3.61
13/08/2007-1837hr								
RPM	927	928	928	930	433	436	435	438
Frequency (Hz)	15.45	15.47	15.47	15.50	7.22	7.27	7.25	7.30
Subharmonics (Hz)	7.73	7.73	7.73	7.75	3.61	3.63	3.63	3.65
14/08/2007-1738hr								
RPM	940	939	939	938	442	441	438	442
Frequency (Hz)	15.67	15.65	15.65	15.63	7.37	7.35	7.30	7.37
Subharmonics (Hz)	7.83	7.83	7.83	7.82	3.68	3.68	3.65	3.68

Abbreviations for main engines and jet shafts are: ME: main engine, JS: jet shaft, PO: port outer, PI: port inner, SI: starboard inner, SO: starboard outer

From the rotational speeds, the fundamental frequencies and their subharmonics were calculated for the main engines and jet shafts. In order to identify the response modal frequency of the vertical bending moment (VBM), elimination of other response components is essential. (The modal frequency of the VBM is the natural frequency of the VBM. However, the VBM natural frequency of the ship varies due to the variation of the ship displacement, loading conditions and surrounding water conditions.) Therefore, the rotational speed log was useful, especially to confirm the subharmonic frequency responses of the jet shaft rotational speed, which appeared to be quite close to the response modal frequency of the VBM. According to the record of main engine rotational speed shown in Figure 6.5, the minimum rotational speed was 720

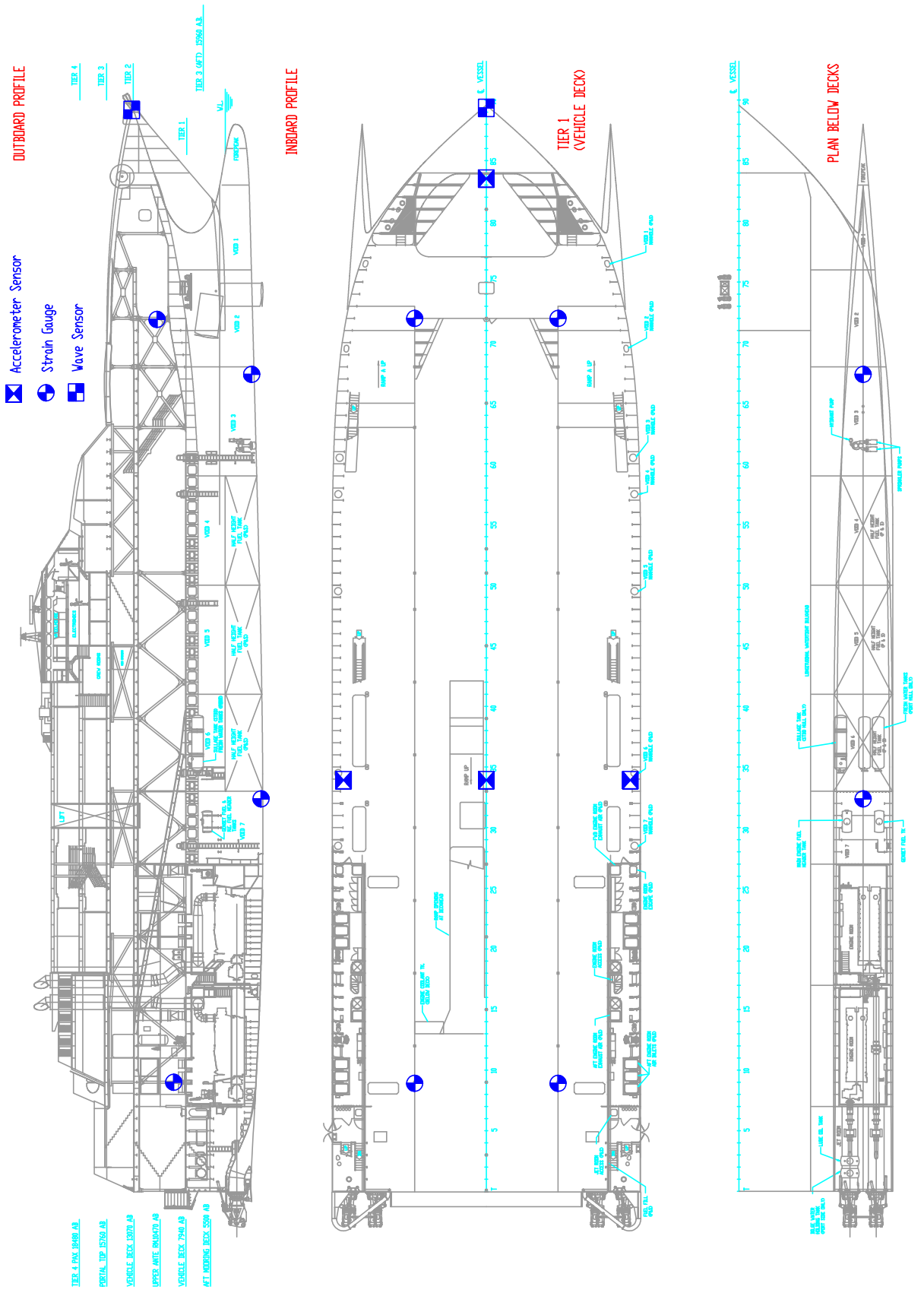

Figure 6.7: INCAT 112 m Hull 064: Sensors General Arrangement

RPM. Hence, the expected subharmonic frequency of the jet shaft was 2.8 Hz. Therefore, the values above 2.8 Hz were eliminated from the response modal frequency of the VBM, which was detected from the power spectral density. The modal frequency identification of the VBM is discussed in Subsection 6.3.3.

6.3.2 Measurement of Slamming Events

When crossing the Bass Strait, Hull 064 experienced the most severe sea conditions during the delivery voyage causing slamming. Slamming phenomena were recorded clearly on the accelerometer sensors, as was the whipping behaviour induced by a slam event. The acceleration did not require any data treatment, such as filtering, for aid detection of slamming and whipping. The strain gauges also showed whipping responses after the slamming. In order to extract the slamming signal from the strain gauge data, a Butterworth low-pass filter was applied to the raw data with the cut-off frequency at 5 Hz. Since the slamming signal from the strain gauges was unclear in the raw data without filtering, this provides a good peak match with the accelerometer signal, since the other higher frequency components can be removed from the raw data to extract the clearer slamming effect.

Slamming was detected by the accelerometers on the vehicle deck, as shown in Figure 6.8. The strain gauge signals from the demi-hull keel are presented in Figure 6.9 during the same event and for the same duration.

In Figure 6.8 , the accelerometer at the forward bow on the vehicle deck shows a clear slamming signal forming a sharp trough after $t = 30$ s. After the first impact, the signal lost the high frequency oscillations with the small amplitudes. Once the signal reaches the trough, the signal suddenly increased to form a peak. After that, the whipping oscillation is clearly observed. Hence, these observations show that the accelerometer arrangement and its system could successfully record the slamming and whipping phenomena.

An advantage of slamming analysis using all four strain gauges in the time domain is that it is different from the analysis on the accelerometer. Time variations of the slamming response signal between the different sensor locations helps determine the slam location and the mechanism of load propagation in the structure, because the strain gauges formed a symmetrical array on the hull.

Strain gauge signals in the time domain for the same duration of accelerometer signals are shown in Figure 6.9. The first sign of the slamming effect can be seen on the strain gauge at the forward starboard keel (FS Keel). From the timing of the slamming peaks it appears that the starboard side demi-hull was subjected to the slamming-induced load first. Subsequently, the aft starboard keel (AS Keel), and then the forward port side keel (FP Keel), were subjected to vibration. The vibration propagated through the hull to the port side, and the aft port side keel (AP Keel) behaved with the clear whipping induced by the slamming impact.

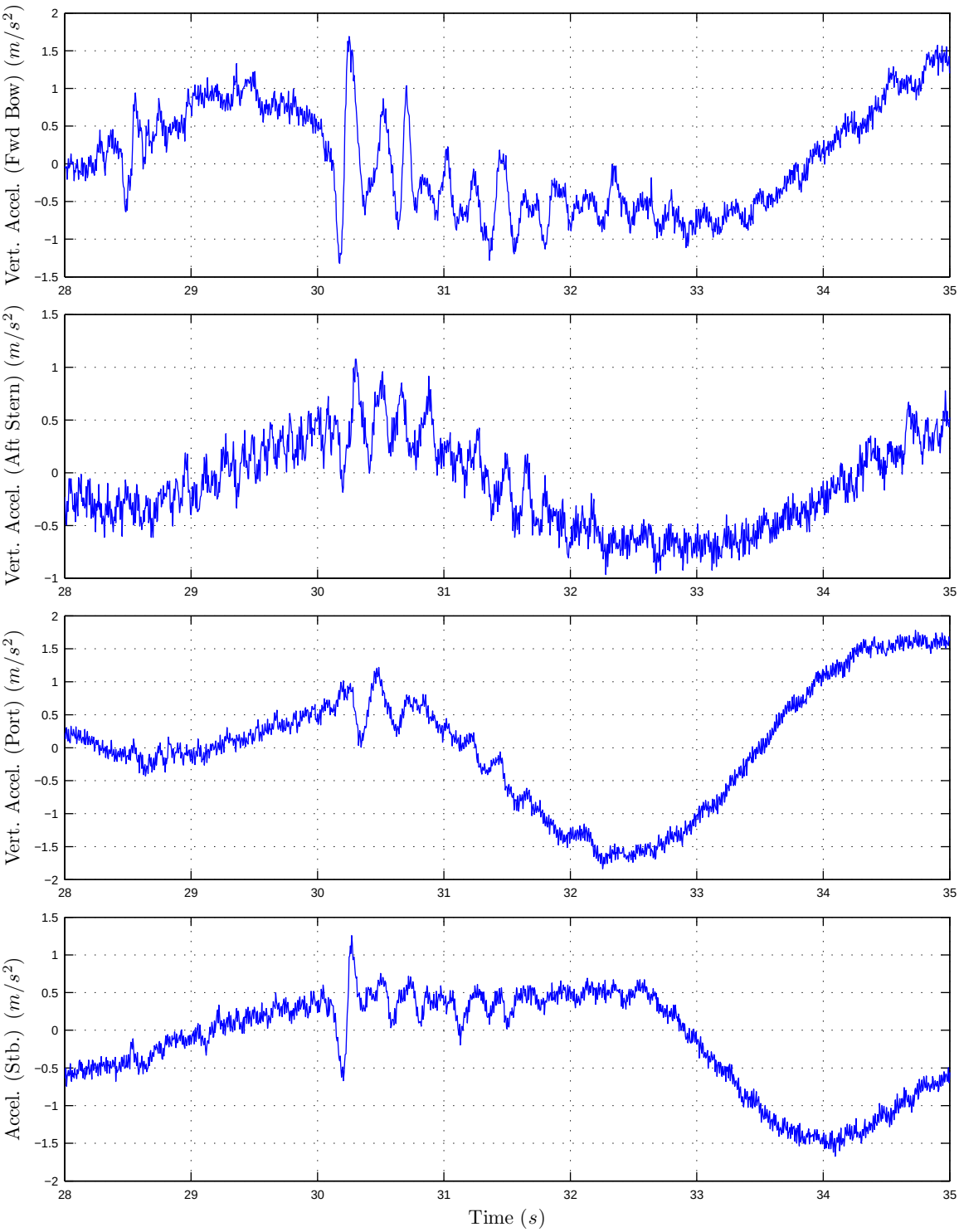

Figure 6.8: Accelerometer data in time domain for the *Hull* 064. Disc No.1 Run No. 062. Slam event recorded at $t = 30.2$ (s) with the subsequent whipping behaviour is clearly visible.

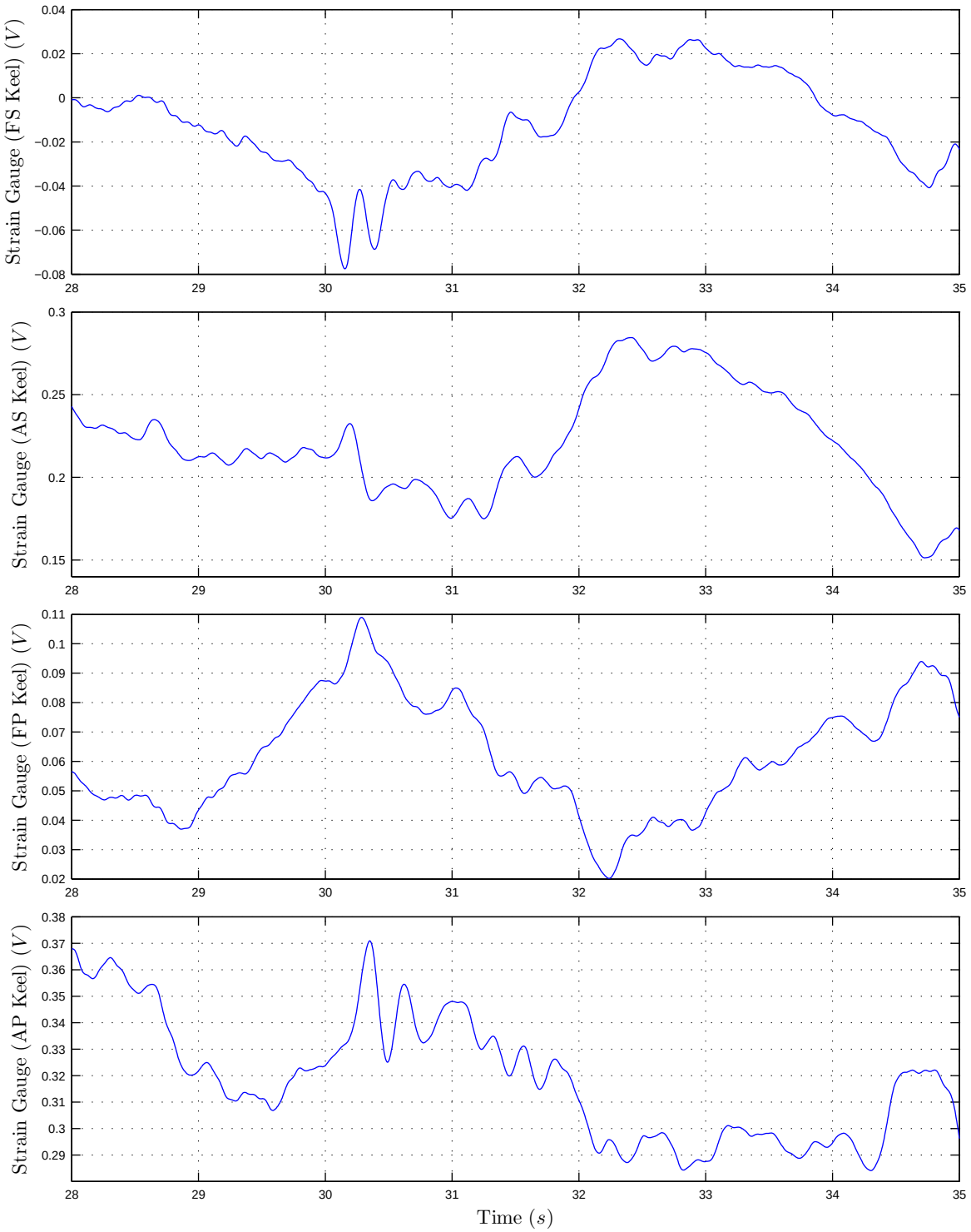

Figure 6.9: Filtered strain gauge data in time domain for *Hull* 064. Butterworth low-pass filter smoothing was applied with cut-off frequencies of 5 Hz. Disc No. 1 Run No. 062.

When the slamming impact occurred, as synchronised between the strain and acceleration as shown in Figure 6.10, a maximum trough of acceleration caused the maximum trough of stain gauge signals which indicated an increase in the hogging vertical bending moment (VBM). As the vertical acceleration for the forward bow sensor sharply decreased around 30.2 seconds, the strain gauge response at the forward starboard keel simultaneously decreased rapidly. Once the acceleration reached the first trough and bounced back to the peak rapidly, the strain gauge signal also responded in the same pattern with acceleration to form the peak. Interestingly, the phase of peak and trough for the slamming signal on the accelerometer coincided with the strain gauge signal. The strain gauge of the aft port side keel did not show the response of the first slam impact, however the whipping phenomena was clearly recorded. With the above analysis on the timing of the slam-induced load propagations recorded by the four strain gauges, it confirms that the slam-induced load generated around the forward area propagated through the keel and hull shell structure to induce the whipping response at the aft port keel area.

Vertical velocity and displacement were determined by numerically integrating from the acceleration measured by the accelerometer, as can be refer to Figure 6.11. As mentioned in Subsection 6.2.4, the presented acceleration data in figures were calculated by subtracting the gravitational acceleration from the total measured acceleration.
Figure 6.11 results from the forward bow accelerometer indicates that the maximum slamming impact occurred after the vertical displacement passed the trough. There is a time delay between the trough of the strain gauge signal and the trough of vertical displacement. This is due to the highest impact of slamming occurring when the centre bow arch was filled with water to give the maximum impact to the centre bow. The vertical velocity shows a small oscillation caused by the slamming impact and whipping. There was a similar signal pattern between the global motion of vertical displacement and the global oscillation of the strain gauge. Since the vertical displacement generally corresponded to global wave motion in the same phase of the oscillation, it indicated that global oscillation of the strain gauge corresponded to the global wave elevation.

According to the dynamic plot analysis using the measured and integrated data to duplicate the ship attitude in the time domain, the ship dynamic attitudes were observed for the slam event shown in Figure 6.8. The ship was in bow-down trim when the vessel experienced slamming. This matched well with the fact that the whipping was detected predominantly on the aft strain gauges rather than the forward strain gauges. The wave piercer and forward demihull region was submerged into the water to increase the damping compared with the aft demi-hull region, therefore the whipping did not occur so clearly.

6.3.3 Spectral Analysis

Spectral analysis, using power spectral density (PSD) functions, was performed on the acceleration and strain gauge data in order to probe the frequencies caused by wave and ship motion,

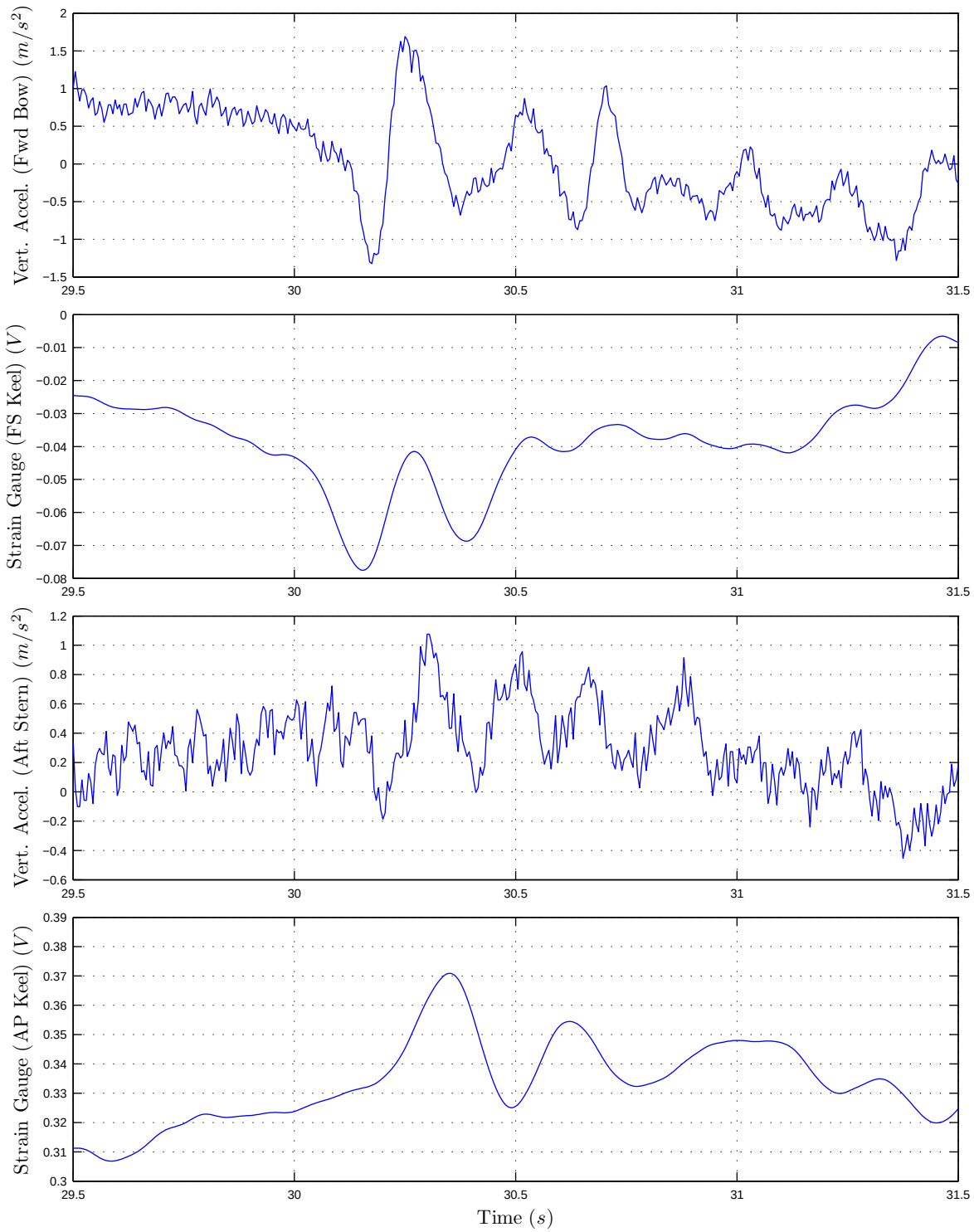

Figure 6.10: Synchronised plot for accelerations raw data and filtered strain gauge data in time domain for $Hull$ 064. Butterworth low pass filter smoothing were applied with the cut off frequencies of $5Hz$. Disc No.1 Run No.062.

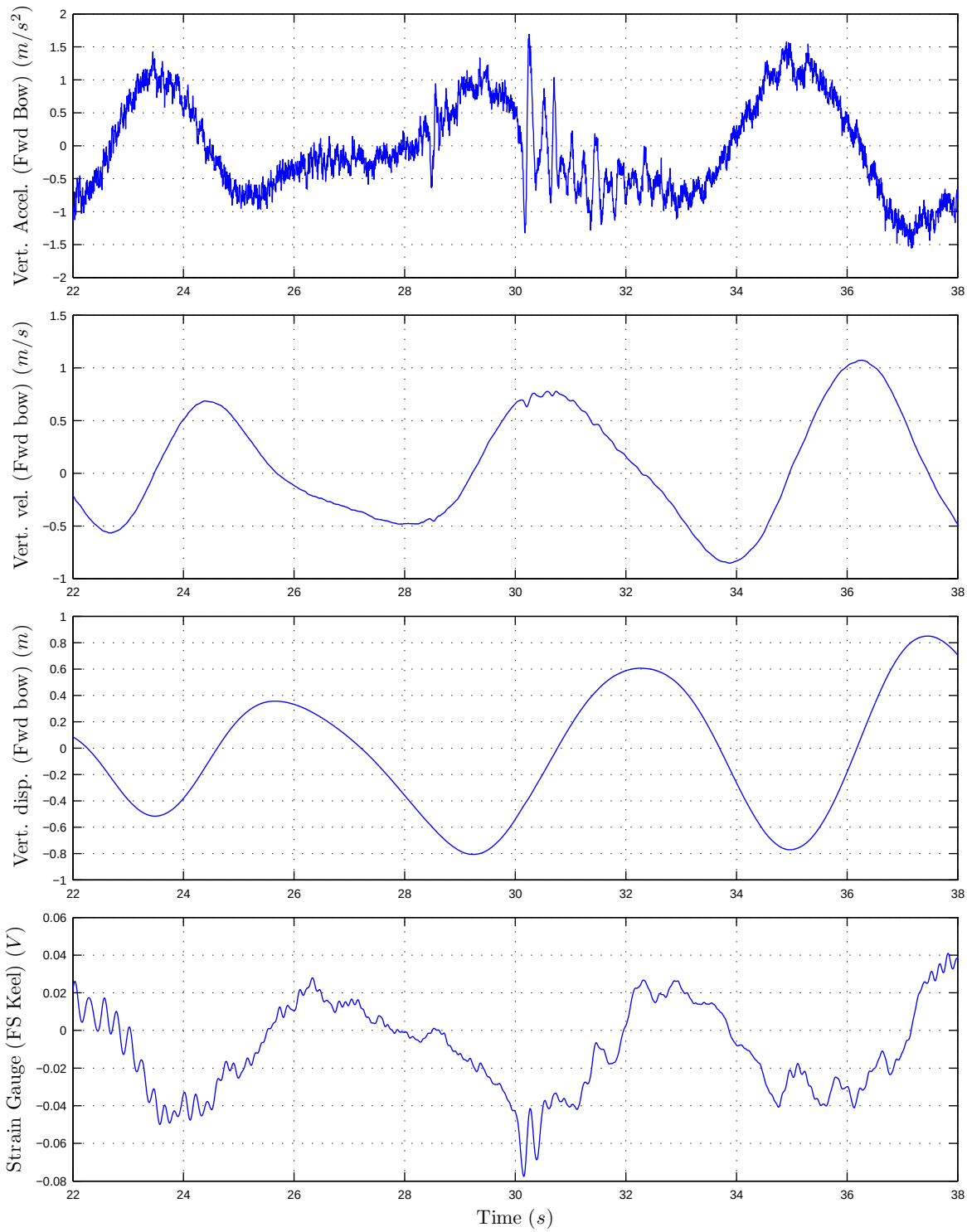

Figure 6.11: Vertical acceleration, velocity, and displacement data and filtered strain gauge data, in time domain for *Hull* 064. Vertical velocity and displacement were calculated by numerical integrations. Butterworth high pass filter smoothing were applied with the cut off frequencies of $0.05Hz$ on the accelerometer data. Disc No.1 Run No.062.

and machinery vibration. In general, under sea conditions of moderate wave heights, without extreme slamming impacts, the wave response component dominated other components caused by the modal response of the vertical bending moment or responses to machinery. Hence, some enhancement techniques on the PSD were required for analysis of the relatively small responses. For the spectral analysis on the wave components, the frequency range was limited in order to display a smaller range where only wave components appeared. Its PSD was obtained on non-filtered data by applying the data taper of a Hamming window in the time domain, and by applying a convolution with smoothing windows in the frequency domain. For the spectral analysis on the other components, whose response frequencies were higher than those of wave components, a bandpass filter was applied to remove the wave components from the data. Then the PSDs were obtained on the filtered data similarly with the Hamming window and convolution smoothing.

Power spectral densities of Disc No. 1 Data No. 062 are presented in Figure 6.12 with three different focuses of response frequency for the overall component, wave component, and other components. Data No. 062 was recorded on the 04/08/2007 at 1615 hr, when the vessel was crossing the Bass Strait as shown in Figure 6.1. Fundamental frequencies and their subharmonic frequencies are presented in Table 6.2, where the main engine RPMs were maintained at 795 to 800 RPM on 04/08/2007 at 1650 hr. The averaged speed log at 800 RPM was 26.7 K_n in GPS speed. The PSD shown in Figure 6.12 shows the response frequencies of the overall component in the top row, response frequencies of wave components in the middle row, and response frequencies of vertical bending moment and machinery vibration in the bottom row.

For the overall component of both the acceleration and strain gauge the most dominant response frequency occurred between 0 and 20 Hz, being caused by the encountered waves. The magnitude of the higher frequency response were relatively negligible to those of the wave component.

The plots in the middle row of Figure 6.12 focused on the frequencies between 0 and 1 Hz, to zoom into the wave response components. The acceleration and strain gauges exhibited response peaks at 0.244 Hz, which was the encountered wave frequency. An intriguing phenomena on the strain gauge on the keel was another clear peak even lower than the response frequency of the encountered wave. This was found to be a second ship harmonic motion cycling with a long period. This periodic ship motion was caused by two possibilities: firstly, the following sea travelling at a similar velocity to the vessel,or secondly, a kind of porpoising mechanism which was also experienced at the model scale. The details of this phenomena will be discussed in Subsection 6.3.5 . Due to its capability the accelerometer sensor could not capture the signal at this lower response frequency.

The bottom row plot of Figure 6.12 shows the PSDs for the data signals which were filtered by a Butterworth filter with a bandpass between 0.8 and 20 Hz. The filtering allowed the wave components to be removed. One frequency clearly shows the response peak on both the acceleration and strain gauge signal at 2.47 Hz. This was the resonance frequency of the vertical bending moment. The peak at 13.3 Hz is the response frequency of the main engine RPM speed, whose

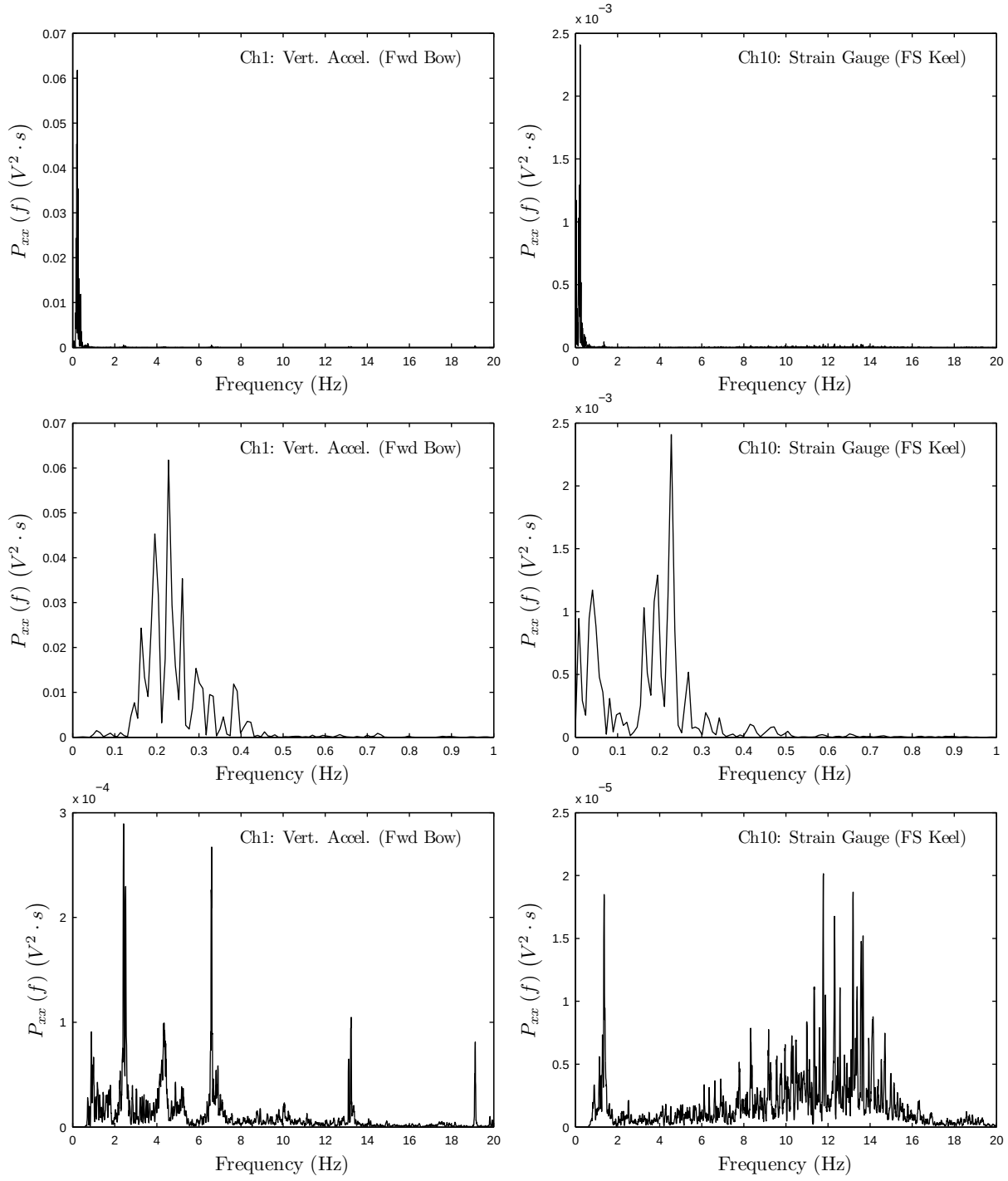

Figure 6.12: Spectral analysis on raw data of accelerometer and strain gauges. Selected power spectral density (PSD), $P_{xx}(f)$ for the acceleration measured at Ch1 on the vehicle deck, and PSD, $P_{xx}(f)$, for strain gauge raw data at Ch10 at the forward starboard side keel. Disc No.1, Data No.062. PSD was obtained by applying the Hamming window for data taper in time domain, and smoothing by a convolution with smoothing windows in frequency domain. No. of the windows can be referred to in Appendix N. The overall components in the top row, the wave components in the middle row, and the vertical bending moment and machinery vibration components in the bottom row

values matched with the calculated value in Table 6.2. The subharmonics of the main engine RPM at 6.67 Hz were also observed as were the jet shaft RPM. The voyage logged data was essential to confirm the identification of the measured fundamental and subharmonic response frequencies of the main engine RPM and jet shaft RPM. Generally, the PSD of the acceleration response was clearer than that of the strain, so the response component analysis utilised the PSD of the accelerometer sensors.

To compare the response frequencies for VBM and machinery vibrations, due to the different sea conditions, the power spectrum density (PSD) for Disc No. 1 Data No. 062, Disc No. 1 Data No. 065 and Disc No. 1 Data No. 154 were selected and are presented in Figures 6.13, 6.14, and 6.15 respectively. There were differences in the sea conditions, speed, and ride control system among the voyage records of Data No. 062, 065 and 154. A summary of the conditions can be seen in Table 6.3.

Table 6.3: Reference summary for Disc and Data No., date, main engine RPM, and speed for presented figures.

Disc	Data	Date& Time	Main engine	GPS speed	T-foil
No.1	No.062	04/08/2007 1615hr	800RPM	26.7Kn	Deployed
No.1	No.065	04/08/2007 1629hr	800RPM	26.5Kn	Deployed
No.1	No.154	06/08/2007 0053hr	840RPM	28.4Kn	Stowed

Firstly, it is important to note several conditional factors for the selected data. Data No. 062 were recorded when the vessel was crossing the Bass Strait, with the vessel was exposed to severe sea conditions. The cruising log speed was around 26.5 Kn with the main engine RPM of around 800 RPM, and the T-foil was deployed to reduce the ship motion. Data No. 065 and 154 were recorded on 4/08/2007 at 1629 hr and 6/08/2007 at 0053 hr, respectively. For Data No. 065, more slamming occurred at 26.7 Kn of GPS speed with the main engine rotational speed of 800 RPM, whose speed and machinery conditions were similar to Data No. 062. In comparison, Data No. 154 were recorded at the speed of 28.4 Kn with 840 RPM of the main engine. The vessel was passing off the coast of Brisbane, as shown in Figure L.2, The wave conditions were calmer than in the Bass Strait allowing comparison of the response magnitude of the VBM. With reduced ship motion for Data No. 154, the T-foil for ride control was stowed.

Comparing Data No. 062 and 065, the main engine RPM and vessel speed were similar, however the time plot of the acceleration for Data No. 065 recorded a larger amplitude of motion response and more occurrences of slamming and whipping than for Data No. 062, hence the vessel response to the wave impact was more noticeable. Therefore, Figure 6.14 showed clearer response frequency peaks in the PSD. The order of magnitude for PSD was 1, indicating stronger responses by Data No. 65. It also indicated the main engine RPM responses and its subharmonic responses at 13.3 Hz and 6.63 Hz, respectively. These values for Ch1 to 4 also matched well with the calculated fundamental and subharmonic frequencies of the main engine rotational speed, as shown in Table 6.2. On acceleration for Ch2 to 4, the sub- harmonic response frequency

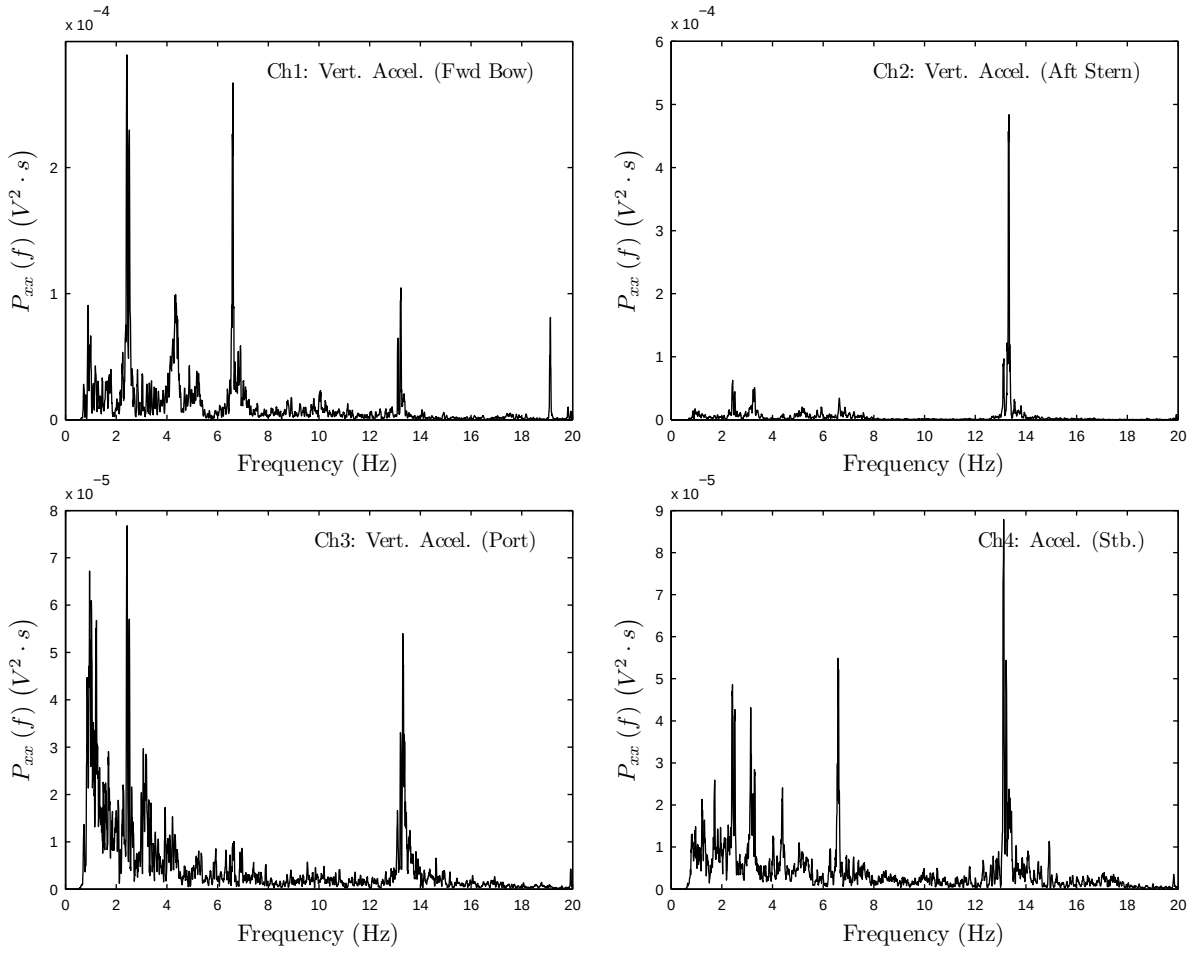

Figure 6.13: Spectral analysis on accelerometer raw data during the delivery voyage of INCAT 112 m. Power spectral density (PSD), $P_{xx}(f)$ for acceleration measured at Ch1, Ch2 Ch3 and Ch4 on the vehicle deck for voyage record disc No.1, Data No.062. PSD was obtained by applying the Hamming window for data taper in time domain, and smoothing by a convolution with five smoothing windows in frequency domain.

of the jet shaft can be observed at 3.14 Hz, however, not on the forward bow accelerometer of Ch1. The subharmonic frequency was also confirmed with the logged data shown in Table 6.2. This subharmonic response frequency by the jet shaft resembled the modal frequency of the vertical bending moment.

After identifying the above machinery response frequencies, the modal response frequency of the vertical bending moment (VBM) in the PSD occurred at 2.48 Hz, which corresponded well to the case of Disc No. 1 Data No. 062. All the accelerometer sensors on the vehicle deck for Data No. 062 and 065 responded in 2.47 and 2.48 Hz, respectively, regardless of its installed location. The strain gauges showed the response modal frequency of the VBM at 2.47 Hz, as shown in N.6. With these consistent results, the response modal frequency of the VBM at a vessel speed of 26.7 Kn can be experimentally determined to be approximately 2.5 Hz.

Data No. 154 provided data for a smaller wave height with no slamming. It showed a relatively

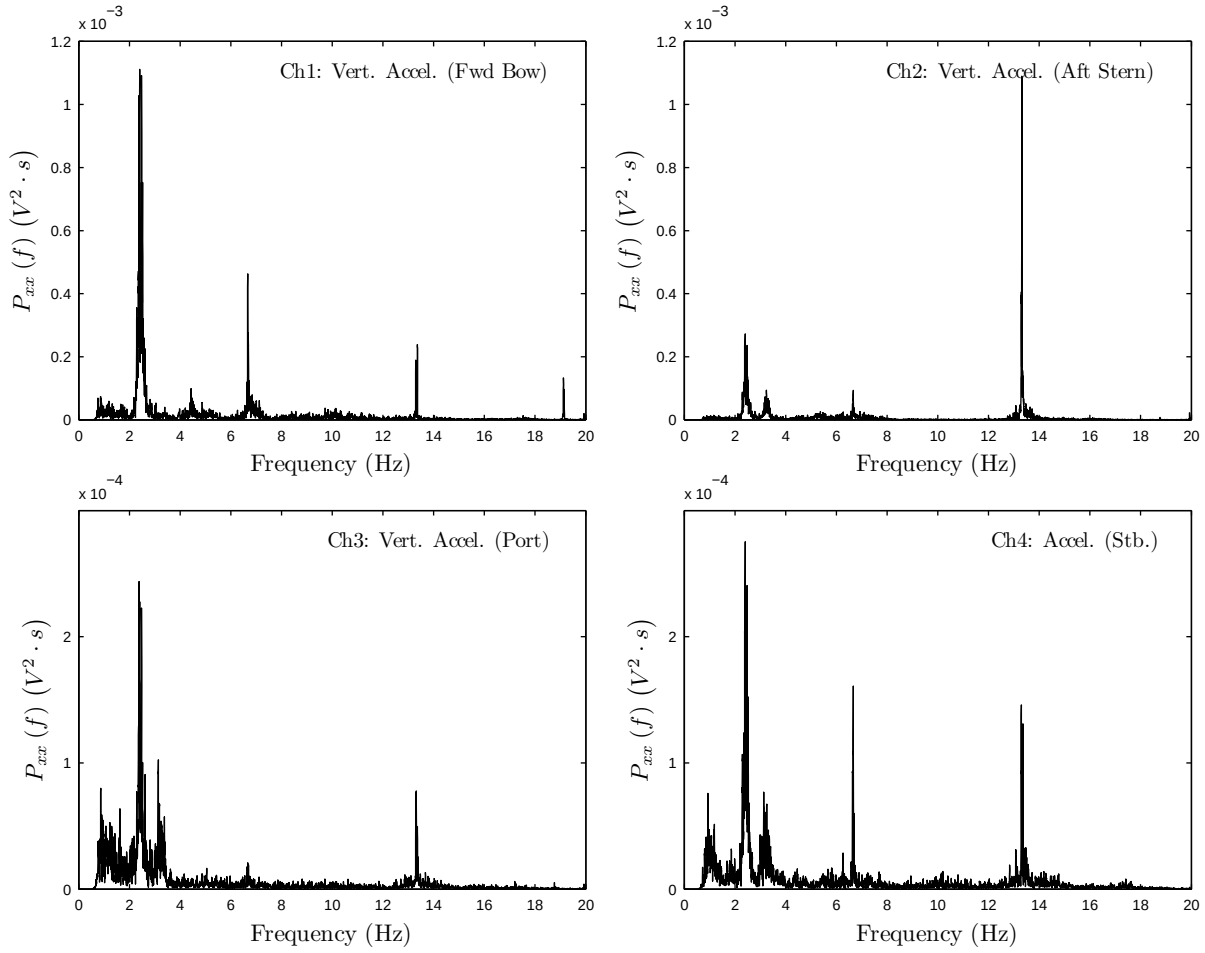

Figure 6.14: Spectral analysis on accelerometer raw data. Power spectral density (PSD), $P_{xx}(f)$ for acceleration measured at Ch1, Ch2 Ch3 and Ch4 on the vehicle deck. Disc No.1, Data No.065. PSD was obtained by applying the Hamming window for data taper in time domain, and smoothing by a convolution with 5 smoothing windows in frequency domain.

smaller response magnitude of the modal frequency for the VBM, as shown in Figure 6.15. The response frequency of the VBM was 2.52 Hz at 26.7 Kn with 840 RPM. The accelerometer results indicated the weak response magnitude of the VBM compared with the responses due to the main engines. The machinery-induced responses of the main engine and its harmonics at 14 Hz and 7.0 Hz, also corresponded well with the fundamental and subharmonic frequency of the main engines as shown in Table 6.2 at 840 RPM. It clearly indicated that the response frequency of the main engine RPM could be detected by the accelerometer sensors on the vehicle deck regardless of the sea conditions or vessel speed. Comparing with Data No. 062 and Data No. 065, a small increase in response frequency of the VBM was observed. The potential reasons for this could due to either variation in the vessel speed or in displacement due to fuel consumption. The primary cause of the response frequency variation for the VBM is discussed in Subsection 6.3.4.

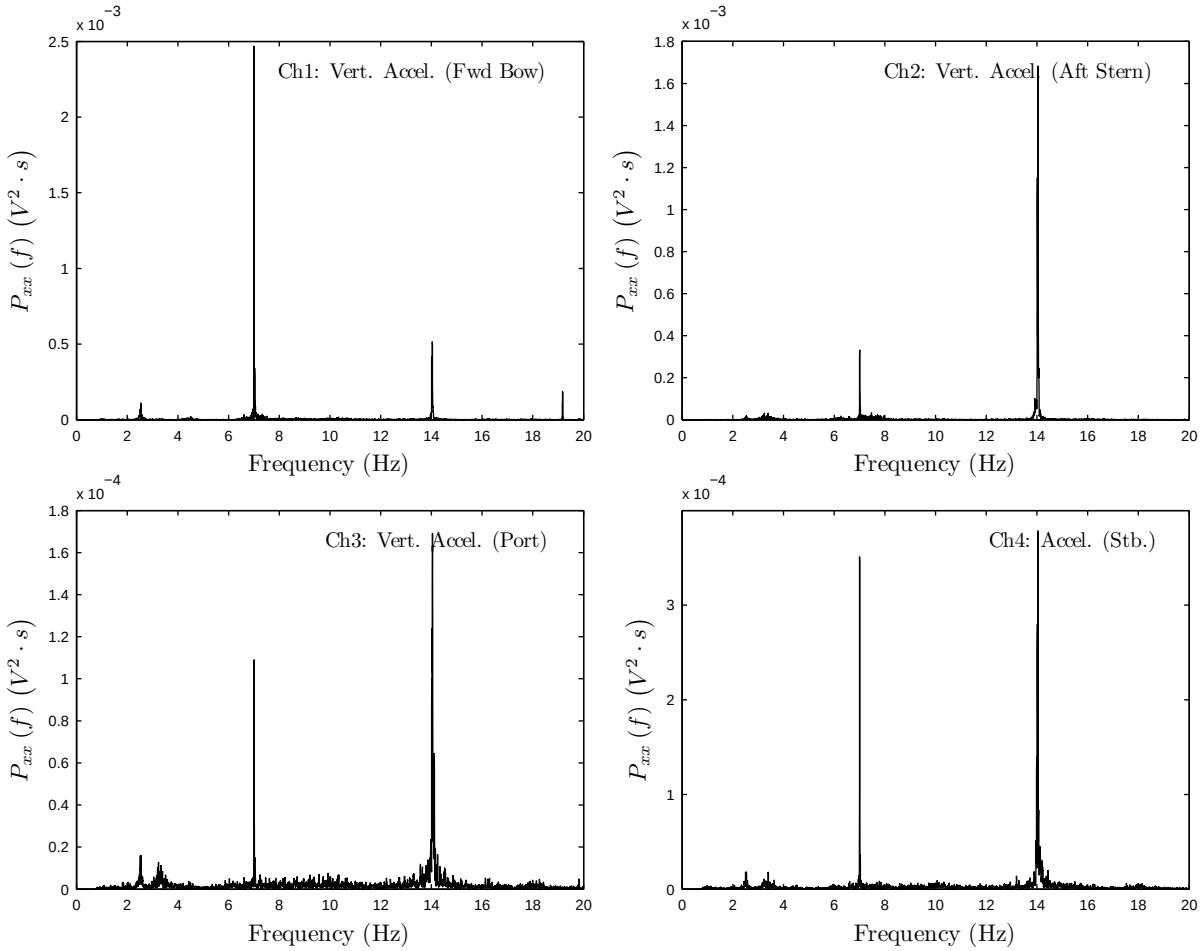

Figure 6.15: Spectral analysis on accelerometer raw data during the delivery voyage of INCAT 112 m. Power spectral density (PSD), $P_{xx}(f)$ for acceleration measured at Ch1, Ch2 Ch3 and Ch4 on the vehicle deck. Disc No.1, Data No.154. PSD was obtained by applying the Hamming window for data taper in time domain, and smoothing by a convolution with 5 smoothing windows in frequency domain.

6.3.4 VBM Frequency Response Variation due to Displacement

The analysis of PSD on all delivery voyage data discovered the distinct influence of the displacement variation on the modal response frequency of the vertical bending moment (VBM), as shown in Figure 6.16. As the vessel displacement decreased its own displacement due to consumption of fuel, the response modal frequency of the VBM increased on average to 2.65 Hz from 2.45 Hz. The whipping is occurred at the natural frequency when ship was induced by the impact excitation. The whipping frequency is the modal frequency, however the mass distribution and surrounding water conditions change the fundamental modal frequency of VBM for the ship being on the water. Hence, the whipping frequency is expected to be varied. The phenomenon compared well with the general rule for the natural frequency of a simple undamped spring-mass system whose natural frequency can be expressed as:

$$f_n = \frac{1}{2\pi}\sqrt{\frac{k}{m}}, \tag{6.1}$$

where m is the mass and k is the stiffness. Hence, a simplified empirical formula of response modal frequency variation based on the delivery voyage data, was obtained with an omission of the stiffness variation as follows:

$$f_{VBN} = C_{VBN}\sqrt{\frac{1}{m}} + C_0, \tag{6.2}$$

using regression analysis, it was found that C_{VBN} was 5.3016 and C_0 was 1.345 for the INCAT 112 m class during the delivery voyage. The coefficient of determination was 11.54. Hence, the fitted line accounts for over 11.5% of the raw variability in displacement, reducing the unexplained variation from 5.35 to 4.73.

Assessment of the effect of vessel speed on the modal frequency of the VBM was attempted, however, it was difficult to obtain the vessel speed accurately by using the engine RPM data to interpolate the vessel speed from the recorded log. The difficulty arose from the fluctuation in the vessel speed during the delivery voyage, hence, developing a system to measure the vessel speed along with acceleration and strain would be useful for future projects, e.g. logging the vessel GPS speed.

The effects of main engine rotational speed on the response modal frequency of VBM were investigated. It did not indicate any clear relationship with the modal frequency of the VBM, as shown in Figure 6.17. The response modal frequencies were scattered over the 2.3 to 2.8 Hz range, and over the measured RPM range.

In conclusion, the full-size scale results provided substantive evidence that the mass distribution of the vessel significantly affected the modal response of the vertical bending moment, by investigation of the effects of displacement and main engine rotational speed variation. An increase in mass generally resulted in a decrease in the response frequency of the VBM, this relationship can seen on the Equation 6.2.

6.3.5 Second Harmonic Ship Motion

During the delivery voyage the author experienced pitch motions with a long period of more than 30 seconds, sometimes almost more than one minute. There was a monitor panel for the MDI ride control system available in the cockpit of INCAT 112 m Hull 064. Displaying the actual and RMS values for the pitch angle. The actual value also showed the very slow variation of the pitch angle which indicated the second harmonic ship motion. After filtering the strain gauge data, the second harmonic ship motion can be observed in the time domain, as shown in Figure 6.18. This can be seen as a cyclic oscillation with a long period of about 30 to 40 s.

Since all four stain gauges presented a similar global cyclic oscillation, it clearly indicated that the strain gauges were subjected to the global loading due to some kind of slow ship dynamic motion. Two potential causes of the ship motion can be considered: one is the ship motion

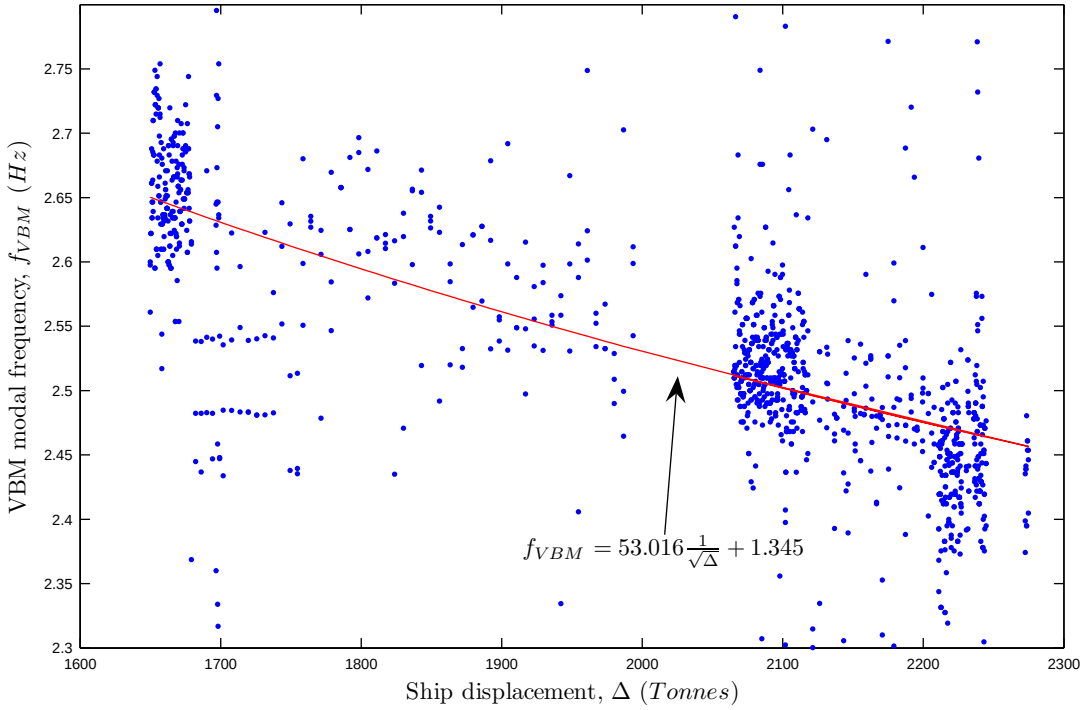

Figure 6.16: Modal frequency (whipping frequency) variation of VBM due to the change in the vessel displacement. The modal frequencies were obtained from peak responses in the power spectral density on Ch01, Ch02, Ch03 and Ch04.

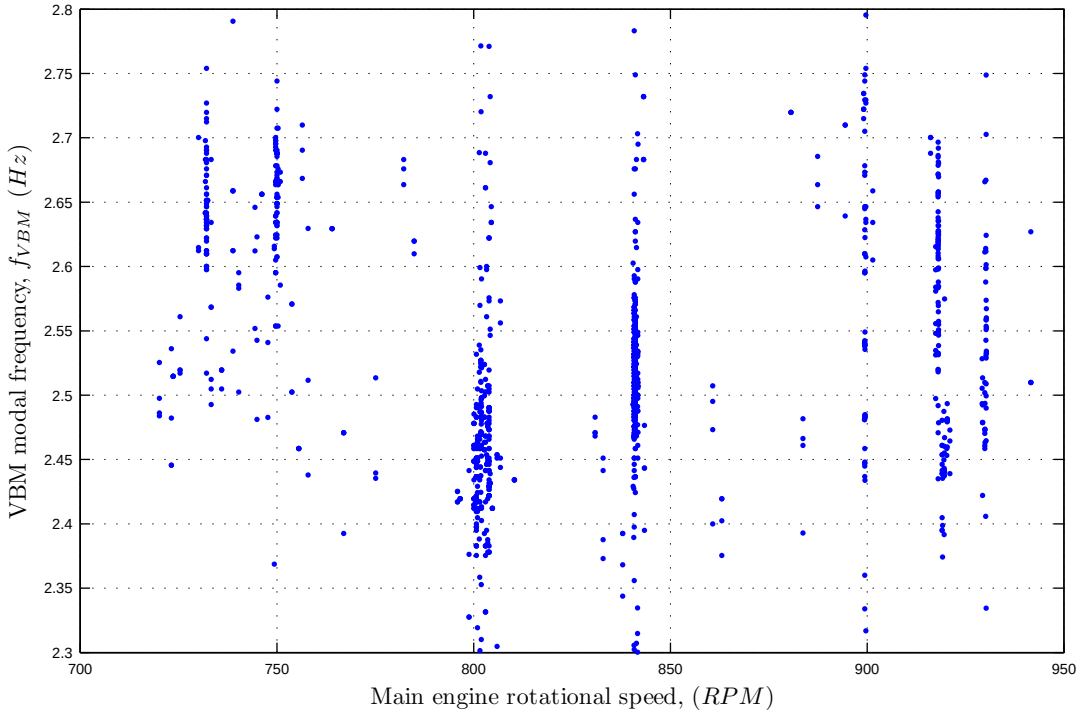

Figure 6.17: Modal frequency (whipping frequency) variation of VBM vs. main engine rotational speed.

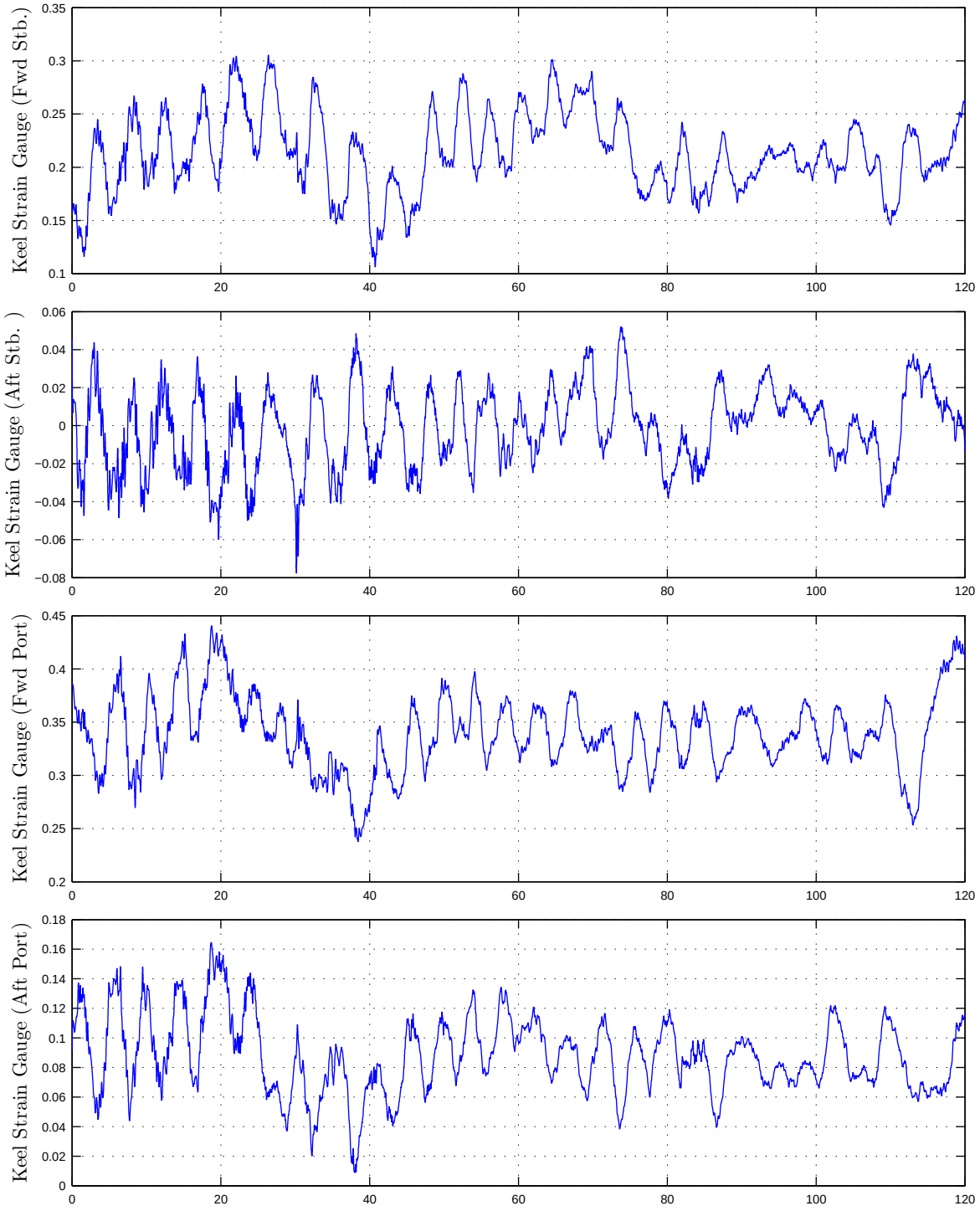

Figure 6.18: Strain gauge raw data in time domain for INCAT 112 m Hull 064 delivery voyage. Butterworth filter smoothing was applied with cut-off frequency of 5 Hz. Data was recorded on Disc No. 1 Run No. 062.

induced by the hydrodynamic lift forces like porpoising, another one is the following wave travelling with a similar speed to the vessel. Since this kind of large period harmonic motion can be seen in many recorded data, the primary cause can be considered as the most likely reason.

In fact, a similar phenomena occurred for the hydroelastic segmented model in the towing tank test, as discussed in Section 3.7. It is the second harmonic ship motion induced by the hull-lift force oscillation which is ascribable to the ship hydrodynamic characteristic of the hull shape and vessel speed. This phenomena occurred in the middle speed range at both the full and model scale.

In order to compare the response frequency of the second harmonic ship motion between the model scale and full scale, the expected scaled frequency was obtained from the hydroelastic segmented model test. Since the exact case Froude number was not available, the frequency of the model size were interpolated with respect to the velocity and scaled as shown in Table 6.4.

Table 6.4: Calculated frequency for second harmonic ship motion for the full scale.

	Fn	Measured Period	Scaled period to full size	Frequency	Run No.
Units		seconds	seconds	Hz	
Model (HSM)	0.32	4.49	30.05	0.0333	Run No.813
Model (HSM)	0.478	8.73	58.43	0.0171	Run No.814
Full size (Hull 064)	0.41	-	46.01	0.0217	Disc No. 1-Run No.062

The frequencies in the model scale for the Fn of 0.32 and 0.478 were used. A frequency was obtained by the interpolation by Froude numbers for Fn of 0.41, which was the voyage speed for the Data No. 062. The expected full-scale frequency for the second harmonic ship motion calculated from the towing tank test data was 0.022 Hz. The expected response frequency of the second harmonic ship motion was marked in the PSD so as to indicate the agreement with the measured values of the response frequency at full scale, as shown in Figure 6.19. The expected response frequency coincided well with the frequency band of the second harmonic ship motion in full scale, therefore the second harmonic ship motion conclusively resulted between model and full scale. This strongly suggest that the second harmonic ship motion exists.

6.4 Conclusion

The delivery voyage measurement of the INCAT 112 m $HULL$ 064 was extremely useful to integrate both experimental results and observations in order to assess the causes of the phenomena both in a laboratory and the actual sea environment.

Slam event and subsequent whipping behaviour were successfully recorded on both accelerometer and strain gauge sensors. According to the dynamic plot analysis using the measured data to duplicate the ship attitude, ship dynamic attitudes were discovered at a slam event. One explanation is that the slam event caused successful subsequent whipping which occurred when the vessel was in bow-down trim. The whipping phenomena predominately occurred at the aft strain gauges as opposed to the forward strain gauges.

Frequency response analysis by spectral analyses were conducted on the acceleration and strain

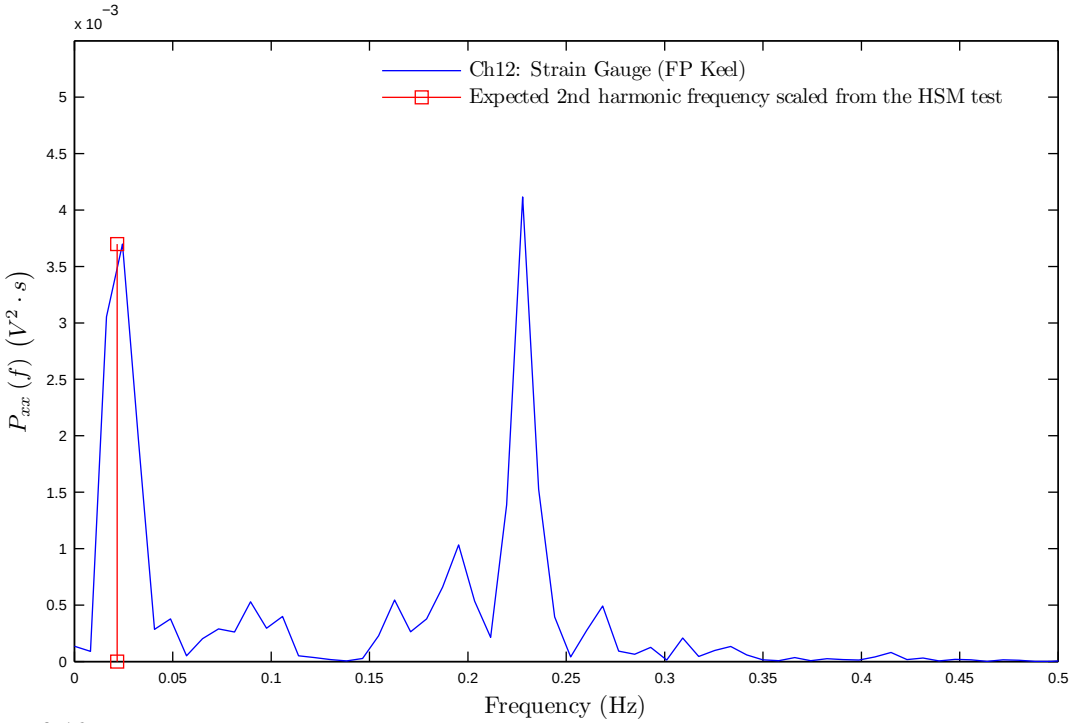

Figure 6.19: Expected second harmonic motion scaled from hydroelastic segmented model test occurred in the lower region of power spectrum density in full scale for the second harmonic motion at 0.022 Hz.

gauge data. Four accelerometer sensors were installed on the vehicle deck and four strain gauges were attached on the keels. The wave-induced responses and machinery vibratory responses were successfully examined. The wave-induced responses were subdivided into the ship motion responses, modal response of the vertical bending moment, and second harmonic ship motion response.

Three types of the wave-induced responses were identified from the delivery voyage data: ship motion response to encountering wave, second harmonic ship motion, and modal response of vertical bending moment. The response frequencies of ship motion to the encountered waves were the most dominate magnitudes in the PSD among the response frequencies of the VBM response and the machinery-induced response for the moderate waves with non-severe slam conditions.

Spectral analysis using power spectral density discovered the response modal frequency of vertical bending moment for INCAT 112 m Hull 064 which varied between 2.45 and 2.65 Hz on average, becoming higher as the displacement became lighter throughout the delivery voyage.

The PSD of the accelerometer sensor detected the response frequency peaks for the main engine rotational speed and its subharmonics, which matched against the calculated frequencies from the rotation speed of the main engine and jet shaft recorded in the delivery voyage log.

The subharmonic of the rotational speed of the jet shaft should be very close to the resonance

frequency of the VBM in order to cause the springing, therefore recording the voyage log data and measuring the sampling frequency to collect the machinery vibratory motion was valuable. In addition, it is recommended to avoid this kind of operational speed in order to reduce unnecessary fatigue.

The power spectral analyses showed that the modal response of the VBM can be induced by vessel speed even under calm water conditions. This phenomena was also discovered in the calm water test at the towing tank, which was discussed in Section 3.7. Hence, the modal response of the VBM for the vessel can be induced even by forward velocity without waves.
In order to identify the VBM component by eliminating the machinery associated components, it was learnt during the analysis that the informations of the machinery-induced responses was an essential data, although they are not primarily forcused.

The second harmonic ship motion was observed in full scale as well as in the model scale of the hydroelastic segmented model. The second harmonic ship motion was likely caused by hydrodynamic hull-lift oscillation similar to porpoising, a characteristic which is significant for ship directional stability.

A recommendation for a future project would be to place the accelerometer near the strain gauges in order to identify a more conclusive cause. It may also recommend the installation of a physical low-pass filter for the strain gauge measurement units.

A response subharmonic frequency of the jet shaft can be coincided with a response modal frequency of the VBM to cause the structural resonance. For example, as shown in the Table 6.2, operating the main engine at 650 RPM was observed in the resonance frequency of the VBM to cause unnecessary springing. In order to avoid springing, which results in fatigue of the ship structure, installing a real-time vibration monitoring and warning system would be extremely usefully to assist the operator in avoiding this unnecessary operational condition.

Chapter 7

Conclusions

A comprehensive study into the motions and loads experienced by large high-speed catamarans has been conducted. The primary conclusion of the work are presented, being split into the main three areas of study.

7.1 Hydroelastic Segmented Model

A novel design for a hydroelastic segmented model for a wave-piercer catamaran with a centre bow was designed in order to acquire the heave and pitch motions, global wave-induced loads and slam-induced loads. The HSM experiments have been successfully conducted in the towing tank at various wave heights and speeds.

Motions and wave load measurements were successfully achieved, hence the hydroelastic segmented model was successfully designed and built, in line with the primary objective. The load measurement mechanisms for the global wave-induced VBMs and slam-induced loads on the centre bow successfully functioned under the conditions of both the wave-induced and calm water flow-induced vibration. The extensive number of calibration tests also determined the good functionality of the HSM mechanisms.In the large wave, the HSM successfully demonstrated the slam with subsequent whipping at the fundamental modal frequency of the VBM.

Ship hydroelasticity was found to affect the vessel motions: the hydroelastic configuration reduced the resonant peak of the heave and pitch motion by 3 to 8%, when compared with the rigid configuration. The time history analysis of the heave, pitch, vertical acceleration, wave-induced VBM, and slam-induced force found a mutual interaction between the fluid-induced motion and structural loads. This mutual interaction was composed of the ship motions induced by the wave harmonic excitation, and the structural load response of the slam-induced impulse excitation with the subsequent whipping response.

The heave and pitch transfer function (TF) results showed strong non-linear responses with respect to the wave height at a constant speed. For the speed effects, strong non-linear responses of the motion to the forward velocity at a constant wave height were obtained; as the wave heights increased, the resonant peak magnitudes for both heave and pitch TF reduced.

Resonant peak comparisons of different wave heights and speeds, showed that the heave and pitch transfer functions for the 45 K_n condition were the maximum values of $z_a/\zeta_a = 1.8$ and $\eta_a/(k\zeta_{5a}) = 1.3$ at $H_w = 0.869\ m$.

A reduction of the response peak magnitude of the heave and pitch transfer function was observed as the wave heights became larger. This showed the effective function of the wave-piercer and centre bow. It confirmed that the hull feature of the wave-piercer catamaran that does not satisfy the linear assumption, resulted in a non-linear response. This non-linearity means that the superposition technique is not appropriate for obtaining the motion in irregular waves, hence the irregular wave model tests are essential for random sea conditions. This data is suitable for validation work on numerical simulations for the model scale. When using the motion responses from experiments, as the expected design values in the full scale, it is recommended confirmation of the numerical simulation in full scale, which is adjusted for damping factors due to Reynolds- and Eddie-making effects and so on. Geometrical similarity tests of the model could also be recommend in order to ensure that the motion transfer function can be used in the full scale.

The wave-induced VBMs on the demi-hull responded to waves in two different ways dependent upon the wave height. In the smaller waves, the wave-induced VBM was proportional to the wave height. In the larger waves, the wave-induced VBM was nearly proportional to the square of the wave height. The VBM did not show a linear relationship to the square of the forward velocity. Due to this variance in the three influential factors, three types of the non-dimensional coefficient for the wave-induced VBMs and slam-induced load for the load responses were proposed for each condition. The three influential parameters were the wave height, wave height squared and velocity squared for the non-dimensional coefficients. Although the slam-induced load was dominated by the vertical force, the vertical velocity was not used for non-dimensionalisation. Since the vertical velocity is difficult to obtain at a preliminary design stage, the forward velocity was used for the non-dimensional coefficient for the wave-induced VBM and slam-induced load.

In the condition of 38 K_n and $H_w = 4.032\ m$ of Run No.457, when the maximum response peak of VBM occurred, the transient VBM oscillation of the whipping phenomena was synchronised with the transient oscillation of the heave acceleration. This experimental result demonstrated that the HSM successfully achieved the ship hydroelasticity; the mutual interaction between fluid-induced motion and wave-induced structural loads. The motion and wave-induced loads of the HSM were induced by the wave harmonic excitation, and the large ship induced motion resulted in the slam impact excitation that caused the oscillation which was synchronised with the inertia of motions.

In the condition which resulted in the maximum response peak of the VBM response, the power spectral density of the spectral analysis on the wave-induced VBM, showed the harmonic series response of the encounter wave response frequency occurring up to the VBM resonant frequency. The experimental results strongly suggested that the ship hydroelastic modelling with scaling structural modal frequency is required to obtain the maximum response loads, since the loads depend on the mutual effects of ship motion and structural response. As a practical implication

of this phenomena, the power spectral analysis could be applied for a diagnostic or detection tool for worst-case scenarios of slamming events in full-scale operation. It could be implemented in a ship information monitoring system, as a warning system to minimise the structural resonance during operation.

Spectral and wavelet analysis were utilised to obtain the dry and wet VBM modal frequency responses for impact excitation tests. Spectral analysis identified the clear response frequency, but was not able to identify the transient modal shape. However, by employing wavelet analysis the transient modal shapes and response frequencies could be identified. It confirmed that the VBM resonant frequencies for dry and wet modes at zero speed in calm water occurred at 16.46 Hz and 13.45 Hz, respectively. It also confirmed that the fundamental mode of resonance for the VBM was excited.

Analysis on the slam resultant force position showed that as the wave height increased, at a constant speed, the slam resultant force position occurred further forward on the centre bow. As the speed increased at a constant wave height, the slam resultant force position occurred farther aft on the centre bow. Using the slam resultant force position and slam-induced force, the slam-induced moments at the elastic links were calculated and compared with the measured wave-induced VBM. The wave-induced VBM and slam-induced moment resulted in a clear linear relationship. This implied that the slam load can be calculated based on the VBM load. In addition, the VBM in large waves showed a linear relationship to the wave height squared.
Overall, the results of the HSM experiments provided critical data allowed the motion and load response to be developed.

7.2 Cross Demihull Loads Model

The cross demihull loads (CDL) model was designed to measure the structural loads between two demi-hulls of a catamaran vessel. It required a novel approach for measuring the pitch connecting, split, and pry moment along with a new the towing mechanism for the model. The NPL5b hull form was selected to obtain the motions and loads response in oblique seas.
Motion responses were found to be linear for heave, pitch and roll motion for the smaller wave heights relative to the ship draught, with respect to wave height. But with respect to the ship speed, the motion response TFs showed non-linearity to the wave height.

The CDL model successfully measured the pitch connecting moment and split moment between the two demi-hulls. For the pitch connecting moment and the split moment, a linear trend with respect to the wave height was observed. Although the split moment was smaller than the PCM, the load response showed a linear response trend around the peak region. The results showed that the novel towing mechanism and model were satisfactory in terms of the original design concept.

The moments was successful obtained by the novel design of CDL measurement system. The

motion sensor application with the acceleration correction based on the Euler transformation successfully provided motion data. From the HSM and PCM experiments, the conclusion could be drawn that the wave-induced load was nearly proportional to the wave height with a smaller wave height-to-draft ratio.

7.3 Delivery Voyage of INCAT 112 m

The full-scale measurements on INCAT 112 m Hull 064 during the delivery voyage contributed to the integration of both the experimental results and observations, in order to understand the cause of the ship hydrodynamics phenomena mutually in the laboratory and actual sea environments.

Slam events and subsequent whipping behaviour were successfully measured. The dynamic plot analysis indicated for the INCAT 112 m that the bow-down trim increased the chance of the slamming leading to a subsequent whipping response. In whipping, the aft strain gauge responded dominantly rather than the forward stain gauges. The full-scale results showed two phases for the increase of slam load at the event, and similar results also occurred in the model test. The full-scale slam event and model-scale slam event resulted in similar whipping phenomena induced by the slam impact excitation. Also the VBM resonant frequency occurred even in calm water, and it was presumed that the resonant frequency was induced by the machinery or the forward velocity. However, the response magnitude was small compared to the wave-induced vibration.

Power spectral analyses were performed to analyses the frequency response on all available data recorded during the delivery voyage from Australia to Japan; the identified response frequencies recognised the encountered wave frequency, the modal frequency of the vertical bending moment, the main engine rotational speed and its subharmonic and the subharmonic of the jet shaft rotational speed. These machinery response frequencies were identified, because the logged data provided the RPM for the machinery. Hence, by eliminating the machinery-dependent frequencies, the VBM frequency was identified. The response modal frequency variation of the vertical bending moment due to a change in the displacement was discovered. The response modal frequency increased from 2.45 to 2.65 Hz as the vessel displacement was reduced from 2250 to 1650 *tonnes* due to fuel consumption. As the mass reduced, the response frequency reduced.

The response frequency induced by machinery in the accelerometer sensor corresponded well with the logged data. These subharmonic response frequency is important to identify the vertical bending moment. Hence, the 20 Hz cut-off frequency was appropriate to include the main engine and jet shaft responses. In addition, recording the logged information of the machinery conditions was essential during the voyage.

A second harmonic ship motion was observed, with similar behaviour was indentified in the

calm water tests for the hydroelastic segmented model. The expected response frequency of the second harmonic ship motion scaled from the model test coincided with the response frequency of the second harmonic ship motion in full scale. The second harmonic ship motion was found to be similar to porpoising. Since the high speed generates the hydrodynamic lift of the hull, the variation in the lift affects the oscillation of the second harmonic ship motion.

7.4 Implications of Research

This research has provided critical data for the motions, wave loads and structural vibration of large high speed catamarans in large waves. The data can be utilised in many areas by designers, classification societies and vessel operators.

The comprehensive seakeeping experimental data, set with a wide range of wave height and speeds, are available for researcher, designers and classification societies to validate numerical seakeeping prediction codes. In particular, these data, under the controlled environment of the towing tank, forms a basis of the ship motion data to validate codes confidently for catamarans with wave-piercer and centrebow. Since the motion responses were strongly non-linear, the availability of many cases for the wave heights and speeds are extremely advantageous.

The wave load data, obtained from the hydroelastic segmented model, contributes to the more reliable prediction of the design loads for structural optimisation. The loads can be used as new design load cases in finite element analysis (FEA) on new vessel designs. The industry partner of this project has already saved approximately 200 *tonnes* of aluminium structures for a similar vessel, based on these experiment results.

The dominate nature of slam loads in generating the large VBM was identified, therefore the researchers and designers should investigate the key influential parameters of the centrebow shape which can be lead to reducing the motions and severe slam occurrence.

Motion and wave loads responses data can be compared with current case loads obtained by the current regulations and rules of classification societies. This will provide the more confidence to expand the design and operational limits. Motion response data can be assed by operators and societies against current route operating manuals. The improving operational limits will results in the increasing the operational capability with confidence in large waves. This will be extremely beneficial for the operator to improve the customer satisfaction with a higher operational rate.

For INCAT 112 m Hull 064, the VBM resonant frequency of between 2.45 to 2.65 Hz was found during the delivery voyage while the displacement varied from 2250 to 1650 *tonnes*. Knowledge of this frequency can contribute to avoiding the springing of demihull due to the rotational vibration of the main engines and water jet shaft. During the delivery voyage, 650 RPM of the main engine and 300 RPM of jet shaft caused the harmonic vibration on the vessel. The

subharmonics frequency of the jet shaft rotation was 2.5 Hz, and this matched with the VBM resonant frequency, hence it resulted in springing. Avoiding the rotational speeds causing the springing will extend the fatigue life of the ship structure.

The full scale measurement were found to be very useful, but it is also difficult to control the environment for the ideal conditions, and many unexpected incidents will disturb the measurement program. The delivery voyage of the Hull 064 was in extremely small waves, except for the Bass Strait. It is clear that establishing an experimental methodology to measure the wave-induced VBM loads and slam loads for high speed catamaran is extremely useful for designers and classification societies to ensure that the design loads for new ship design can be obtained in the future.

A novel experimental methodology to successfully measure the cross demihull loads of a catamaran was established. This data set also forms a basis of the validation data, for example, the numerical code and this test methodology can be extended for other directions and conditions. Large wave height with the slam events; the different oblique angles and random sea conditions can be tested.

7.5 Recommendations

Use of the experimental HSM for the load measurement is strongly recommended to model ship hydroelasticity. The resonance frequency scale of the VBM can be modelled successfully, however flexural rigidity scaling is challenging. Installing the accelerometer sensor at each segment would be useful to calculate the inertia force of each segment.

In order to measure the VBM loads without the slamming influence and to ensure the scaling of the wave-induced loads due to global waves, three different sizes of hydroelastic models could be experimented for the geometrical similarity (GeoSim) test. This would increase confidence in scaling the measured load in the model scale to the full scale. Transom hollows and rooster tails were generated at the stern, and this may have Reynolds effects due to the boundary layer generated around the stern area. Water separation at the stern generates the damping force with heave and pitch oscillatory motions, this damping mechanism could be investigated. Therefore, the GeoSim test and numerical simulation would be beneficial to increase confidence.

Similarly, a slamming dedicated model could be assessed with a forcing oscillatory device. Although the hydroelasticity would be eliminated, the rigid demi-hulls and centre bow with load sensors would provide useful information for the slam load.
The systematic approach investigation on different centrebow shape effects on the ship motion and slam loads will be extremely usefully for advancing the centrebow shape. The centrebow arch height, bow jaw location, centrebow buoyancy distribution and centrebow truncation bulkhead position can be investigated. The reduction in slam loads and occurrence and motions will results in the increasing the operational envelope in large waves. This will be extremely beneficial for the operator to improve the customer satisfaction with a higher operational rate.

For the full-scale measurement, the accelerometer could be placed adjacent to a strain gauge to obtain the displacement and acceleration information. More strain gauges and accelerometer sensor units could be placed over the keel and deck to form a sensor array grid for measuring the modal shape experimentally. The data acquisition system could be integrated to the ship information monitoring system, and the comprehensive integration with the monitoring data of the propulsion control system and ride control system, would be useful to understand the relationship among the measured data.

The delivery voyage was found to be an excellent opportunity to obtain and to diagnostic the ship structure response with the large displacement variation due to fuel consumption. This is strongly recommended for future vessels to be delivered. An non-recommenced operational RPM speeds based on the ship displacement variation can be provided to operators. In addition, a dynamic monitoring warning system can be developed and installed to measure the engine and jet shaft rotational frequency and keel vibration. Operator can utilised the warning system to select appropriate operational speeds for machineries. For the use of classification society and operators, such kind of the dynamic monitoring warning system can provide the information of severe whipping and springing time to asses the structural life and its durability period for a planned maintenance system.

References

Aarsnes, J. (1996), Experimental techniques for local and global hydroelastic effects on ships, *in* 'Seminar on Hydroelasticity in Marin Technology', Trondheim, Norway.

Allday, W. (1991), Methods of avoiding common problems with aluminium structures, *in* 'Proceeding of the FAST'91 Conference', Trondheim, Norway, pp. 765–780.

Amin, W. (2009), Non-Linear Unsteady Wave Loads on Large High-Speed Wave Piercing Catamarans, PhD thesis, The University of Tasmania.

Barenbaltt, G. (1996), *Scaling, self-similarity, and intermediate asymptotics*, 1 edn, Cambridge University Press, Cambridge, Cambridge.

Bishop, R. & Price, W. (1979), *Hydroelasticity of Ships*, 1 edn, Cambridge University Press, Cambridge, Cambridge.

Chamberlin, K. (2008), Characterisation of high-speed catamaran slam events in irregular waves, Technical report, Thesis, The University of Tasmania, Australian Maritime College.

Colwell, J., Datta, I. & Rogers, R. (1995), Head seas slamming tests on a fast surface ship hull form series, *in* 'Proceeding of RINA Seakeeping and Weather', London,UK.

Couser, P. (1996), An investigation into the performance of high-speed catamarans in calm water and waves, PhD thesis, The University of Southampton.

Davis, M. (2005), 'Notes on triple beam system'.

Davis, M. & Holloway, D. (2003), 'The influence of hull form on the motions of high speed vessels in head seas', *Ocean Engineering* **30**, 2091–2115.

Davis, M., Holloway, D. & Watson, N. (2005), Validation of non-linear wave loads predicted by time domain methods in sea trials of an 86 m catamaran., *in* 'Proceeding of the FAST'05 Conference'.

Davis, M., Watson, N. & Holloway, D. (2004), 'Measurement and prediction of wave loads on a high speed catamaran fitted with active stern tabs', *Marine Structure* **17**, 503–535.

Davis, M., Watson, N. & Holloway, D. (2005a), 'Measurement of response amplitude operators for an 86 m high-speed catamaran', *Journal of Ship Research* **49**, 121–143.

Dessi, D., Mariani, R., & Coppottelli, G. (2007), 'Experimental investigation of the bending vibrations of a fast vessel', *Australian Journal of Mechanical Engineering* **4**(2), 125–144.

Dessi, D., Mariani, R., Coppottelli, G. & Rimondi, M. (2005), Experimental identification of wet bending modes with segmentated model tests, *in* 'Proceeding of the FAST'05 Conference', St. Petersburg, Russia, pp. 1–8.

Dessi, D., Mariani, R., Gala, F. & Benedetti, L. (2003), Experimental analysis of the wave-induced response of fast monohull via a segmented-hull model, *in* 'Proceeding of the FAST'03 Conference', Ischia island, Italy, pp. 75–82.

Doctors, L. (1986), Application of the collocation and galarkin approaches to potential-flow solution by the boundary element method, *in* 'Proceeding of the Ninth Australian Fluid Mechanics Conference', Auckland, New Zealand, pp. 400–403.

Doctors, L. (1987), Application of the boundary-element method to bodies oscillating near a free surface, *in* 'Proceeding of International Symposium on Computational Fluid Dynamics ISCFD-Sydney', pp. 377–386.

Doctors, L. (1999), The hydros/4.1 programs: Description and documentation, Technical report, The University of New South Wales.

Faltinsen, O. (1971), A rational strip theory of ship motions: Part ii, Technical report, Department of Naval Architecture and Marine Engineering College of Engineering, The University of Michigan, No.113.

Faltinsen, O. (1974), 'A numerical investigation of the ogilvie-tuck formulas for added mass and damping coefficients', *Journal of Ship Research* **18**, 73–84.

Faltinsen, O. (2005), *Hydrodynamics of High-Speed marine Vehicles*, 1 edn, Cambridge University Press, Cambridge, Cambridge.

Faltinsen, O. & Zhao, R. (1991), 'Numerical prediction of ship motion at high forward speed', *Philosophical Transactions: Physical Sciences and Engineering, The Royal Society* **334**, 241–252.

Fletcher, C. (1991), *Computational Techniques for Fluid Dynamics*, 2 edn, Springer, Verlag, Germany.

Ge, C., Faltinsen, O. & Moan, T. (2002), Global hydroelastic response of a catamaran due to wetdeck slamming accounting for forward speed, *in* 'Proceeding of 21st International Conference on Offshore Mechanics and Arctic Engineering', Oslo, Norway, pp. 221–230.

Ge, C., Faltinsen, O. & Moan, T. (2005), 'Global hydroelastic response of a catamaran due to wetdeck slamming', *Journal of Ship Research* **49**, 24–42.

Gerritsma, J. & Beukelman, W. (1963), 'Distribution of damping and added mass along the length of a ship model', *International Shipbuilding Progress* **10**, 73–84.

Gerritsma, J. & Beukelman, W. (1967), 'Analysis of the modified strip theory for the calculation of ship motions and wave bending moments', *International Shipbuilding Progress* **14**, 319–337.

Grande, K. & Xia, J. (2002), Prediction of slamming occurrence on catamaran cross structure, *in* 'Proceeding of 21st International Conference on Offshore Mechanics and Arctic Engineering', Oslo, Norway, pp. 1–9.

Handbook, N. (2010), Measurement uncertainty analysis principle and methods, nasa measurmenet quality assurance handboook annex, Technical report, National Aeronautics and Space Administration, NADA-HDBK-8739,19-3.

Hansen, P., Jensen, J. & Pedersen, P. (1995), Long term springing and whipping stresses in high speed vessels, *in* 'Proceeding of the FAST'95 Conference', Luebeck-Travemuende, Germany, pp. 473–485.

Heggelund, S. & Moan, T. (2002), 'Analysis of global load effects in catamarans', *Journal of Ship Research* **46**, 81–91.

Heggelund, S., Moan, T., Hoff, J. & Oma, S. (2001), Practical calculation of global design loads and load effects for large high speed catamarans, *in* 'Proceeding of the FAST'01 Conference', Southampton, UK, pp. 203–217.

Hermundstad, O. (1995), Theoretical and Experimental Hydroelastic Analysis of High Speed Vessels, PhD thesis, The Norwegian Institute of Technology.

Hermundstad, O., Aarsnes, J. & Moan, T. (1995a), Hydroelastic analysis of a flexible catamaran and comparison with experiment, *in* 'Proceeding of the FAST'95 Conference', Luebeck-Travemuende, Germany, pp. 487–500.

Hermundstad, O., Aarsnes, J. & Moan, T. (1997), Hydroelastic analysis of a high speed catamaran in regular and irregular waves, *in* 'Proceeding of the FAST'97 Conference', Sydney, Australia, pp. 447–454.

Holloway, D. (1998), A High Froude Number Time Domain Strip Theory Applied to the Seakeeping of Semi-SWATHs, PhD thesis, The University of Tasmania.

Holloway, D., Lavroff, J. & Davis, M. (2006), Global structural design of hydrodynamics models, *in* 'Proceeding of 5^{th} International Conference on High Performance Marine Vehicles', Launceston, Australia, pp. 253–261.

Hughes, O. (1998), *Ship Structural Design, A Rationally-Based, Computer-Aided Optimisation Approach*, Society of Naval Architects and Marine Engineers, New Jersey,USA.

ITTC (1999), Testing and extrapolation methods, high speed marine vehicles, structural loads, Technical report, International Towing Tank Conference, 22nd, HSMV Committee.

Kaplan, P. (1991), Structural loads on advanced marine vehicles, including effects of slamming, *in* 'Proceeding of the FAST'91 Conference', Trondheim, Norway, pp. 781–795.

Kaplan, P. & Dalzell, J. (1993), Hydrodynamic loads prediction (including slamming) and relation to structural reliability, *in* 'Proceeding of Ship Structure Symposium'93, SNAME', Arlington, VA, USA, pp. A1–A10.

Kapsenberg, G. & Brizzolara, S. (1999), Hydro-elastic effects of bow flare slamming on a fast monohull, *in* 'Proceeding of the FAST'99 Conference', Seattle,USA, pp. 699–708.

Keuning, J. (1990), 'Distribution of damping and added mass along the length of a ship model moving at high forward speed', *International Shipbuilding Progress* **37**(410), 123–150.

Keuning, J. (1994), The Nonlinear Behaviour of Fast Monohulls in Head Waves, PhD thesis, Technische Universiteit Delft.

Korvin-Kroukovsky, B. (1955), 'Investigation of ship motions of a ship in regular waves', *Trans. of SNAME* **63**, 590–632.

Korvin-Kroukovsky, B. (1961), *Theory of seakeeping*, Society of Naval Architects and Marine Engineers, New York,USA.

Korvin-Kroukovsky, B. & Jacobs, W. (1957), 'Pitching and heaving motions of a ship in regular waves', *Trans. of SNAME* **65**, 590–632.

Kvålsvold, J. & Faltinsen, O. (1993), Hydroelastic modelling of slamming against the wetdeck of a catamaran, *in* 'Proceeding of the FAST'03 Conference', Yokohama, Japan, pp. 681–697.

Kväolsvold, J., Svensen, T. & Hovem, L. (1996), 'Bow impact loads on ro-ro vessels', *Transactions of the Royal Institution of Naval Architects* **222**, 33–50.

Kyyrö, K., Hakala, M., Helasharju, H., Rantanen, A. & Holopainen, T. (1997), Determination of structural dimennstioning loads of a fast catamaran using rigidbackbone segmented model testing techniques, *in* 'Proceeding of the FAST'97 Conference', Sydney, Australia, pp. 317–323.

Lavroff, J. (2009), The Slamming and Whipping Vibratory Response of a Hydroelastic Segmented Catamaran Model, PhD thesis, The University of Tasmania.

Lloyd, A. (1989), *Seakeeping: Ship Behaviour in Rough Weather*, Ellis Horwood Limited, New York.

Maeda, H. (1991), 'Modelling techniques for dynamics of ships', *Philosophical Transactions, The Royal Society* **334**, 307–317.

McTaggart, K., Datta, I., Stirling, A., Gibson, S. & Glen, I. (1997), 'Motion and loads of a hydroelastic frigate model in servere seas', *Trans. of SNAME* **105**, 427–453.

Miyamoto, T. & Tanizawa, K. (1984), 'A study of the impact load on ship bow', *Trans. Society of Naval Architecture of Japan* **156**, 297–305.

Miyamoto, T. & Tanizawa, K. (1985), 'A study of the impact load on ship bow (2nd report)', *Trans. Society of Naval Architecture of Japan* **158**, 270–279.

Moan, T., Skallerud, B. & Skjastad, O. (1991), Structural analysis and design of hydrofoils and struts, *in* 'Proceeding of the FAST'91 Conference', Trondheim, Norway, pp. 743–764.

Nakos, D. & Sclavounos, P. (1994), 'Kelvin wakes and wave resistance of cruiser- and transom-stern', *Journal of Ship Research* **38**, 9–29.

Ogilvie, F. & Tuck, E. (1969), A rational strip theory of ship motions: Part i, Technical report, Department of Navla Architecture and Marine Engineering College of Engineering The University of Michigan, No.013.

Okada, S. & Sumi, Y. (1995), 'Experimental study on the maximum pressure and duration time of the horizontal water impact of flat plate', *Trans. Society of Naval Architecture of Japan* **178**, 381–389.

Økland, O., Moan, T. & Aarsnes, J. (1998), Structure response in large twin hull vessels exposed to severe wet deck slamming, *in* 'Proceeding PRADS Conference', The Hague, pp. 69–78.

Olkinuora, P., Knuuttila, E., Hakala, M., Rintala, S. & Vuorio, J. (1991), Structural design of an aluminium missile boat, *in* 'Proceeding of the FAST'91 Conference', Trondheim, Norway, pp. 727–741.

Pedersen, T. (2000), Wave Load Prediction- a Design Tool, PhD thesis, Technical University OF Denmark.

Salvesen, N., Tuck, E. & Faltinsen, O. (1970), 'Ship motions and sea loads', *Trans. of SNAME* **70**, 250–287.

Sebastiani, L., Valdenazzi, F., Grossi, L. & Kapsenberg, G. (2001), A theoretical / experimental investigation of the slamming pressures on fast monohull vessels, *in* 'Proceeding of the FAST'01 Conference', Southampton, UK, pp. 109–116.

Smith, W. (1967), 'Computation of pitch and heave motions for arbitrary ship forms', *International Shipbuilding Progress* **14**, 267–291.

Smith, W. & Salvesen, N. (1970), 'Comparison of ship-motion theory and experiment for destroyer with large bulb', *Trans. of SNAME* **14**, 67–76.

Sueoka, H., Tozawa, S., Sakai, F. & Kabata, T. (1995), Structural responses of mitsubishi supershuttle 400, *in* 'Proceeding of the FAST'95 Conference', Luebeck-Travemuende, Germany, pp. 501–511.

Takagi, K. (1994), 'Influence of elasticity on hydrodynamic impact problem', *Journal of the Kansai Society of Naval Architect, Japan* **222**, 99–106.

Takemoto, H., Miyamoto, T., Y., H., Oka, S. & Ohsawa, N. (1993), Slamming impact loads and hull-girder response of a large-speed craft in waves, *in* 'Proceeding of the FAST'03 Conference', Yokohama, Japan, pp. 723–731.

Thomas, G., Davis, M., Holloway, D., Roberts, T., Matsubara, S., Lavroff, J., Amin, W., Chamberlin, K. & Dove, T. (2009), Characterisation of slam events of a high-speed catamaran in regular waves, *in* 'Proceeding of the FAST'09 Conference', Athens, Greece.

Thomas, G., Davis, M., Holloway, D., Watson, N. & Roberts, T. (2003a), 'Slamming response of a large high-speed wave-piercer catamaran', *Marine Technology* **40**, 126–140.

Thomas, G., Winkler, S., Davis, M., Holloway, D., Matsubara, S., Lavroff, J. & French, B. (2010), 'Slam events of high-speed catamarans in irregular waves.', *Journal of Marine Science and Technology, Society of Naval Architecture of Japan* **Accepted: 12 August 2010**.

Thomas, T., Davis, M., Holloway, D. & Roberts, T. (2003), Transient dynamic slam response of large high speed catamarans, *in* 'Proceeding of the FAST'03 Conference', Ischia island, Italy, pp. 1–8.

Thomas, T., Davis, M., James, W. & Roberts, T. (2001), Slamming response of large high speed wave catamaran, *in* 'Proceeding of the FAST'01 Conference', Southampton, UK, pp. 1–8.

Tønnessen, R., Vada, T. & Nestegård, A. (1993), A comparison of an extended strip theory with a three-dimensional theory for computation of response and loads, *in* 'Proceeding of the FAST'03 Conference', Yokohama, Japan, pp. 671–680.

Vada.T. (1995), Hydroelastic response of ships with forward speed in waves, *in* 'Proceeding of the FAST'95 Conference', Luebeck-Travemuende, Germany, pp. 463–471.

von Karman, T. (1929), The impact on seaplane oats during landing, Technical report, NACA, Technical Note, No.321, SITDL, TR1854.

Vossers, G., Swaan, W. & Riken, H. (1961), 'Vertical and lateral bending moment measurements on series 60 models (n.s.m.b. wageningen holland n.200)', *International Shipbuilding Progress* **8**(3).

Wagner, H. (1932), 'Ueber stoss-und gleitvorgaenge an der oberflache von flussigkeiten', *Zeitschrift fur Angewandte Mathematik und Mechanik* **12**, 193–215.

Wahab, I. R. (1967), Amidships forces and moments on a cb = 0.80 series 60 model in waves from various directions, Technical report, Netherlands Ship Research Centre, Report 100S.

Watanabe, I., Tanizawa, K. & Sawada, H. (1988), 'An observation of bottom impact phenomena by means of high speed video and transparent model', *Transaction of the Society of Naval Architecture of Japan* **164**, 120–126.

Whelan, J. (2004), Wetdeck Slamming of High-Speed Catamarans with a Centre Bow, PhD thesis, The University of Tasmania.

Winkler, S. (2009), Classification of high-speed catamaran slam events in irregular waves, Technical report, Thesis, The University of Tasmania, Australian Maritime College.

Wu, M.-K., Aarsnes, J., Hermundstad, O. & Moan, T. (1997), A practical prediction of wave-induced structural reponses in ship with large amplitude motion, *in* 'Proceeding of the Twenty-First Symposium on Naval Hydrodynamics', Fukuoka, Japan, pp. 438–452.

Wu, M.-K., Hermundstad, O. A. & T., M. (1993), Hydroelastic analysis of ship hulls at high forward speed, *in* 'Proceeding of the FAST'03 Conference', Yokohama, Japan, pp. 699–710.

Yamaoto, Y. (1980), Structure-fluid interaction problems for a ship among waves, *in* 'Proceeding of International Union of Theoretical an Applied Mechanics', Toronto, Canada, pp. 209–222.

Yoshimoto, H. andOhmatsu, S., Hoshino, K. & Ikebuchi, T. (1997), 'Slamming load on a very large floating structure with shallow draft', *Journal of Marine Science and Technology, Society of Naval Architecture of Japan* **2**, 163–172.

Appendix A

INCAT 112 m Class: Functions

The INCAT 112 m class is a catamaran type of high-speed vessel. A catamaran has two hulls one on the starboard side and one on the port side, and each hull is called a demihull. Starboard and port side demi-hulls are connected through a cross-bridge deck. The cross-bridge deck is also called a slamming deck in some contexts. The cross-bridge deck provides an extremely large and wide area compared to a conventional monohull deck. The widely spread demihull separation with the cross-bridge deck, contributes to the high stable capability under listing conditions. Hence, the stability of the catamaran is generally appreciated and utilised for large high-speed vessels. Since the cross-bridge can generate enough volume space for cargo and passengers, demi-hulls of the catamaran can be significantly thinner than monohull ships. The thinner demi-hull can contribute to generating less wave-making resistance by coalescing innovative features, such as a wave-piercer bow. The wave piercer is a fine sharp bow, as it literary penetrates through some ranges of wave. Thus, the wave making resistance can decline to an extremely small portion in the high-speed range compared with other components of resistance, such as frictional or viscous resistance. The wave piercer penetrating through the wave reduces the ship motion significantly, therefore, it reduces the increase in resistance due to the wave as well. As the wave-piercer bow is equipped at the tip of the thinner bow of the demi-hull, the wave-piercer bow clearly possess reduced reserve buoyancy compared with the bow of a conventional monohull. Especially in the case of following seas, the lack of reserve buoyancy of the wave-piercer bow might cause the problem of a nosedive. In order to avoid this potential problem, a centre bow can be equipped between the starboard and port side wave-piercer bow. The centre bow provides the reserve buoyancy, when sea conditions require this function to ensure the safety of the vessel. As the bow of the vessel happens to plummet deep into the water, the centre bow also submerges into the water and simultaneously generates extra buoyancy to lift up the bow of the vessel. This innovative function of the centre bow has been found to perform well in real sea conditions. The reliance on the reserve buoyancy ensures the safety and confidence in the high-speed operated vessel.

The features of the centre bow and wave-piercer bow result in a unique hull shape around the bow region. The centre bow arch is a concave surface region facing the water surface. The bow jaw is a concave shape of leading edge between the centre bow and wave-piercer bow. The centre bow arch is exposed to the slamming in large waves.

The centre bow has a significant purpose for achieving high-speed ferry operation in large waves. In order to achieve the high-speed operation, the demi-hull is equipped with the wave-piercer bow. The wave-piercer bow is shaped like a sharp and slender spear. The wave-piercer bow penetrates into some waves, therefore, the vessel avoids climbing over the waves. As a result, ship motion is reduced, and added resistance can be reduced as well. The centre bow was initially developed to avoid the nosedive, when the large wave lifts the transom of the vessel in following seas. Since the wave-piercer bow catamaran features a thinner bow, its reserve buoyancy is smaller compared with the reserve buoyancy of conventional hulls. Also the demihull is significantly thinner than a conventional monohull ship. The lack of buoyancy on the wave-piercer bow is countered by equipping the catamaran with a centre bow. The centre bow can provide the reserve buoyancy when responding to certain sea conditions.

The centre bow has a significant purpose for achieving high-speed ferry operation in large waves. In order to achieve the high-speed operation, the demi-hull is equipped with the wave-piercer bow. The wave-piercer bow is shaped like a sharp and slender spear. The wave-piercer bow penetrates into some waves, therefore, the vessel avoids climbing over the waves. As a result, ship motion is reduced, and added resistance can be reduced as well. The centre bow was initially developed to avoid the nosedive, when the large wave lifts the transom of the vessel in following seas. Since the wave-piercer bow catamaran features a thinner bow, its reserve buoyancy is smaller compared with the reserve buoyancy of conventional hulls. Also the demihull is significantly thinner than a conventional monohull ship. The lack of buoyancy on the wave-piercer bow is countered by equipping the catamaran with a centre bow. The centre bow can provide the reserve buoyancy when responding to certain sea conditions.

Appendix B

Building of the Hydroelastic Segmented Model

In addition to numerous refinements during the design stage, the hydroelastic segmented model also went through the following stages during the building phase:

1. Frame and bulkhead cut out for the male plug.
2. Building the male plug.
3. Building the female mould from the male plug.
4. Layering up the carbon fibre and PVC core on the female mould.
5. Embedding the internal structure.
6. Segmentation cut.
7. Building appendatage.

The male plug was made of timber planking and a frame arrangement in order to produce the female mould. Using the female mould, the hull surface of the experimental model was layered up with carbon fibre and core materials. After the outer surface of the model was extracted from the female mould, the assembly of the backbone beam, frame and bulkhead were installed into the model. Once the internal structure of the model was complete, the segmentation cut was produced. The model was painted in the AMC towing tank standard colour of yellow.

Prior to building the male plug, the half frames were cut out using the 3D CNC machine at the School of Architecture at the University of Tasmania. The 3D CNC machine is capable of cutting a section out of a large size (2400 x 1200 mm) plywood sheet. The program, called Visual Mill, controls the CNC machine for the cut-out. Prior to the CNC machine cut-out, the nesting of the half frame was required. The nesting was carried out in the AutoCAD program to create the input data for the CNC machine. The input ?les used the dxf format. The geometry in the file should conform with Polyline and Plygon with closed loops. Generally, the rotational drawing direction of the polyline loop should be constant for all the geometries drawn in the files. The thickness of the plywood sheet used was 10 mm. Since the planking was to be carried

out at the next step, a margin of 3 mm needed to be removed from the half frames, where the planking was to be carried out.

Next, the framing was carried out to form the male plug. With the horizontal plywood sheet as a base, a vertical wall was constructed out of a plywood sheet. On the each side of the vertical wall, the half frames were placed according to their own locations for starboard and port side. Once the framing process was complete, the planking was carried out. The planking was made of many thin strips of timber, 3 mm thick. Filler was used to fill the gaps in the planking surface, and then sanded down. When a smooth surface was obtained, the epoxy resin was applied on the planked surfaces of the male plug, followed by a finishing sand. When the male plug was complete, the vertical wall had an excess area well out of the surface of the male plug, as this was important for the alignment mechanism. The male plug was finished as such a statuesqueness.

The next stage was to build the female mould. The female mould was made using the shape of the male plug, and was made of a glass fibre layer and resin. Firstly, the PVA releasing agent was applied over the surface of the male plug, and then two layers of gel coat were applied. Next, the fibreglass sheet and resin were applied. The fibreglass was laid over, not only the hull surface, but also over the vertical wall. Hence, the vertical wall parts of the female mould on both sides, matched each other after the male plug was removed. Once the resin was cured and hardened, the female mould was ready to be removed. But before removing this, the alignment bolt holes were drilled on the vertical walls of the excess area. Since the alignment mechanism with bolts and holes was prepared before releasing the male plug from the female mould, the female mould was aligned using the alignment mechanism after removal of the male plug. Once this was done, any cavities were filled and sanded to obtain a smooth surface.

When the female mould was complete, the next step was to build the actual model. The PVA release agent was applied to the surface of the female mould, and two layers of gel coat spread over the surface, then a carbon ?bre woven mat sheet and resin was applied. The sheets of the closed-cell core material were laid over the carbon fibre woven mat sheet, becoming the outer surface of the model. Therefore, the typical layering of the materials from the outer to inner side of the model, were two layers of gel coat, a carbon fibre sheet, the core material, and a carbon fibre sheet. The number of extra carbon fibre layers applied depended on the location of the geometry, if it was required. When excessive carbon composite was applied, the excess composite was removed and cut away from the edge of the female mould, so that the starboard and port sides of the female moulds could be matched to join the carbon composite surface on both sides. When joining the starboard and port sides, the alignment mechanism was utilised. The alignment mechanism of bolting up both sides contributed to pressurising the composite surfaces in order to assist adhesion. Once the bonding process of both sides of the composite was complete, the female mould was removed. Now the carbon fibre composite hull appeared. Any cavities were filled with the filler and sanded down to a smooth surface.

Internal structures such as the frame and bulkhead were required, and the carbon fibre composite sheet was cut out to its required shape. The carbon sheet was vacuum bagged to make the sheet thin and remove excessive resin. Prior to cutting out the frame, the frame design and nesting were carried out. Firstly, the margin on some edges of the frame, where it had contact with the hull surface and gannel, needed to be removed. 3.5 mm was removed as a margin, which was equivalent to the hull thickness which was made from the carbon fibre and PVC core composite. After re-trimming the frame and bulkhead, the nesting work was carried out. Good nesting contributes to reduced waste material, thus saving costs. The nesting was carried out in the AutoCAD program.

The backbone beam was gently tucked into the frames and bulkheads as a unit, for the demi-hull. The unit should be placed in the carbon fibre composite hull. However, the inner surface of the carbon composite hull was not a smooth surface, hence it required readjustment on the edge of the frame and bulkhead. It needed several readjustments to obtain the appropriate placement of the backbone beams into the hull. Once the backbone beam, frame and bulkhead were set into the required position in the demi-hull, the centre bow segments were also attached to the cantilever beam. Adjustment was carried out until the centre bow was placed in the appropriate position.

Once the frame and bulkhead were glued into the demi-hull and centre bow using the resin filler, the return decks (with a width of 25 mm) were installed. The trim tab was attached on the transom wall. Since the trim tab was recessed into the transom, a cut-out was made on the transom walls and a small area at the bottom of the hulls. Once the trim tab unit was placed in the required position, the base unit of the trim tab was fixed to the hull. The trim tab was designed to be replaceable.

Finally, the segmentation cut was made after removing the solid link for assembly. The demi-hull was cut between two adjacent bulkheads. The lips of the hull surface were removed and resin was used to seal any cavities on the watertight bulkhead, which may be exposed to water. Finally, the surface was painted yellow.

Building the hydroelastic segmented model from carbon fibre was mainly carried out by the AMC model maker, Stuart Phillips, under supervision and instruction from the author.

Appendix C

Detailed Mass and Mass Moment of Inertia Distribution

The components that related to the tow mechanism are considered as point mass loaded at the hinge points of the tow posts, therefore the mass moments of inertial about its were not considered. The individually measured mass properties and mass properties that were obtained from the Rhino model are presented in Table C.1.

The local coordinate systems for the location of the centre of gravity are based on its segments. The origins of the coordinate systems are set at the intersection of the longitudinal transoms, the baseline and vessel centre-line. The mass moment of inertia was obtained about its centre of gravity. In the table, "R" and "PM" in the column for "Swing period" indicates the measurement method of mass properties. "R" indicates that the mass properties were obtained from the Rhino Model and "PM" indicates that the mass was measured by scales and treated as a point mass.

In order to determine the mass moment of inertia, there are two ways of determining the mass properties. The first method is to experimentally measure the entire segment assembly, and the second method is to measure each individual component of the segment and calculate the assembled value for the segment. The first method causes a problem with the assembled forward and aft segment due to the cables attached to the elastic links. Therefore, the mass, the location of centre of gravity and mass moment of inertia were difficult to measure accurately. In order to avoid this error associated with the mass properties of the cables, the second method was used to calculate the input values for the mechanical dynamics system with three rigid bodies and two elastic links. The aft segments were not transversely connected, therefore the mass properties were determined by the second method. The mass properties for the assembled aft segment were calculated, since the mass properties of the starboard and port side were summed to form the aft segment for the mechanical dynamics system. Although the second method required many measurements of the mass properties, it increased confidence in the obtained values.

The measurements were conducted extensively based on the segments and entire assembled model. All the carbon fibre composite segments were individually measured. The location of the centre of gravity was determined by the balance mechanism on the rod. The mass moment

of inertia was obtained on the individual segment by the bifilar method. Since the mechanical dynamic method of calculating the natural frequency utilises the three rigid body system, both sides of the demi-hull is considered as a single rigid body in terms of simplifying the inputs. Because the forward segments and aft segment could not be measured as one single rigid body, the segments were decomposed into the individual components to measure the mass, centre of gravity and mass moments of inertia. When the components could not use the bifilar method, the mass moment of inertia was obtained by the Rhino model. The Rhino can produce the volume moment of inertia, to which a density of aluminium of $2700kg/m^3$ was multiplied to gain its mass moment of inertia. In addition to the problem associated with the extra mass of the strain gauges, the other reason why the Rhino model data was used, was that the bifilar method was rather difficult to apply to the pitch radius of gyration on a segmentation, which is assembled with both starboard and port side demi-hulls. The difficulties arised from the curved side hull shapes around the bow area, so that it was rather difficult to parallel the bifilar beam and the experimental model segments due to each centre of gravity being too far apart from each other. In addition, the centre of gravity was rather difficult to determine as an assembled segment. Therefore, each individual demi-hull measurement was conducted to increase the confidence. Since some components were very small, in order to find out the centre of gravity and radius of gyration, the Rhino model was utilised to determine these values. The total mass summed the mass of both individually measured values and the Rhino model values of all parts of the mid segments, then compared to the mass of the assembled mid segments and the difference was only 4 grams. Hence, using the Rhino model increased the accuracy of the mass distribution measurement. The components that related to the tow mechanism were considered as a point mass loaded at the hinge points of the tow posts, therefore their mass moments of inertia were not considered. The individually measured mass properties and mass properties that were obtained from the Rhino model are presented in Table C.1 in Appendix C.

Table C.1: Mass moment of inertia calculated from the bifilar method and the Rhino model.

Components	Mass	CG @ Local coordinate system			Swing period [1]		Mass moment of inertia	
		LCG	TCG	VCG	Pitch	Yaw	Pitch	Yaw
(*Unit*) / Segments	(kg)	(m)	(m)	(m)	(s)	(s)	$(kg \cdot m^2)$	$(kg \cdot m^2)$
Fwd Segment								
FSDH Stb.	1.681	0.329	0.271	0.125	1.66	1.65	0.053100	0.048105
FSDH Port	1.615	0.324	-0.269	0.126	1.67	1.66	0.048110	0.040883
CBS	2.085	0.436	0.000	0.173	1.65	1.70	0.103457	0.127177
FTB System (Fwd)	0.541	0.453	0.000	0.197	R	R	0.000284	0.025844
FTB System (Aft)	0.541	0.229	0.000	0.197	R	R	0.000284	0.025844
FTB System Bolts (Fwd)	0.074	0.453	0.000	0.156	R	R	0.000000	0.000000
FTB System Bolts (Aft)	0.074	0.229	0.000	0.156	R	R	0.000000	0.000000
ELDH Stb Fwd sets	0.114	0.019	-0.275	0.136	R	R	0.000027	0.000027
ELDH Port Fwd sets	0.114	0.019	0.275	0.136	R	R	0.000027	0.000027
Segment Gap Sealing	0.100	0.260	0.000	0.111	PM	PM	0.000000	0.000000
Mid Segment								
MSDH Stb.	1.724	0.286	0.279	0.118	1.63	1.59	0.043643	0.025083
MSDH Port	1.747	0.286	-0.281	0.118	1.59	1.58	0.027665	0.023252
Mid Cross Bridge Deck	2.992	0.233	0.000	0.181	1.50	1.55	0.122086	0.157313
Aft Cross Bridge Deck	0.938	-0.462	0.000	0.169	1.90	1.91	0.042609	0.050163
ELDH Stb Fwd sets	0.114	0.554	-0.275	0.136	R	R	0.000027	0.000027
ELDH Port Fwd sets	0.114	0.554	0.275	0.136	R	R	0.000027	0.000027
ELDH Stb Aft sets	0.114	0.019	-0.275	0.136	R	R	0.000027	0.000027
ELDH Port Aft sets	0.114	0.019	0.275	0.136	R	R	0.000027	0.000027
Fwd Tow Post (Fwd TP)	1.440	0.121	0.000	0.236	PM	PM	0.000000	0.000000
Load cell (Fwd TP)	0.308	0.121	0.000	0.236	PM	PM	0.000000	0.000000
LVTD core (Fwd TP)	0.257	0.121	0.000	0.236	PM	PM	0.000000	0.000000
Bolts & Nuts (Fwd TP)	0.076	0.121	0.000	0.236	PM	PM	0.000000	0.000000
Aft Post (Aft TP), No.8	0.758	-0.308	0.000	0.251	PM	PM	0.000000	0.000000
LVTD core (Aft TP)	0.278	-0.308	0.000	0.251	PM	PM	0.000000	0.000000
Bolts & Nuts (Aft PT)	0.039	-0.308	0.000	0.251	PM	PM	0.000000	0.000000
Fwd TP Pin Joint	0.216	0.121	0.000	0.231	PM	PM	0.000000	0.000000
Aft TP Joint & Slider	0.323	-0.308	0.000	0.231	PM	PM	0.000000	0.000000
Ballast Port 03 (moving)	0.152	0.121	-0.327	0.205	PM	PM	0.000000	0.000000
Ballast Stb 03 (moving)	0.152	0.121	0.327	0.205	PM	PM	0.000000	0.000000
Segment Gap Sealing	0.100	0.287	0.000	0.145	PM	PM	0.000000	0.000000
Aft Segment								
ASDH Stb.	4.088	0.239	0.278	0.102	1.53	1.53	0.273149	0.266470
ASDH Port	4.110	0.235	-0.282	0.099	1.53	1.52	0.271457	0.263920
ELDH Stb Aft sets	0.114	0.806	-0.275	0.136	R	R	0.000027	0.000027
ELDH Port Aft sets	0.114	0.806	0.275	0.136	R	R	0.000027	0.000027
Segment Gap Sealing	0.100	0.412	0.000	0.148	PM	PM	0.000000	0.000000
Total mass	27.420							
Weight measurement	27.430							
Reference Coordinate System		Zero @ local transom	Zero @ vessel centre-line	Zero @ base line	Local CG	Local CG	Local CG	Local CG

[1] R indicates for the mass moment of inertia obtained from the Rhino model, and PM indicates that the component is considered to be a point mass. Therefore, the bifilar methods were not applied for the components marked by R or PM.

Appendix D

Results of Forward Velocity Induced Load in Calm Water Conditions

D.0.1 Power spectram density on VBM

D.0.2 Dynamic Attitude

Dynamic attitude is plotted in the Figure D.5.

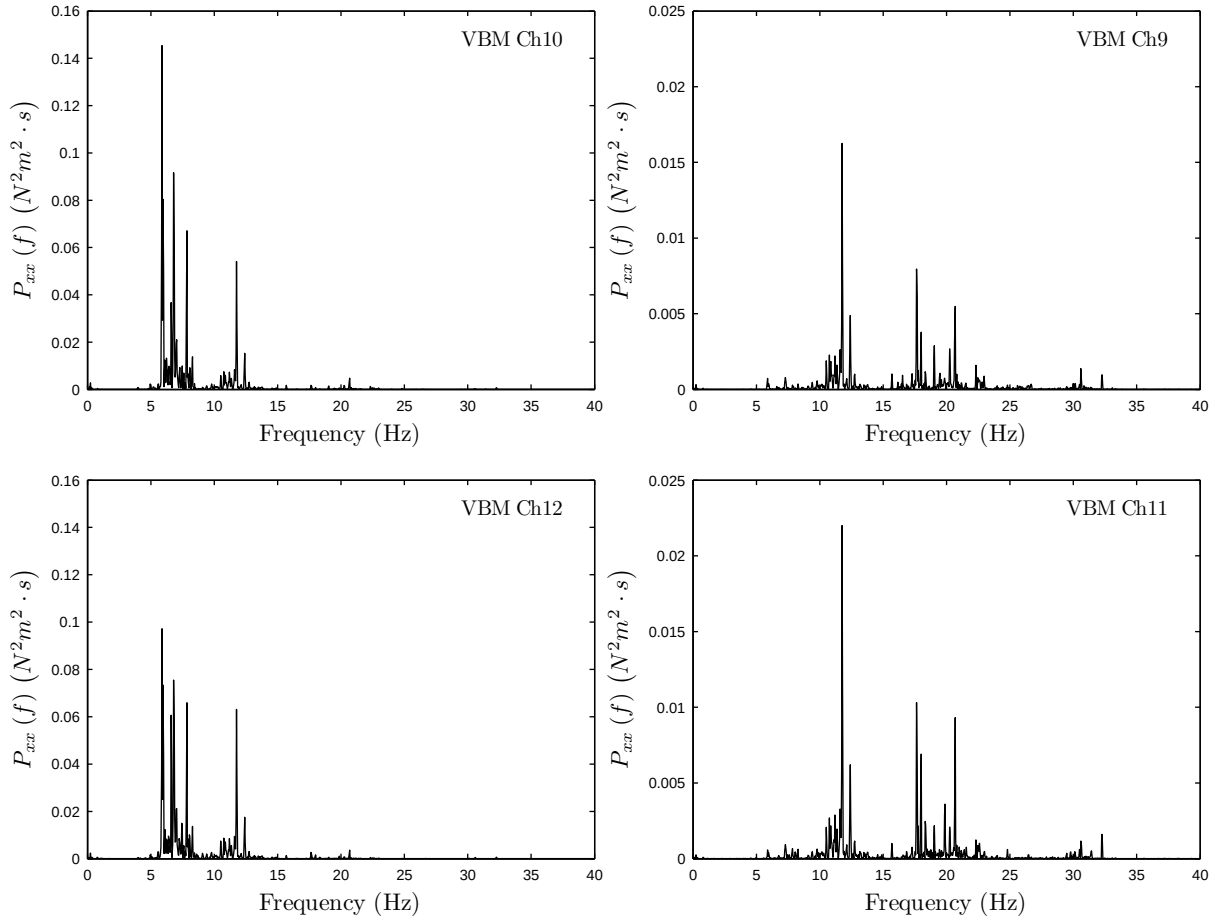

Figure D.1: Power spectral density (PSD), $P_{xx}(f)$ for vertical bending moment (VBM) measured at strain gauges at Ch9, Ch10, Ch11 and Ch12 in calm water run at $F_n = 0.32$, Run No.813. PSD was obtained by applying the Hamming window for data taper in the time domain, and no smoothing by a convolution in the frequency domain.

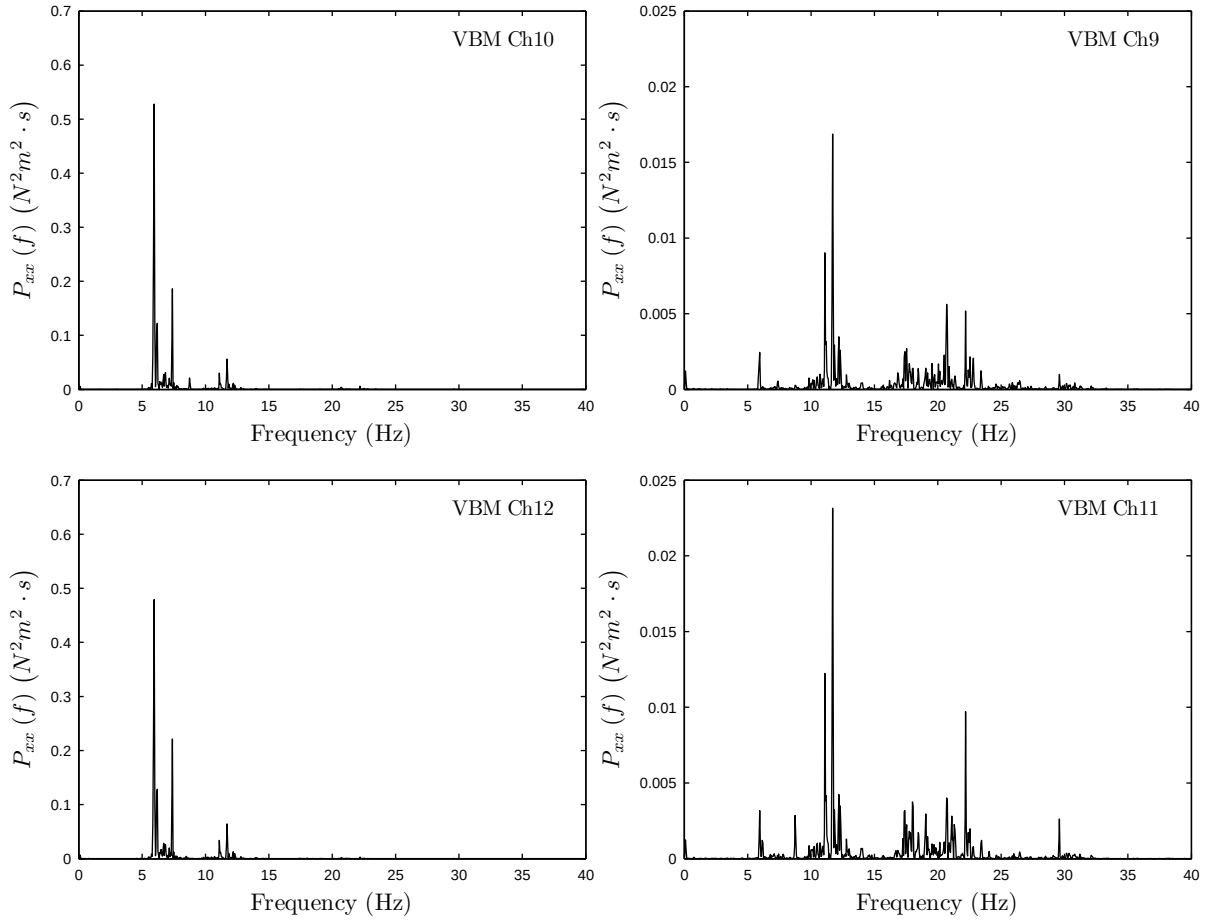

Figure D.2: Power spectral density (PSD), $P_{xx}(f)$ for vertical bending moment (VBM) measured at strain gauges at Ch9, Ch10, Ch11 and Ch12 in calm water run at $F_n = 0.478$, Run No.814. PSD was obtained by applying the Hamming window for data taper in the time domain, and No smoothing by a convolution in the frequency domain.

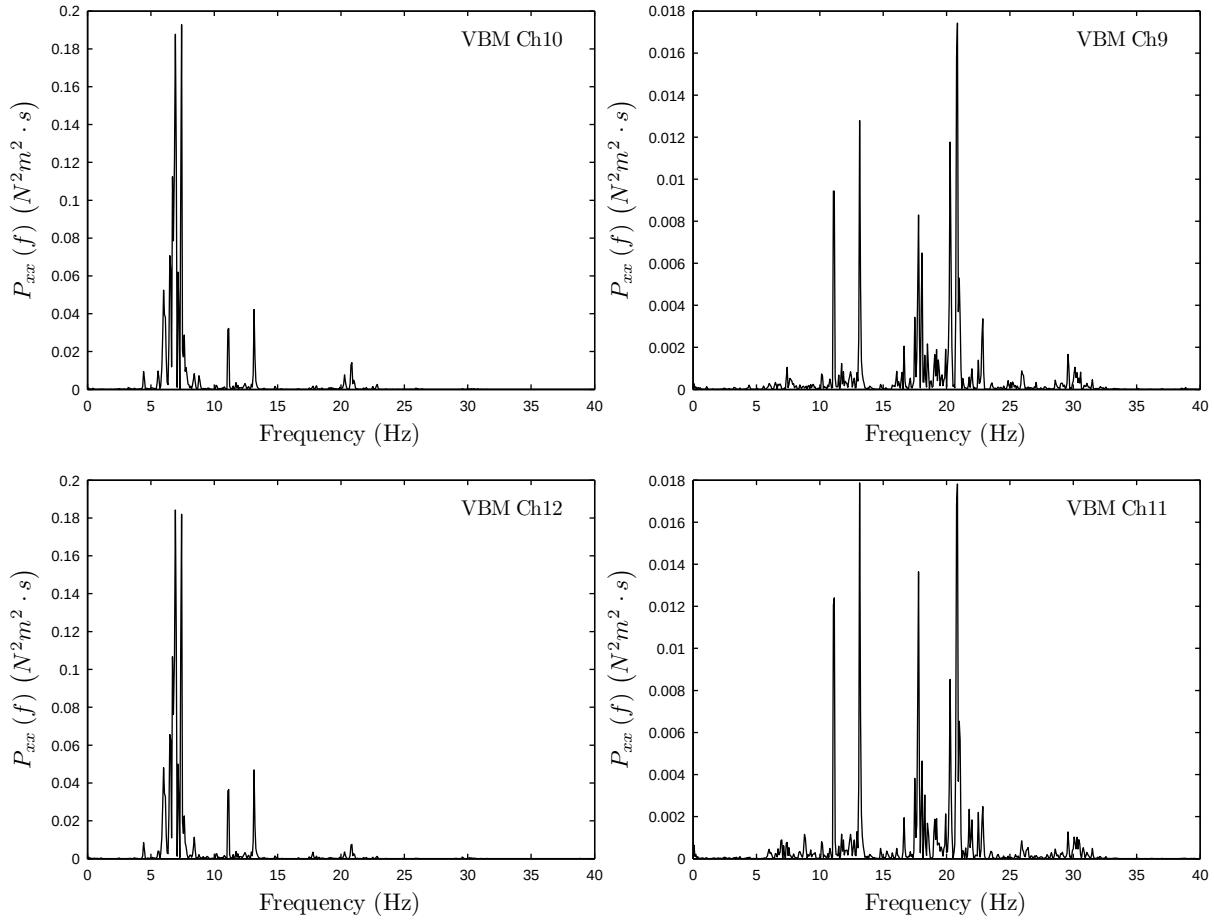

Figure D.3: Power spectral density (PSD), $P_{xx}(f)$ for vertical bending moment (VBM) measured at strain gauges at Ch9, Ch10, Ch11 and Ch12 in calm water run at $F_n = 0.717$, Run No.816. PSD was obtained by applying the Hamming window for data taper in the time domain, and no smoothing by a convolution in the frequency domain.

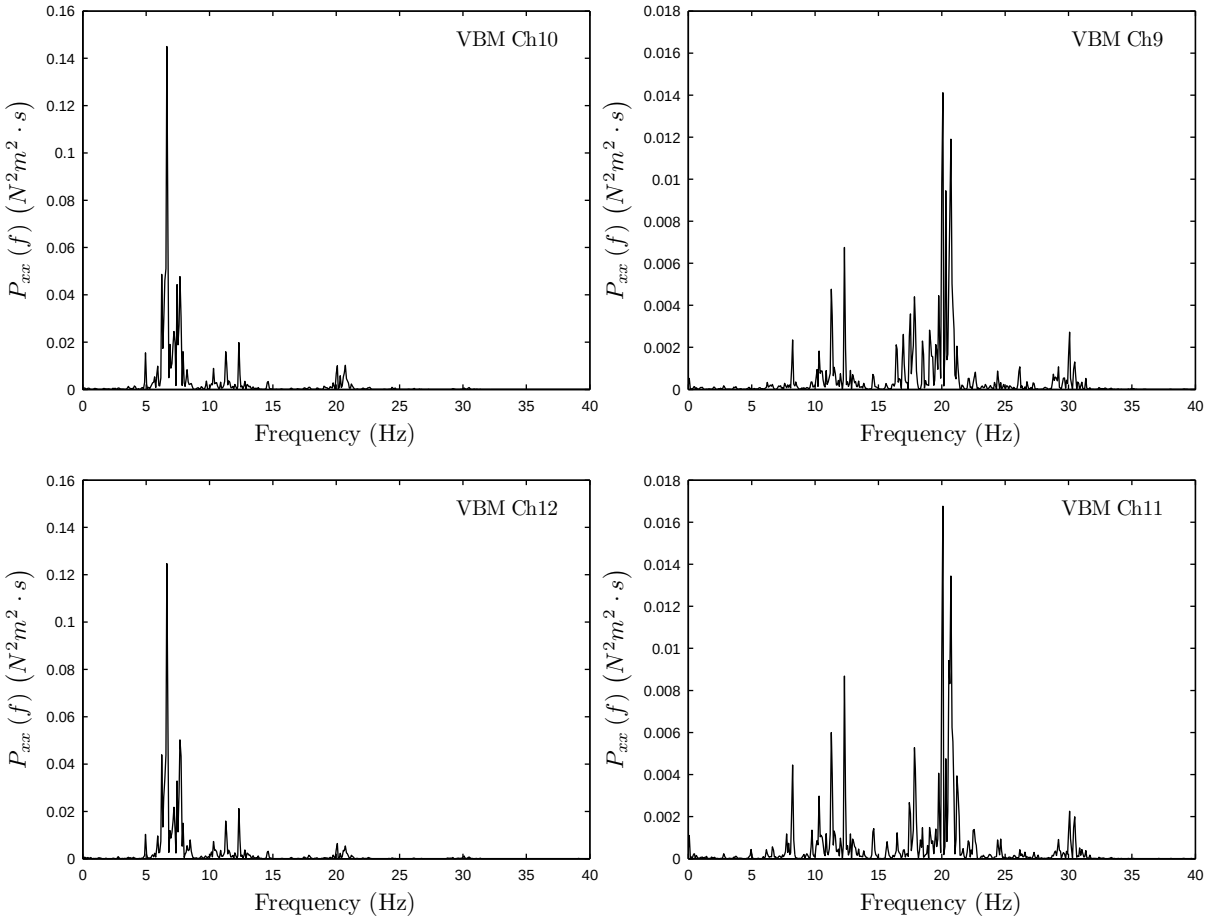

Figure D.4: Power spectral density (PSD), $P_{xx}(f)$ for vertical bending moment (VBM) measured at strain gauges at Ch9, Ch10, Ch11 and Ch12 in calm water run at $F_n = 0.797$, Run No.817. PSD was obtained by applying the Hamming window for data taper in the time domain, and no smoothing by a convolution in the frequency domain.

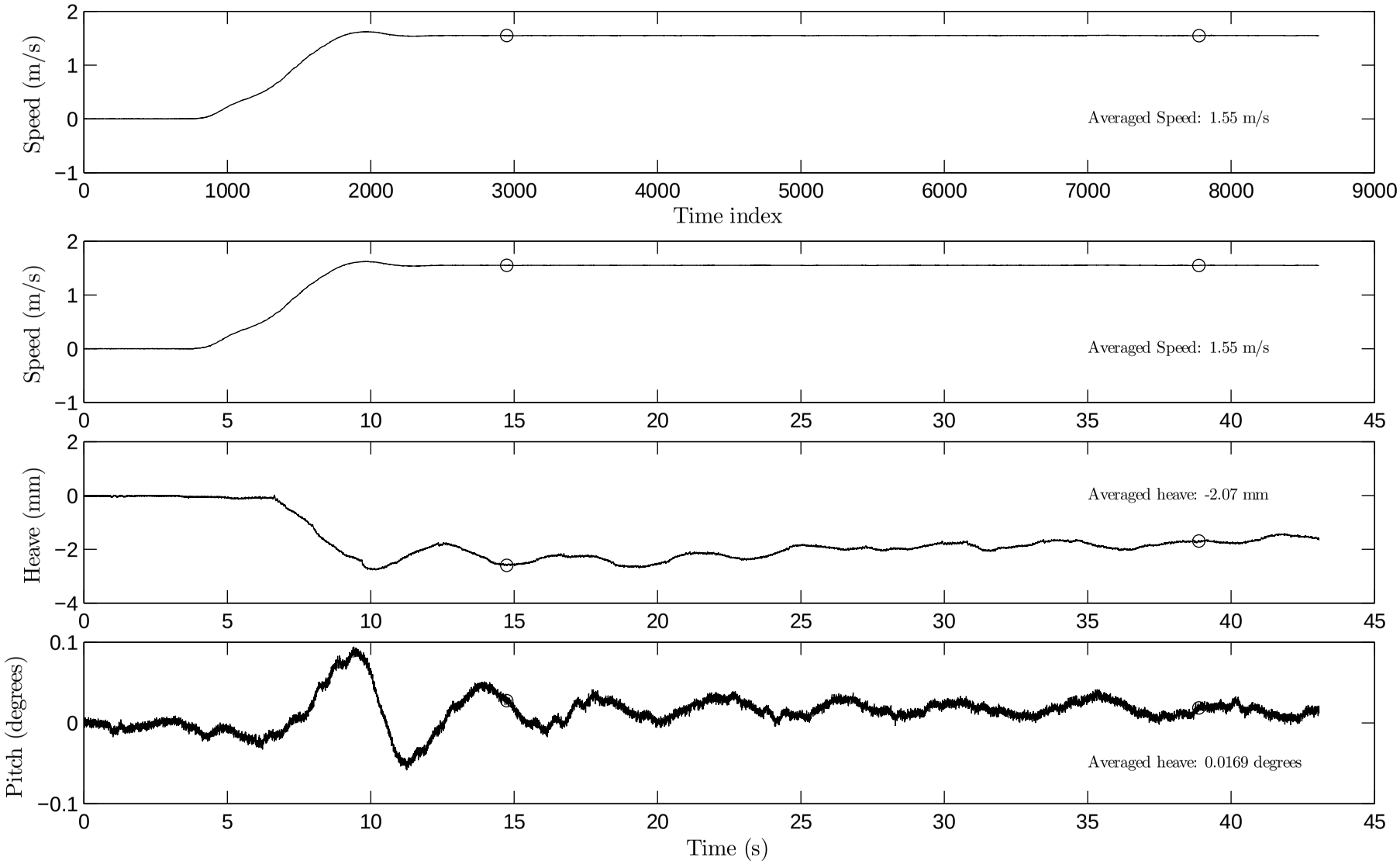

Figure D.5: Dynamic attitude of calm water run with steady speed maintained at $F_n = 0.320$ for Run No. 813. Averaged values are calculated between two circles.

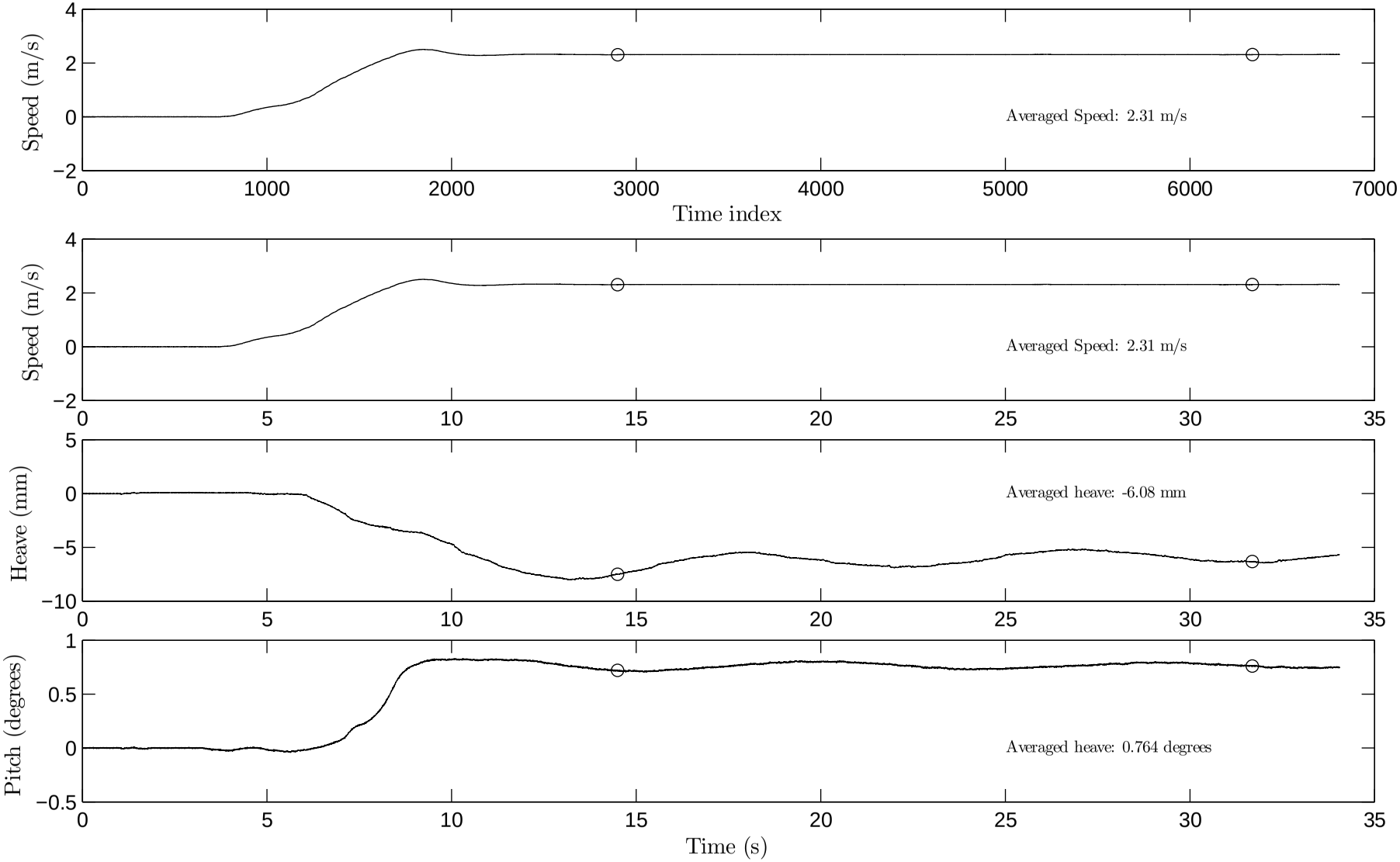

Figure D.6: Dynamic attitude of calm water run with steady speed maintained at $F_n = 0.478$ for Run No. 814. Averaged values are calculated between two circles.

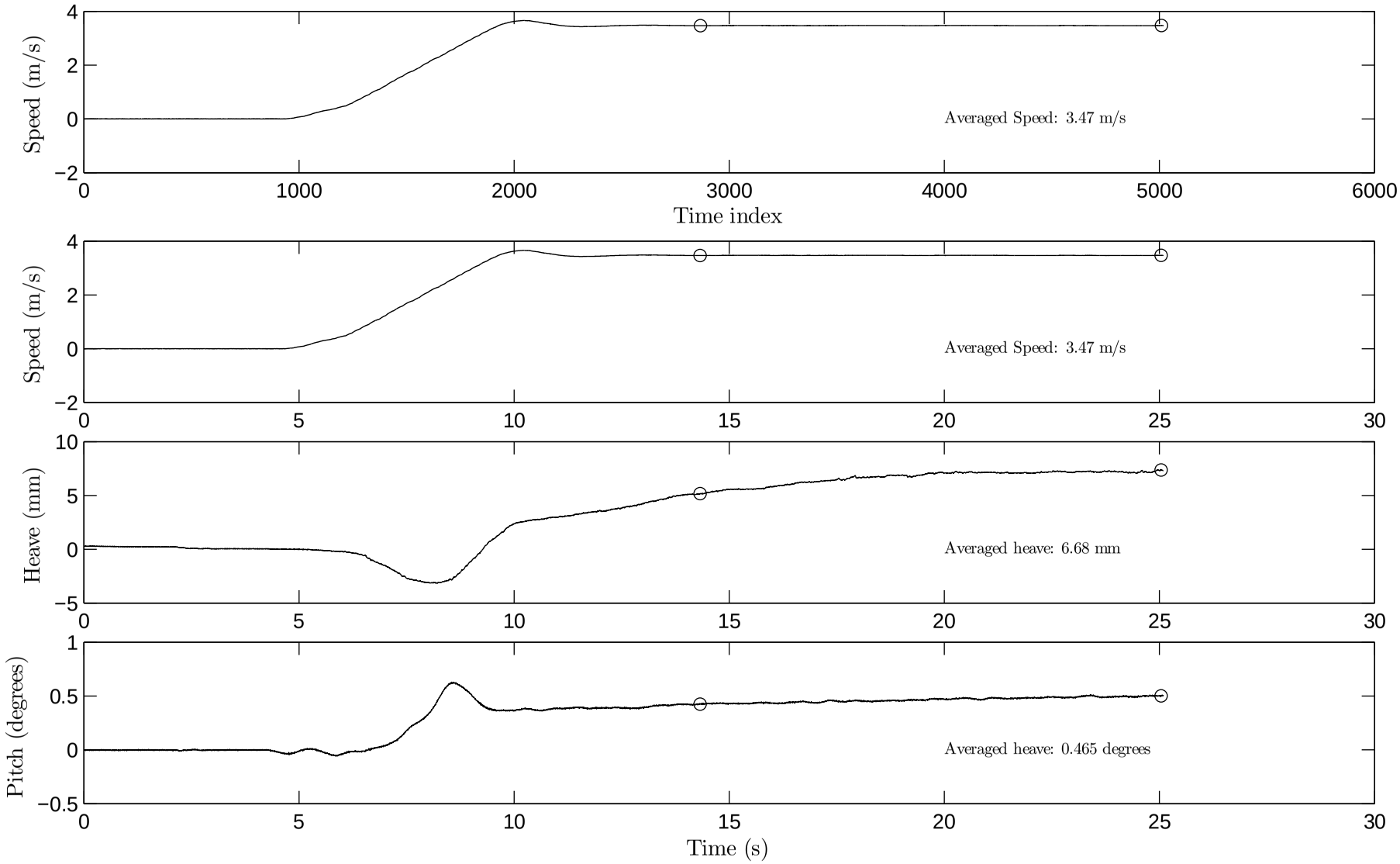

Figure D.7: Dynamic attitude of calm water run with steady speed maintained at $F_n = 0.717$ for Run No. 816. Averaged values are calculated between two circles.

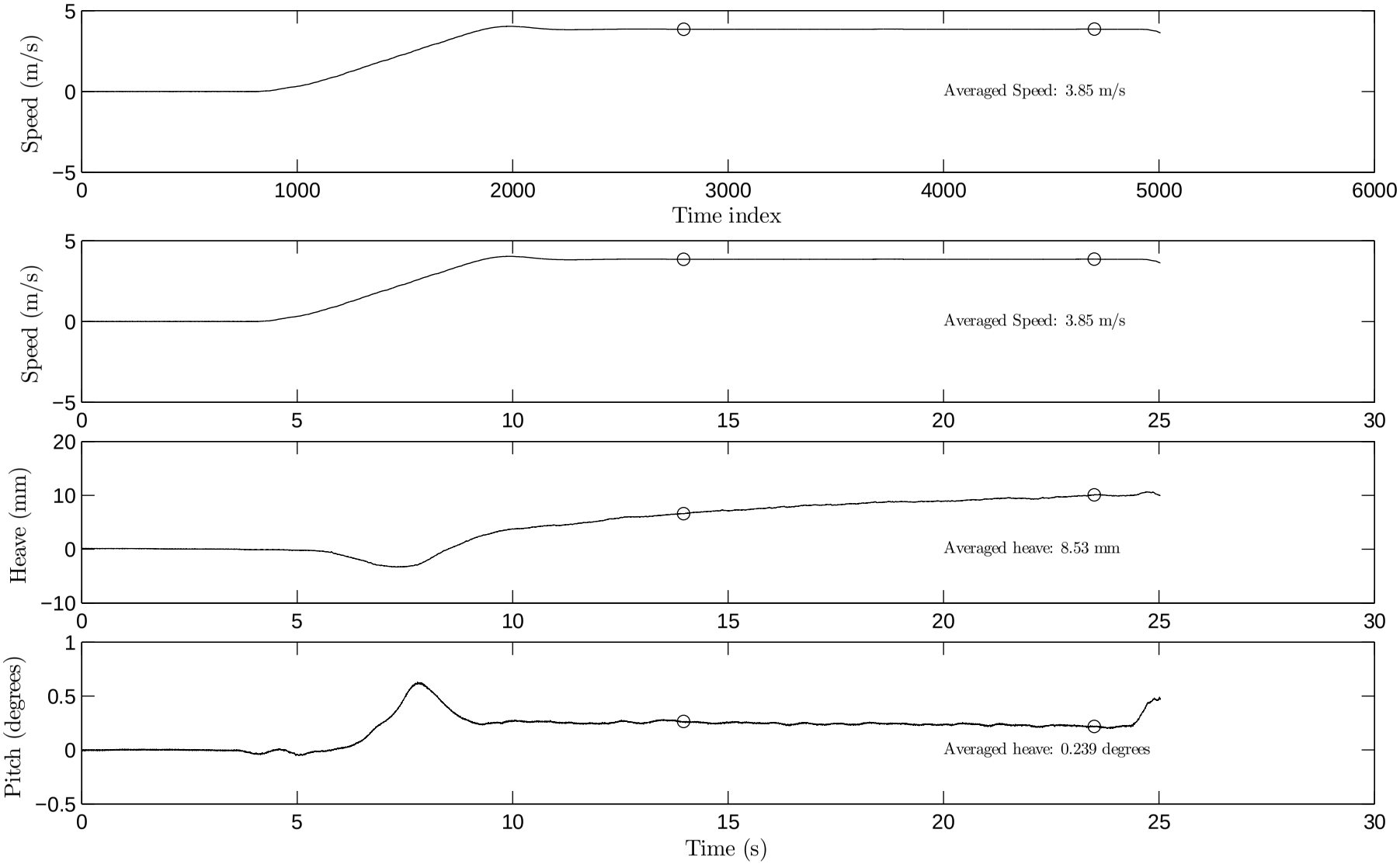

Figure D.8: Dynamic attitude of calm water run with steady speed maintained at $F_n = 0.797$ for Run No. 817. Averaged values are calculated between two circles.

D.0.3 Vertical Bending Moment at Segmentation Gaps in Time

Hogging and Sagging VBM were plotted in Figure D.9.

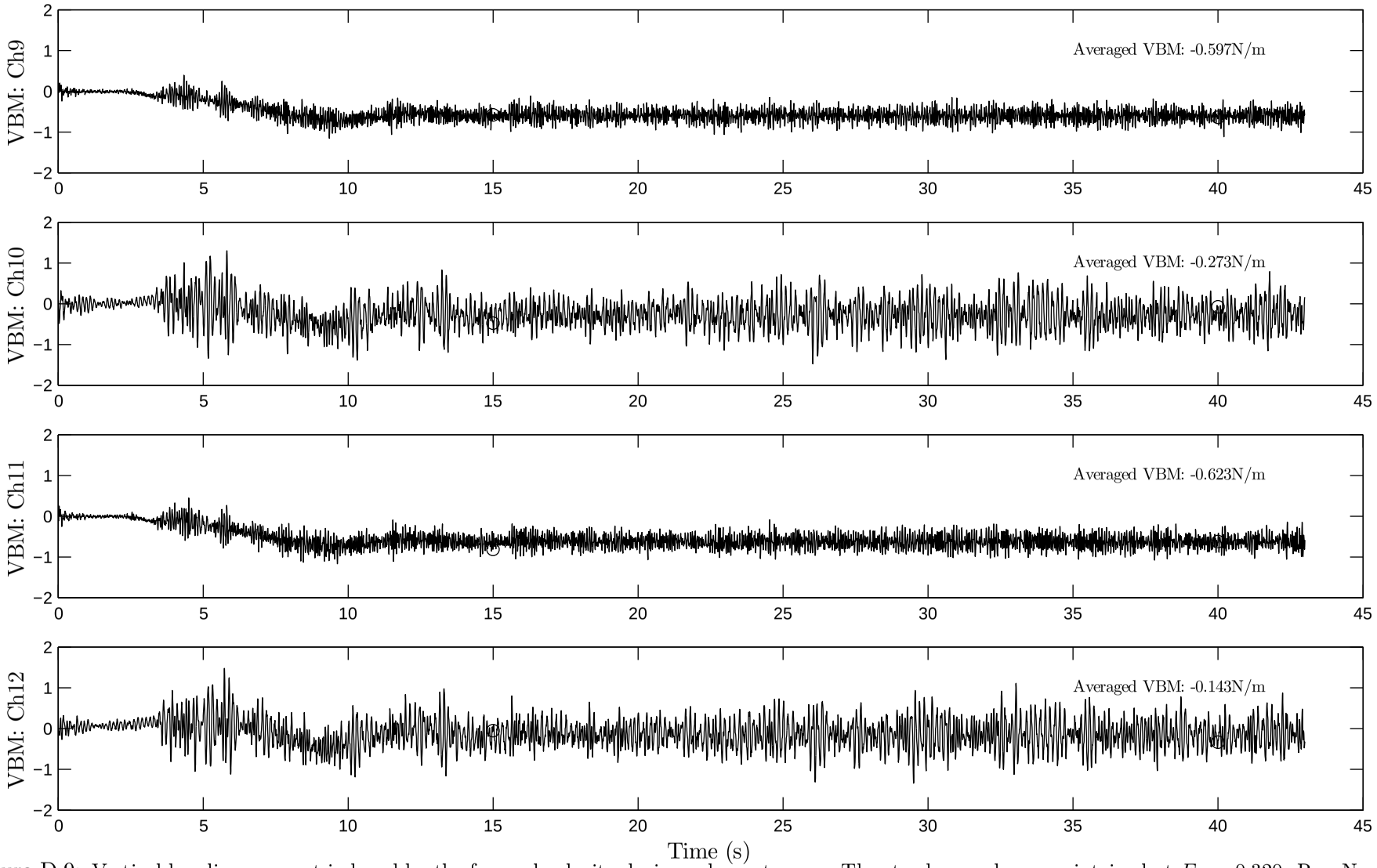

Figure D.9: Vertical bending moment induced by the forward velocity during calm water run. The steady speed was maintained at $F_n = 0.320$. Run No. 813. Positive and negative values indicate the hogging and sagging VBM, respectively.

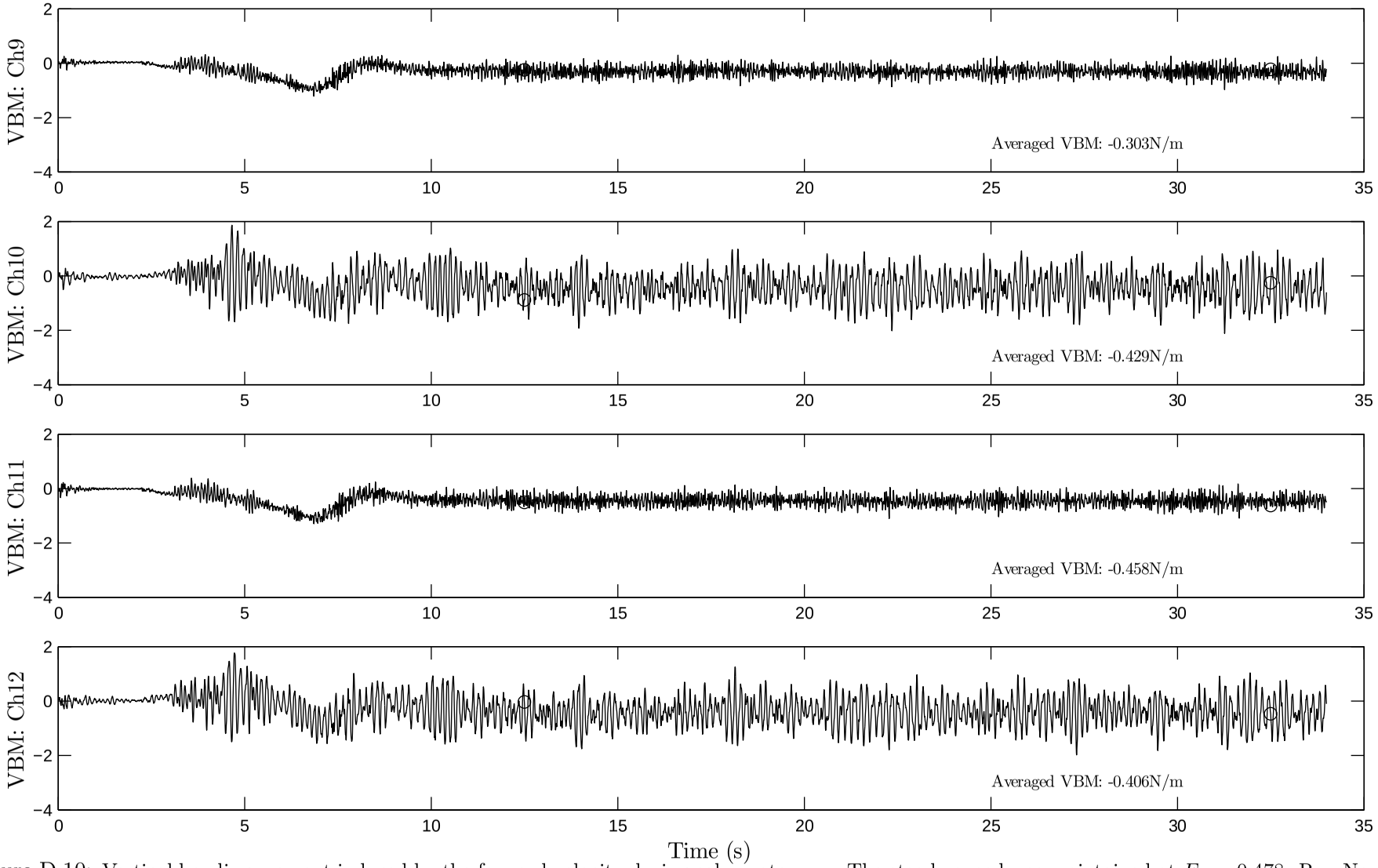

Figure D.10: Vertical bending moment induced by the forward velocity during calm water run. The steady speed was maintained at $F_n = 0.478$. Run No. 814. Positive and negative values indicate the hogging and sagging VBM, respectively.

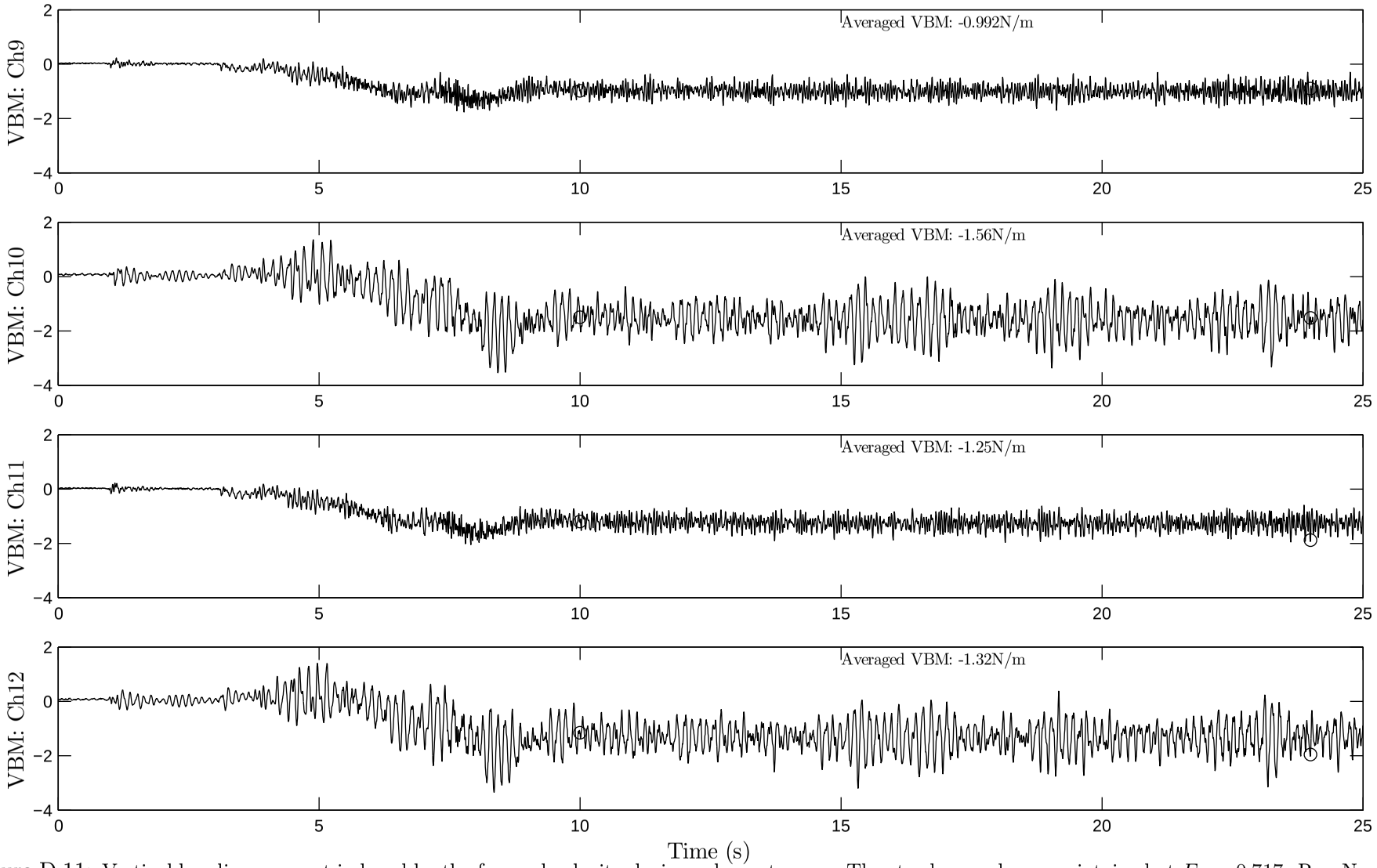

Figure D.11: Vertical bending moment induced by the forward velocity during calm water run. The steady speed was maintained at $F_n = 0.717$. Run No. 816. Positive and negative values indicate the hogging and sagging VBM, respectively.

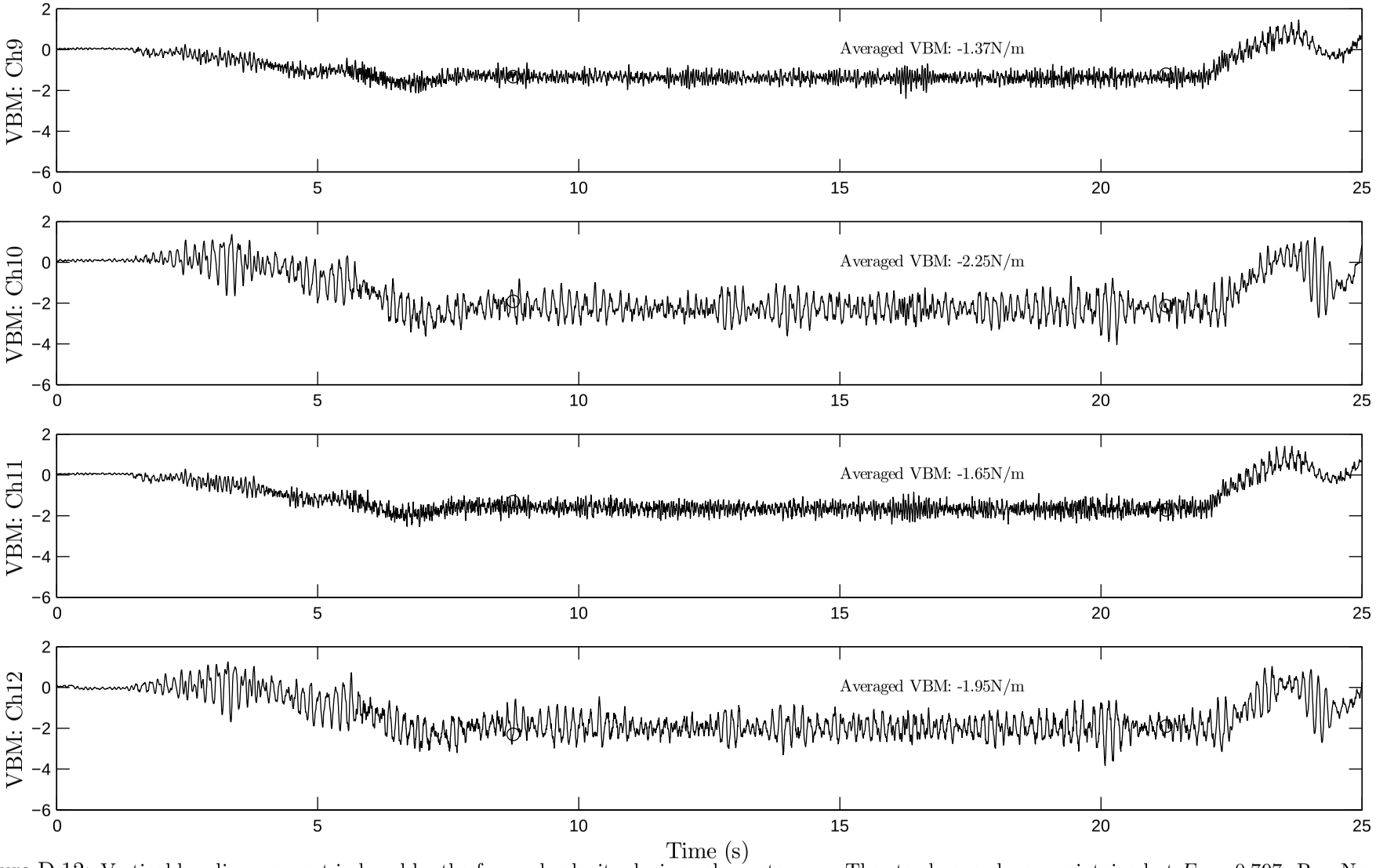

Figure D.12: Vertical bending moment induced by the forward velocity during calm water run. The steady speed was maintained at $F_n = 0.797$. Run No. 817. Positive and negative values indicate the hogging and sagging VBM, respectively.

Appendix E

Continuous Wavelet Transform and Morlet Wavelet Function

The continuous wavelet transform (CWT) of a signal $s(t)$ is represented as the CWT coefficient, $C(a, b)$:

$$C(a,b) = \int_R s(t)\frac{1}{\sqrt{a}}\Psi(\frac{t-b}{a})dt \tag{E.1}$$

where a is scale, which corresponds to the frequency calculated by Equation E.3, and b is the time position.

For a mother wavelet function for the CWT, the Morlet wavelet was selected as follows:

$$\Psi(x) = e^{-x^2/2}cos(5x) \tag{E.2}$$

The CWT is the cross-correlation of the signal $s(t)$ with the scaled and time shifted wavelet, $\frac{1}{\sqrt{a}}\Psi(\frac{t-b}{a})$. The cross-correlation can be considered as a measure of the similarity (resemblance) between the signal and the scaled and shifted wavelet. The CWT coefficient can be presented in the Jet colormap. The x-axis indicates the position along the signal(time), the y-axis represents scale a, and the colour at each x-y coordinate indicates the magnitude of the CWT coefficient, C(a,b). If the magnitude of the coefficient is large, the resemblance is strong. The magnitude of CWT is given by the colorbar.

Conversion from the scale a to frequency can be calculated by following:

$$F_a = \frac{F_c}{a \cdot \Delta} \tag{E.3}$$

where Δ is the sampling period, F_c is the centre frequency of a wavelet in Hz and F_a is the pseudo-frequency corresponding to the scale a. The scale a and the frequency has a relationship based on the Equation E.3 as presented in Figure E.1.

In order to examine the CWT with the Morlet wavelet function, dummy signals were assembled to represent wave loads and slam events. A dummy wave signal can be calculated as follows:

$$S_w = A_w sin(2\pi f_w t) \tag{E.4}$$

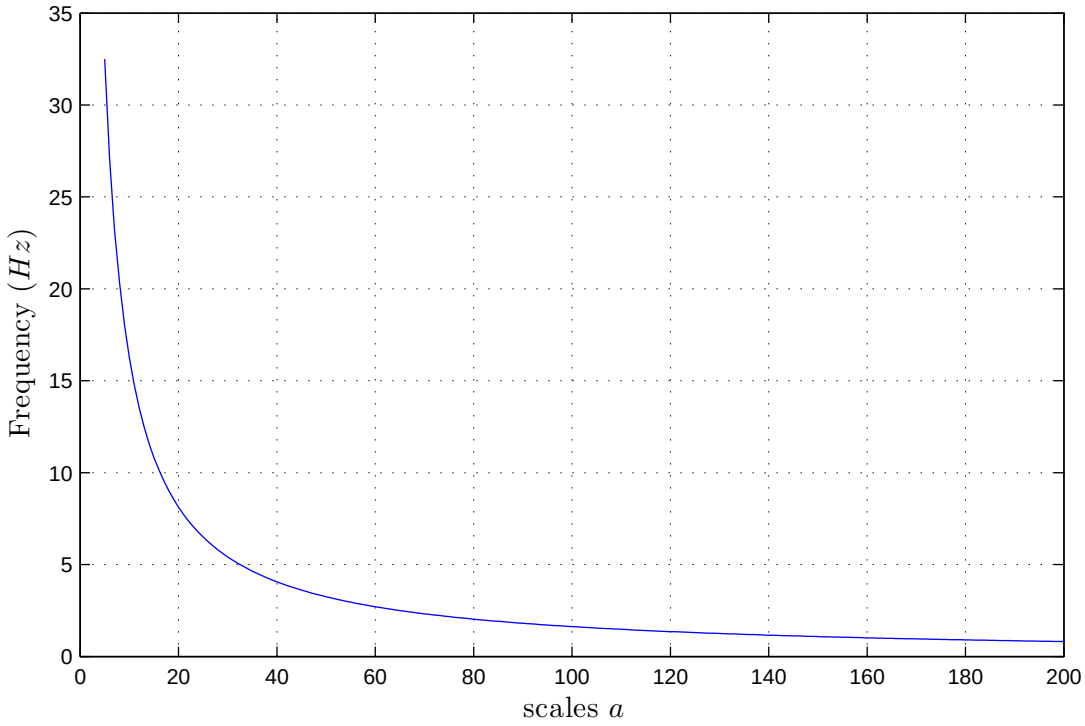

Figure E.1: Pseudo-frequencies (Hz) corresponding to the scales a.

where f_w is the wave frequency in Hz and A_w is the wave amplitude. A slam signal can be generated by the following equation.

$$S_s = A_s e^{-\zeta\omega_n t} \sin(\sqrt{1-\zeta^2}) \tag{E.5}$$

where ζ is the damping ratio, A_s is an amplitude, $\omega_n = 2\pi f_s$ and f_s is the slam whipping frequency. Combined wave signal and slam signal were simply superimposed as follows:

$$S_c = S_w + S_s \tag{E.6}$$

The wave signals were generated as shown in Figures E.2 with the inputs of $f_w = 1.5\ Hz$, $A_w = 20$, $f_s = 12.5\ Hz$, $\zeta = 0.025$, $A_s = 30$.

The CWT results with Morlet mother function for the mathematically generated signals by Equations E.4 and E.6, are presented in Figure E.3 and Figure E.4 for the zoomed view. The CWT of "wave" shows the CWT results for the wave signal, the CWT of "slam" is for the slam signal. Whilst "wave+Slam" shows the CWT coefficient for the combined wave and slam signal. The slam signal is weaker when compared with the wave signal, requiring an enhancement technique to intensify the weaker signal. The CWT of "wave+slam", enhanced shows the slam whipping signal clearly.

Colours indicate the magnitude of the CWT coefficients, $C(a,b)$ according to an adjacent colour bar. Red in colour indicates the peak of the signal and blue colour indicates the trough of the signal. These CWT corlourmaps and the time signals in Figures E.2 can be compared to

understand the CWT response to the signals.

The maximum CWT coefficient of the wave signal occurred at scale $a = 108$, which is corresponds to 1.504 Hz. Similarly, the maximum CWT coefficient of the slam signal occurred at scale $a = 13$, which corresponds to the 12.500 Hz. These frequencies agreed with the input frequencies to the mathematically generated signals. In addition, the power spectral density were obtained for the three different waves signals as shown in Figures E.5. The results show that the response frequency of the wave occurred at 1.5 Hz and the response frequency of the slam whipping occurred at 12.5 Hz. These combinations of PSD and CWT were useful for detecting the response frequency in both the frequency and time domain.

In general, two or more phenomena have a distinct difference in the frequency response, the CWT can successfully recognise the response frequency and temporal occurrence information. This is a significant advantage of the CWT. In addition, the power spectral densities (PSD) of these signals were obtained and plotted in Figures E.5. The response frequency occurred at 1.5 and 12.5 Hz and thus confirmed the frequency response as calculated by the CWT coefficient. Hence, the CWT can be used effectively to analyse of the global wave and slam response.

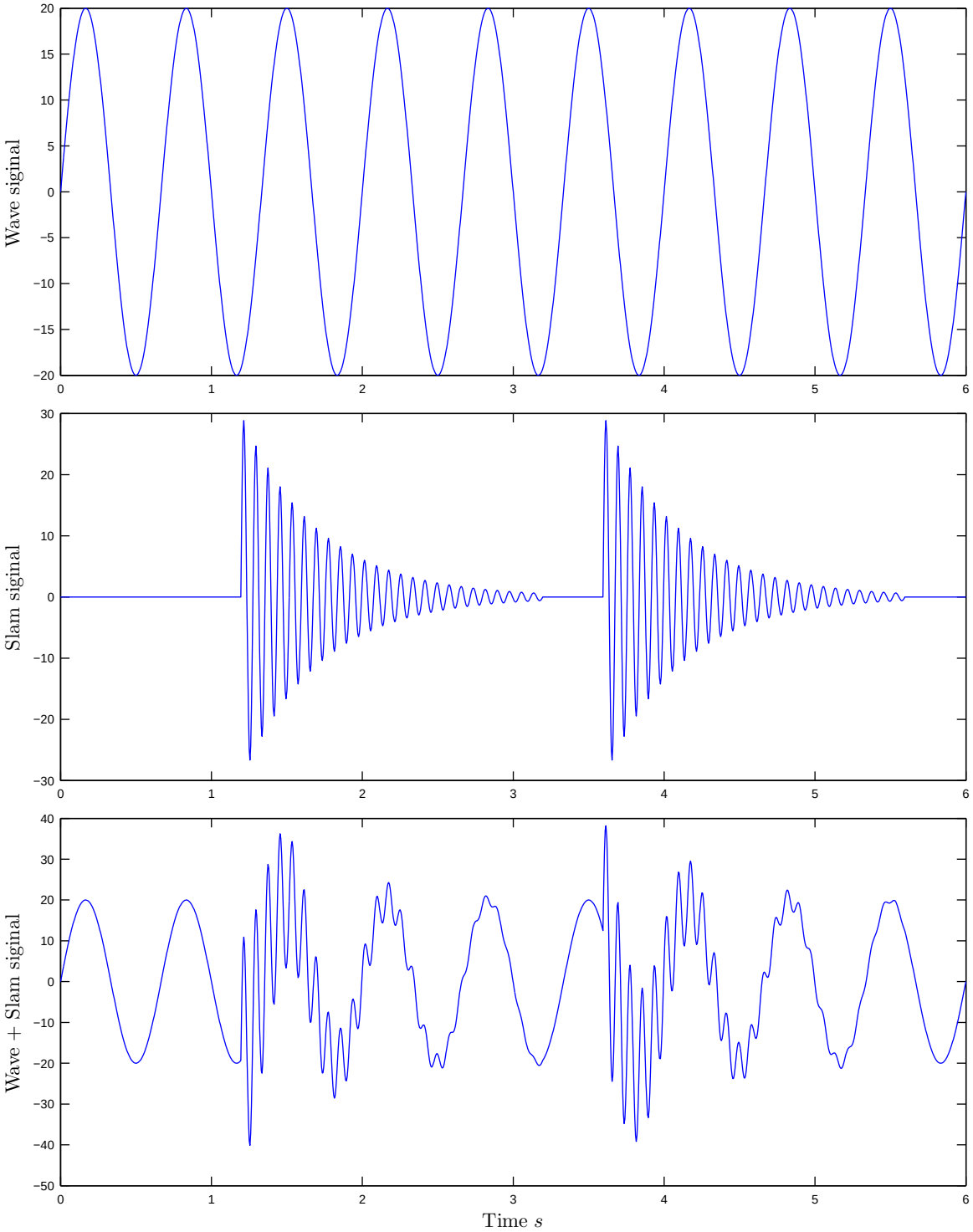

Figure E.2: Wavelet test on the mathematically generated waves.

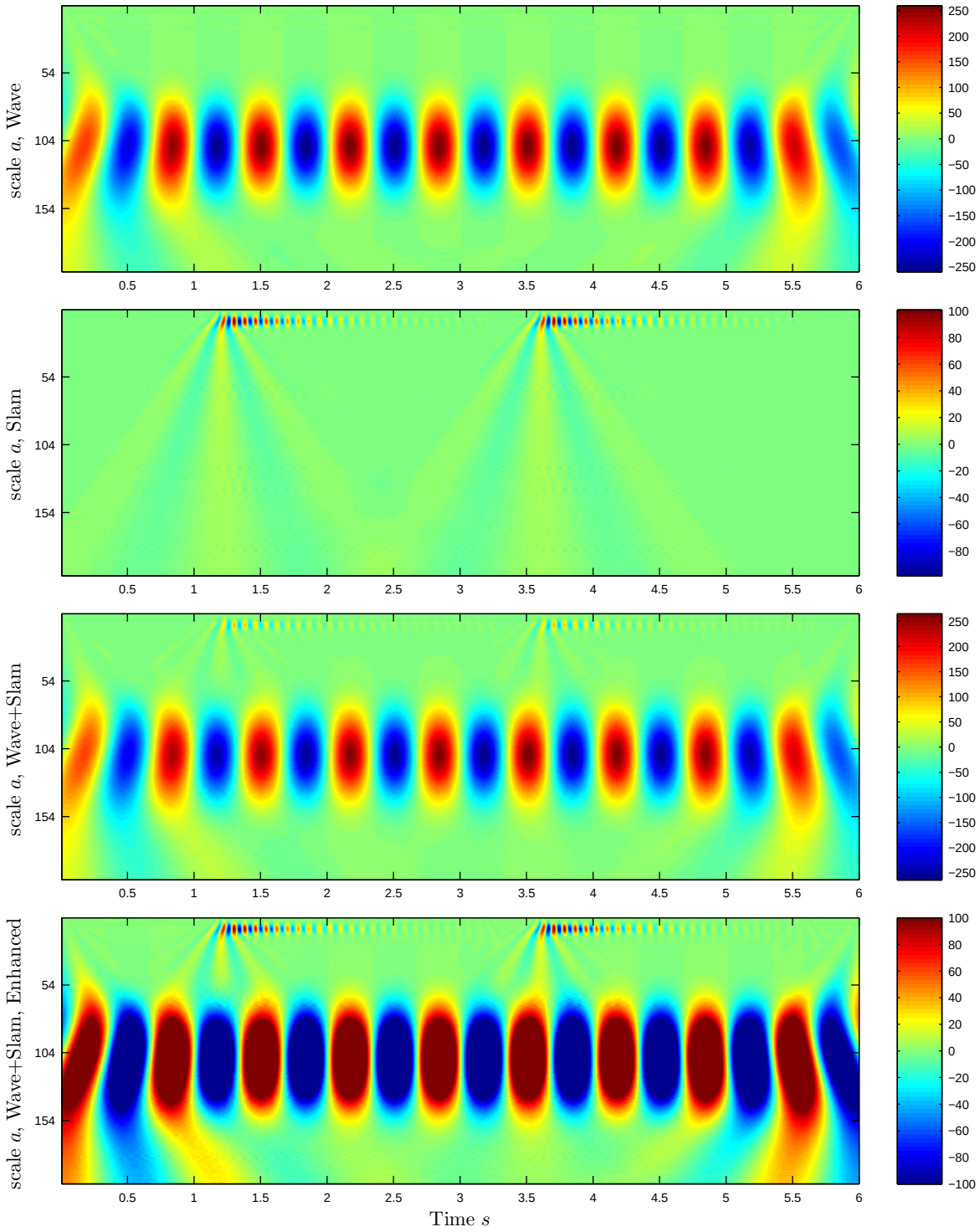

Figure E.3: Wavelet test on the mathematically generated waves.

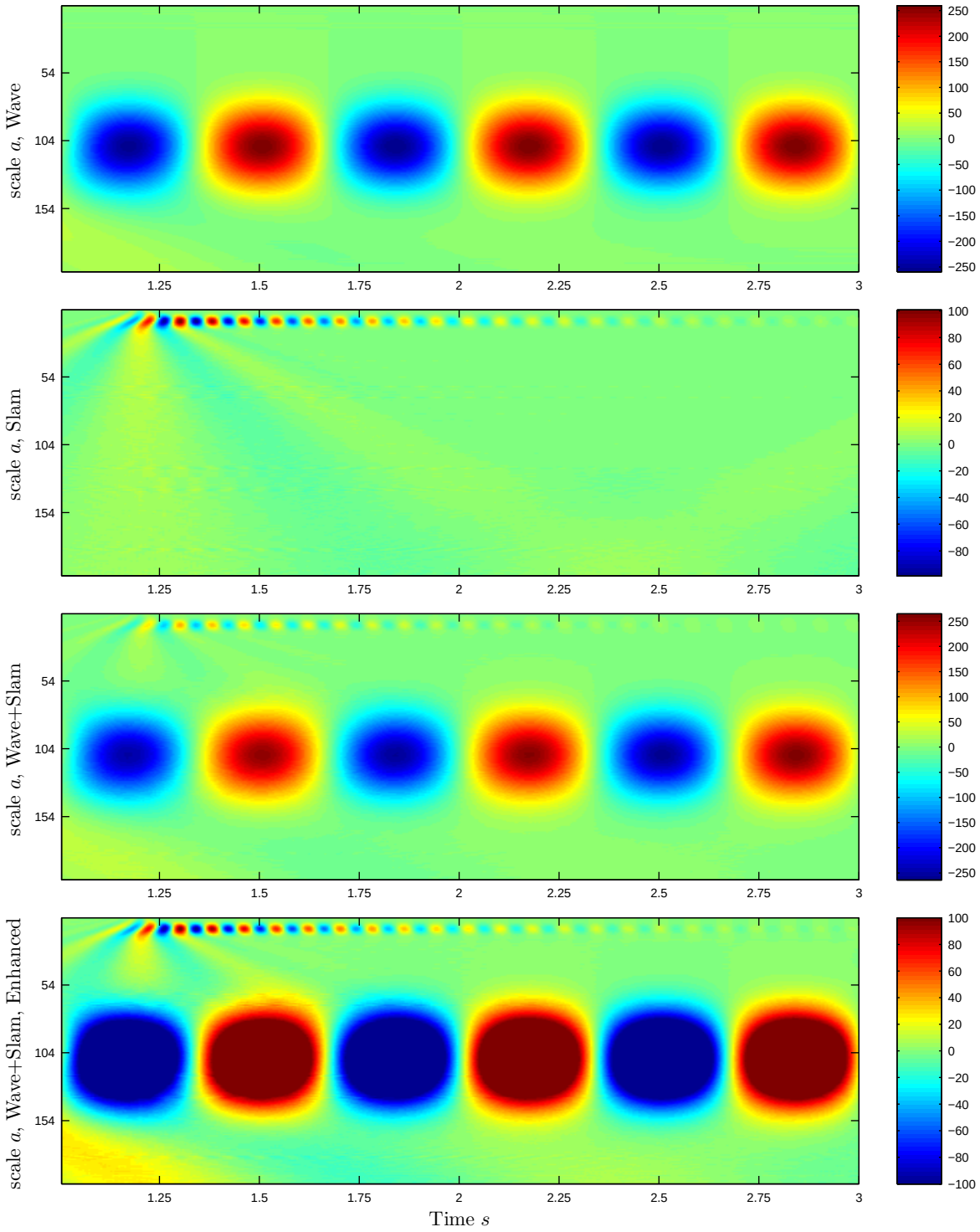

Figure E.4: Wavelet test on the mathematically generated waves.

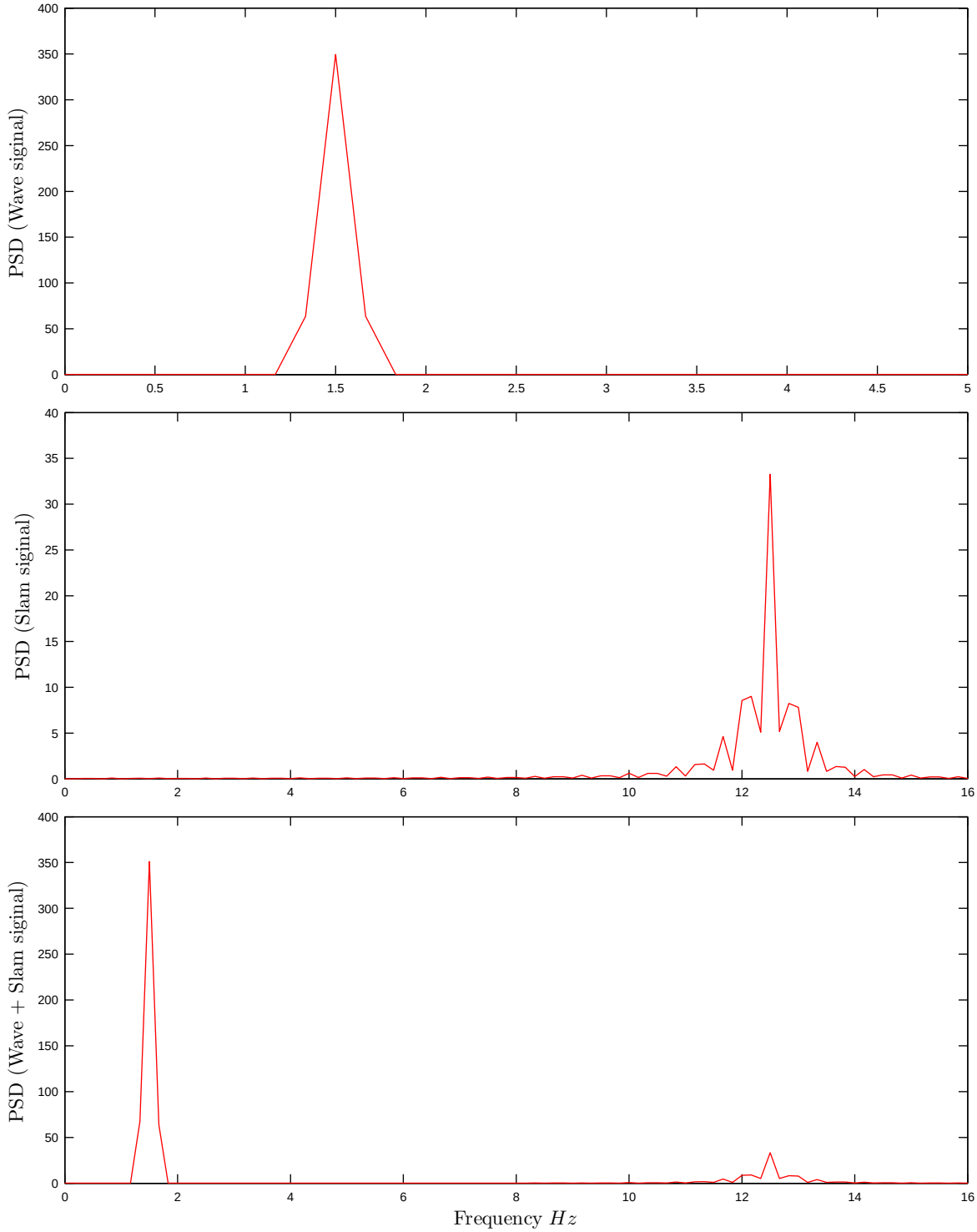

Figure E.5: Wavelet test on the mathematically generated waves.

Appendix F

Hydroelastic Effects of the HSM

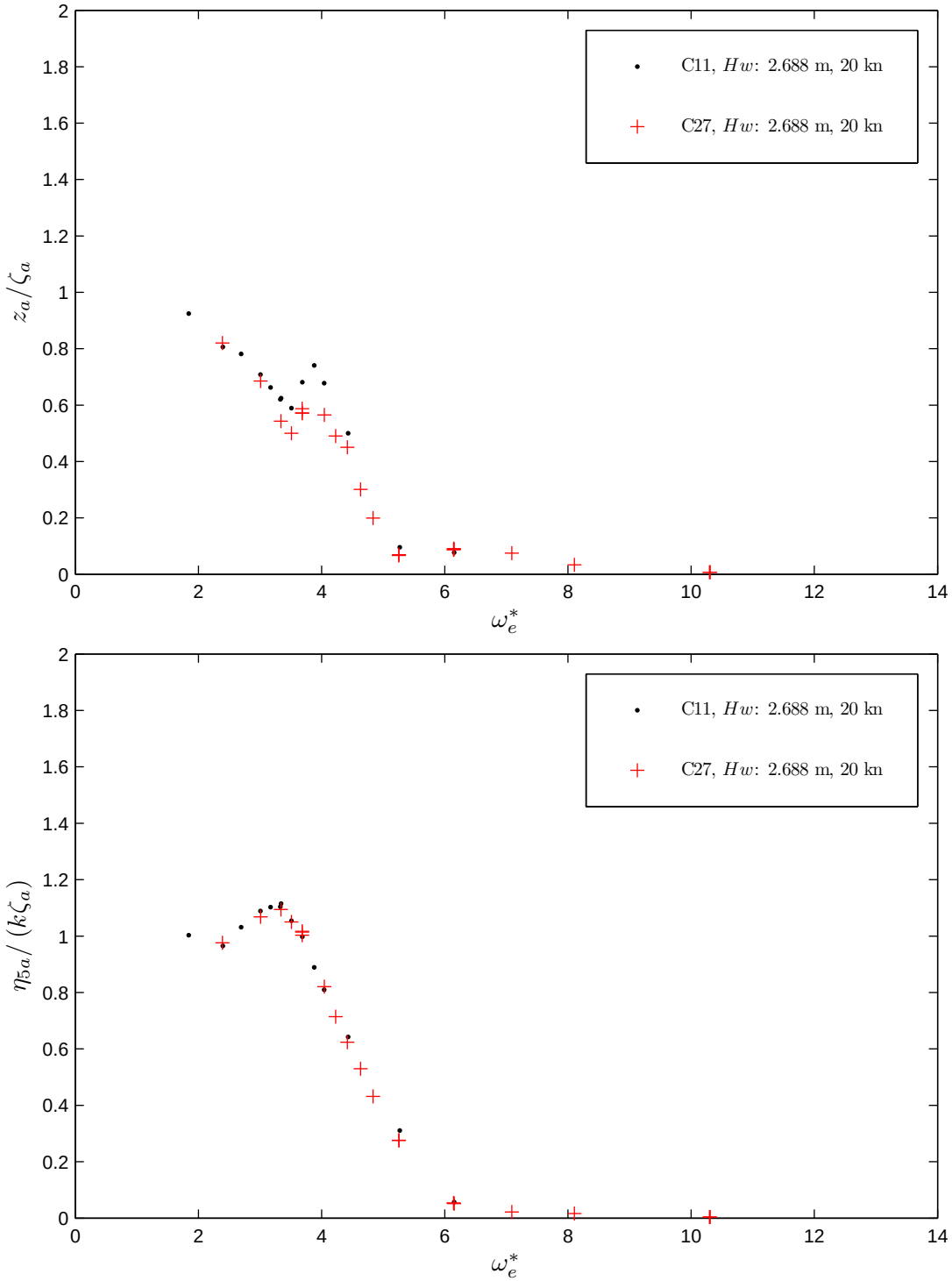

Figure F.1: Elastic link influence on the TFs for heave and pitch motions for the wave height, $H_w/T = 0.79$ plotted as a function of the non-dimensional encounter angular wave frequency, ω_e^*. $F_n = 0.32$.

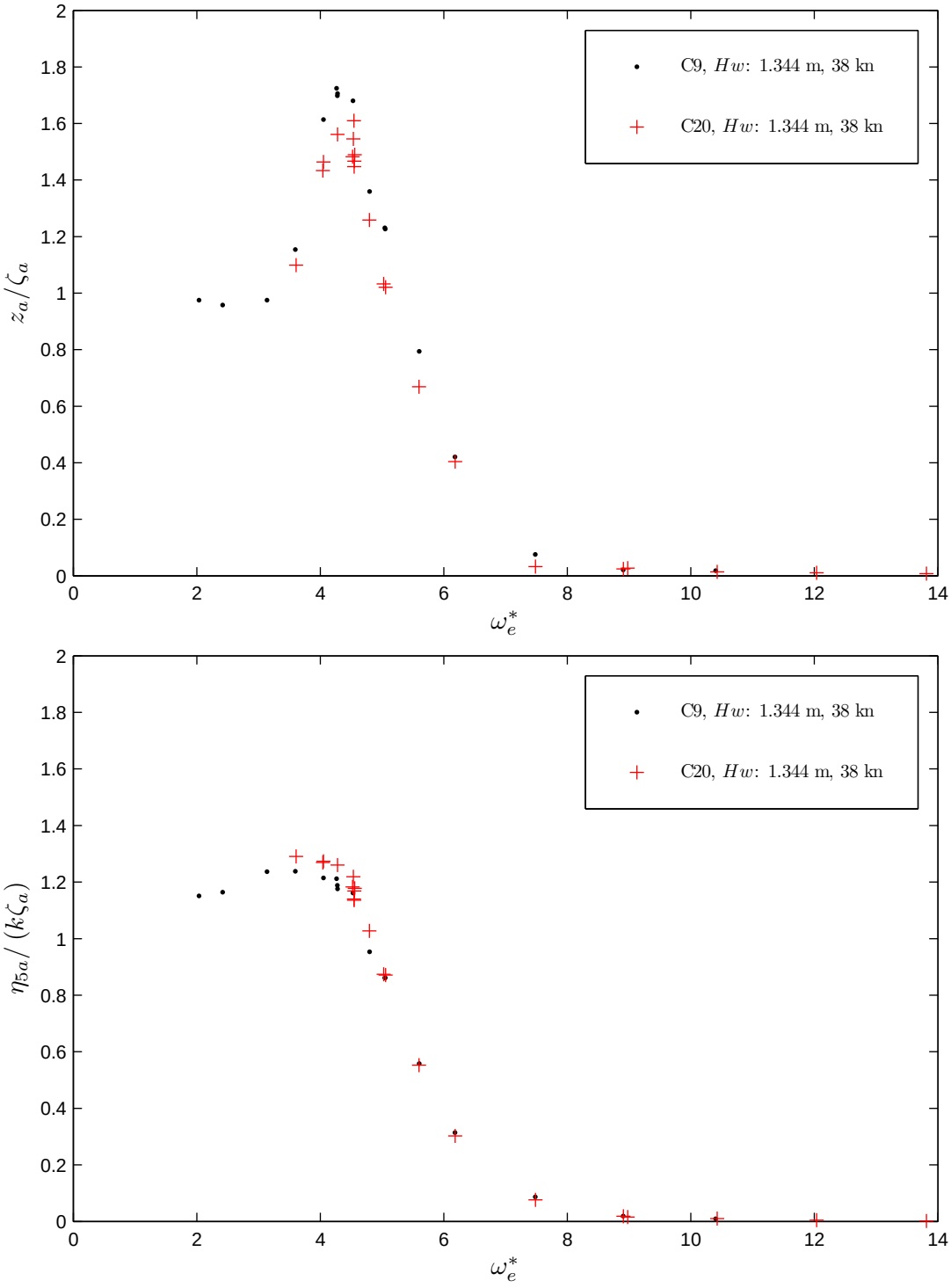

Figure F.2: Elastic link influence on the TFs for heave and pitch motions for the wave height, $H_w/T = 0.39$ plotted as a function of the non-dimensional encounter angular wave frequency, ω_e^*. $F_n = 0.60$.

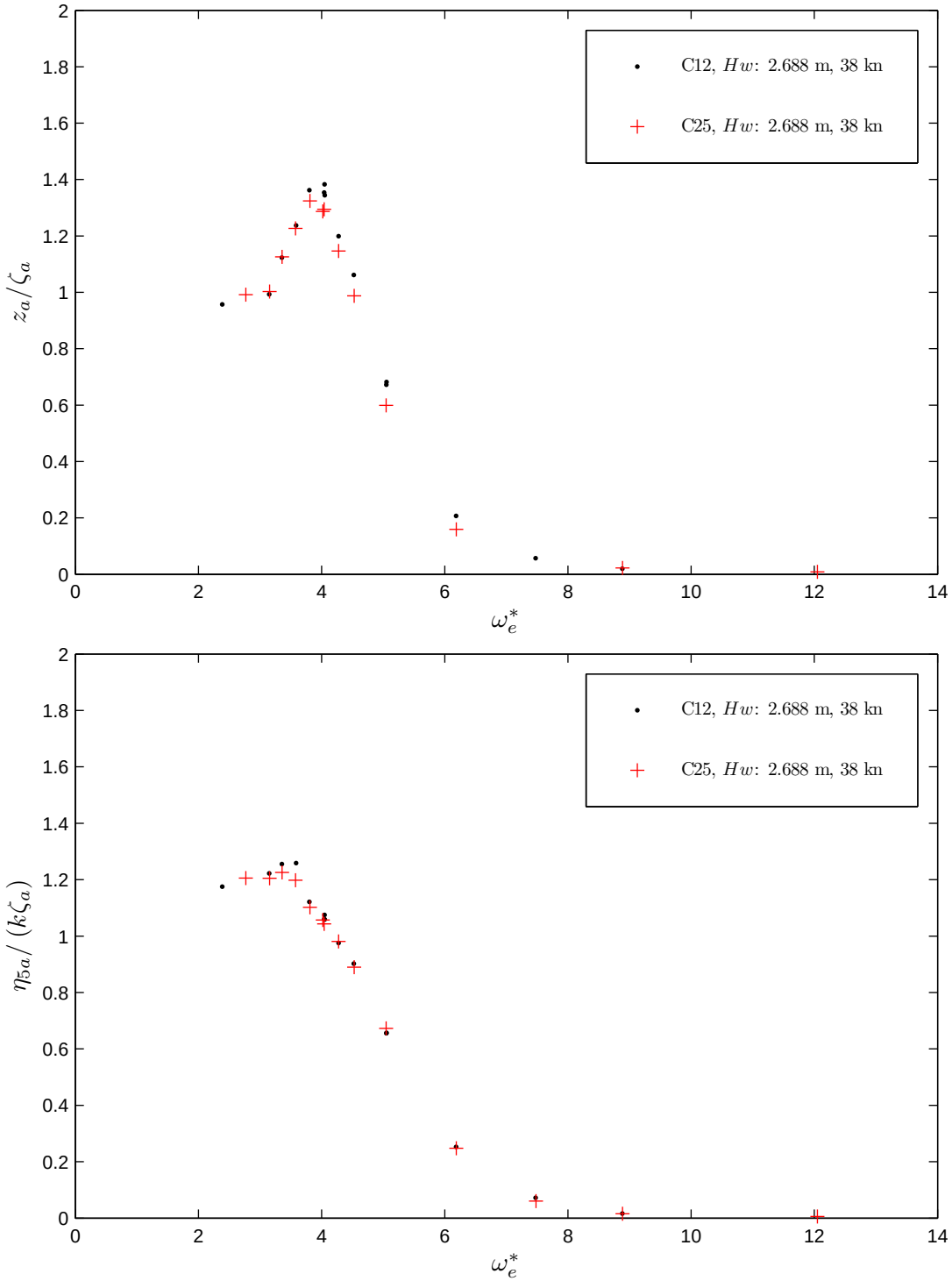

Figure F.3: Elastic link influence on the TFs for heave and pitch motions for the wave height, $H_w/T = 0.79$ plotted as a function of the non-dimensional encounter angular wave frequency, ω_e^*. $F_n = 0.60$.

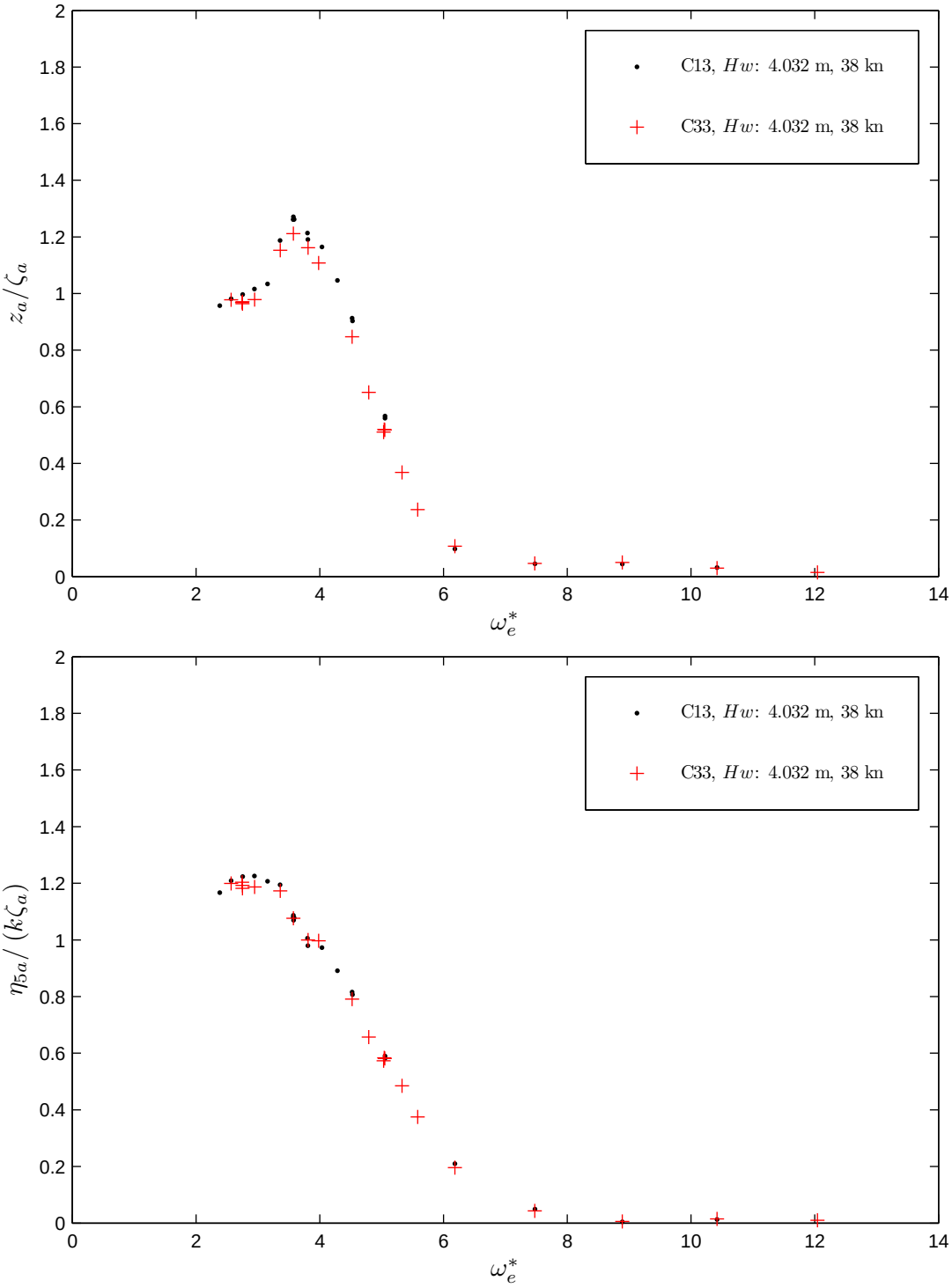

Figure F.4: Elastic link influence on the TFs for heave and pitch motions for the wave height, $H_w/T = 1.18$ plotted as a function of the non-dimensional encounter angular wave frequency, ω_e^*. $F_n = 0.60$.

Appendix G

Vertical Bending Moment for Small and Large Waves

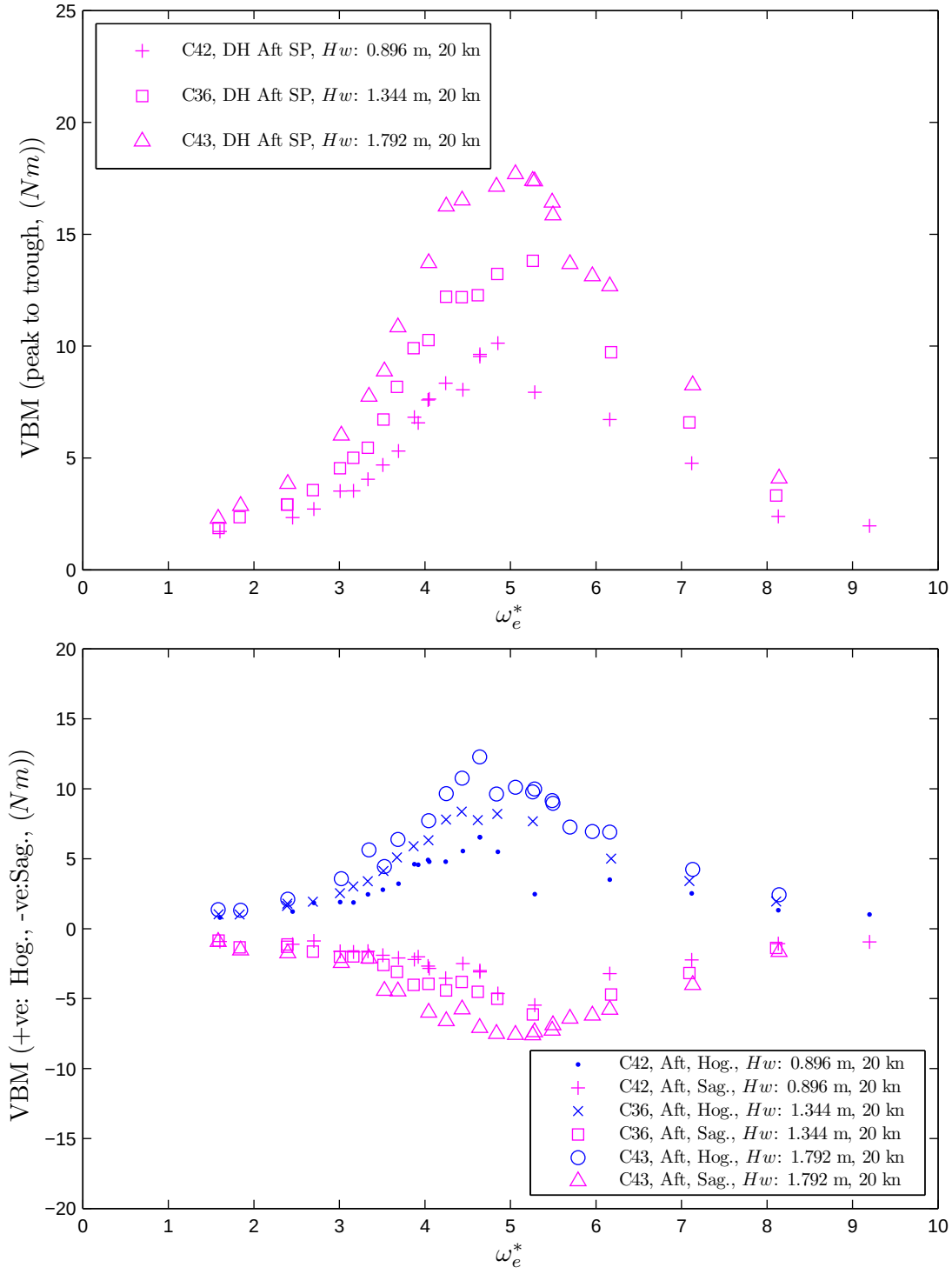

Figure G.1: Vertical bending moment (peak to trough) and hogging and sagging vertical bending moment at aft elastic links by varying the wave height, are plotted with respect to non-dimensional encounter angular wave frequency, ω_e^*. The model speed was maintained at the constant speed of $F_n = 0.32$.

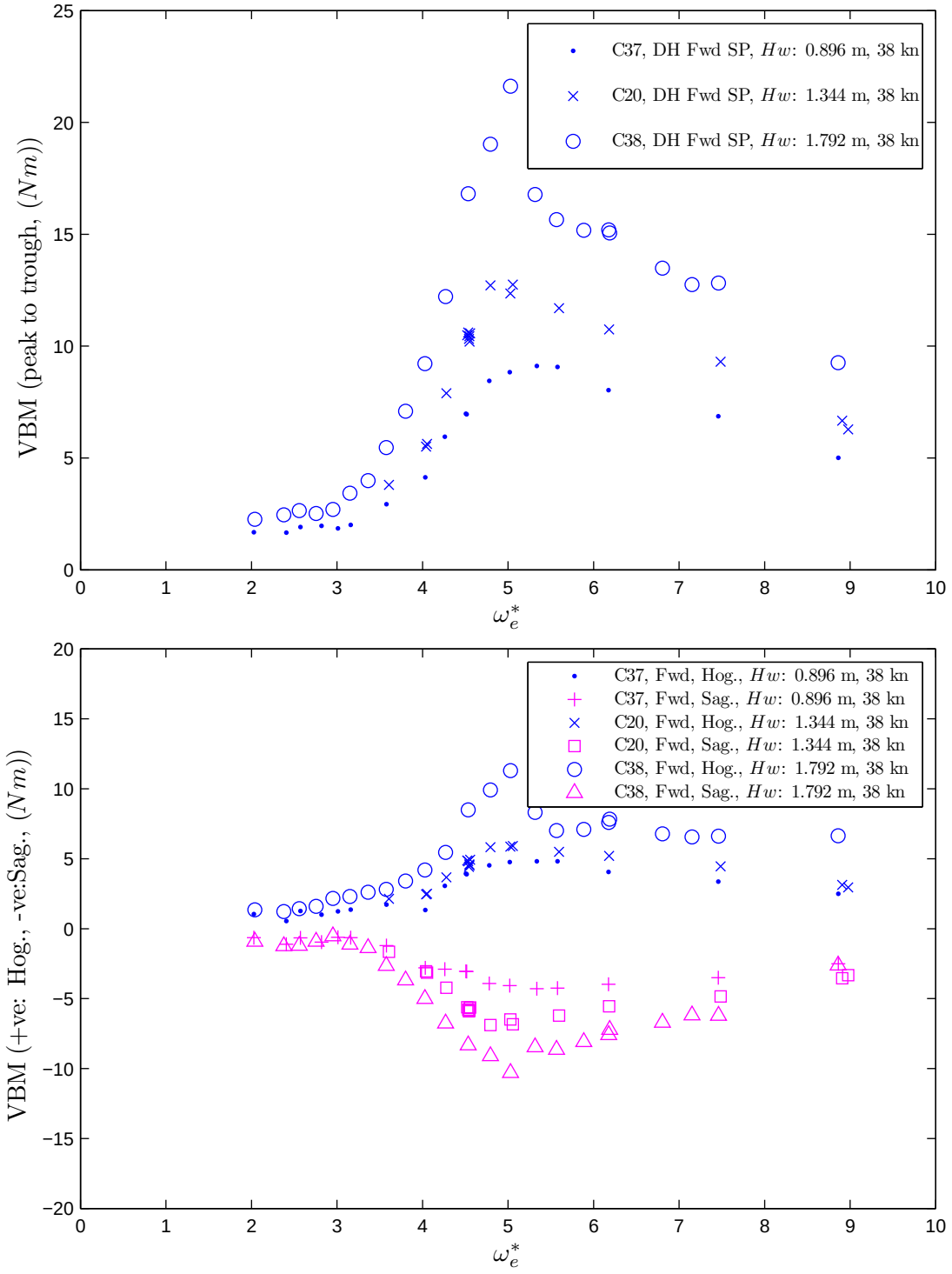

Figure G.2: Vertical bending moment (peak to trough) and hogging and sagging vertical bending moment at forward elastic links by varying the wave height, are plotted with respect to the non-dimensional encounter angular wave frequency, ω_e^*. $F_n = 0.60$.

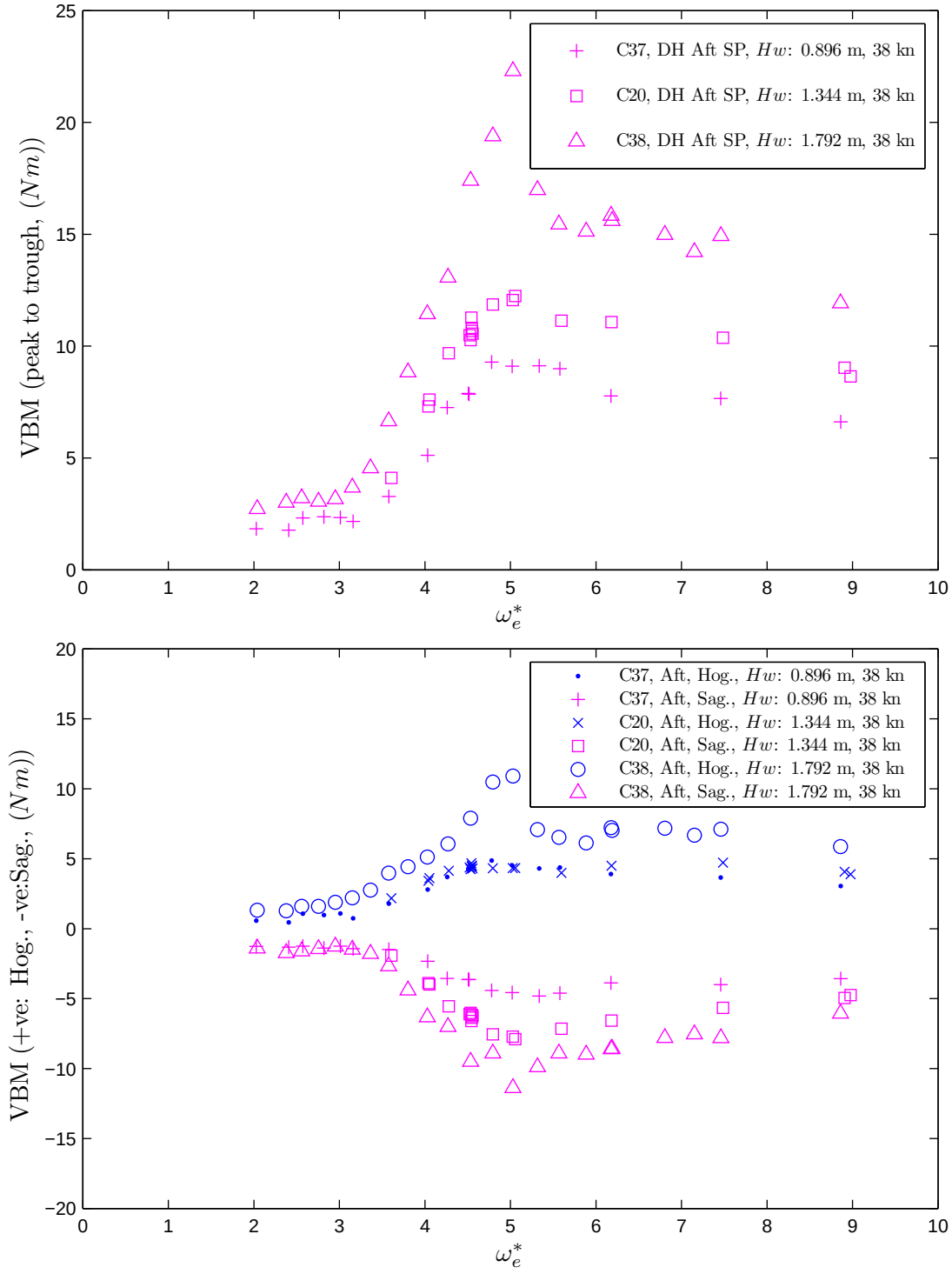

Figure G.3: Vertical bending moment (peak to trough) and hogging and sagging vertical bending moment at aft elastic links by varying the wave height, are plotted with respect to the non-dimensional encounter angular wave frequency, ω_e^*. $F_n = 0.60$.

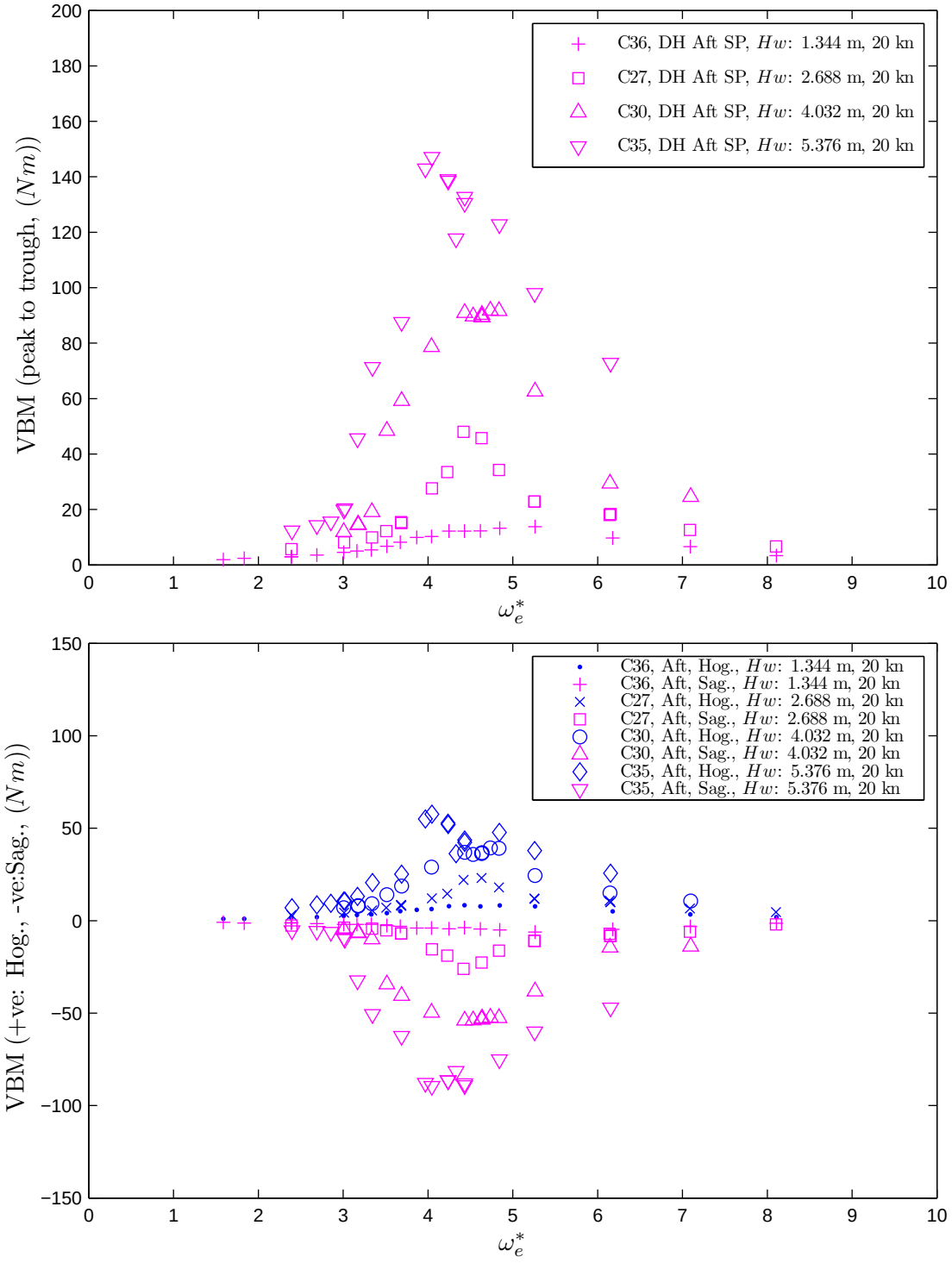

Figure G.4: Vertical bending moment (peak to trough) and hogging and sagging vertical bending moment at aft elastic links by varying the wave height, are plotted with respect to the non-dimensional encounter angular wave frequency, ω_e^*. $F_n = 0.32$.

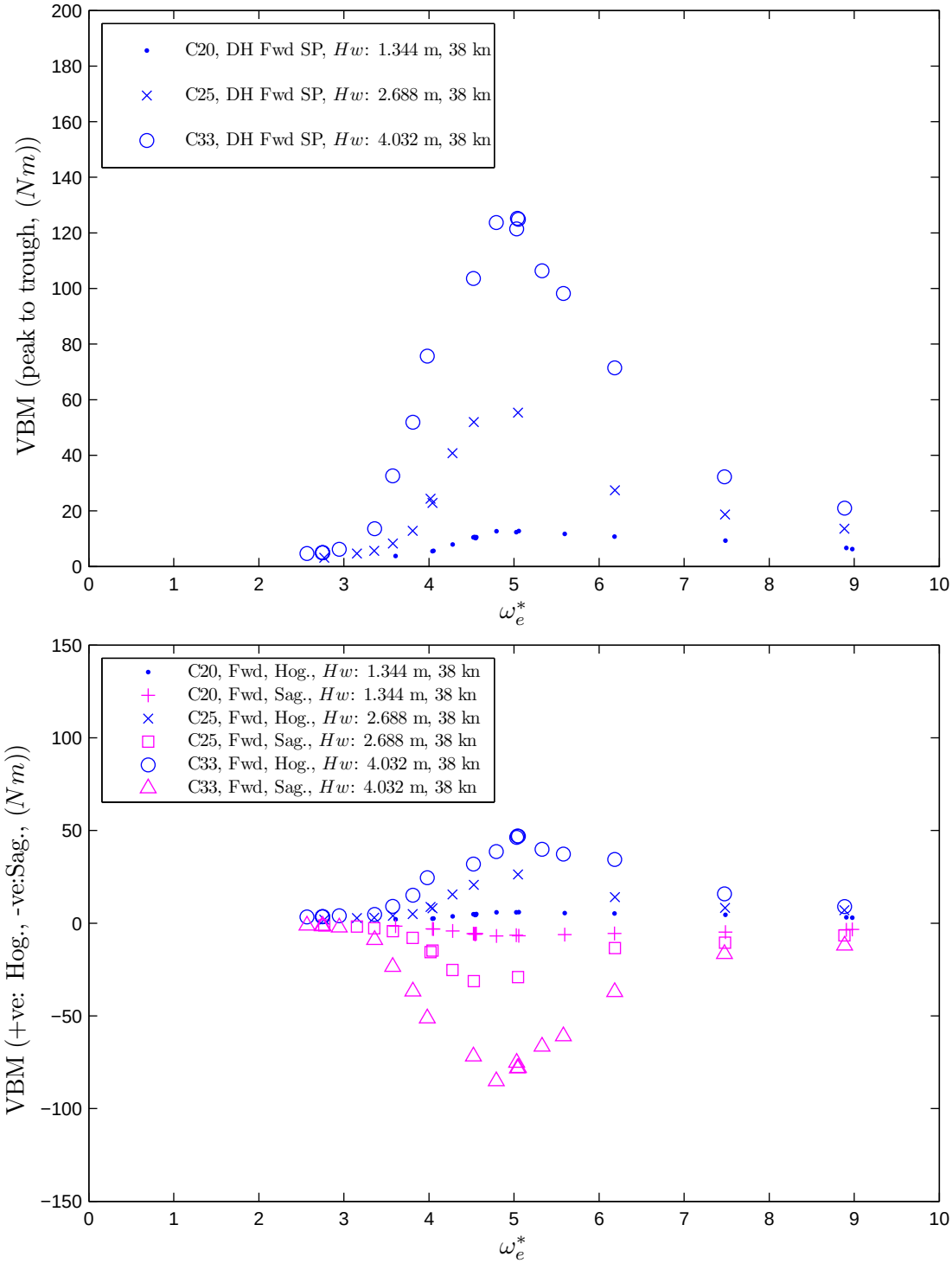

Figure G.5: Vertical bending moment (peak to trough) and hogging and sagging vertical bending moment at forward elastic links by varying the wave height, are plotted with respect to the non-dimensional encounter angular wave frequency, ω_e^*. $F_n = 0.60$.

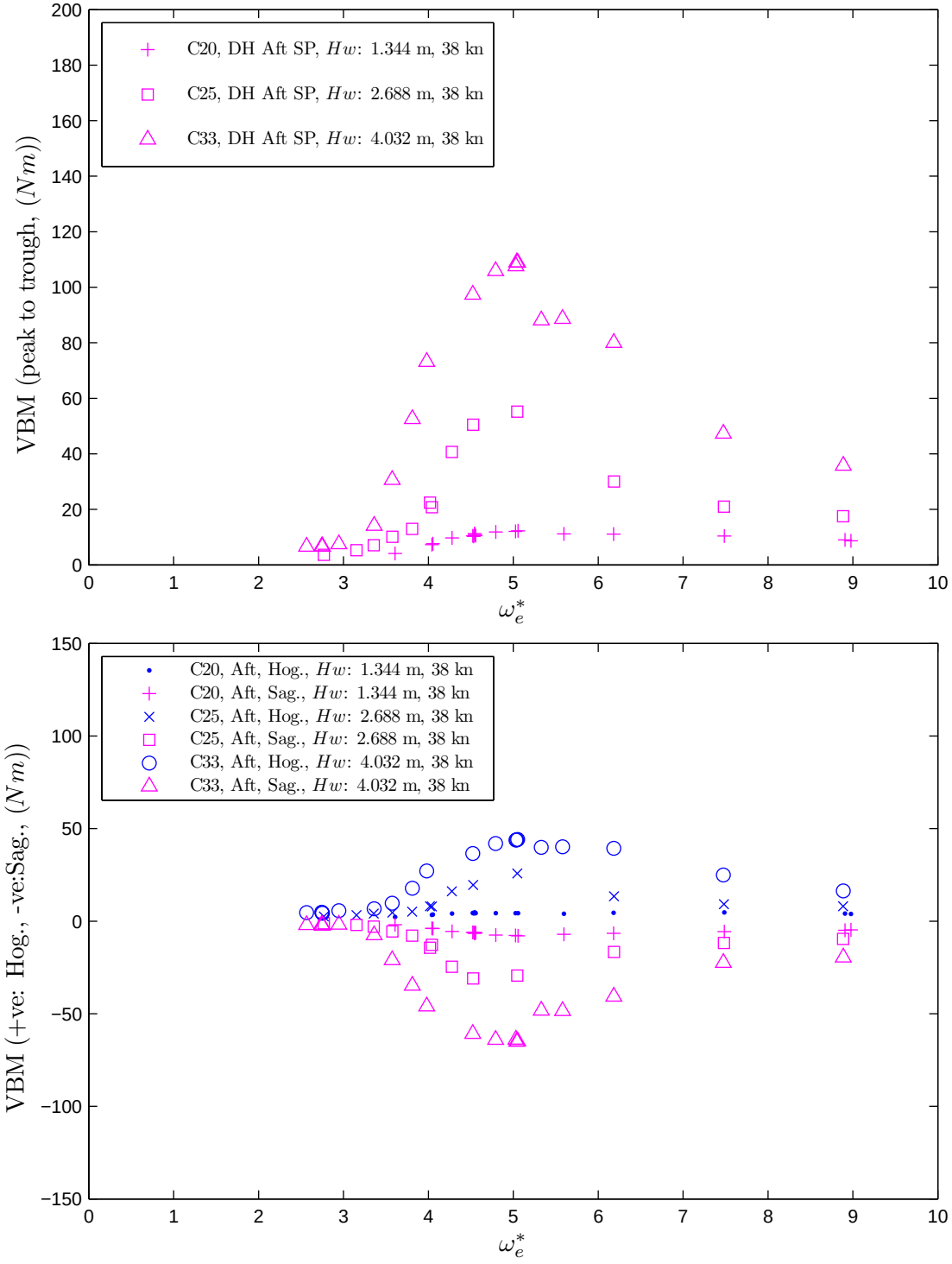

Figure G.6: Vertical bending moment (peak to trough) and hogging and sagging vertical bending moment at aft elastic links by varying the wave height, are plotted with respect to the non-dimensional encounter angular wave frequency, ω_e^*. $F_n = 0.60$.

Appendix H

Vertical Bending Moment Coefficients for Small Waves Heights

The non-dimensional vertical benging moment coefficient for small wave heights were obtained based on Equation 3.46. The wave height was varied at $H_w = 0.896$, 1.344, and 1.792 m. The constant model velocities for the comparison of wave variation were 20, 30 38 45 and 50 kn.

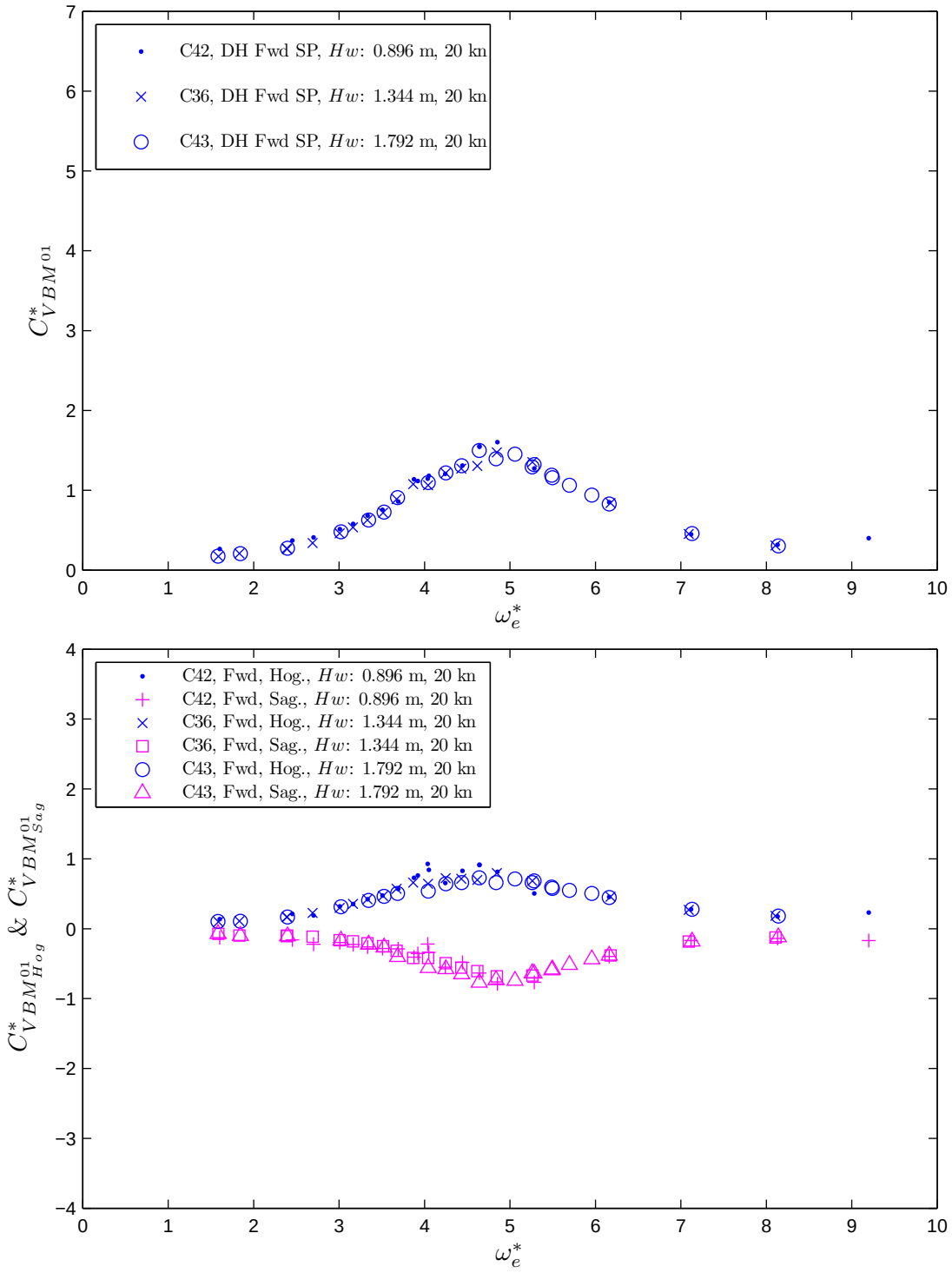

Figure H.1: Non-dimensional vertical bending moment coefficient (peak to trough), $C^*_{VBM^{01}}$ and non-dimensional hogging and sagging vertical bending moment coefficients, $C^*_{VBM^{01}_{Hog}}$ & $C^*_{VBM^{01}_{Hog}}$, at forward elastic links by varying the wave height, are plotted with respect to the non-dimensional encounter angular wave frequency, ω^*_e. $F_n = 0.32$.

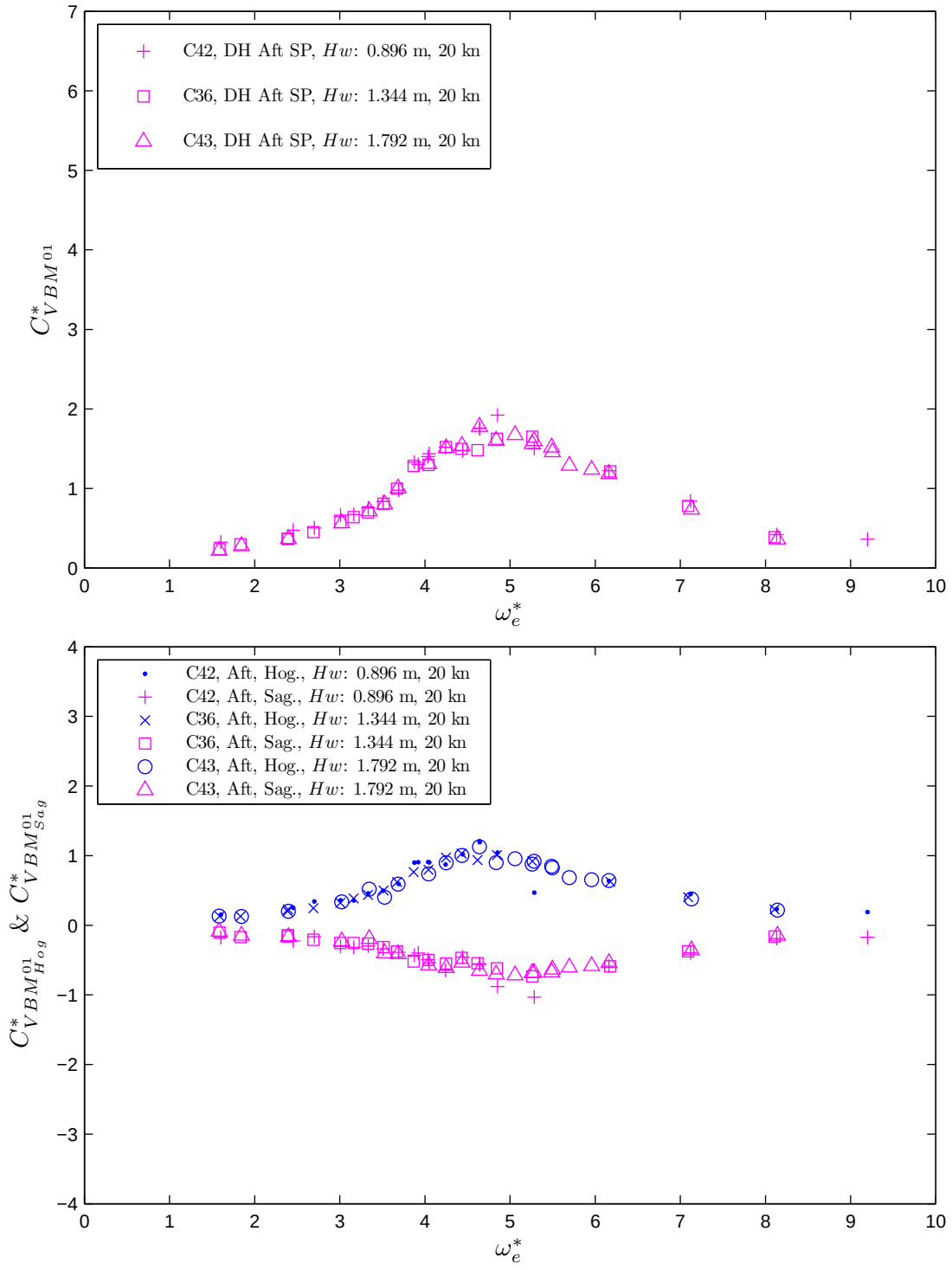

Figure H.2: Non-dimensional vertical bending moment coefficient (peak to trough), $C^*_{VBM^{01}}$ and Non-dimensional hogging and sagging vertical bending moment coefficient, $C^*_{VBM^{01}_{Hog}}$ & $C^*_{VBM^{01}_{Hog}}$ at aft elastic links by varying the wave height, are plotted with respect to non-dimensional encounter angular wave frequency, ω^*_e. The model speed was maintained at the constant speed of $F_n = 0.32$.

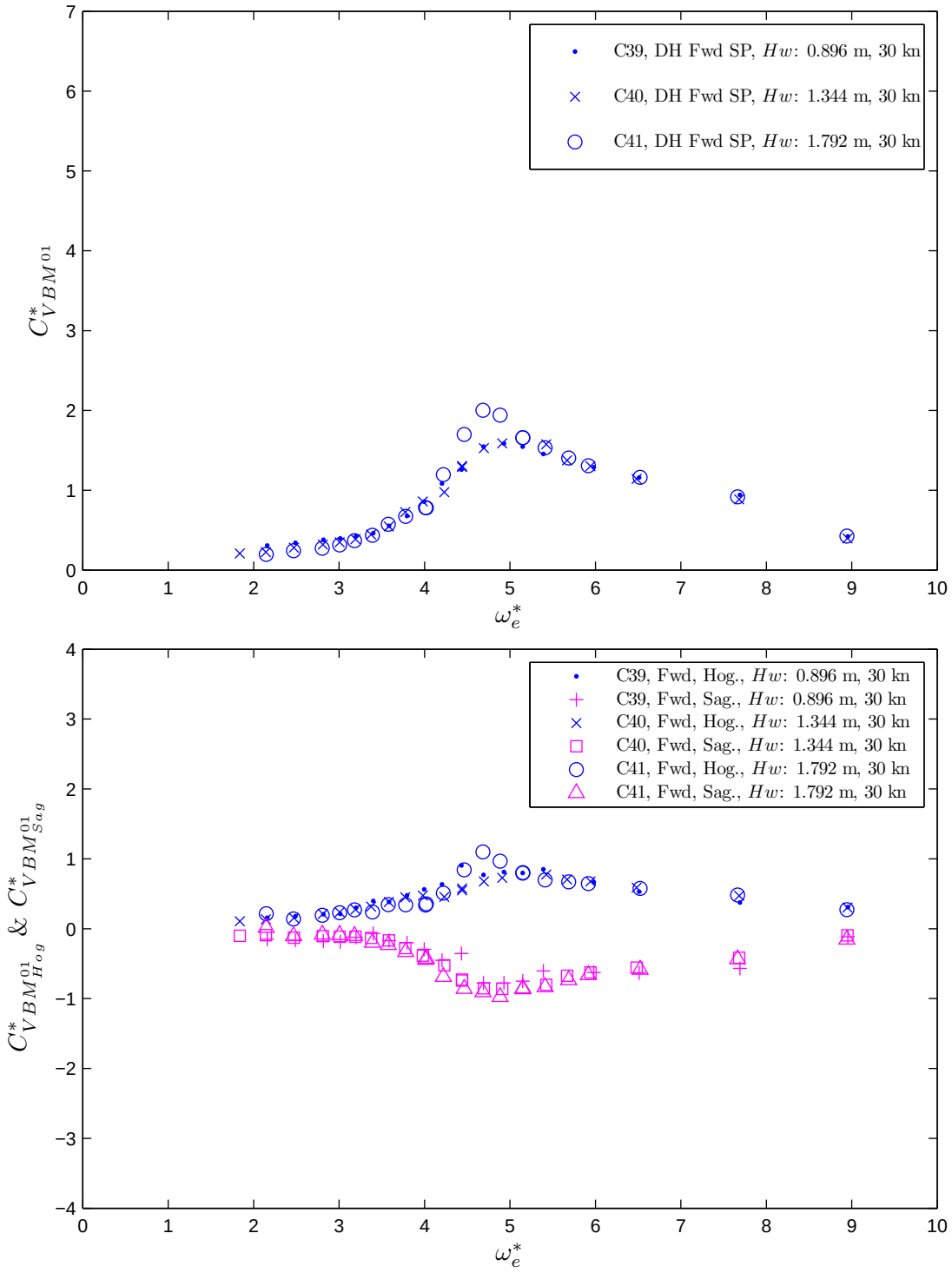

Figure H.3: Non-dimensional vertical bending moment coefficient (peak to trough), $C^*_{VBM^{01}}$ and non-dimensional hogging and sagging vertical bending moment coefficients, $C^*_{VBM^{01}_{Hog}}$ & $C^*_{VBM^{01}_{Hog}}$, at forward elastic links by varying the wave height, are plotted with respect to the non-dimensional encounter angular wave frequency, ω^*_e. $F_n = 0.48$.

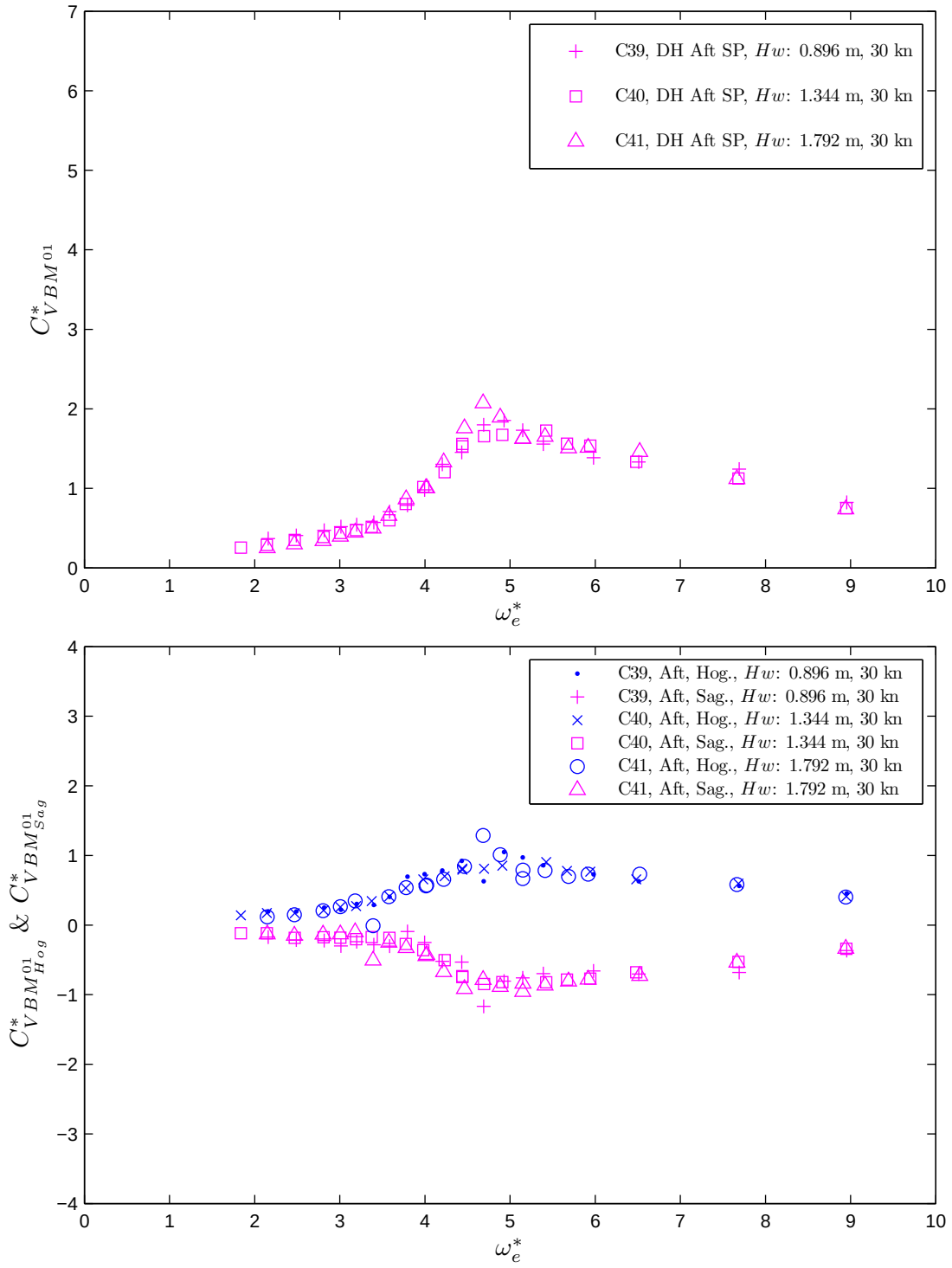

Figure H.4: Non-dimensional vertical bending moment coefficient (peak to trough), $C^*_{VBM^{01}}$ and non-dimensional hogging and sagging vertical bending moment coefficients, $C^*_{VBM^{01}_{Hog}}$ & $C^*_{VBM^{01}_{Hog}}$, at aft elastic links by varying the wave height, are plotted with respect to the non-dimensional encounter angular wave frequency, ω^*_e. $F_n = 0.48$.

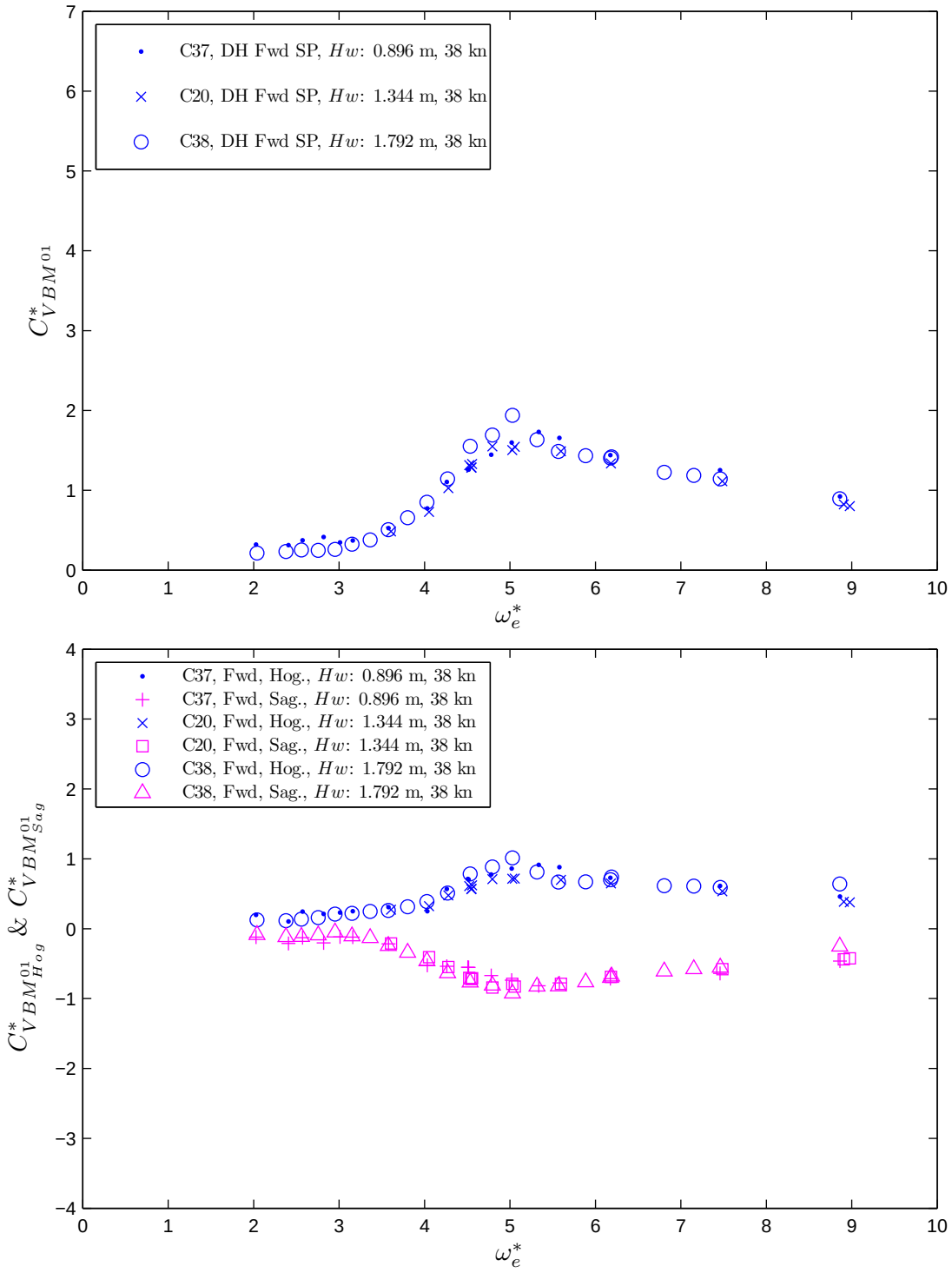

Figure H.5: Non-dimensional vertical bending moment coefficient (peak to trough), $C^*_{VBM^{01}}$ and non-dimensional hogging and sagging vertical bending moment coefficients, $C^*_{VBM^{01}_{Hog}}$ & $C^*_{VBM^{01}_{Hog}}$, at forward elastic links by varying the wave height, are plotted with respect to the non-dimensional encounter angular wave frequency, ω^*_e. $F_n = 0.60$.

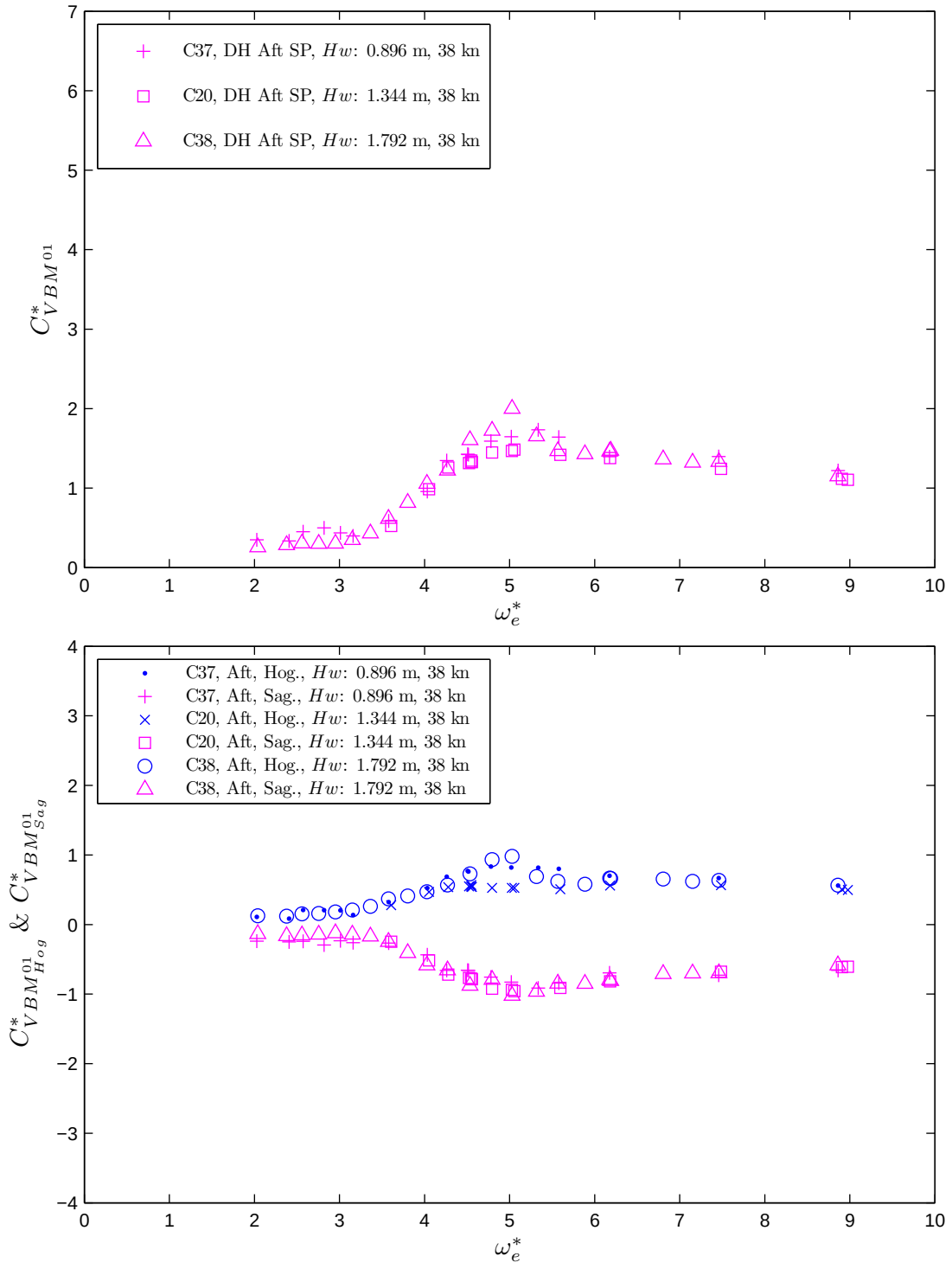

Figure H.6: Non-dimensional vertical bending moment coefficient (peak to trough), $C^*_{VBM^{01}}$ and non-dimensional hogging and sagging vertical bending moment coefficients, $C^*_{VBM^{01}_{Hog}}$ & $C^*_{VBM^{01}_{Hog}}$, at aft elastic links by varying the wave height, are plotted with respect to the non-dimensional encounter angular wave frequency, ω^*_e. $F_n = 0.60$.

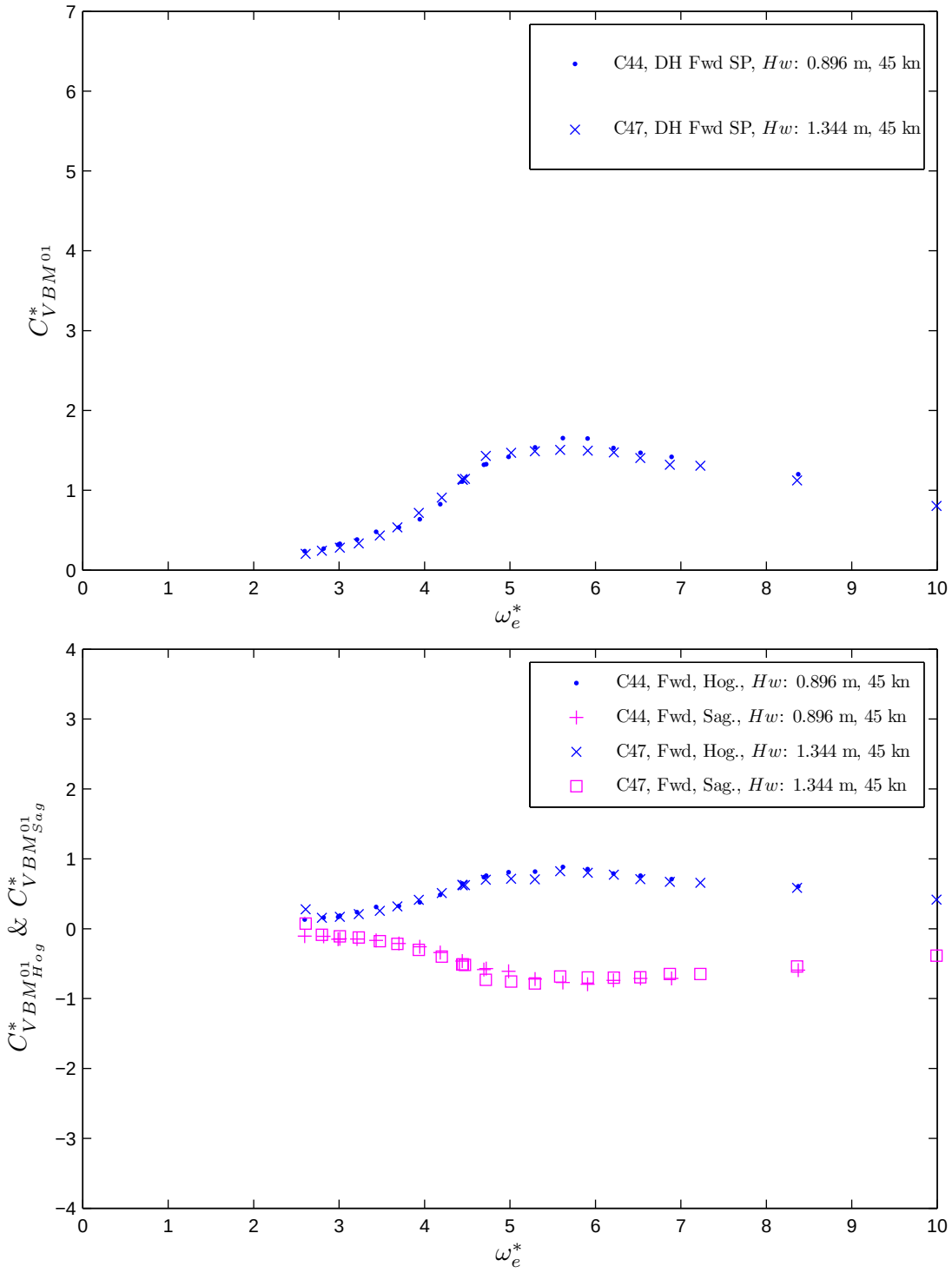

Figure H.7: Non-dimensional vertical bending moment coefficient (peak to trough), $C^*_{VBM^{01}}$ and non-dimensional hogging and sagging vertical bending moment coefficients, $C^*_{VBM^{01}_{Hog}}$ & $C^*_{VBM^{01}_{Hog}}$, at forward elastic links by varying the wave height, are plotted with respect to the non-dimensional encounter angular wave frequency, ω^*_e. $F_n = 0.72$.

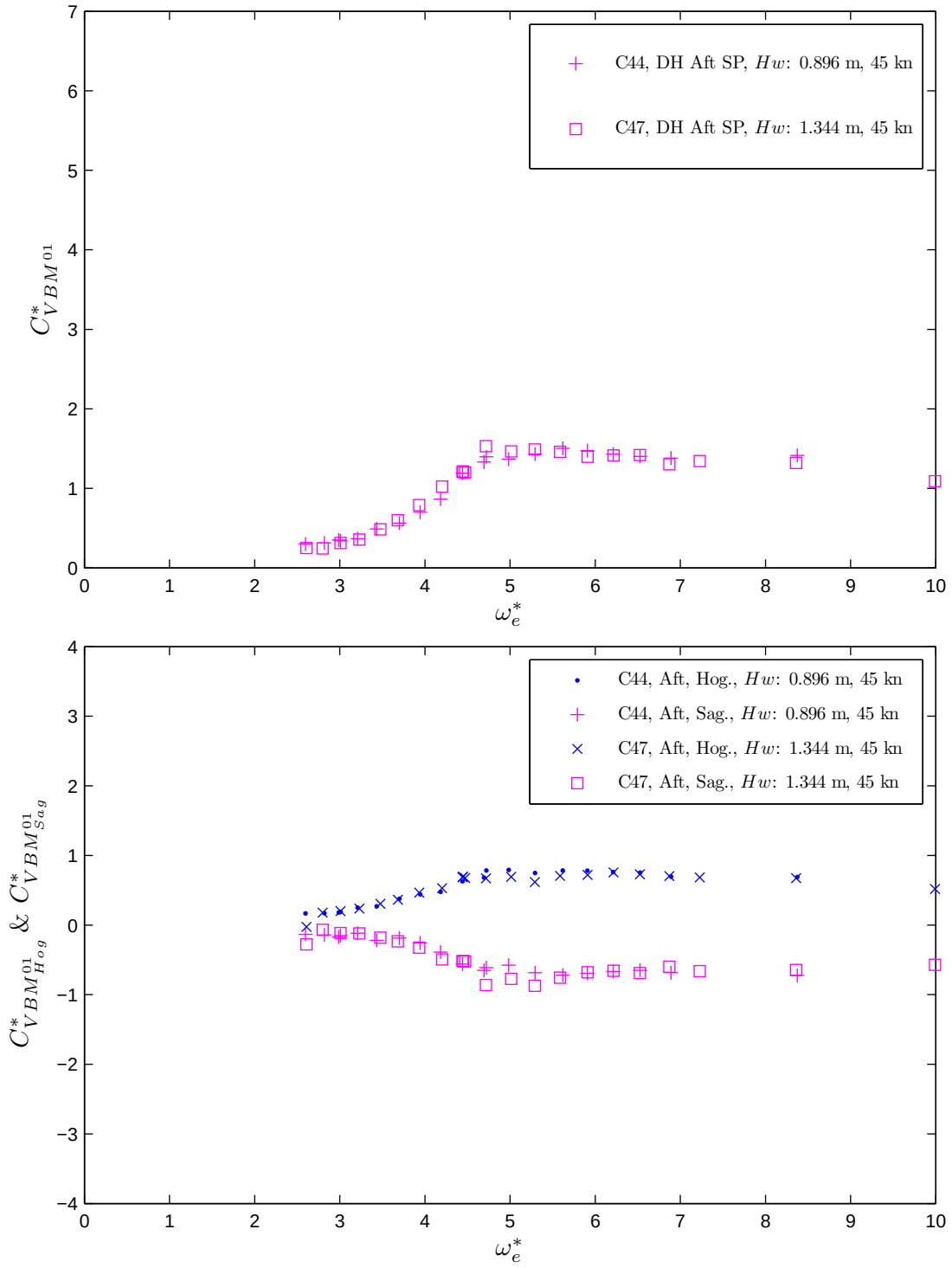

Figure H.8: Non-dimensional vertical bending moment coefficient (peak to trough), $C^*_{VBM^{01}}$ and non-dimensional hogging and sagging vertical bending moment coefficients, $C^*_{VBM^{01}_{Hog}}$ & $C^*_{VBM^{01}_{Hog}}$, at aft elastic links by varying the wave height, are plotted with respect to the non-dimensional encounter angular wave frequency, ω^*_e. $F_n = 0.72$.

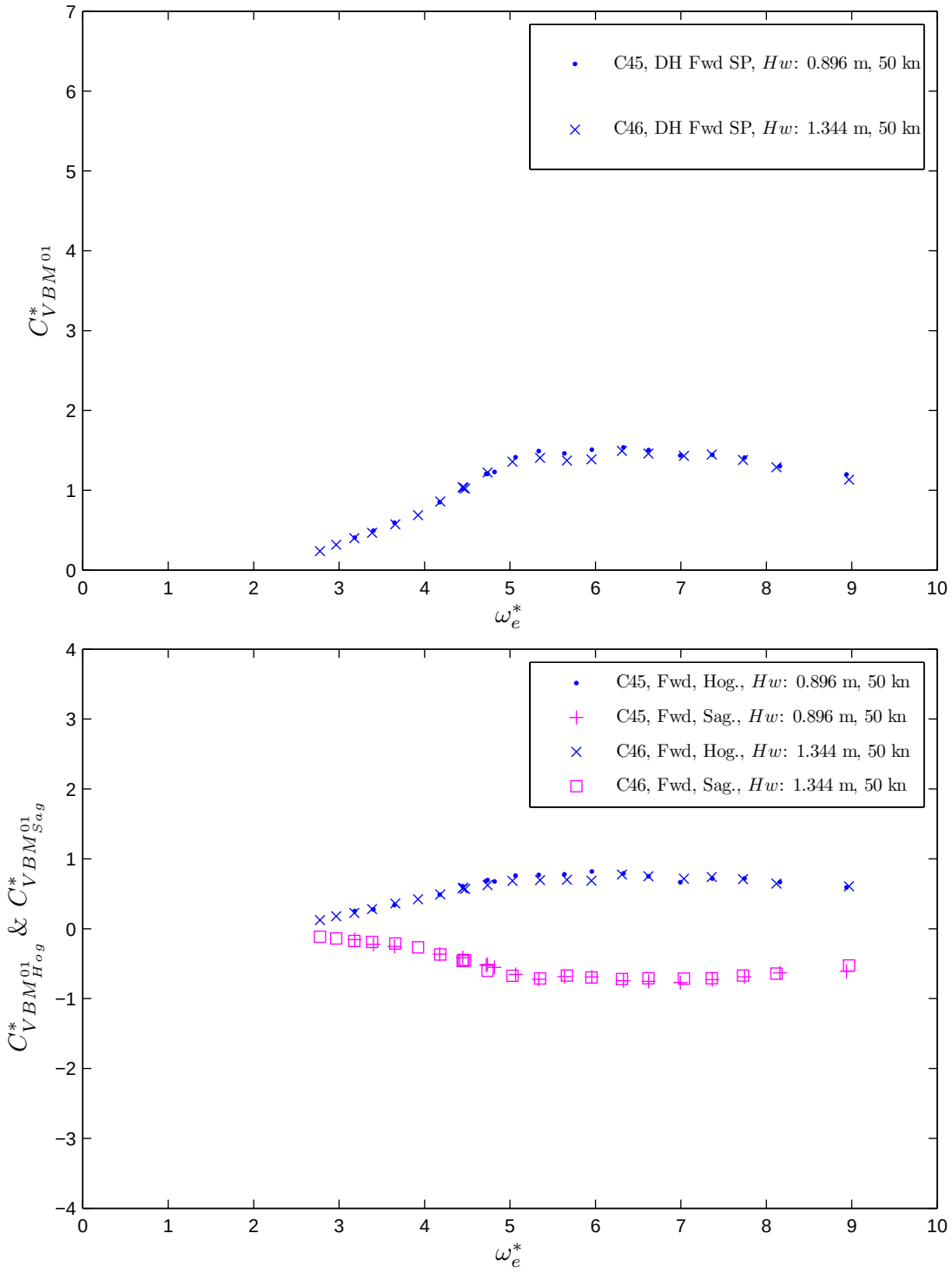

Figure H.9: Non-dimensional vertical bending moment coefficient (peak to trough), $C^*_{VBM^{01}}$ and non-dimensional hogging and sagging vertical bending moment coefficients, $C^*_{VBM^{01}_{Hog}}$ & $C^*_{VBM^{01}_{Hog}}$, at forward elastic links by varying the wave height, are plotted with respect to the non-dimensional encounter angular wave frequency, ω^*_e. $F_n = 0.79$.

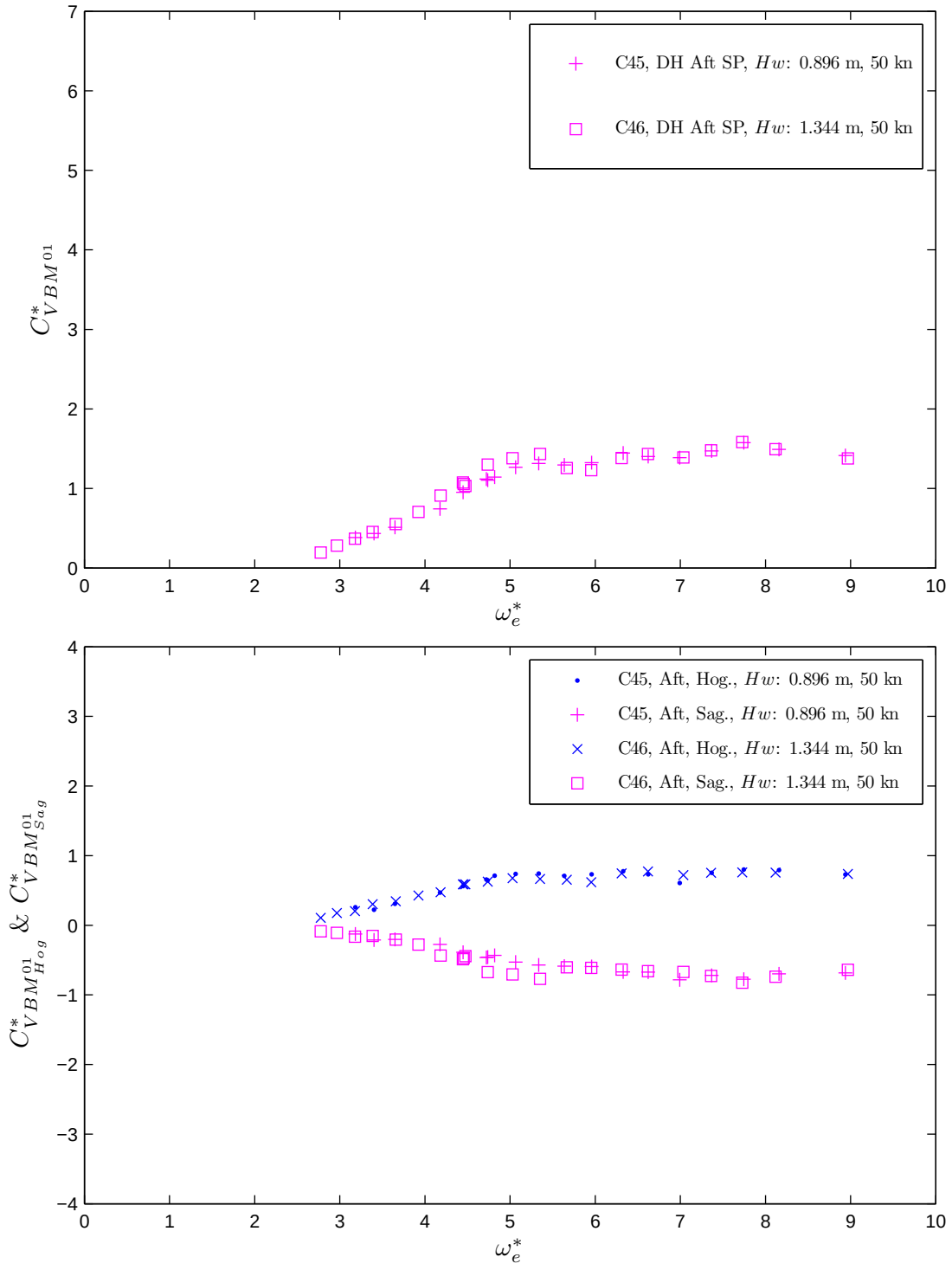

Figure H.10: Non-dimensional vertical bending moment coefficient (peak to trough), $C^*_{VBM^{01}}$ and non-dimensional hogging and sagging vertical bending moment coefficients, $C^*_{VBM^{01}_{Hog}}$ & $C^*_{VBM^{01}_{Hog}}$, at aft elastic links by varying the wave height, are plotted with respect to the non-dimensional encounter angular wave frequency, ω^*_e. $F_n = 0.79$.

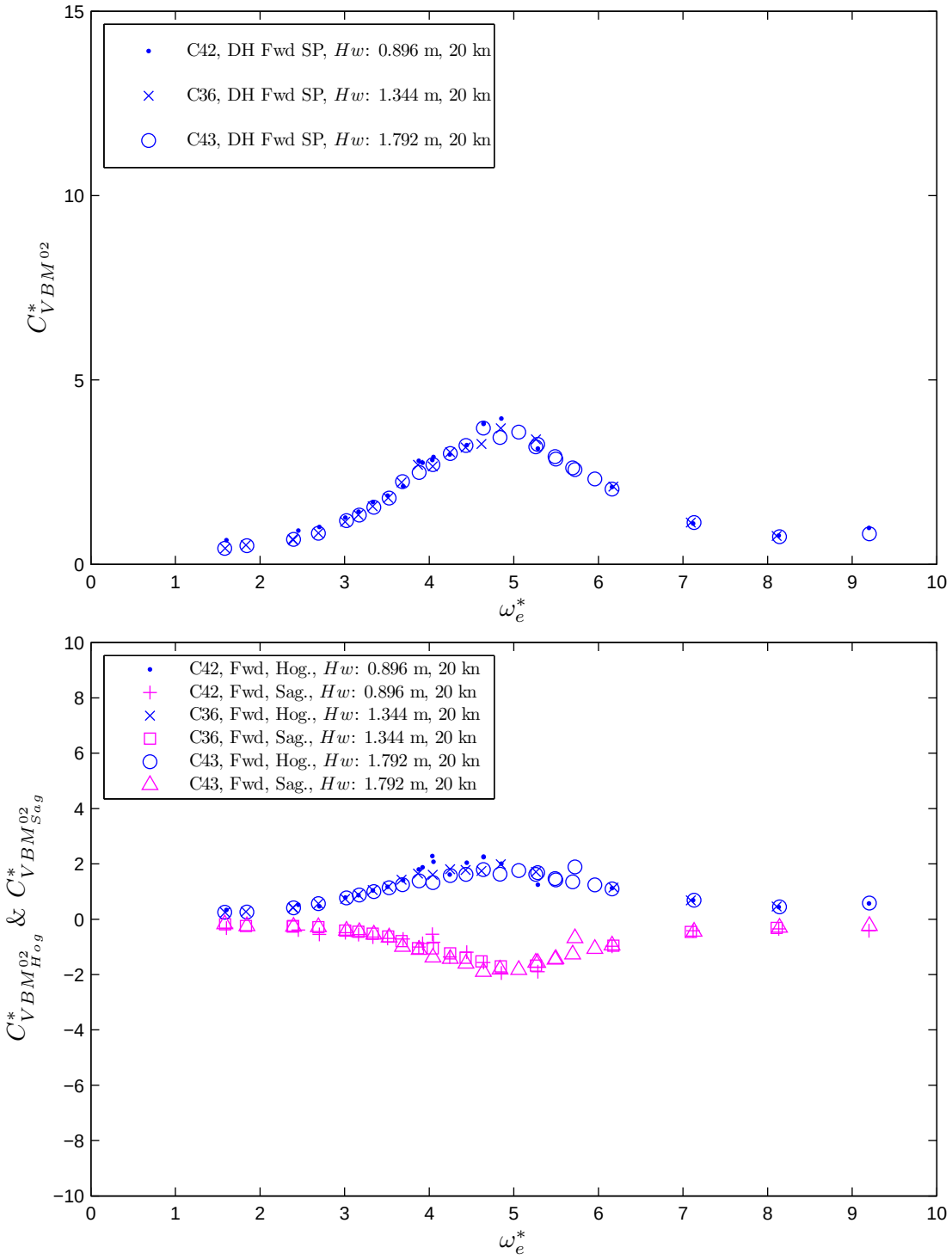

Figure H.11: Non-dimensional vertical bending moment coefficient (peak to trough), $C^*_{VBM^{02}}$ and non-dimensional hogging and sagging vertical bending moment coefficients, $C^*_{VBM^{02}_{Hog}}$ & $C^*_{VBM^{02}_{Hog}}$, at forward elastic links by varying the wave height, are plotted with respect to the non-dimensional encounter angular wave frequency, ω^*_e. $F_n = 0.32$.

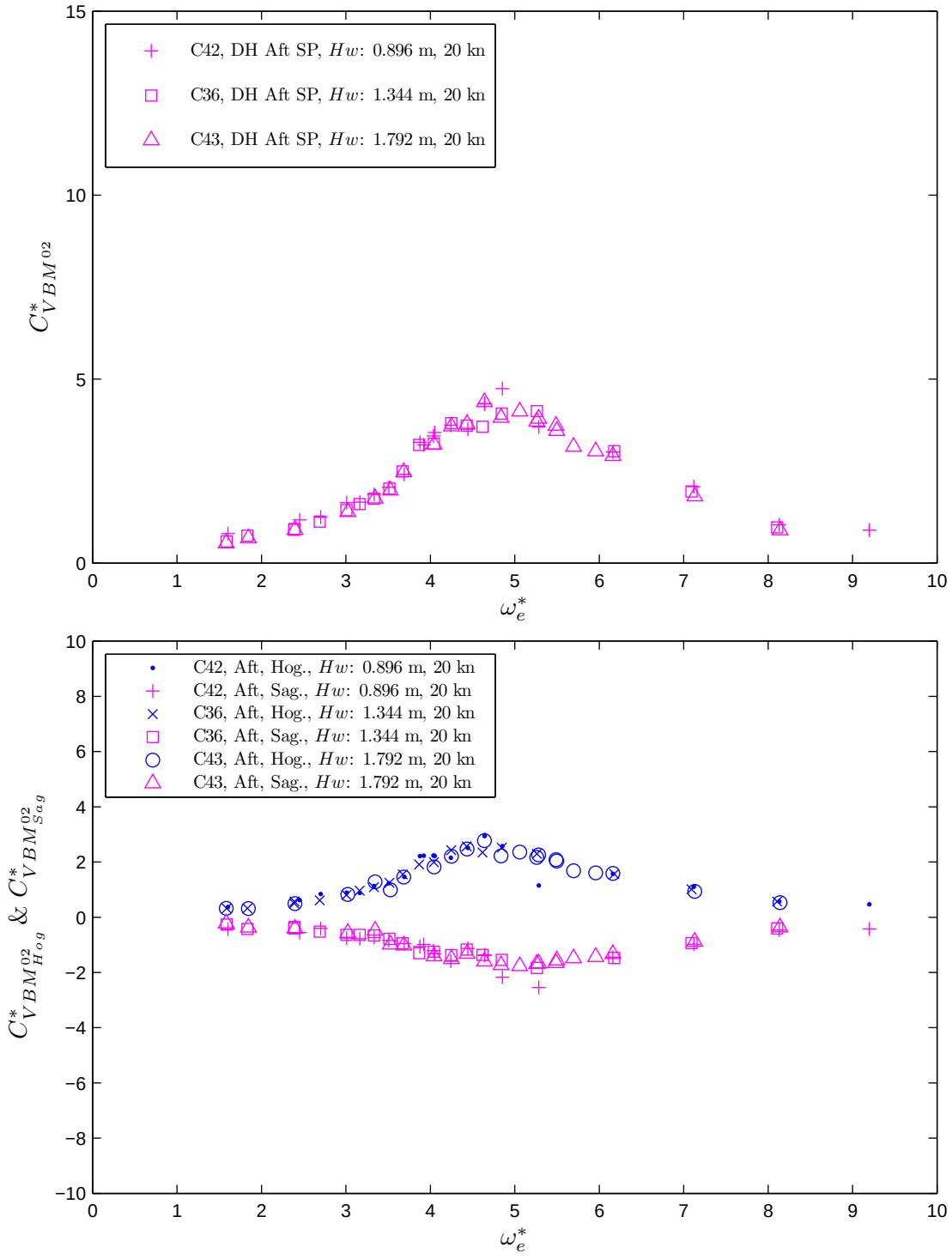

Figure H.12: Non-dimensional vertical bending moment coefficient (peak to trough), $C^*_{VBM^{02}}$ and Non-dimensional hogging and sagging vertical bending moment coefficient , $C^*_{VBM^{02}_{Hog}}$ & $C^*_{VBM^{02}_{Hog}}$ at aft elastic links by varying the wave height, are plotted with respect to non-dimensional encounter angular wave frequency, ω^*_e. The model speed was maintained at the constant speed of $F_n = 0.32$.

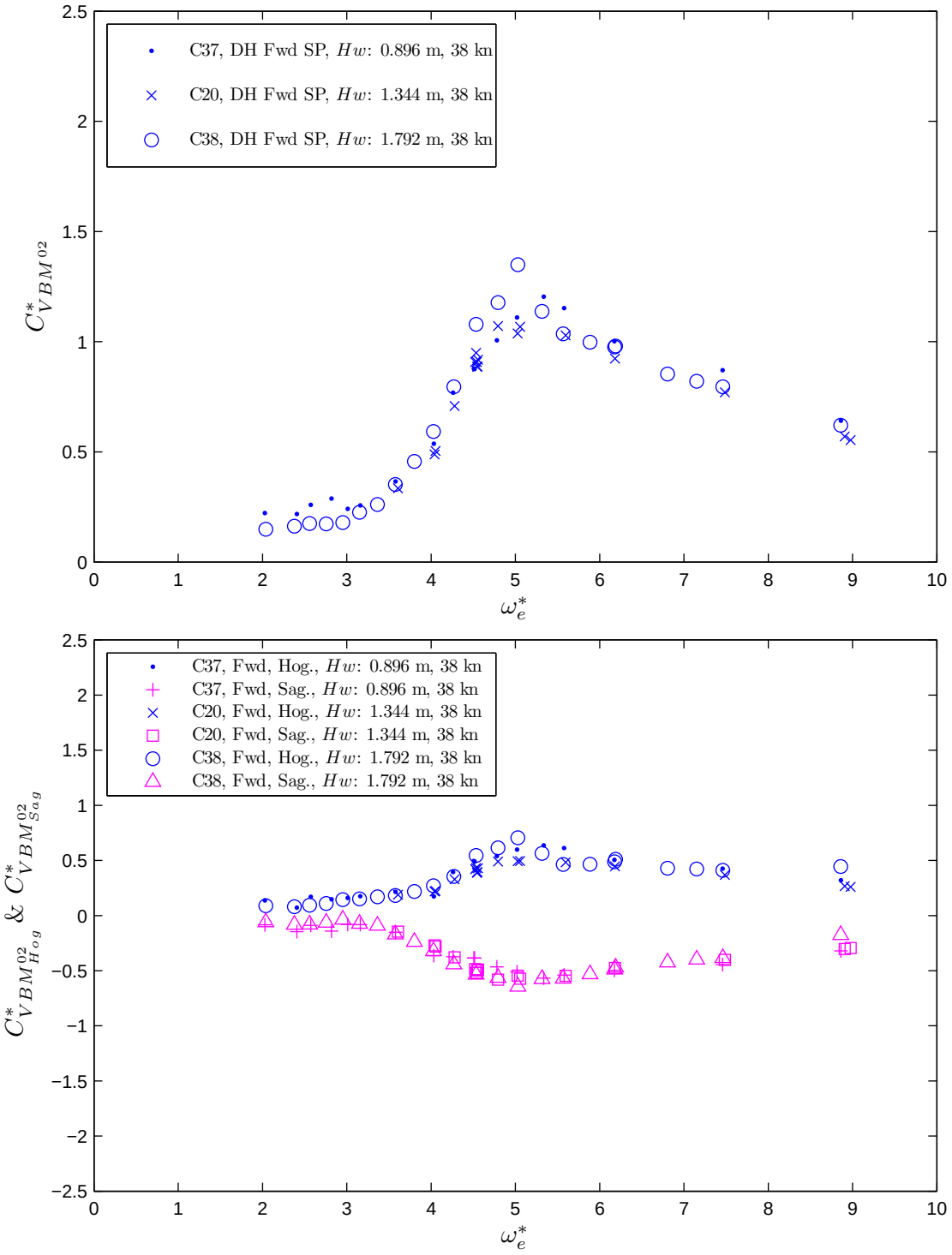

Figure H.13: Non-dimensional vertical bending moment coefficient (peak to trough), $C^*_{VBM^{02}}$ and non-dimensional hogging and sagging vertical bending moment coefficients, $C^*_{VBM^{02}_{Hog}}$ & $C^*_{VBM^{02}_{Hog}}$, at forward elastic links by varying the wave height, are plotted with respect to the non-dimensional encounter angular wave frequency, $\omega^*_e.F_n = 0.60$.

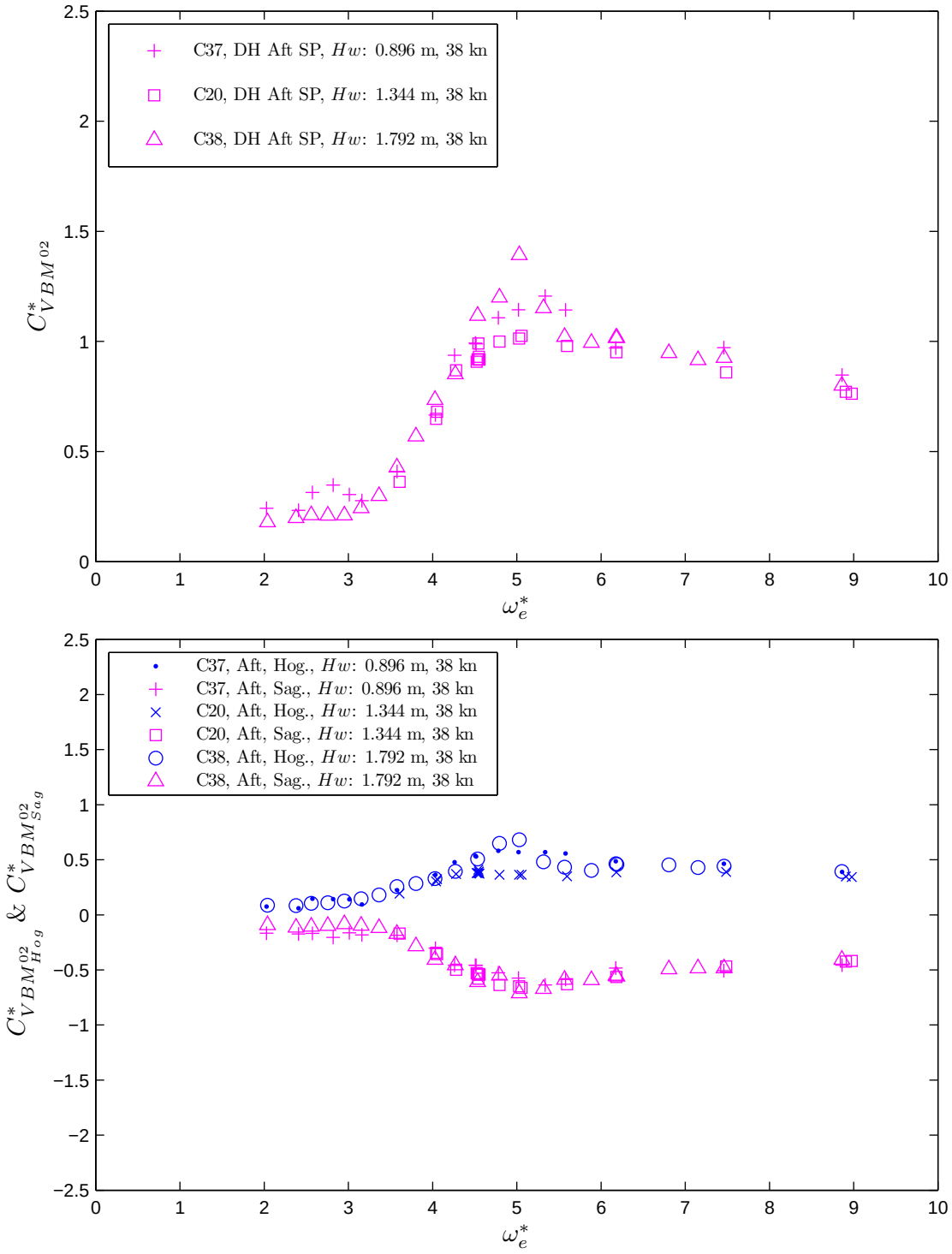

Figure H.14: Non-dimensional vertical bending moment coefficient (peak to trough), $C^*_{VBM^{02}}$ and non-dimensional hogging and sagging vertical bending moment coefficients, $C^*_{VBM^{02}_{Hog}}$ & $C^*_{VBM^{02}_{Hog}}$, at aft elastic links by varying the wave height, are plotted with respect to the non-dimensional encounter angular wave frequency, ω^*_e. $F_n = 0.60$.

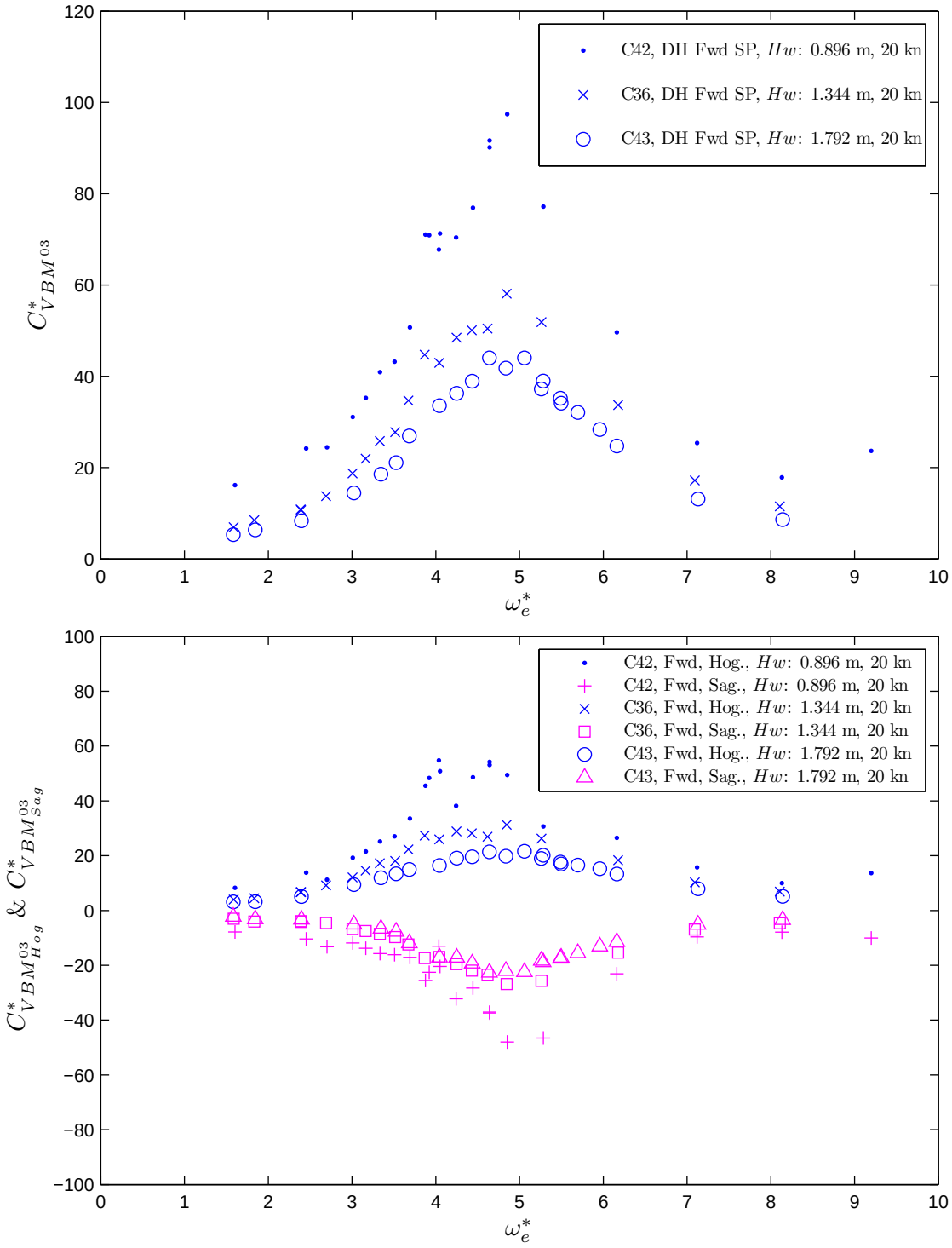

Figure H.15: Non-dimensional vertical bending moment coefficient (peak to trough), $C^*_{VBM^{03}}$ and non-dimensional hogging and sagging vertical bending moment coefficients, $C^*_{VBM^{03}_{Hog}}$ & $C^*_{VBM^{03}_{Hog}}$, at forward elastic links by varying the wave height, are plotted with respect to the non-dimensional encounter angular wave frequency, ω^*_e. $F_n = 0.32$.

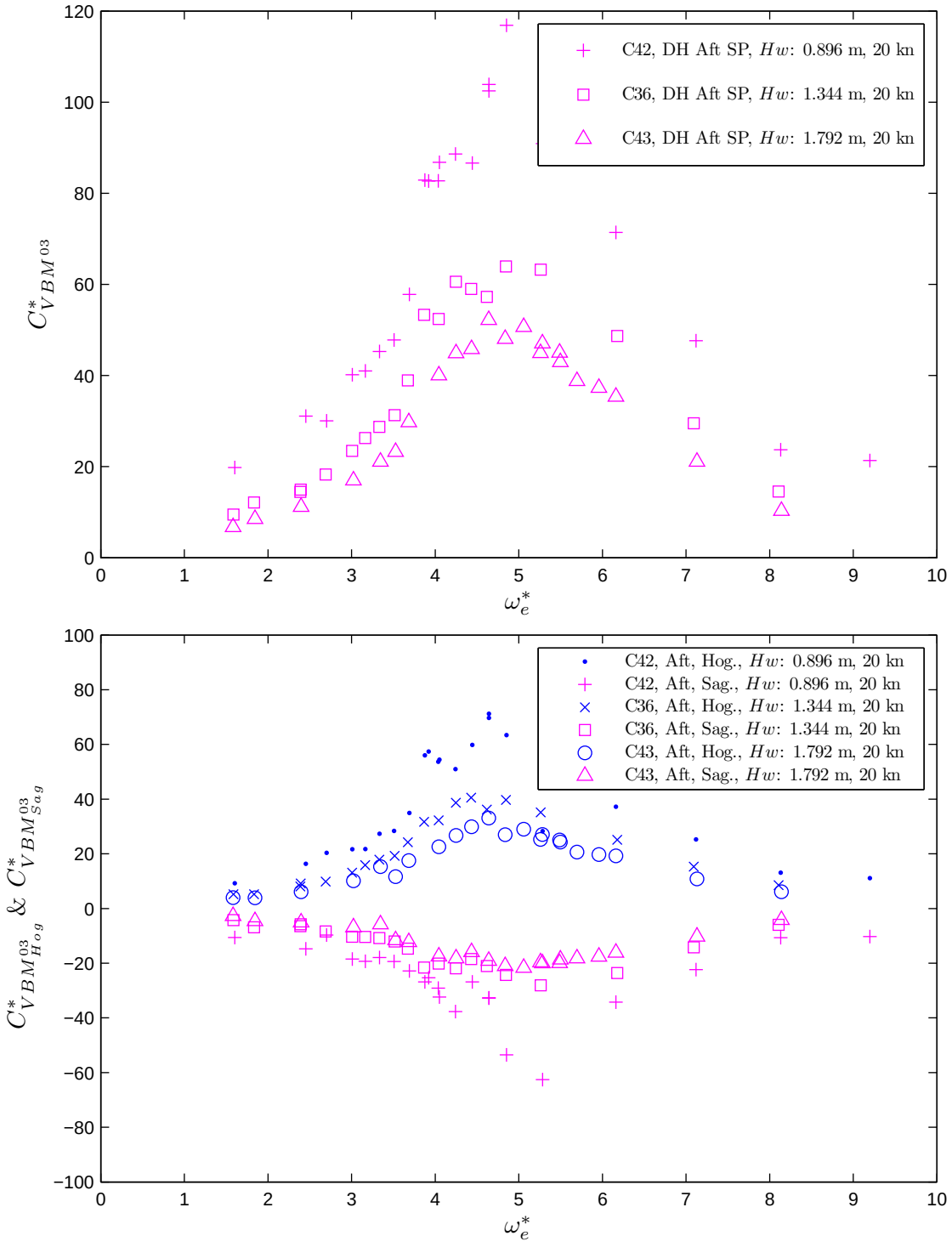

Figure H.16: Non-dimensional vertical bending moment coefficient (peak to trough), $C^*_{VBM^{03}}$ and non-dimensional hogging and sagging vertical bending moment coefficients, $C^*_{VBM^{03}_{Hog}}$ & $C^*_{VBM^{03}_{Hog}}$, at aft elastic links by varying the wave height, are plotted with respect to the non-dimensional encounter angular wave frequency, ω^*_e. $F_n = 0.32$.

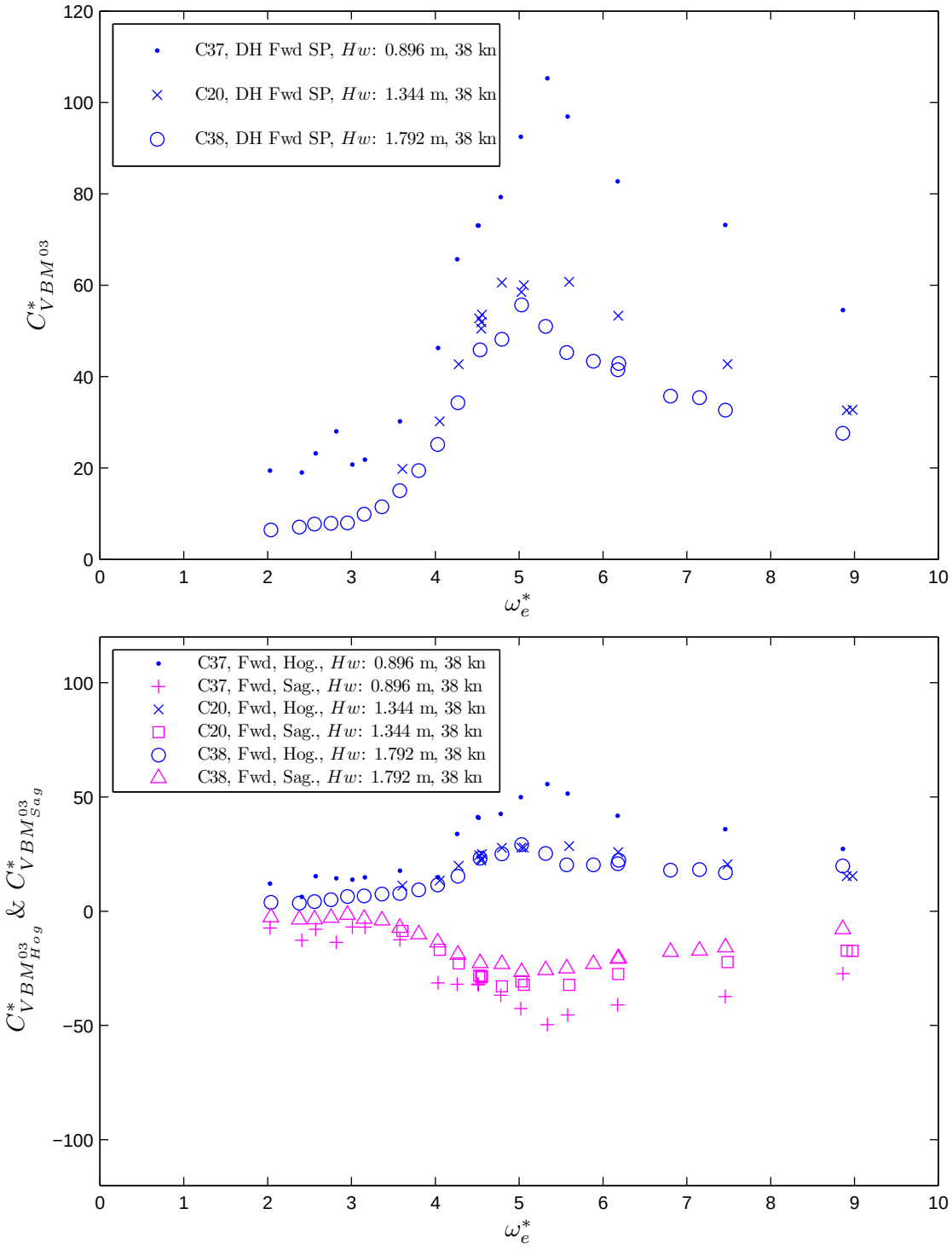

Figure H.17: Non-dimensional vertical bending moment coefficient (peak to trough), $C^*_{VBM^{03}}$ and non-dimensional hogging and sagging vertical bending moment coefficients, $C^*_{VBM^{03}_{Hog}}$ & $C^*_{VBM^{03}_{Hog}}$, at forward elastic links by varying the wave height, are plotted with respect to the non-dimensional encounter angular wave frequency, ω^*_e. $F_n = 0.60$.

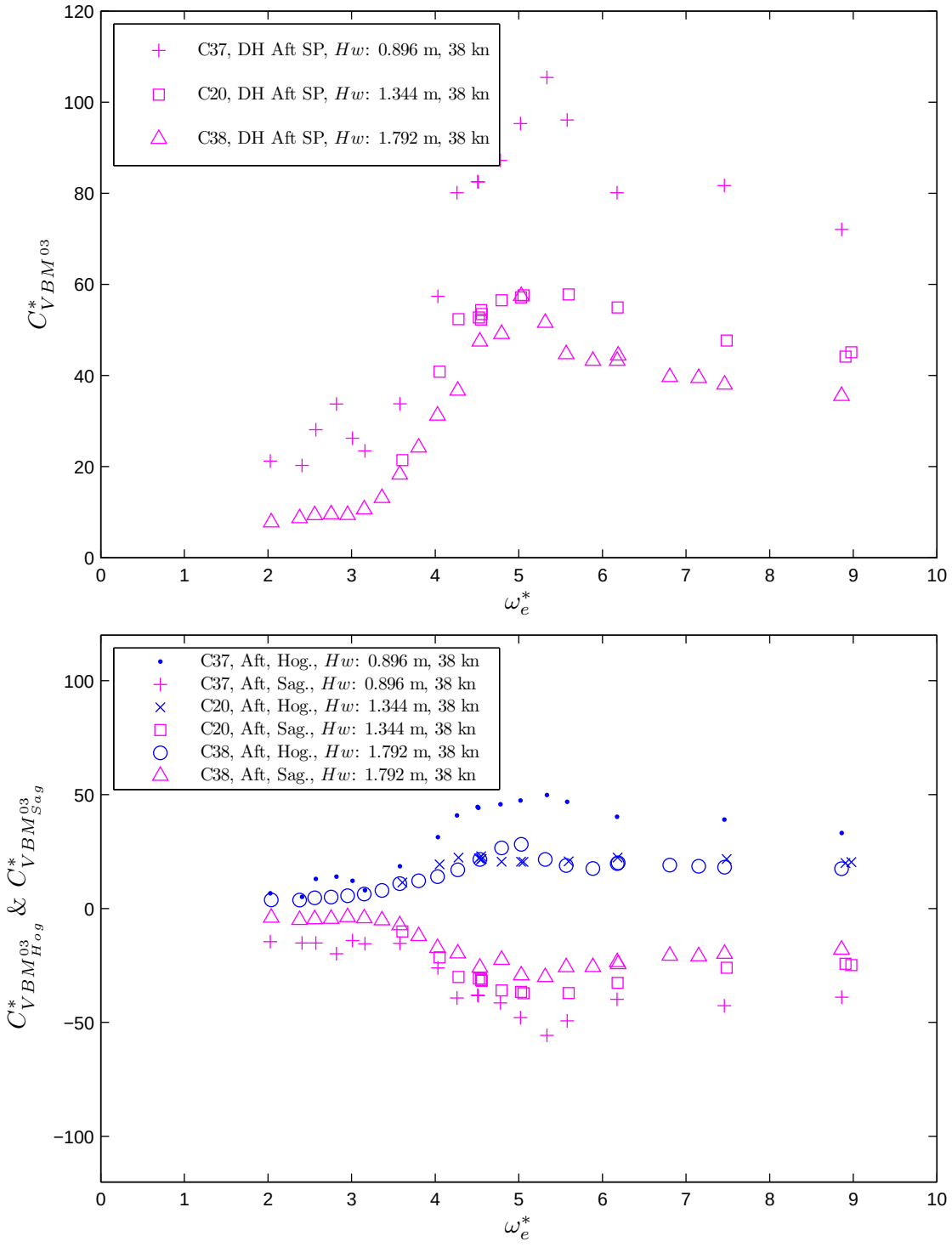

Figure H.18: Non-dimensional vertical bending moment coefficient (peak to trough), $C^*_{VBM^{03}}$ and non-dimensional hogging and sagging vertical bending moment coefficients, $C^*_{VBM^{03}_{Hog}}$ & $C^*_{VBM^{03}_{Hog}}$, at aft elastic links by varying the wave height, are plotted with respect to the non-dimensional encounter angular wave frequency, ω^*_e. $F_n = 0.60$.

Appendix I

Vertical Bending Moment Coefficients for Large Waves Heights

The non-dimensional vertical binging moment coefficient for large wave heights were obtained based on the Equation 3.46. The wave height was varied at H_w = 1.344, 2.688 4.032 and 5.376 m. The constant model velocities for the comparison of wave variation were 20 and 38 kn.

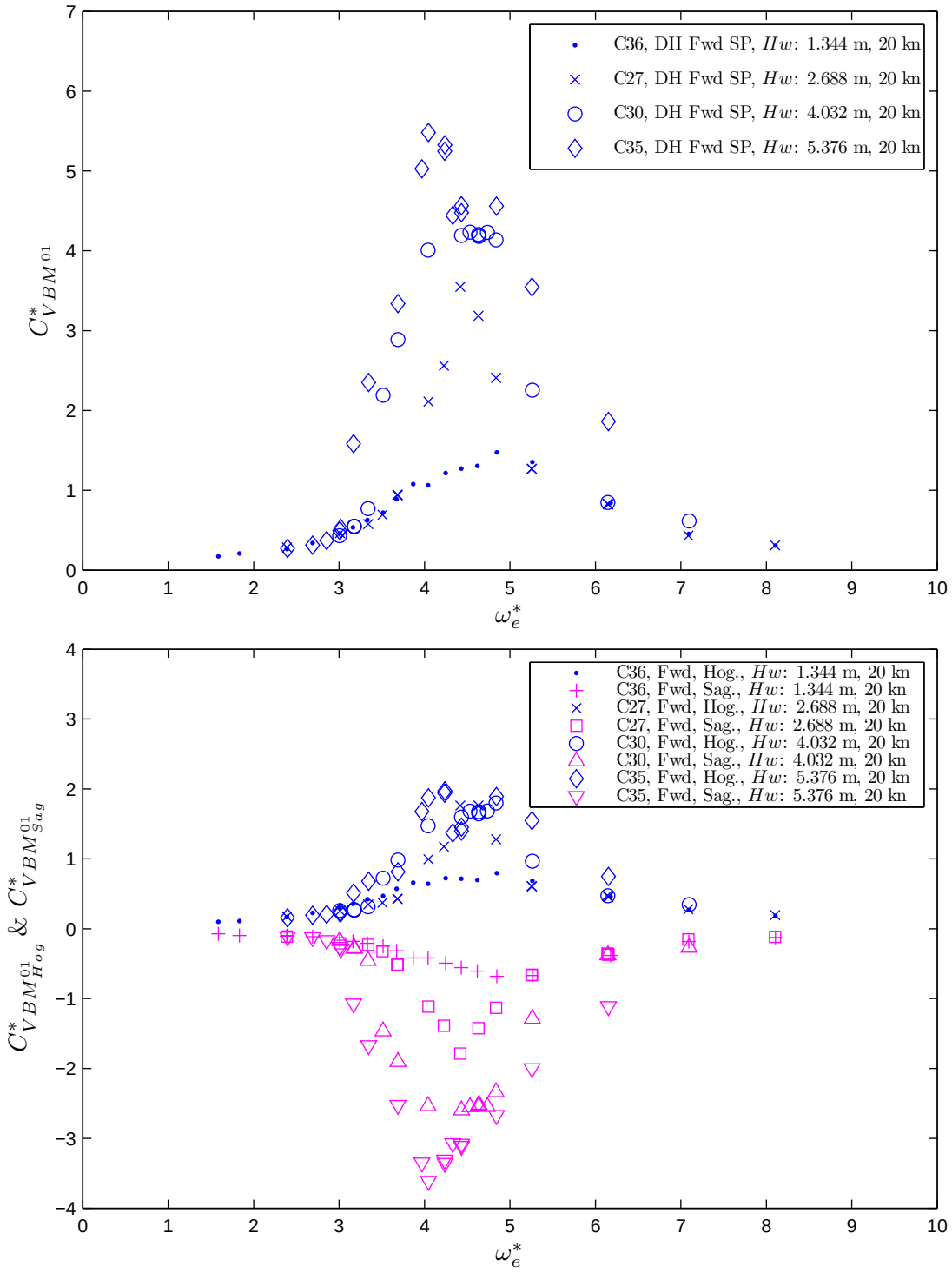

Figure I.1: Non-dimensional vertical bending moment coefficient (peak to trough), $C^*_{VBM^{01}}$ and non-dimensional hogging and sagging vertical bending moment coefficients, $C^*_{VBM^{01}_{Hog}}$ & $C^*_{VBM^{01}_{Hog}}$, at forward elastic links by varying the wave height, are plotted with respect to the non-dimensional encounter angular wave frequency, ω^*_e. $F_n = 0.32$.

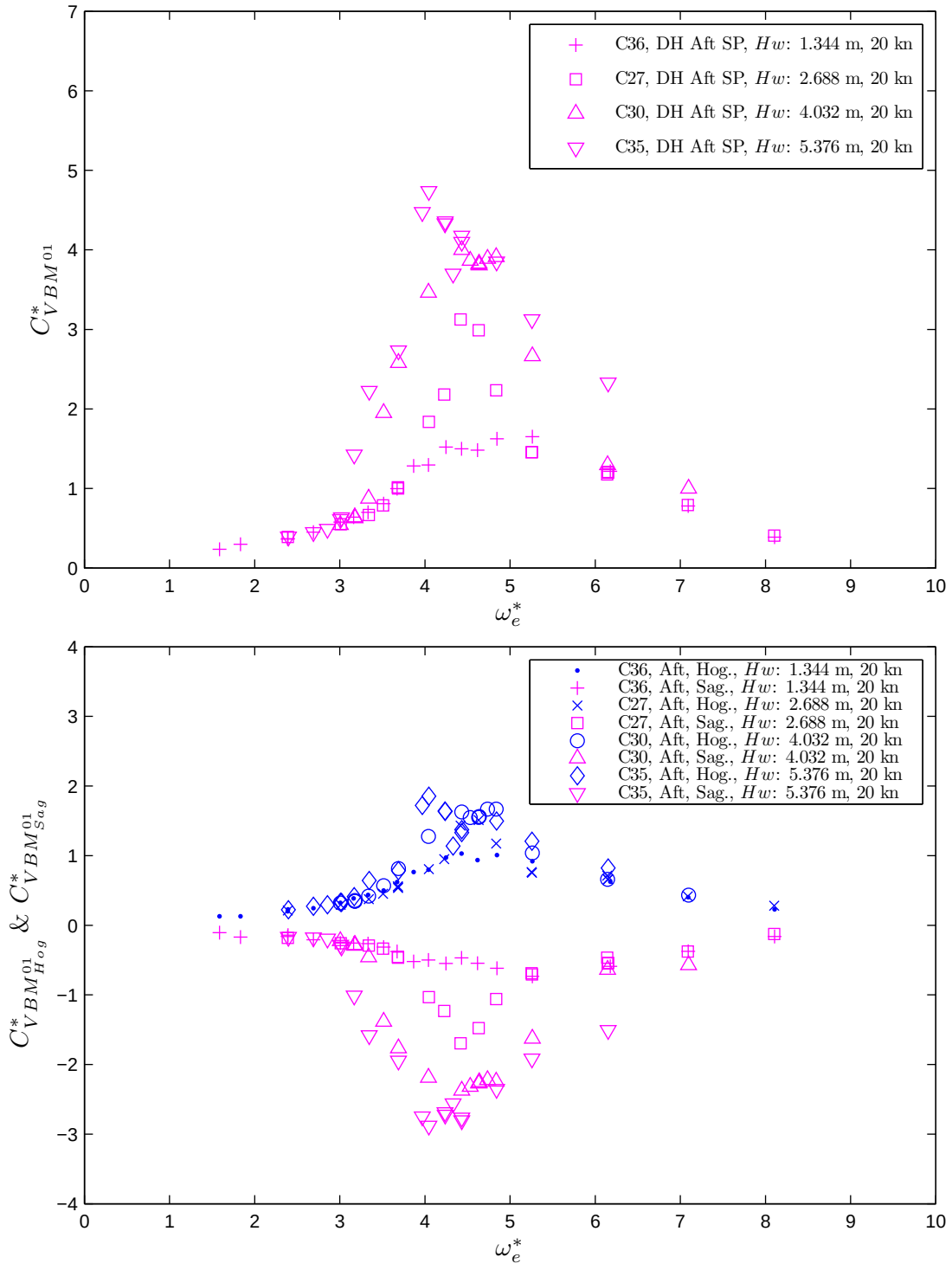

Figure I.2: Non-dimensional vertical bending moment coefficient (peak to trough), $C^*_{VBM^{01}}$ and non-dimensional hogging and sagging vertical bending moment coefficients, $C^*_{VBM^{01}_{Hog}}$ & $C^*_{VBM^{01}_{Hog}}$, at aft elastic links by varying the wave height, are plotted with respect to the non-dimensional encounter angular wave frequency, ω^*_e. $F_n = 0.32$.

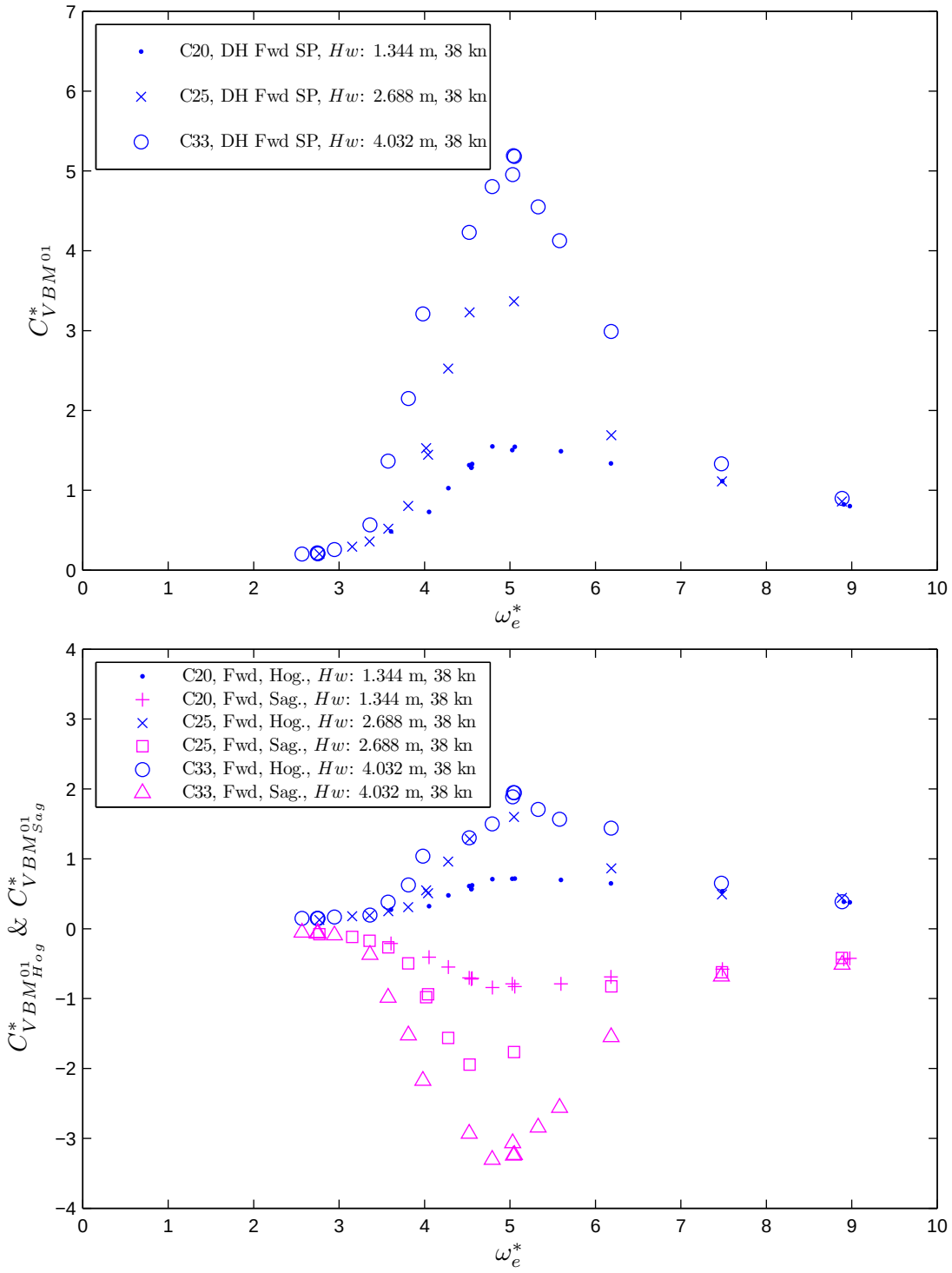

Figure I.3: Non-dimensional vertical bending moment coefficient (peak to trough), $C^*_{VBM^{01}}$ and non-dimensional hogging and sagging vertical bending moment coefficients, $C^*_{VBM^{01}_{Hog}}$ & $C^*_{VBM^{01}_{Hog}}$, at forward elastic links by varying the wave height, are plotted with respect to the non-dimensional encounter angular wave frequency, ω^*_e. $F_n = 0.60$.

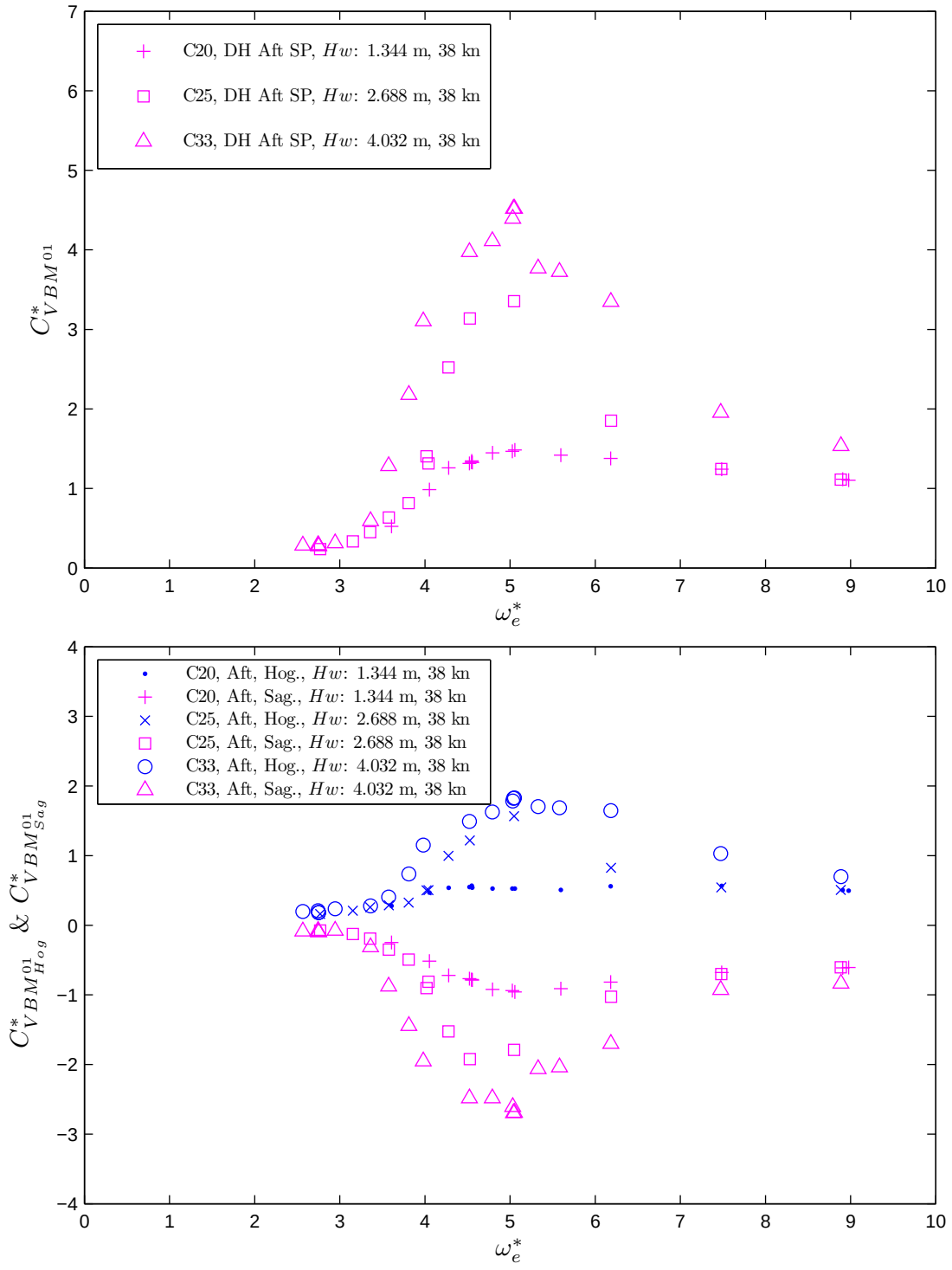

Figure I.4: Non-dimensional vertical bending moment coefficient (peak to trough), $C^*_{VBM^{01}}$ and non-dimensional hogging and sagging vertical bending moment coefficients, $C^*_{VBM^{01}_{Hog}}$ & $C^*_{VBM^{01}_{Hog}}$, at aft elastic links by varying the wave height, are plotted with respect to the non-dimensional encounter angular wave frequency, ω^*_e. $F_n = 0.60$.

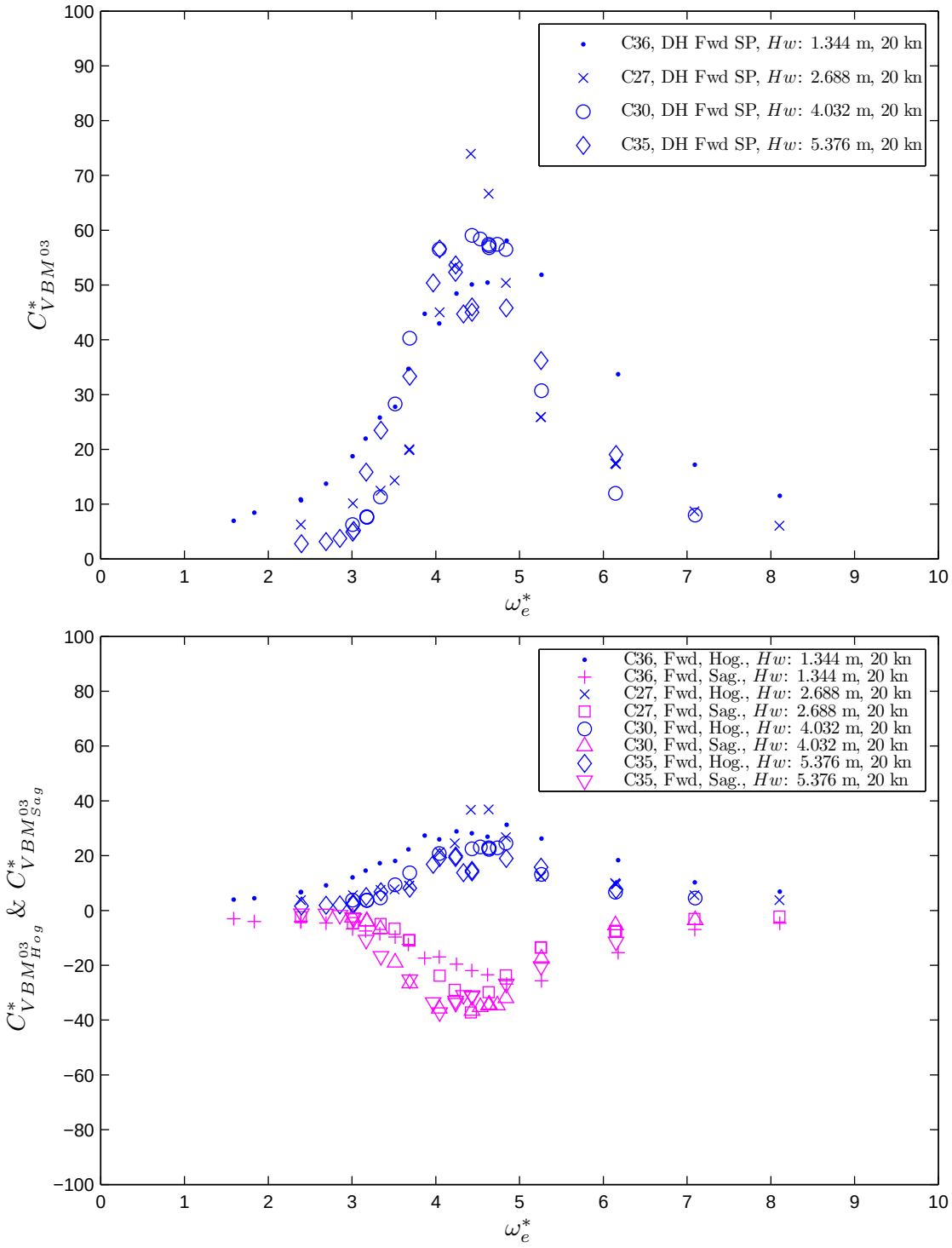

Figure I.5: Non-dimensional vertical bending moment coefficient (peak to trough), $C^*_{VBM^{03}}$ and non-dimensional hogging and sagging vertical bending moment coefficients, $C^*_{VBM^{03}_{Hog}}$ & $C^*_{VBM^{03}_{Hog}}$, at forward elastic links by varying the wave height, are plotted with respect to the non-dimensional encounter angular wave frequency, ω^*_e. $F_n = 0.32$.

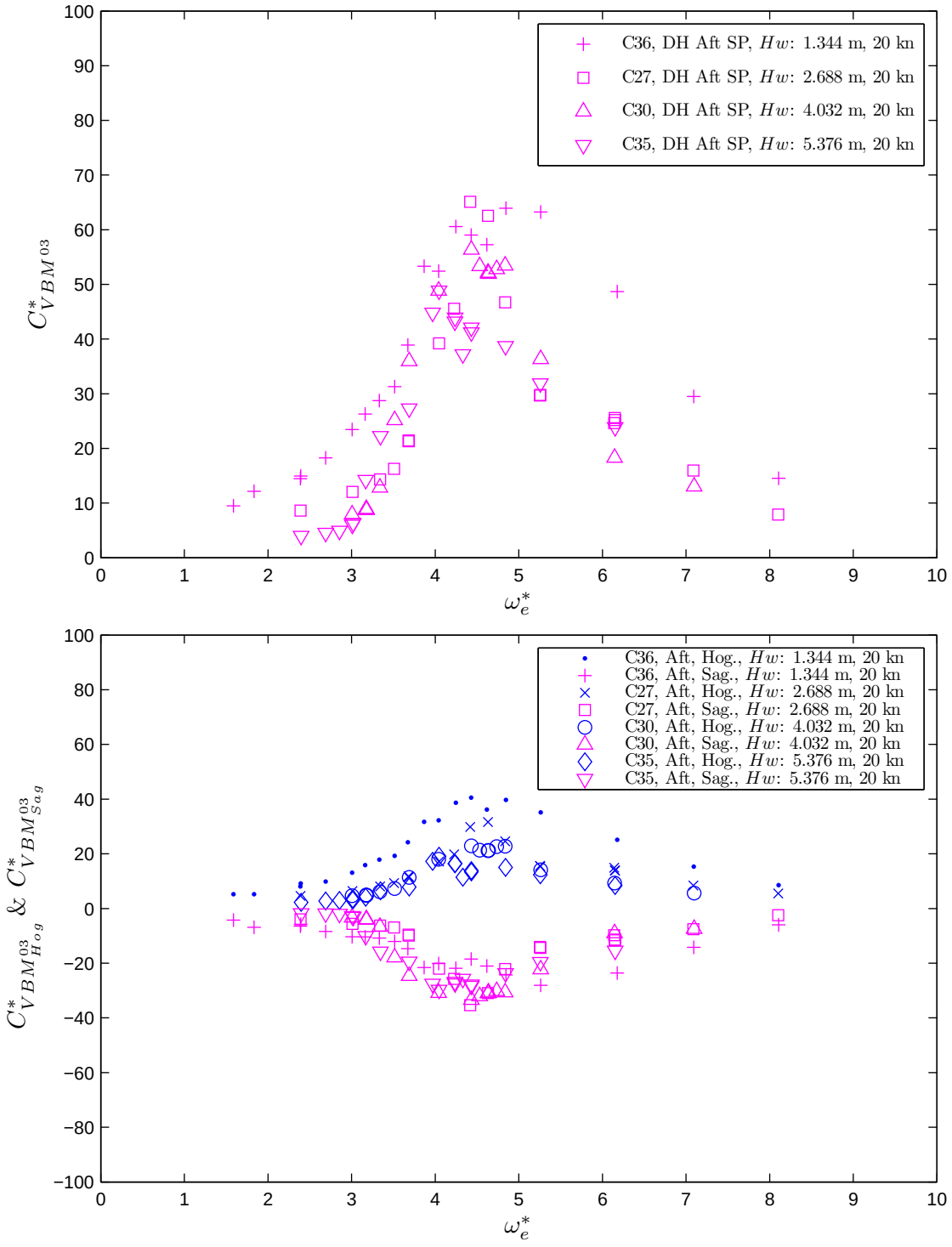

Figure I.6: Non-dimensional vertical bending moment coefficient (peak to trough), $C^*_{VBM^{03}}$ and non-dimensional hogging and sagging vertical bending moment coefficients, $C^*_{VBM^{03}_{Hog}}$ & $C^*_{VBM^{03}_{Hog}}$, at aft elastic links by varying the wave height, are plotted with respect to the non-dimensional encounter angular wave frequency, ω^*_e. $F_n = 0.32$.

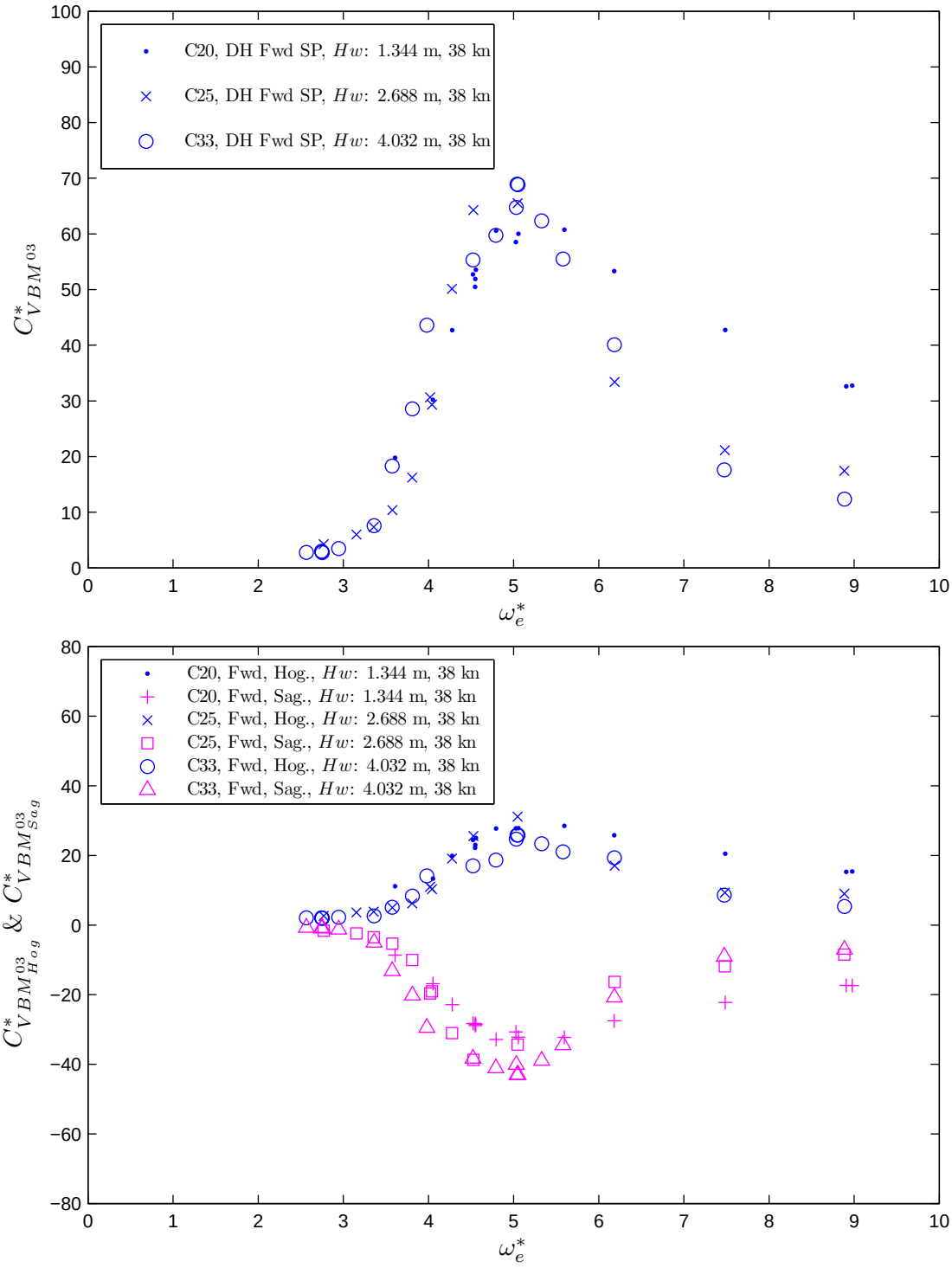

Figure I.7: Non-dimensional vertical bending moment coefficient (peak to trough), $C^*_{VBM^{03}}$ and non-dimensional hogging and sagging vertical bending moment coefficients, $C^*_{VBM^{03}_{Hog}}$ & $C^*_{VBM^{03}_{Hog}}$, at forward elastic links by varying the wave height, are plotted with respect to the non-dimensional encounter angular wave frequency, ω^*_e. $F_n = 0.60$.

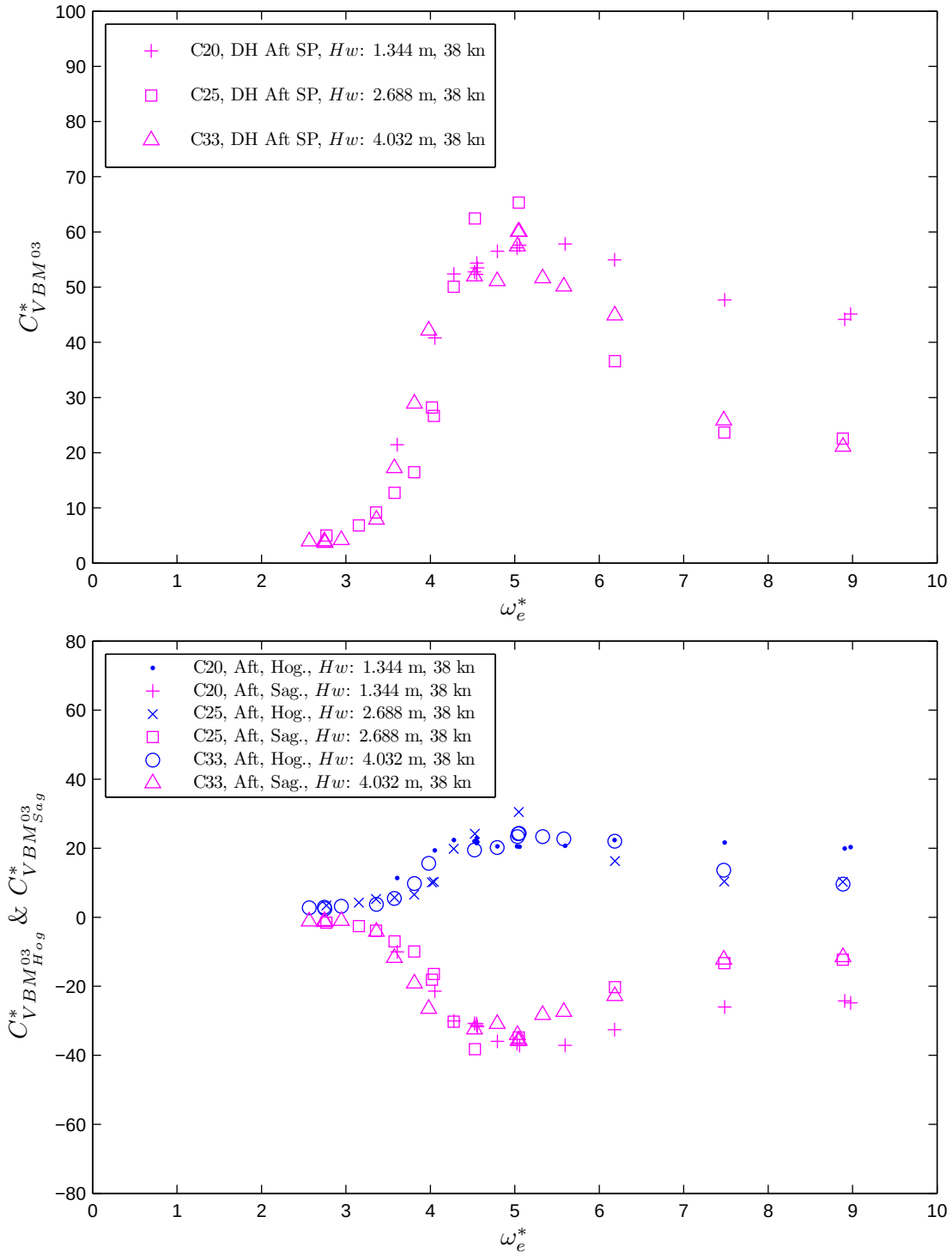

Figure I.8: Non-dimensional vertical bending moment coefficient (peak to trough), $C^*_{VBM^{03}}$ and non-dimensional hogging and sagging vertical bending moment coefficients, $C^*_{VBM^{03}_{Hog}}$ & $C^*_{VBM^{03}_{Hog}}$, at aft elastic links by varying the wave height, are plotted with respect to the non-dimensional encounter angular wave frequency, ω^*_e. $F_n = 0.60$.

Appendix J

Forward Velocity Effects on the Vertical Bending Moment Coefficients

The non-dimensional vertical binging moment coefficient for small and large wave heights were obtained based on the Equation 3.46. The model velocities were varied at 20, 30 , 38, 45, and 50 k_n. The constant wave height for the comparison of the velocity variation were 0.896, 1.344, 1.792, 2.688, and 4.032 m.

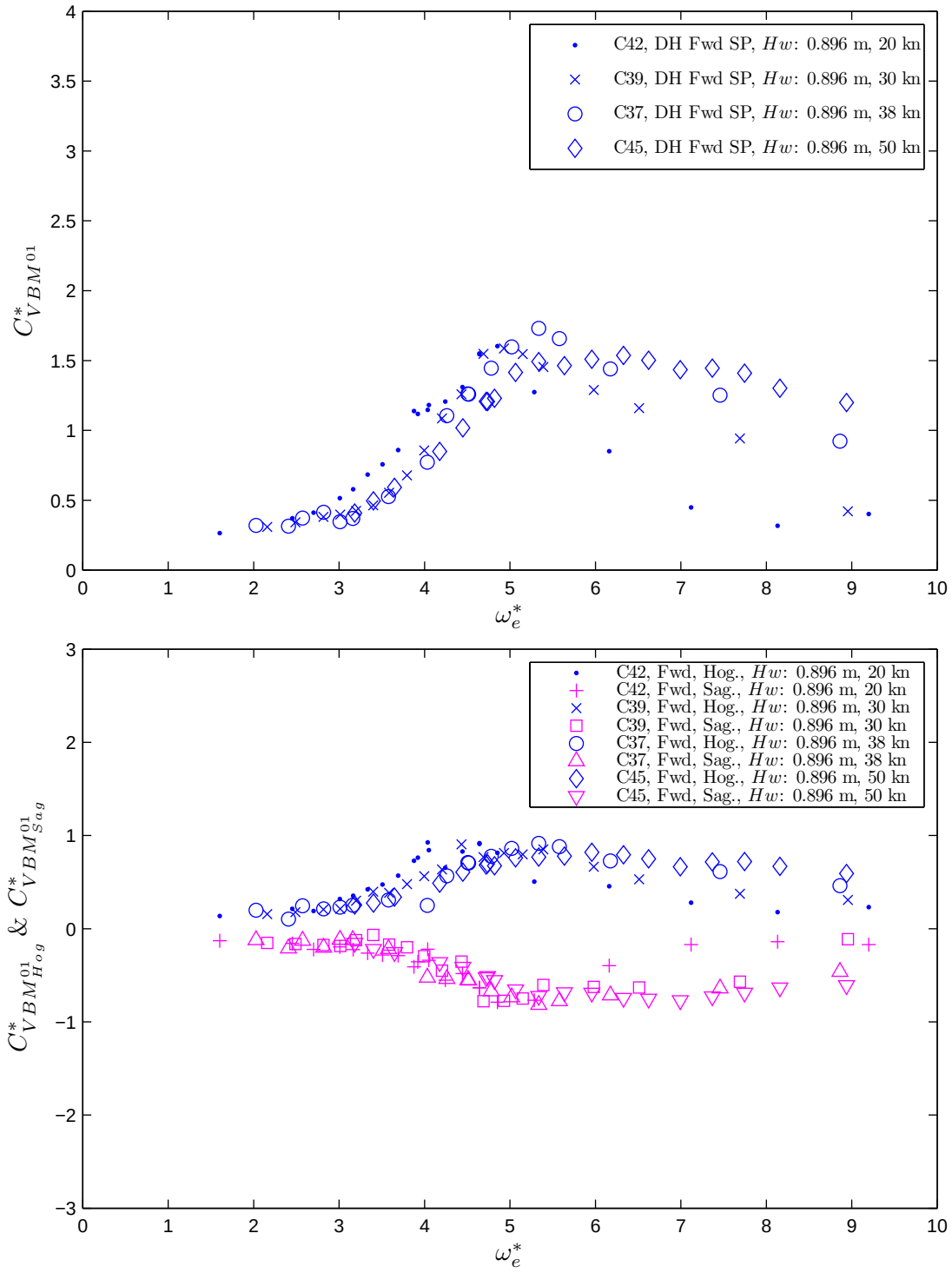

Figure J.1: Non-dimensional vertical bending moment coefficient (peak to trough), $C^*_{VBM^{01}}$ and non-dimensional hogging and sagging vertical bending moment coefficients, $C^*_{VBM^{01}_{Hog}}$ & $C^*_{VBM^{01}_{Hog}}$, at forward elastic links by varying the velocity, with respect to the non-dimensional encounter angular wave frequency, ω^*_e. The wave height to draft ratio, H_w/T was maintained at 0.26.

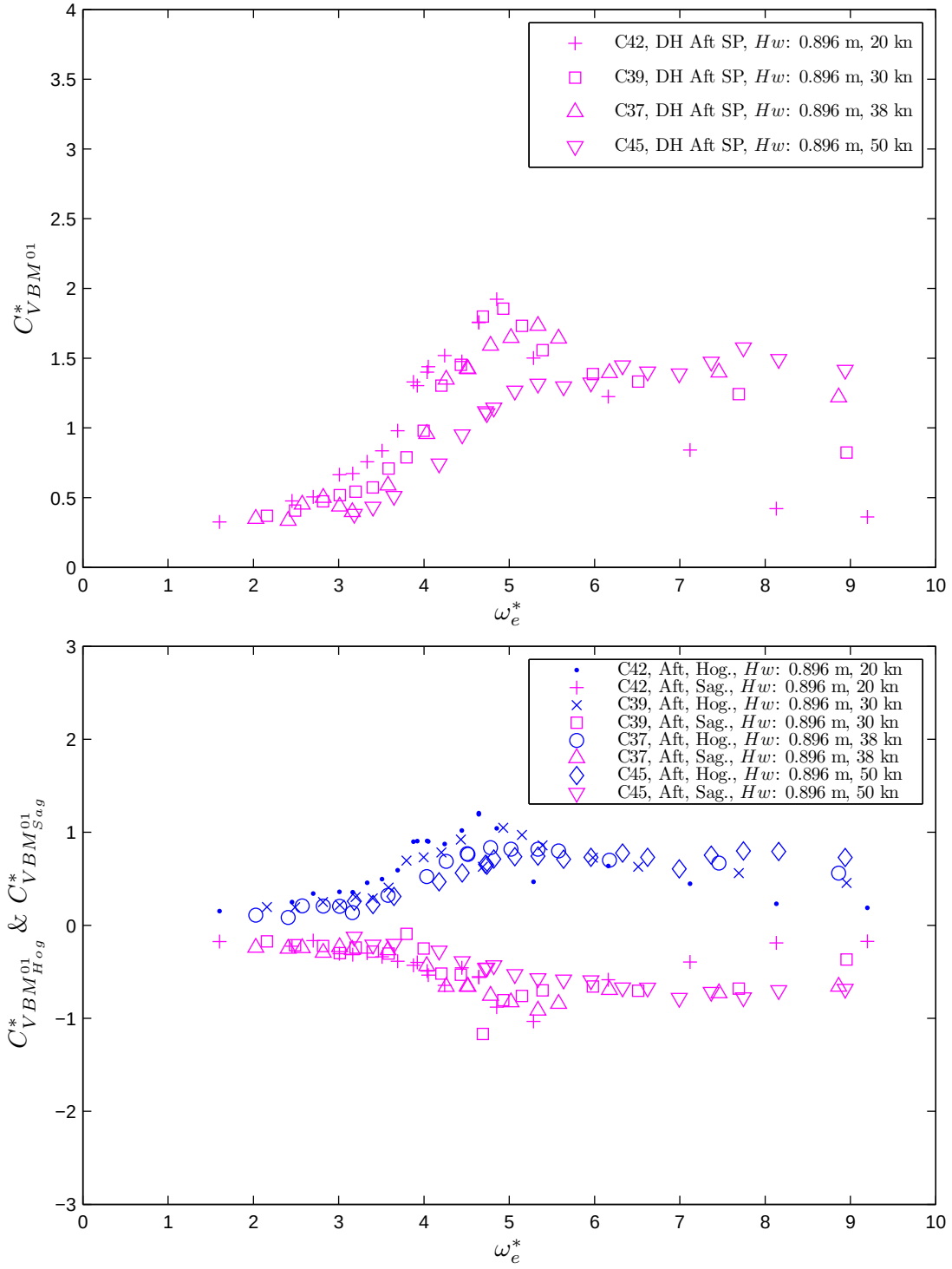

Figure J.2: Non-dimensional vertical bending moment coefficient (peak to trough), $C^*_{VBM^{01}}$ and non-dimensional hogging and sagging vertical bending moment coefficient, $C^*_{VBM^{01}_{Hog}}$ & $C^*_{VBM^{01}_{Hog}}$, at aft elastic links by varying the velocity, with respect to the non-dimensional encounter angular wave frequency, ω^*_e. The wave height to draft ratio, H_w/T was maintained at 0.26.

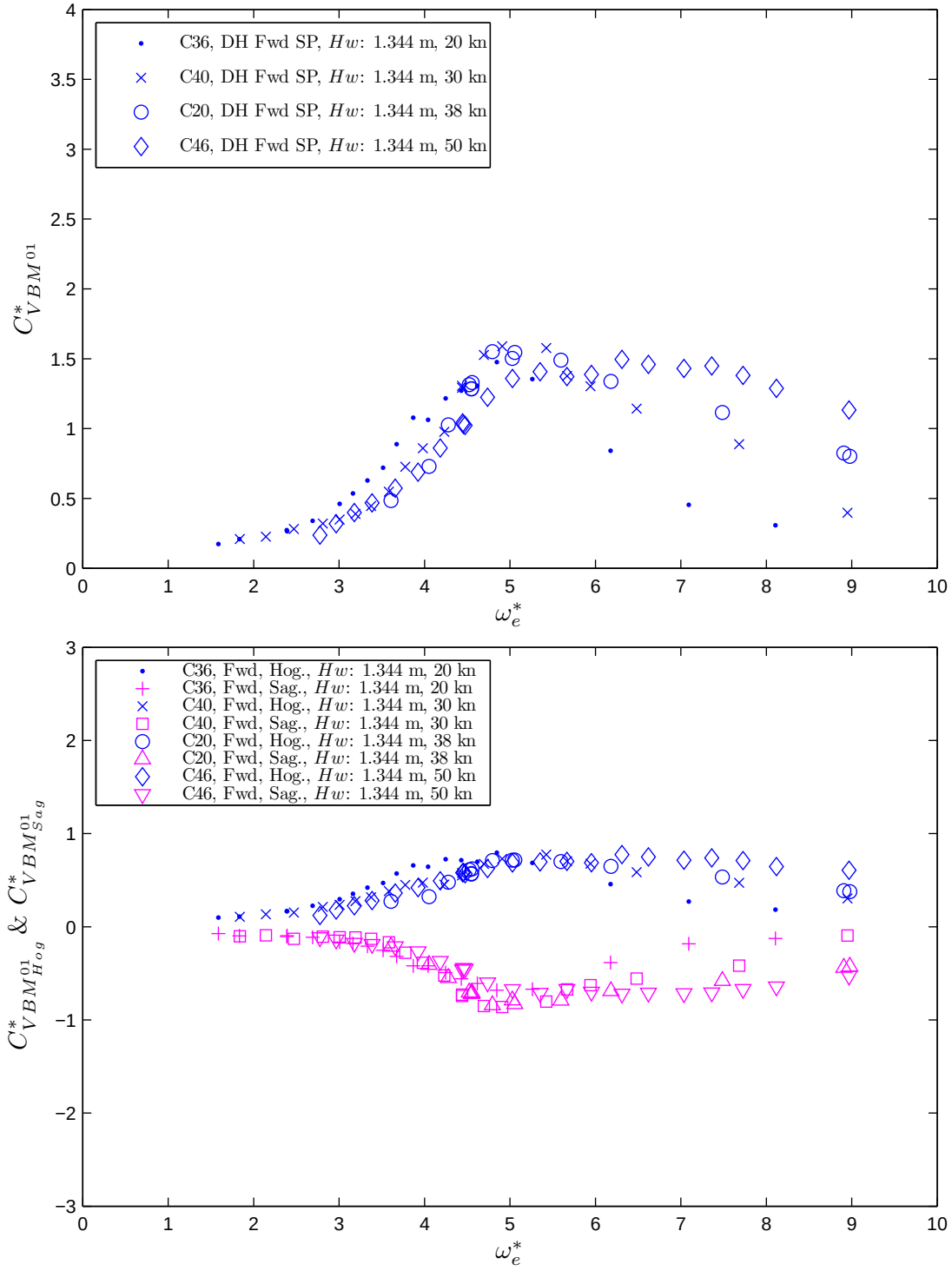

Figure J.3: Non-dimensional vertical bending moment coefficient (peak to trough), $C^*_{VBM^{01}}$ and non-dimensional hogging and sagging vertical bending moment coefficient, $C^*_{VBM^{01}_{Hog}}$ & $C^*_{VBM^{01}_{Hog}}$, at forward elastic links by varying the velocity, with respect to the non-dimensional encounter angular wave frequency, ω^*_e. The wave height to draft ratio, H_w/T was maintained at 0.39.

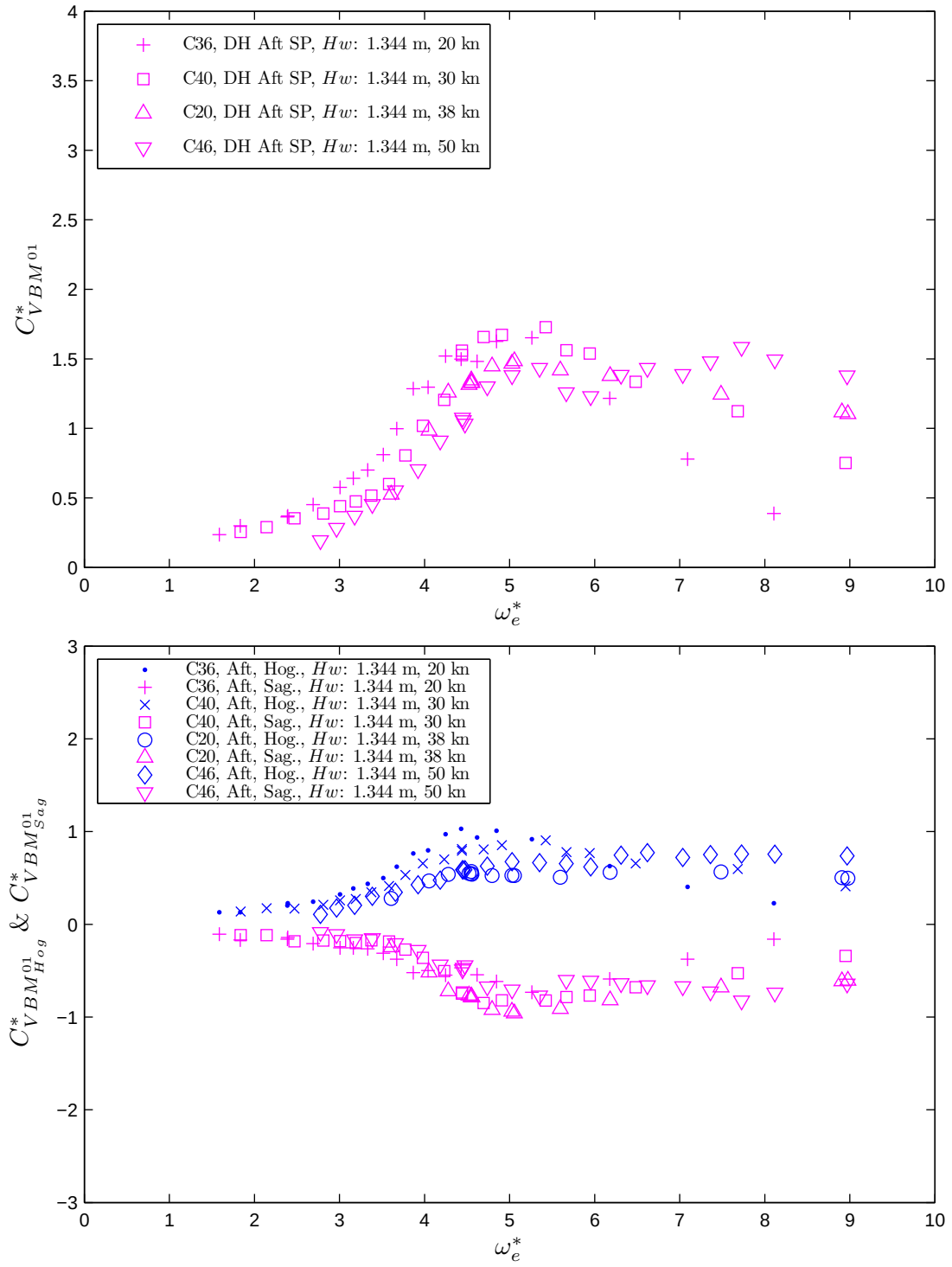

Figure J.4: Non-dimensional vertical bending moment coefficient (peak to trough), $C^*_{VBM^{01}}$ and non-dimensional hogging and sagging vertical bending moment coefficient, $C^*_{VBM^{01}_{Hog}}$ & $C^*_{VBM^{01}_{Hog}}$, at aft elastic links by varying the velocity, with respect to the non-dimensional encounter angular wave frequency, ω^*_e. The wave height to draft ratio, H_w/T was maintained at 0.39.

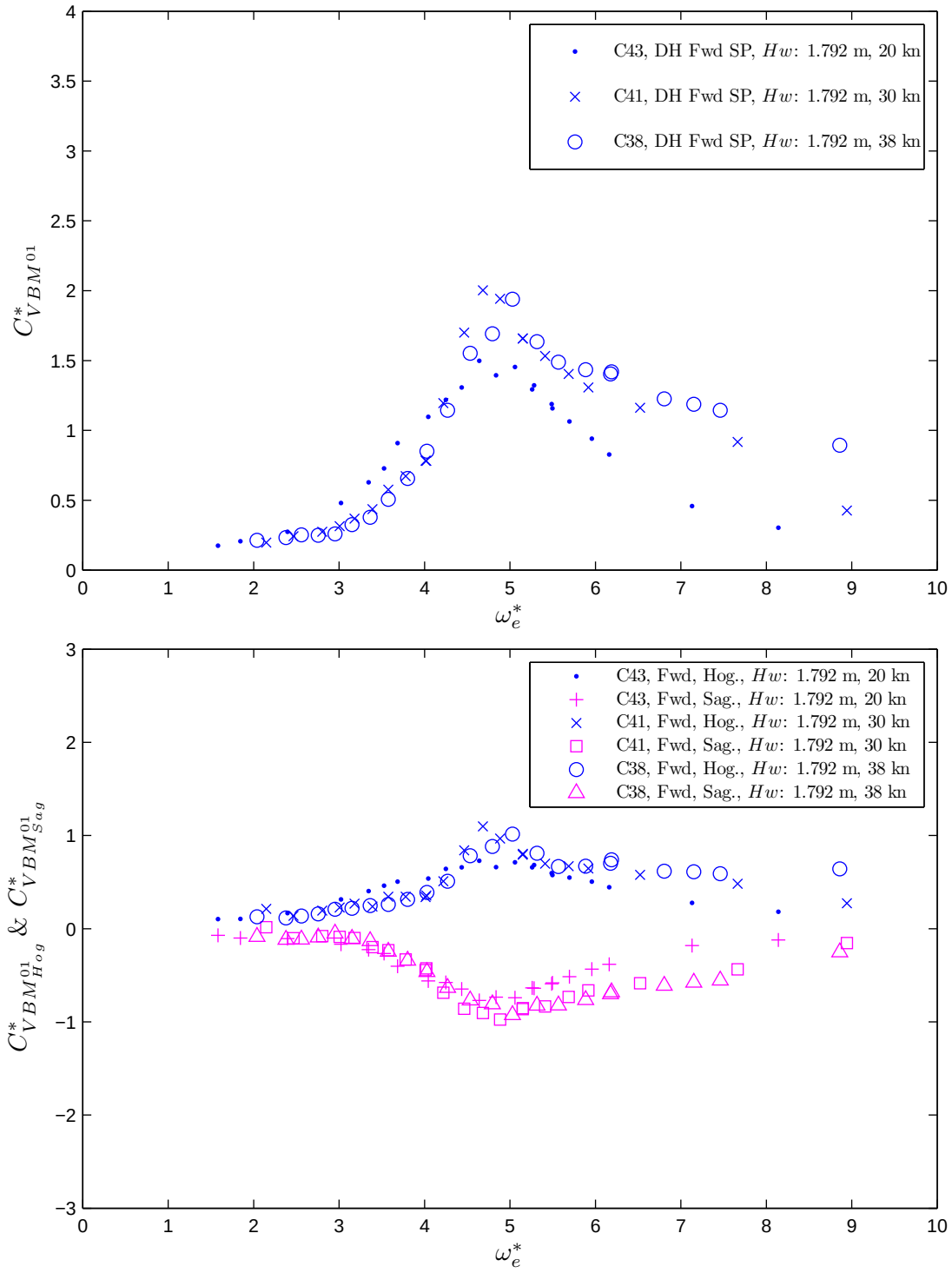

Figure J.5: Non-dimensional vertical bending moment coefficient (peak to trough), $C^*_{VBM^{01}}$ and non-dimensional hogging and sagging vertical bending moment coefficient, $C^*_{VBM^{01}_{Hog}}$ & $C^*_{VBM^{01}_{Hog}}$, at forward elastic links by varying the velocity, with respect to the non-dimensional encounter angular wave frequency, ω^*_e. The wave height to draft ratio, H_w/T was maintained at 0.52.

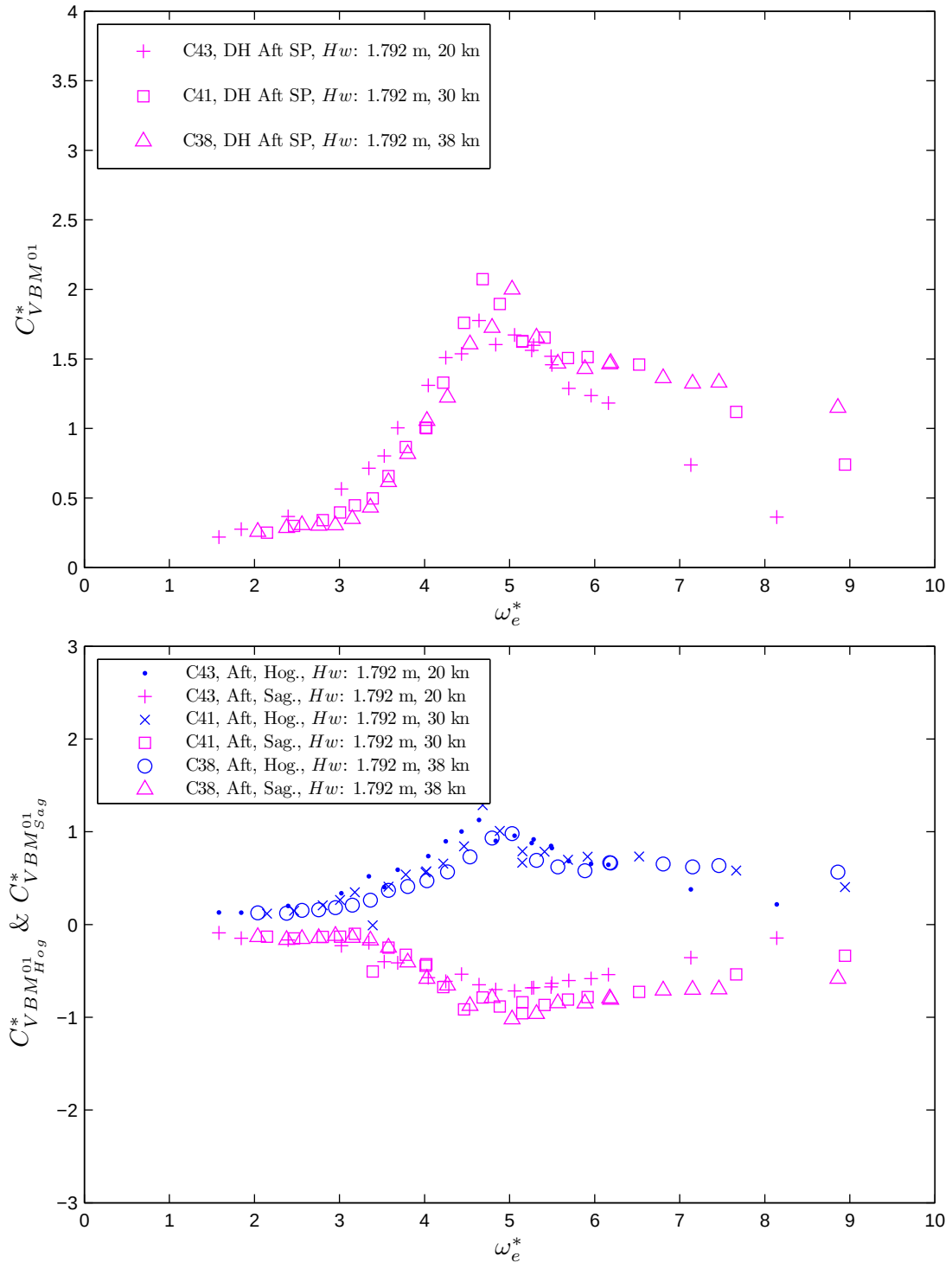

Figure J.6: Non-dimensional vertical bending moment coefficient (peak to trough), $C^*_{VBM^{01}}$ and non-dimensional hogging and sagging vertical bending moment coefficient, $C^*_{VBM^{01}_{Hog}}$ & $C^*_{VBM^{01}_{Hog}}$, at aft elastic links by varying the velocity, with respect to the non-dimensional encounter angular wave frequency, ω^*_e. The wave height to draft ratio, H_w/T was maintained at 0.52.

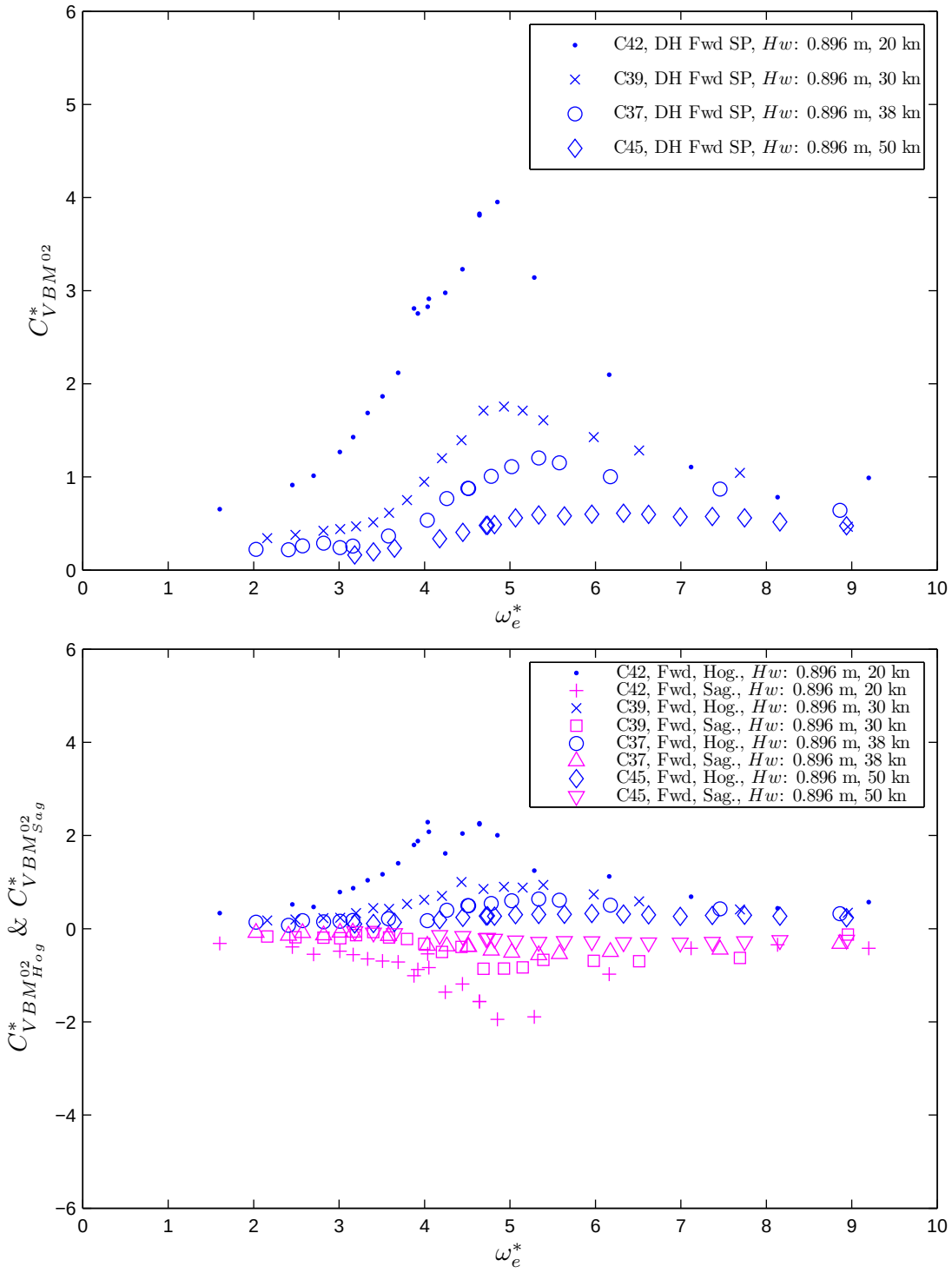

Figure J.7: Non-dimensional vertical bending moment coefficient (peak to trough), $C^*_{VBM^{02}}$ and non-dimensional hogging and sagging vertical bending moment coefficient, $C^*_{VBM^{02}_{Hog}}$ & $C^*_{VBM^{02}_{Hog}}$, at forward elastic links by varying the velocity, with respect to the non-dimensional encounter angular wave frequency, ω^*_e. The wave height to draft ratio, H_w/T was maintained at 0.26.

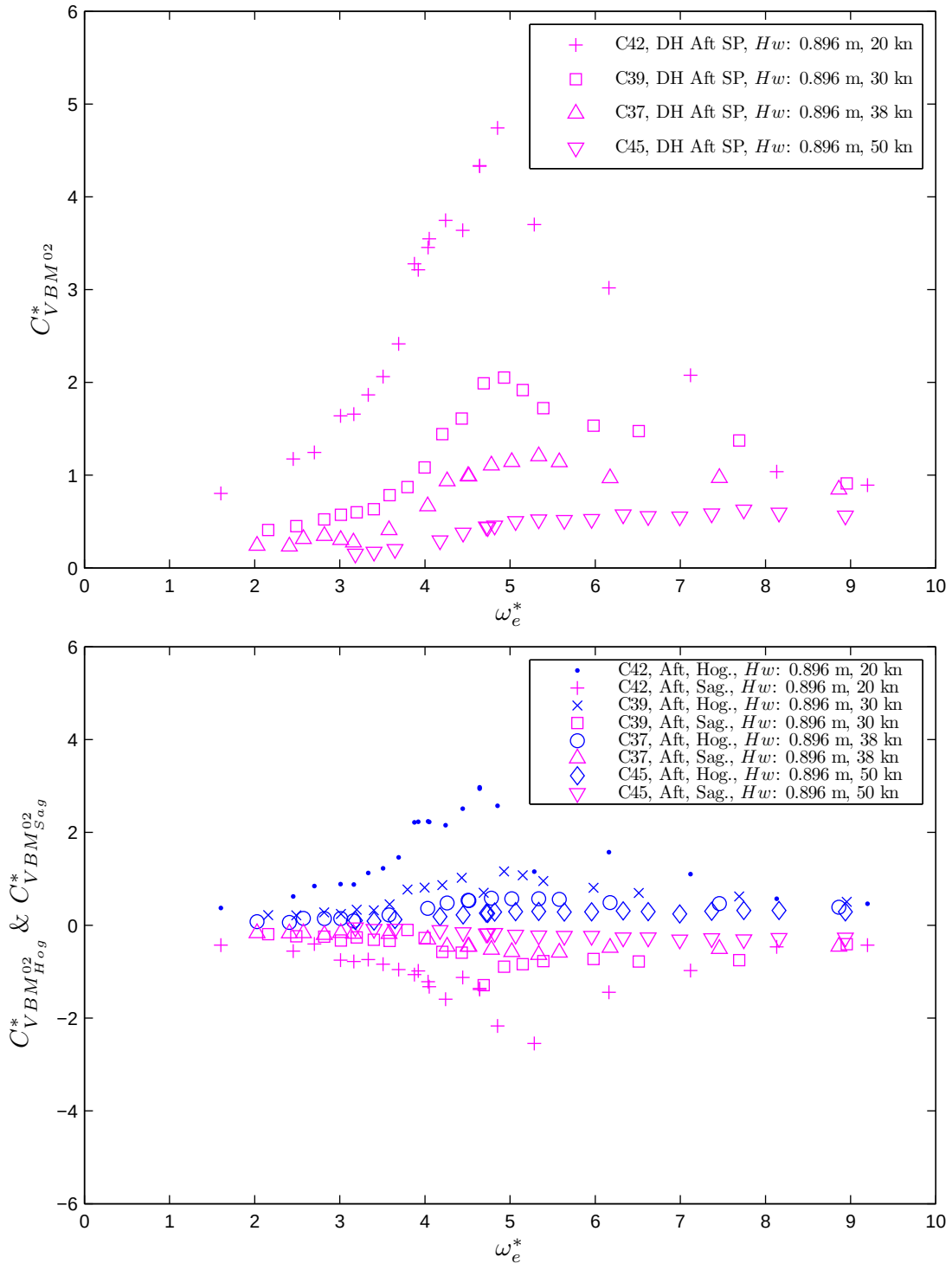

Figure J.8: Non-dimensional vertical bending moment coefficient (peak to trough), $C^*_{VBM^{02}}$ and non-dimensional hogging and sagging vertical bending moment coefficients, $C^*_{VBM^{02}_{Hog}}$ & $C^*_{VBM^{02}_{Hog}}$, at aft elastic links by varying the velocity, with respect to the non-dimensional encounter angular wave frequency, ω^*_e. The wave height to draft ratio, H_w/T was maintained at 0.26.

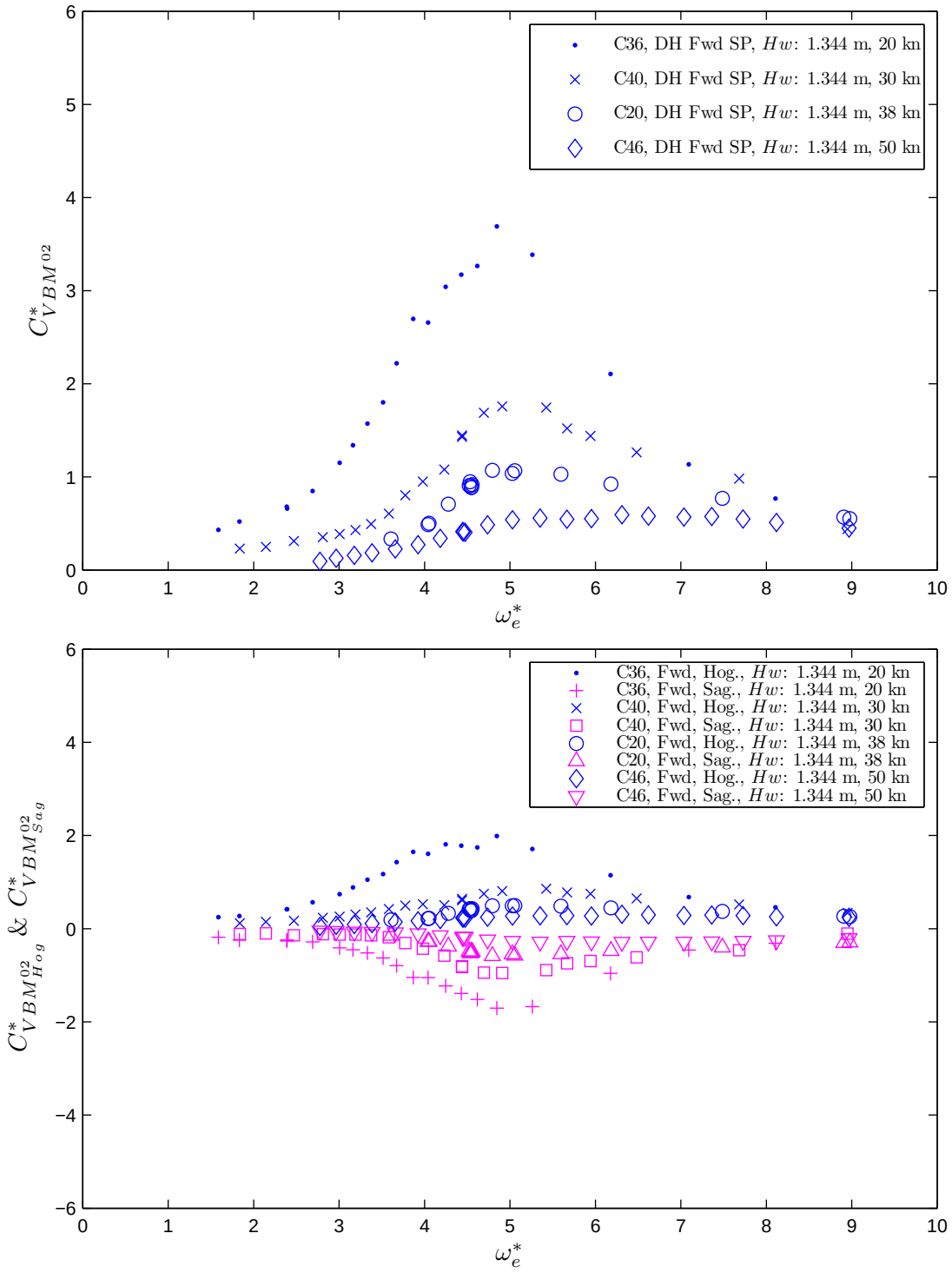

Figure J.9: Non-dimensional vertical bending moment coefficient (peak to trough), $C^*_{VBM^{02}}$ and non-dimensional hogging and sagging vertical bending moment coefficients, $C^*_{VBM^{02}_{Hog}}$ & $C^*_{VBM^{02}_{Hog}}$, at forward elastic links by varying the velocity, with respect to the non-dimensional encounter angular wave frequency, ω^*_e. The wave height to draft ratio, H_w/T was maintained at 0.39.

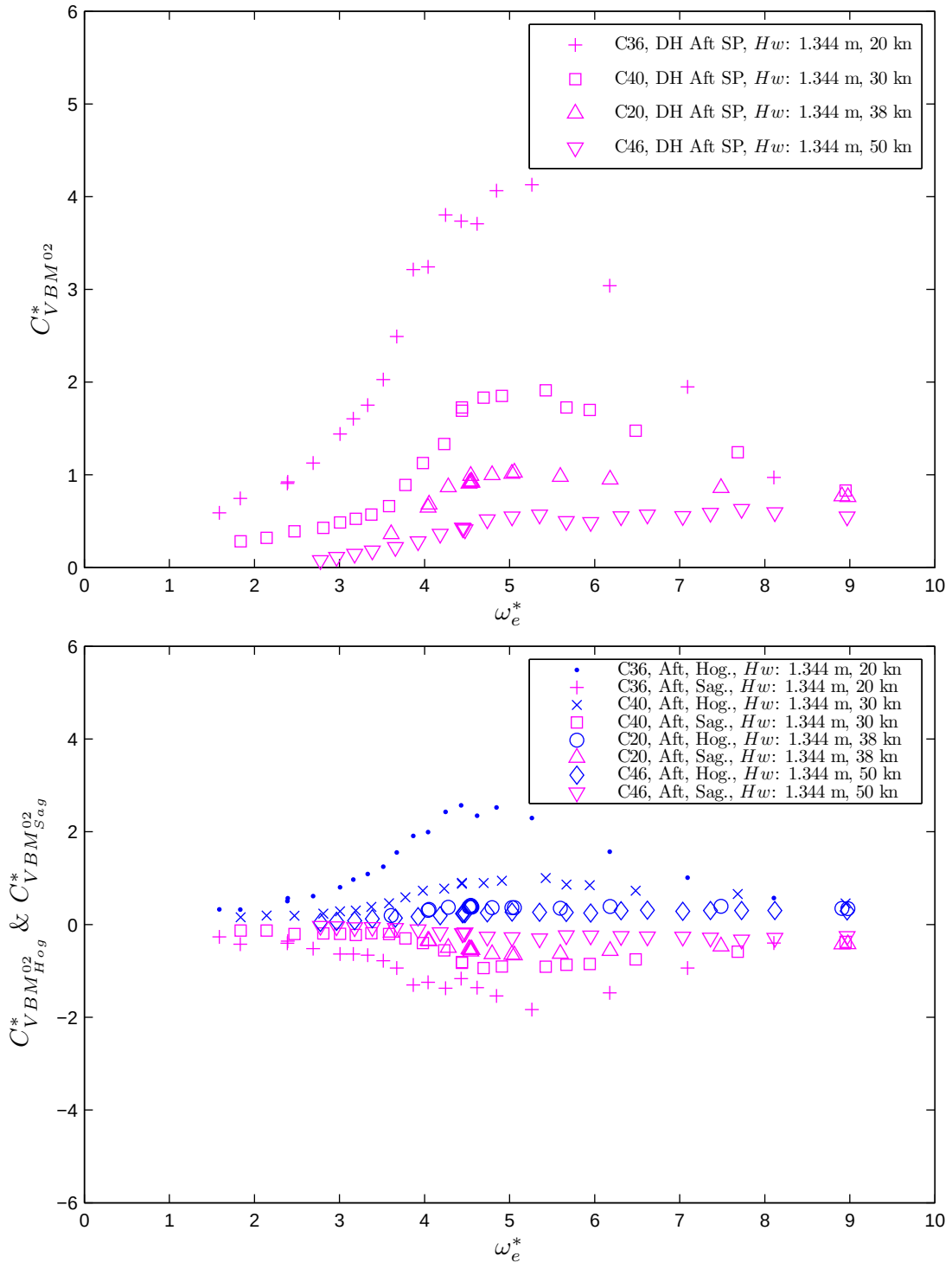

Figure J.10: Non-dimensional vertical bending moment coefficient (peak to trough), $C^*_{VBM^{02}}$ and non-dimensional hogging and sagging vertical bending moment coefficient, $C^*_{VBM^{02}_{Hog}}$ & $C^*_{VBM^{02}_{Hog}}$, at aft elastic links by varying the velocity, with respect to the non-dimensional encounter angular wave frequency, ω^*_e. The wave height to draft ratio, H_w/T was maintained at 0.39.

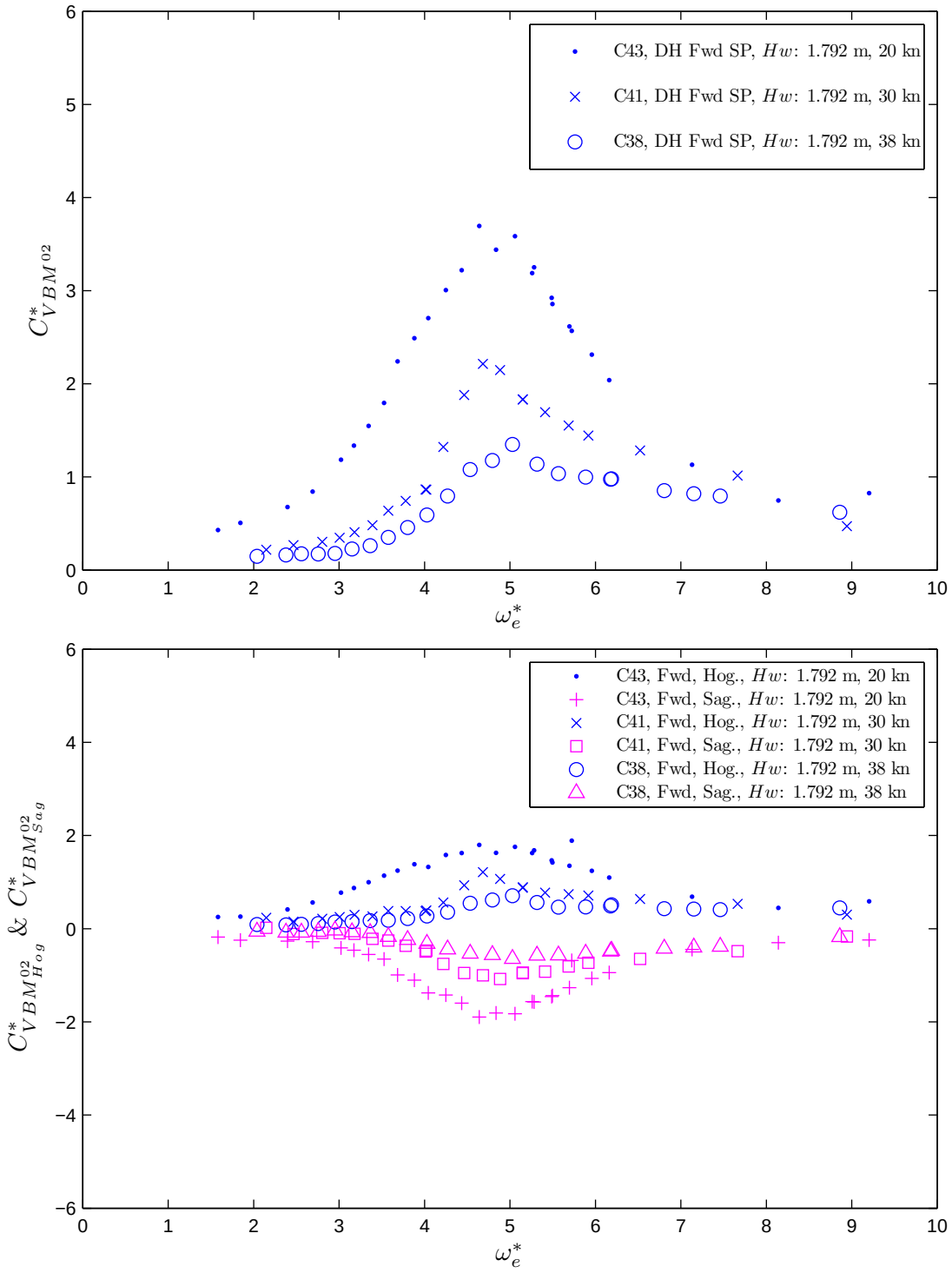

Figure J.11: Non-dimensional vertical bending moment coefficient (peak to trough), $C^*_{VBM^{02}}$ and non-dimensional hogging and sagging vertical bending moment coefficients, $C^*_{VBM^{02}_{Hog}}$ & $C^*_{VBM^{02}_{Hog}}$, at forward elastic links by varying the velocity, with respect to the non-dimensional encounter angular wave frequency, ω^*_e. The wave height to draft ratio, H_w/T was maintained at 0.52.

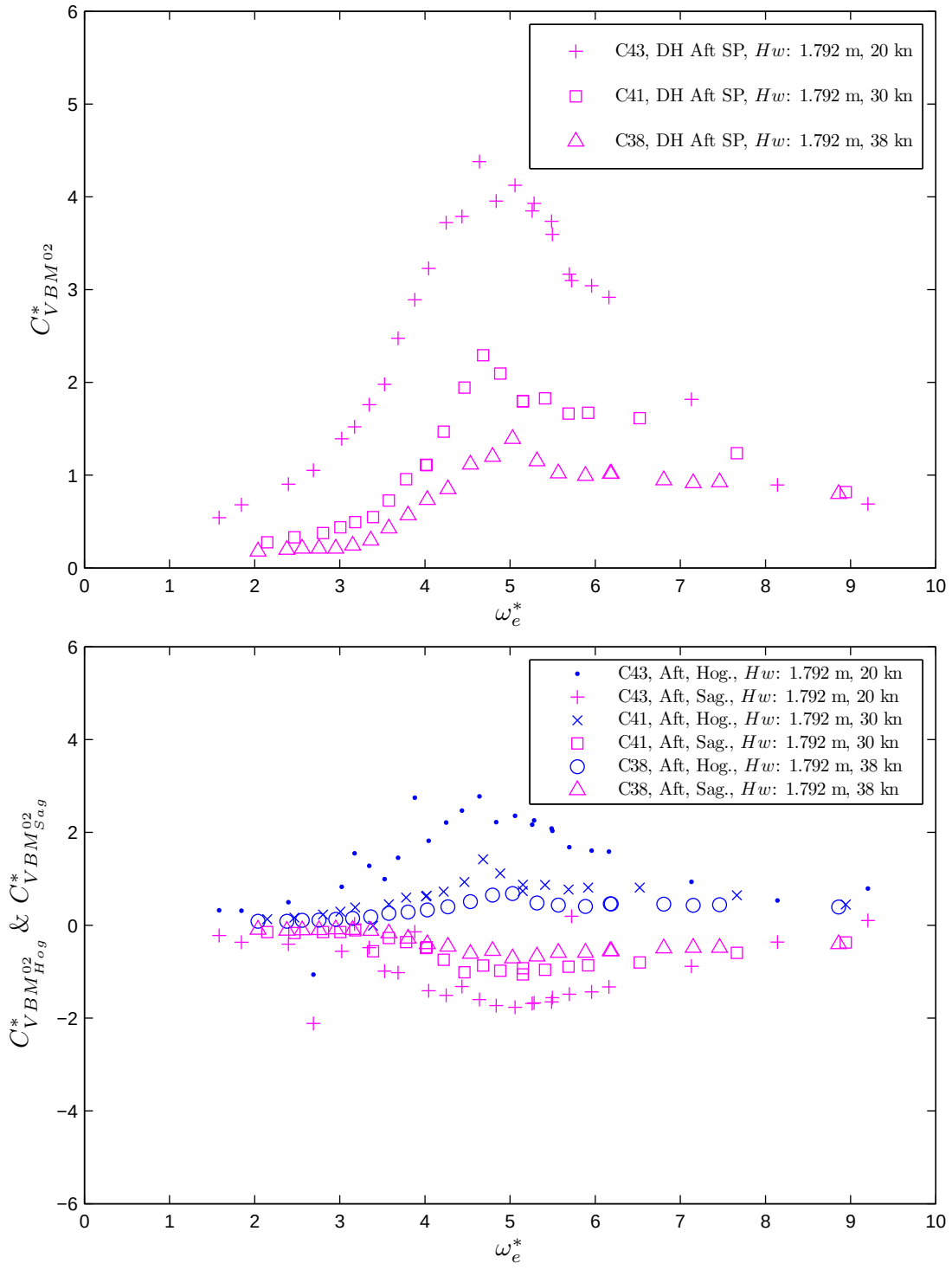

Figure J.12: Non-dimensional vertical bending moment coefficient (peak to trough), $C^*_{VBM^{02}}$ and non-dimensional hogging and sagging vertical bending moment coefficients, $C^*_{VBM^{02}_{Hog}}$ & $C^*_{VBM^{02}_{Hog}}$, at aft elastic links by varying the velocity, with respect to the non-dimensional encounter angular wave frequency, ω^*_e. The wave height to draft ratio, H_w/T was maintained at 0.52.

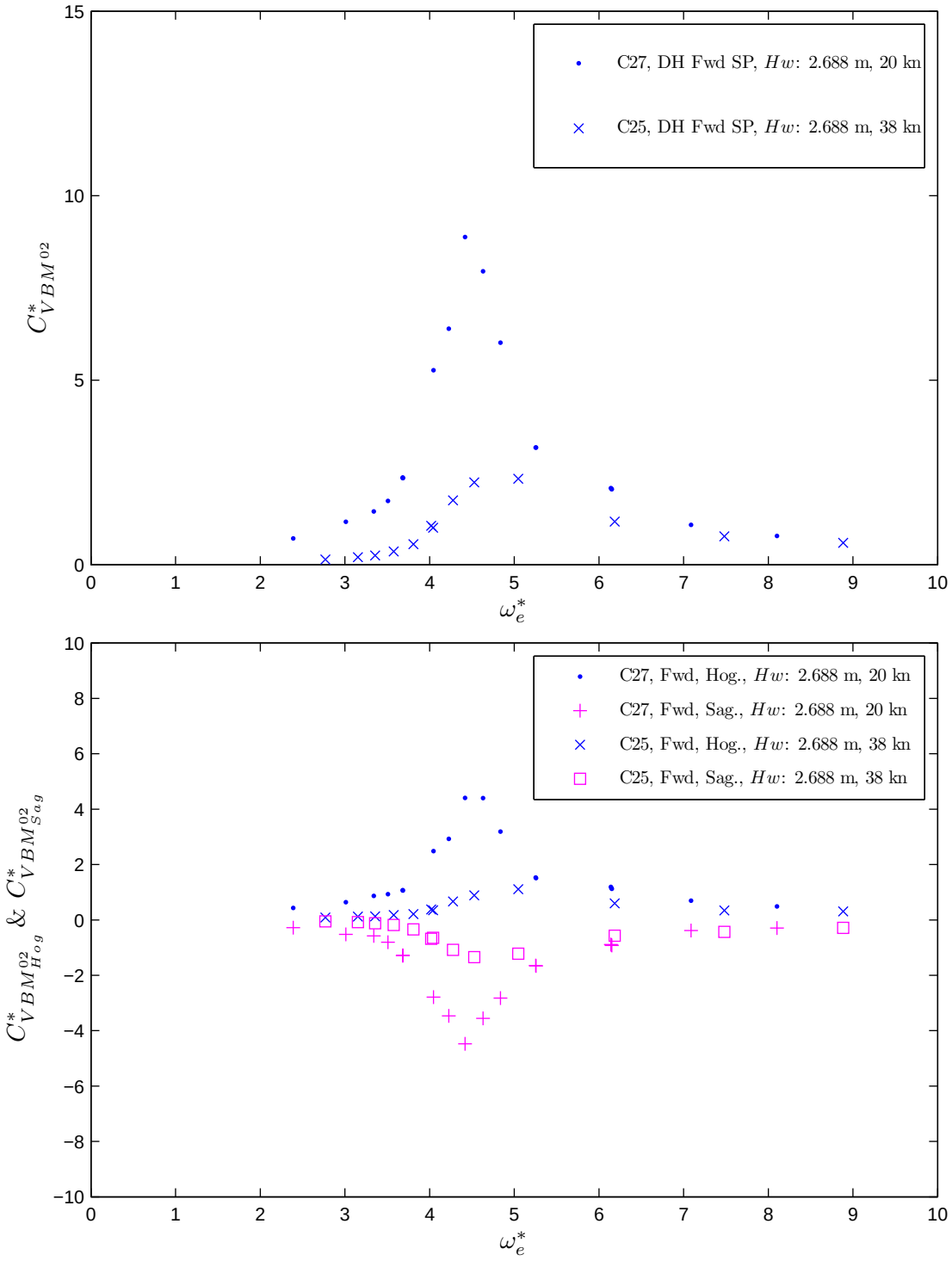

Figure J.13: Non-dimensional vertical bending moment coefficient (peak to trough), $C^*_{VBM^{02}}$ and non-dimensional hogging and sagging vertical bending moment coefficient, $C^*_{VBM^{02}_{Hog}}$ & $C^*_{VBM^{02}_{Hog}}$, at forward elastic links by varying the velocity, with respect to the non-dimensional encounter angular wave frequency, ω^*_e. The wave height to draft ratio, H_w/T was maintained at 0.79.

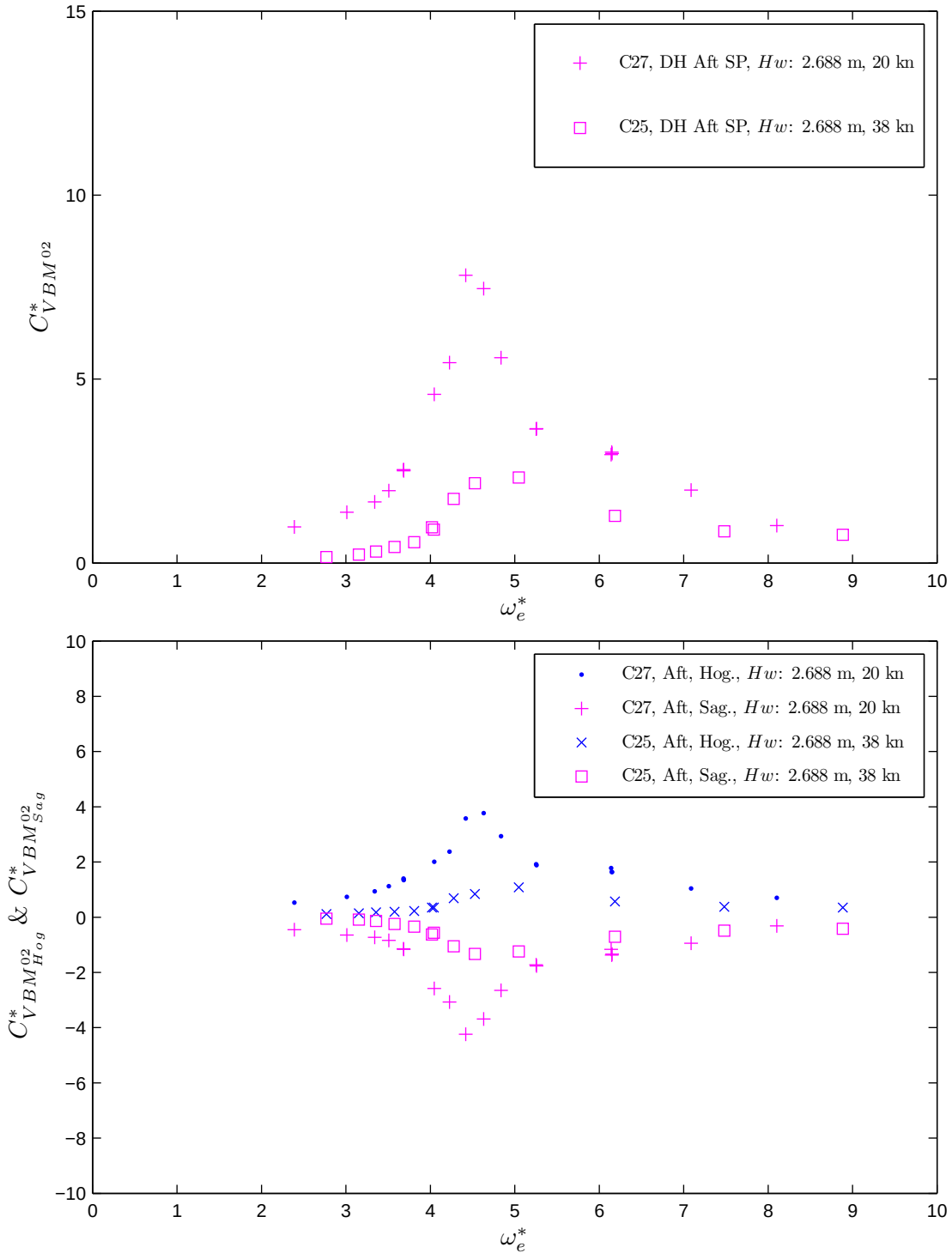

Figure J.14: Non-dimensional vertical bending moment coefficient (peak to trough), $C^*_{VBM^{02}}$ and non-dimensional hogging and sagging vertical bending moment coefficients, $C^*_{VBM^{02}_{Hog}}$ & $C^*_{VBM^{02}_{Hog}}$, at aft elastic links by varying the velocity, with respect to the non-dimensional encounter angular wave frequency, ω^*_e. The wave height to draft ratio, H_w/T was maintained at 0.79.

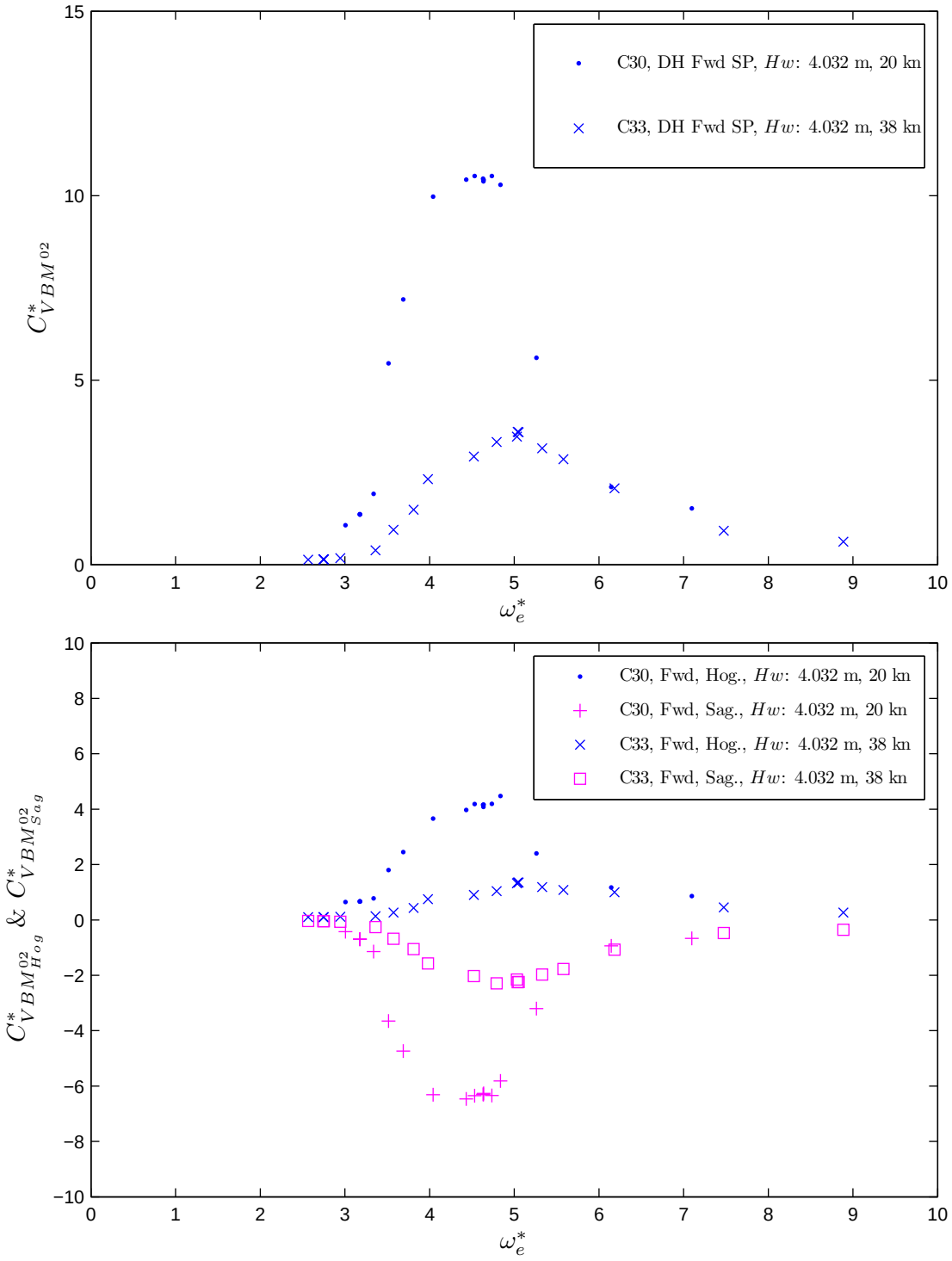

Figure J.15: Non-dimensional vertical bending moment coefficient (peak to trough), $C^*_{VBM^{02}}$ and non-dimensional hogging and sagging vertical bending moment coefficients, $C^*_{VBM^{02}_{Hog}}$ & $C^*_{VBM^{02}_{Hog}}$, at forward elastic links by varying the velocity, with respect to the non-dimensional encounter angular wave frequency, ω^*_e. The wave height to draft ratio, H_w/T was maintained at 1.18.

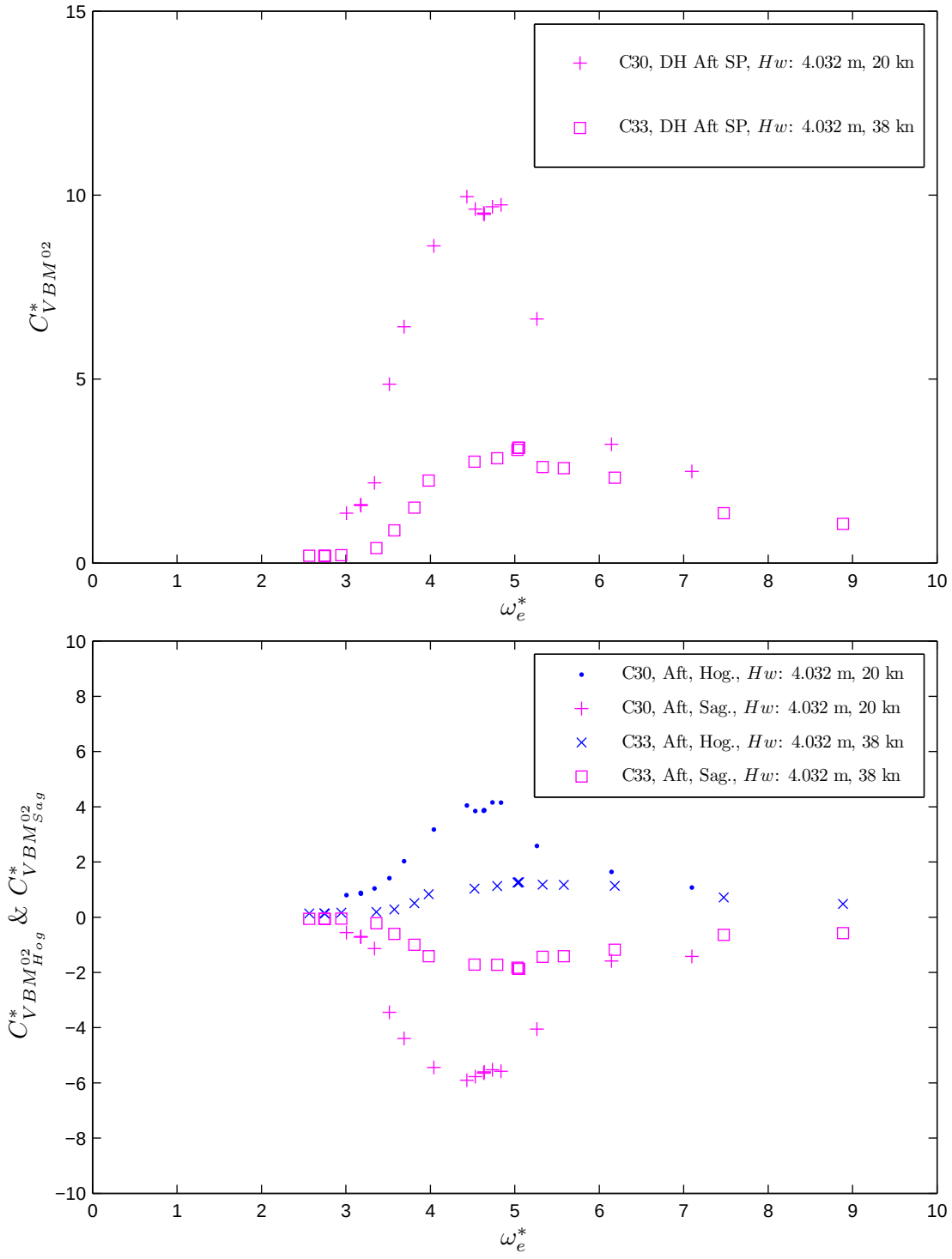

Figure J.16: Non-dimensional vertical bending moment coefficient (peak to trough), $C^*_{VBM^{02}}$ and non-dimensional hogging and sagging vertical bending moment coefficient, $C^*_{VBM^{02}_{Hog}}$ & $C^*_{VBM^{02}_{Hog}}$, at aft elastic links by varying the velocity, with respect to the non-dimensional encounter angular wave frequency, ω^*_e. The wave height to draft ratio, H_w/T was maintained at 1.18.

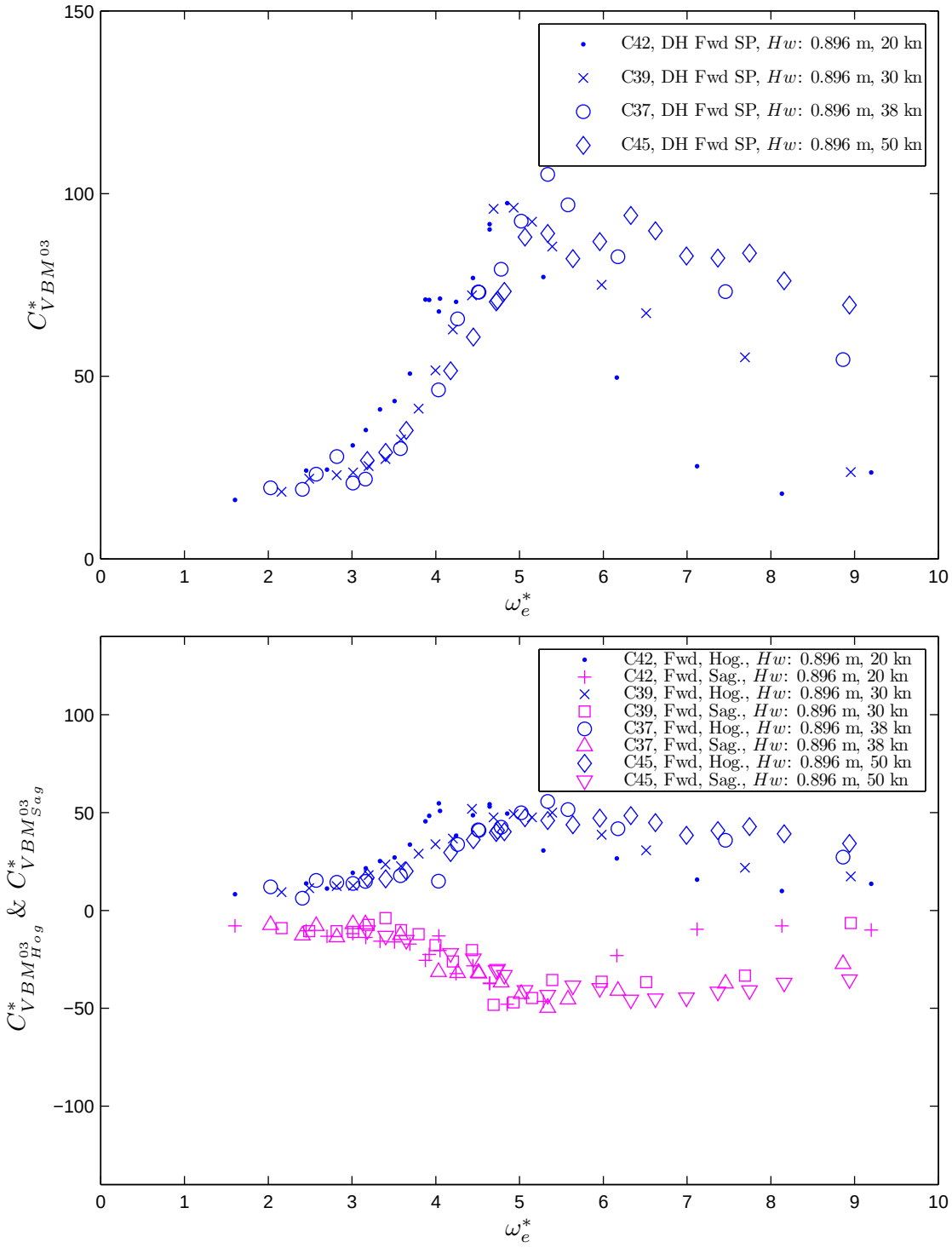

Figure J.17: Non-dimensional vertical bending moment coefficient (peak to trough), $C^*_{VBM^{03}}$ and the non-dimensional hogging and sagging vertical bending moment coefficients, $C^*_{VBM^{03}_{Hog}}$ & $C^*_{VBM^{03}_{Hog}}$, at forward elastic links by varying the velocity, with respect to the non-dimensional encounter angular wave frequency, ω^*_e. The wave height to draft ratio, H_w/T was maintained at 0.26.

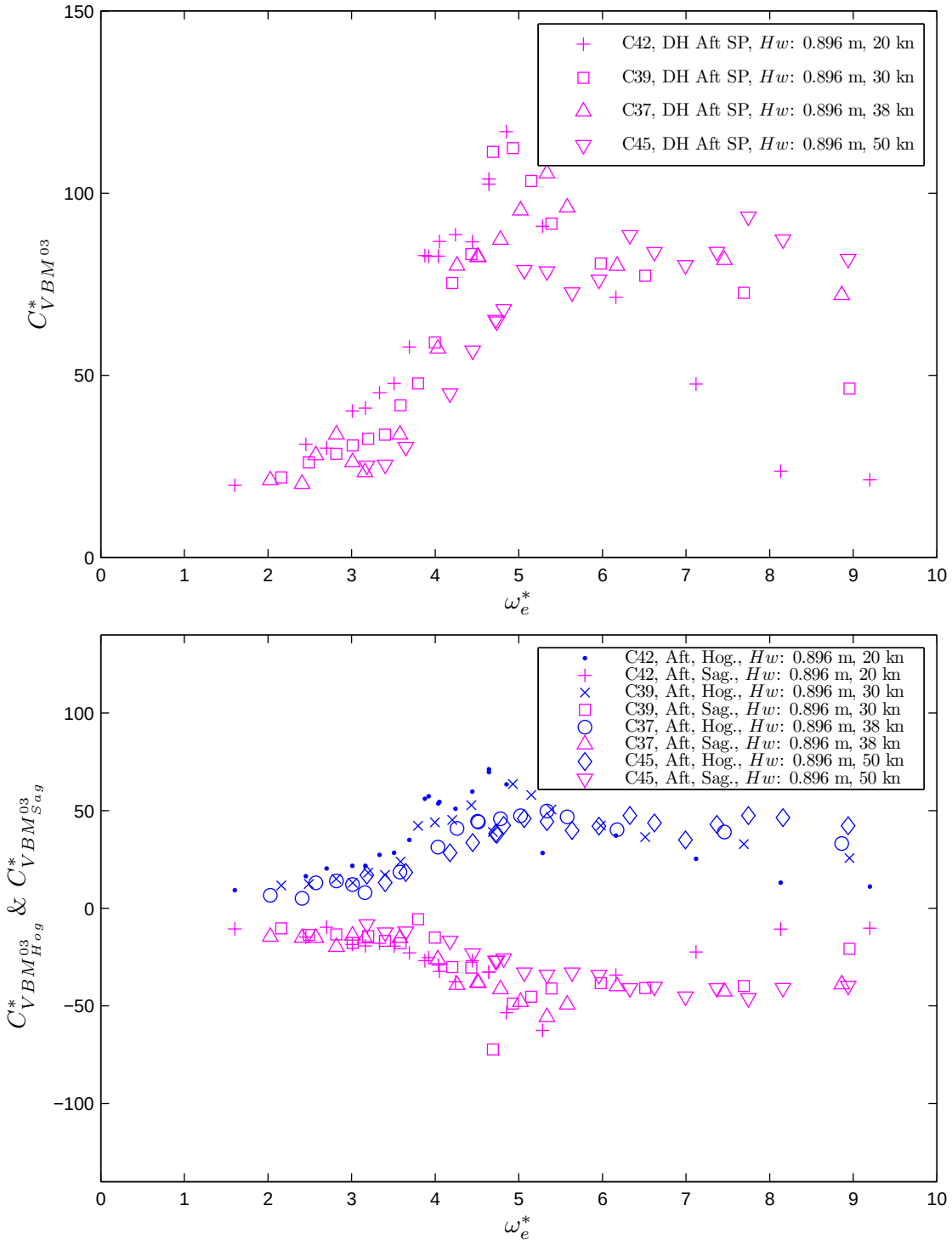

Figure J.18: Non-dimensional vertical bending moment coefficient (peak to trough), $C^*_{VBM^{03}}$ and non-dimensional hogging and sagging vertical bending moment coefficients, $C^*_{VBM^{03}_{Hog}}$ & $C^*_{VBM^{03}_{Hog}}$, at aft elastic links by varying the velocity, with respect to the non-dimensional encounter angular wave frequency, ω^*_e. The wave height to draft ratio, H_w/T was maintained at 0.26.

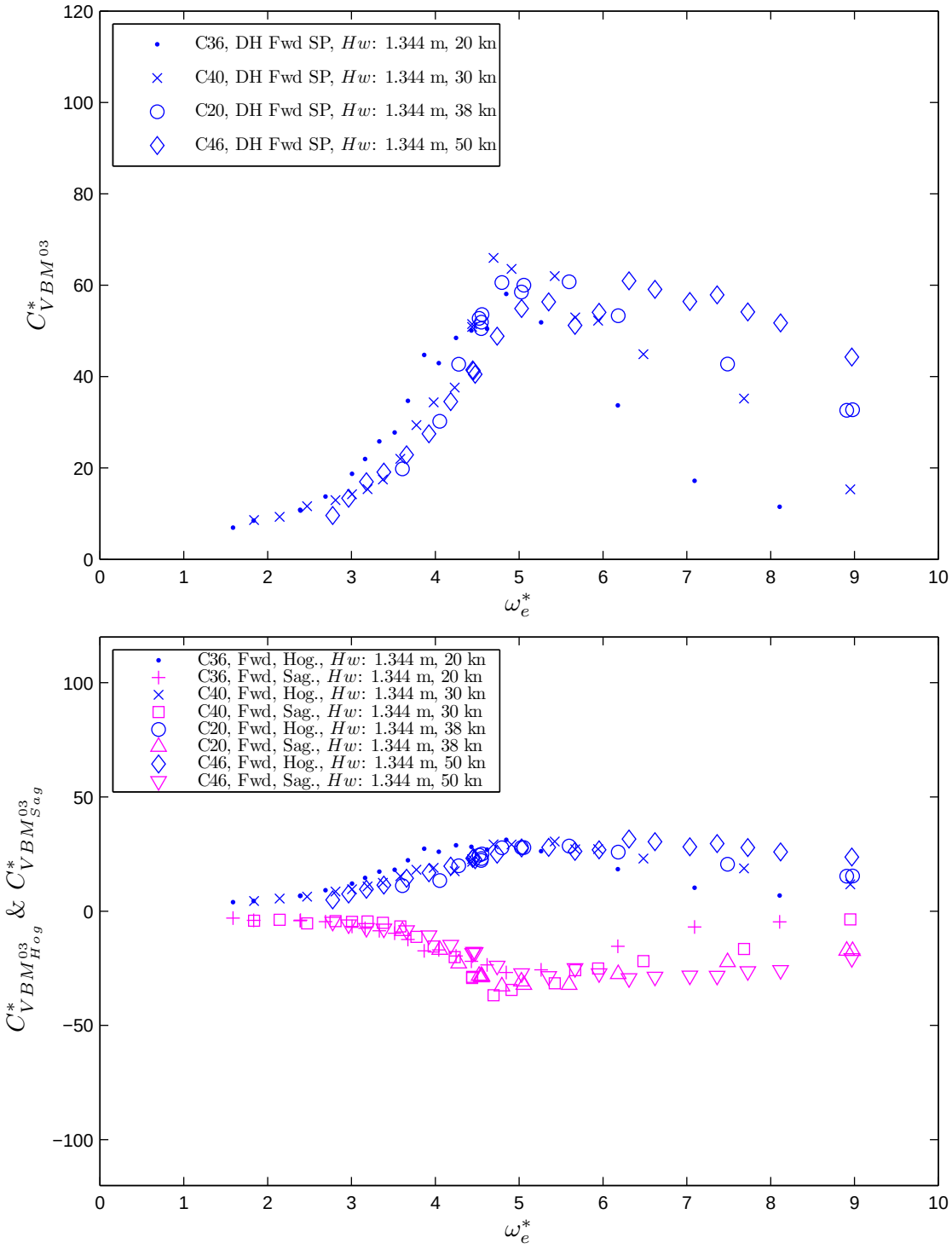

Figure J.19: Non-dimensional vertical bending moment coefficient (peak to trough), $C^*_{VBM^{03}}$ and non-dimensional hogging and sagging vertical bending moment coefficients, $C^*_{VBM^{03}_{Hog}}$ & $C^*_{VBM^{03}_{Hog}}$, at forward elastic links by varying the velocity, with respect to the non-dimensional encounter angular wave frequency, ω^*_e. The wave height to draft ratio, H_w/T was maintained at 0.39.

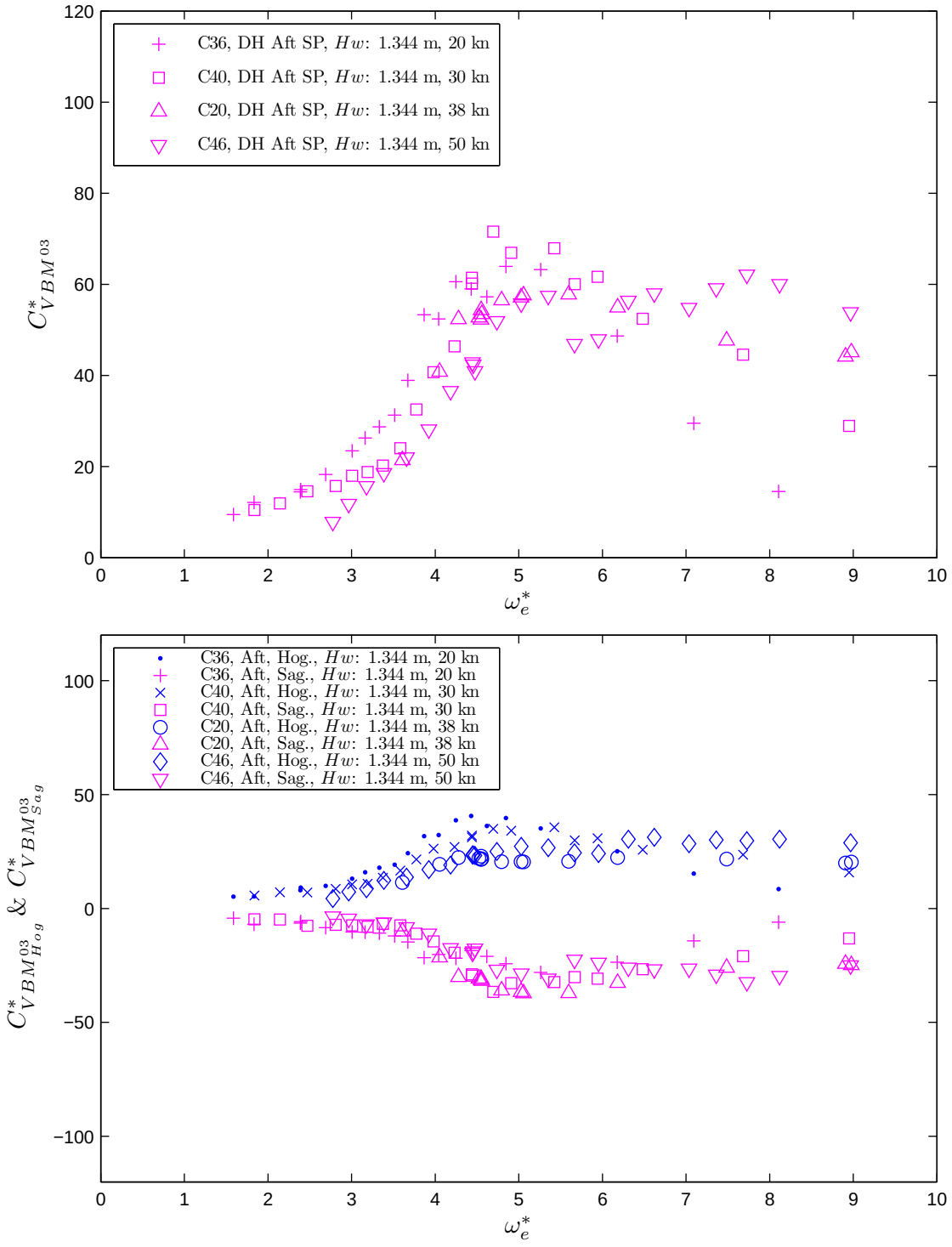

Figure J.20: Non-dimensional vertical bending moment coefficient (peak to trough), $C^*_{VBM^{03}}$ and non-dimensional hogging and sagging vertical bending moment coefficients, $C^*_{VBM^{03}_{Hog}}$ & $C^*_{VBM^{03}_{Hog}}$ at aft elastic links by varying the velocity, with respect to the non-dimensional encounter angular wave frequency, ω^*_e. The wave height to draft ratio, H_w/T was maintained at 0.39.

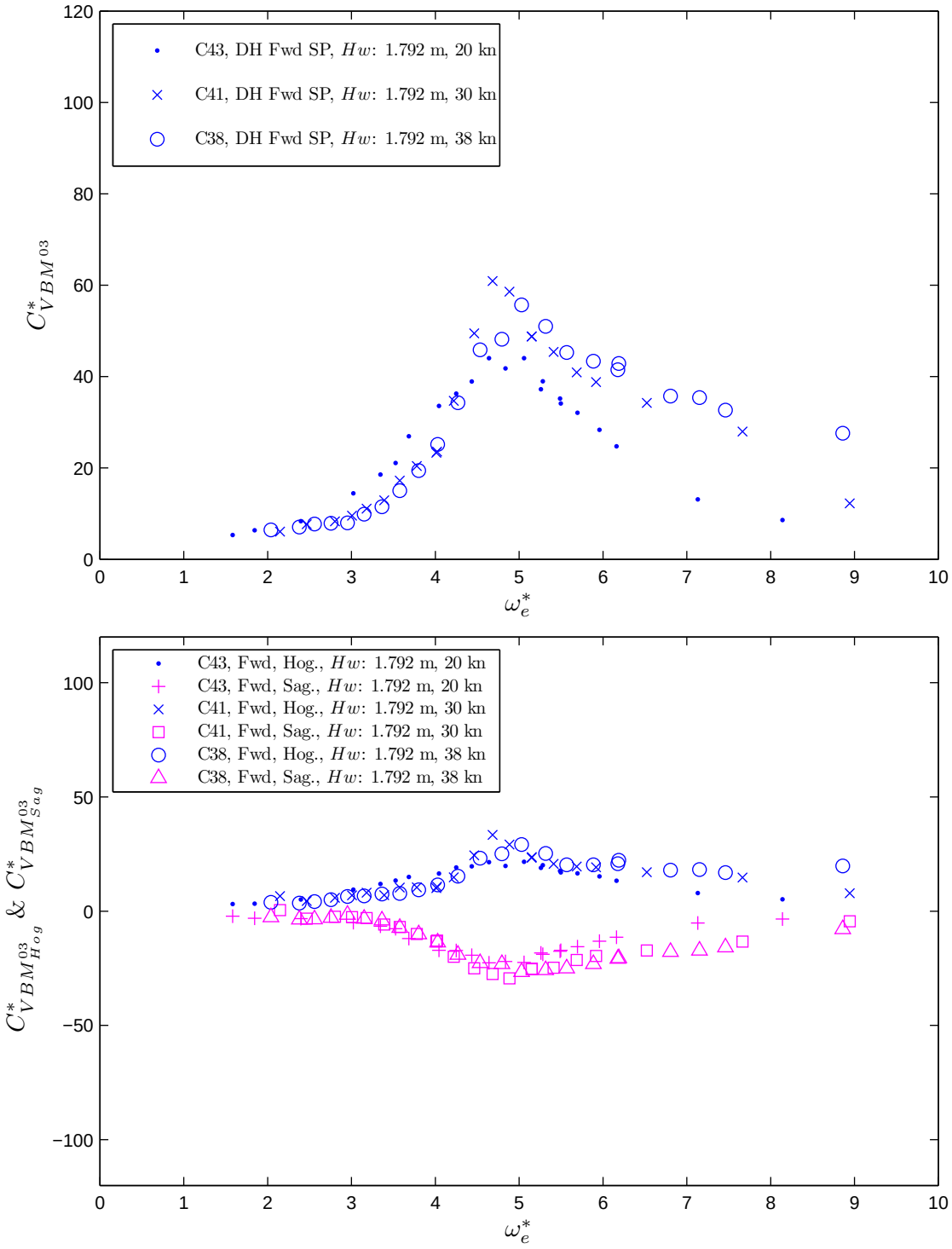

Figure J.21: Non-dimensional vertical bending moment coefficient (peak to trough), $C^*_{VBM^{03}}$ and non-dimensional hogging and sagging vertical bending moment coefficients, $C^*_{VBM^{03}_{Hog}}$ & $C^*_{VBM^{03}_{Hog}}$, at forward elastic links by varying the velocity, with respect to the non-dimensional encounter angular wave frequency, ω^*_e. The wave height to draft ratio, H_w/T was maintained at 0.52.

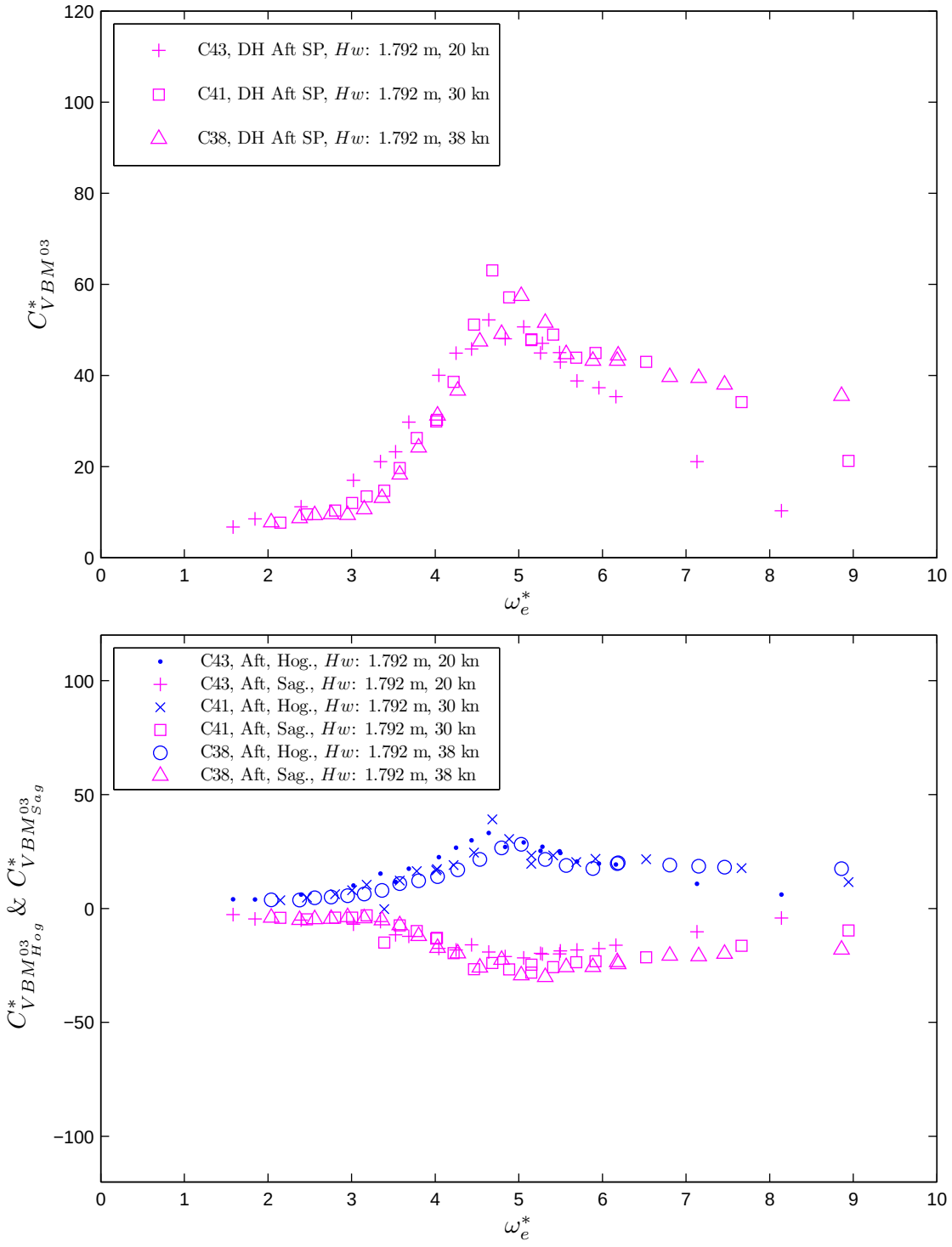

Figure J.22: Non-dimensional vertical bending moment coefficient (peak to trough), $C^*_{VBM^{03}}$ and non-dimensional hogging and sagging vertical bending moment coefficients, $C^*_{VBM^{03}_{Hog}}$ & $C^*_{VBM^{03}_{Hog}}$, at aft elastic links by varying the velocity, with respect to the non-dimensional encounter angular wave frequency, ω^*_e. The wave height to draft ratio, H_w/T was maintained at 0.52.

Appendix K

Slam Force Coefficients

The slam force coefficients for large wave heights were obtained based on Equation 3.48 for wave heights of 1.344, 2.688, 4.032, and 5.376 at 20 and 38 K_n.

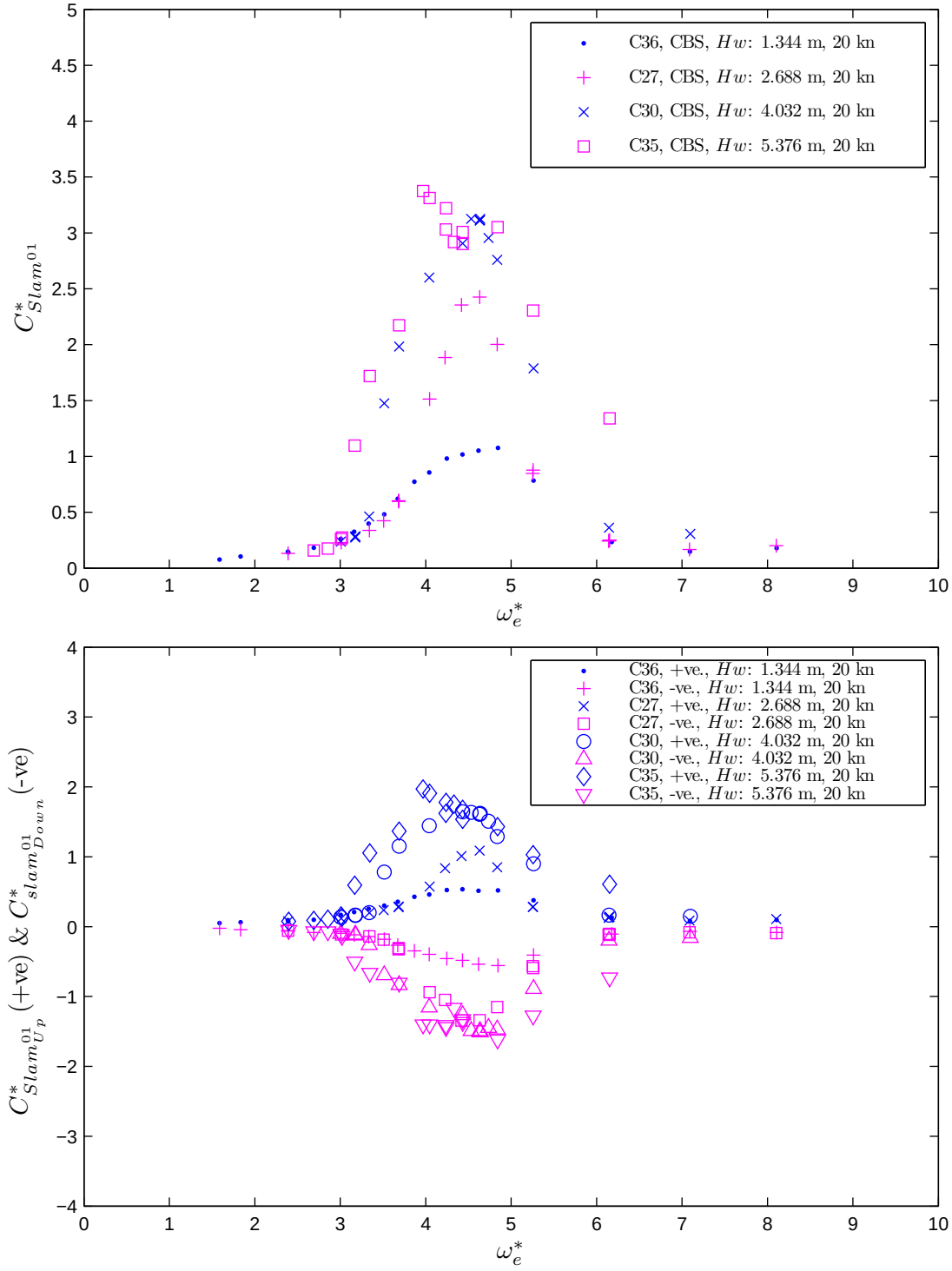

Figure K.1: Coefficients for Slam force (peakto trough) and positive and negative slam force by varying the wave height, are plotted with respect to the non-dimensional encounter angular wave frequency, ω^*_e. The model speed was maintained at a constant speed of $F_n = 0.32$.

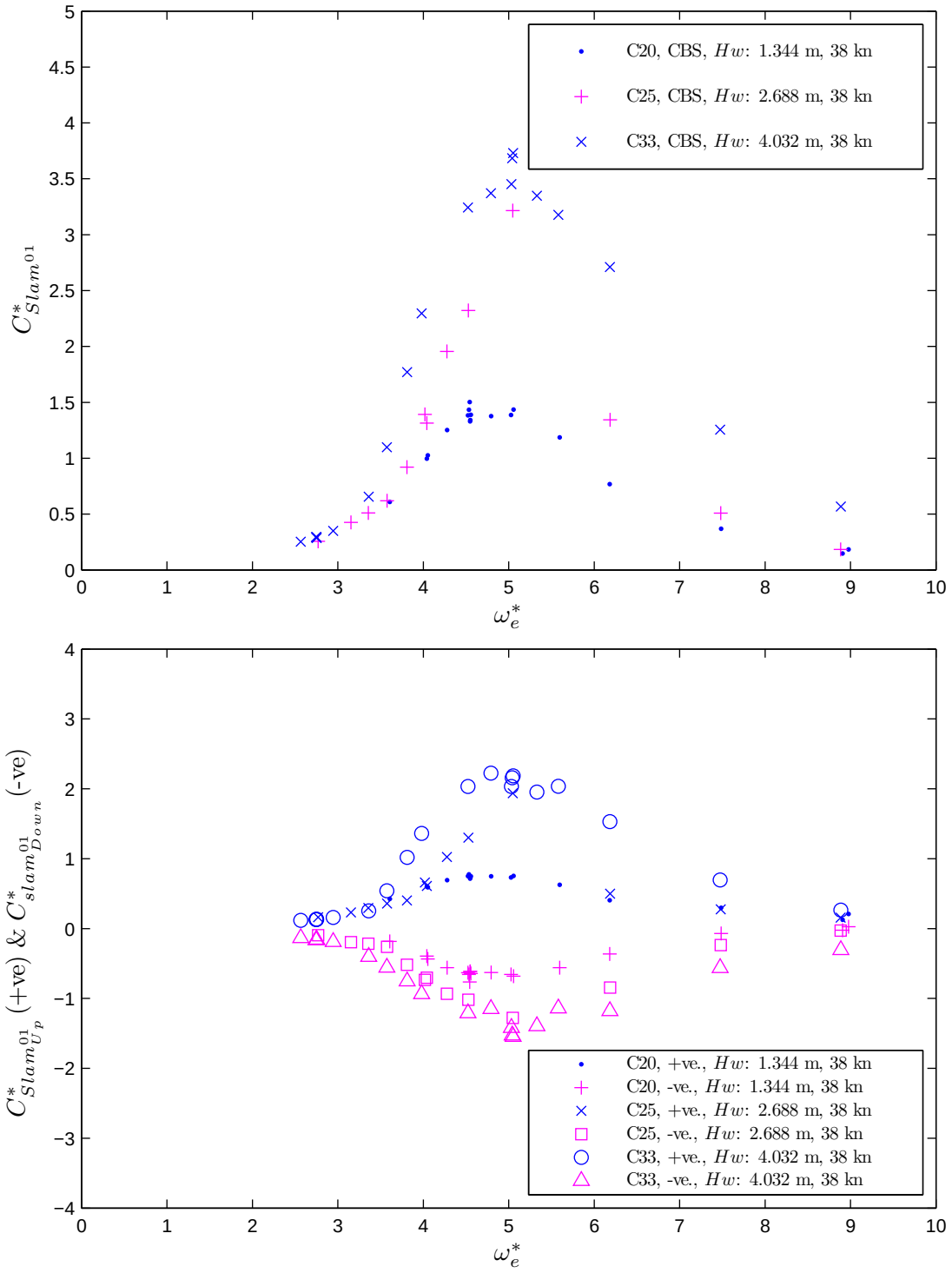

Figure K.2: Coefficients for Slam force (peak to trough) and positive and negative slam force by varying the wave height, are plotted with respect to non-dimensional encounter angular wave frequency, ω^*_e. The model speed was maintained at the constant speed of $F_n = 0.60$.

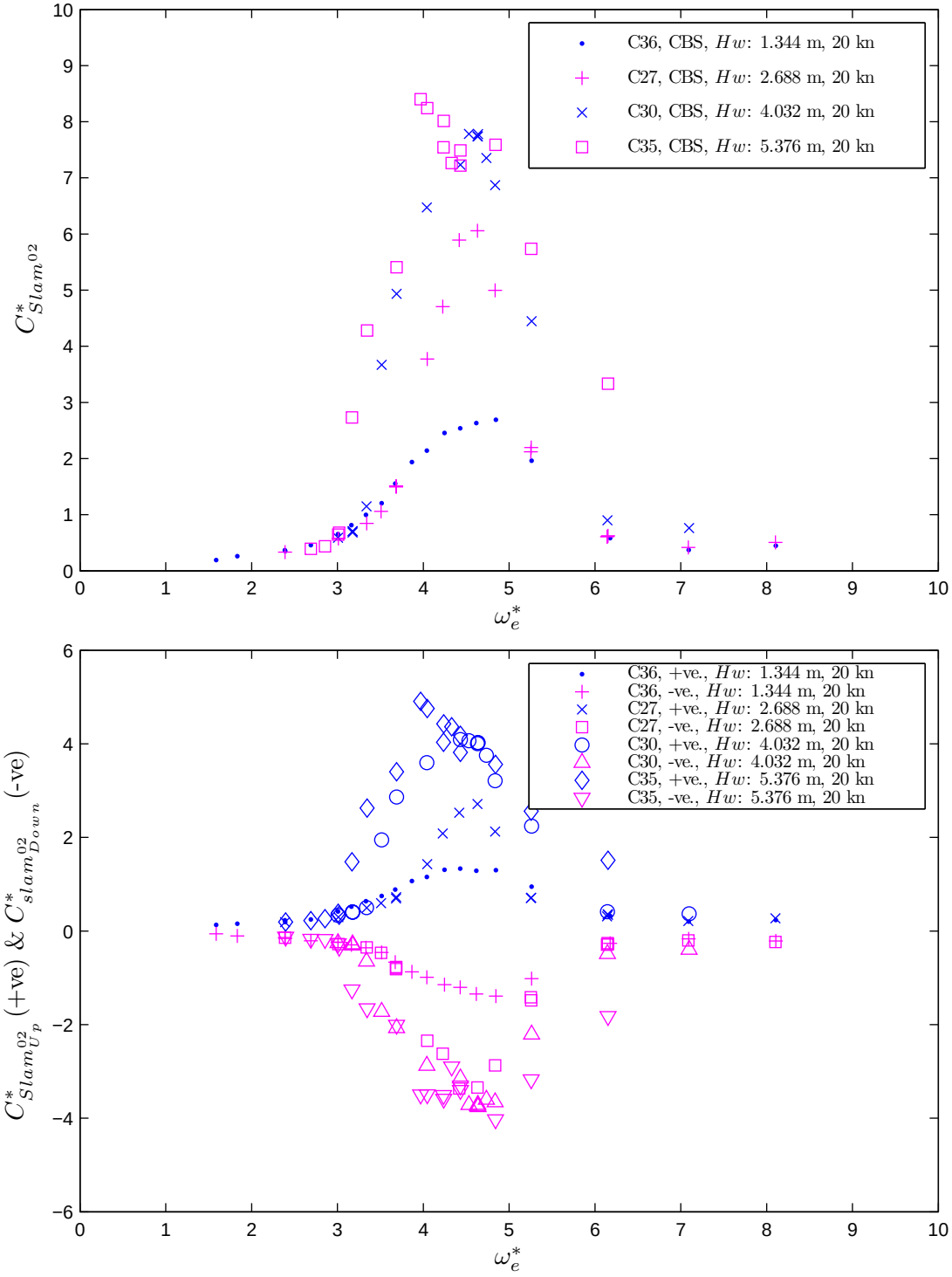

Figure K.3: Coefficients for Slam force (peak to trough) and positive and negative slam force by varying the wave height, are plotted with respect to the non-dimensional encounter angular wave frequency, ω^*_e. The model speed was maintained at a constant speed of $F_n = 0.32$.

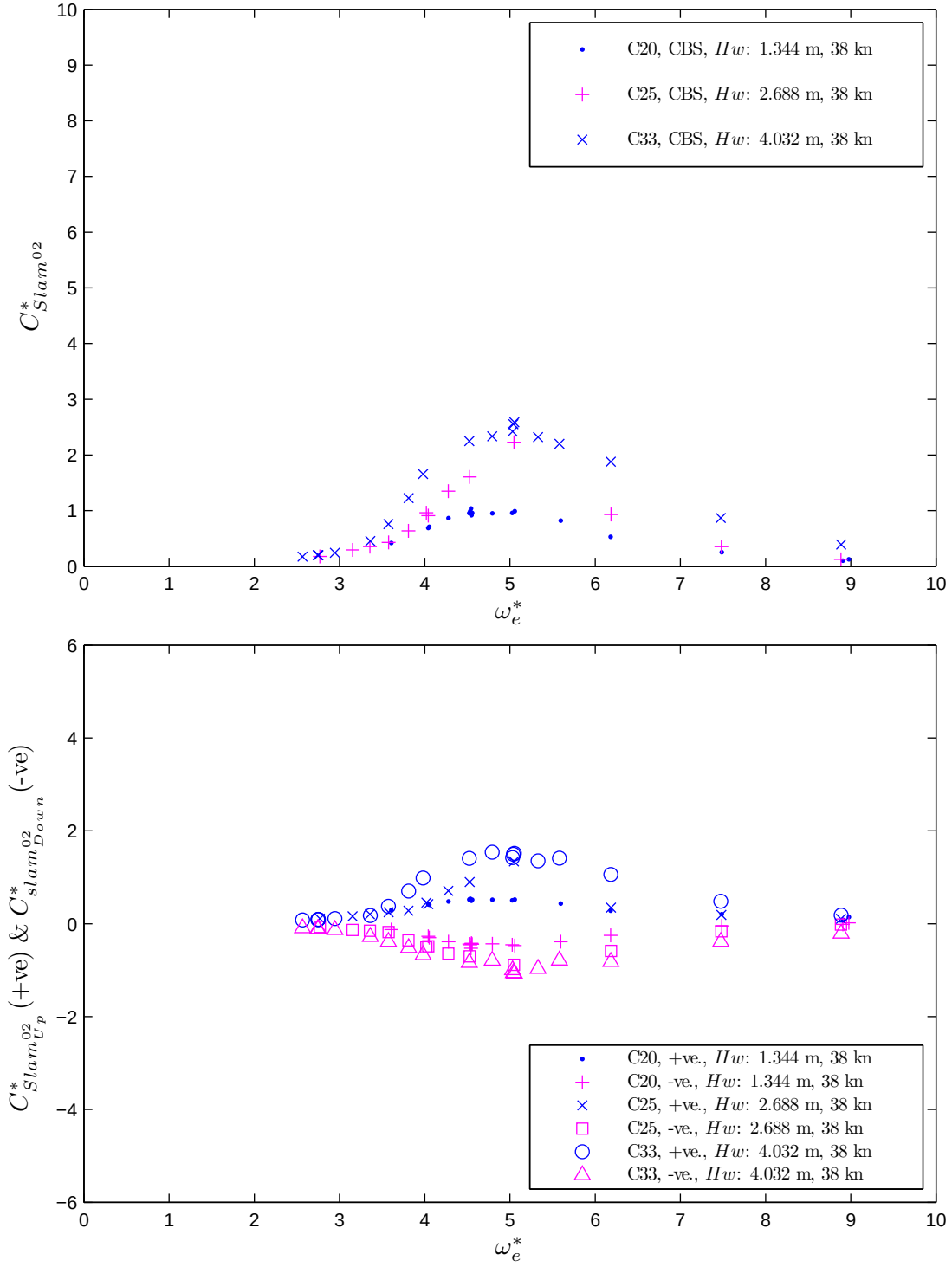

Figure K.4: Coefficients for Slam force (peak to trough) and positive and negative slam force by varying the wave height, are plotted with respect to the non-dimensional encounter angular wave frequency, ω^*_e. The model speed was maintained at a constant speed of $F_n = 0.60$.

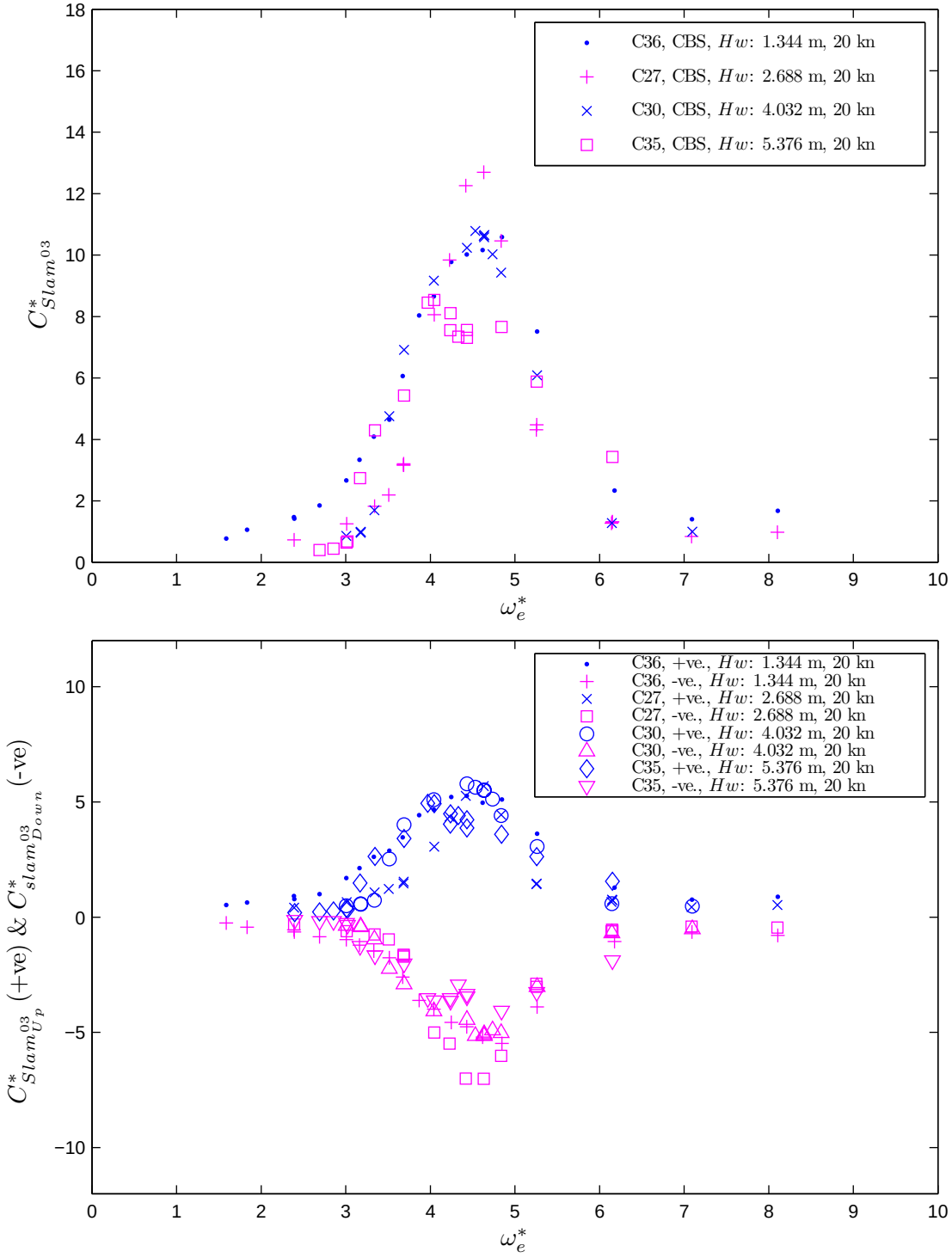

Figure K.5: Coefficients for Slam force (peak to trough) and positive and negative slam force by varying the wave height, are plotted with respect to the non-dimensional encounter angular wave frequency, ω^*_e. The model speed was maintained at a constant speed of $F_n = 0.32$.

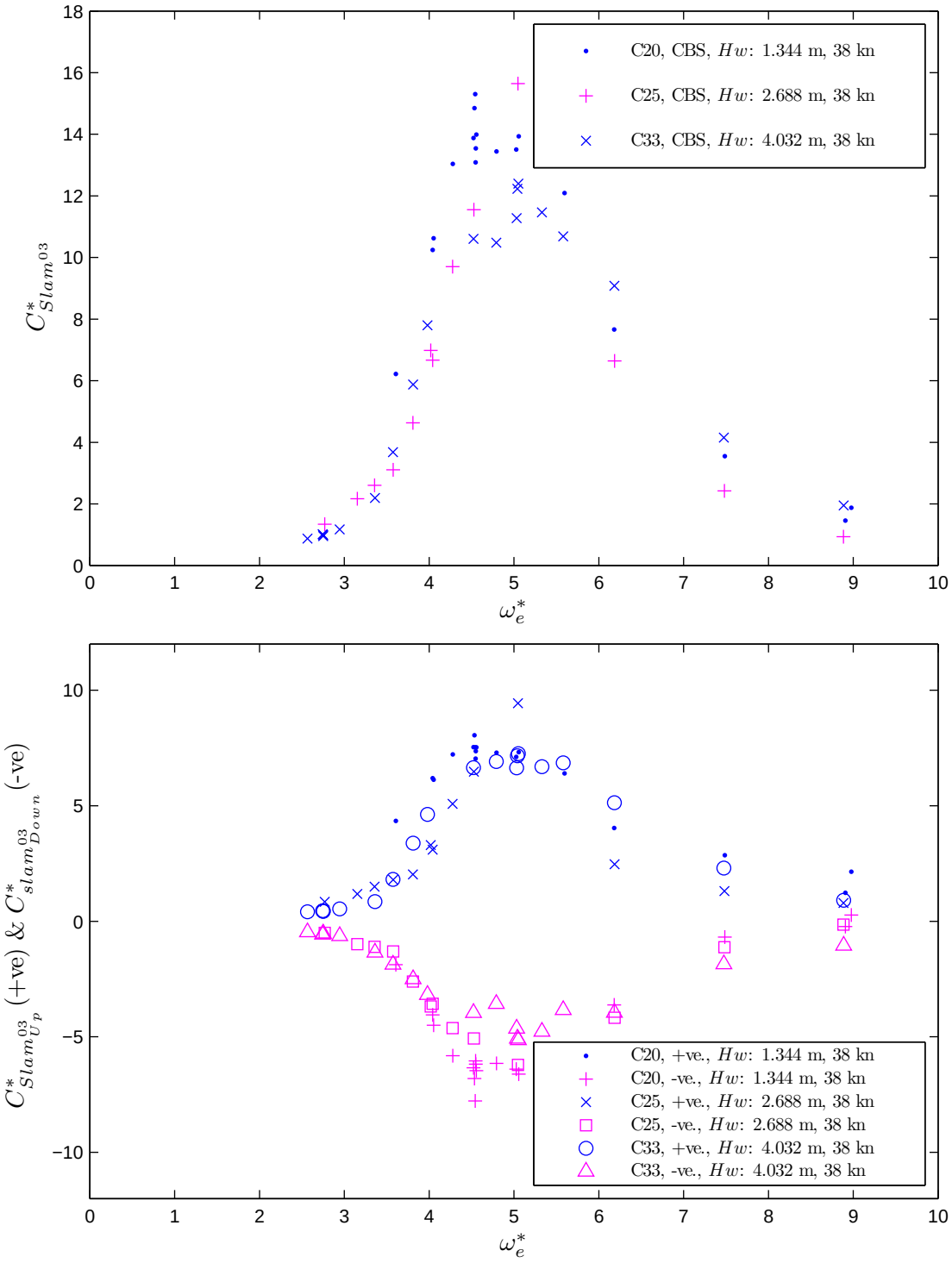

Figure K.6: Coefficients for Slam force (peak to trough) and positive and negative slam force by varying the wave height, are plotted with respect to the non-dimensional encounter angular wave frequency, ω^*_e. The model speed was maintained at a constant speed of $F_n = 0.60$.

Appendix L

INCAT 112 m Hull 064, Delivery Voyage Route

The location of the delivery voyage routes were plotted based on the date and time according to the GPS locations recorded on the voyage log. The date and time can be used as reference information of the delivery voyage log to determine the GPS speed, log speed, main engine and jet shaft RPM speed, fuel gauges, for example.

Figure L.1: Vessel locations crossing Bass Strait during the voyage from Hobart to off the coast around Sydney.

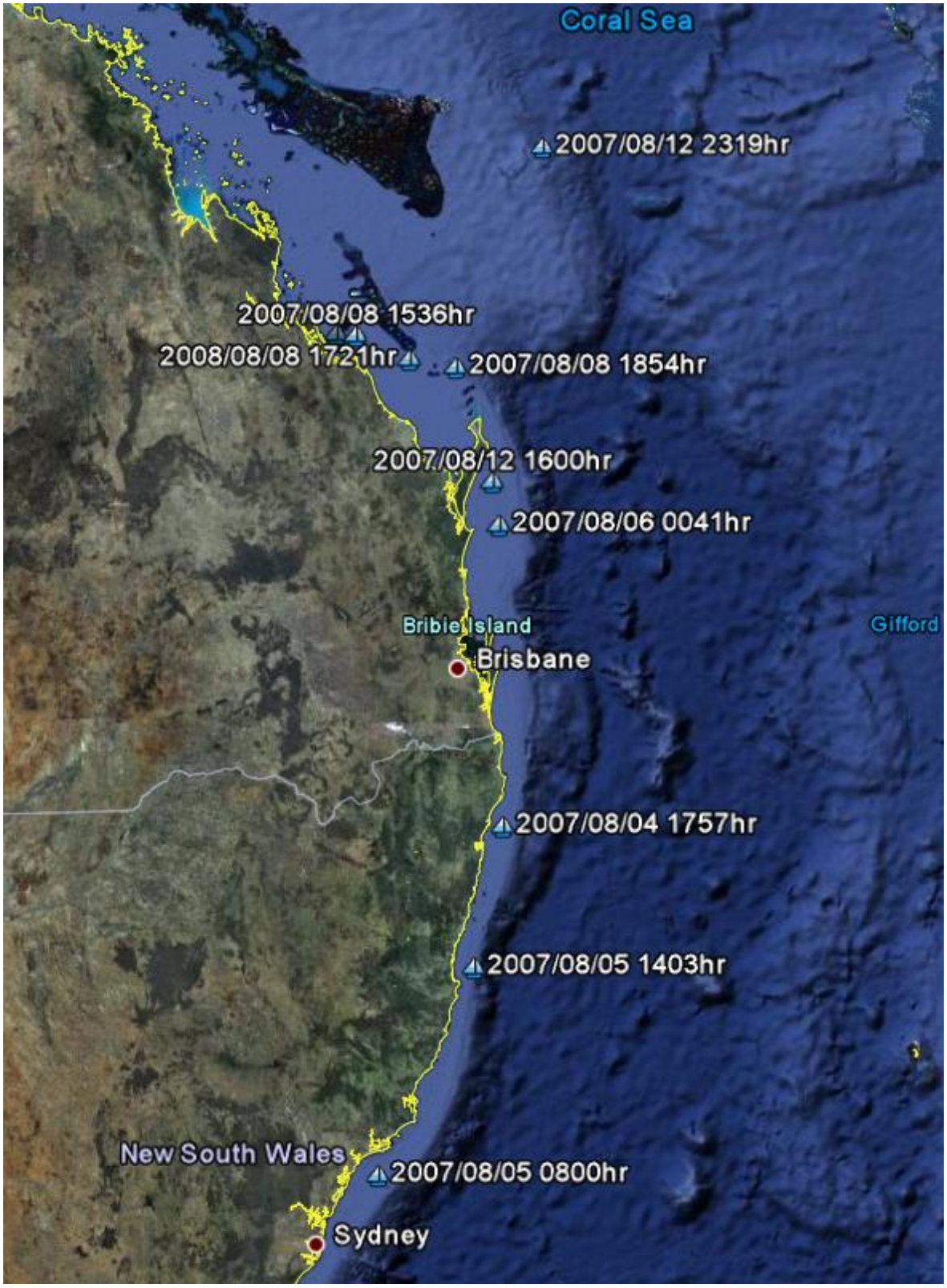

Figure L.2: Vessel locations travelling from off the coast around Sydney to the Coral Sea.

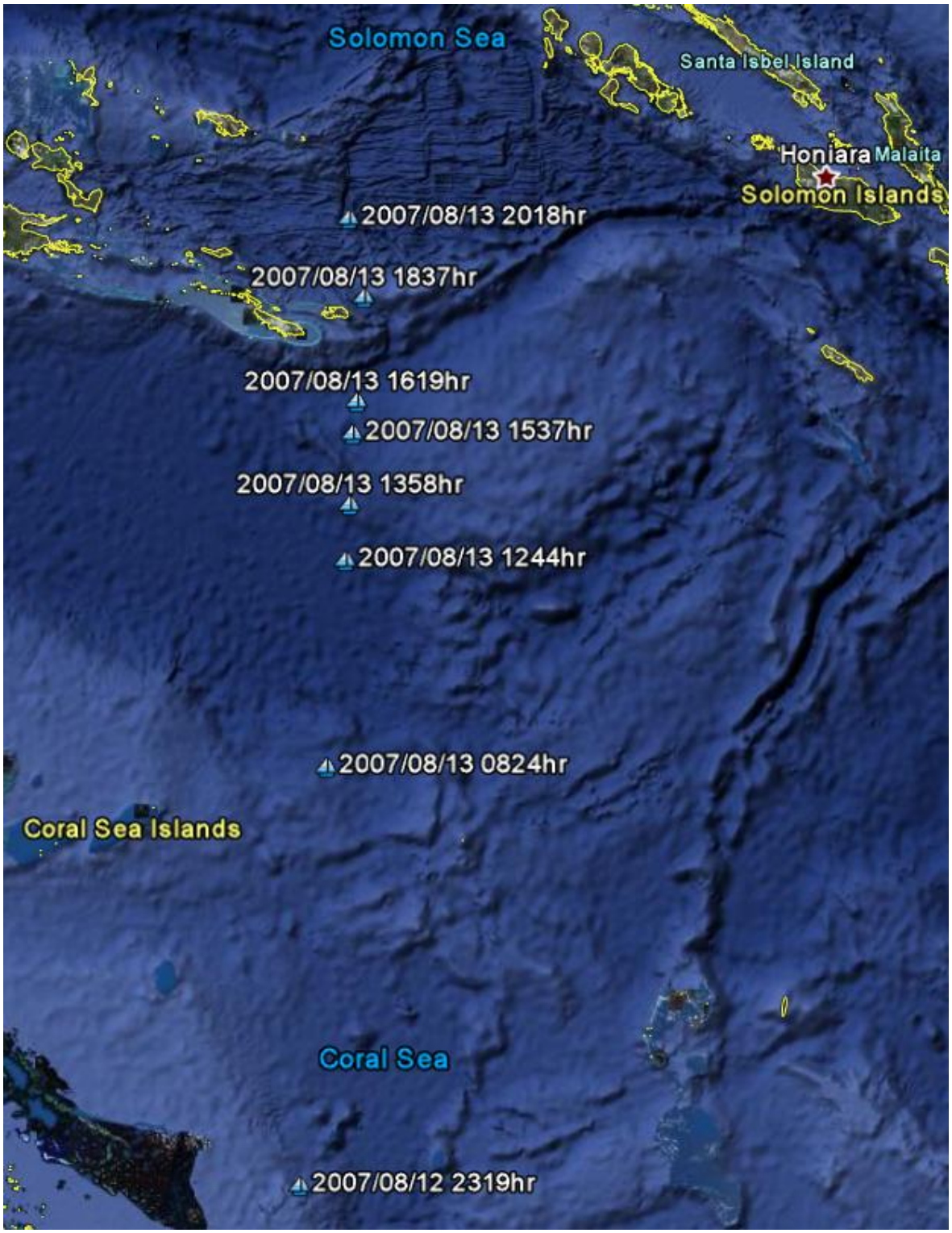

Figure L.3: Vessel locations travelling from the Coral Sea to the Solomon Sea

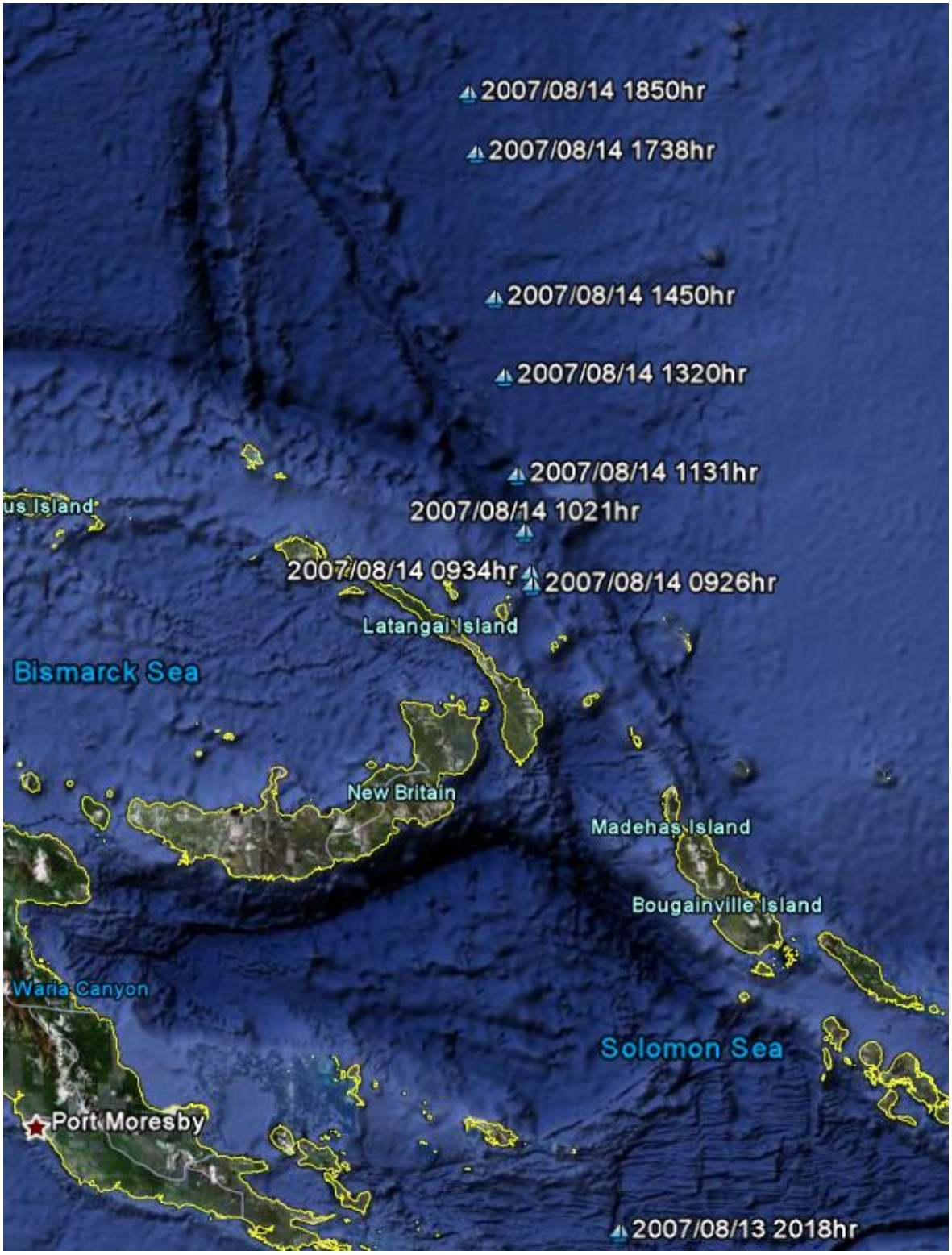

Figure L.4: Vessel locations travelling from the Solomon Sea to Bismarck Island.

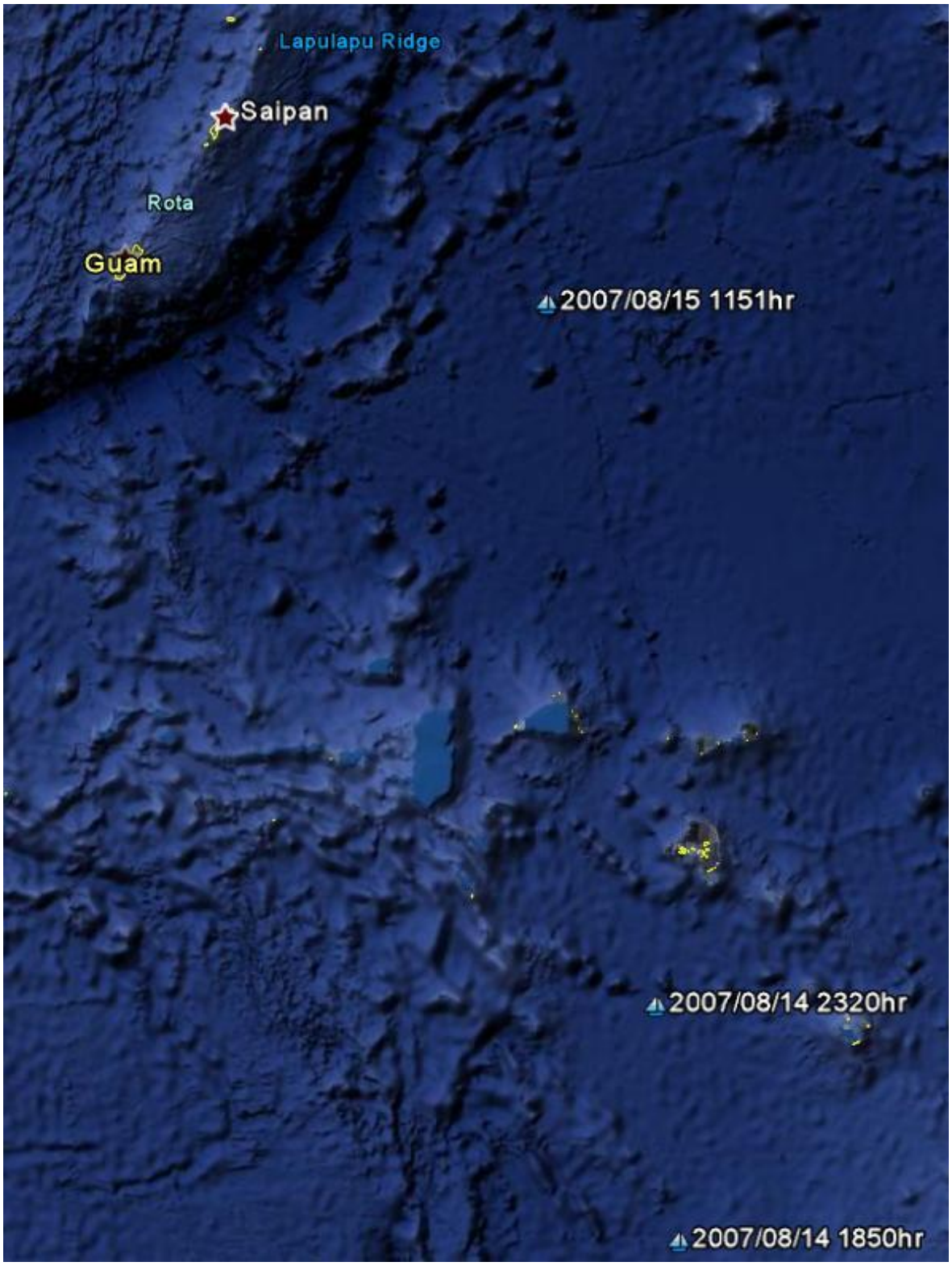

Figure L.5: Vessel locations travelling from Bismarck Island to off the coast of Saipan.

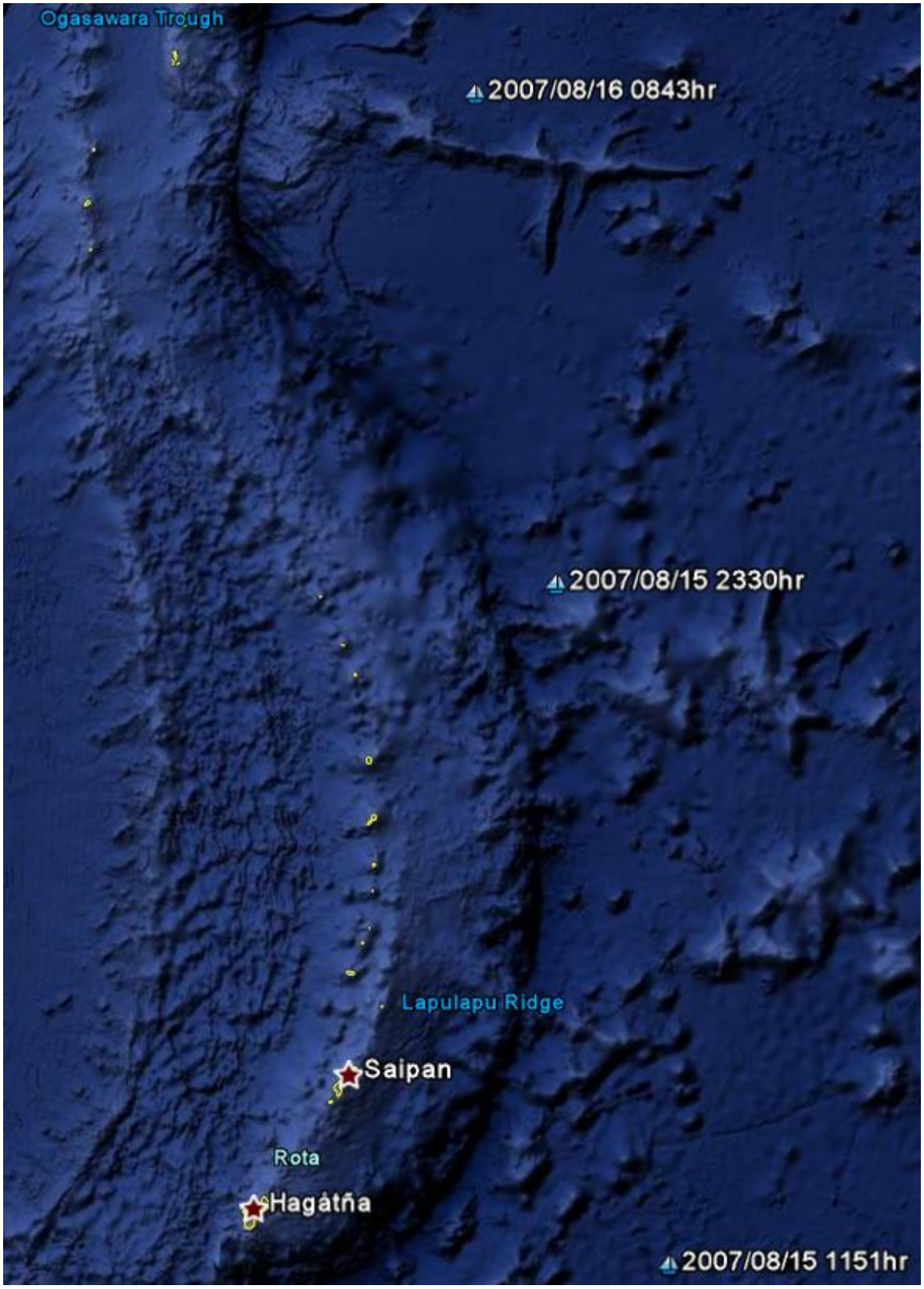

Figure L.6: Vessel locations travelling from off the coast of Saipan to off the coast of the Ogasawara Islands.

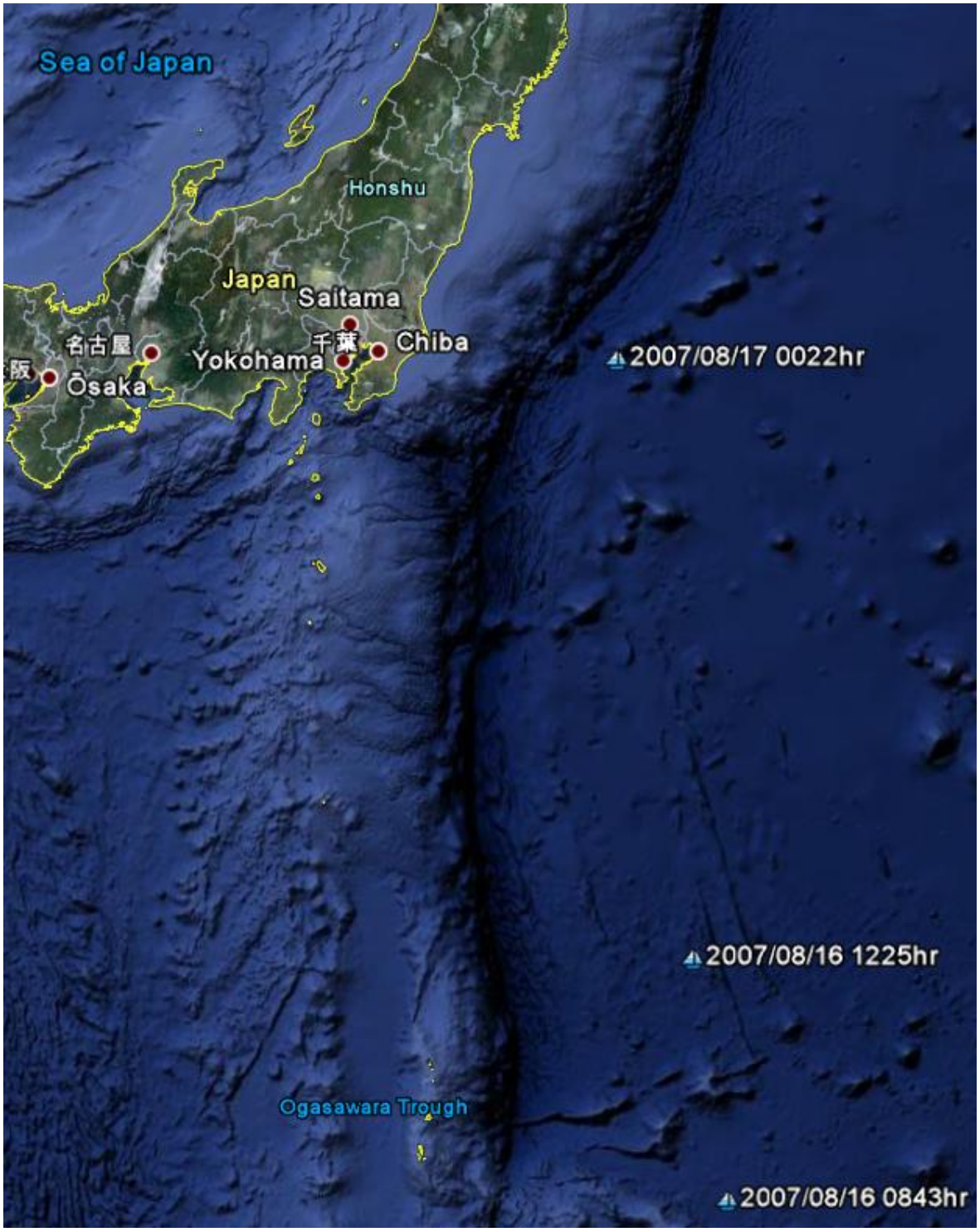

Figure L.7: Vessel locations travelling from off the coast of Saipan to off the coast of Ogasawara Islands.

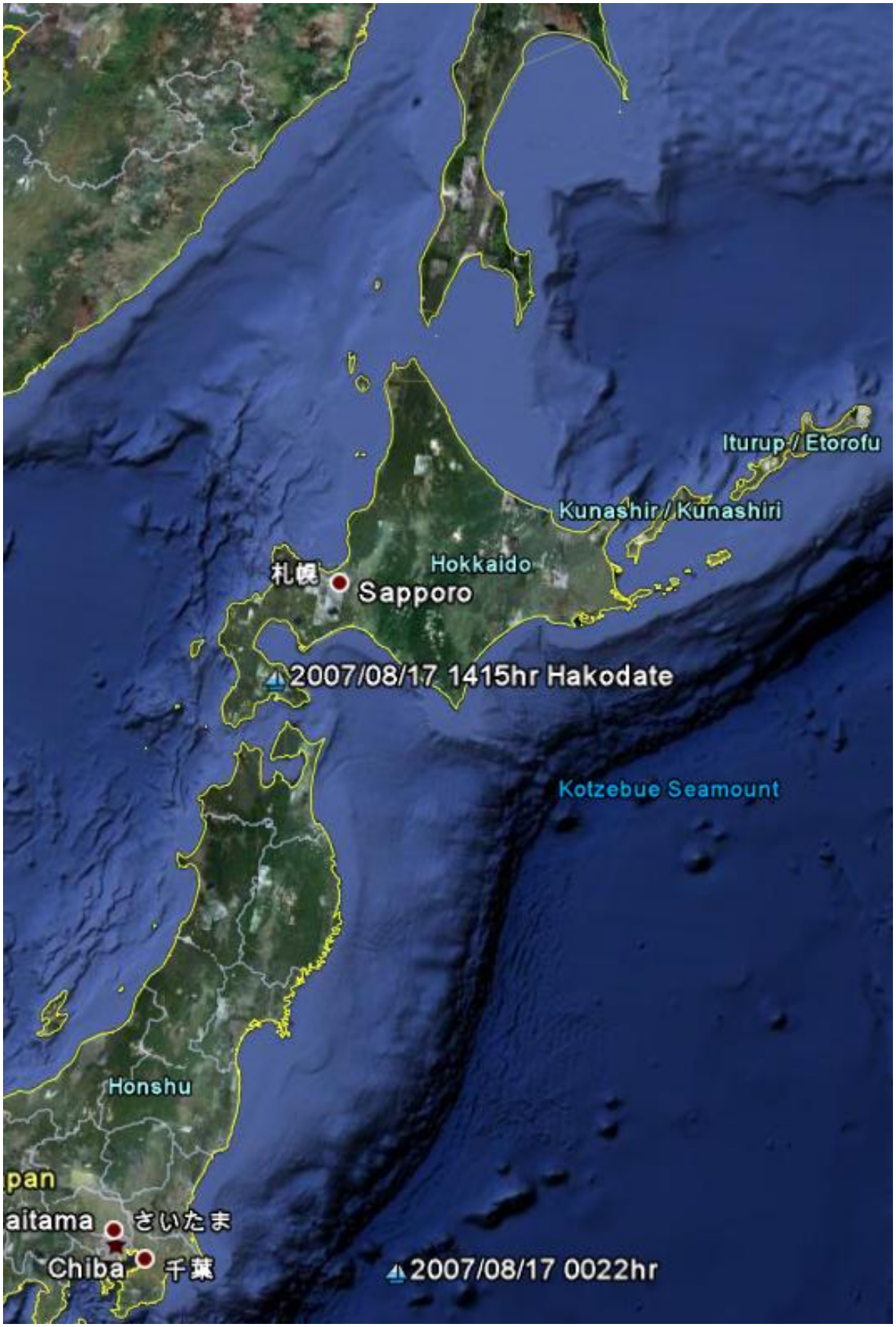

Figure L.8: Vessel locations travelling from near Honshu Island to Hakodate in Hokaido.

Appendix M

INCAT 112 m Hull 064 Delivery Voyage Data

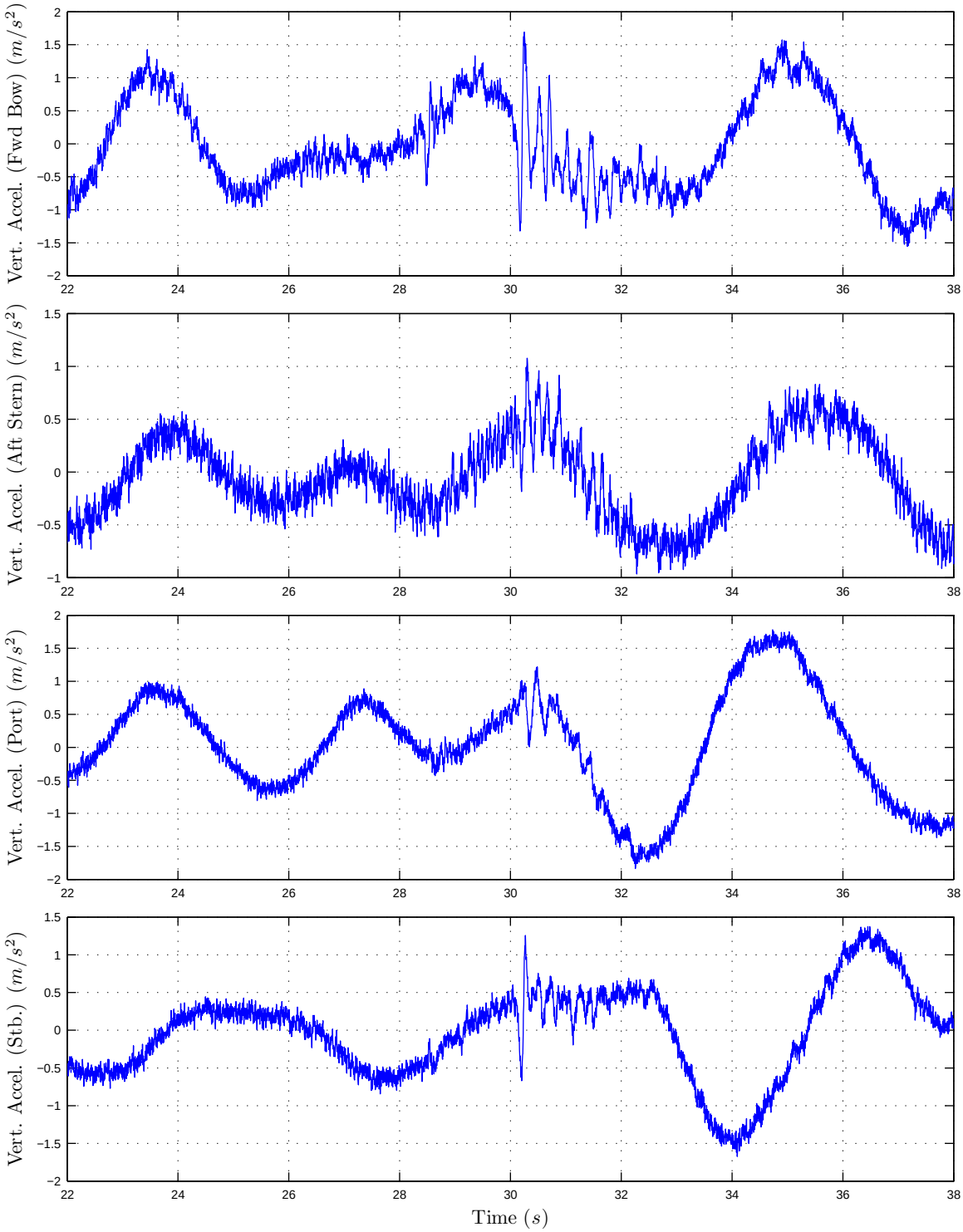

Figure M.1: Vertical accelerometer data in the time domain for INCAT 112 m Hull 064 delivery voyage. Data was recorded on Disc No. 1 Run No. 062.

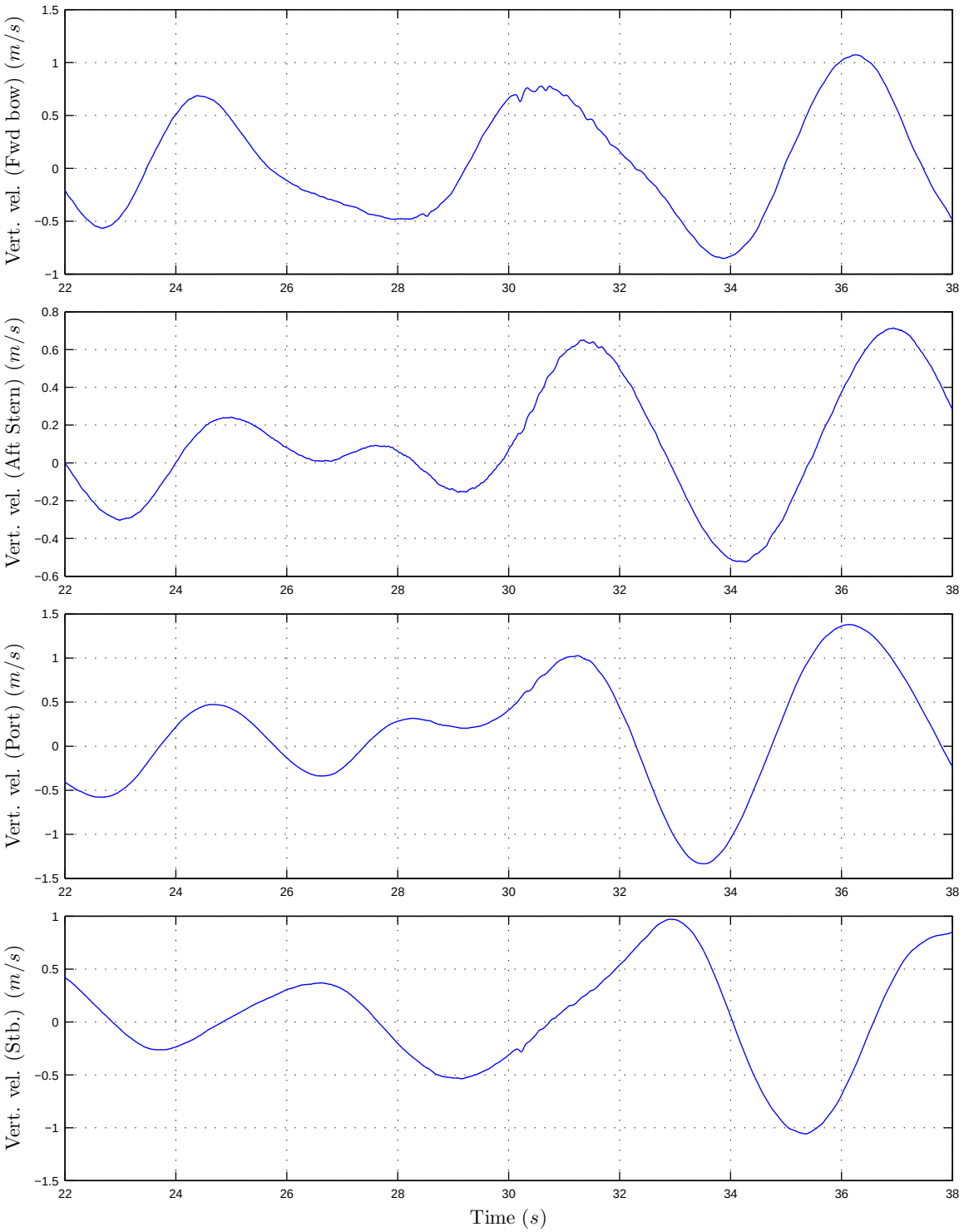

Figure M.2: Vertical velocity data in the time domain numerically integrated for INCAT 112 m Hull 064 delivery voyage. Data was recorded on Disc No. 1 Run No. 062.

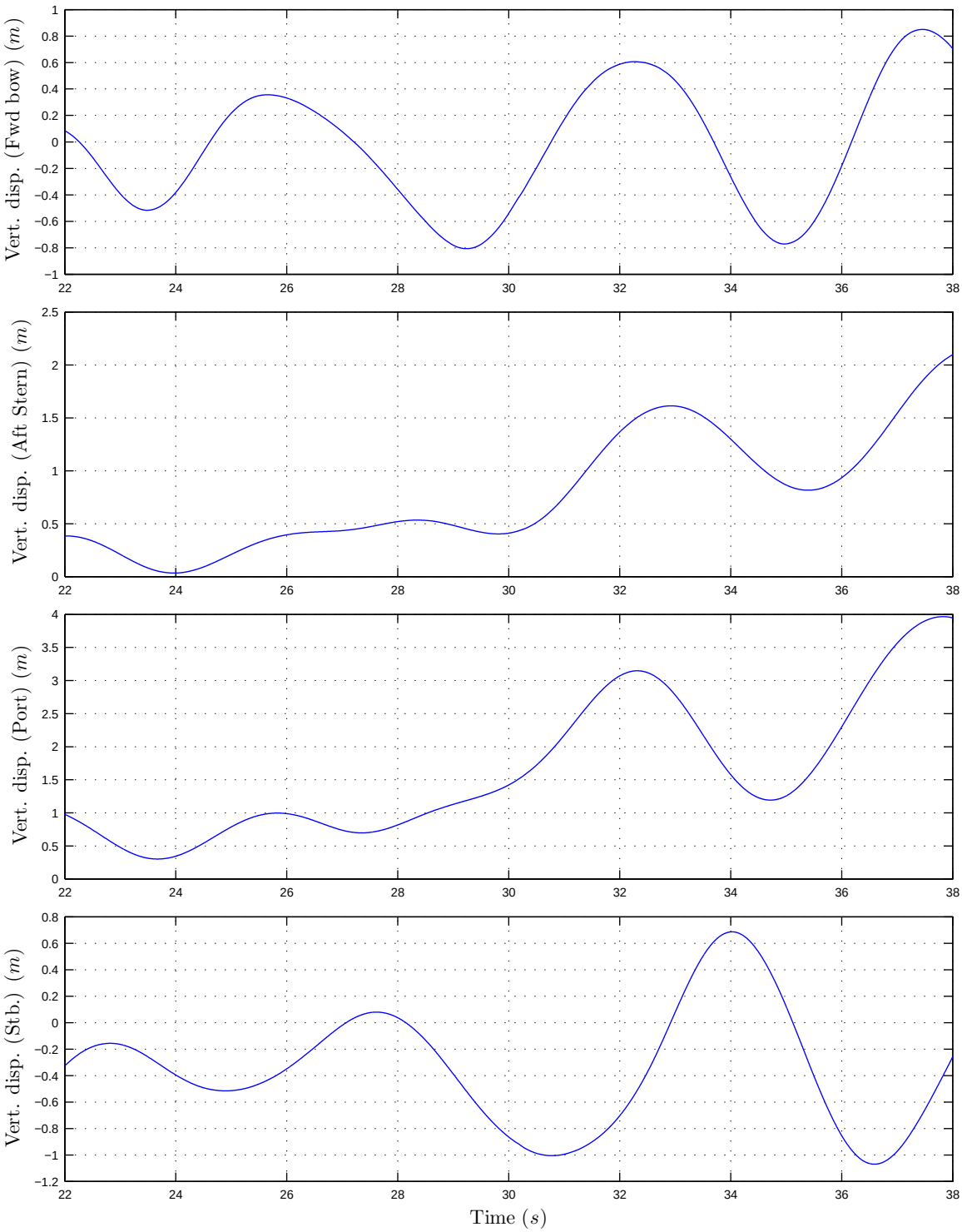

Figure M.3: Vertical displacement data in time domain numerically double-integrated for INCAT 112 m Hull 064 delivery voyage. Data was recorded on Disc No. 1 Run No. 062.

Appendix N

Power Spectrum Density for Delivery Voyage Data

PSD: Overall range

Spectral analysis on the accelerometers and strain gauges were carried out. The power spectral density (PSD) shows the response from 0 to 20 Hz for the dominant frequency for accelerometers and strain gauges shown in Figures N.1 and N.2. The power spectrum density shows strong peaks in the lower frequencies for both analyses of accelerometers and strain gauges, and other response frequency components cannot be seen in these figures. This indicates that the strongest effects were caused by the encounter wave.

PSD: Wave frequency response range

The PSDs in Figures N.3 and N.4 focused on the wave frequency response range by eliminating the higher frequency range.

PSD: VBM frequency response range

The PSDs in Figures N.5 and N.6forcused on the VBM response by removing the dominant response from the encounter wave frequency.

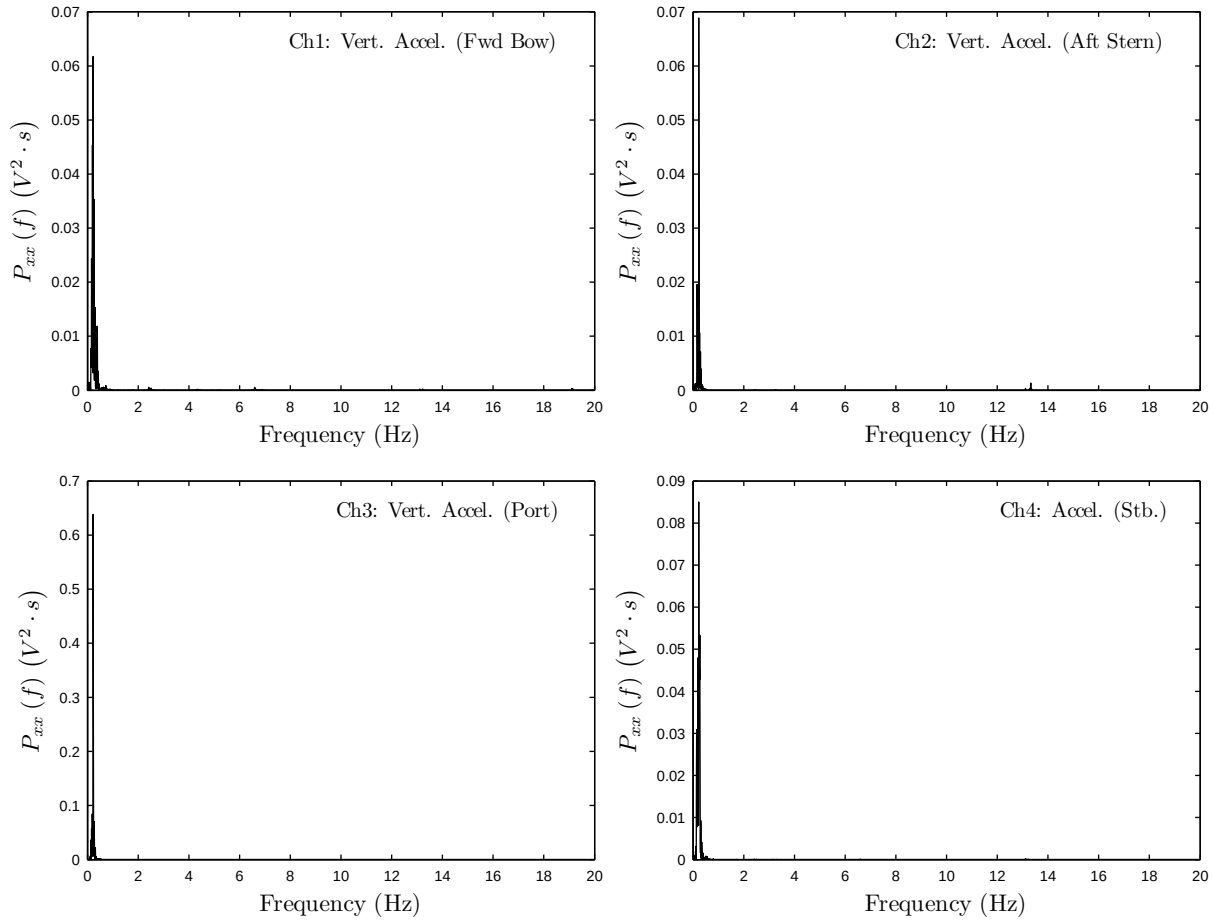

Figure N.1: Spectral analysis on accelerometer raw data during the delivery voyage of INCAT 112 m. Power spectral density (PSD), $P_{xx}(f)$ for acceleration measured at Ch1, Ch2 Ch3 and Ch4 on the vehicle deck for Voyage record disc No.1, Data No.062. PSD was obtained by applying the Hamming window for data taper in the time domain, and smoothing by a convolution with 1 smoothing window in the frequency domain.

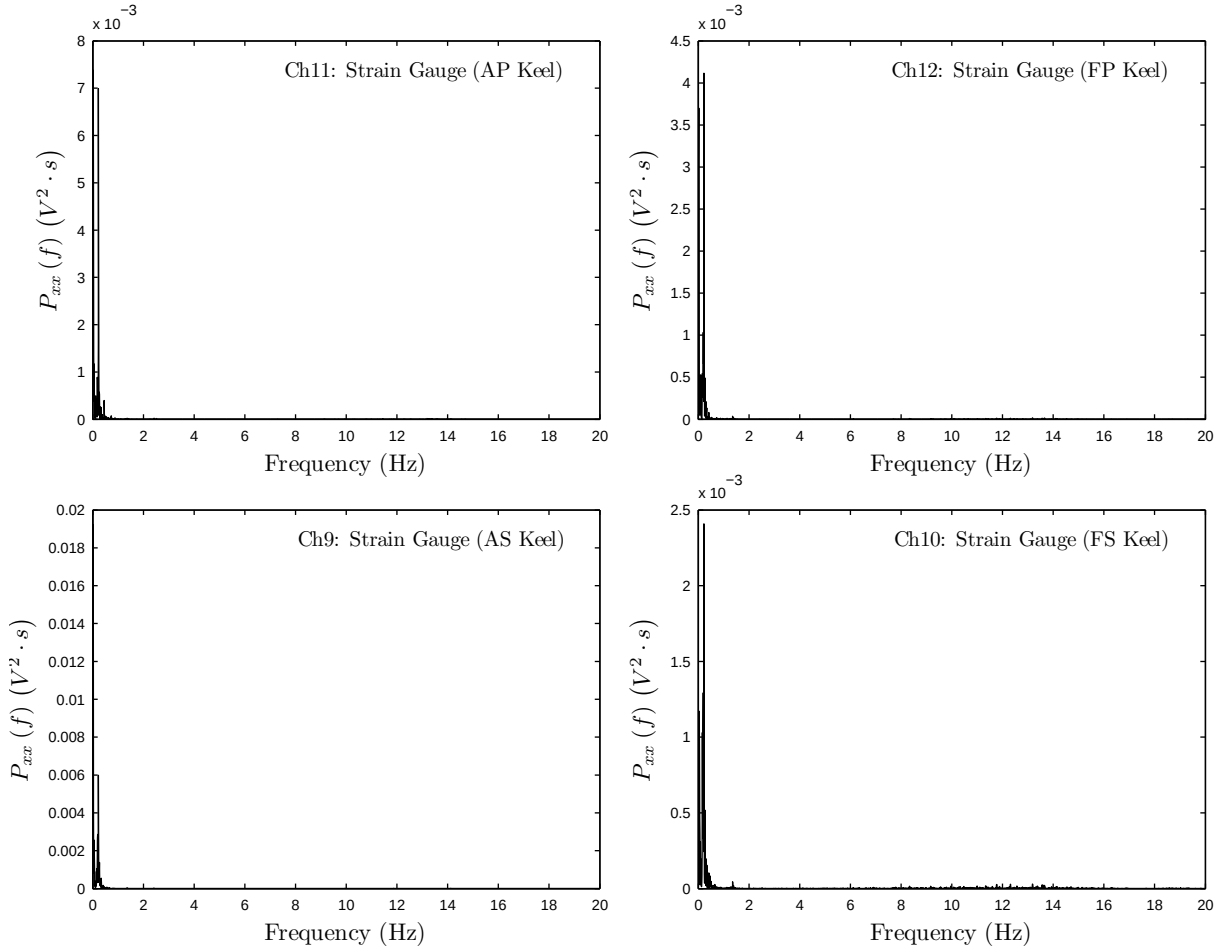

Figure N.2: Spectral analysis on raw data of strain gauges on the keel during the delivery voyage of INCAT 112 m. Power spectral density (PSD), $P_{xx}(f)$ for acceleration measured at Ch9, Ch10 Ch11 and Ch12 on the viechle deck for Voyage record disc No.1, Data No.062. PSD was obtained by applying the Hamming window for data taper in the time domain, and smoothing by a convolution with 1 smoothing windows in the frequency domain.

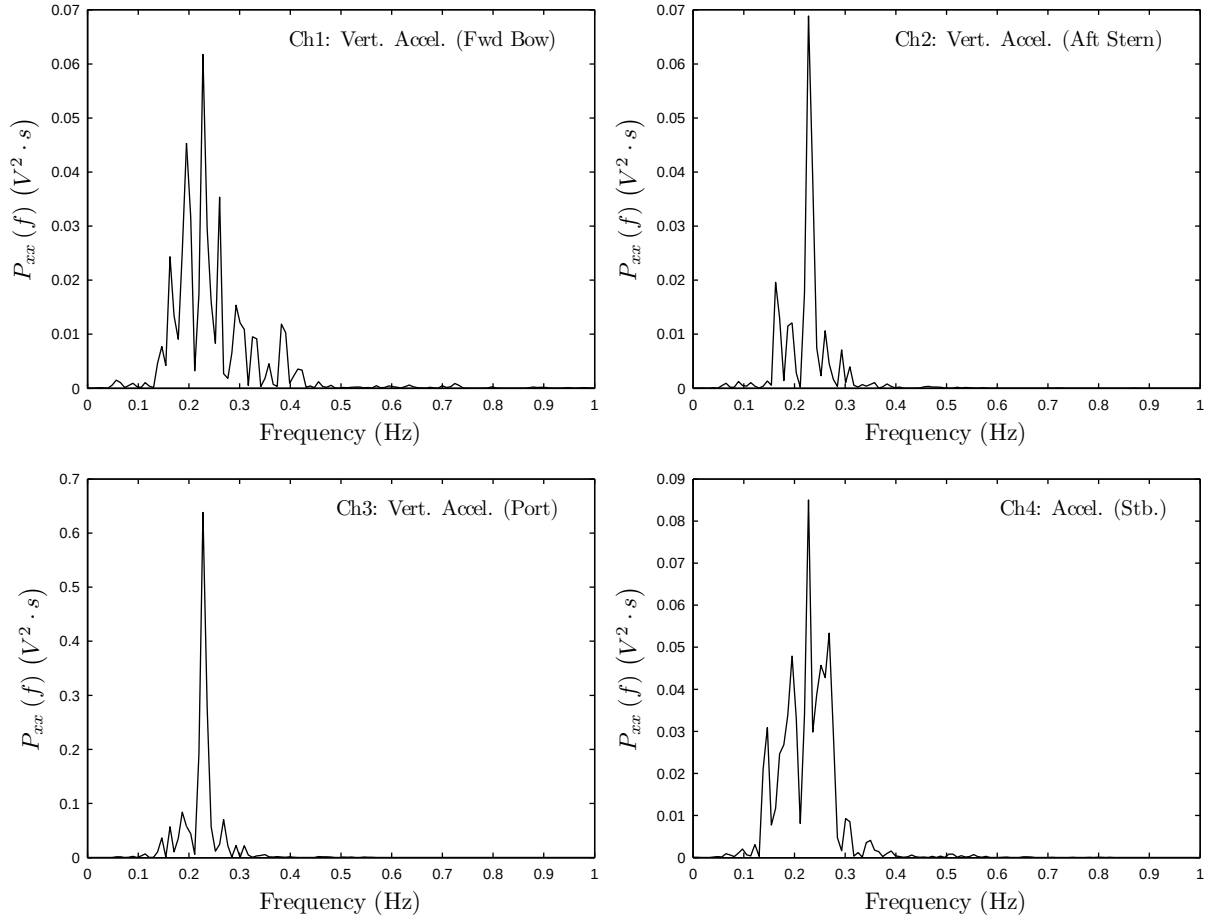

Figure N.3: Spectral analysis on accelerometer raw data during the delivery voyage of INCAT 112 m. Power spectral density (PSD), $P_{xx}(f)$ for acceleration measured at Ch1, Ch2 Ch3 and Ch4 on the vehiicle deck for Voyage record disc No.1, Data No.062. PSD was obtained by applying the Hamming window for data taper in the time domain, and smoothing by a convolution with 1 smoothing windows in the frequency domain.

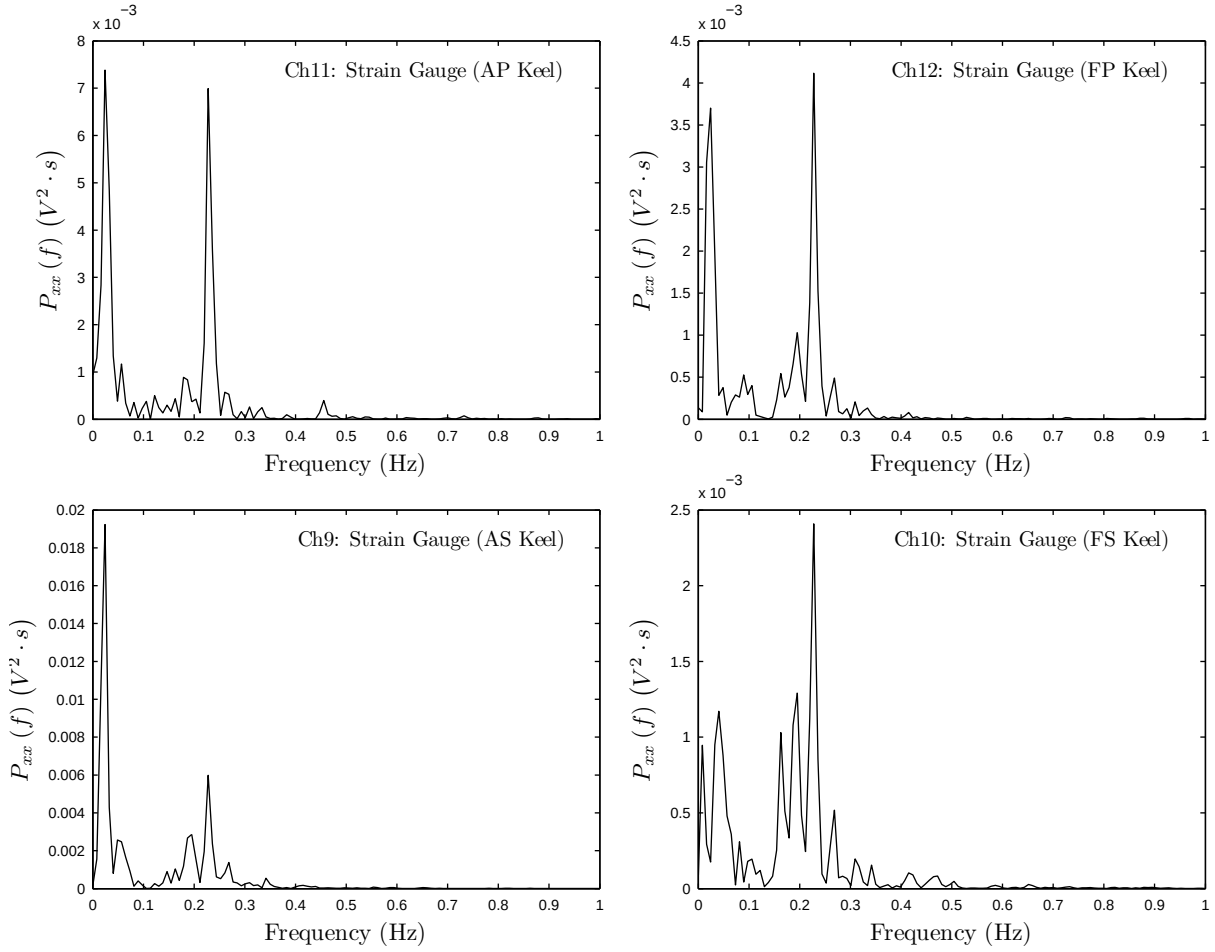

Figure N.4: Spectral analysis on raw data of strain gauges on the keel during the delivery voyage of INCAT 112 m. Power spectral density (PSD), $P_{xx}(f)$ for acceleration measured at Ch9, Ch10 Ch11 and Ch12 on the viechle deck for Voyage record disc No.1, Data No.062. PSD was obtained by applying the Hamming window for data taper in the time domain, and smoothing by a convolution with 1 smoothing windows in the frequency domain.

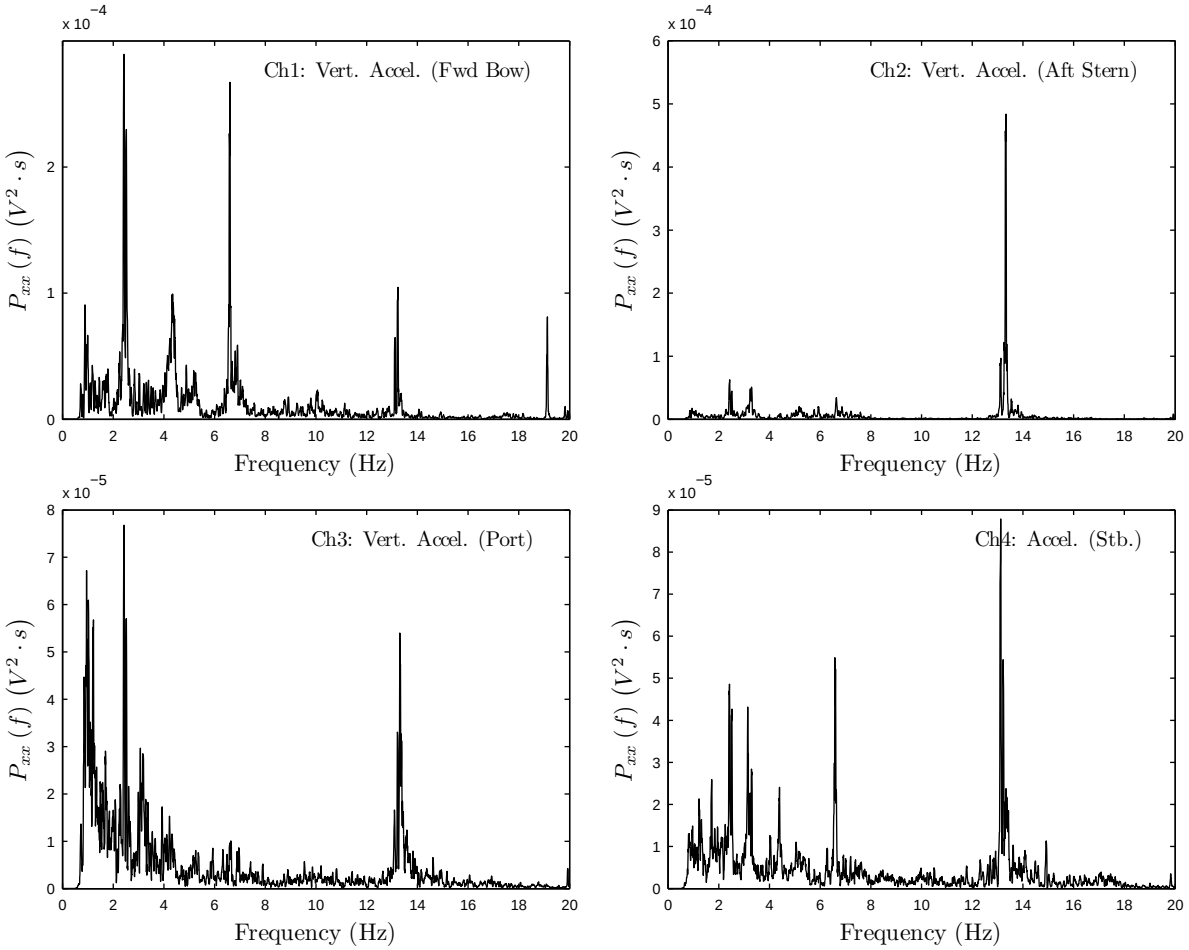

Figure N.5: Spectral analysis on accelerometer raw data during the delivery voyage of INCAT 112 m. Power spectral density (PSD), $P_{xx}(f)$ for acceleration measured at Ch1, Ch2 Ch3 and Ch4 on the viechle deck for Voyage record disc No.1, Data No.062. PSD was obtained by applying the Hamming window for data taper in the time domain, and smoothing by a convolution with 5 smoothing windows in the frequency domain.

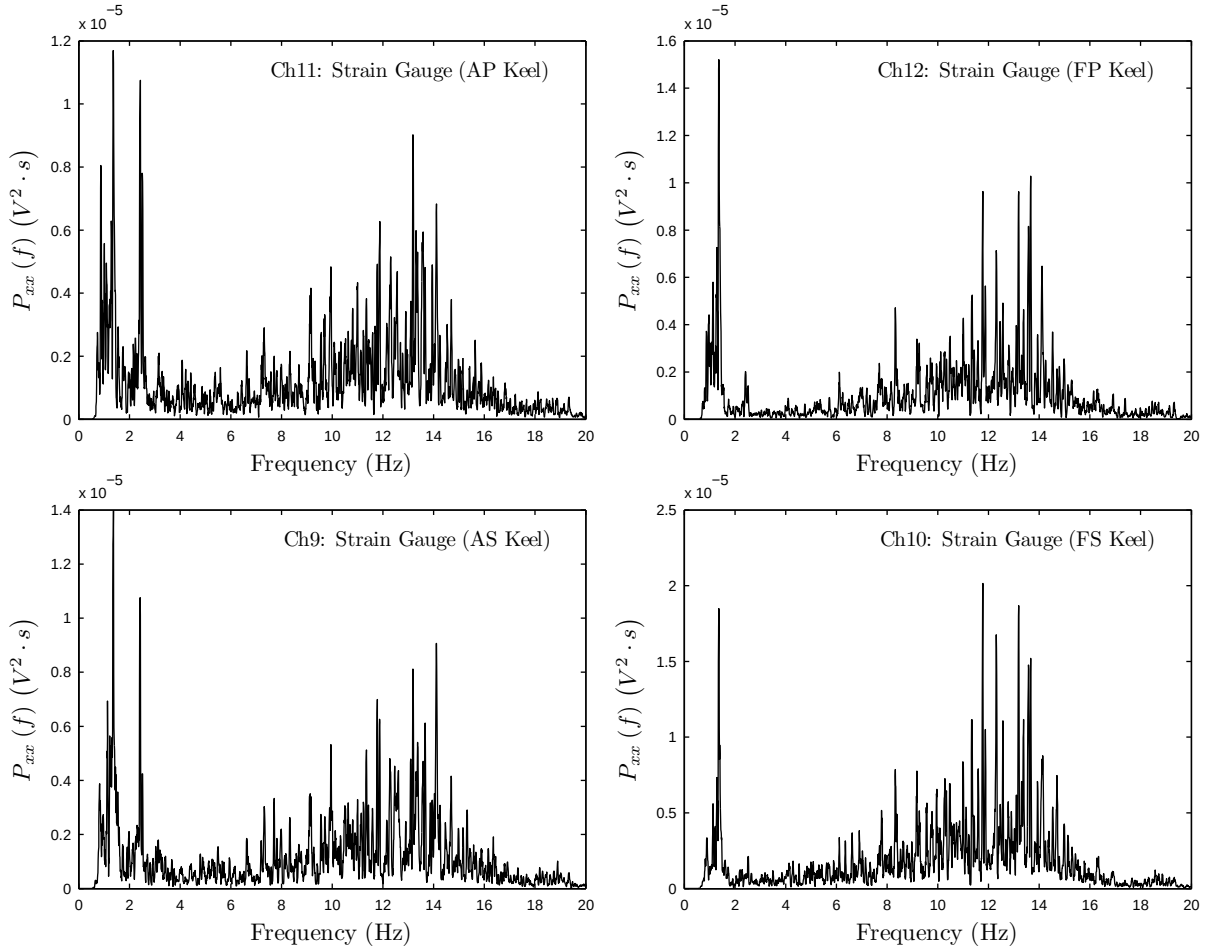

Figure N.6: Spectral analysis on raw data of strain gauges on the keel during the delivery voyage of INCAT 112 m. Power spectral density (PSD), $P_{xx}(f)$ for acceleration measured at Ch9, Ch10 Ch11 and Ch12 on the vehicle deck for Voyage record disc No.1, Data No.062. PSD was obtained by applying the Hamming window for data taper in the time domain, and smoothing by a convolution with 5 smoothing windows in the frequency domain.

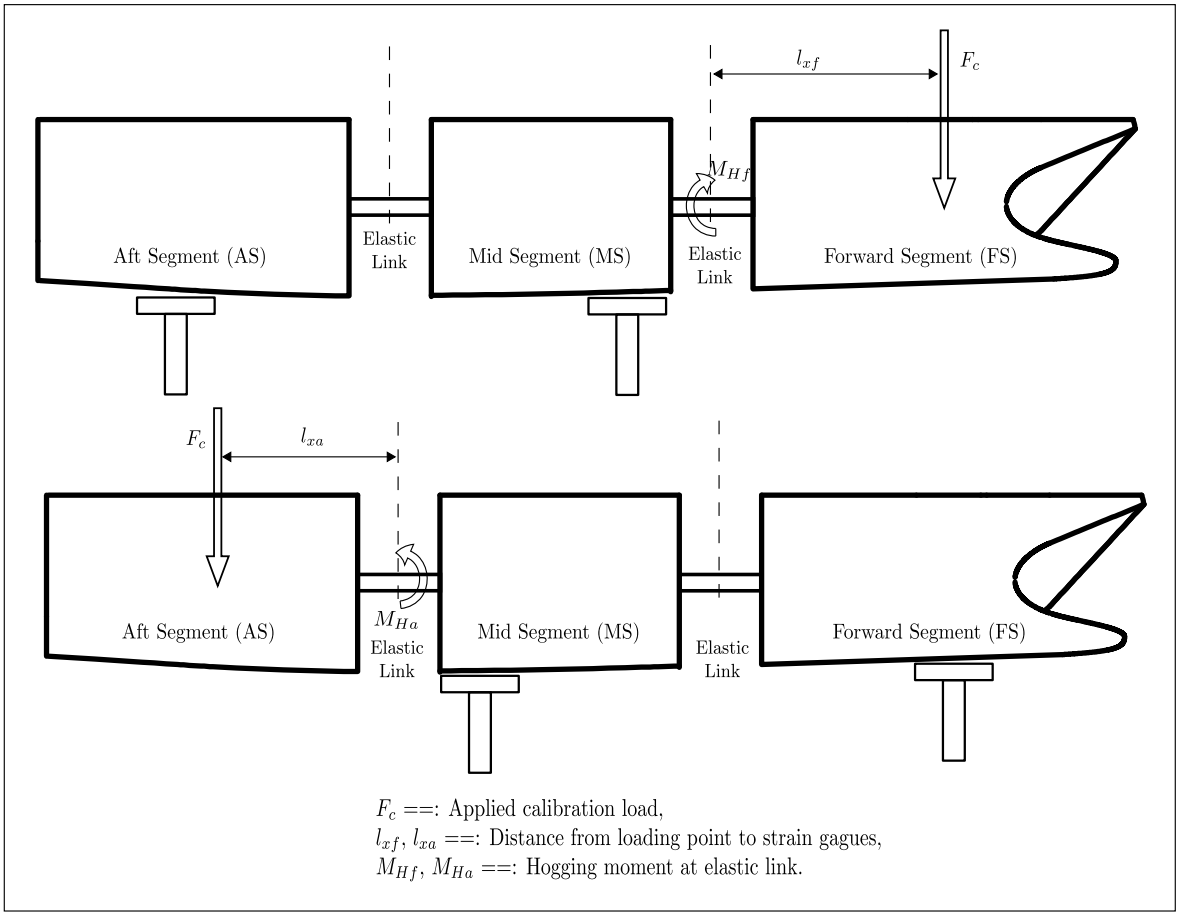

Figure 3.5: Calibration schematic diagram for the strain gauges on the elastic link on the demi-hull segment gap under hogging.

where the i is for ith channel of recorded data signals. The location of the elastic link and corresponding channel of the data signal are listed in Table 3.6. The calibration factors were obtained from the least-square method by fitting the linear regression line to the applied moment against the measured microstrain. Many sets of calibration were conducted to increase confidence in the calibration factors.

In order to obtain reliable calibration factors, several di erent types of jig were tested as follows:

1. Jig Type - 1: Direct loading cables and calibration weight boxes. Applying the calibration loads simultaneously on both demi-hulls.

2. Jig Type - 2: Even-distribution loading bar and rods. Applying the calibration loads simultaneously on both demi-hulls.

3. Jig Type - 3: Direct loading cable and calibration weight box. Applying the calibration loads on one side of the demi-hull only.

An advantage of Jig Type - 1 is that the calibration can proceed at any hook point on the model, however, the transverse alignment of applied load to the demi-hull centre-line is rather di cult, except for applying the calibration loads on the wave-piercer bow and transom stern

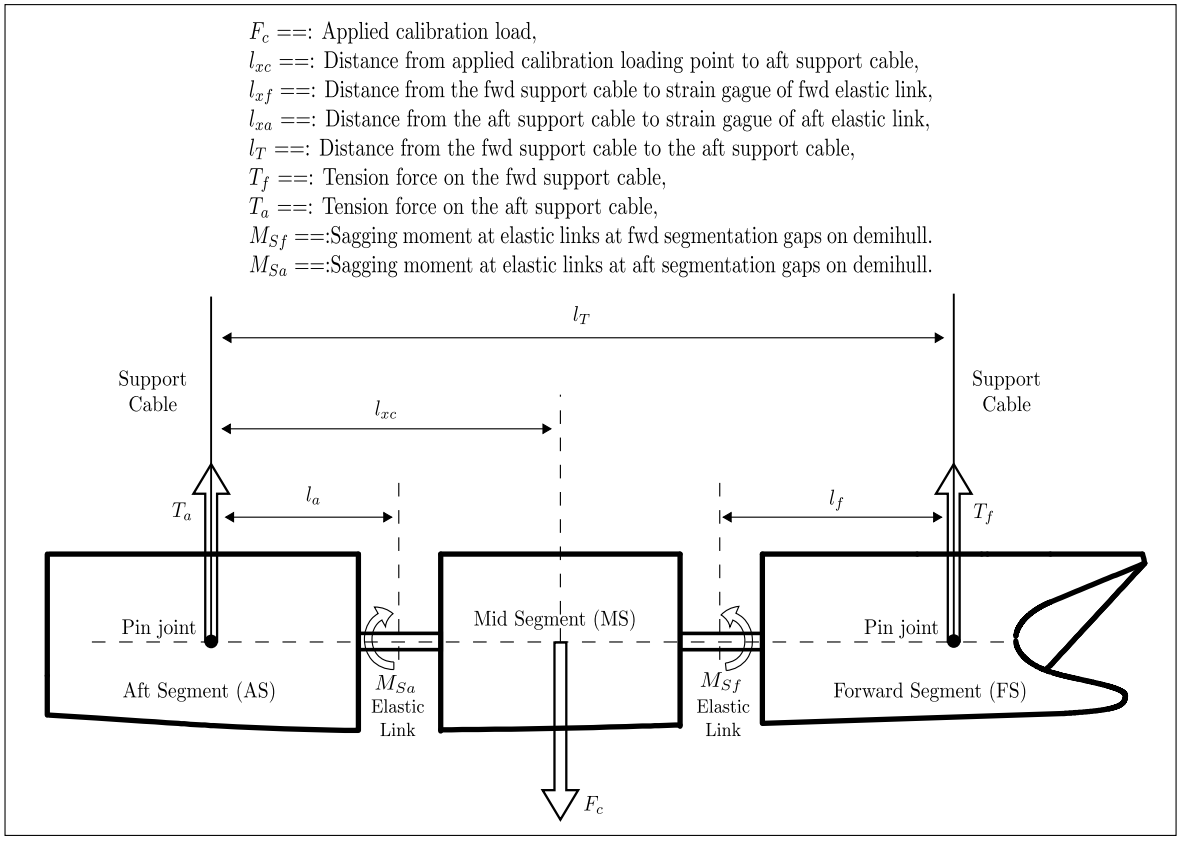

Figure 3.7: Calibration schematic diagram for strain gagues of elastic link on demihull segment gap under hogging

Next, calculating the moments at the elastic links are as follows:

$$M_{Sf} = T_f l_f \tag{3.11}$$

$$M_{Sa} = T_{fa} l_a \tag{3.12}$$

The strain of the elastic link can be obtained from the strain gauges of the elastic link, introducing the calibration factor to calculate the vertical bending moment. The following equation can be obtained for the forward and aft elastic links respectively:

$$M_{Sf} = C_{EL_{CH09}} \epsilon_{CH09} + C_{EL_{CH11}} \epsilon_{CH11} \tag{3.13}$$

$$M_{Sa} = C_{EL_{CH10}} \epsilon_{CH10} + C_{EL_{CH12}} \epsilon_{CH12} \tag{3.14}$$

Substituting Equations 3.7, 3.10, 3.13, and 3.14 into Equations 3.11 and 3.12, the following relationship can be obtained for calibration:

$$C_{EL_{CH09}} \epsilon_{CH09} + C_{EL_{CH11}} \epsilon_{CH11} = \frac{F_c l_{xc}}{l_T} l_a \tag{3.15}$$

$$C_{EL_{CH10}} \epsilon_{CH10} + C_{EL_{CH12}} \epsilon_{CH12} = \frac{F_c \left(l_T - l_{xc}\right)}{l_T} l_a \tag{3.16}$$

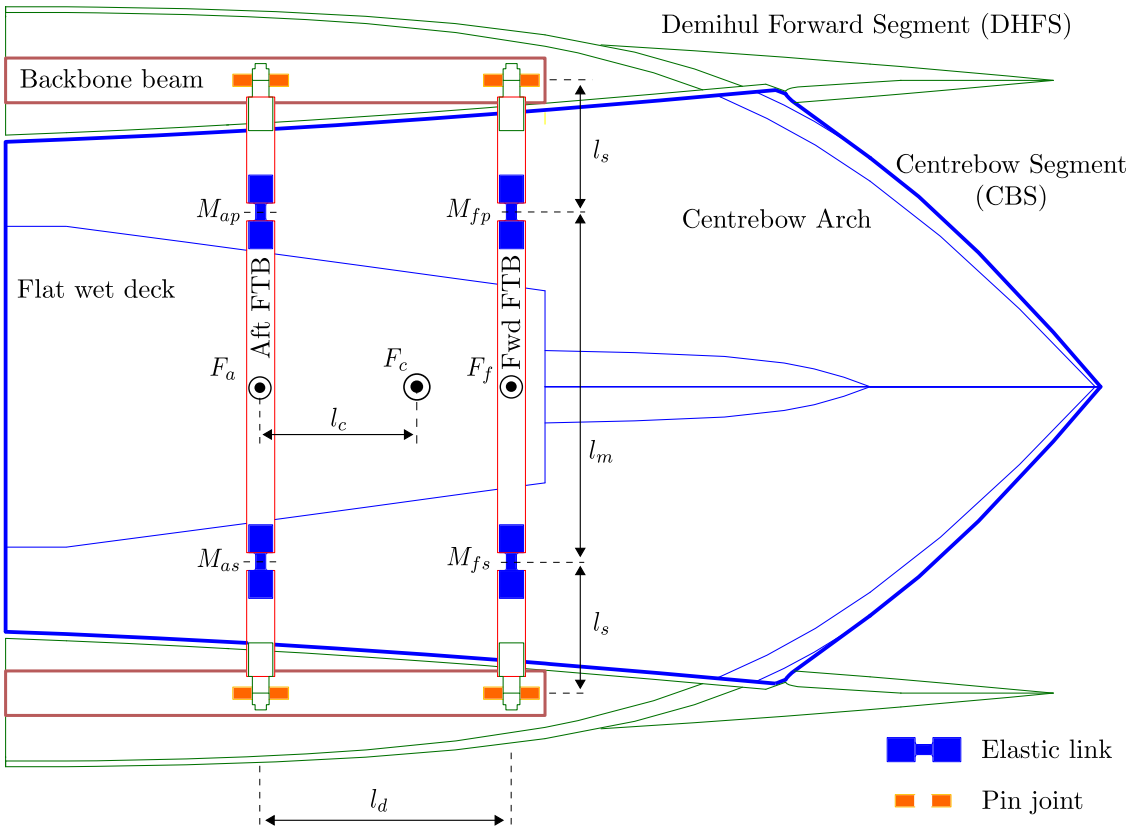

Figure 3.9: Calibration schematic diagram for strain gauges of elastic link on centrebow segmentation.

the demi-hull mid segments and demi-hull aft segments were supported by the workbench for the free condition on the centre bow segment and demi-hull forward segments, so that the centre bow segment and demi-hull forward segments were free to move. The centre bow mount was used for applying calibration loads, since the centre bow shape did not have a flat region.

The calibration and slamming force calculation equations were developed as follows, and the force diagram is presented in Figure 3.10.
The reaction force at the forward port pin joint can be expressed as:

$$R_{fp} = -\frac{M_{fp}}{l_s} \tag{3.17}$$

The vertical force equilibrium of the port forward FTB is:

$$R_{fp} = V_{fp} \tag{3.18}$$

Taking a moment equilibrium on the mid segment of the FTB about the starboard side elastic link is calculated as:

$$\frac{F_f l_m}{2} + V_{fp} l_m + M_{fs} - M_{fp} = 0 \tag{3.19}$$

Substituting Equations 3.17 and 3.18 into Equation 3.19, and simplifying the equation, the force on the forward FTB can be calculated as follows:

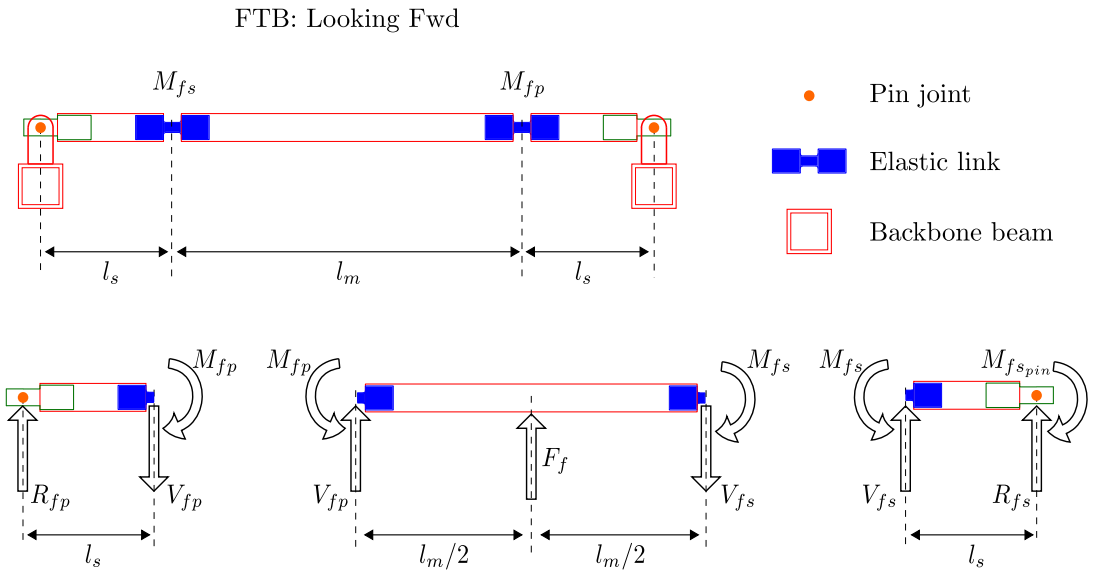

Figure 3.10: Forces diagram for loads acting on the forward FTBs on the centrebow for centrebow mount calibration. The subscript $_f$ is replaced with $_a$ for the aft FTB.

$$F_f = \frac{2M_{fp}}{l_s} + \frac{2\left(M_{fp} - M_{fs}\right)}{l_m} \tag{3.20}$$

Similarly, the force acting on the aft FTB can be calculated as:

$$F_a = \frac{2M_{ap}}{l_s} + \frac{2\left(M_{ap} - M_{as}\right)}{l_m} \tag{3.21}$$

The moment at the elastic link can be calculated with individual calibration factors:

$$M_{fp} = C_{EL_{CH13}} \epsilon_{CH13} \tag{3.22}$$

$$M_{ap} = C_{EL_{CH14}} \epsilon_{CH14} \tag{3.23}$$

$$M_{fs} = C_{EL_{CH15}} \epsilon_{CH15} \tag{3.24}$$

$$M_{as} = C_{EL_{CH16}} \epsilon_{CH16} \tag{3.25}$$

Finally, the total force on the centre bow can be calculated as:

$$F_c = F_f + F_a \tag{3.26}$$

Once the total force is calculated, then the force acting position of the total force can be calculated as:

$$l_c = \frac{F_f l_d}{F_c} \tag{3.27}$$